** From April 1, 1997, **High Energy Accelerator Research Organization (KEK)** was newly established. The new organization is restructured of three reseach institutes, National Laboratory for High Energy Physics (KEK), Institues of Nuclear Study (INS), Univ. of Tokyo and Meson Science Laboratory, Faculty of Science, Univ. of Tokyo.*

KEK Reports are available from:

Information Resources Division
High Energy Accelerator Research Organization (KEK)
1-1 Oho, Tsukuba-shi
Ibaraki-ken, 305
JAPAN

Phone: 0298-64-5137
Fax: 0298-64-4604
Cable: KEK OHO
E-mail: Library@kekvax.kek.jp (Internet Address)
Internet: http://www.kek.jp

Table of Contents

JLC Design Study Group

N. Akasaka, M. Akemoto, S. Anami, Y. Chin, S. Fukuda, Y. Fujii, J. Fujimoto, Y. Funahashi, Y. Hashimoto, H. Hayano, Y. Higashi, T. Higo, S. Kamada, S. Kato, S. Kawabata, M. Kikuchi, S. Koike, S. Koizumi, T. Korhonen, K. Kubo, Y. Kurihara, S. Kuroda, T. Matsui, H. Matsumoto, S. Matsumoto, S. Michizono, A. Miyamoto, H. Mizuno, M. Muto, T. Naito, H. Nakayama, Y. Namito, J. Odagiri, K. Oide, T. Omori, Y. Otake[1], Y. Saito, S. Sakanaka, T. Shintake, Toshikazu Suzuki, K. Takata, T. Takatomi, Seishi Takeda, Shigeru Takeda, M. Tejima, E. Takasaki, Yasunori Takeuchi, S. Tokumoto, N. Toomi, K. Tsukamoto, T. Tauchi, M. Tawada, N. Terunuma, N. Toge[2], J. Urakawa, M. Yamamoto[3], N. Yamamoto, Y. Yamazaki, K. Yokoya, M. Yoshioka; *High Energy Accelerator Research Organization (KEK), Tsukuba, Ibaraki, Japan*

I. Watanabe; *Akita Keizaihoka University Junior College, Akita, Japan*

S. Kashiwagi; *School of Mathematical and Physical Science, Graduate University for Advanced Studies, Hayama, Japan*

I. Endo, K. Matsukado, T. Ohgaki, T. Takahashi; *Department of Physics, Faculty of Science, Hiroshima University, Hiroshima, Japan*

T .Watanabe; *Kogakuin University, Tokyo, Japan*

N. Sasao; *Department of Physics, Faculty of Science, Kyoto University, Kyoto, Japan*

T. Nakanishi, S. Okumi, C. Takahashi, K. Togawa, C. Suzuki; *Department of Physics, Faculty of Science, Nagoya University, Nagoya, Japan*

[1]Now at Earthquake Research Institute, University of Tokyo
[2]Editor in chief
[3]Now at IHI, Co. Ltd.

H. Horinaka, K. Wada; *Department of Physics and Electronics, College of Engineering, Osaka Prefecture University, Sakai, Japan*

T. Kon; *Institute of Physics, Faculty of Engineering, Seikei University, Tokyo, Japan*

T. Takeshita, N. Matsuda; *Department of Physics, Faculty of Science, Shinshu University, Nagono, Japan*

F. Hinode, T. Nakazato, M. Oyamada; *Laboratory of Nuclear Science, Tohoku University, Sendai, Japan*

M. Higuchi; *Department of Applied Physics, Faculty of Technology, Tohoku-Gakuin University, Tagajo, Japan*

F. Tamura; *Department of Physics, Faculty of Science, University of Tokyo, Tokyo, Japan*

T. Hirose, T. Okugi; *Department of Physics, Tokyo Metropolitan University, Tokyo, Japan*

Preface

A research program in high energy physics at electron-positron collisions aiming at TeV energy region physics was first recommended by the Japanese High Energy Physics Committee in 1986, as a long-term project in the post-TRISTAN era. In Japan this recommendation initiated a systematic accelerator R&D program centered at High Energy Accelerator Research Organization (KEK).[1] The accelerator R&D work by KEK, in collaboration with a number of universities and laboratories in and outside Japan, has produced a series of encouraging results during the past ten years.

In the meanwhile, recent high-precision measurements of masses of Z^0 and $W^{\pm}$ particles have come to strongly suggest the Grand Unified Theory of the Strong, Weak and Electromagnetic interactions based on Supersymmetry (SUSY GUT). SUSY GUT predicts that the mass of the Higgs boson that is responsible for the electroweak symmetry breaking should be below 150 GeV. In addition, SUSY GUT postulates the existence of supermultiplets, and thus the existence of superpartner particles for all known elementary particles, leading to a great possibility of a new and rich class of particle spectroscopy to be studied in the O(TeV) energy region.

With notions on future directions of high energy physics research, including the serious likelihood of the validity of SUSY GUT or other scenarios, a consensus has by now widely grown in the world high energy physics community that complementary experiments at pp and e^+e^- collisions which explore the sub-TeV to TeV energy range would provide a solid and balanced strategy for reaching the new frontier in the field of high energy physics research. As for pp experiments, the construction of the LHC in Europe has already been authorized. Thus, an early construction of a corresponding e^+e^- collider is a remaining world-wide issue.

In Japan, the research programs at TRISTAN ($E_{CM} \simeq 60$ GeV electron-positron collider) were

[1] On 1st of April, 1997, KEK, formerly known as "National Laboratory for High Energy Physics" is newly established as "High Energy Accelerator Research Organization" by a cabinet decree.

concluded in 1995. Currently, the construction of a high-luminosity asymmetric B-factory, called KEKB, which reuses the accelerator tunnel and other infrastructure inherited from TRISTAN, is vigorously proceeding. It aims to start initial runs in late 1998. Thus, the successful completion and operation of KEKB is the immediate highest priority task for the Accelerator Laboratory of KEK at this moment. However, efforts for a realistic design of a 500 GeV - 1 TeV scale electron-positron LC is another clearly identified task that has strong support by the entire high energy physics community in Japan towards the early 21st century.

This report, "JLC Design Study," was prepared in this context. The Design Study presents a collection of survey work that has been conducted towards the design and construction of an electron-positron linear collider (LC), which will allow immediate studies of 250 to 500 GeV energy region, and is energy-extendable to the 1 TeV region, by the JLC Group in Japan. It aims to serve as a reference document that summarizes the results of the past accelerator R&D efforts and that presents a fundamental conceptual design of a realistic LC in a coherent single-volume form. Attempts are made to present major technical and theoretical milestones that have been achieved so far, and to identify the remaining key issues that will have to be addressed in the near future. It is expected that this Design Study will become a basis for more advanced conceptual and engineering LC design work in the next several years.

Acknowledgments

Research and development of linear colliders, since its early stage, has been a substantially international activity. As such, a large number of ideas and schemes presented in this design study have been developed through scientific interactions of the members of this study group with scientists and engineers from institutes outside Japan, in addition to collaborative work with colleagues in Japan. They include: SLAC in U.S., DESY in Germany, CERN in Europe, BINP-Protvino and BINP-Novosibirsk in Russia, PAL in Korea, IHEP and Tsing-Hua University in China. Attempts are made to attribute proper credits in the reference section of each chapter to those who contributed important ideas to the development of JLC, irrespective of countries or organizations. However, due to an extensive amount of the work, it is not necessarily possible to always accurately identify the true original sources of the ideas or schemes. The JLC design study group expresses gratitude to their contributions, and apologies, in advance, for possible omissions.

The JLC design study group would like to thank the directorate of High Energy Accelerator Research Organization (KEK), Prof. H. Sugawara, Prof. Y. Kimura, Prof. S. Iwata and Prof. M. Kihara, for continuous encouragement throughout this work. We are also thankful to the morale support which was extended by the community of high energy physics researchers in Japan, spear-headed by the Japanese High Energy Physics Committee.

This work was financially supported in part by: Grant-in-Aid for Scientific Research, Grant-in-Aid for International Scientific Research, Foundation for High Energy Accelerator Science (FAS), the Japan Society for the Promotion of Science, Tsukuba EXPO'85 Memorial Foundation "Bannpaku-Zaidan", and US.-Japan Collaboration Program in High Energy Physics Research.

Also, part of the work was supported by "Joint Research with the Private Sector", the program under Ministry of Education, Science, Culture and Sports with the following organizations:

Hitachi Corporation on the C-band structure, Hitachi Shipbuilding Corporation on R&D for the damping ring vacuum chamber, Mitsubishi Electric Corporation on simulation of 300 MW power line system and stabilization of linac system, Mitsubishi Heavy Industry on the S-band and X-band accelerating structures, Nichicon Corporation on the modulator capacitor, Nihon Chemicon Corporation on the modulator capacitor, Nihon Koshuha Corporation on the C-band modulator, NKK Corporation on the positron target design, Sumitomo Heavy Industry Ltd. on R&D for the damping ring DC septum magnets, Toshiba Corporation on the development of high-power klystrons, Shimizu Corporation, Kumagai Gumi Co. Ltd. and Takenaka Corporation on the tunnel facilities. Their support is greatly appreciated.

CHAPTER 1

Introduction

Contents

1.1 Project History, Background and Goal

R&D on e^+e^- linear colliders (LC) in Japan started officially in 1986, in response to a recommendation by the Japanese High Energy Physics Committee. Until that time, several possible options were being considered for the main acceleration mechanism of a linear collider. However, after some discussions it was decided to select the conventional rf linac approach using beam pulses with multiple bunches. The desired center-of-mass energy was to start with 500 GeV and eventually to reach $\simeq$ 1.5 TeV; also, an rf system at 11.4 GHz (X-band) was chosen for the main linacs to achieve this goal [1].

Starting in 1992, as the Japanese physics community became increasingly interested in lower center-of-mass energies (E_{CM}), two alternate lower rf frequencies for the main linacs, namely 2.9 GHz (S-band) and 5.7 GHz (C-band), were also chosen for consideration. They are reported in [2]. Some parameter surveys were conducted, and pilot design studies were made.

However, the bulk of the hardware development for the main linacs has remained focused on X-band technology. This has in part been due to the limited resources, and due to the strong desire to obtain good perspectives of the required technology by consistently pursuing an initially chosen scheme. This work has been continuing up to now in parallel with the construction of the Accelerator Test Facility (ATF) at KEK, which is an accelerator complex that includes a multi-bunch-capable gun and a buncher, followed by a 1.54 GeV S-band linac and an ultra-low emittance damping ring prototype. Formal hardware R&D of the C-band scheme started later in 1996 as the development of a realistic back-up technology for the main linacs. While the operational experiences of multi-bunch acceleration are being accumulated at the S-band ATF linac, more advanced studies on the S-band linac technology for JLC are currently limited to its application in the injectors, bunch compressors and pre-linacs.

Many discussions have taken place in the Japanese high energy physics community during the past few years on the energy range to be targeted by the LC. The present "Action Plan" [3] by the Japanese High Energy Physics Committee requests to aim at an E_{CM} range of 250 - 500 GeV as the first phase of the project for the discovery of a light Higgs boson and studies of the top quark; eventually an effort will be made to reach the TeV energy region as the second phase for studies of particles predicted by SUSY GUT or other phenomena.

Equally important is the time-scale of the project. Driven by the desire to conduct high energy physics experiments at JLC within the time frame concurrent with that of LHC, the "Action Plan" calls for starting construction of LC in the year 2001[3]. To be compatible with this schedule, the "Action Plan" asks to complete a basic design of the LC by early 1997. One of the main purposes of this JLC Design Study is to respond to this specific request.

The "Action Plan" also points out the need for the construction of the LC by an international organization. It is naturally anticipated that the real engineering design of the LC be carried out in some form of an international collaboration, and various technological ideas and schemes will be brought in from laboratories outside of Japan. As such, the JLC Design Study group feels that it is essential to

document the present design scheme conceived by this group in a coherent reference form, so that more specific discussions on the design details with future collaborators can be conducted in an intelligent and productive way.

To reiterate, the salient points that are binding in this Design Study report are summarized as follows:

1. The project goal of the LC accelerator construction is to provide the best research facility for conducting experimental research in high energy physics at e^+e^- collisions at initial E_{CM} of around 250 - 500 GeV in phase-one, and eventually at around 1 TeV in phase-two.

2. The phase-one accelerator construction is desired to be started in '2001. Consequently, the technology choices to be adopted in the LC design need to be sufficiently realistic, reliable and affordable within this time frame. Specifically, for the main linac design we consider the X-band technology with realistic peak rf power specifications to be the main scheme, and will focus on it.

3. The transition from the phase-one to phase-two should be adiabatic. This is so that an accelerator complex with a reasonably long life-span can be proposed in a persuasive way, without compromising the time-scale goal for the initial phase-one operation.

4. Due to the amount of remaining technological issues to address, and due to the ambiguities of their outcome, presenting a total project cost estimate is not yet possible, nor adequate, at this moment. Therefore, it will not be done in this Design Study Report. Rather, this report focuses on presenting the design scheme of the LC that is currently conceived by the JLC Design Group, while showing major research milestones that have been achieved so far, and identifying the issues and tasks that need to be attacked in the near future. The goal here is to present a concrete basis for more advanced design work to be carried out in the next several years.

5. We treat the C-band main linac design as a back-up scheme, and, thus, give some serious thoughts to this possibility. The whole system designs of the X-band and C-band JLC are mostly similar, except, of course, for the main linacs. Another important difference between the X-band and C-band JLC system designs lies in the bunch compressors and pre-linacs. This is due to the fact that the required bunch length in the X-band main linacs is 90 μm, while that in the C-band main linacs is 200 μm. However, due to the limitation of time and manpower resources, in this report, no study results on C-band-specific designs of the bunch compressor and pre-linac systems are given.

Some discussions exist concerning the project name "JLC" which originally meant "Japan Linear Collider." It has been pointed out that if the project is to be carried out within the framework of an international collaboration, it would be worthwhile reconsidering the use of a country-specific word, "Japan," even while our primary goal is to have this machine built in Japan and the continued efforts would be made towards that. The accelerator study group responsible for this Design Study considers that it is the task of the Japanese high energy physics community and the leadership of KEK to examine the situation and to make a revision of the project name if and when doing so is found to

— Fundamental Parameters —			
Main accelerating frequency	f_{rf}	11.424	GHz
Number of particles per bunch	N	0.70×10^{10}	
Number of bunches per pulse	m_b	85	
Bunch spacing	t_b	1.40	nsec
Repetition frequency	f_{rep}	150	Hz
Normalized emittance at damping ring exit	$\gamma\varepsilon_x/\gamma\varepsilon_y$	$3\times10^{-6}/3\times10^{-8}$	m·rad
R.m.s. bunch length	σ_z	90	μm
— Main Linac —			
Nominal accelerating gradient	G_0	73.0	MV/m
Effective accelerating gradient	G_{eff}	55.6	MV/m
Injection energy	E_{inj}	10	GeV
Klystron peak power		67	MW
Required klystron output pulse length		750	nsec
Assumed efficiency from AC to structure input		28	%
Peak power into a structure		130	MW
Structure length		1.31	m
Single-bunch full energy spread after off-crest correction		0.30	%

Table 1.1: *A shortened table of parameters for the X-band JLC which are independent of the beam energy. For a more detailed table, see Table 2.1 in Chapter 2 (next chapter).*

be appropriate. For now, throughout this Design Study the word "JLC" is meant to be the code-name for the electron-positron linear collider design that is conceived by this study group. When the next-generation electron-positron linear collider designs need to be collectively named, a generic term, "LC," will be used.

1.2 Outline of the JLC Design

Figure 1.1 shows a schematic layout diagram of JLC. Table 1.1 and 1.2 give a shortened version of parameter set that are relevant to the X-band JLC. A full parameter set will appear as Tables 2.1 in Chapter 2.

As shown in Figure 1.1 the electron beam is to be created by either a thermionic gun, and rf gun or a laser-driven photocathode gun which can produce polarized electrons. The positron beam is to be produced from a 10 GeV electron beam that is accelerated by an S-band linac and that impinges on a target. Both electron and positron beams are supposed to consist of multi-bunch trains for maximizing the luminosity for a finite power efficiency in linac operation. The electron beam is injected directly into a damping ring, whereas the positron beam, having a larger emittance, must first be "cooled

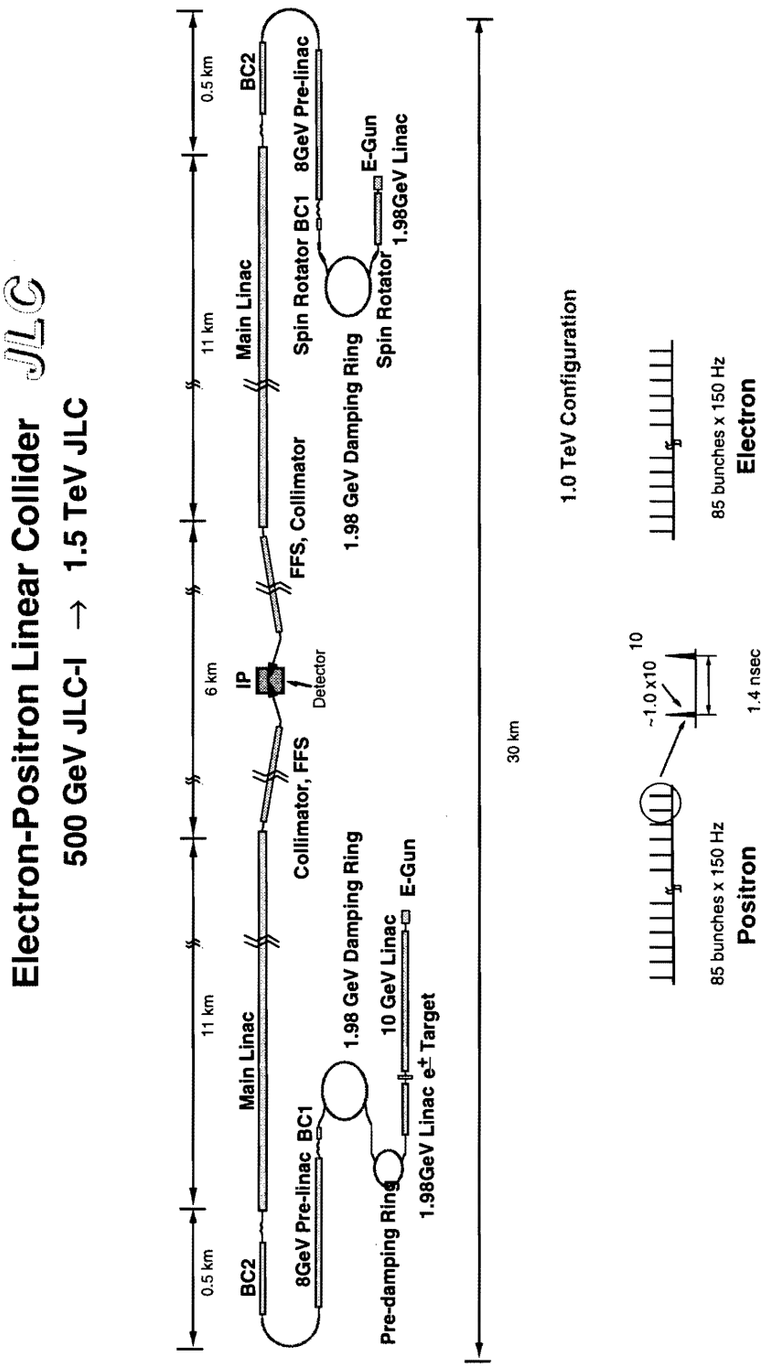

Figure 1.1: *Schematic layout of JLC.*

Center-of-mass energy	E_{CM}	250	500	1000	GeV
Active length of each main linac	L_{acc}	2.07	4.33	8.81	km
Number of klystrons per beam		1052	2200	4482	
Number of structures per beam		1578	3300	6726	
Wall-plug power for two linacs		55	115	234	MW
Number of particles per bunch	N	0.7	0.7	0.7	$\times 10^{10}$
Assumed normalized emittance	$\gamma\varepsilon_x^*$	3.3×10^{-6}	—	—	m·rad
	$\gamma\varepsilon_y^*$	4.8×10^{-8}	—	—	m·rad
Beta function at IP	β_x^*	10	—	—	mm
	β_y^*	0.10	—	—	mm
R.m.s. beam size	σ_x^*	367	260	184	nm
	σ_y^*	4.43	3.14	2.28	nm
Crossing angle (full angle)	ϕ_{cross}	8.0	—	—	mrad
Disruption parameter	D_x	0.106	—	—	
	D_y	8.81	8.79	8.57	
Average energy loss by beamstrahlung	δ_{BS}	[1.54]	[4.40]	[9.90]	%
Average number of photons per electron	n_γ	[0.83]	[1.12]	[1.43]	
Maximum Upsilon parameter	Υ_{max}	[0.119]	[0.336]	[0.950]	
Geometric luminosity reduction factor	H_{geo}	[0.855]	[0.855]	[0.855]	
Pinch enhancement factor	H_D	[1.581]	[1.585]	[1.599]	
Luminosity	$\mathcal{L}$	[4.13]	[8.28]	[16.72]	$10^{33}/\mathrm{cm}^2/\mathrm{s}$

Table 1.2: *A shortened table of parameters for the X-band JLC which are dependent on the beam energy. The numbers in brackets [ ] mean that the values are quoted in the case where crab-crossing is used at the interaction point. For a more detailed table, see Table 2.1 in Chapter 2 (next chapter).*

down" to an invariant emittance of $\gamma\epsilon_x \simeq 10^{-4}$ m in a pre-damping ring.

The beam energy of the damping rings has been chosen to be 1.98 GeV and the equilibrium emittances are, respectively, $\gamma\epsilon_x = 3 \times 10^{-6}$ and $\gamma\epsilon_y = 3 \times 10^{-8}$ m. The damping is provided mainly by a long wiggler section and the small emittance by arcs with a FOBO lattice.

The $\sim$ 5 mm-long bunch from the damping ring is compressed to 90μm by a two-stage bunch compressor consisting of rf sections, chicane sections and an arc. The first stage bunch compression takes place immediately downstream of the damping ring at 1.98 GeV. Adequate spin manipulation sections are incorporated to support physics runs with polarized electrons. The 8 GeV pre-accelerator linac is based on S-band technology. The second-stage bunch compression takes place at the energy of 10 GeV. The energy spread at the exit of the entire bunch compression section is approximately 1.3 %.

To make the total length of the facility reasonably short, the unloaded gradient in the main linac is set to be high in as much as realistic rf technology is considered to allow: 40 MV/m for C-band and 73 MV/m for X-band. The beam-loading is approximately 25 % . Constant-gradient structures will be

adopted for the C-band and detuned structure for the X-band. Pulse compression will be achieved by one of, or a combination of, three alternate schemes, namely two-port SLED, SLED with disk-loaded energy storage cavities (SLED-III) and DLDS. The transient beam-loading will be compensated by structures using frequency-shifted cavities, stagger-timed triggering klystrons, or by modulating the rf phases of a pair of klystrons whose power is combined to drive a set of accelerating structures.

The current JLC design with the X-band main linacs has adopted the same accelerating gradient (after subtracting the beam-loading effects, $G_{eff} = 55.6$ MV/m), independent of the target center-of-mass energy. This means that the organization of individual power units will not undergo any major conceptual changes as energy-upgrades from $E_{\rm CM} = 250$ GeV up to 1 TeV are performed. There, the length of the linacs is simply extended in proportion to the target energy, introducing additional power sources, power distribution systems, accelerating structures and associated linac beam-line components.

The scheme of the currently considered high-power klystrons and high-precision accelerating structures is such that, if they come to sufficiently mature in the next several years, they are quite adequate for building a linear collider which can eventually reach $E_{\rm CM} \sim 1$ TeV within a reasonable site length below 30 km. If a land of this size is, indeed, available as the site of JLC, in the initial stage of operation with $E_{\rm CM} = 250 \sim 500$ GeV, the simplest solution would be to use a bypass beam line along the main linac tunnel to deliver the relatively low-energy beams to the interaction region, while the linac extension work is in progress during the machine down time. While this type of details on the construction scenario need to be carefully examined in the near future, a more immediate task is to investigate the technical feasibility of the fundamentals of the X-band linac hardware organization in conjunction with the related beam-dynamics issues; and that is the focus of this design study.

The beam delivery system consists of so-called "big bends," collimators and the final focus system. The first two are inserted in order to reduce beam-induced background at the experiments. The "big bends" also make it possible to have two collision points, one of which may be used for collisions other than e^+e^-, such as γ-e and γ-γ. The final focus system is based on a two-family non-interleaved sextupole scheme and is designed to give a final spot size ($\sigma_x^* \times \sigma_y^*$) as small as 260 nm $\times$ 3 nm in operation with $E_{\rm CM} = 500$ GeV.

More detailed parameters are tabulated in Table 2.1 and 2.2 of Chapter 2 (next chapter).

1.3 Organization of the Design Study Report

The organization of this design study report is as follows.

After this introduction (Chapter 1), Chapter 2 summarizes the basic machine parameters in the JLC designs for cases where the main linacs are based on RF technologies of X-band and the C-band frequencies. Rationale for the choice of various parameters, such as the bunch length, emittance,

beta-function values at the interaction point and others, is given.

Chapter 3 presents the design of multi-bunch-capable electron sources (both unpolarized and polarized electrons). It covers the region that starts with the electron gun, going through the bunchers, and injector linacs up to the entrance of the damping rings.

Chapter 4 treats the design issues of the positron source. After a brief discussion on the 10 GeV linac that accelerates electrons to impinge on the positron production target, a conceptual design of the positron production system is presented. It is followed by a discussion on the 1.98 GeV positron linac and a positron pre-damping ring which damps the positron emittance to the level that is acceptable for the positron main damping ring.

Chapter 5 discusses the design of 1.98 GeV damping rings. Advanced design ideas are given based on experience being accumulated from operation of the ATF (Accelerator Test Facility) 1.54 GeV damping ring prototype at KEK.

Chapter 6 is for the bunch compressor systems and the pre-linac of JLC when its main linacs are built based on X-band technologies. The bunch compression is done in two steps; the first step (BC1) at 1.98 GeV using L- or S-band cavities, and the second step (BC2) at 10 GeV using an S-band linac. An 8-GeV S-band linac, called pre-linac, and an arc section are inserted between BC1 and BC2 to bring the beam energy up to 10 GeV and to apply a suitable phase-space rotation in the longitudinal bunch phase space. A design of the spin-manipulation system to be incorporated near the injection and extraction points of the electron damping ring is also presented.

Chapter 7 through Chapter 11 are dedicated to discussion on the X-band main linacs. Chapter 7 presents the overall scheme in the X-band linac system design and summarizes the relevant system design parameters. Chapter 8 discusses issues related to the beam dynamics in the main linacs, followed by evaluation of required tolerances on structure fabrication, hardware alignment and operational conditions. Chapter 9 gives a detailed view on the design and development of the "Detuned Structure" as the accelerating structure for use in the main linacs. Chapter 10 presents the design and development status of the power-source system, including the modulators, klystrons and the power-distribution scheme. Chapter 11 presents some discussions on the main linac support systems.

Chapter 12 presents the status of development of the design and hardware for the main linacs based on the C-band RF technologies, whose work was formally initiated in 1996.

Chapter 13 discusses the design of the so-called "Beam Delivery," which includes the beam collimation sections and the final-focus system.

Chapter 14 treats the issues related to the interaction region and the detector interface. It evaluates the beam-induced background, produced through various mechanisms, to the experimental facility. It also presents an idea on the beam-profile measurement technique near the collision point, which takes advantages of low-energy electron-positron pairs that are abundantly produced in the beam-beam collision. Finally, this chapter discusses the issue of "luminosity spectrum" (differential luminosity with respect to the center-of-mass energy).

The use of the second interaction region for studies of γ-γ collision physics is discussed in Chapter 15. Significant progress has been made during the recent years on understanding of the beam-beam interaction issues, including laser-electron interaction and such properties as luminosity distribution and beam background.

Chapter 16 consolidates the development status of beam diagnostic and instrumentation for various portions of linear colliders.

The issues related to the tunnel facility for JLC are discussed in Chapter 17. Several tunnel excavating techniques are examined.

Finally, Chapter 18 attempts to present the remaining tasks in the areas of R&D and design improvement of JLC, which are required to be performed in the immediate future.

References for Chapter 1

[1] International Linear Collider Technical Review Committee Report 1995, G.A. Loew and T. Weiland, ed., 1995.

[2] JLC-I, KEK Report 92-16, December, 1992.

[3] HEP Committee of Japan's Action Plan (May, 1996) in its entirety is reproduced here (Original text is in Japanese. Quoted here is an official translation by S.Kurokawa, approved by Chairperson Y.Nagashima):

1. We aim at the total center of mass energy range of 250-500 GeV as the first phase of the project and eventually try to reach the TeV energy region as the second phase.
2. The LC should be built in the Asian-Pacific region. The institution to carry out the LC project should be an international organization and its facilities should be open to the international user community. We express our intention to host the project.
3. We aim at starting the construction of the LC in the year 2001. In order to achieve this goal, we should complete the basic design of the LC by early 1997 or by the end of JFY1996 and then proceed to a more detailed design.
4. The ATF (Accelerator Test Facility) currently under construction at KEK should be fully utilized in order to identify technical issues with respect to the LC. R&D on the main linac will be centered on the X-band system, whereas R&D on the C-band system will be strengthened as a realistic backup technique.
5. An "LC project office" should be established within KEK to lead the project. An "LC Project Council" consisting of representatives from both universities and KEK will steer the project in close collaboration with the LC project office.
6. We should aim to build a new "International Accelerator Center" (name tentative). For its realization and also in view of a possibility that KEK could be expanded and converted to an international organization, an initiative should be promptly taken to further internationalize KEK.

[4] Zeroth-Order Design Report for the Next Linear Collider, LBNL-PUB-5424, also SLAC Report 474 or UCRL-ID-124161, May 1996.

Author and Major Contributers of Chapter 1

- Nobu Toge
- Hitoshi Hayano
- Yasuo Higashi
- Toshiyasu Higo
- Shigeru Kashiwagi
- Mitsuo Kikuchi
- Kiyoshi Kubo
- Shigeru Kuroda
- Hiroshi Matsumoto
- Hajime Mizuno
- Tsutomu Nakanishi
- Katsunobu Oide
- Toshiyuki Okugi
- Tsumoru Shintake
- Toshikazu Suzuki
- Seishi Takeda
- Toshiaki Tauchi
- Junji Urakawa
- Kaoru Yokoya

CHAPTER 2

Machine Parameters

Contents

Table 2.1 summarizes the basic parameters of JLC when its main linacs are based on X-band technologies. The parameters that depend on the collision energy are given for three center-of-mass energies: 250, 500 and 1000 GeV.

2.1 Beam Parameters

2.1.1 Beam Structure

The electron/positron beam in the present design consists of a bunch train that is made of $m_b = 85$ bunches per pulse. A bunch, separated by $t_b = 1.4$nsec (16 buckets), contains $N = 0.7\times10^{10}$ particles each. The repetition rate of the machine is maximum 150 Hz. Some numerical juggling of the parameters, such as (N, m_b, t_b), are still possible (by a factor of two or so), while maintaining essentially the same luminosity. However, many factors impose constraints on the choice of these parameters:

- The total beam-loading is mainly determined by m_bN and to some extent by m_bt_b.
- The beam-loading per unit time, which must be small enough for loading compensation, depends on N/t_b.
- Single-bunch collective phenomena such as bunch-lengthening in the damping ring and the single-bunch transverse blow-up in the linac, is related to N.
- The cure for multibunch beam breakup in the linac by means of the detuned structure mainly depends on m_b. (The total frequency spread is proportional to $1/t_b$ and the frequency interval to $1/m_bt_b$. Thus, the number of different frequencies is proportional to m_b.)
- The limitation of the positron production comes from the pulse charge, m_bN.
- The required response time of fast monitors, which discriminates each bunch or a fraction of the whole pulse, is proportional to t_b or m_bt_b.
- The beamstrahlung at the collision point is determined by N.
- Finally, the luminosity is proportional to m_bN^2.

One of the problems of the present parameter set is the cure of the multibunch beam breakup by the simple detuned structure does not seem to be enough. A design with halved m_b, doubled t_b and N larger by factor of $\sqrt{2}$ gives essentially the same luminosity performance as the present design except that at high energies ($E_{CM} \sim 1$TeV) the present design is better because beamstrahlung is less serious. The problem of the multibunch beam breakup should better be solved by the detuned structure with interleaved frequency distribution or by the damped detuned structure.

2.1.2 Bunch Length

There is no wide range of possible bunch lengths σ_z. A short bunch length below $\sim 80\mu$m would help to reduce the transverse wake in the linac and to increase the luminosity, if β_y^* can be reduced at the same time. However, the design of the bunch compressors will become very difficult. On the other hand, a σ_z longer than $\sim 100\mu$m will degrade the luminosity, because of the hour-glass effect at the interaction point (IP).

2.1.3 Emittance

The design (normalized) emittance at the exit of the damping rings is $\gamma\varepsilon_x = 3\times10^{-6}$ and $\gamma\varepsilon_y = 3\times10^{-8}$ rad·m. These values were set several years ago, when systematic studies on the linear collider design were started, and have been fixed, considering the design of the damping rings.

According to the results of later design studies of the damping rings, $\gamma\varepsilon_y = 3\times10^{-8}$ rad·m appears to be feasible. This should be verified in experiments at ATF of KEK. If it turns out to be the case, making use of better emittance values will become a more important issue; in that case, the direction of the parameter revisions will be to relax the focusing system for the quad misalignment tolerance and to make a/λ larger in order to reduce the wake.

2.2 The Main Linac

2.2.1 Accelerating Gradient

Since several years ago, the trend concerning the accelerating gradient of the X-band main linac has been set to a relatively high value (unloaded gradient ~70 MV/m, loaded gradient ~50 MV/m).[1] The fundamental reason for the high gradient is the desire to keep the entire facility within an acceptable site length, which is considered ~30 km or less.

In order to achieve a high gradient with a relatively small number of components, we had demanded klystrons of very high power exceeding 100 MW. With the observation of the present status of klystron development we have decided in this design study report to relax the peak-power requirement by factor of two, and, instead, to combine the outputs of two klystrons, leaving a possibility that higher-power klystrons may be used at a later stage.

The high gradient allows the iris aperture radius of the accelerating structure to be relatively small, $a/\lambda \sim 0.16$, as a weighted average over the structure. This is to be compared with the aperture in

[1] The JLC-I report is an exception where technologies immediately available were demanded for the comparison with other possible frequency ranges.

the JLC-I report, $a/\lambda \sim 0.18$ at $G_0 = 40$MV/m.

Actually, the above-mentioned requirement on the site length imposes a constraint on the gradient only at the highest target energy. The choice of gradient at lower energies in earlier stages is, in principle, a separate problem. It may in fact be a reasonable strategy to adopt a lower gradient at lower energies with a lower peak power of the klystrons.

However, once the structure design is fixed, the charge to be contained in each bunch should be approximately proportional to the gradient. This is so as to maintain the relative beam-loading and the structure alignment tolerance within a reasonable range. Therefore, if one reduces the gradient by a factor of $1/\sqrt{2}$, the luminosity will be reduced by a factor of $1/2$. Some portion of this reduction can be compensated for, for instance, by adopting a smaller horizontal beta value at the IP. Reducing the IP beta for the lower energy operation is not a serious difficulty from the stand-point of beam optics. However, in any case, such remedies are also possible at high gradient; thus, the "luminosity scaling" with respect to the accelerating gradient still remains valid. In summary, once the structure designs are given and fixed, it is reasonable to consider that the available luminosity will be proportional to the gradient.

Thus, we have come to adopt the same accelerating gradient independent of the target energy, meaning that the linac length must be made larger in proportion to the energy. As a side note, going back to a lower energy after construction of the full-length linac is another issue, which has not yet been fully examined. The use of a bypass beam line is a possible solution.

A consequence of the energy-independent gradient is that the alignment tolerance of structures is almost independent of the energy. Only a minor revision to this scenario is that if the emittance increase is to be maintained at the same level for both 500 GeV and 1 TeV operation, the tolerance will be slightly tighter at higher energies, because of the increased number of units. Another consequence of this "constant gradient strategy" is that the beam structure (such as the charge per bunch, charge per pulse) will be independent of the energy.

2.2.2 Injection Energy to the Main Linac

The beam energy at the injection point to the main linacs in the JLC-1 design was $E_{inj} = 20$GeV. However, after recent studies on the bunch compressor design and on the beam blow-up at the low-energy part of the main linac, we changed the injection energy to 10 GeV. Since the full design of the intermediate linac still requires much work, this choice remains tentative at this moment.

2.2.3 Pulse-Compression Scheme

We adopt the 4/3 DLDS (Delay Line Distribution System) scheme, meaning the outputs of 8 klystrons within the RF power source block are added and cut into 3 pieces in time and distributed to 3 clusters of the accelerating structures. An obvious advantage of the DLDS is the extremely low power-loss rate. The issues to be addressed are that the RF phase accuracy has to satisfy a tight tolerance on

3.2 Polarized Electron Source

3.2.1 Specifications

The operating specifications for the polarized electron source (PES) are given in Table 3.2. A beam intensity of about $2 \times 10^{10} e^-$/bunch, which is equivalent to a peak current of 3.2 A (assuming a bunch-width of 700 ps and a cathode area of $3\,cm^2$), must be extracted from the source to provide $1 \times 10^{10} e^-$/bunch at the interaction point.[1] The maximum peak current is determined by the space-charge limit of the gun, if the effect of surface charge is not the limitation. The space charge limit will be about 30 A for the gun, which is designed to operate at 200 kV, corresponding to an extraction field gradient of 3.2 MV/m. For a given extraction voltage, the surface charge limit is related to the negative electron affinity (NEA) of the cathode surface, and it is considered to determine the practical peak current of the gun. The activated NEA surface is extremely sensitive to surface contamination. To maintain a good operating condition, an ultra-high-vacuum (UHV) environment with a total pressure of $\sim 10^{-11}$ Torr is required around the cathode.

For the same reason, the creation of contaminants by a field emission dark current induced at the high-voltage electrodes must be minimized so as to avoid degradation of the NEA. In practice, the average dark current should be kept below 20 nA. The desired $1/e$ decay rate of the quantum efficiency (defined as cathode lifetime) is longer than 200 hours for a suitable operational efficiency. The electron spin polarization should be greater than 85% for the beam intensity specified in the table.

3.2.2 Photocathode

Important parameters for photocathodes operated at linear colliders include:

1. Electron spin polarization (ESP),
2. Quantum efficiency (QE),
3. Extracted current (I_p), and
4. the cathode life time (τ).

The JLC polarized gun group has been conducting development work on various types of photocathodes during the past several years.[1]. The maximum electron spin polarization is limited by the fine energy splitting of the band structure in the valence band of the cathode crystal. To overcome the 50% limitation of bulk-GaAs, several different types of photocathodes have been developed up to

[1] Table 2.1 in Chapter 2 assumes $0.7 \times 10^{10} e^-$/bunch at the interaction point. Thus, about a 40 % margin is considered here.

Table 3.1: Parameters of the HV pulser for the thermionic electron gun.

Peak power output	24 MW
Average power output	8.4 kW
Maximum pulse voltage	240 kV
Operating pulse voltage	200 kV
Maximum pulse current	100 A
Output impedance	2.4 kΩ
Load impedance	2.4 kΩ
Transformer ratio	1:15
Pulse width	7 μs
Pulse flat top	3 μs
Maximum repetition rate	150 pps
Pulse height deviation	
flatness	$\leq \pm 0.3$ %
Pulse amplitude drift	
Short term	$\leq$0.2 %
Long term	$\leq$0.5 %

3.1.3 Grid Pulser

A grid pulser is installed on the HV station set up near to the electron gun. Grid pulses are produced by gating the output of a 714 MHz signal generator that is synchronized with sub-harmonic bunchers. An optical signal transmitter and receiver system are used to transmit 85 cycles of rf at 714 MHz rf frequency to the high-voltage deck of the gun HV pulser. A 5 kW rf amplifier amplifies the pulses from the ECL level to an rf voltage of 400 V peak-to-peak at the 50 Ω load impedance. The band width of the rf amplifier should be as wide as possible. This is so as to shorten the rise and fall times of the pulse. A rectangular pulse a the pulse width of 119 ns is combined into a pulse with a fine structure. This is done in order to eliminate any satellite pulses subsisted at the rise and fall of the pulse train.

The beam energy of the gun system is 200 KeV in the normal operating mode. Since the pulse width of a beam is 1 ns FWHM, the length of the pulse beam is estimated to be 209 mm at an energy of 200 KeV. The peak current of a short pulse beam is 3.8 A (2.1×10^{10} electrons/bunch). The flatness of each short pulse beam, except for the rising and falling parts, is estimated to be about $\pm$1% peak-to-peak. In order to eliminate any satellite bunches that appear during the rising and falling parts of the pulse, a beam-deflector system with a collimator will be installed downstream of the electron gun.

3.1 Thermionic Electron Gun

3.1.1 Overview

The design of a conventional (non-polarized) electron gun for JLC consists of a cathode stem, a HV insulator, a vacuum chamber with an anode and magnetic lenses. The cathode stem and Wenelt electrode should be made of "Clean Stainless-Steel" to reduce the out-gassing during high-voltage operation.

The diameter of the insulator is chosen to match the ICF253 flange. The length of the insulator is 360 mm, which is determined so as to avoid HV breakdown in the atmosphere along the outer surface of the insulator. The key issue concerning the gun design is the alignment of the cathode, anode and magnetic lenses with respect to the beam axis of the preinjector.

The alignment of both axes of the cathode and anode are realized by a precise machining of the flanges at both ends of the insulator. The cathode stem has a mover for a precise alignment of their axis. As a result, the axes of the cathode and anode would be aligned within 100 μm. The anode and magnetic lenses are fixed on a SUS316L support-block, which is also precisely machined so as to align its axis within a mechanical accuracy of 50 μm. The electron gun is installed on a support table equipped with a remotely-controlled fine-alignment mechanism. The axis of the beam that is extracted from the anode can be aligned by measuring the beam profile in the preinjector so that the beam is injected to the axis of the magnetic fields of the preinjector linac.

The EIMAC Y646-E or Y796 grid-cathode assembly is installed on the cathode stem. Activation of the cathode after completing the assembly of the entire system is made by a computer-controlled automatic processing system under a vacuum condition at a pressure below 6×10^{-7} Torr.

3.1.2 Gun HV Pulser

The gun HV pulser consists of a 240 kV pulse modulator, a HV station with a grid pulser and a control system. Table 3.1 shows the specifications for the HV pulser. The HV pulse is generated by the HV modulator with a line-type, 16-section pulse-forming network. A de-Q'ing circuit is introduced to stabilize the pulse amplitude with drifting of less than 0.2% within the short term, and less than 0.5% in the long term. A high-power dummy-load is installed in a pulse transformer to decrease the impedance and to reduce the sag of the output voltage.

CHAPTER 3

Electron Source

Contents

Author of Chapter 2

- Kaoru Yokoya

Center-of-mass energy	E_{CM}	250	500	1000	GeV
— Structures —					
Number of structures per beam		2004	4184	5864	
Peak power into a structure		84.3	84.3	165.	MW
Structure type		CG Choke-mode $3\pi/4$			
Structure length		1.80	-	-	m
Average iris radius / wavelength[a]	a/λ	0.148	-	-	
range (entrance – exit)		0.173 – 0.125			
Average group velocity	v_g/c	0.023	-	-	
Filling time	T_f	286	-	-	nsec
Attenuation parameter	τ	0.53	-	-	
Average Q factor	Q	9670	-	-	
Elastance	s	1.95×10^{14}	-	-	Ω/m/s
Shunt impedance	R_s	53.1	-	-	MΩ/m
— Linac beam dynamics —					
Off-crest angle for single-bunch energy compensation[b]	ϕ_{rf}	14.5	14.5	10.0	deg
Single-bunch full energy spread after off-crest correction		0.35	0.35	0.28	%
Transverse wake at $z = 2\sigma_z$		4.64×10^{15}	-	-	V/C/m^2
Structure misalignment tolerance		30.	-	-	μm
— Parameters at the Interaction Point[c] —					
Number of particles per bunch	N	1.11×10^{10}	1.11×10^{10}	1.39×10^{10}	
Assumed normalized emittance	$\gamma\varepsilon_x^*$	3.3×10^{-6}	-	-	m·rad
	$\gamma\varepsilon_y^*$	4.8×10^{-8}	-	-	m·rad
Beta function at IP	β_x^*/β_y^*	10/0.20	15/0.20	30/0.20	mm
R. m. s. beam size	σ_x^*/σ_y^*	367/6.26	318/4.43	318/3.14	nm
Crossing angle (full angle, crab crossing)	ϕ_{cross}	8.0	-	-	mrad
Disruption parameter	D_x/D_y	0.373/21.9	0.250/17.9	0.157/15.9	
†Average energy loss by beamstrahlung	δ_{BS}	2.09	4.09	8.34	%
†Average number of photons per electron	n_γ	1.41	1.51	1.73	
Maximum Upsilon parameter	Υ_{max}	0.0955	0.210	0.506	
Nominal luminosity[d]	$\mathcal{L}_{00}$	3.07	5.02	5.53	10^{33}/cm^2/s
Geometric luminosity reduction factor[e]	H_{geo}	0.863	-	-	
†Pinch enhancement factor of luminosity[f]	H_D	1.78	1.66	1.60	
†Luminosity[g]	$\mathcal{L}$	4.71	7.18	7.65	10^{33}/cm^2/s

[a] weighted by the contribution to the single-bunch transverse wake
[b] average over the whole linac
[c] Those with † are results of simulation
[d] $\mathcal{L}_{00} = f_{rep} m_b N^2 / 4\pi\sigma_x^*\sigma_y^*$
[e] Includes the crossing angle effect and the hourglass effect
[f] $H_D = \mathcal{L}/H_{geo}\mathcal{L}_{00}$
[g] Assumes that crab crossing is used

Table 2.2: Basic Parameters of C-band Collider

— Fundamental Parameters —					
Main accelerating frequency	f_{rf}	5.712	-	-	GHz
Center-of-mass energy	E_{CM}	250	500	1000	GeV
Number of particles per bunch	N	1.11	1.11	1.39	$\times 10^{10}$
Number of bunches per pulse	m_b	72	-	-	
Bunch spacing	t_b	2.80	-	-	nsec
Repetition frequency	f_{rep}	100	100	50	Hz
Normalized emittance at damping ring exit	$\gamma\varepsilon_x/\gamma\varepsilon_y$	$3\times10^{-6}/3\times10^{-8}$	-		m·rad
R. m. s. bunch length in main linac	σ_z	200.	-	-	μm
— Main Linac —					
Nominal accelerating gradient	G_0	40.0	40.0	56.0	MV/m
Effective accelerating gradient[a]	G_{eff}	31.9	31.9	46.4	MV/m
Active length of each main linac	L_{acc}	3.61	7.53	10.55	km
Injection energy	E_{inj}	10	-	-	GeV
RF unit (number of modulator/klystron/structure)		2/2/4			
— Total Power —					
Wall-plug power for two linacs		73.4	153	133	MW
Total efficiency from AC to structure input		22.6	22.6	35.2	%
Average beam power for two linacs	P_B	3.20	6.41	8.01	MW
— Klystrons and Modulators —					
Number of klystrons per beam		1002	2092	2932	
Klystron peak power		50.3	50.3	98.6	MW
Required klystron output pulse length		2.44	-	-	μsec
Efficiency of modulators	η_{mod}	75	-	-	%
Efficiency of klystrons	η_{kly}	45.	45.	70.	%
— Pulse compressor —					
Pulse compression scheme		multi-cell coupled cavity			
Pulse compression ratio		5	-	-	
Pulse compression efficiency		67.	-	-	%

[a]net acceleration per structure including single-bunch and multi-bunch energy compensation

lowered the injection energy from 20 GeV to 10 GeV.[2] However, what frequency range should be adopted for the pre-linac is unknown yet. It might be that C-band can also be used for the pre-linac. In this case, a single-stage compressor may turn out to be feasible. Investigations on these issues are left for future studies.

For energies in the range $E_{CM} = 250 \sim 500$ GeV we will use the same RF system. Above this energy we consider an upgrade to the klystron power source to ~100 MW/tube. This will push up the effective accelerating gradient from ~32 MV/m to ~46 MV/m. Together with an extension of the linac length by 40 %, we can reach E_{CM}=1 TeV.

At $E_{CM} = 1$ TeV or higher we have to reduce the repetition rate to half, in order to limit the total power comsumption to below ~200 MW, and we must increase the horizontal beta function at the collision point larger by a factor of two. In spite of these facts, the luminosity will be slightly higher than at $E_{CM} = 500$ GeV, because of the adiabatic damping and the increased number of particles per bunch (25 %). The latter is possible because of the increased accelerating gradient.

[2]The C-band chapter still uses $E_{inj} = 20$ GeV so that there is an inconsistency of a few percent between the parameter set here and those in the C-band chapter.

2.4 C-band Linear Collider

The possibility of using the C-band for the main linacs has been discussed since several years ago. The decision was made in 1996 to pursue R&D of the C-band scheme as a realstic back-up technology for JLC, and formal hardware development work was started at KEK.

The parameter set for the C-band collider is given in Table 2.2 for three center-of-mass energies in a manner similar to the case of the X-band table.

An advantage of the C-band is that various aspects of the microwave technology is expected to be substantially easier than that with the X-band. For example, alignment tolerance of the accelerating structure is considerably looser. Another issue to note is that the C-band design prefers the choice of lower accelerating gradient for maximizing the luminosity per power. This means that the C-band design tends to result in longer linacs for a given target luminosity.

Up to now intensive studies of the whole system have not yet been made. In this report we present the recent study of the RF system only.

Linear collider designs with lower frequency usually assume a greater number of bunches, more particles per bunch, and a larger emittance. However, we do not adopt the last item (larger emittance), because the low emittance beam adopted in the X-band design does not look hard to obtain in the damping ring, and preserving that emittance in the main linacs is even easier than in the case with X-band. Thus, we assume the same emittance as in the case of the X-band. Although the number of particles per bunch is larger than in the X-band, the number of bunches per pulse is smaller, because the total number of particles per pulse is limited by the positron production rate. The latter has no large margin in the present design of the positron system.

The bunch length is chosen to be 200 μm, twice as long compared to the X-band case. This is required in order to compensate for the single-bunch longitudinal wake by using off-crest acceleration. This longer bunch, compared with old designs of the C-band, brings about three changes:

- Firstly, the iris aperture was made larger in order to relax the single-bunch transverse wake-field.
- Secondly, the vertical beta function at the interaction point (IP) became larger in order to avoid the hour-glass effect.
- Finally, the use of crab crossing at the interaction point became highly desirable, or, in a way, inevitable. The luminosity quoted in Table 2.2 assumes that crab crossing is used.

On the other hand, the beamstrahlung emission at IP is reduced by using a longer bunch length. Another change is that the design of the bunch-length compressor will become significantly easier. However, we have not yet revisited the design of this part. As in the X-band case, we have tentatively

Table 2.1(continued)

— Energy-dependent Parameters of the X-band Main Linac —					
Center-of-mass energy	E_{CM}	250	500	1000	GeV
Active length of each main linac	L_{acc}	2.07	4.32	8.81	km
Number of klystrons per beam		1053	2197	4485	
Number of structures per beam		1579	3295	6727	
Wall-plug power for two linacs		55	115	234	MW
— Parameters at the Interaction Point[a] —					
Center-of-mass energy	E_{CM}	250	500	1000	GeV
Number of particles per bunch	N	0.7	0.7	0.7	$\times 10^{10}$
Assumed normalized emittance	$\gamma\varepsilon_x^*$	3.3×10^{-6}	3.3×10^{-6}	3.3×10^{-6}	m·rad
	$\gamma\varepsilon_y^*$	4.8×10^{-8}	4.8×10^{-8}	4.8×10^{-8}	m·rad
Beta function at IP	β_x^*	10	10	10	mm
	β_y^*	0.10	0.10	0.10	mm
R. m. s. beam size	σ_x^*	367	260	184	nm
	σ_y^*	4.43	3.14	2.28	nm
Crossing angle (full angle)	ϕ_{cross}	8.0	8.0	8.0	mrad
Disruption parameter	D_x	0.106	0.106	0.106	
	D_y	8.81	8.79	8.57	
†Average energy loss by	δ_{BS}	1.34	3.40	6.90	%
beamstrahlung		[1.54]	[4.40]	[9.90]	%
†Average number of photons	n_γ	0.74	0.91	1.04	
per electron		[0.83]	[1.12]	[1.43]	
Maximum Upsilon parameter	Υ_{max}	0.114	0.319	0.894	
		[0.119]	[0.336]	[0.950]	
Nominal luminosity[b]	$\mathcal{L}_{00}$	3.06	6.11	12.2	$10^{33}/\mathrm{cm}^2/\mathrm{s}$
Geometric luminosity	H_{geo}	0.646	0.541	0.429	
reduction factor[c]		[0.855]	[0.855]	[0.855]	
†Pinch enhancement factor	H_D	1.596	1.566	1.460	
of luminosity[d]		[1.581]	[1.585]	[1.599]	
†Luminosity	$\mathcal{L}$	3.15	5.18	7.66	$10^{33}/\mathrm{cm}^2/\mathrm{s}$
		[4.13]	[8.28]	[16.72]	$10^{33}/\mathrm{cm}^2/\mathrm{s}$

[a]The numbers in square brackets are those with crab crossing. Items with † are results of simulation.
[b]$\mathcal{L}_{00} = f_{rep} n_b N^2 / 4\pi\sigma_x^*\sigma_y^*$
[c]Includes the crossing angle effect and the hourglass effect
[d]$H_D = \mathcal{L}/H_{geo}\mathcal{L}_{00}$

the change of the wave-guide length, and that the system becomes complex when one aims at a high compression ratio.

Another problem, which has not yet been studied fully, is the scheme of beam-loading compensation. The so-called staggered timing method (change the timing of fill from structure to structure) seems to be difficult, because to change the timing for the structures within one DLDS system independently is very hard. The beam-loading compensation and RF phase controls in general might be too 'non-local', particularly in the low-energy portion of the main linacs, for establishing adequate operability of the machine. We are now investigating two other possibilities, ΔT and ΔF methods.

2.3 Final Focus System and Interaction Point

The final focus system is designed such that the same magnet sequence can be used for any collision energies up to E_{CM} = 1.5 TeV, except for the needs to replace the last few quadrupole magnets in a few steps. The beta functions at the IP are chosen to be β_x^*=10 mm and β_y^*=0.1 mm.

The choice of the β-function values at the IP is independent of energy up to E_{CM} = 1.5 TeV. For energies above E_{CM}=1 TeV, β_x^* has to be increased in order to reduce the beamstrahlung. This naturally decreases the luminosity. An obvious remedy is to adopt a smaller β_y^*. However, it will require a shorter bunch length to accomplish the desired luminosity increase, and it will impose a significant challenge in the design of the bunch compressor system.

In the present design stage there is a large uncertainty concerning the choice of the number of particles per bunch at the IP and the emittances.

We assumed that the particle loss after the damping ring is negligible as far as the luminosity is concerned. The tolerance on the total charge in a bunch train to avoid fluctuation of beam-loading is as tight as ±0.5 %. This means that if there is a loss of 10 %, for example, the loss must be stable from pulse to pulse within ±5 % of its average value. Although the loss fluctuation in the later part of the main linac and the final focus system is more acceptable in this respect, large beam losses are more likely to occur upstream. This "stable loss" looks quite unreasonable. We thus assume no loss for the luminosity computation. Note that the charge fluctuation before the damping ring should be (and can be) compensated for by a feed-forward system that detects the beam current stored in the damping ring, and adjusts the RF phases and other parameters in the main linacs.

A larger uncertainty is associated with the emittance blowup across the entire linear collider complex. In the table we assume 10 % increase in ε_x and 60 % in ε_y from the damping ring exit to the IP. One could assume a larger blowup in light of considerations of the operational margins. In fact, the actual blowup will be much larger than the above values, at least in the beginning of operation. However, we think that it is more reasonable to assume a moderate value of emittance blowup in the standard parameter set. If we expect a large emittance blowup, say several hundred percent, in

item	value
Gun vacuum	$\leq 10^{-11}$ Torr
Operating voltage	≥ 150 kV
Cathode area	3.0 cm^2
Extraction field	3.2 MV/m
Maximum field on cathode electrode	≤ 5.4 MV/m
Space charge limit	~30 A
Peak current at gun	3.2 A
Number of bunches	90
Bunch width at gun	~ 700 ps (FWHM)
Bunch spacing	1.4 ns
Macropulse repetition rate	150 pps
Intra-pulse energy variation	$\leq 1\%$
Gun normalized edge emittance	≤ 30 mm-mrad
Dark current	≤ 20 nA
Cathode life-time	~ 200 hours
Polarization	$\geq 85\%$

Table 3.2: *Specifications of the electron gun for JLC.*

now. They are categorized into two groups, strained GaAs and super-lattice. The former contains strained GaAs, strained GaAsP, strained GaAs with DBR (distributed Bragg reflector); the latter contains AlGaAs-GaAs super-lattice, the same super-lattice with modulated doping, and InGaAs-GaAs strained layer super-lattice.

These efforts were assisted by semiconductor physicists of Osaka Prefecture University and of research laboratories of Daido-Steel and NEC. Co. They have instruments that can measure the spin relaxation time, fabricate the strain GaAs cathodes by the MOCVD method, and the super-lattice cathodes by the MBE method, respectively.

The NEA surface plays an essential role in the emission of electrons from the cathode. The QE is mainly determined by the property of this NEA surface. The best-achieved performance of these photocathodes in terms of the maximum ESP and the QE at the same laser wavelength that has been obtained by us are shown in Table 3.3.

Cathode-type	Polarization	QE	Ref.
Strained GaAs on GaAsP	~ 85 %	~ 0.1 %	[2]
Strained GaAs with DBR	~ 85 %	~ 1.0 %	[3]
Super-lattice (AlGaAs-GaAs)	~ 70 %	~ 1.0 %	[4]
Strained Layer Super-lattice (InGaAs-GaAs)	~ 90 %	~ 0.05 %	[5] [8]

Table 3.3: *Performances of different kinds of photocathodes.*

In the most recent development it was demonstrated that a polarization of 90% can be achieved by the InGaAs-GaAs strained layer super-lattice, as shown in Figure 3.1 [8].

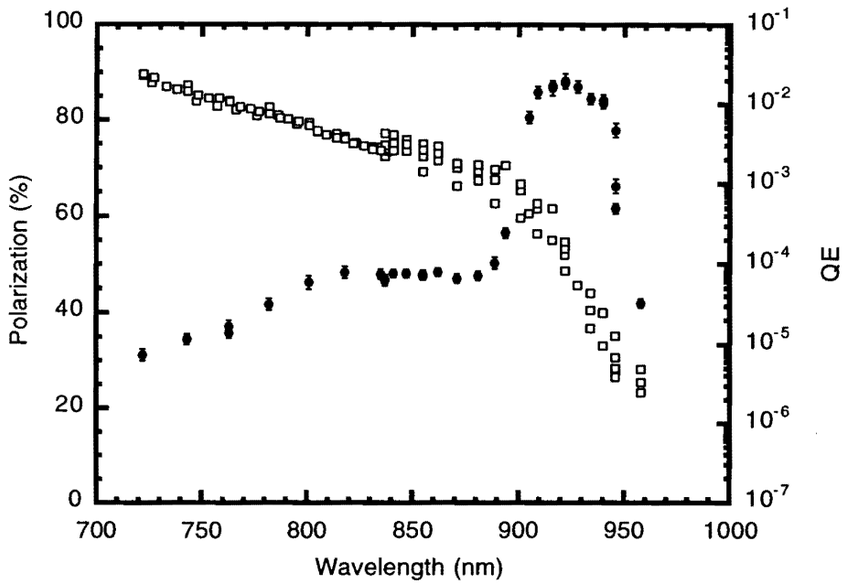

Figure 3.1: *Polarization (filled circles) and quantum efficiency (white rectangles) obtained by an InGaAs-GaAs strained layer super-lattice.*

We thus consider the strained GaAs and the strained layer super-lattice to be the most promising candidates of photocathodes for JLC. This is because of their high polarization, in excess of 85 %. The QE of an InGaAs-GaAs strained layer super-lattice is not sufficiently high at this moment, as shown in Table 3.3. However, its QE value will be improved by another kind of strained layer super-lattice having a wider band gap than that of the InGaAs-GaAs super-lattice.

The maximum current, extracted from an NEA-activated cathode, is limited by the so-called "surface charge limit (SCL)", rather than by the space charge limit[6]. It has been suggested that SCL depends on the NEA status, or conditions of the band-bending region, as well as the extraction field gradient. The AlGaAs-GaAs super-lattice with a highly p-doped NEA surface showed a higher resistance against SCL than that of strained GaAs[7]. Further studies on various ideas for reducing the SCL effect are planned in experiments at 100 kV and 200 kV polarized guns.

The decay rate of QE, defined as the cathode lifetime, is the most important parameter for the operation and maintenance of the polarized electron source. A wider band-gap semiconductor cathode is considered to have a better lifetime, due to the larger NEA. In this respect, a photocathode with a strained layer super-lattice and wide band gap structures is again considered to be the most promising, and a study of such cathodes is continuing.

3.2.3 Gun Design Layout

A schematic plan view of the polarized gun system is shown in Figure 3.2. This system consists of components contained in three distinct vacuum chambers: the gun itself to produce a beam of up to 200 keV polarized electrons; a preparation chamber for heat cleaning and activation of the photocathode by successive depositions of Cs and O_2; a reservoir to store several spare photocathodes. Three chambers are isolated by two gate valves during normal gun operation. Two transporters are used to move the photocathodes between them without breaking the ultra-high-vacuum.

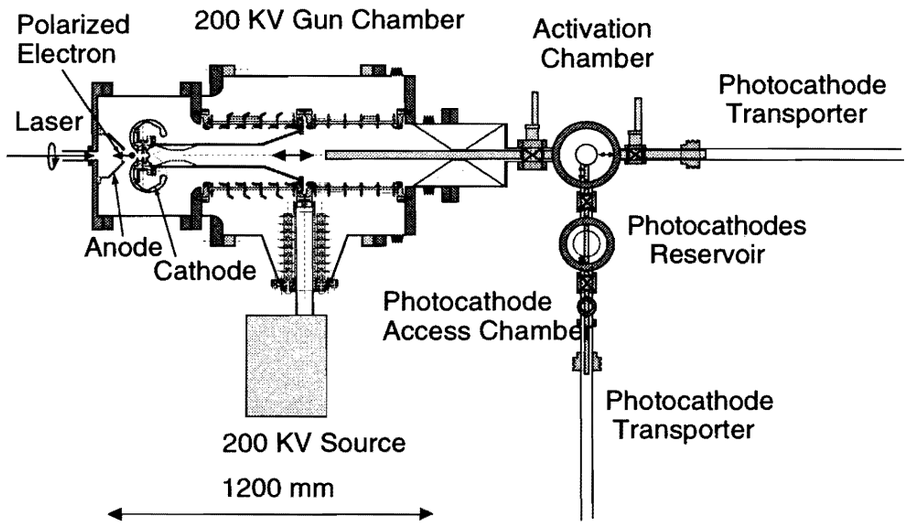

Figure 3.2: *Schematic of the polarized electron gun system.*

The activation chamber and the load-lock system are indispensable for reducing the increase in the rate of the dark current, which is due to repetitive depositions of Cs atoms into the gun chamber to re-activate the NEA surface. An advantage of this design is that the load-lock system is kept connected to the gun body at the ground potential. A schematic view of the gun structure is shown in Figure 3.3. Its main components are a stainless-steel gun chamber; an anode electrode; a cathode electrode supported on a horn-tube that is fixed to the center flange of high voltage ceramics; a replaceable photocathode crystal mounted on a transport "pack"; a pair of insulating ceramic segmented into 5 stages; a high-voltage bushing supported by a 250 kV power supply; and an insulating gas tank filled with SF_6.

A high-voltage of up to 250 kV can be applied to the center of a pair of identical ceramic structures. Each ceramic structure is divided into five segments longitudinally in order to reduce the leakage current that flows along the ceramic surface. A gun voltage much higher than 100 kV is desirable

for increasing the output electron current with a relaxed space charge limit and surface charge limit. However, an improved technology for reducing the dark current is required in that case.

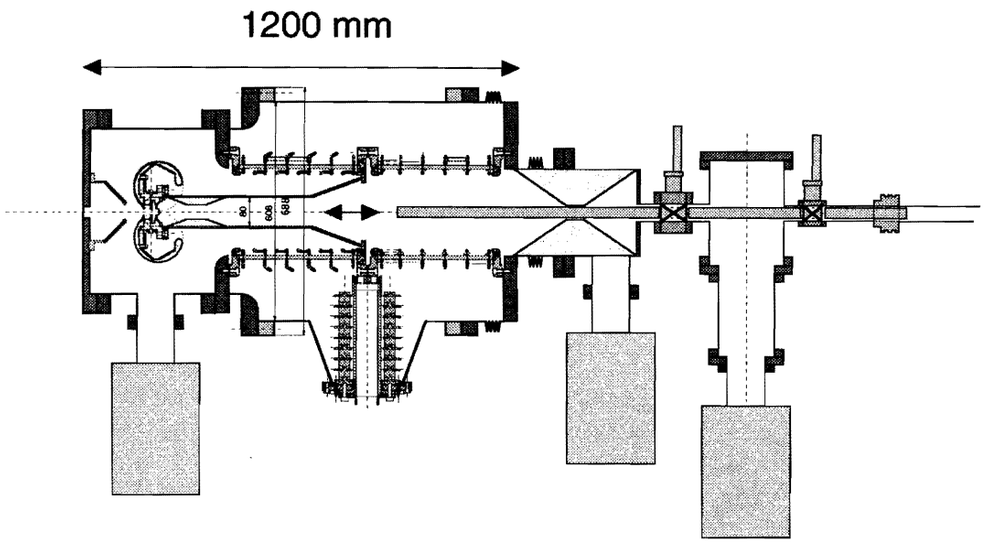

Figure 3.3: *Schematic of the polarized electron gun chamber.*

Circularly-polarized photons are injected from the left side onto the cathode surface, and the produced electrons are extracted in the direction opposite to the laser photons.

3.2.4 Dark-Current Problem

Dark currents are caused by field emission from the metal surface of an electrode. It is known that if they reach a level of 100 nA, they significantly degrade the photocathode lifetime and irreversibly reduce the QE. Thus, the key point for achieving the long lifetime of photocathodes required for stable operation of the polarized gun is a reduction of the field emission dark current from electrodes.

Although there is still no definitive agreement on the nature of emitting sites of dark current among researchers, it is considered that the local electric field can be enhanced by several orders of magnitudes (defined as a microscopic filed enhancement factor, β) by the presence of microscopic irregularities (pitting and scratches), impurity materials with the non-metallic energy band structures, or dust deposited on the surface.

The JLC polarized gun group has been conducting basic research on the dark-current issue with a compact test-apparatus, as shown in Figure 3.4. Here, a test electrode piece is arranged in a demountable way, so that a variety of electrodes can be easily tested. The electrodes are made of different materials and machined by different procedures of surface treatment and finished by a different rinsing method. The geometrical shapes of the electrodes are also shown in Figure 3.4. They

are common to all tested samples.

The selection of material to build the electrodes is important. It has been demonstrated that a special SUS material made by vacuum induction or a vacuum arc re-melting method is useful as the electrode material. This is because it contains a much smaller amount of non-metallic contamination (C, Si, P, S etc.) than the standard SUS-316L material.

In order to fabricate a super-clean SUS (stainless-steel) electrodes, special methods were developed for surface polishing using the electrochemical-buffing method and surface rinsing with ultra-pure water.

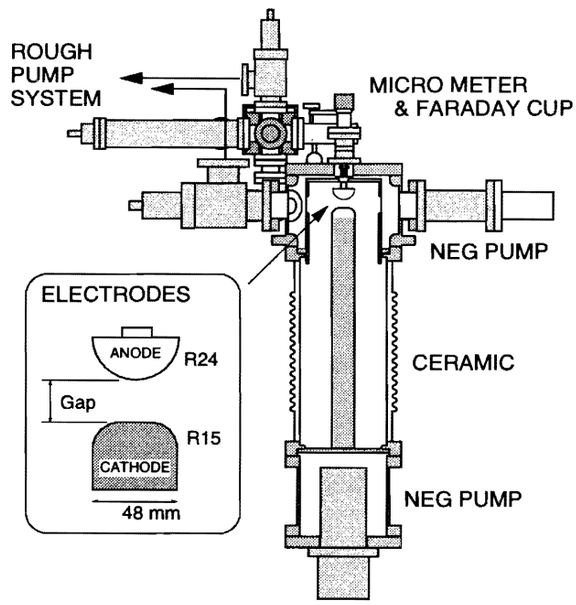

Figure 3.4: *Test apparatus used for the dark-current study.*

Measurements of the dark current can be performed in a UHV ($\leq 3 \times 10^{-11}$ torr) under various field gradients which are set by the electrode-gap-length and the bias voltage. The best record taken for the sample electrodes made of stainless steel shows that the dark current can be reduced to a level of less than 90 pA under a field gradient of 34 MV/m.

The microscopic field enhancement factor, $\beta \sim 40$, was estimated by using a Fowler-Nordheim plot, as shown in Figure 3.5, where (a) and (b) were taken at the initial and final stage of " current" conditioning, respectively[8].

A standard procedure for fabricating stainless steel electrode is expected to be established from this study, and will be applicable for not only the DC electrodes, but also for other high-voltage devises. The apparatus is now used for a study to reduce the dark current from the copper surface of an RF cavity.

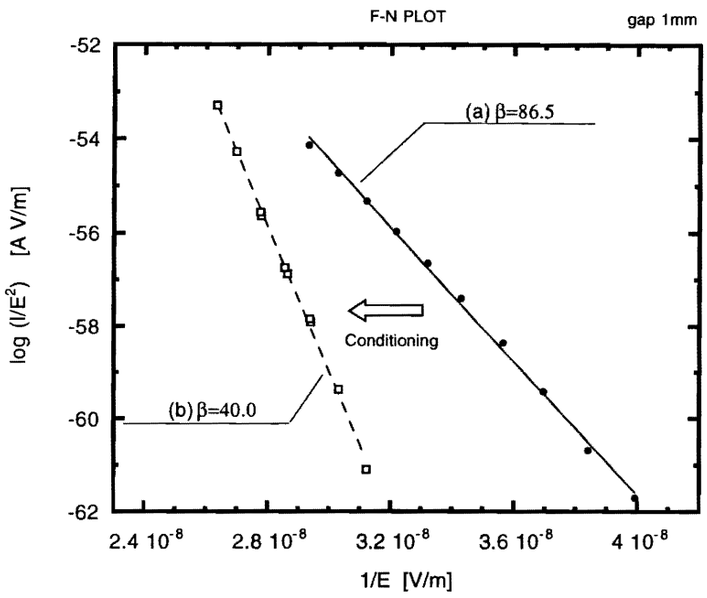

Figure 3.5: *Fowler-Nordheim plot of the dark current emitted from the stainless steel electrodes. (a) before conditioning, and (b) after conditioning.*

3.2.5 Load-lock and Cathode Preparation Chamber

Baking the gun chamber is required for achieving a UHV. Also, a high voltage processing of the electrodes is required to reduce the dark current. There, the voltage is slowly ramped up while discharges are taking place. Care must be taken, however, since both of these activities tend to damage the photocathode. The increase in the dark current from the cathode electrode caused by repetitive supplies of Cs atoms into the gun chamber must be also avoided in order to achieve a long cathode lifetime.

The use of activation chamber with load-lock system is an obvious solution to those problems. It allows us to remove the photocathode during baking and high-voltage processing, and to replace it while maintaining a UHV. The preparation chamber has functions for thermal cleaning, first surface activation and the QE evaluation of the photocathode.

A notable feature of the preparation chamber is an induction heating station with a docking mechanism similar to the gun's. A schematic view is shown in Figure 3.6.

The preparation chamber has provision for making the NEA surface by Cs and O_2 deposition. The Cs flux is easily controlled by varying the dispenser current, and O_2 can be introduced into the vacuum through a standard leak valve. The preparation chamber vacuum is provided by a $30\,l/s$ ion pump with a $100\,l/s$ NEG pump mounted on a large bottom port.

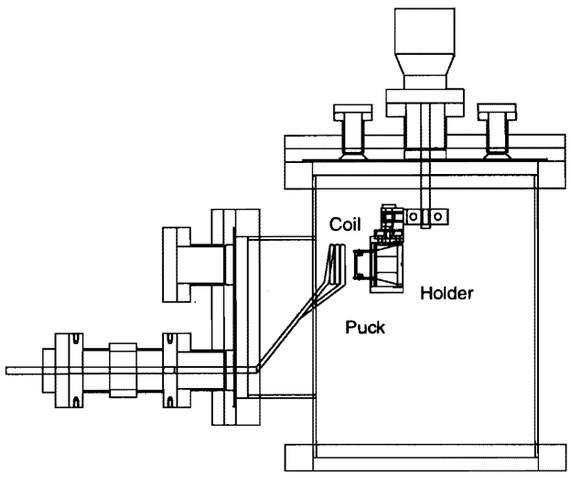

Figure 3.6: *Cathode preparation chamber with an induction heating station and docking mechanism*

3.2.6 Laser System

The requirements for the laser system are determined by the specifications on the polarized electron beam to be produced at the photocathode. The laser-photon wavelength that gives the maximum electron polarization depends on the type of photocathode. For instance, it is ~870 nm for strained GaAs, and ~740 nm for an AlGaAs- GaAs super-lattice. It is thus desirable for the laser system to cover the wavelength range from 720 nm to 890 nm. The preferred bunch shape is rectangular, since the total charge extracted per bunch is the integral of the peak current, which is limited by the surface charge limit properties of the NEA cathode. Thus, the bunch shape should be as rectangular as possible. The required laser photon energy flux is determined by the cathode quantum efficiency that is assumed to be 0.1%. A simple calculation shows that it is preferred to be higher than 20μJ. The laser spot size on the cathode should be made variable during operation. This is so that the saturated current can be matched to the required beam current. The specifications for the laser system are given in Table 3.4.

Two schemes are in principle possible for producing the multi-bunch laser beam required at JLC. One is to use laser pulses of 126 ns width at a repetition rate of 150 Hz. In this case each pulse is sliced into multi-bunches using a Pockels cell pulse shaper. The other scheme is to produce laser light that oscillates at a frequency of 714 MHz (1.4 ns spacing) first. Out of these, up to 90 bunches per each pulse are retained to form macro-pulses at a rate of 150 Hz.

No laser systems that meet the specifications mentioned above are readily available at this moment. Both schemes should be investigated in parallel as possible candidates. A schematic diagram of a laser system based on the latter scheme is shown in Figure 3.7. The mode-locked semiconductor diode laser oscillates at 714 MHz, where each micropulse is assumed to have a 100~200 ps width.

item	value
Laser wavelength	720 nm to 890 nm
Circular Polarization	$\geq$ 99.5 %
Bunch train length	up to 126 ns
Bunch separation	1.4 ns (714 MHz) or 2.8 ns (357 MHz)
Bunch width	700 ps
Bunch photon energy	$\geq 20\,\mu$ J
Laser spot size on cathode	tunable from 10 mm to 20 mm diameter
Repetition rate	150 Hz

Table 3.4: *Laser cpecifications for a polarized electron source.*

The 150 Hz macropulses, which consist of 90 bunch trains, can be created by the pulse-shaping unit. Then, a bunch with a width of ~700 ps can be obtained by combining the original micropulse and the delayed pulse by a method of successive splitting and delaying of the original micropulse. The bunch energy is then amplified to meet the energy requirement by a multi-pass laser amplifier comprising a Ti:Sapphire crystal, which is pumped by a high power Nd:YAG laser system.

An advantage of this scheme is due to the fact that this laser system can be compatible with the future polarized RF gun scheme, since a pulse width shorter than 50 ps can be produced by replacing the mode-locked diode laser. However, it should be noted that the technology for a high repetition rate diode laser is not yet fully conventional[9], and some further developments will be required to establish this scheme.

3.2.7 Research and Development Plan

A number of R&D programs on both the photocathode and polarized gun have been conducted by a KEK-Nagoya collaboration. A base-line design of the polarized electron source, as described in previous sections, has resulted from such R&D. However, the gun system that can produce a multi-bunch beam has not yet been constructed, and the development of additional technologies is still required to achieve the design values needed for a polarized electron gun for JLC.

Photocathode Development

Polarization that exceeds 85% and a quantum efficiency higher than 0.3% have been operational by photocathodes made of strained GaAs and a strained layer superlattice. The most recent result obtained by a InGaAs-GaAs superlattice has been already discussed.

However, challenging issues still remain: (a) a new cathode structure that can mitigate the surface charge limit effect, and (b) a new surface structure that can give a higher stability to the NEA states against the adsorption of residual impurities in an ultra-high-vacuum. These studies can be performed

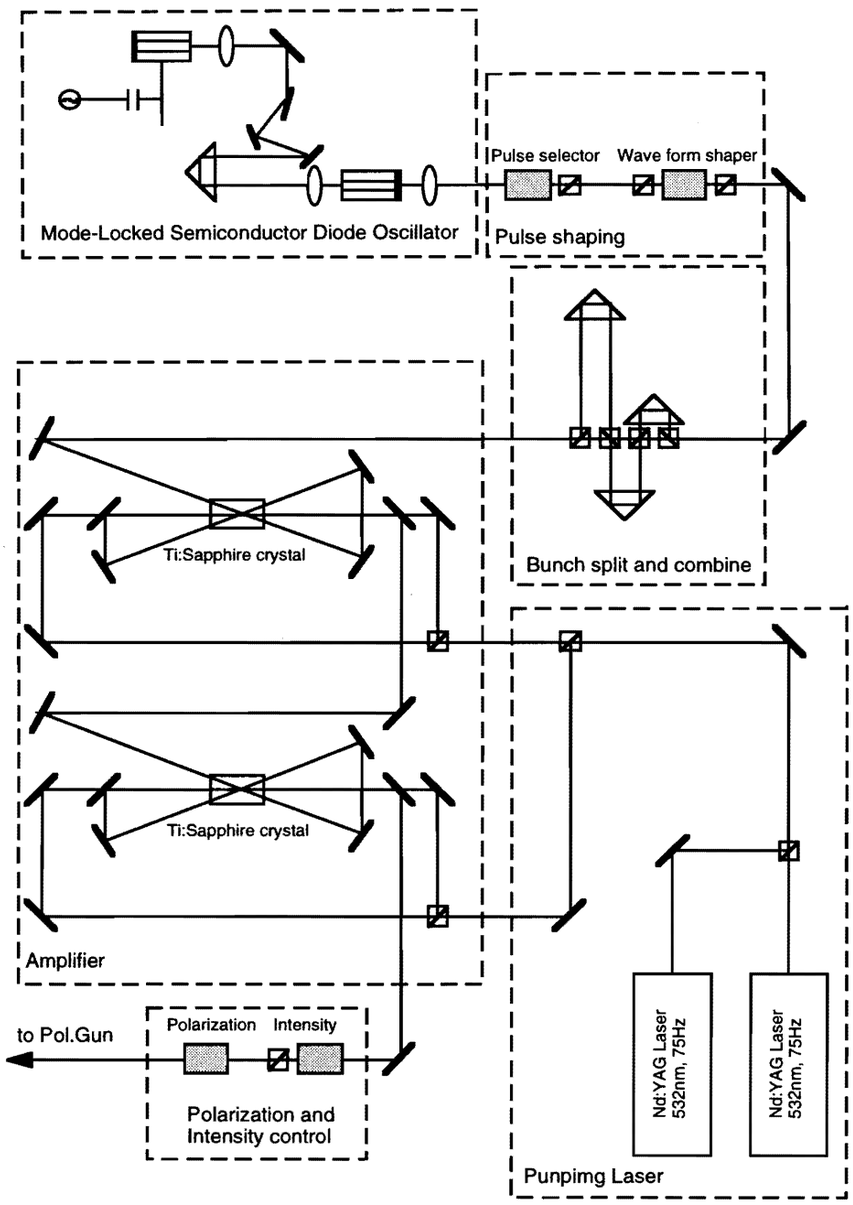

Figure 3.7: *Schematic of the laser system proposed for JLC.*

using the cathode-test-systems operated at Nagoya Univ. and KEK, respectively.

Construction and Beam Experiments of the 200 kV Gun System

A 100 kV polarized gun is currently being operated with a Ti:Sapphire pulse (5 ns width) laser system at Nagoya Univ.; it is used for studies of surface charge limit effect using different types of photocathodes.

The design work of the 200 kV gun system has been progressing. It is almost completed, and some components of the gun have already been constructed. For example, a cathode preparation chamber with heat-cleaning and activation mechanisms (Figure 3.6) has been built, and the first extraction of a photo-current was already successfully achieved.

A key issue in building the 200 kV gun system (shown in Figure 3.3) is considered to be the field emission dark current from the cathode electrode. A pilot study to master the techniques of " how to reduce the dark current under high gradient DC field" has been continued by the Nagoya-KEK collaboration. Some experiments on stainless steel electrodes have already been finished, as explained earlier; the obtained techniques will be applied for the fabrication of electrodes for the 200 kV gun.

After completion of the 200 kV gun system, studies on the dark current and the lifetime of photocathodes must be conducted under a high gradient (≥ 3 MV/m) with a bias of 200 kV. This is to ensure the system reliability.

The evelopment of the laser system must be done in parallel with the gun construction. First, the feasibility of the scheme proposed in Figure 3.7, must be established. Then, the key components of a 714 MHz mode-locked diode laser system should be built for various test measurements. Important topics concerning the study are the available range of the pulse width, which is desired to be as close as possible to 700 ps, and stability of the amplitude and frequency for 714 MHz oscillation. If the multi-bunch-structure is realized by pulses from the diode laser, these seed pulses will be amplified by the conventional multi-pass amplification procedure to meet the energy requirements.

The 200 kV gun system, combined with this laser system, will be able to produce a polarized electron beam with the multi-bunch structure required at JLC. It is highly desirable to implement this system as the injector of an actual accelerator for studying the long-term stability and other aspects in operation.

Development of Polarized RF Gun

As an upgraded design of a polarized electron gun, the concept of a polarized RF gun is an attractive idea. In an RF gun the field gradient of a conventional DC gun is replaced by a much higher RF-field gradient[10]. The RF gun has the possibility of significantly reducing the emittance of the beam extracted from the gun. These low emittance beams from the gun will greatly mitigate the required operating condition of the damping ring, in addition to elimiating the need for a bunching system. The simulation results show that the normalized emittance of 1×10^{-6} m-rad for a 1 nC bunch (10 to 20 ps width) can be achieved[11]. Many laboratories in the world are planning to develop RF guns, driven primarily by the needs for FEL's high brightness electron sources.

A prototype RF gun assembly with a double Nd:YAG laser system exists at KEK. It was constructed in order to investigate its feasibility for the production of a low emittance beam without polarization[12]. The laser-driven 3 GHz RF gun has been developed at CERN as an electron source for the CLIC test facility (CTF). It can produce a single pulse of 35 nC in 8 ps[13]. However, due to the technical difficulties listed below, the feasibility of a polarized RF gun has not yet been demonstrated.

(a) **Survivability of the activated NEA photocathodes**

For the successful and reliable operation of a polarized electron source, the vacuum in the vicinity of the NEA cathode must be extremely low, on the order of 10^{-11} Torr; thereby the dark current generated by field emission and/or RF breakdown must be reduced to an extremely low level.

Some interesting results have been obtained at KEK in selecting an appropriate copper material and treating it with pressurized ultra-pure water to achieve vacuum levels of 2×10^{-10} Torr in the S-band standing-wave cavity[14]. A surface gradient of 337 MV/m has been achieved without arcing or any rise in the pressure in the presence of RF power. A plan to construct an RF gun cavity with an extremely low dark current has been started by an international collaboration of CERN/KEK-Nagoya/SLAC using such techniques, to demonstrate the survivability of the NEA cathode in the RF gun.

(b) **Photoemission response time of the NEA photocathode**

The NEA surface allows the conduction-band electrons to make multiple attempts to escape into the vacuum, leading not only to a higher quantum efficiency, but also to a longer response time as a drawback. Measurements of response time for a thin layer of GaAsP photocathodes were recently made at Mainz, by using a conventional 100 kV gun[15]. The result shows that a response time of less than ~30 ps was observed for a 8 fC bunch charge using a laser pulse width of 5 ps.

The JLC injector requirement for the bunch width must not exceed 20 ps, and the response time of the photocathode must be less than 10 ps. Therefore, more exact response time measurements are highly required for a thin-layer cathode of strained GaAs with a high quantum efficiency under the high-intensity beam-extraction condition.

(c) **Peak-current limit of the NEA photocathode**

Studies on the surface-charge effect at SLAC have shown that the charge limitation in a 2 ns pulse depends almost linearly on the bias voltage, or equivalently, on the extraction field graidient at the surface, although the data were taken in a limited region of the field gradient, less than 1.8 MV/m.[6].

The JLC specifiations for the beam intensities of the RF gun are 6.4 nC in a 10 to 20 ps bunch 1.4 ns apart in a train of 126 ns. Therefore, the pulse width is about two orders of magnitude shorter than that used by the conventional SLC gun, and obviously the surface charge limit will set an upper limit on the current density extracted from the cathode. This means that the field gradient in the RF gun must be sufficiently large so as to overcome this charge limit. In the RF gun, the extraction field at the cathode surface is on the order of 100 MV/m, which is about two orders of magnitude higher than that of the DC gun.

At present, an accurate estimation of the charge limit for the RF gun is not possible, because there are no experimental data to measure the pulse-length dependence of the surface-charge limit in the 10 ps$\sim$1 ns range. Thus, it is highly desirable to conduct such measurements in the nearest possible future.

As another remark, the surface-charge limit is considered to be affected by various parameters of the photocathodes, such as the cathode thickness, dopant density, magnitude of the band gap, and the NEA magnitude, besides the cathode bias voltage. Experimental studies are also required to find a better semiconductor material and/or structure to mitigate the surface-charge limit.

3.3 Buncher System

3.3.1 Overview

The specifications for the 80 MeV preinjector are mainly driven by the energy acceptance and dynamic aperture of the damping ring.

Although the energy spread among multi-bunches will be compensated for by a $\pm\Delta$f energy-compensation system in the 1.98 GeV linac, the energy spread within a single bunch is determined by the bunch length at the exit of the preinjector.

The dynamic aperture of the damping ring determines the maximum emittance allowed for the beam from the injector linac. Assuming no emittance growth in the 1.98 GeV linac, the specifications of the maximum emittance will be applied to the preinjector.

Table 3.5 shows the required specification of the 80 MeV preinjector. The maximum bunch population produced by the 80 MeV preinjector linac should be 3.0×10^{10}, allowing for the beam loss to the interaction point.

Beam energy	80 MeV
Number of pulses	85
Bunch population	3.0×10^{10}
Bunch separation	1.4 ns
Bunch length (FWHM)	<10 ps
Normalized emittance	$<3\times10^{-4}$rad m (1σ)
Energy spread (Full Width of 90% beam)	<1% (each bunch at 1.98 GeV)

Table 3.5: *Required specifications of the 80 MeV preinjector.*

As shown in Figure 3.10, the preinjector consists of a thermionic electron gun, two sub-harmonic bunchers, four single-cell bunchers, an accelerating structure, a matching section of the beam lattice, an energy analyzer and beam instrumentation.

3.3.2 Buncher System for Multi-bunch Operation

The multi-bunch beam from the gun is extracted by applying an rf voltage to the grid. Due to the frequency response of the grid-cathode assembly, the beam has a bunch length of 1 ns FWHM, while the bunch spacing is 1.4 ns. As a result, a completely separated multi-bunch can not be produced by using the triode thermionic gun system.

The buncher system consists of three 714 MHz subharmonic bunchers (SHB), and a 1428 MHz traveling wave buncher. In order to realize the bunch length required for the preinjector, beam-loading of the multi-bunch is a key issue to be solved. Each bunch contains more than 3×10^{10} electrons. Such a high current produces a cumulative loading voltage in the bunching cavity, which distorts the cavity voltage. To avoid phase shifting of the bunching voltage due to this beam-loading, a new type of SHB cavity will be adopted. An SHB cavity is driven by two rf systems. One rf system feeds a 714 MHz rf pulse to produce the bunching field in the cavity. The other rf system feeds a pulse at the injection of the beam in order to cancel the beam induced field. As a result, all the multi-bunches are bunched by the bunching field with both the same amplitude and phase.

Figure 3.8 shows the configuration of the SHB rf system. To maintain efficient bunching effects, three 714 MHz SHB cavities are to be installed at optimum Z-positions. A 1428 MHz traveling buncher is to be installed before the 3 m-long 2856 MHz S-band accelerating structure.

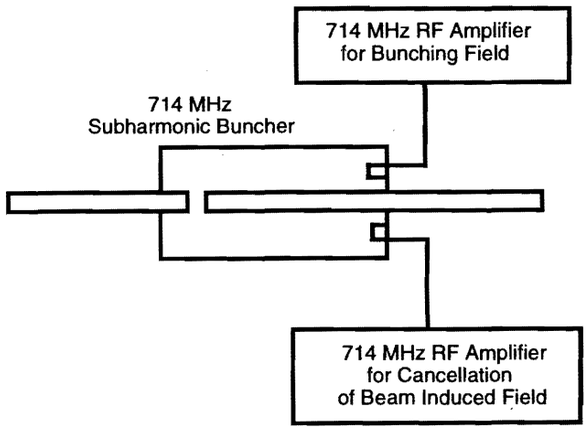

Figure 3.8: *Schematic drawing of the SHB rf system.*

3.3.3 RF System of the Buncher

The rf system of 80-MeV preinjector linac consists of six 714 MHz power amplifiers for three SHB cavities, a 60 MW 1428 MHz L-band klystron for a traveling-wave buncher and a 100 MW 2856 MHz S-band klystron. Three 715 MHz amplifiers of the SHB's are 20 kW electric-tube amplifiers for generating the bunching field. The pulse length is 30 μs. Three solid-state amplifiers are used to produce 30 kW output pulses with a first rise time for canceling the beam-induced field. The required pulse length for the cancellation is slightly longer than 119 ns. The phase and amplitude of the SHB cavities are controlled by a low-level circuit at the input stage of the power amplifiers.

3.3.4 Accelerator Section

The accelerator section of the 80-MeV preinjector consists of a 3 m-long constant-gradient accelerating structure. This is associated with a 1 m-long accelerating structure for the energy-compensation system. The geometrical dimension of the constant-gradient structures is identical to the structure of the 1.54 GeV ATF linac.

When the beam is injected 119 ns before the filling time of the rf power into the accelerating structure, the energy spread of 85 bunches is estimated to be 7.1 %, as shown in Figure 3.9. By using an energy-compensation scheme based on the ΔT technique, the energy spread is reduced to 2.7 %.

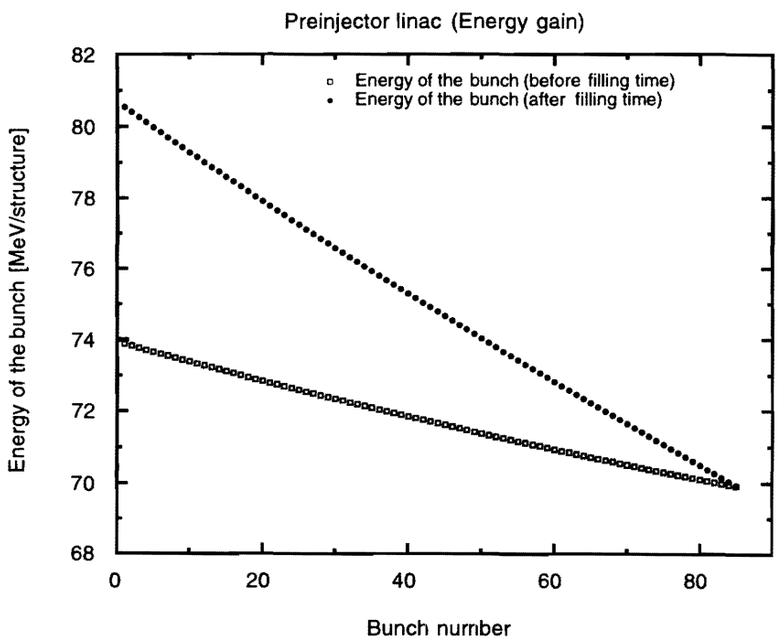

Figure 3.9: *Energy spread of the 80 MeV preinjector linac.*

3.3.5 Preinjector Instrumentation

The beam instrumentation of the preinjector consists of current-transformer monitors, wall-current monitors, phosphor screen monitors, strip-line type BPMs, optical transition radiation (OTR) monitors and a wire scanner. All of the instrumentation is similar to that which has been developed and is currently being used at the 1.54 GeV ATF linac.

The bunch intensity is measured by using an amorphous core monitor and wall-current monitors. The beam position is observed by a strip-line position monitor. The OTR monitor and the wire scanner

are installed downstream of the 1 m-long ECS structure. The bunch-by-bunch beam energy and its energy spread are analyzed at a 45-degree energy analyzer magnet and observed by the OTR monitor with a fast-gate camera. The bunch length is measured by the OTR monitor with a streak camera. A wire scanner is routinely used for emittance measurements. The bunch-by-bunch emittance is also obtained from the OTR profile as a function of the strength of the magnetic field of the quadruple magnet located upstream of the OTR monitor.

3.4 1.98 GeV Damping Ring Injector Linac

The 1.98 GeV damping ring injector linac has to accelerate multi-bunch electrons for injection to a low-emittance damping ring. Table 3.6 gives the basic parameters of the beam required based on the operation of the damping ring. A multi-bunch consists of a bunch train, each consisting of 85 bunches. The bunch population is $\sim 1 \times 10^{10}$ electrons and the bunch spacing is 1.4 ns. A maximum energy spread of 90 % of the electrons in a multi-bunch is 1.0% full width, and the normalized emittance at the end of the linac is required to be less than 1×10^{-4} m·rad (1σ). The linac is operated at a repetition rate of maximum 150 pps.

Beam energy	1.98 GeV
Bunch population	1×10^{10} electrons/bunch
Bunches/train	85
Bunch spacing	1.4 ns
Repetition rate	150 pps
Energy spread (Full Width)	<1.0 % (90% beam)
Normalized beam emittance	1×10^{-4} m·rad (1σ))

Table 3.6: *Basic Parameters of 1.98 GeV damping ring injector linac.*

As shown in Figure 3.10, the 1.98 GeV electron injector linac consists of two 80-MeV preinjector linacs, each equipped with 16 units of regular accelerator sections and a $\pm\Delta F$ energy-compensation system. The two 80 MeV preinjectors are installed in parallel so as to offer high maintainability of the injector complex. One of the 80 MeV preinjector linacs can provide a beam during maintenance of the other preinjector. The parameters of the 1.98 GeV injector linac are summarized in Table 3.7.

Beam Energy for DR	1.98 GeV
Total length	158 m
Preinjector	18 m
Linac	140 m (active length: 96 m)
80-MeV Preinjector	
Beam Energy	80 MeV
Number of Bunches	85

Bunch Population	$<3\times10^{10}$ electrons
Bunch Separation	1.4 ns
Klystron	
Klystron Peak Power	100 MW
Klystron Pulse Length	1.0 μs
Number of Klystrons	1 / Preinjector
RF Pulse Compression	none
Klystron Modulator	
Total Number	1
Regular Accelerating Sections	
Accelerating Structure	$2\pi/3$ mode constant gradient
Total length	3 m
Total number	32
Accelerating Field*	
Maximum Field	52 — 38 MV/m
Average	33 MV/m
RF Frequency	2.856 GHz
Feed Peak Power	200 MW/Structure
Klystron	
Klystron Peak Power	80 MW
Klystron Pulse Length	4.5 μs
Number of Klystrons	16
RF Pulse Compression	SLED–I
Power Gain	5.0 at peak
Klystron Modulator	
Total Number	16

Table 3.7: *Parameters of the 1.98 GeV injector linac. *The quoted value of the maximum field is for the case with no beam-loading. The "average field" is with beam-loading.*

3.4.1 Accelerator Section of the 1.98 GeV Injector Linac

The accelerator section of the 1.98 GeV injector linac is to be located downstream of the 80-MeV pre-injectors. It consists of 16 rf units feeding 32 accelerating structures, and an additional 4 rf units for 8 energy-compensation structures. Also, a series of quadrupole magnets to form the linac lattice, beam instrumentation and active alignment systems are included. The beam-transport lines are located between two 80 MeV preinjector linacs and the accelerator section. A beam scraper in the beam-transport line is introduced to eliminate any low-energy component in a bunch tail. The configurations of the accelerating structures and $\pm\Delta F$ energy-compensation structures are shown in Figure 3.11.

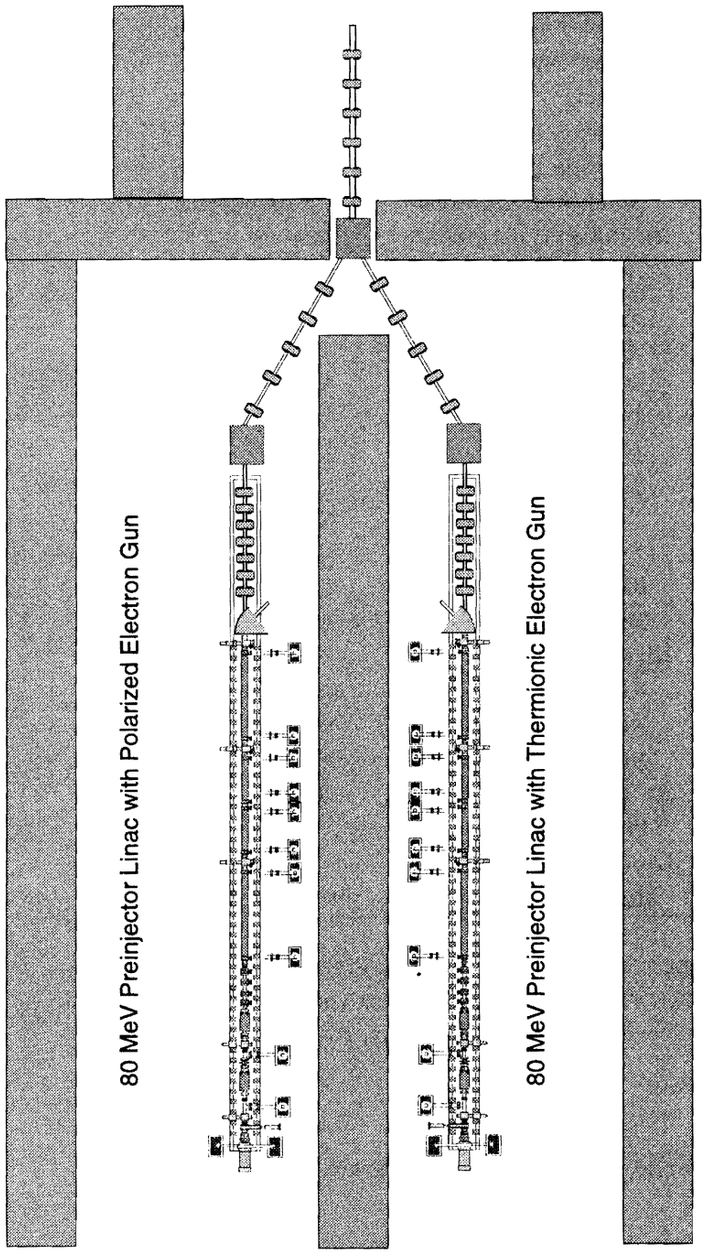

Figure 3.10: *Schematic Drawing of the 80-MeV Preinjectors.*

RF System of the Accelerator Section As shown in Figure 3.11, the rf system of the accelerator section consists of 16 rf units. The rf unit consists of an 80 MW klystron, a klystron modulator, a SLED cavity, rf waveguides, two 3 m-long accelerating structures and rf dummy loads, as shown in

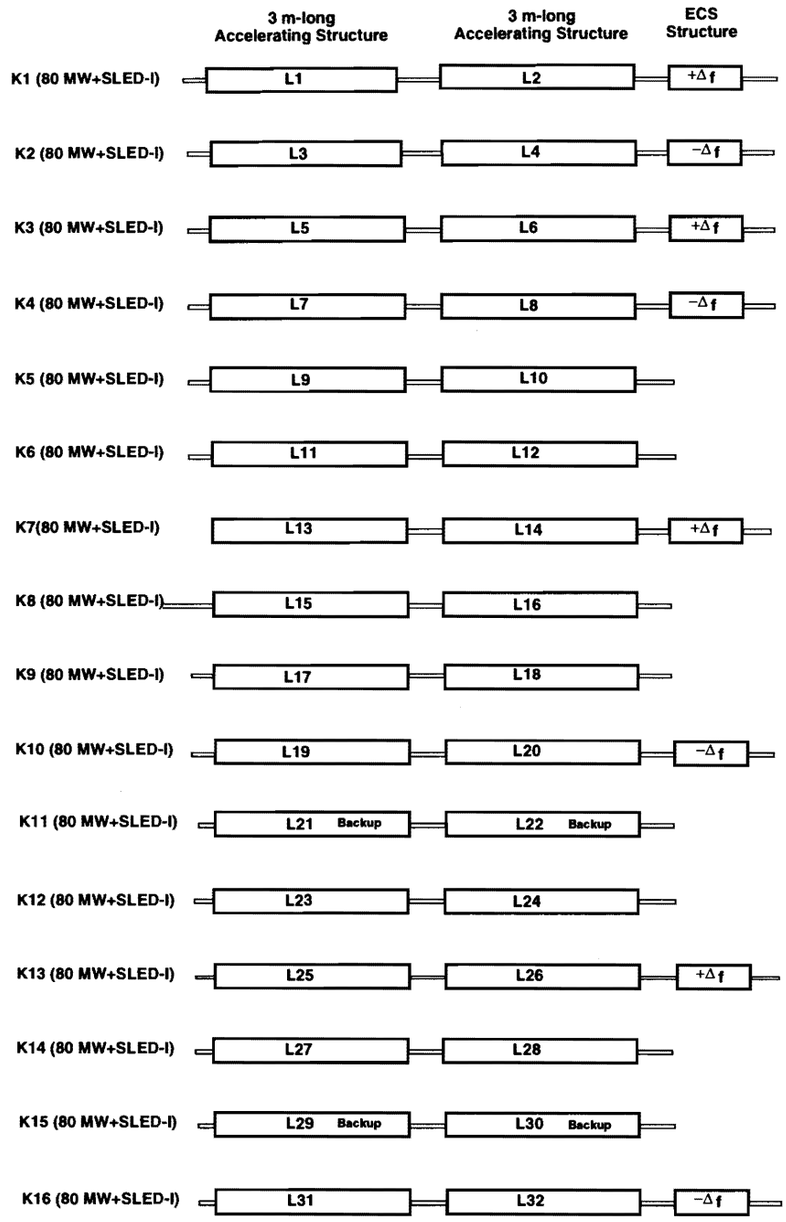

Figure 3.11: *Configuration of accelerator section of 1.98 GeV Linac.*

Figure 3.12. The klystron produces an rf peak power of 80 MW with a pulse duration of 4.5 μs. The rf power is fed into a SLED cavity. To conduct SLED operation, the rf phase is reversed at 3.5 μs for each machine pulse. A peak power of 400 MW with a pulse duration of 1.0 μs is extracted from the SLED cavity. The rf power from the SLED is divided into two rf waveguides, and feed a peak power

of 200 MW into a 3 m-long accelerating structure.

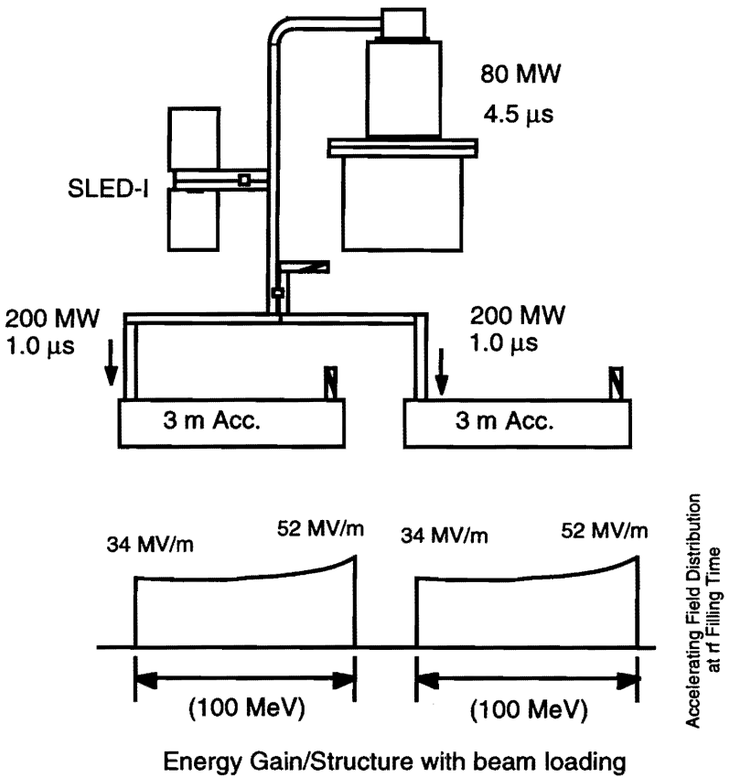

Figure 3.12: *RF unit of accelerator section of the 1.98 GeV Linac.*

The damping ring injector linac should be designed for a wide rage of bunch populations. The $\pm\Delta F$ energy-compensation system has high flexibility to cope with bunch populations from near-zero to 4×10^{10} electrons/bunch. This is accomplished by adjusting the RF power of the klystrons.

The rf unit for an energy-compensation system consists of a 60 MW klystron modulator. The accelerating structures are designed to work at slightly different frequencies from the canonical frequency 2856 MHz, with a phase velocity equal to the velocity of light. The total length of four $\pm\Delta F$ accelerating structures at the low-energy section is 1 m. The length of four $\pm\Delta F$ accelerating structures at high energy section is 3 m. The rf power from an rf unit is fed into two structures. The klystron produces a rectangular rf pulse of 60 MW peak rf power of 1 μs pulse duration.

Accelerating Structures The main parameters of the accelerating structures are listed in Table 3.8. In order to obtain a wide operational margin for emittance preservation, three types of

accelerating structures having mutually different dimensions of the beam aperture ($2a$) have been fabricated for studies. Table 3.9 shows the size of the disk apertures of the accelerating structures.

Table 3.8: *Main parameters of the accelerating structures.*

Operating frequency	2856 MHz
Phase shift/cell	$2\pi/3$
Electric-field distribution	Constant gradient
Structure length	3 m
Number of cells	84 cells + 2 couplers
Quality factor	13,000
Shunt impedance	60 MΩ/m
Attenuation parameter	0.57
Group velocity	$0.0204 \sim 0.0065c$
Filling time	0.83 μs

Table 3.9: *Disk aperture of three types of accelerating structures.*

Structure Type	A	B	C
Aperture of 1st Disk (mm)	25.251	25.269	25.287
Aperture of Last Disk (mm)	18.376	18.414	18.453

Active Alignment System In order to keep any emittance growth in the linac at the minimal level, the accelerating structures should be aligned to less than 200 μm r.m.s. for both the vertical and horizontal directions. The support tables of the accelerator section of the linac need to be equipped with an active mover mechanism and wire-position sensors. The 140 m-long wires are stretched in both sides of the accelerator section of the 1.98 GeV linac. One of its ends is fixed to the preinjector stage, which does not have an active mover mechanism; the other end is stretched by a tension weight. Figure 3.13 shows a schematic diagram of the active alignment system.

Each position sensor consists of a pair of induction coils that are electrically connected in series, and mounted on a vertically movable offset stage fixed on a support stage. The center position of a pair of induction coils is pre-calibrated on the calibration stand. The sensors are installed at four corners of the support table for Q-magnets and beam monitors, and a short support table for an accelerating structure. As for the long support table for the two accelerating structures, six sensors are installed at four corners of the support table, and both sides of the center of the table.

The wire position is detected by a synchronous detection of the signal from the differential coils using a 60 kHz, 100 mA AC current on the wire. A frequency of 60 kHz is chosen as the frequency range suitable for the use of a lock-in amplifier in order to obtain a stable and reproducible measurement. The resolution of the position sensor is 2.5μm. The dynamic range of the sensors is $\pm$2.5 mm. This is determined by the gap length between two induction coils. Figure 3.14 shows the expected signals to

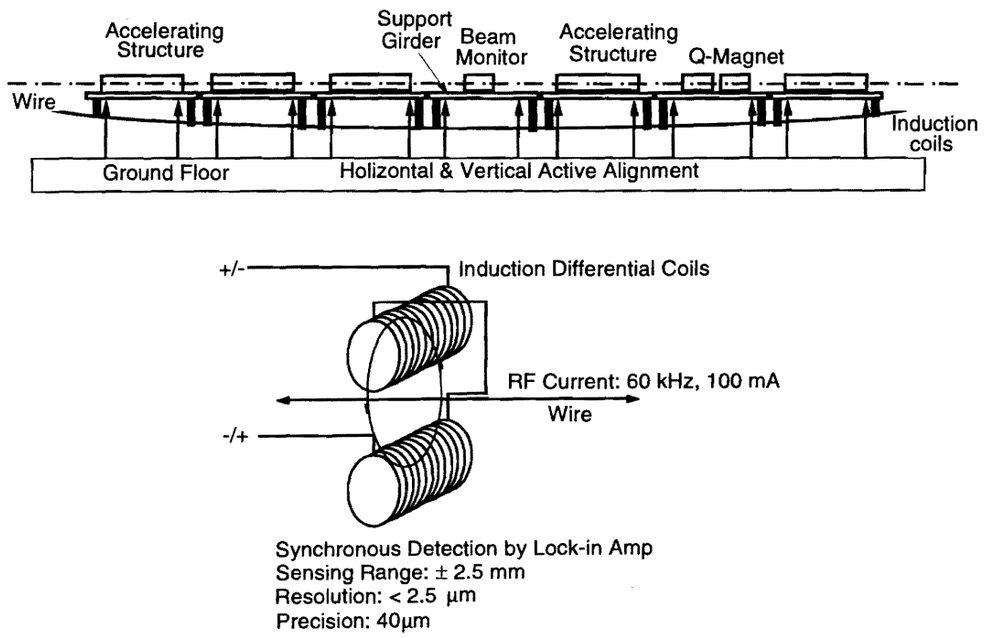

Figure 3.13: *Schematics of the active alignment system of the 1.98 GeV linac.*

be observed with differential coils as function of the support displacement. The performance similar to this expectation has been confirmed with the support system of the 1.54 GeV ATF injector linac at KEK.

The linac support tables are machined with an accuracy better than $\pm 10\mu$m. The left side of the support table has a reference line parallel to the beam axis. The accelerating structures, Q-magnets and beam monitors are aligned to the reference line with an accuracy of less than $\pm 10\mu$m. Each sensor installed on the left side of the linac has two pairs of induction coils to detect the vertical and horizontal positions from the wire. These sensors are aligned along the sag of the wire with a vertical offset. Therefore, the reference line is aligned in a straight line. Each sensor installed on the right side of the linac stages has a pair of induction coils for measuring only the vertical position. As a result, the support tables are vertically and horizontally aligned with an accuracy of less than 20μm r.m.s.

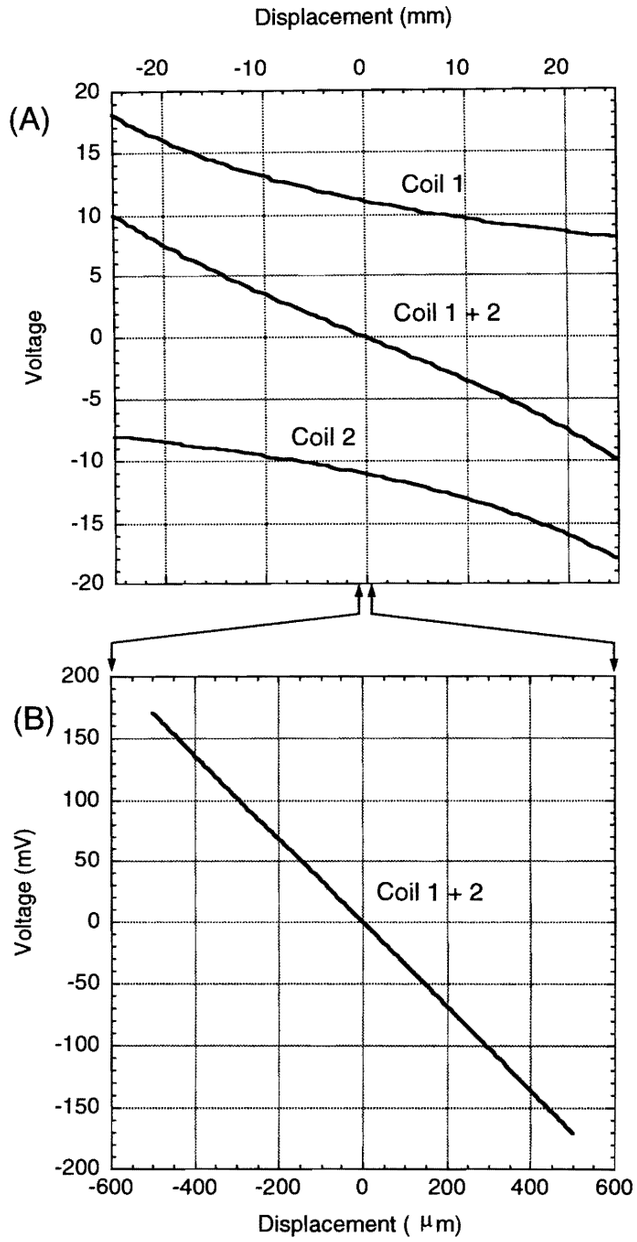

Figure 3.14: *Calculated voltage to be induced on induction coils as function of the support displacement. Case (A) shows the behavior with displacement* $< \pm 25$ *mm. Signals from the two differential coils, as well as the combined data are shown. Case (B) shows the behavior within displacement* $< \pm 500 \mu m$.

References for Chapter 3

[1] T. Nakanishi, A lecture note for Joint US-CERN-Japan International School published in "Frontiers of Accelerator Technology" (1996, World Sci.Pub.) 665-680

[2] T. Nakanishi et al., Phys. Lett. A158 (1991) 345-349
H. Aoyagi et al., Phys. Lett. A167 (1992) 415-420

[3] T. Saka et al., Jpn. J. Appl. Phys. 32 (1993) L1837-40.

[4] T. Omori et al., Phys. Rev. Lett. 67 (1991) 3294-97.

[5] T. Omori et al., Jpn. J. Appl. Phys. 33 (1994) 5676-80

[6] R. Alley et al., Nucl. Instrum. and Math. A365 (1995) 1-27
Independent of space charge limit, there is another limit to the current density extracted from the NEA semiconductor photocathodes. This limit is here called the "surface charge limit", because this effect was observed only in the NEA cathode. It depends on the rate of arrival of conduction-band electrons at the NEA surface and the rate of discharge due to the escape into vacuum or due to the recombinations with holes. This phenomenon was first observed at SLC.

[7] Y. Kurihara et al., Jpn. J. Appl. Phys. 34 (1994) 355-358.

[8] T. Nakanishi et al., DPNU-96-60 (Nov.1996), published in Proc. of 12th high energy spin physics symposium (September, 1996, Amsterdam).

[9] H. Avramopoulos, Published in Proc. of 12th high energy spin physics symposium (September, 1996, Amsterdam),
M. Poelker, Appl. Phys. Lett. 67 (1995) 2762-2764,
J. Hoffmann et al, Nucl. Instrum. and Meth. A383 (1996) 624-626

[10] J. Clendenin et al., Nucl. Instrum. and Math. A340 (1994) 133-138

[11] D. T. Parmer et al., Proceedings of PAC-95 (1995)

[12] M. Yoshioka et al., Int. J. Mod. Phys. A (Proc. Suppl.) 2A (1993) 120-123

[13] H. Braun, Proceedings of LC-95 (1995) 482-501

[14] H. Matsumoto, Proceedings of Linac-94 (1994) 302-304,
H. Matsumoto, Proceedings of Linac-96 (1996) 626-630

[15] P. Hartmann et al., Nucl. Instrum. and Math. A379 (1996) 15-20

Authors and Major Contributers of Chapter 3

- Hitoshi Hayano
- Takashi Naito
- Seishi Takeda
- Tsutomu Nakanishi
- Shoji Okumi
- Kazuaki Togawa
- Chihiro Suzuki
- Chikako Takahashi
- Tsunehiko Omori
- Yoshimasa Kurihara
- Masakazu Yoshioka
- Hiroshi Matsumoto
- Yasunori Takeuchi
- Masafumi Tawada
- Hiromichi Horinaka
- Kenji Wada

The authors would like to express their gratitude to Mr. Kazuharu Nishitani of ATC Corporation for his help in preparing and conducting experiments on the polarized electron source. The authors would like to thank Dr. Takashi Saka and Dr. Toshihiro Kato of New Material Research Laboratory, Daido Steel Co. and Dr. Toshio Baba and Dr. Masashi Mizuta of Fundamental Research Laboratory of NEC Corporation for fabricating photocathodes for the polarized electron source and for measuring their characteristics.

CHAPTER 4

Positron Source

Contents

4.1 Introduction

The JLC positron source needs to produce an intense positron beam at a repetition rate of 150 Hz. The required total charge per pulse is of about 6×10^{11} positrons. The parameters relevant to the positron source system are summarized in Table 4.1.

Number of particles per bunch (at IP)	7×10^9
Number of bunches per rf-pulse	85
Number of particles per pulse	5.95×10^{11}
Repetition rate[Hz]	150
Bunch spacing [ns]	1.4
Damping Ring injection energy [GeV]	1.98
Damping Ring acceptance (normalized) [rad·m]	1×10^{-4}

Table 4.1: *JLC parameters related to the positron source*

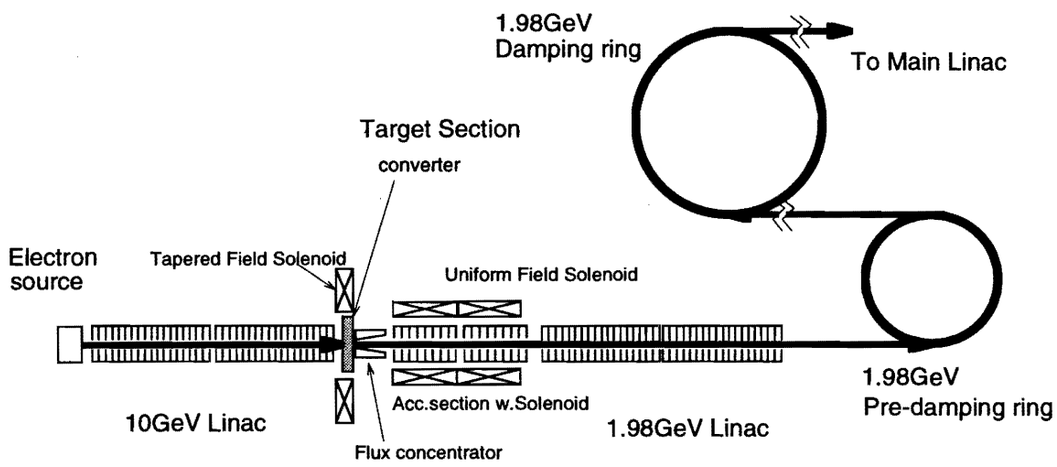

Figure 4.1: *Schematic diagram of the positron source system for the JLC.*

The method adopted in this design study for producing positrons is a conventional scheme, which exploits electro-magnetic cascade showers initiated by high-energy electrons that impinge on a converter target. A schematic view of the system is shown in Figure 4.1. The system consists of a 10 GeV electron injector, a target section, a 1.98 GeV pre-linac, and a pre-damping ring. The target section consists of the converter target and a phase-space transformer, followed by an accelerator section which is placed within a uniform solenoid magnetic field.

In the following sections, outlines of the design of individual subsystems are presented.

4.2 10 GeV Electron Injector

The 10 GeV positron production linac is designed to accelerate multi-bunch electrons to the positron target. Table 4.2 gives the basic parameters of the beam for positron production. Each multi-bunch train consists of 85 bunches. The bunch population is 1×10^{10} electrons and the bunch spacing is 1.4 ns.

Beam energy	10 GeV
Bunch population	1×10^{10} electrons/bunch
Bunches/train	85
Bunch spacing	1.4 ns
Repetition rate	150 pps
Energy spread (Full Width)	<1.0 % (90% beam)
Normalized beam emittance	$<3\times10^{-4}$ m·rad (1σ)

Table 4.2: *Basic parameters of 10 GeV positron production linac.*

As shown in Figure 4.3–4.4, the 10 GeV electron injector linac consists of two 80-MeV preinjector linacs, 80 units of regular accelerating sections and $\pm\Delta$f energy-compensation systems. The two 80 MeV preinjectors are installed in parallel to obtain high maintainability of the injectors, as shown in Figure 4.2. One of the 80 MeV preinjector linacs can provide a beam during maintenance of the other preinjector. The electron sources would be a thermionic gun or photocathode gun. The beam-transport lines are located between two 80 MeV preinjector linacs and the accelerator section. The beam scraper in the beam transport line is useful for removing the low-energy component in a bunch tail. The parameters of the 10 GeV injector linac are summarized in Table 4.3.

Beam Energy	10 GeV
Total length	158 m
Preinjector	18 m
Linac	350 m (active length: 240 m)
80-MeV Preinjector	
Beam Energy	80 MeV
Number of Bunches	85
Bunch Population	$<3\times10^{10}$ electrons
Bunch Separation	1.4 ns
Klystron	
Klystron Peak Power	100 MW
Klystron Pulse Length	1.0 μs
Number of Klystrons	1 / Preinjector
RF Pulse Compression	none
Klystron Modulator	

Total Number	1
Regular Accelerating Sections	
Accelerating Structure	$2\pi/3$ mode constant gradient
Total length	3 m
Total number	160
Accelerating Field*	
Maximum Field	52 - 38 MV/m
Average	33 MV/m
RF Frequency	2.856 GHz
Feed Peak Power	200 MW/Structure
Klystron	
Klystron Peak Power	80 MW
Klystron Pulse Length	4.5 μs
Number of Klystrons	80
RF Pulse Compression	SLED–I
Power Gain	5.0 at peak
Klystron Modulator	
Total Number	80

Table 4.3: Parameters of the 10 GeV injector linac. *Maximum accelerating field means the unloaded accelerating field gradient. Average accelerating field takes the field reduction due to beam-loading into account.

4.2.1 Accelerator Section of the 10 GeV Injector Linac

The accelerator section of the 10 GeV linac is located downstream of the 80-MeV pre-injectors. It consists of 80 rf units for 160 accelerating structures, 12 rf units for 12 energy-compensation structures, a linac lattice, and beam instrumentation and active alignment systems. The configuration of the accelerating structures and $\pm\Delta F$ energy-compensation structures is shown in Figures 4.3 and 4.4.

Accelerating Structures The main parameters of the accelerating structures are listed in Table 4.4. These structures are based on the same design as the 8 GeV pre-accelerator linac.

RF System of the Accelerator Section The role of the accelerator section of the linac is to accelerate a multi-bunch beam from 80 MeV to 10 GeV with a minimum energy spread and a minimum emittance growth to obtain a small spot size at the positron target. The rf unit consists of an 80 MW klystron, a klystron modulator, a SLED cavity, rf waveguides, two 3 m-long accelerating structures

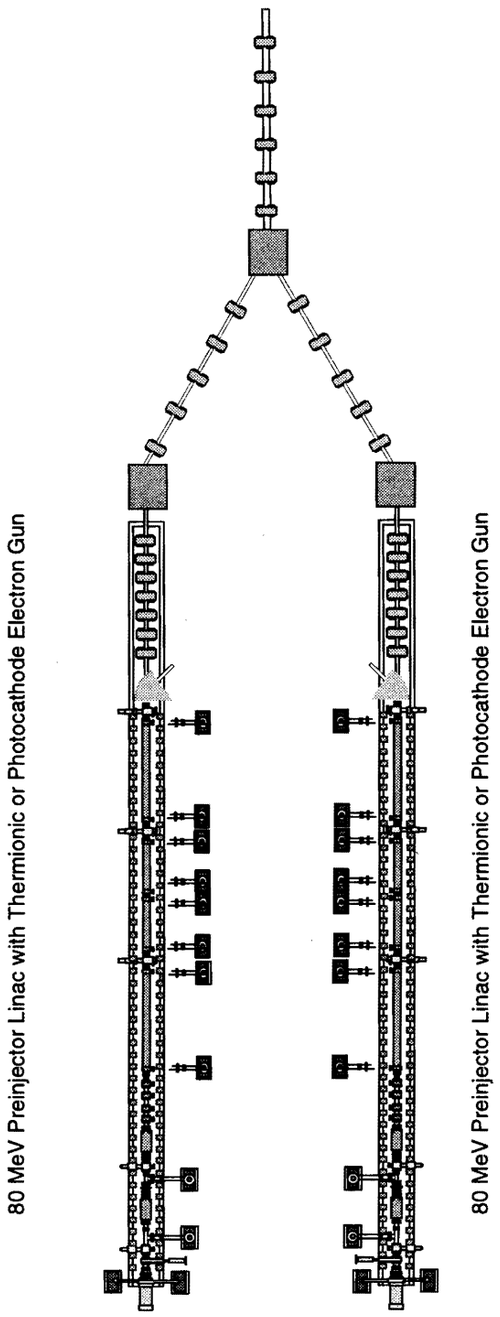

Figure 4.2: *Schematic Drawing of the 80-MeV Preinjectors for positron production.*

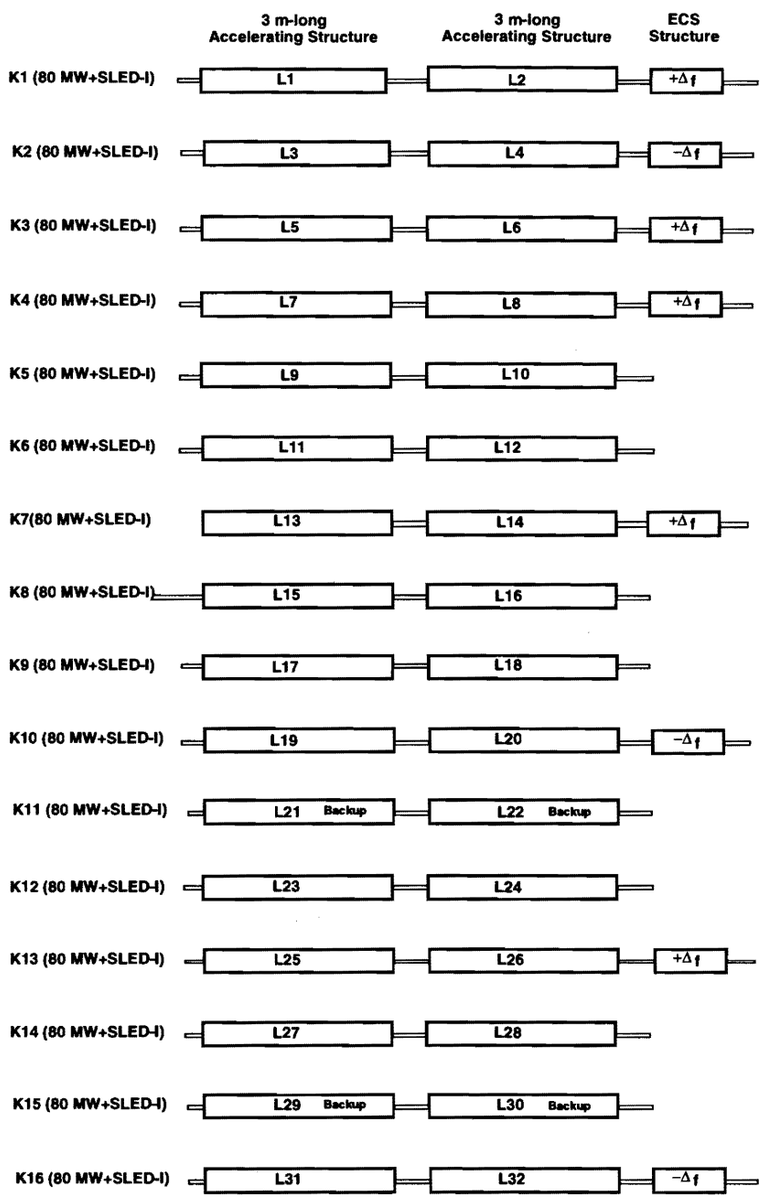

Figure 4.3: *Configuration of accelerator section of the 10 GeV Linac. (Sections from 80 MeV to 2 GeV)*

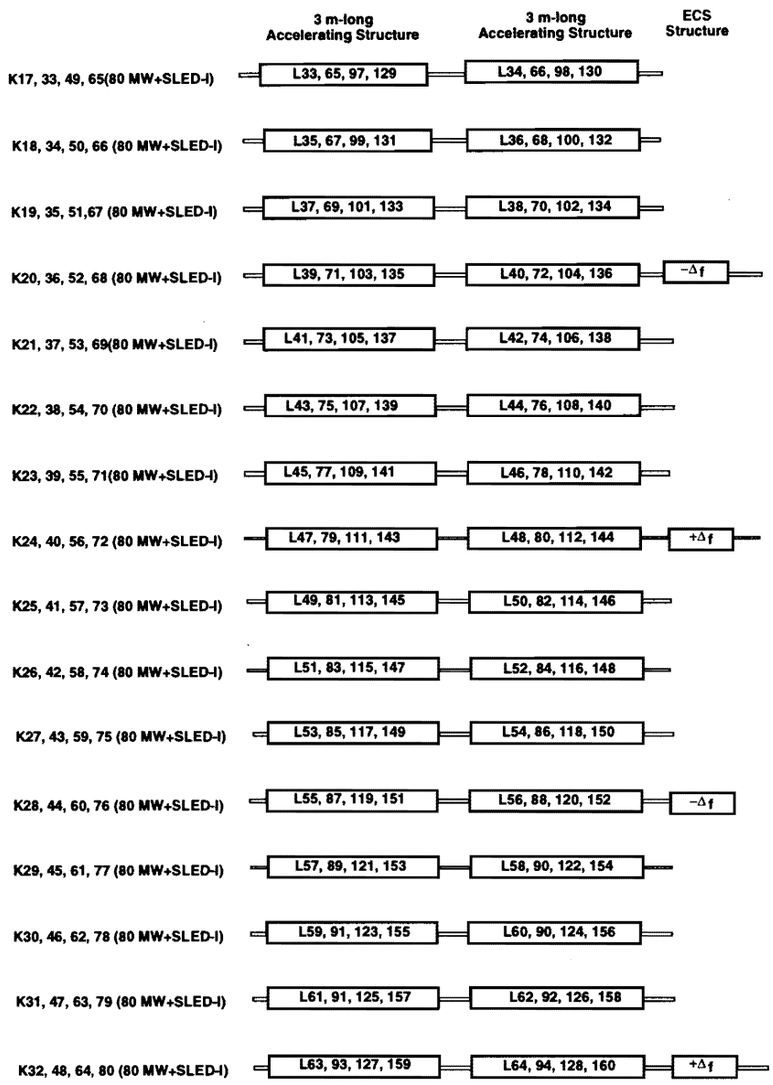

Figure 4.4: *Configuration of the accelerator section of the 10 GeV Linac. (Sections from 2 to 10 GeV)*

Table 4.4: *Main parameters of the accelerating structures.*

Operating frequency	2856 MHz
Phase shift/cell	$2\pi/3$
Electric-field distribution	Constant gradient
Structure length	3 m
Number of cell	84 cells + 2 couplers
Quality factor	13,000
Shunt impedance	60 MΩ/m
Attenuation parameter	0.57
Group velocity	$0.0204 \sim 0.0065c$
Filling time	0.83 μs

and rf dummy loads, as shown in Figure 4.5. This configuration is the same as that of 8 GeV pre-accelerator linac. The klystron produces an rf peak power of 80 MW with a pulse duration of 4.5 μs. The rf power is fed into a SLED cavity, and the rf phase is reversed at 3.5 μs. A peak power of 400 MW with a pulse duration of 1.0 μs is extracted from the SLED cavity. The rf power from the SLED is divided into two rf waveguides to feed a peak power of 200 MW into a 3 m-long accelerating structure.

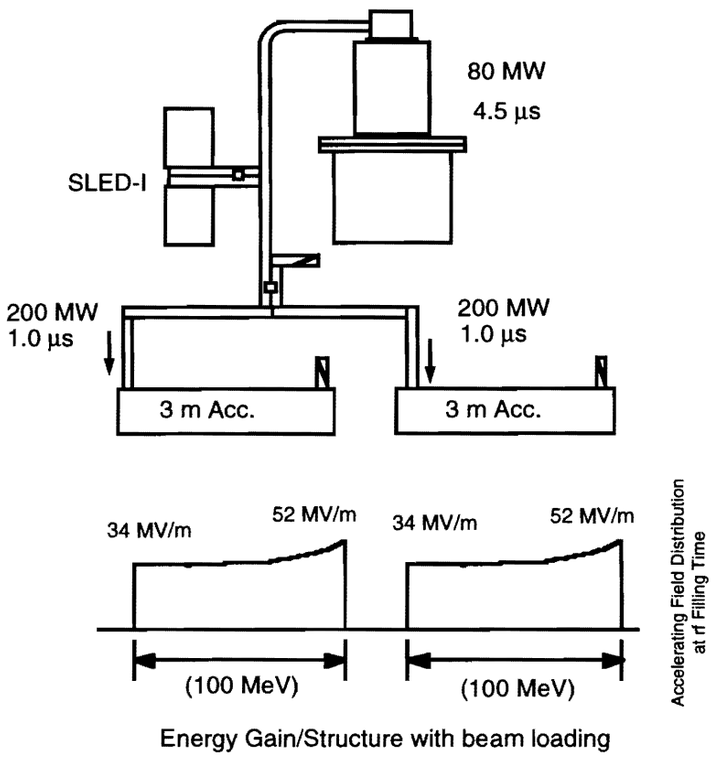

Figure 4.5: *RF unit of accelerator section of the 10 GeV Linac.*

4.3 Target Section

The scheme of the positron source[3] section adopted here is similar to what has been used for the SLC positron source, which had been successfully operated for several years[4]. However, the requirement at JLC is such that 20-times more positrons need to be produced per pulse, as compared to the operating condition at SLC. Meeting this requirement generally leads to the use of a more intense primary electron beam. Here, careful attention must be paid to an increased power dissipation on the converter target in terms of both the instantaneous and DC power.

In the design presented here the electron-beam spot size on the converter is increased so as to limit the energy density on the unit area of the target, while increasing the total beam energy. In addition, the magnetic field strength of the positron capture section is increased so as to obtain a higher collection efficiency. Also, as described later, a pre-damping ring is introduced to reduce the positron beam emittance so as to better match the injection acceptance of the damping ring.

Injected Electron Beam	
Energy [GeV]	10
Intensity [/ bunch train]	$\sim 6 \times 10^{11}$
rms beam radius [mm]	1.2
Beam power [kW]	147
Target Section	
Material	W–Re
Thickness [mm]	21 (6 Radiation length)
Phase-space Transformer Section	
Initial magnetic field [T]	8
Length [mm]	180
Accelerating Section With Solenoids	
Accelerating frequency [MHz]	2856
Repetition rate [Hz]	150
Accelerating gradient [MV/m]	30
Structure length [m]	1.5 (×2)
Iris diameter at the exit [mm]	26
Constant solenoid field [T]	0.8
Beam Transport To Pre-damping Ring	
Transverse acceptance [rad · m]	0.027
Energy acceptance [%]	± 1
Number of e^+ to the Pre-damping Ring per e^-	3.0

Table 4.5: *Main parameters of the JLC positron source .*

The positron production efficiency was studied using a Monte-Carlo program based on the TOPAZ[5] detector simulator, which covers the target section and the 1.98 GeV linac. The EGS[6] is used to

simulate an electro-magnetic shower in the converter. The main parameters of the positron source are summarized in Table 4.5.

A schematic view of the target section is shown in Figure 4.6. It comprises the converter, the tapered-field solenoid and the flux concentrator for the phase-space transfer of produced positrons, and the accelerating section with the Uniform field solenoid. Each subsystem is described below.

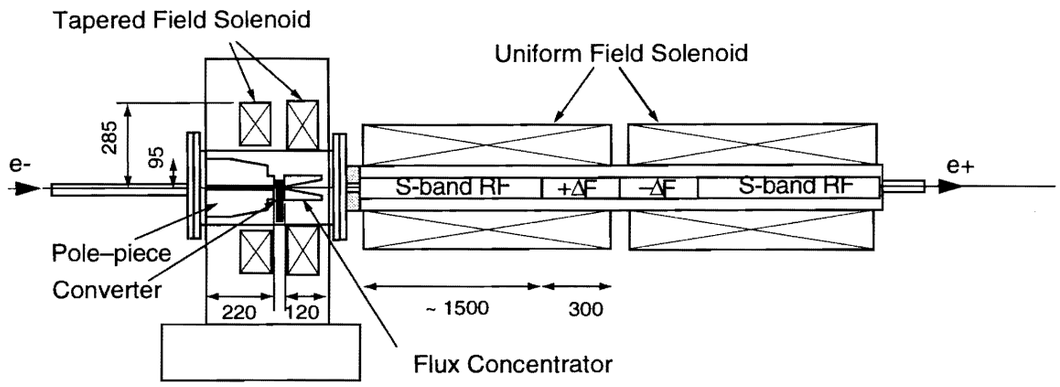

Figure 4.6: *Schematic diagram of the target section. The unit of component dimensions shown is in mm.*

4.3.1 Converter Target

A Tungsten-Rhenium alloy (W-Re) has been adopted as the converter material for this design. This W-Re material has a good track record as the target body at the SLC positron system.

S. Ecklund[7] has studied the thermal-stress limit of various materials. According to this study, no damage of a W-Re converter was observed for a beam energy density (ρ) of up to 2.0×10^{12} GeV/mm^2. Here, ρ is given by

$$\rho = \frac{NE}{\pi\sigma^2}, \tag{4.1}$$

where N is the number of incident electrons per pulse, E is its energy, and σ is the rms beam radius on the converter. In our design, ρ is chosen to be $\sim 1.4 \times 10^{12}$ GeV/mm^2, so as to stay within the limit quoted in[7].

As listed in Table 4.5, the thickness of the considered target is 6 radiation-lengths. According to simulation studies using EGS, about 1/3 of the total beam energy is expected to be absorbed by the converter.

	TFS 1	TFS 2
Inner radius (mm)	280	250
Outer radius (mm)	560	570
Coil height (mm)	100	100
Number of turns	14×10	16 × 10
Current (A)	900	900
Power (KW)	49	54

Table 4.6: *Parameters for TFS solenoid. TFS1 is the upstream solenoid and TFS2 is the downstream.*

4.3.2 Tapered Field Solenoid and Flux Concentrator

The positrons that emerge from the target are geometrically confined within a relatively small spatial cross section of radius that is comparable to that of the primary electron beam. However, they have a large transverse momenta of $\sim$ 3 MeV/c. The phase space of these positrons needs to be reduced so that they are acceptable for the accelerating sections downstream.

This phase-space transformation is accomplished by the combined use of a DC solenoid magnet and a pulsed magnet (flux concentrator), which produce an adiabatically varying magnetic field.

The tapered-field solenoid is a DC field solenoid magnet that surrounds the converter and the flux concentrator, as shown in Figure 4.6. Its field is peaked at 1.2 T immediately downstream of the converter. Then, the field gradually decreases along the beam direction. The flux concentrator provides an additional pulsed magnetic field.

A prototype positron target system that incorporates these concepts was developed for testing at ATF (Accelerator Test Facility) of KEK. Its cross-sectional view is shown in Figures 4.7 (A) and (B). A photograph is shown in Figure 4.8.

For operation at JLC, the target converter needs to be axially rotated so that localized heat accumulation will not build up, leading to damage of the target material. However, this mechanism has not been incorporated in the prototype. For testing at ATF, since the beam power and the repetition rate is low, the converter target is physically fixed in position, and the simple use of water cooling is sufficient.

A prototype coil for the flux concentrator was also built for testing at ATF. A schematic diagram is shown in Figure 4.9. The specifications of the TFS solenoid and the power source for the flux concentrator are summarized in Tables 4.6 and 4.7.

In a simulation study of the positron efficiency, we assumed that the longitudinal component of the magnetic field in the adiabatic device is given by

$$B_z = \frac{B_i}{1 + (\frac{B_i}{B_0} - 1)\frac{Z}{L}}, \tag{4.2}$$

where B_i is the initial magnetic field at the target exit, B_0 is that of the uniform field solenoid, and

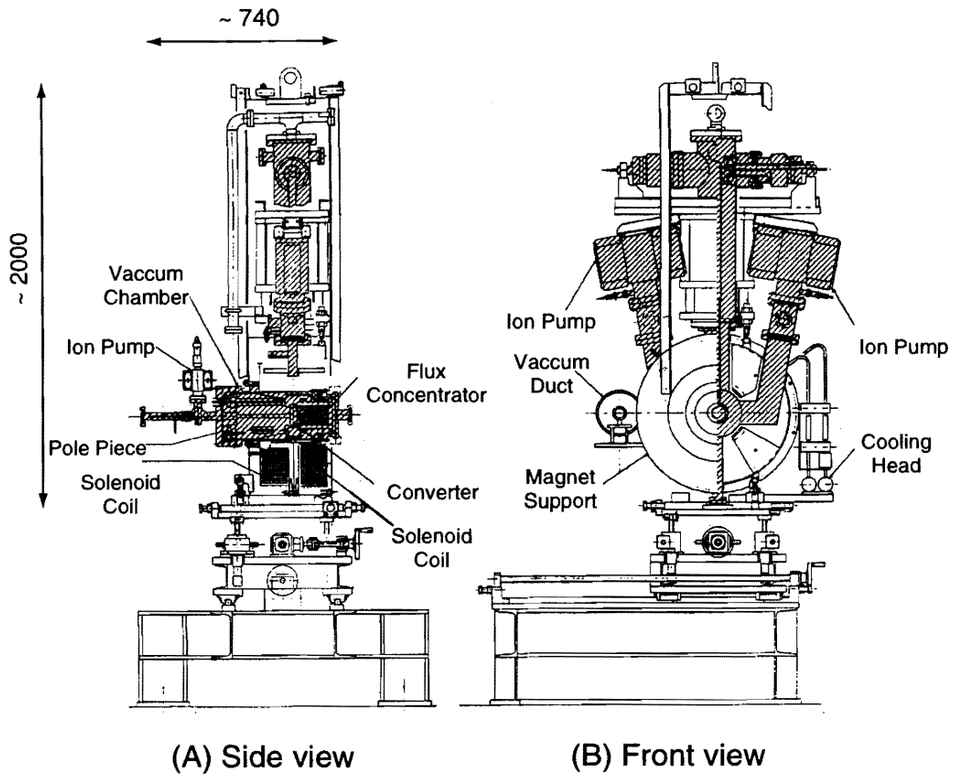

Figure 4.7: *Side (A) and front (B) views of the prototype target system.*

Maximum pulse current (kA)	16
Maximum pulse voltage (kV)	12
Pulse width (μs)	5 (100kHz half-sine wave)
Maximum Pulse frequency (Hz)	180
Inductance (μH)	1.1
Maximum field (Tesla)	5.8

Table 4.7: *Parameters of the power source of the Flux Concentrator.*

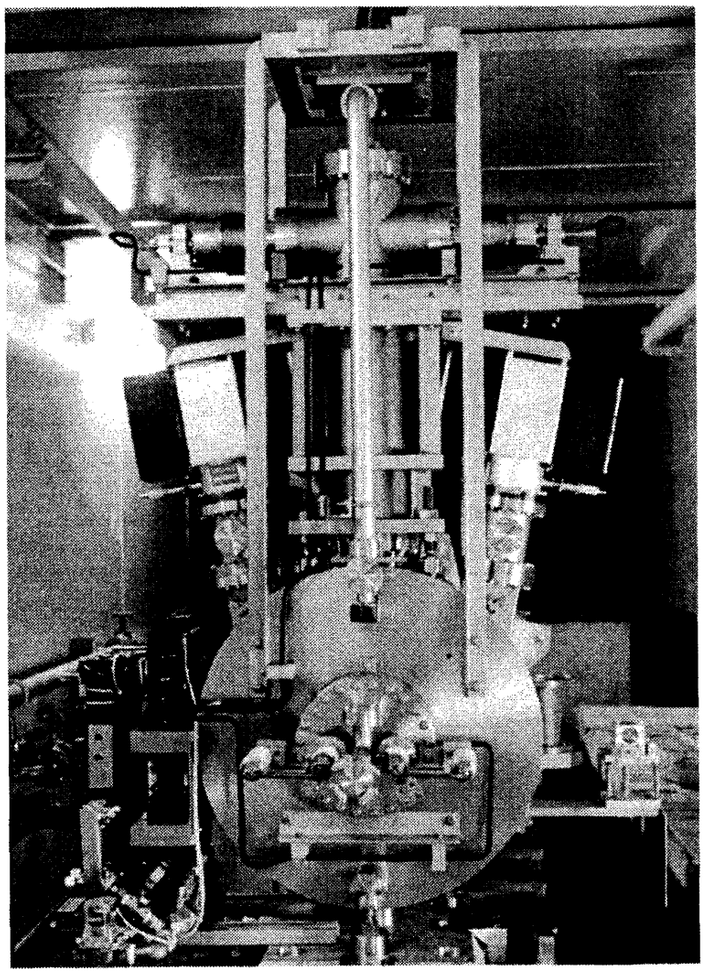

Figure 4.8: *Photograph of the prototype positron target built at KEK.*

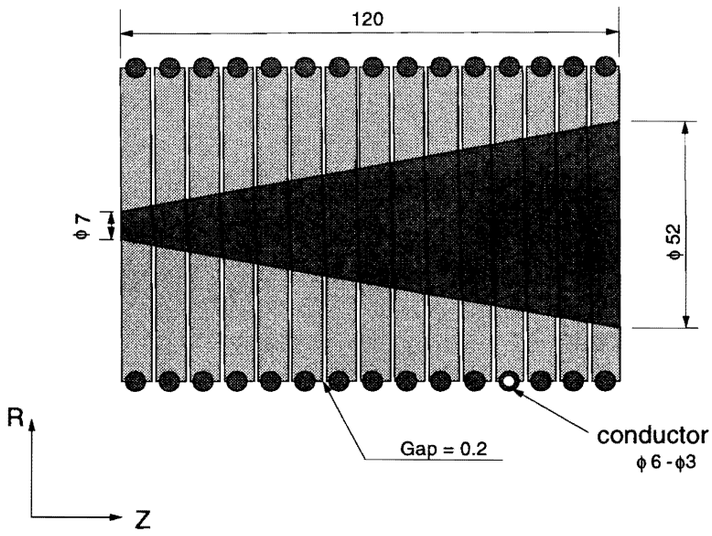

Figure 4.9: *Schematic view of the flux concentrator.*

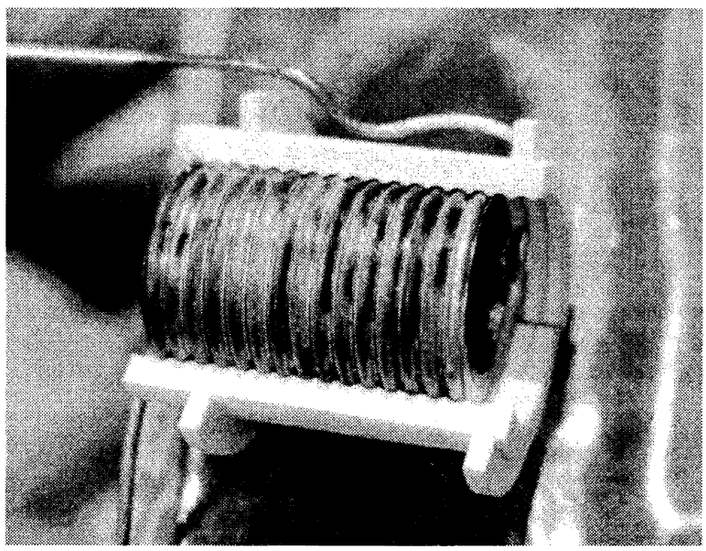

Figure 4.10: *Picture of the flux concentrator coil.*

L is the length of the flux concentrator. Figure 4.11 shows a scatter plot of positrons x and x_p at the entrance and exit of the flux concentrator. The phase-space transfer is clearly visible.

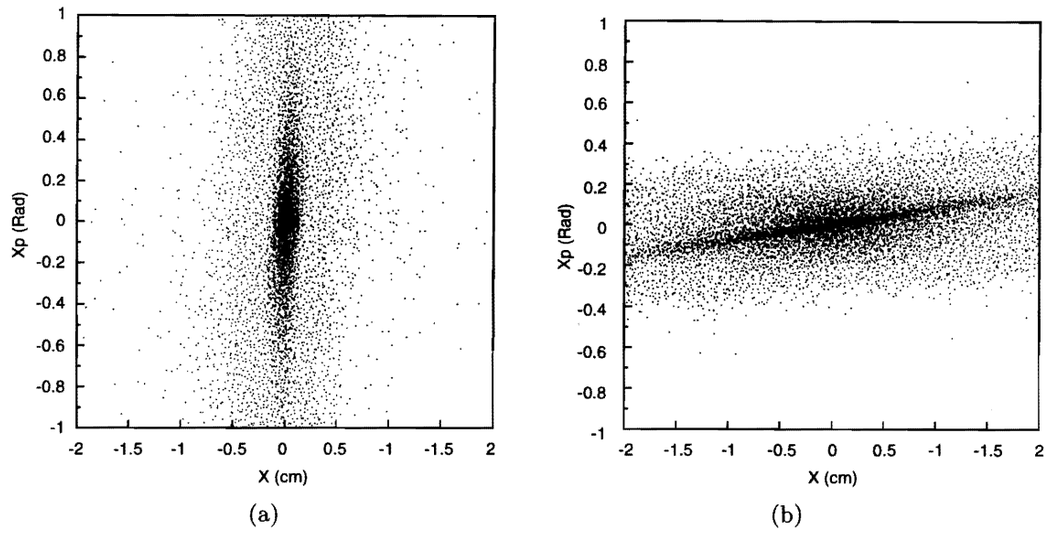

Figure 4.11: *Scatter plot of positrons's x position and direction at the entrance (a) and the exit (b) of the flux concentrator.*

Figure 4.12 shows the radial distribution of positrons at various points of the system. It is clearly seen from the figure that, the sharp spectrum at the exit of the converter is widened by the Flux Concentrator, then cut by the iris aperture of the RF structure. The radius of the Flux concentrator soon after the converter is 3.5mm. We lose only 5% of the positrons due to the aperture of the Flux concentrator. Due to the small radiation length of the converter material, the positrons' radial distribution at the exit of the converter is mainly determined by the spot size of the incident electrons. Since the Flux Concentrator can accept a fatter beam without any significant loss of the capture efficiency, we may increase the electron-beam spot size in the case when the energy-deposit density turned out to be too high for a stable target operation.

The number of positrons per electron are 22, 12 and 6.8 at the exit of the converter, the entrance of the accelerator section with the solenoid, and the exit of the 1.98 GeV linac, respectively. We used an aperture of 1.2 cm for the accelerator section with the solenoid to estimate the yield conservatively. Since we lose a huge amount of positrons around the flux concentrator, the radiation safety issue must be carefully considered.

4.3.3 Accelerator Section with Uniform Solenoid Field

The positrons emerging from the phase-space transformer are accelerated by an S-band RF field surrounded by a uniform magnetic field until their energy is high enough to be focused by the usual FODO optics. To contain positrons within the radius of the iris, a solenoid field of 0.8 Tesla is applied.

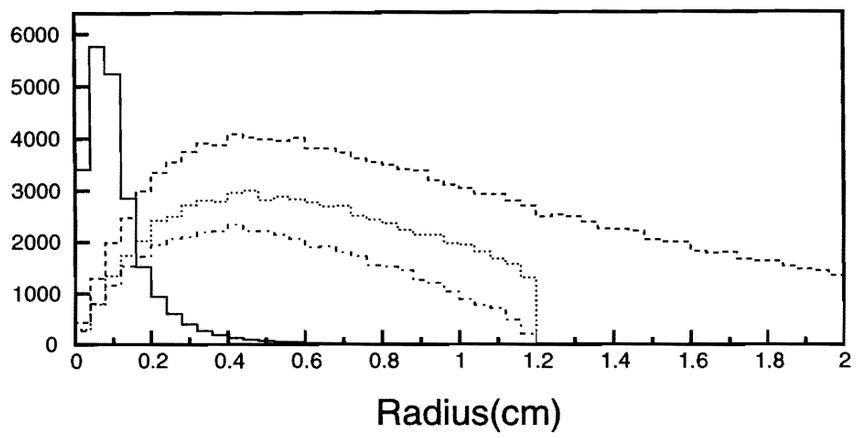

Figure 4.12: *Positron distribution with respect to the radius at several points of the system. The solid histogram is for soon after the converter, the dashed one at the end of the flux concentrator, the dotted one at the entrance of the accelerator section with solenoid, and the dot-dashed at the end of 1.98 GeV Linac. The solid histogram is scaled by 0.1.*

The RF structures consists of two 1.5 m length S-band structure with 30 MV/m accelerating field, inter-positioned by a $\pm\Delta F$ energy-compensation structure.

In this section, both positrons and electrons are co-accelerated. Electrons are separated after this section. Since the net charge of the beam is almost 0, space-charge effect in this section will not be significant. However, since this section must accelerate about twice as many particles compared to the other section, the beam-loading effect can not be neglected. In this respect, the use of lower frequency RF should be considered in the near future.

The longitudinal momentum spectrum of positrons is shown in Figure 4.13. At the exit, the momentum spread is about 5 MeV in rms.

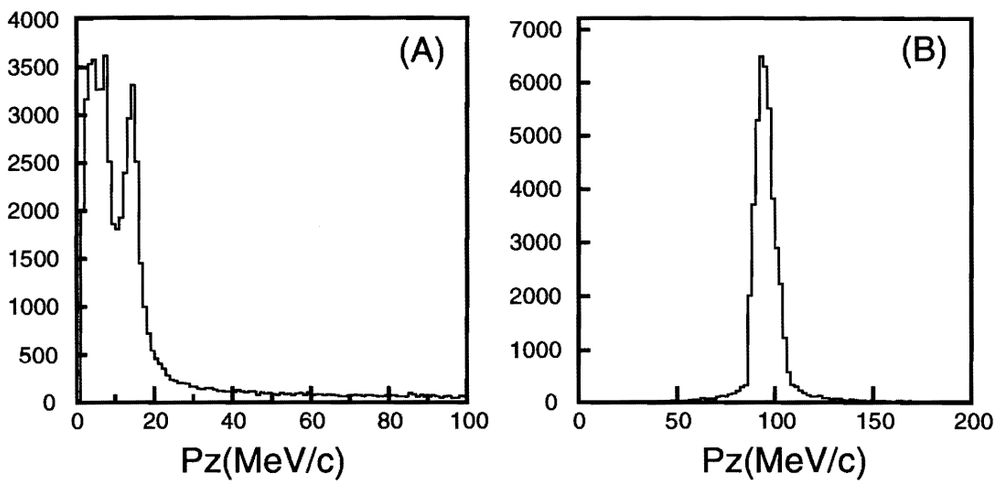

Figure 4.13: *Longitudinal momentum distribution of the positrons at the entrance(A) and the exit(B) of the accelerating section with a solenoid.*

4.4 1.98 GeV Linac

The 90 MeV positrons are accelerated up to 1.98 GeV by an S-band pre-injector linac, and are transported to the pre-damping ring. The linac has an accelerating gradient of 30 MV/m, provided by a series of 3 m-long constant-gradient accelerating structures with an iris aperture of 26 mm. In order to achieve a large transverse acceptance for a maximized positron yield, the linac should be equipped with 9 FODOs around the first accelerating structure and $3 \sim 6$ more around the subsequent structures.

The distribution of the normalized emittance and the momentum at the exit of 1.98 GeV Linac is shown in Figure 4.14. The normalized emittance (1σ) of the positron beam there is estimated to be 3×10^{-3} m. This beam is first injected into the positron pre-damping ring to reduce the emittance, so that the positrons from it can be stored and damped in the main damping ring without significant beam loss (the target value of the beam acceptance of the main damping ring is 1×10^{-4} m (normalized)).

If the pre-damping ring has a phase-space acceptance of 0.027 m (this corresponds to 3σ of expected beam from the positron 1.98 GeV injector linac) and an energy acceptance of ± 1 %, it follows that three positrons would survive for each primary electron that impinges on the production target. This corresponds to a total positron population of 16×10^{11} per pulse. This is more than twice as large as those required in Table 4.1.

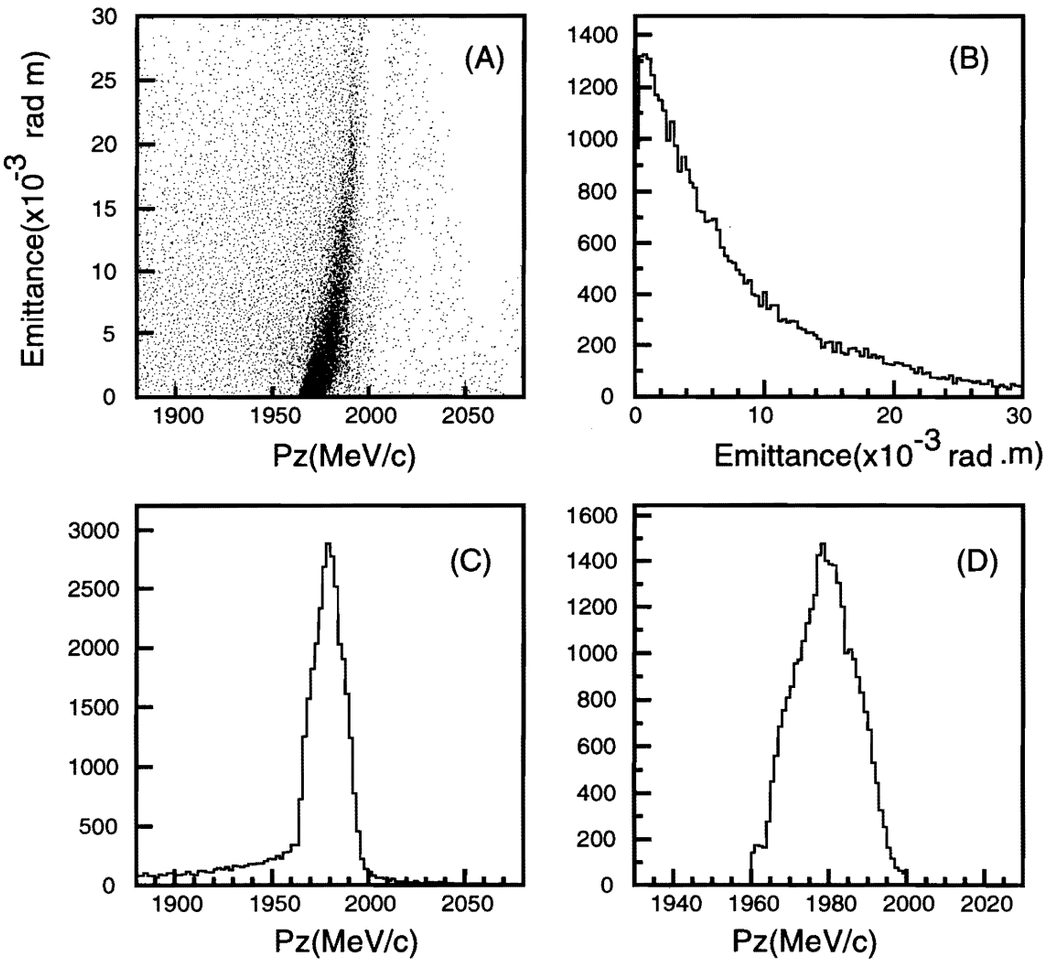

Figure 4.14: *Emittance(ϵ_n) and momentum(p) distribution at the exit of the 1.98 GeV Linac. Figure (A) is a scatter plot of ϵ_n, Figures (B) and (C) show the ϵ_n and p distribution, respectively, and Figure (D) is the p_Z distribution with momentum and emittance cuts of the pre-damping ring acceptance.*

4.5 Pre-damping Ring

The role of the pre-damping ring for positrons is to produce a low-emittance positron beam so that the main damping ring can accept it, without loosing the beam to the extent that affects the integrity of the JLC design.

The main damping ring assumes that the injected positron beam has a normalized emittance ($\gamma\epsilon_x$) of 1×10^{-4} m. On the other hand, the emittance of the positron beam from the source, after accelerated to 1.98 GeV with the positron injector linac, is expected to be $\gamma\epsilon_x = 3 \times 10^{-3}$ m (1σ, normalized emittance). Thus, for the positrons, a pre-damping ring is required to reduce the transverse beam emittance. This section gives a preliminary results of some design considerations concerning the positron pre-damping ring.

The whole layout and the optics Twiss parameters or the pre-damping ring, considered here, are shown in Figures 4.15 and 4.16. The ring has the shape of a racetrack and has a superperiodicity of 2. Each arc consists of 12 FODO cells, and each cell has the phase advance of 144 and 36 degrees for horizontal and vertical plane, respectively. The total tune for the ring is selected to be 11.47 and 4.09 for horizontal and vertical plane, respectively. These tune values have been chosen to given optimum dynamic aperture.

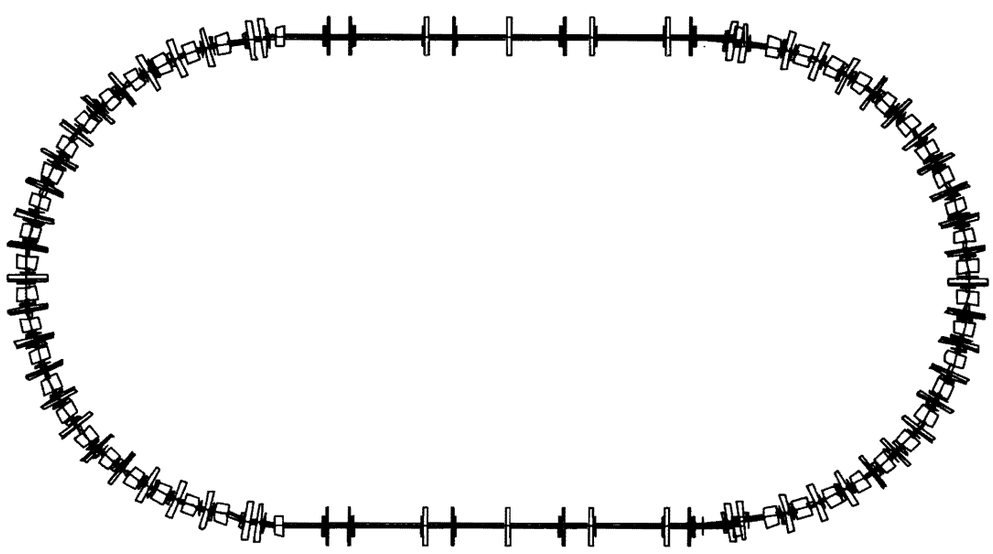

Figure 4.15: *Schematic plan view of the entire positron pre-damping ring.*

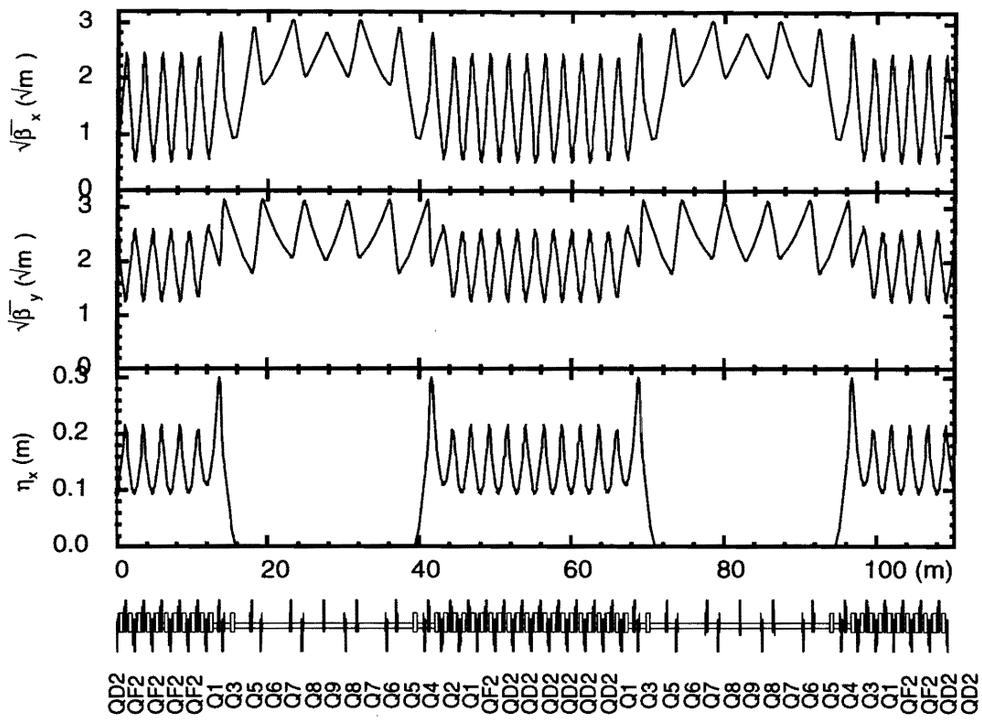

Figure 4.16: *Twiss parameters of the entire positron pre-damping ring.*

Energy	1.98 GeV
Repetition Rate	150 Hz
Number of Bunch Trains	2
Kicker Rise/Fall Time	60 nsec
Circumference	110.43 m
Equilibrium Emittance (unnormalized)	2.9×10^{-8} m
Equilibrium Emittance (normalized)	1.12×10^{-4} m
Horizontal/Vertical Damping Time	4.2/4.2 msec
Momentum Compaction Factor	6.92×10^{-3}
RF Frequency	714 MHz
Harmonic Number	263
Energy Loss/Turn	0.356 MeV
RF Voltage	2 MV
Energy Spread	8.55×10^{-4}
Bunch Length	6.1 mm

Table 4.8: *Parameters of the JLC Pre-Damping Ring*

4.5.1 Parameters

The main parameters are tabulated in Table 4.8. An equilibrium emittance of 2.9×10^{-8} m corresponds to $\gamma\epsilon_x = 1.12 \times 10^{-4}$ m at E= 1.98 GeV. The beam stays in the ring for 13.3 msec (2 bunch trains/150 Hz). Then, at extraction the normalized horizontal beam emittance is expected to be 1.17×10^{-4} m (see Equation 5.5 in Chapter 5). This is close to satisfy the specifications, although some more efforts would be required to reduce the nominal emittance. The circumference has been determined to accommodate just two bunch trains, while assuming the kicker rise/fall times of 60 nsec; some additional length might also be needed, here.

4.5.2 Arc Cell

For the arc periodic cell, an ordinary FODO lattice is adopted. The Twiss parameters of the arc cell are shown in Figure 4.17.

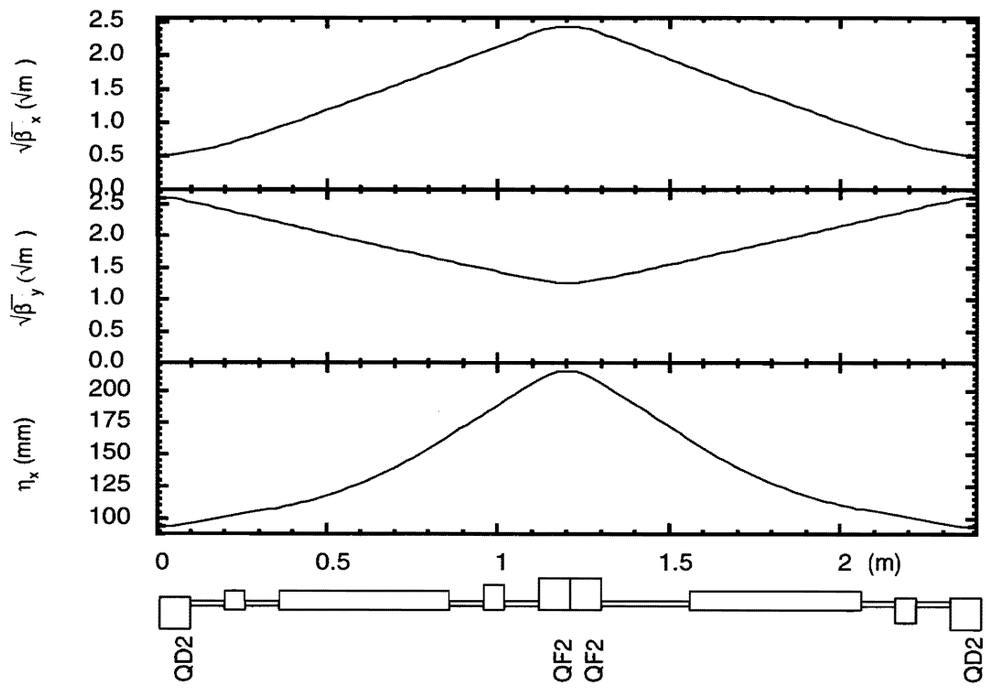

Figure 4.17: *Twiss parameters of a single cell in the arc sections of the positron pre-damping ring.*

The dimensions and the field strengths of the magnets are summarized in Table 4.9. The bending field is 1.73 T, and the strongest field gradient of the quadrupole magnet is 59.54 T/m for Q_D. These values seem to be slightly large, and may be adjusted by the length of the magnet in the future.

Magnet	Length[m]	Angle[degree]	k[1/m]
Bend	0.50	7.5	
Q_F	0.18		-0.983
Q_D	0.18		1.624

Table 4.9: *Summary of the magnets of the normal cell*

4.5.3 Dynamic Aperture

The positron beam to be injected into the pre-damping ring is expected to have a normalized emittance ($\gamma\epsilon$) of 3×10^{-3} m (1σ emittance). According to discussions in section 4.4, the pre-damping ring should accept a beam of 3σ size at that time (i.e. 0.027 m of normalized emittance envelope), with a momentum spread of $\pm 1.0\%$. We note here that 3σ of the injection beam is expressed as $3\sqrt{30}\sigma_0 \sim 16\sigma_0$ in terms of the equilibrium emittance, $\gamma\epsilon_0 = 1 \times 10^{-4}$, of the ring. Here, $\sigma_0 = \sqrt{\beta\epsilon_0}$.

The dynamic aperture of the ring has been studied using the program code SAD. The initial condition for the momentum deviation is selected to be between $-1.5\,\%$ and $1.5\,\%$. For each energy deviation, the transverse deviation is set so that

$$dx = n\sqrt{\beta_x\epsilon_0}, \qquad dy = n\sqrt{\beta_y\epsilon_0}, \tag{4.3}$$

where $\epsilon_0 = 1 \times 10^{-4}\,\mathrm{m}/\gamma$. By using the tracking code SAD, we find the maximum value of the coefficient n such that the particles, whose initial phase-space coordinate is determined by n, can be stored in the ring over a certain number of revolutions[1]

dp[%]	-1.5	-1.0	-0.5	0.0	0.5	1.0	1.5
n_{max}	22	32	28	28	28	26	24

Table 4.10: *Summary of tracking studies.*

Table 4.10 indicates that for a momentum deviation of $1.0\,\%$, the n value is found to be ~ 26. It must be noticed that if a round shape is assumed for the dynamic aperture in the transverse plane, the dynamic aperture will be given by $\sqrt{2}n_{max}$. If it is the case, the estimated dynamic aperture would be

$$26^2 \times 1 \times 10^{-4} \times 2 = 0.135\,\mathrm{m}. \tag{4.4}$$

Thus, an ample amount of dynamic aperture exists, in as much as possible construction and operational errors of the pre-damping ring are ignored.

[1]Typically 1000-turns was used as the criteria. Calculations, where 100-turns was used as the criteria, were also made for comparison. The differences in obtained n_{max} values were found to be small.

4.5.4 Effect of a Misalignment

This subsection discusses on the effect of a misalignment in the pre-damping ring. The errors listed in Table 4.11 are considered. The errors are distributed according to a Gaussian distribution with the standard deviations as tabulated in Table 4.11. Large errors beyond 3 standard deviations are truncated. After a calculation with errors, some corrections were tried to cure the effects. First, the tunes were adjusted by arc quadrupole magnets. Then, the closed-orbit distortion was corrected by using steering dipole magnets. The statistics were taken by 100 trials, using different random seeds for specifying the errors.

Displacement Errors for Q and SX	$\sigma_x = 50\ \mu m$
	$\sigma_y = 60\ \mu m$
Rotational Errors for B,Q,SX and C	$\sigma_\theta = 0.5\ mrad$
Monitor Setting Errors	$100\mu m$
Magnetic Field Errors for B,Q,SX and C	0.1 %

Table 4.11: *Errors for Simulation. B, Q, SX and C represent the bending, quadrupole, sextupole and corrector magnets, respectively.*

The horizontal emittance before a correction is 3.5×10^{-8} m at the 90 % confidence level. After a correction, it is recovered to 2.95×10^{-8} m, quite close to the nominal value.

The dynamic aperture in the presence of alignment errors was also studied. Here, the threshold revolution number is set to be 100 turns. The results of the tracking are given in Table 4.12.

dp[%]	-1.5	-1.0	-0.5	0.0	0.5	1.0	1.5
n_{max}(with errors)	8	8	8	8	8	8	6
n_{max}(corrected)	12	12	12	12	10	10	12

Table 4.12: *Summary of Tracking with Errors. The values are at the 90 % CL.*

Without applying corrections, the obtained n_{max} value is ~ 8 for 1.5 % momentum error. Assuming a round shape of the dynamic aperture, this means the dynamic aperture of

$$8^2 \times 1 \times 10^{-4} \times 2 = 0.008\,\mathrm{m}. \tag{4.5}$$

This corresponds to 2.1σ of the injected beam. If corrections are applied, n_{max} is recovered to about 12. This means the dynamic aperture of

$$12^2 \times 1 \times 10^{-4} \times 2 = 0.028\,\mathrm{m}, \tag{4.6}$$

corresponding to 3.1σ of the injected beam.

It can be concluded that the ring performance is acceptable for the errors tabulated in Table 4.11. The alignment within those errors is thought to be realistic, though it is not trivial. It is expected that by using the beam-based alignment method, the alignment and ring performance can be improved.

4.6 Remaining Issues

As can be found in the preceding sections, the JLC positron source system is expected to produce more than 2-times higher positrons than required. However, this estimation is based on relatively simple simulations. The items listed below should be seriously considered when starting the construction of the JLC.

- We are planing to inject about 7-times more beam energy with 3-times greater energy density than those of SLC. According to a study prior to the SLC construction[7], the converter will not suffer damage even with this condition. However, since the incident beam parameters, such as the bunch length, the number of bunches per pulse, and the spot size, were different, another test with a beam parameter similar to that of JLC is desired. If the beam energy density is too high according to such a test, a possible cure is to increase the beam spot size. In this case, the intensity or energy of the incident electron should be increased so as to overcome the loss of the positron capture efficiency.

- The designs of the 10 GeV electron linac, the 1.98 GeV linac and the pre-damping need more systematic work.

- The number of positrons in the accelerator section in the uniformed field solenoid is about twice as large as in the downstream sections. The same number of electrons also pass through the RF structure. The expected performance of this section must be reviewed from an RF-technological point of view.

- The magnetic field in the simulation assumes the ideal field shape. A realistic field shape for the flux concentrator and the effect of the gaps among the solenoid coils should be included.

- While, it appears possible to conceive a positron pre-damping ring that is close to satisfy the design criteria, some design refinements are required. First, the design needs to improve the equilibrium emittance, and the damping time. The expected dynamic aperture appears large enough to guarantee the required beam acceptance. Nonetheless, a less error-prone lattice design or a design with an even larger dynamic aperture from the beginning would be nice.

- The circumference of the present pre-damping ring is just long enough to accommodate two full bunch trains. It leaves very little room for kicker magnets and other devices in straight sections. Adopting a longer ring circumference is an obvious solution to this problem, and it can also help relax the requirement on the damping time, if three (or more) bunch trains can be simultaneously stored. However, its impact on the dynamic aperture needs to be carefully examined. It is also worthwhile considering improvements on the damping time and the dynamic aperture of the main damping ring.

- Issues associated with the so-called photo-electron-induced instability (PEI) in the positron pre-damping ring need to be examined, and, if the problem could be serious, adequate hardware

design measures must be taken. Possible solutions include a careful shaping of the vacuum chamber, implementing a bunch feedback system and others. This task applies to the design work of the main damping ring, as well.

References for Chapter 4

[1] JLC-I, KEK Report 92-16, December, 1992.

[2] Zeroth-Order Design Report for the Next Linear Collider, LBNL-PUB-5424, also SLAC Report 474 or UCRL-ID-124161, May 1996.

[3] H. Ida, et al., in the "Proceedings of 17th Linac Conference - Volume I - ", Tsukuba, KEK, August 21-26, 1994, p.366. H. Ida, et al., KEK-Preprint 92-56, July, 1992.

[4] J.E. Clendenin, SLAC-PUB-4743, April 1989 ; J.De Lamare, et al., SLAC-PUB-5472, June 1991 ; A.V. Kulikov, et al, SLAC-PUB-5473, June 1991 ; R. Pitthan, et al., SLAC-PUB-5547, June 1991 ; E. Reuter, et al., SLAC-PUB-5369, December 1991.

[5] TOPAZ Collab., TRISTAN-EXP-02, 1983.

[6] W.R. Nelson, et al, SLAC-Report-265, December 1985.

[7] S. Ecklund, SLAC-CN-128, 1981.

Authors and Major Contributers of Chapter 4

- Akiya Miyamoto
- Seishi Takeda
- Shigeru Kuroda

We express our gratitude to Mr. H. Ida of NKK Corporation for his contributions to the design studies of the JLC positron production system.

CHAPTER 5

Damping Rings

Contents

5.1 Introduction

The role of the damping ring is to reduce the beam emittance in a short period that is compatible with the repetition time of the accelerator system. The target values for the beam emittance are $\gamma\epsilon_x = 3 \times 10^{-6}$ m and $\gamma\epsilon_y = 3 \times 10^{-8}$ m. This means a vertical/horizontal coupling of 1 %. Naturally, it requires an accurate alignment of the ring components. The energy of the ring is chosen to be 1.98 GeV so as to avoid the spin-depolarization resonance.

The equilibrium emittance of an electron ring is generally given by

$$\epsilon_x = \frac{5}{5} 32\sqrt{3} \frac{h}{2\pi mc} \left(\frac{E}{mc^2}\right)^2 \frac{I_5}{I_2 - I_4}, \tag{5.1}$$

where

$$I_2 = \oint \frac{1}{\rho^2} ds, \tag{5.2}$$

$$I_4 = \oint \left(\frac{2K_x}{\rho} + \frac{1}{\rho^3}\right) \eta_x ds, \tag{5.3}$$

$$I_5 = \oint \frac{\gamma_x \eta_x^2 + 2\alpha_x \eta_x \eta_x' + \beta_x \eta_x'^2}{|\rho|^3} ds. \tag{5.4}$$

These equations show that the emittance of the ring is determined mainly by the optics in the arc region if the dispersion is suppressed in other sections (e.g. straight sections). To obtain an ultra-low emittance the design of the JLC damping ring adopts the FOBO cell for the arc region, where a small dispersion is maintained inside the bending magnet.

After beam storage for a time period of t, the emittance of the extracted beam is given by

$$\epsilon = \epsilon_i e^{-2t/\tau} + (1 - e^{-2t/\tau}) \epsilon_{eq}, \tag{5.5}$$

where ϵ_i, ϵ_{eq}, and τ are the emittance of the injected beam, the equilibrium emittance of the ring, and the damping time of the betatron amplitude, respectively.

In JLC the injected beam is assumed to have an initial emittance $\gamma\epsilon_i$ of 1×10^{-4} m for both the horizontal and vertical planes. Then, to obtain the required emittance of the extracted beam the damping time must practically satisfy the condition $\tau_y < t/7$. (The injection beam emittance of 1×10^{-4} m is readily available for the electrons. However, in order to achieve the above emittance for the positron beam, a pre-damping ring is required. See discussions in Chapter 4.)

The adequate store time t is determined from the repetition rate $f_{\rm rep}$ and the number of bunch trains N_t that are simultaneously stored in the ring. Their relationship is given by $t = N_t/f_{\rm rep}$. With $N_t = 5$ and a repetition rate of 150 Hz, the damping time τ_y is required to be less than 4.76 msec. In order to obtain such a short damping time, a long series of wiggler magnets need to be introduced in the dispersion free section.

The threshold impedance of the longitudinal single-bunch instability is given by [1]

$$|Z/n|_{th} = \frac{(2\pi)^{3/2}\sigma_\tau \alpha E \sigma_\epsilon^2}{e^2 N}, \tag{5.6}$$

where σ_τ is the bunch length, α the momentum compaction factor, E the beam energy, σ_ϵ the relative energy spread, and N the number of particles per bunch. However, in a study of the ATF damping ring, it was found that the above formula overestimated the threshold by factor ~ 3, compared with the results from a Vlasov equation analysis with a potential-well distortion[2]. In the case of JLC, the beam energy is chosen to be 1.98 GeV, which is about 4/3 of the ATF beam energy. Consequently, in order to obtain a the higher threshold than in the case of ATF for the same values ($\sigma_\tau, \sigma_\epsilon$ and N), the momentum compaction factor α should be kept larger than 0.26 times the ATF, namely 5×10^{-4}.

5.2 Lattice and Optics

The layout of the entire damping ring is shown in Figure 5.1. Overall, the ring has a race-track shape. Each arc consists of 19 FOBO cells, where 'B' means combined-function bending magnets.

A special half cell having a half bending magnet will be placed at two ends of each arc. The ring has two long straight sections, which are filled with wiggler magnets that are placed so as to reduce the damping time. The ring has a superperiodicity of 2, and the RF cavities and wiggler magnets are placed symmetrically. However, the locations of the injection and extraction positions are not symmetric. This is done so that the RF cavities would always see the same total charge of the stored beam when the bunch trains are injected and extracted. According to experience of the ATF damping ring operation, the maximum β_y in the wiggler and septum region should be kept at a relatively small value of 10 m. This is so as to retain a sufficiently large physical aperture relative to the beam size there, while the pole gaps of the wiggler magnets are made small so as to reduce the magnet fabrication and operational costs.

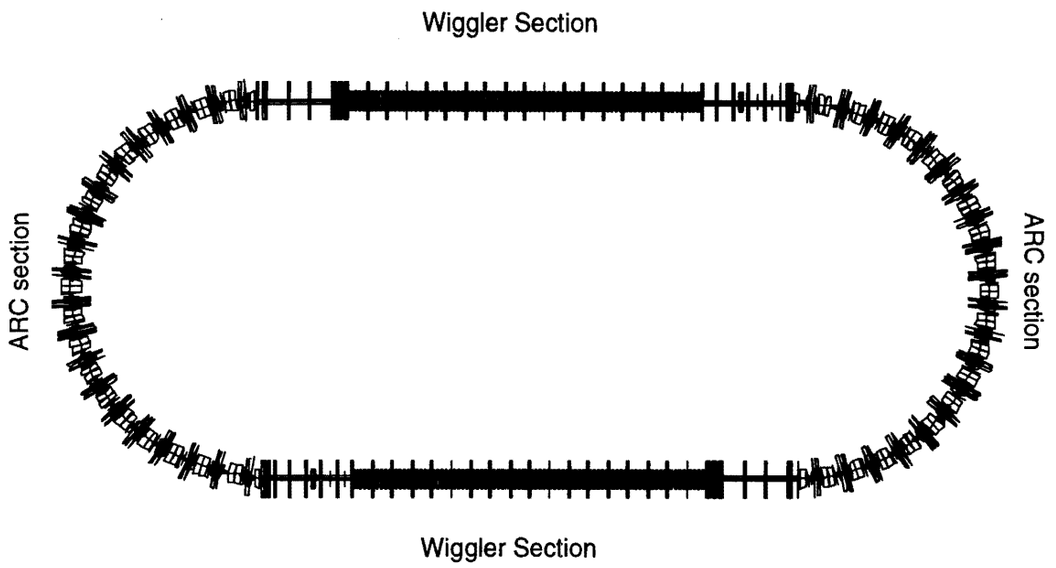

Figure 5.1: *Geometry of the JLC damping ring (plan view).*

5.2.1 Parameters

The main parameters of the damping ring are given in Table 5.1. The ring has a total circumference of 277 m. This will allow us to simultaneously store five bunch trains, as discussed earlier. An equilibrium emittance of 6.50×10^{-10} m would correspond to $\gamma\epsilon_x = 2.52 \times 10^{-6}$ m at E= 1.98 GeV. A momentum compaction factor α of 8.02×10^{-4} is well above the threshold value of 5×10^{-4} in terms of the longitudinal single-bunch beam instability. Figure 5.2 shows the Twiss parameters across the entire damping ring.

5.2.2 Arc Cell

The Twiss parameters of the arc cell are shown in Figure 5.3. Each cell consists of a combined-function bending magnet and two flavors of quadrupole magnets. One of the quadrupole magnets is used for a fine adjustment of the optics. It is beneficial to have such magnets, since the quadrupole field component of the bending magnet is fixed by its pole-face geometry. The field strengths of the magnets are determined according to an optimum tune setting. The equilibrium emittance and the momentum compaction factor of the cell, itself, are 1.23×10^{-9} m and 1.99×10^{-3}, respectively. The presence of the wiggler section in the ring makes both values smaller than those given in Table 5.1.

The dimensions and the field strength of the magnets are summarized in Table 5.2. In this Table, k is defined as

$$k = \frac{B'l}{B_0\rho}. \tag{5.7}$$

Parameter	Value
Energy	1.98 GeV
Number of Bunches/Train	85 (max.)
Repetition Rate	150 Hz
Number of Bunch Trains	5
Bunch Spacing	1.4 nsec
Kicker Rise/Fall Time	60 nsec
Circumference	277.12 m
Equilibrium Emittance (not normalized)	6.50×10^{-10} m
Equilibrium Emittance (normalized)	2.52×10^{-6} m
Horizontal/Vertical Coupling	≤ 1 %
Horizontal/Vertical Damping Time	4.22/4.83 msec
Damping Partition ($J_x/J_y/J_z$)	1.14 / 1.00 / 1.86
Momentum Compaction Factor	8.02×10^{-4}
RF Frequency	714 MHz
Harmonic Number	660
Energy Loss/Turn	0.758 MeV
RF Voltage	1.2 MV
Energy Spread	8.62×10^{-4}
Bucket Height	1.25 %
Bunch Length	4.85 mm

Table 5.1: *Parameters of the JLC Damping Ring*

Magnet	Length[m]	Angle[degree]	k[1/m]
Bend	1.20	9	-1.338
Q_F	0.30		0.7259
Q_D	0.15		0.003

Table 5.2: *Summary of the magnets of a normal cell*

The nominal bending field is 0.86 T. The field gradient of the bending magnets is 7.36 T/m. If the same beam pipe as that of ATF is to be used (outer radius 16 mm) in this bending magnet, the field of the bending magnet at radius δr=32 mm is about 1.1 T, which is considered to be a comfortable condition. The largest field gradient of quadrupole magnet in the design here is found to be 48.39 T/m for QM1 (quadrupole magnet in the matching section). For a bore radius of 16 mm, the corresponding pole tip field is 0.77 T. Its design is considered not to be difficult.

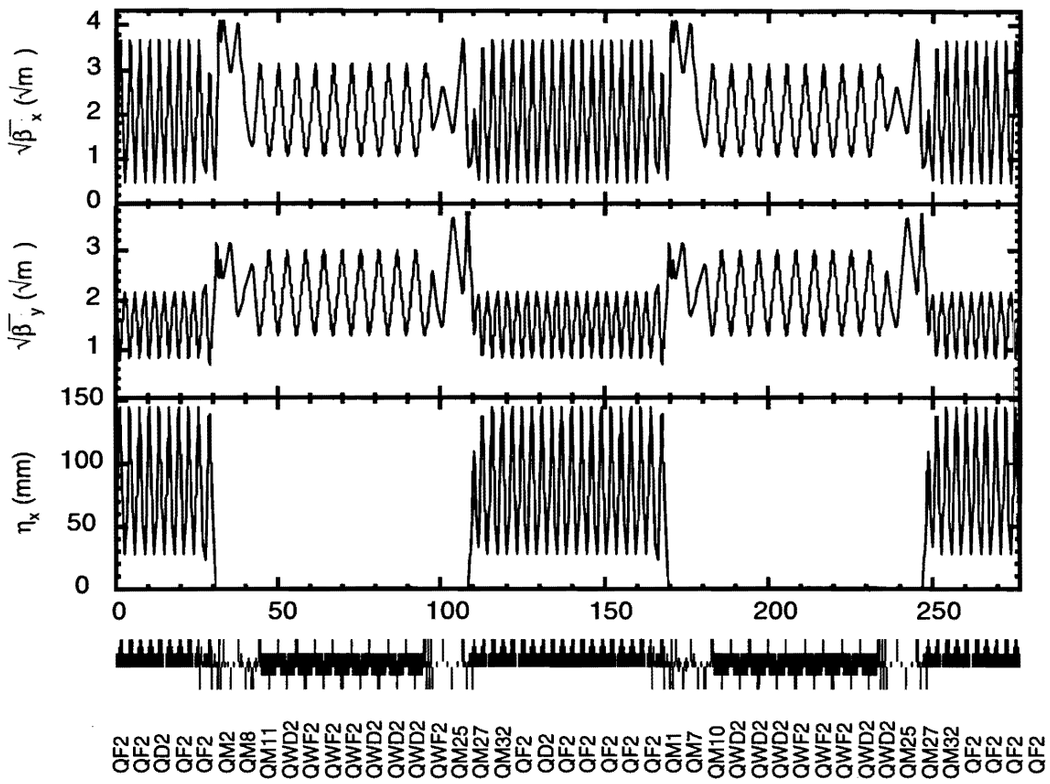

Figure 5.2: *Twiss parameters of an entire damping ring.*

5.2.3 Comparison of Various Cell Configurations

Before settling on the FOBO arc lattice design, various types of arc cell configurations have been studied. This section presents a mini-review of these studies.

TME (Theoretical Minimum Emittance) Lattice

First we consider the TME (Theoretical Minimum Emittance) lattice [3]. The lattice and its Twiss parameters are shown in Figure 5.4.

Starting with the FOBO lattice in the previous section, if an extra quadrupole magnet is added, and if the entire single cell is symmetrized, a TME lattice configuration is topologically realized, except that the field signs of the quadrupole magnets are reversed. For comparison, the same combined functioned magnet as in the FOBO case is assumed here. In order to reach the minimum emittance, β_x and η_x at the center of the bending magnet must be

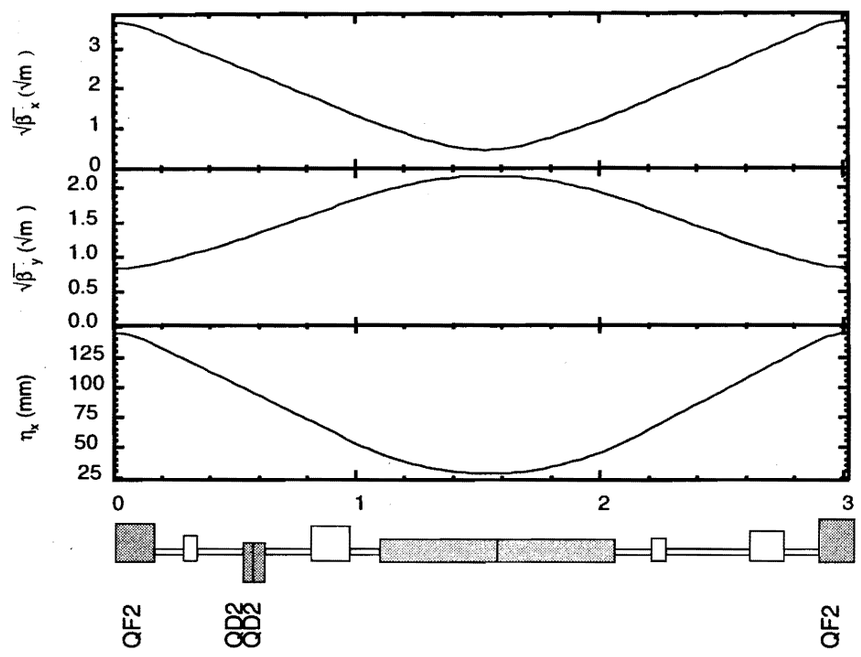

Figure 5.3: *Twiss parameters of a single arc cell in the damping ring.*

$$\beta_x = \beta_{\rm TME}, \quad \eta_x = \eta_{\rm TME}, \tag{5.8}$$

where

$$\beta_{\rm TME} \equiv \frac{l_B\sqrt{l_B^4 + 20l_N^2\rho^2 + 120\rho^4}}{5\sqrt{2}(l_B^2 + 12\rho^2)}, \tag{5.9}$$

$$\eta_{\rm TME} \equiv \frac{l_B^2(7l_B^2 + 60\rho^2)}{120\rho(l_B^2 + 12\rho^2)}. \tag{5.10}$$

Then, the minimum emittance is given by

$$\begin{aligned}\epsilon_{\rm TME} &= l_B^4(-x + \sinh x)(4 + x^2 - 4\cosh x + x\sinh x)) \\ &\quad /(x^2(\rho^4x^3K^2 + 2x\sinh^2(x/2) - 8\rho^4xK^2\sinh^2(x/2) \\ &\quad +2(1 + 2K\rho^2)^2\sinh^2(x/2)\sinh x)) \qquad (5.11) \\ &\rightarrow \frac{l_B^4}{3\sqrt{2}\sqrt{l_B^4 + 20l_B^2\rho^2 + 120\rho^4}}. \qquad (5.12)\end{aligned}$$

It has been found that in our case the minimum-emittance condition is given by $\beta_{\rm TME} = 0.095$ m and $\eta_{\rm TME} = 0.0037$ m. However, because of the stability requirement (i.e. periodic boundary condition), this minimum-emittance condition cannot be satisfied. From scanning in the (β_x, η_x) parameter plane, a point with (β_x, η_x)=(4.5 $\beta_{\rm TME}$, 3.5 $\eta_{\rm TME}$) has been found to be a possible candidate for a small emittance and a large momentum compaction factor. The parameters of the lattice are

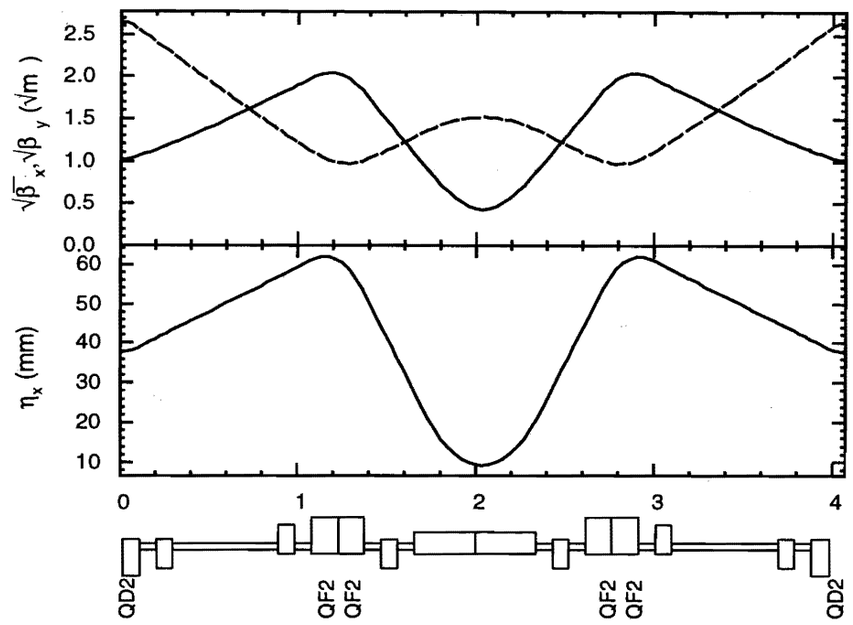

Figure 5.4: *Twiss parameters of a TME arc cell.*

summarized in Table 5.3 with those of the FOBO lattice. Although the TME lattice has a slightly smaller equilibrium emittance, it also has a relatively small momentum compaction factor which is somewhat of a concern in the light of single-bunch longitudinal instabilities. The momentum compaction factor can be increased by using a longer bending magnet. However, this revision tends to increase the cell length; for a ring design with a fixed circumference, it leads to reduction of the beam line length available for the wiggler magnets and injection / extraction sections.

The trace of the vertical transfer matrix of a lattice, as shown in Figure 5.4, has a denominator factor,

$$32l\eta_{x0} - \theta((16 + 8k_Bl + 2k_Bl_B + kB^2ll_B)\beta_{x0}^2 + 4ll_B). \tag{5.13}$$

Here, l_B denotes the bend-magnet length, and l represents the sum of the length of the bend magnet l_B and the half thickness of the QD magnet, as shown in Figure 5.4. This is the singularity that prevents us from adopting the true TME condition for the lattice design in a straightforward manner. To stay sufficiently far away from this singularity, a bending magnet with very high field gradient is needed. It should be noted that adding another quadrupole magnet to the TME lattice has little effect in terms of avoiding this singularity. However, this revision helps make the momentum compaction factor larger.

The minimum emittance seems not to heavily depend on the choice of k_B. The parameters of the TME with a normal bending magnet with (β_x, η_x)=(2 $\beta_{\rm TME}, \eta_{\rm TME}$) is also shown in Table 5.3.

FODO Lattice

FODO lattice configurations, as shown in Figure 5.5, have also been studied. Here, the bending field is provided by pure dipole magnets without any field gradient. It has been found that to obtain an

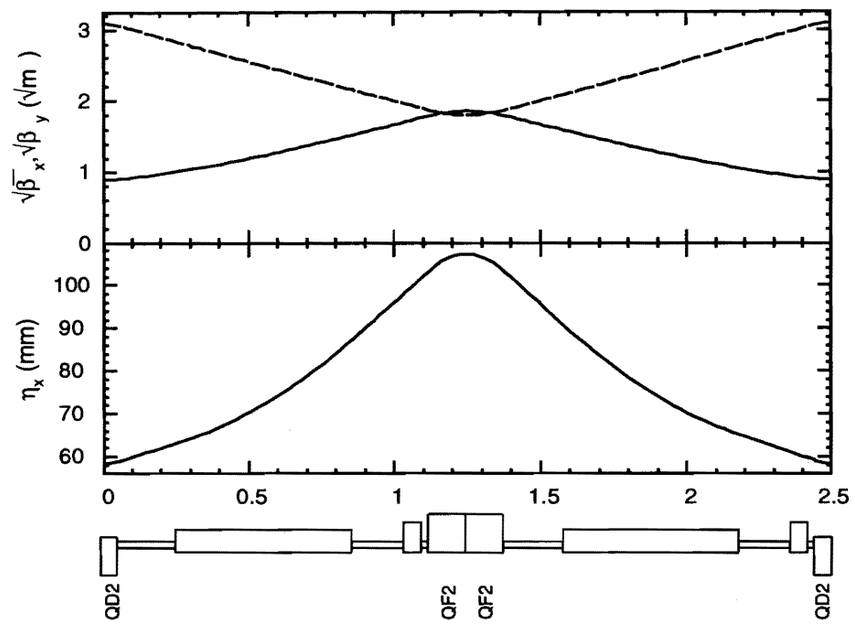

Figure 5.5: *Twiss parameters of a FODO arc cell.*

equilibrium normalized emittance comparable with those of the FOBO or TME lattice, more than 80 cells are needed. The parameters are also summarized in Table 5.3. The momentum compaction factor is very large, because the ratio of the beam-line length that is occupied by the bending magnet in a cell is larger than FOBO and TME lattice. The energy loss is smaller because of the larger number of cells, i.e. a large bending radius. Consequently, longer wiggler-magnet sections are required to obtain a short damping time. This leads to a difficulty in the overall ring design if its circumference is to be fixed at 277 m (if the construction of a big ring is considered not to be a problem, then it will be of no concern.)

However, there may be still room for optimizing the drift space between the magnets. For example, a shorter drift length between bend and defocusing quadrupole magnet makes the cell length similar to that of the FOBO, and may reach better performance. This is one of the study items for the near future.

	FOBO	TME(combined B)	TME(normal B)	FODO
Number of cell	56	56	56	80
Cell Length[m]	2.42	3.38	4.54	2.5
Arc Length[m]	135.5	189.3	254.2	200
$\epsilon_{equil,x}$[m]	5.11×10^{-10}	4.45×10^{-10}	2.19×10^{-10}	5.93×10^{-10}
α_C	7.69×10^{-4}	5.62×10^{-4}	1.71×10^{-4}	1.23×10^{-3}

Table 5.3: *Comparison of various lattices. In the table, $\epsilon_{equil,x}$ and α_C represent the horizontal equilibrium emittance and the momentum compaction factor of the cell, respectively.*

Discussions

In summary, both the FOBO and TME lattice designs with similar damping performance are possible. For now, the FOBO lattice has been chosen since it appears to be more compatible with the prescribed ring circumference of 227 m. Also, operational experience concerning a damping ring with the same conceptual design is expected to be obtained in the near future at ATF to help further refine the design.

The expected emittance, as shown in Table 5.3, is very small compared to what is actually required in the overall JLC design. However, the quoted values of the momentum compaction factors are also uncomfortably small. Table 5.3 should be interpreted only as a representation of the general trends of parameters in these lattice configurations. For their practical applications to the damping ring, much more design tuning work is required to increase the momentum compaction in exchange for the increased equilibrium emittance within the acceptable range.

5.2.4 Wiggler Cell

Length	2 m
Period	0.4 m
Field Strength	1.8 T

Table 5.4: *Specification of the wiggler magnet*

The Twiss parameters of the wiggler cell are shown in Figure 5.6. This cell contains two wiggler magnets. The ring has $7 + 7$ wiggler cells, i.e. 28 wiggler magnets. The wiggler magnets considered here are of the same type as that used for the ATF damping ring. The specifications of the wiggler magnet are summarized in Table 5.4.

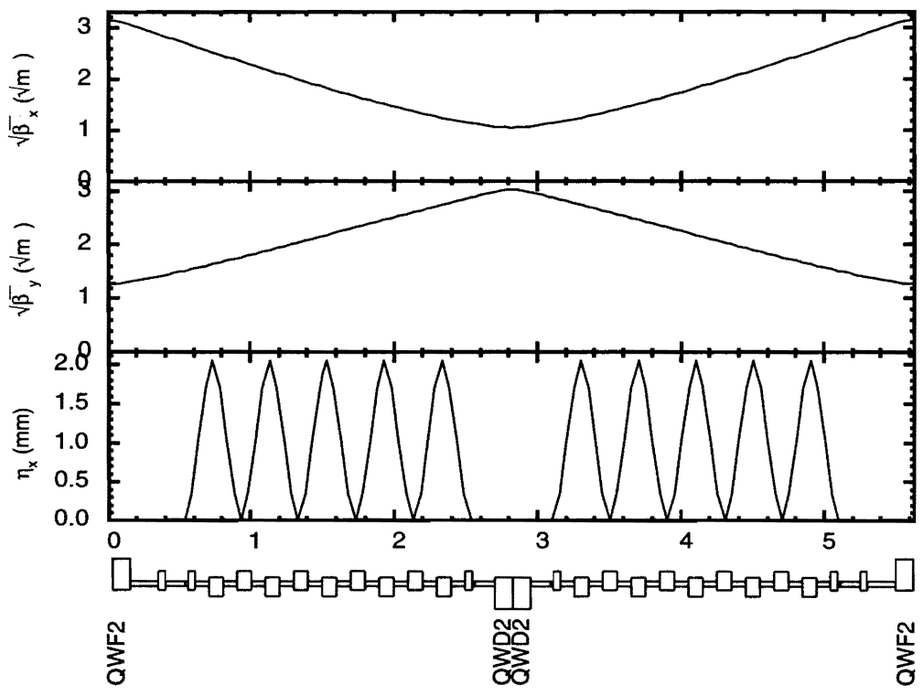

Figure 5.6: *Twiss parameters in the wiggler section of the damping ring.*

5.3 Magnet System

The damping ring requires some strict conditions on the magnet system and its alignment. As discussed in the previous section, to achieve the desired emittance and damping time, the present damping ring design has adopted a combined FOBO lattice and damping wigglers. This section discusses the design considerations related to these magnets.

5.3.1 Damping Wiggler

The low emittance and fast damping of the damping ring require high-field, short-pitch wigglers. These conditions conflict with each other, because a high field requires much space for flux sources, whether iron cores with coils or permanent magnets. Studies on the effects of the geometrical configurations of the wigglers on the emittance have been conducted. It was found that the choice of free spaces between adjacent wiggler poles has little effect on the emittance in the lowest order approximation. This fact relaxes the requirement on the wiggler pitch. Our choice of the pitch is 0.4 m.

Studies have been made on two types of damping wigglers. One is a hybrid magnet scheme that uses permanent magnetic materials as flux sources. The other is the usual electric magnet scheme, which uses compact coils excited by intense electric currents. Field calculations with the 2-dimensional codes PANDIRA and POISSON show that it is possible to achieve $B_{\rm peak}$, $B_{\rm eff} > 2$ T for both types, where $B_{\rm eff}$ is defined as $\sqrt{\ll B^2 \gg}$. Here , $\ll B^2 \gg$ is an integral of the field over the whole wiggler length divided by the pole length, *i.e.* $\int B^2 ds / L_{pole}$.

We chose the electric option, since its adjustability during operation is an important asset. In the design of the damping ring optics, the wiggler field strengths are set to $B_{\rm peak}$ and $B_{\rm eff}$ 1.7~1.8 T (the calculated value by POISSON) in consideration of power consumption.

A prototype wiggler magnet was built, and the field profiles were measured as a function of the current. The measured $B_{\rm peak}$ of the prototype wiggler is smaller than the POISSON design value by about 15 %. This is considered to be because of a limitation in the 2-dimensional calculation, whose accuracy is compromised for magnets with short poles as this wiggler magnet. However, 3-dimensional codes, such as OPERA-3D and TOSCA, could reproduce the field-measurement results very well.

Calculations with OPERA3D have shown that $B_{\rm peak}$ can be increased to $\sim$ 1.6T by using wider poles. Hence, the pole shapes of the wiggler after the prototype studies have been revised so as to have a larger pole width. The final parameters of the damping wigglers are listed in Table 5.5. The whole structure of the wiggler and its cross section along the beam line are shown in Figure 5.7. Figure 5.8 shows the results of a field measurement with calculated values. The final mechanical design of the wiggler magnets will have to take the installation aspects of these magnets on an active mover system into account.

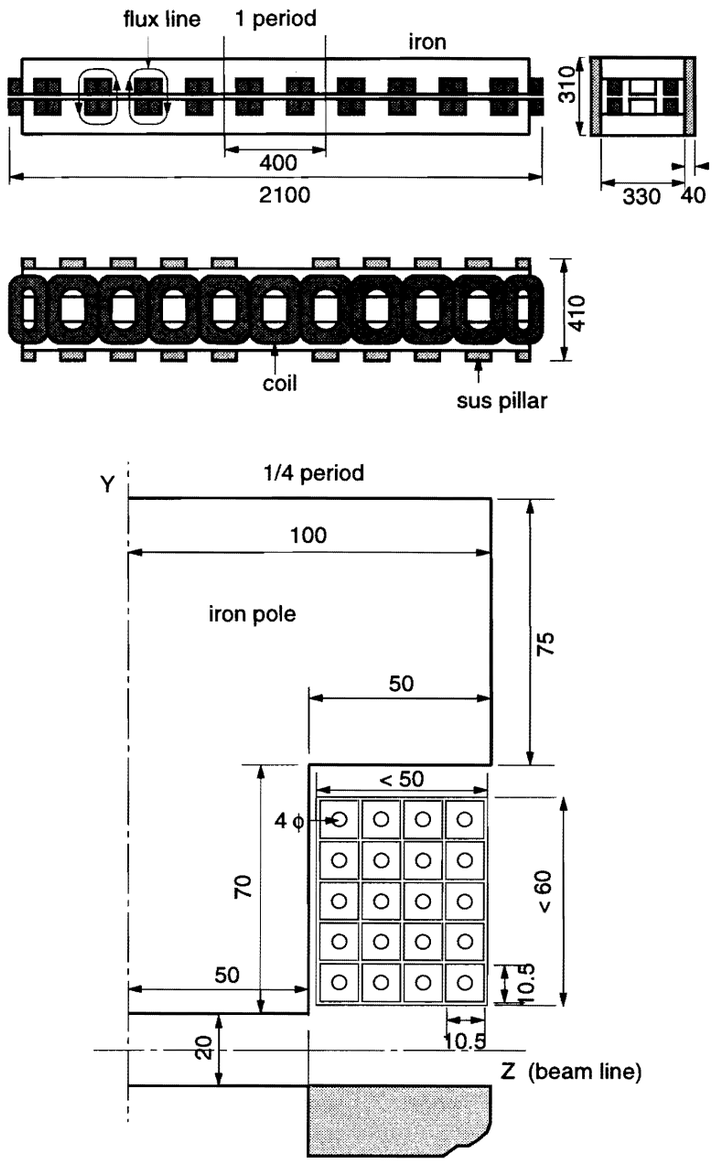

Figure 5.7: *Wiggler Magnet.*

total length	2.1 m
one period	0.4 m
full gap	20 mm
Bpeak	1.6 T
Beff	1.8 T
current/pole	20 kA (1000 A × 20)
number of wigglers	28

Table 5.5: *Damping wiggler parameters.*

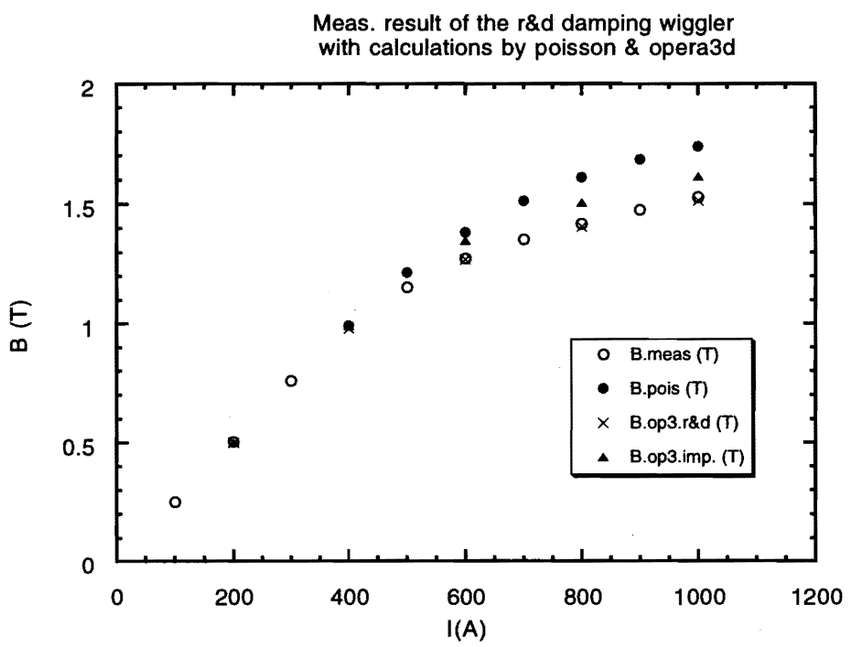

Figure 5.8: *Measurement results of the R&D damping wiggler with calculations by POISSON and OPERA-3d.*

effective length	1.2 m
central gap	32 mm
dipole field B_0	0.86 T
field gradient B'	-7.36 T/m
bending radius	7.67 m (for a 1.98 GeV/c beam)
current / pole	12000 A (1000 A $\times$ 12)
number of dipoles	40

Table 5.6: *Bending-magnet parameters.*

5.3.2 Combined-Function Bending Magnet

By introducing combined-function bending magnets having a defocus quadrupole field, we can make the D parameter (which appears in damping partition) negative, which can reduce the transverse emittance. The parameters of the combined-function bending magnets are given in Table 5.6.

This combined-function bending must be of the sector type because of the large sagitta of about 22 mm; otherwise, the beam feels a varying field of as much as 15 % of B_0 for a 1.2 m bending. The logarithmic pole profiles were obtained for sector-type combined-function bend magnets by solving the Poisson equation in cylindrical coordinates. The field distribution, its dependence on the coil positions, shimming and the field changes due to some manufacturing errors were studied using POISSON. These studies showed that the accuracy of the poles must be better than 20 μm to obtain the required field quality, and which kinds of errors are critical. One R&D combined-function bending magnet was produced; its entire shape and cross section are shown in Figure 5.9.

Precise field measurements have been carried out using a 1 mm Hall probe. The field-measurement results showed some interesting features: a saturation effect, an asymmetry of the field distribution due to the coil configuration, etc. The final design of the combined bending-function magnets will be completed by taking account of the field-measurement results and further calculations using computer codes.

5.3.3 Quadrupole Magnets

The total number of the quadrupole magnets required for the DR is about 200. After examining the optics results concerning the quadrupole magnets, we reduced the number of quadrupole magnet types to be produced. These are shown in Table 5.7.

The uniformity of the quadrupole fields in 12 mmϕ is required to be better than 0.1 %. This needs a manufacturing accuracy of better than 30 μm to achieve the required field quality. Two R&D quadrupole magnets were constructed with an accuracy of 20 μm. The parameters are listed in Table 5.8.

Rough field measurements were made using a Hall probe; the results show that the field strength is

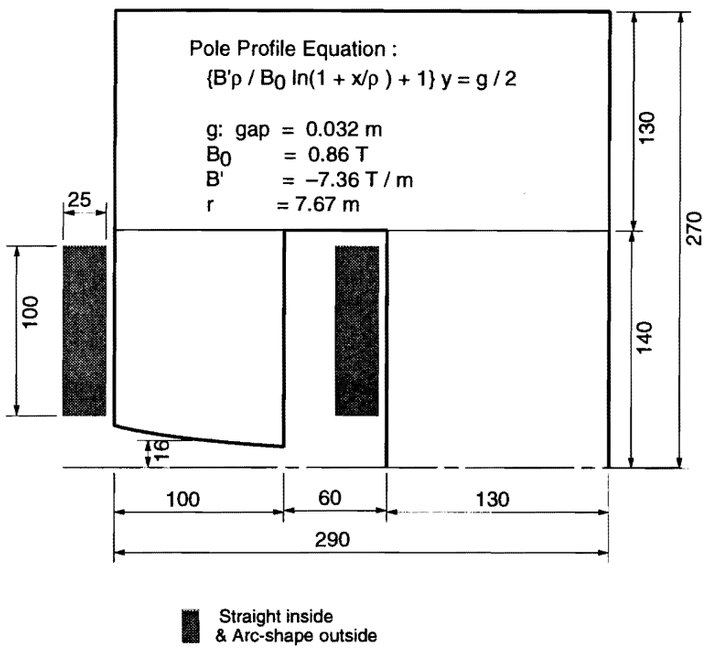

Figure 5.9: *A half cross-section view of a dipole magnet.*

Table 5.7: *Choices of r_{bore} for the quadrupole magnets.*

r_{bore} (m)	B' (T/m)	length (m)
0.016	55	0.25, 0.05, (0.15)
0.021	26	0.25, 0.05, (0.15)
0.021 (skew)	26	0.25, (0.15)

* The 0.15 m long quadrupole magnets will possibly be replaced by 0.25 m or 0.05 m quadrupole magnets by modifying the optics.

Table 5.8: *Quadrupole magnet.*

	type1	type2
pole length (m)	0.06	0.06
r_{bore} (m)	0.016	0.016
B' design (T/m)	52	55
current/pole (AT)	5576 (328A×17)	6000

Table 5.9: Sextupole magnet.

r_{bore} (m)	B'' (T/m^2)	length (m)	current/pole for R&D (A_{turns})
0.016	6000	0.122	3900 (325A × 12)

about 10 % less than the design value calculated by POISSON. However, the integrated field gradient satisfies the required strength due to the effective length being longer than the pole length. The discrepancy between the measurement and the POISSON calculation is due to the short pole length; this fact implies that a 2-dimensional calculation is no longer valid. The field-measurement results were well reproduced by OPERA3D. The measurement results and the calculations by the OPERA3D were taken into account for the final designs.

5.3.4 Sextupole Magnets

The damping ring requires about 120 sextupole magnets; their parameters are listed in Table 5.9. The required manufacturing accuracy is the same as that of the quadrupole magnets. One R&D sextupole was constructed with an accuracy of 20 μm. The field measurements were made in the same way as that of the quadrupole magnets, giving similar results. Although the measured field strength is about 10 % less than the design value by POISSON, the integrated sextupole field satisfies the required strength. The measurement results were also well reproduced by OPERA3D. The measurement results and further calculations by OPERA3D will be taken into account for the final designs.

5.3.5 Field Measurements

The orthodox methods of the field measurement use rotating coils or flip coils. The rotating coils are for the quadrupole magnets and sextupole magnets, and the flip coils are for the bend magnets. The use of a laser and quadrant photo-diodes is effective in the positioning and alignment processes. Although these methods can work in principle, some magnets are too short to be equipped with surveying devises in this case. Furthermore, the end-field effects become important when the magnets are short. Also, the narrow spaces between the magnets may cause some field interference with adjacent elements. An evaluation of the end-field effects using a 3-D computer code (TOSCA), field measurements of the actual configuration, the development of some methods to measure the integral of B and B' along an arc for the combined function bend magnets, etc... are important subjects.

5.4 Alignment

Figure 5.10: *Active Support Tables for the Arc Section*

For obtaining a very low-emittance beam, the magnets of the ring must be aligned within 30 μm. The relative movement of the magnets due to ground motion is, however, shown to be of the same order as the tolerance mentioned above [2]. We must therefore correct the relative movement between the magnets automatically. For this purpose, we will install a set of magnets on an active support table, whose position can be controlled so as to keep the relative alignment between the tables stably. We will also mount each wiggler magnet on an active support in order to control its position and orientation.

5.4.1 Design of the Tables

Tables for the Arc Section

Figure 5.10 shows the tables for the arc section. The table comprises a base plate, three movers, a surface plate, and joints between the movers and the surface plate. A set of magnets, i.e. one bending magnet, two quadrupole magnets, and two sextupole magnets, are mounted on each table.

The alignment of the magnets on the table is carried out in an alignment hut in the ring tunnel. The table with magnets is then moved and installed in the beam line.

Base Plate

The base plate made of iron with a thickness of 30 mm. This thickness was chosen so that the magnet alignment will not be disturbed due to any distortion of the base plate during movement from the alignment hut to the beam line.

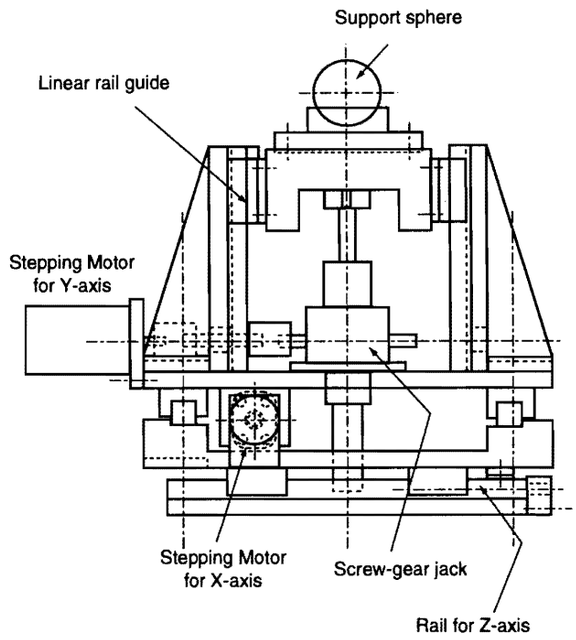

Figure 5.11: *Assembly Drawing of the Mover.*

Mover

Three movers are bolted onto the base plate. One of them has three stages: the lowest stage moves in the beam direction (in z-direction), the middle one horizontally and perpendicularly to the beam (in x-direction), and the highest one vertically (in y-direction). The other two have only two stages, each: an x-stage and a y-stage. Each stage moves along linear rail guides. The z-stage is manually driven, while the x- and y-stages are moved by ball screws driven by pulse motors. The range of the movement is ± 2.5 mm.

Surface Plate

The surface plate has a non-magnetic top plate and an iron bottom plate. A non-shrink mortar is filled between the plates. We made three types of surface plates for a trial: one has an aluminum upper plate, another a stainless one, and the other a mortar surface in which several small plates of stainless steel are attached to mount and bolt the magnets. Comparing these three mutually, we have chosen the stainless upper plate because it is convenient for alignment work and hard to be scratched. The thicknesses of the upper and bottom plates are 20 mm and 15 mm, respectively. The surface plate has a total thickness of 170 mm and a weight of about 1 t.

Joints between the Movers and the Surface Plate

Joints are inserted between the movers and the surface plate to make the table movement smooth. Each joint consists of a ball bearing and a cradle. The ball bearing is for conveying heavy goods, and comprises a large ball to hold weight and small balls to make the rotation of the large ball smooth. It is fixed on the top of the mover, and the cradle is attached to the bottom surface of the surface plate.

To make the mover design simple and to reduce the cost, we use three types of cradles. The cradle for mover A (see Figure 5.13) has a conical hollow in which the ball fits. Therefore, this joint has degrees of freedom for rotation around the center of the ball, but no degree of freedom for movement in the x-z plane. The cradle for mover B has a V-shaped groove where the ball fits. Although the surface plate can move freely along the direction of the groove (z-direction), it is constrained in the transverse direction (x-direction). Since the cradle for mover C is a flat plate, the surface plate can slide in any direction.

Support for the Wiggler Magnet

What is important concerning the wiggler magnet is to maintain its vertical position. For this purpose, each wiggler magnet is installed on a support comprising a base plate and three movers. The mover has only a y-stage, whose design is basically the same as that of the mover for the arc section. We use ball joints between the movers and the wiggler magnet for smooth movement. With this support, we can control the vertical position, roll (rotation around the z-axis), and pitch (rotation around the x-axis) of the wiggler magnet. We gave up trying to control the yaw (rotation around the y-axis), because small effects due to a misalignment of the yaw can be corrected by horizontal steering and quadrupole magnets.

5.4.2 Safety against Earthquakes

The accelerator components must be earthquake-proof. The wiggler magnet on its support is top-heavy, and seems to be rather weak against earthquakes. We have therefore carried out a shaking test and have made sure of the safety [2].

5.4.3 Test of the Positioning Resolution

Table for the Arc Section

Tests were carried out with a dummy weight of 865 kg on the table instead of the magnets. The vertical displacements were measured at points a, b, c, and d shown in Figure 5.13 with an accuracy of 2 μm.

First, the vertical positioning was tested. The surface plate was raised and then lowered by about

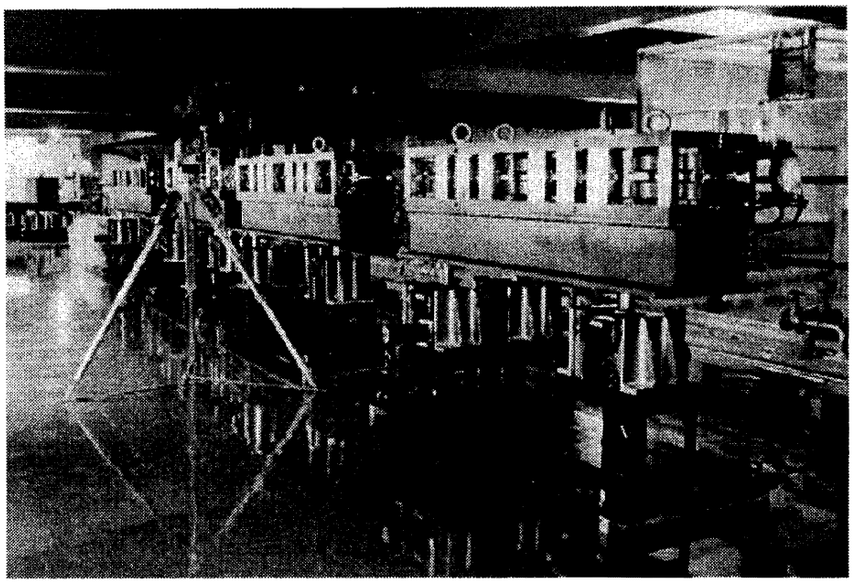

Figure 5.12: *Support for the Wiggler Magnet*

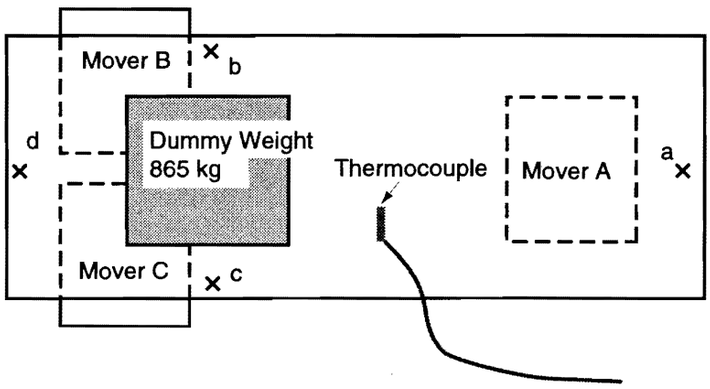

Figure 5.13: *Position of the Measurement*

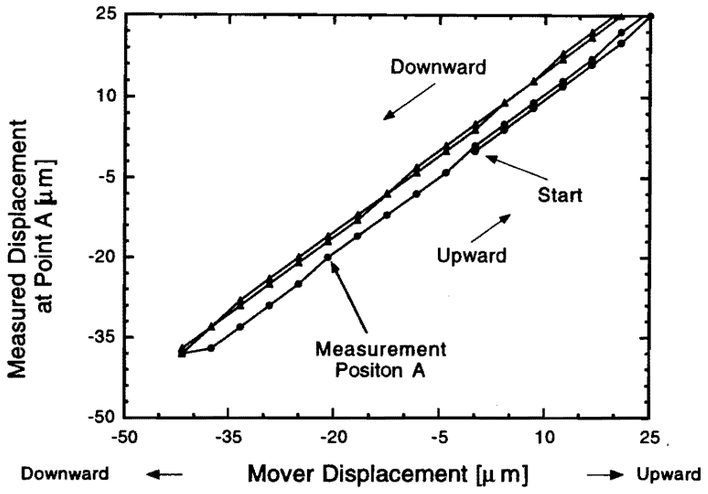

Figure 5.14: *Results of the test of vertical positioning with a magnet mover.*

1.3 mm; this up-and-down cycle was repeated once more. Although the results show good linearity, it moves on different trajectories when it is raised and lowered (Figure 5.14). Although two trajectories are apart from each other by about 5 μm, the reproducibility of each trajectory is very good. We consider that this phenomenon is due to backlash of the ball screw of the y-stage. In order to estimate the performance of the table, we chose one trajectory and made a linear fit. The deviation from the fitted line is shown in Figure 5.15. The vertical position of the table can be controlled within an accuracy of better than 2 μm.

Tests of the roll and pitch were carried out as well. The results also show double trajectories due to backlash. A linear fit was made with the data on each single trajectory. Deviations from the fitted lines are shown in Figures 5.16 and 5.17 for the pitch and roll, respectively. The pitch angle can be controlled within 2.5 μrad, while the error in the roll angle becomes about 10 μrad.

We suppose that the reason for this difference between the pitch and roll is that the joint having the cradle with the V-shaped groove does not function well for rotation around the axis parallel to the direction of the groove.

As for this problem, a new joint comprising a ball joint and a linear rail guide has been developed. Preliminary results show that it works well. We expect that the deviation of the roll will be reduced with the new joints to the same level as that of the pitch.

Support of Wiggler Magnets

The wiggler magnet was mounted on its support and moved up-and-down twice. The range of the movement was about 1.3 mm. The results show the same features as those of the support table: good

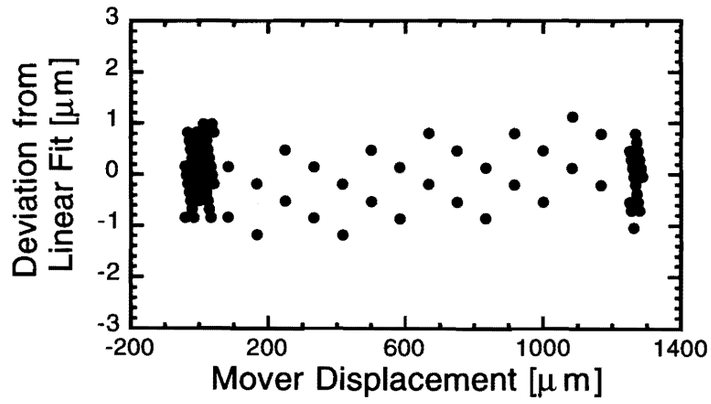

Figure 5.15: *Deviation from the Fitted Line: Vertical Movement*

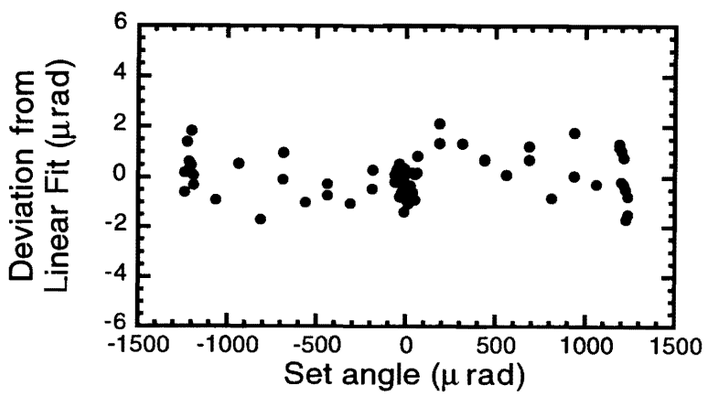

Figure 5.16: *Deviation from the Fitted Line: Pitch*

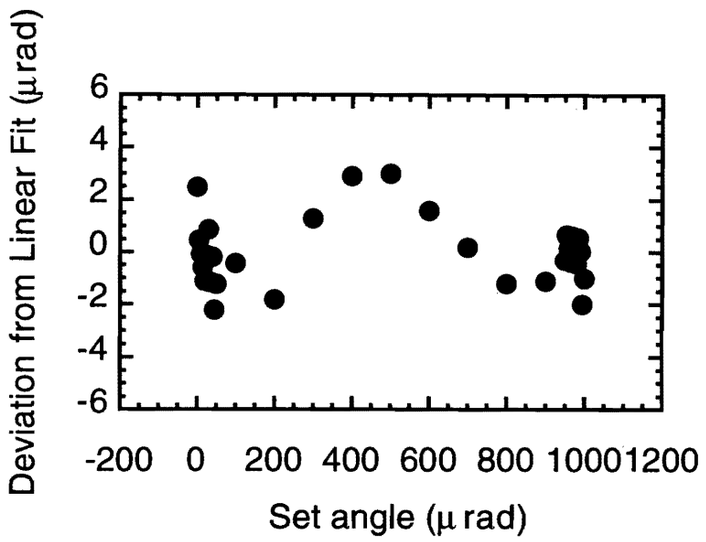

Figure 5.17: *Deviation from the Fitted Line : Roll*

linearity and a double trajectory due to backlash. The fit to one trajectory shows that the vertical position can be controlled to within 3 μm, (Figure 5.18).

Preliminary Results of ATF Alignment

About 300 magnets for the ATF damping ring were roughly aligned within an accuracy of 200μm in January, 1997. Since one combined bending magnet, two quadrupole magnets and two sextupole magnets were set on one active girder within an accuracy of 31μm, we could align them precisely using a beam-based alignment and movers. A scattered plot of the setting error of the transverse position and longitudinal setting error are shown in Figures 5.19.

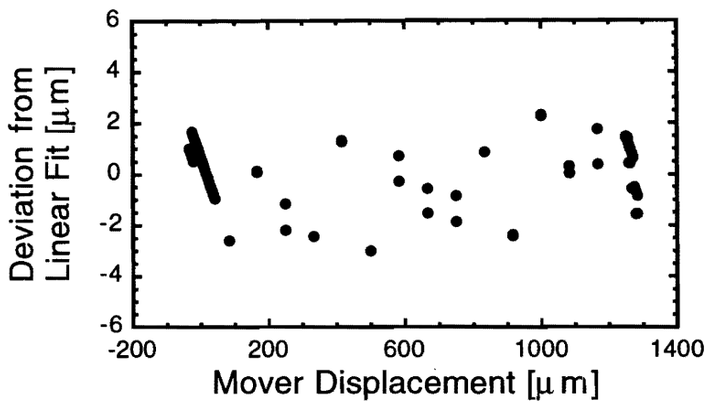

Figure 5.18: *Deviation from the fitted line: vertical movement (wiggler support)*

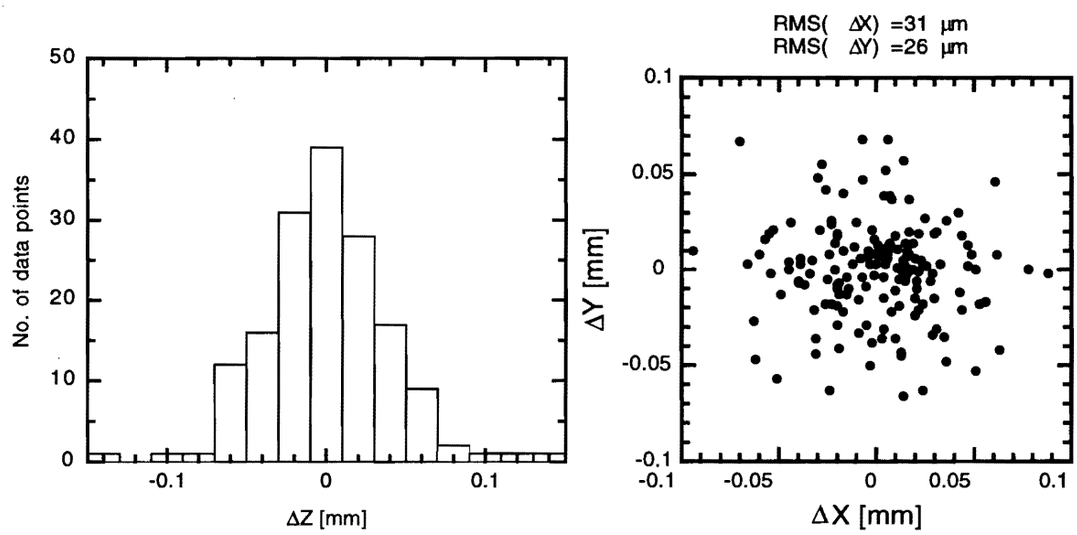

Figure 5.19: *Scattered plot of the transverse setting error and longitudinal setting error, which were measured on magnets of the ATF 14 active girders using a 3D mobile tracking system*

5.5 RF System

5.5.1 General Description

The damping-ring RF system must be reliably operated so as to provide a sufficiently stable accelerating voltage as well as to accommodate a suitable low-impedance environment for the beam. The design should be made while taking the following requirements into account:

1. Provide a sufficient voltage to obtain an energy acceptance of more than 1.2% and to obtain a short bunch length of less than 5 mm.
2. Provide sufficient power to compensate for a synchrotron- radiation loss of 758 keV/turn and parasitic mode loss.
3. Avoid any longitudinal and transverse coupled-bunch instabilities caused by higher order modes (HOMs) of the accelerating cavities up to the maximum beam current of 553 $\sim$ 790 mA. Also, the broad-band impedance of the cavity section should be sufficiently small to avoid turbulent bunch lengthening.

The choice for the accelerating frequency is determined by the bunch spacing of the beam, and by the availability of klystrons or other RF devices. The frequency should be a sub-harmonic of 2856 MHz, the injector linac frequency, in order to synchronize the beam to the linac RF during injection and extraction. Since the bunch spacing is 1.4 nsec, frequencies of 714 MHz and 1428 MHz are candidates. The frequency of 714 MHz is considered to be adequate for the following reasons [2]:

a) With a lower RF frequency, the growth rate of the coupled-bunch instability caused by the accelerating-mode impedance of the cavities is small. Also, the shifts in the stable bunch positions, which arise from the modulation of the accelerating voltage induced by the gaps between the bunch trains, becomes small with a lower RF frequency.

b) High-power devices, such as a klystron and an input coupler, can easily be realized for a lower RF frequency.

c) The 714 MHz RF systems have already been built for the SLC damping ring at SLAC and for the ATF damping ring at KEK, and many key devices have already been developed.

We consider here the 714 MHz RF system, which is based on the technologies developed for the ATF damping ring. The principal parameters of the RF system are given in Table 5.10.

By using four HOM-damped cavities, which have been developed for the ATF, a total gap voltage of 1.2 MV can be produced. The synchrotron radiation loss of 758 keV/turn is about five times larger

RF frequency	f_{RF} [MHz]	714.000
Harmonic number	h	660
Total gap voltage	V_c [MV]	1.2
Number of cavities	N_c	4
Maximum beam current	$(I_0)_{max}$ [mA]	600
Beam Energy	E_0 [GeV]	1.98
Radiation loss/turn	U_0 [MeV]	0.758
Revolution frequency	f_r [MHz]	1.0818
Longitudinal radiation damping time	τ_ε [msec]	2.6
Natural energy spread	$(\sigma_\varepsilon/E)_0$	8.62×10^{-4}
Momentum compaction factor	α	8.02×10^{-4}
RF bucket height	$(\Delta E/E)_{max}$	1.25×10^{-2}
Natural bunch length	σ_s [mm]	4.85
Synchrotron frequency	f_s [kHz]	6.8
Synchronous phase*	ϕ_s [deg.]	140.8
Shunt impedance/cavity**	R_{sh} [$M\Omega$]	4.0
Unloaded-Q	Q_0	24,000
Loaded-Q	Q_L	3,400
Cavity coupling coefficient	β	6.0
Cavity filling time	T_f [μs]	1.53
Wall loss/cavity	$(P_c)_{cell}$ [kW]	22.5
Beam-loading/cavity	$(P_b)_{cell}$ [kW]	114
Transmission power/window	P_{window} [kW]	136
Total generator power (at 600 mA)	P_g [kW]	545
Cavity tuning angle (at 600 mA)	ψ [deg.]	-41.5
Cavity detuning amount (at 600 mA)	Δf [kHz]	-92

* $\sin\phi_s = U_0/eV_c$

** $R_{sh} = V^2/P_c$

Table 5.10: *RF system parameters of the damping ring.*

than that of the ATF damping ring. As a result, the beam-loading per cavity becomes much heavier. The input coupler, which can handle a transmission power of more than 140 kW, should be newly developed. The total power required for the power source amounts to 550 kW. CW klystrons capable of providing more than 100 kW are not immediately available, and should thus be developed.

Because of the very narrow beam pipe used in the damping ring, the cutoff frequencies are very high, for example, 9.56 GHz for the TM01-mode in the case of an inner diameter of 24 mm. In order to store a high beam current of 600 mA without experiencing coupled-bunch instabilities, it is essential to reduce the higher-order-mode (HOM) impedances of the cavities up to this cutoff frequency. It is also very important to design the beam-line components carefully in order to avoid resonance structures.

5.5.2 Damped Cavity

The requirements for the cavity HOMs are roughly given by:

$$\begin{aligned} (R_{sh}/Q)\cdot Q\cdot f_{res} &< 40\ [\mathrm{k\Omega\cdot GHz/ring}] \quad \text{for monopole modes,} \\ (R_T/Q)\cdot Q &< 200\ [\mathrm{k\Omega/m/ring}] \quad \text{for dipole modes,} \end{aligned}$$

where R_{sh} is the shunt impedance ($= V^2/P$), f_{res} the resonant frequency of the HOM, and R_T the transverse impedance. We assumed that a single HOM resonance contributes to the growth of the instability. We consider here the use of the 714-MHz HOM-damped cavity, which was developed for the ATF damping ring [2, 7]. It was demonstrated that this cavity can provide a gap voltage of more than 400 kV/cavity, and has an excellent performance of low HOM impedances.

The 714-MHz HOM-damped cavity has four HOM-damping ports to extract HOM power. Figure 5.20 shows a cross-section of one cavity unit. Each damping port is a flat waveguide of 170 × 20 mm, with round corners of 5 mm in radius. The cutoff frequency of the waveguide was chosen to be 887 MHz, higher than the accelerating frequency of 714 MHz and lower than the lowest HOM frequency. The HOM power is extracted from the damping ports and is absorbed in the dummy loads, while an accelerating field is trapped in the cavity due to the high-pass characteristics of the waveguide. In order to effectively damp all of the harmful HOMs, it is essential to locate the damping ports at a the location where magnetic fields of the HOMs are strong. We designed the inner shape of the cavity so that the field patterns of the HOMs are not deformed too much from those of the cylindrical pill-box cavity. Then, the damping ports are put at the outer corner of the cavity where the magnetic fields of the HOMs are strong in the case of a pill-box cavity. In addition, a beam pipe damping scheme was introduced for the high-frequency HOMs. The power of the high-frequency HOMs are also absorbed in microwave absorbers installed in a large beam pipe (100 mm in diameter) located beside the cavity.

The HOM-damping characteristics were first investigated with the computer code MAFIA, using Slater's tuning method [4]. Then, the HOM-damping characteristics were experimentally investigated using a cold model cavity [5]. The characteristics of the most harmful HOMs are given in Table 5.11. Figure 5.21 shows the damped resonance spectrum measured on a cold model cavity. The HOM characteristics seems to be excellent, at least up to a frequency of 2.5 GHz.

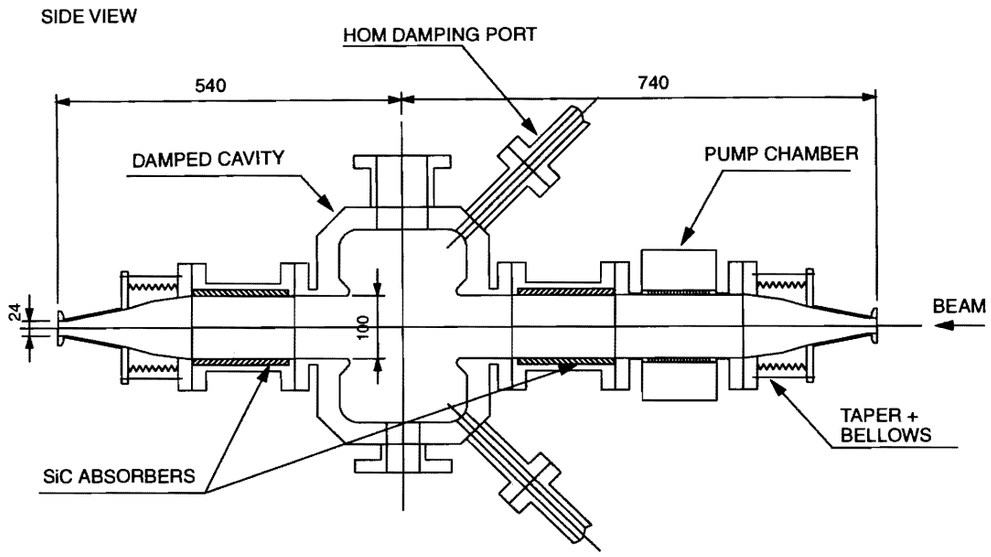

Figure 5.20: *Cross section of one cavity unit.*

Mode	Calculated			Measured	
	f (GHz)	Q_{ex}	R_{sh}/Q or R_T/Q	f (GHz)	Q_L
TM011	1.075	7.1	62.5 (Ω)	not visible	
TM110	1.160	24	263 (Ω/m)	1.158	24
TM111	1.363	24	726 (Ω/m)	1.363	19

Table 5.11: *Characteristics of the strongest HOMs.*

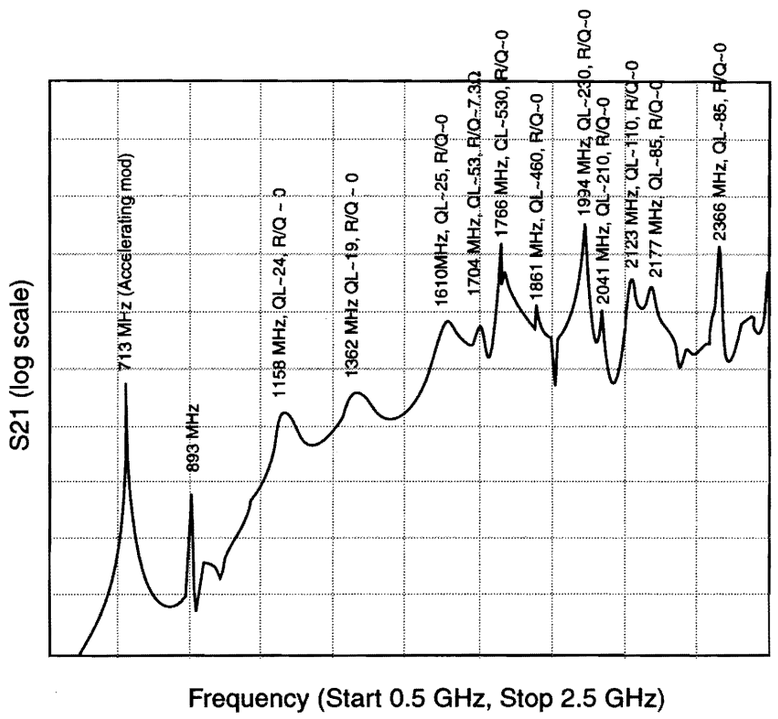

Figure 5.21: *Damped resonance spectrum with four waveguides and loads measured on the cold model. The measured S_{21} parameter between two rod antennas placed at both end plates is shown Abscissa: frequency, 0.5 - 2.5 GHz. Ordinate: $|S_{21}|$, 10 dB/ division.*

Although good HOM damping characteristics are expected for higher frequency range of 2.5 - 10 GHz, further investigations, both on the calculation and the measurement, are needed for a verification.

A high-power cavity was designed [6], fabricated and tested under high power [7]. The basic fabrication method was machining from copper blocks and assembling by brazing. Table 5.12 shows the principal parameters of the high-power cavity.

Resonant frequency	f_{res} [MHz]	714.000
Unloaded-Q	Q_0	24,000
Shunt impedance/Q	R_{sh}/Q	166 Ω
Shunt impedance	R_{sh}	4.1 MΩ

Table 5.12: *Parameters of the HOM-damped cavity.*

It was demonstrated that this cavity can be operated under up to a dissipated power of 50 kW, the maximum available power at the test bench, without any problems. This corresponds to a gap voltage of about 440 kV/cavity. Two cavities of this type were installed in the ATF damping ring, and are undergoing operation. Figure 5.22 is a photograph of the damped cavity installed in the ATF damping ring.

To absorb the HOM power, two types of HOM loads have been developed [8, 9]. One is a broadband waveguide load which terminates the HOM damping port. Tiles of silicon-carbide (SiC) are brazed in a copper waveguide, and are used as microwave absorbers. The SiC's are cooled by heat transfer to cooling water pipes, which are brazed on a side wall. For the other type of the loads, a beam-pipe HOM load, a cylinder of SiC is used as a microwave absorber. It was fit in a copper pipe by a shrink-fit technique, and is cooled by heat transfer to a cooling water pipe brazed on the copper pipe.

Beside using the HOM-damped cavities developed for the ATF DR, the use of the ARES (Accelerator Resonantly-coupled with an Energy Storage) is another solution. The ARES is a three coupled-cavity system, which was developed as a powerful countermeasure to the heavy beam-loading in the B-factory. Because of its large electromagnetic stored energy, the ARES is effective for minimizing the modulation in the cavity voltage induced by missing buckets in the damping ring. Since two types of 508 MHz ARES's have been successfully developed at KEK, it will be possible to scale these designs to the frequency of 714 MHz.

5.5.3 Power Sources

An output power of 550 kW is required for the 714 MHz power source. In order to supply this power below 80 % of the saturation level of the klystron, the maximum power of about 700 kW is required. Since there are no CW klystrons that are capable of providing more power than 100 kW, a new klystron should be developed. In the original design of the ATF damping ring, it is planned to use a

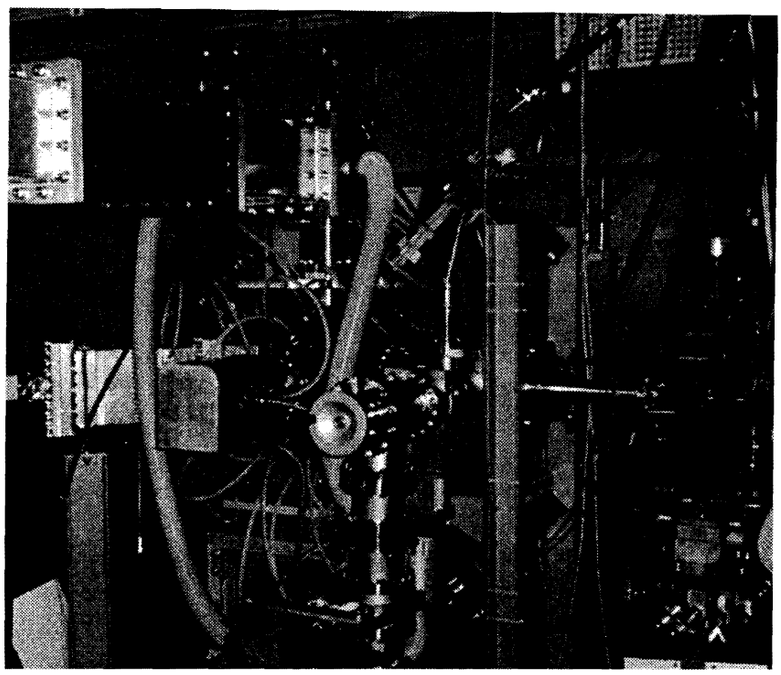

Figure 5.22: *714 MHz HOM-damped cavity installed in the ATF damping ring.*

714-MHz 250 kW klystron which would be newly developed. However, due to the shortage of fund, this plan was frozen, and a commercial 50 kW klystron was used for the initial operation. For the damping ring, we consider here the use of four 200-kW class klystrons. Some of the design parameters of the klystron, which was considered for the ATF DR, are given in Table 5.13.

Frequency range	f	714 ± 1 MHz
Beam voltage	E_b	44.9 kV
Beam current	I_k	11.1 A
Output power	P_0	250 kW
Efficiency	η	51 %
Current density	J_c	0.88 A/cm^2
Perveance		1.17 μA/V$^{3/2}$

Table 5.13: *Some of the design parameters of the 250-kW klystron.*

Because fast control of the cavity voltage and phase will be required to compensate for any sudden change in the beam-loading during injection, a wide bandwidth of more than 1 MHz will be required. For a quick and economical development, the design will adopt as many components of those of the present klystrons as possible. Each klystron is connected to each cavity, being isolated from each

other by using a circulator.

In the damping ring, beams are injected by a train of 90 bunches. When the ring is initially filled, the beam current increases by a step of 120 mA. Since this causes a sudden change in the cavity voltage and phase, a compensation of this change is needed to fill the ring. A low-level system having this function has been developed and will be tested in the ATF.

5.5.4 Summary

The 714-MHz damping ring RF system can be basically realized based on the technologies developed for the ATF damping ring and for the KEKB. For the accelerating cavities, there are two candidates, the HOM-damped cavity for the ATF, and the ARES cavity developed for the KEKB. Both of them are damped cavities in which the higher order modes are heavily damped. The former cavities are already under operation in the ATF, and are readily available. On the other hand, the ARES has a unique advantage in that it can minimize the modulation of the cavity voltage induced by the empty buckets. In this case, some developments are needed to realize a 714-MHz ARES, since the RF frequency of the KEKB (508.6 MHz) is different from that of the damping ring. In both cases, there is a need for extensive R&D to evaluate HOM impedances at high frequency up to 10 GHz.

High-power 714-MHz klystrons capable of providing 200-kW class power should be developed. A fast control for a sudden change in the beam loading is required for the low-level RF system. It is expected that much experience, that will be extracted from the operation of ATF damping ring, is reflected to the detail design of the RF system.

5.6 Vacuum System

The vacuum system of the damping ring must be designed so as to achieve a pressure that does not cause an unacceptable emittance growth through beam-gas scattering. The gas desorption in an electron storage ring is dominantly induced by the irradiation of synchrotron radiation (SR), which is called photo-desorption.

The damping ring will have circulating beam currents of 600 mA. The density of the SR photons at the chamber wall will reach 2×10^{19} and 1×10^{19} photons per meter per second in the wiggler section and bending sections, respectively. The photo-desorption rate of the chamber wall is conservatively assumed to be 1×10^{-5} molecules per photon. The aimed average pressure of our ring is below 6×10^{-6} Pa. Therefore, the required pumping speed of the ring was found to be 140 and $70\,l/\mathrm{s/m}$ for the above two sections, respectively. The basic design concept of the ring is summarized as follows:

1. First, suitable materials for some of the vacuum components must be selected. Most of the vacuum chambers will be made of the extruded aluminum alloy. Copper will be used for the SR

absorbers and a vacuum chamber that will be set under the hard radiation fan. Stainless steel will be used for the bellows. All of the vacuum chamber will be baked to 150 °C for 24 hours before assembly at the beam line.

2. The vacuum chambers must be connected using optimized clamp-chain flanges that have no gap in the beam channel. The chambers will not be welded *in situ* due to the limitation of connection space.

3. The synchrotron radiation should be localized using photon absorbers, especially in the arc section. This has a merit that it will be possible to minimize the area of high gas desorption.

4. The basic cross section of the beam duct is a circle of ϕ24 mm, except for the straight section. The wiggler chamber has a race-track shape, 15 mm high × 47 mm wide. These different cross sections should be connected with shallow transitions to keep the impedance contribution low.

5. Two types of bellows with a race-track and circular aperture should be used that are the same as that of the chamber's. The RF shield should be inserted into the bellows and gate valves.

6. A cold-cathode gauge should be installed in each cell to monitor the pressure of the ring. Additional information can be obtained by monitoring the ion-pump currents, using B-A gauges and residual-gas analyzers.

5.6.1 Vacuum Chambers

A cross-sectional view of the wiggler chamber is shown in Figure 5.23 (a). The beam duct has cooling channels on both horizontal sides. Along the beam duct, two side channels for non-evaporable getter (NEG) pumps are installed. They are connected to the beam duct through slots that are created in the space between the cooling channel and the outer chamber wall. Three pumping ports are provided on the inner side of the ring to install ion pumps, some vacuum gauges and the roughing pump systems.

The cross section of a bending chamber is shown in Figure 5.23 (b). The bending magnet is a combined type, and the gap between the magnet poles is open to the outside of the ring. We will add an ante-chamber to the beam chamber in order to localize the area irradiated by SR photons. Ion pumps and NEG pumps will be installed near to the photon absorber in order to evacuate the out-gas effectively.

With a beam current of 600 mA, the maximum linear power density along the beam duct becomes 1.5 kW/m for both the wiggler and arc sections. These chambers are cooled by water. In the ante-chamber the maximum temperature at the surface of the copper photon absorber will reach 130 °C.

An important issue concerning the vacuum system is to handle a large SR power load from wiggler magnets. It will exceed 5 kW at the crossing point of the chamber wall of the first bending chamber and an extrapolated center line of wigglers, a SR beam line. This load has to be removed from the ring to a specially designed cooling section through an extracted SR beam line, like SR light source rings. To make this beam line, we need specially designed quadrupole magnets and sextupole magnets, because the SR line interferes with these magnets.

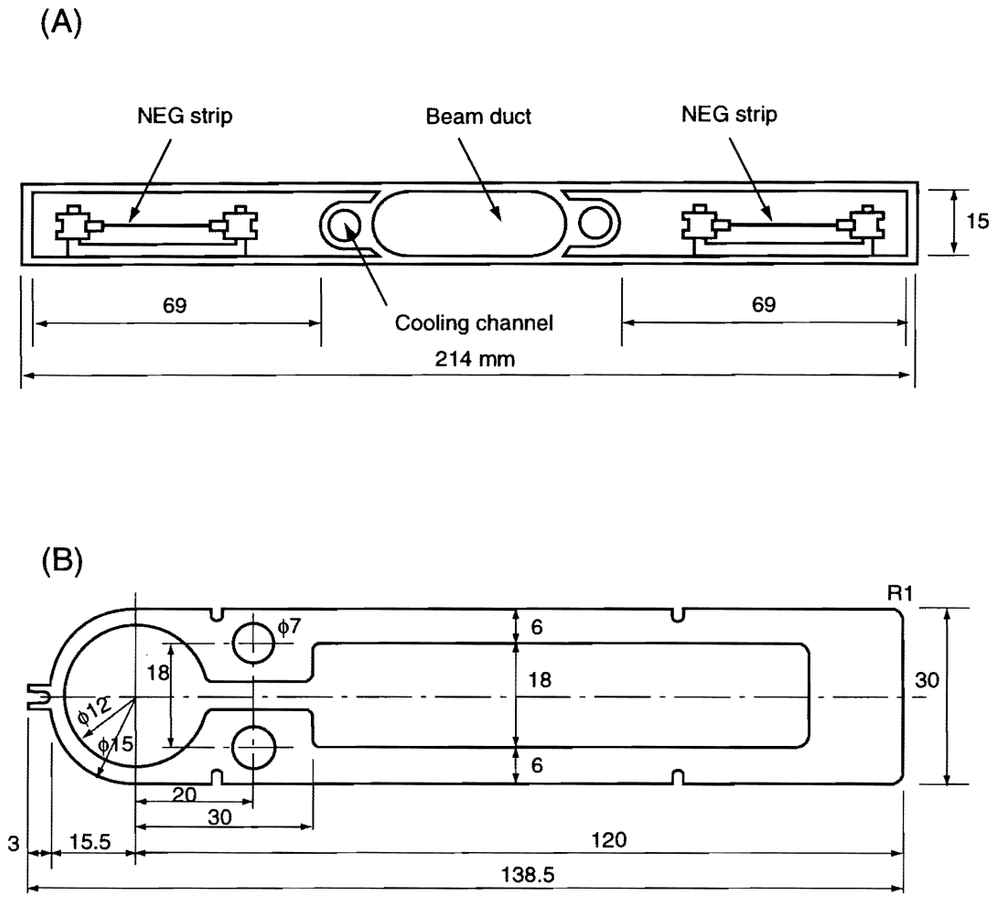

Figure 5.23: *Cross-sectional views of the chambers (a) for the wiggler magnet (b) for the bending magnet.*

5.6.2 Pumping scheme

The roughing pump system is connected to vacuum chambers by manually operated valves. The system consists of an oil-free turbomolecular pump with magnetic bearings and a dry pump. The pump will be mounted on a cart and disconnected from the vacuum chamber during operation, except for NEG pump activation.

Sputter ion pumps (SIPs) will be mainly used in the ring. They will be placed just before the photon absorber so as to effectively evacuate desorped gases. The SIPs will have a 60 l/s nominal pumping speed for straight chambers and 100 l/s for ante-chambers. Linear NEG ribbons will be installed in two side channels of the wiggler chamber. They should effectively evacuate the desorped gases along the beam duct. Additional lumped NEG modules will be installed in the normal cell to support the SIPs.

5.6.3 Beam-Gas Scattering

Scattering of the beam with residual gases in the vacuum chamber leads to a beam loss and an emittance growth of the beam.

Regarding the emittance issue, several persons [2] have evaluated the distribution function of an electron bunch. The result is different from a Gaussian, and has a long tail distribution. Since we are interested in the central region of the bunch, the effect to the beam emittance is not very large. If we accept a vertical emittance growth of 10%, an average pressure of the ring below 6×10^{-6} Pa is needed, which is a realistic pressure to achieve in the ring.

For the beam loss, the beam lifetime is calculated by formulae of elastic scattering, Bremsstrahlung and ionization of the gases. The calculated beam lifetime is 40 minutes at an average pressure of 6×10^{-6} Pa. There is sufficient time to store the beam in the ring, because the electron bunch will be extracted 200 ms after injection.

5.7 Beam Instabilities

5.7.1 Single-Bunch Instabilities

A single-bunch instability, especially in the longitudinal plane, must be avoided in a damping ring. If the intensity exceeds some threshold, it can damage not only the longitudinal emittance, but also may cause a so-called saw-tooth phenomena, which totally degrades the performance of the linear collider. Therefore, the impedance of the vacuum chamber and components should be carefully evaluated.

First, a rough estimation of the threshold is given by the formula

$$|Z/n|_{\rm th} = \sqrt{\frac{\pi}{2}} \frac{\gamma Z_0}{r_e} \frac{\alpha_p \sigma_\delta^2 \sigma_z}{N} \ , \tag{5.14}$$

where Z_0 is the vacuum impedance and r_e is the classical electron radius. In the case of the damping ring, Equation 5.14 gives 0.15 Ω at $N = 1 \times 10^{10}$.

The impedance sources in the ring are listed in Table 5.7.1. They were estimated by TBCI and ABCI

	$\lvert Z/n\rvert$/unit (mΩ)	Number of units	$\lvert Z/n\rvert$/ring (mΩ)
Rf cavities	40	5	200
Vacuum pump slots	6×10^{-4}	3600	2
Monitor electrodes	0.02	4×100	8
Bellows	0.4	80	32
Septum chamber	0.7	2	1
Rf quadrupoles	6.4	2	13
Tapered transitions	1.5	4	6
Clamp flanges	0.04	60	2
Gate valves	0.8	6	5
Photon masks	0.5	20	10
Kicker chambers	2.1	2	4
Rf absorbers			≈ 50
Total			331

Table 5.14: *Impedance sources.*

codes. Although the specific impedance ($|Z/n|$) reaches 0.33 Ω, 2/3 of the total comes from the rf cavities, whose major contribution is capacitive. We thus expect that the actual threshold is higher than that given by Equation 5.14.

5.7.2 Multi-bunch Instabilities

In the case of a high current and a large number of bunches in the ring, a cure for the coupled-bunch effect must be considered. The possible effects of the RF cavities are:

1. Longitudinal coupled-bunch instabilities caused by the accelerating mode,
2. A shift of the longitudinal bunch position due to beam-loading, and
3. Longitudinal and transverse coupled-bunch instabilities due to the higher order modes.

In addition, the wake-field of the resistive wall of the vacuum chamber has an important effect on the transverse coupled-bunch motion.

Because of the high beam current and large circumference, the band width and detuning frequency of the cavities should be comparable with the revolution frequency. Then, the growth rate of the "-1" mode, excited by the tail of the impedance of the accelerating mode, can be higher than the radiation-damping rate under some conditions. This instability can be avoided by using a low RF frequency, high accelerating voltage with low-R/Q cavities. The design of our RF system will achieve this condition. Another solution is RF feedback for specific oscillation modes. The growth rate of the coupled-bunch motion has been analytically estimated to be less than $100\,\mathrm{s}^{-1}$ in the case of the highest current, which is less than the radiation-damping rate. The stability of bunches has been checked by tracking simulations of rigid bunches, including the wake-field of the accelerating mode. Since the bunches are not uniformly distributed over the ring because of the gap between the trains, each bunch feels a different wake-field (beam-loading) induced by the preceding bunches. The bunch energies are the same, so as to keep the revolution frequency unchanged. As a result, the head bunch in a train delays and tail bunch advances from the nominal positions. The shift in the positions would become comparable with the bunch length under some conditions. A high accelerating voltage with low R/Q can reduce this shift. In addition, an RF system for beam-loading compensation will be installed to test the minimization of the shift. This system has an idling cavity (no power is fed) having a resonance frequency of $f_{main} - N_t f_{rev} - D_f$, where f_{main} is the frequency of the main RF and N_t the number of trains, f_{rev} the revolution frequency and D_f the detuning frequency. The required peak voltage is about 50 kV. It is possible to install more than one cavity with frequency $f_{main} - nN_t f_{rev} - D_f, n = 1, 2, 3, \ldots$ to obtain more precise compensation. The behavior of bunches with this beam-loading compensation system has been studied by tracking simulations.

The longitudinal instabilities caused by the higher-order modes (HOM) can be suppressed by the damped cavity (cavity with low Q values of HOMs). In the case of the highest beam current, the threshold Q of HOMs estimated by a tracking simulation is

$$(R/Q) \times Q \times f \sim 10^4 \qquad \text{for each monopole mode,}$$

where f is the frequency of each mode in GHz and R/Q is in Ω. This value agrees with analytic calculations for uniformly distributed bunches having the same total current.

The transverse instabilities can be suppressed by a damped cavity and the bunch-to-bunch tune spread in each train. The requirements were estimated by a tracking simulation to be:

$$(R/Q) \times Q \sim 10^6 (\Omega/m) \qquad \text{for each dipole mode, and}$$
$$D_n \sim 1 \times 10^{-3},$$

where D_n is the peak-to-peak betatron tune difference in a train. These values also agree with the analytic result for uniformly distributed bunches having the same total current, assuming that the bunches in a train are decoupled because of different tunes. These requirements concerning the RF cavities can be satisfied, as described later, and the tune spread can be obtained by an RF quadrupole. The tune difference is also expected to suppress the transverse coupled-bunch instabilities due to the

resistive wall wake-field. In these estimations, bunches were assumed to be rigid point charges. Some single-bunch effects, for example a head-tail effect with positive chromaticity, are expected to increase the damping rate of coherent oscillation and to relax the requirements. These effects will be tested in the ring.

The thresholds of the longitudinal and transverse coupled-bunch instabilities caused by a higher-order resonance with impedances $R_\parallel$ and $R_\perp$ at the resonant frequency (f_r) are roughly estimated by the formulae

$$\begin{aligned} R_{\parallel,\mathrm{th}} &= \frac{E\nu_z}{I\tau_z\alpha_p f_r e}, \\ R_{\perp,\mathrm{th}} &= \frac{ET_0}{I\tau_\beta\beta e}, \end{aligned} \tag{5.15}$$

where β is the beta function at the cavities. Equation 5.15 assumes a uniform distribution of bunches; the worst case is when the coupled-mode hits the resonance exactly. In the case of the ATF damping ring, this threshold is

$$\begin{aligned} R_{\parallel,\mathrm{th}} &= 1.4\left(\frac{1\ \mathrm{GHz}}{f_r}\right)\mathrm{k}\Omega, \\ R_{\perp,\mathrm{th}} &= 16\mathrm{k}\Omega/\mathrm{m}, \end{aligned} \tag{5.16}$$

where we have used $\beta = 8$ m and $\tau_\beta = \tau_y = 4.8$ ms. The longitudinal threshold is satisfied by the damped cavity in the longitudinal direction, as discussed later. The transverse is cured by a damped cavity together with a bunch-to-bunch tune spread of $\Delta\nu_\beta \sim 10^{-3}$ introduced by an rf quadrupole. According to the tune-spread, the transverse threshold is effectively increased to be N_b-times bigger than Equation 5.16.

The actual threshold with a real bunch-train distribution including transient phenomena has been studied by multi-rigid-bunch simulations. The results show that conditions 5.15 and 5.16 are acceptable for the threshold.

The resistive wake of the vacuum chamber is another source of the coupled-bunch instability. The growth rate is estimated by

$$\begin{aligned} \nu &= \nu_0\left[1 - \frac{Ne^2\beta^2 G^*(2\pi,\nu)}{\pi b^3\gamma m\sqrt{R}\omega_0^2\nu_0^2}\sqrt{\frac{c}{4\pi\sigma\beta}}\right], \\ G^*(2\pi,\nu) &= 2\sqrt{\pi}\sum_{n=1}^{\infty}\frac{\exp(i\nu 2\pi n)}{(2\pi n)^{1/2}}, \end{aligned} \tag{5.17}$$

where $\sigma = 3.5 \times 10^7\Omega^{-1}\mathrm{m}^{-1}$ is the conductivity of aluminum. The growth rate is 10 ms for $N = 1 \times 10^{10}$.

5.8 Remaining Issues

Here is a partial list of remaining issues to consider in the design of the damping rings.

- For making the final choice of the lattice scheme, obviously some more systematic and comparative studies of several lattice configurations, as discussed in section 5.2, are required.
- A series of experiments are planned at the ATF damping ring. Without doubt, a large amount of operational experience to be gained there would be fed back to all aspects of the final design of the damping rings.
- In particular, injection and extraction kicker magnets with a high-quality flat top and fast rise- and fall-times for multi-bunch operation of the damping rings are crucial for stable operation of the system. A thorough understanding of this issue will require more hardware R&D and prototype studies.
- Use of long sections of wiggler magnets in the real-life damping rings is very likely, as discussed in section 5.2. In the light of operational flexibility, possibilities must be considered for cases where the damping rings are operated at various excitations of those wiggler magnets. This leads to a varying ring circumference, depending on the operating condition of the wigglers. Provisions must be made to adjust the ring circumference and/or the ring RF frequency to cope with such possibilities.
- Dynamic aperture and its sensitivity to the construction and operational errors of the damping rings needs much more systematic studies. For the positron system, this issue needs to be considered in conjunction with the design of the pre-damping ring, and the expected positron beam emittance from the production area.
- Potential problems with the Fast Ion Instabilities (FEI) in the electron damping ring, and the Photo-electron-Induced Instabilities (PEI) in the positron damping ring could be quite serious. Their expected magnitudes and possible cures must be investigated. Experience to be gained from operation of the ATF damping ring, as well as that of KEKB and PEP-II B-factory rings, would be extremely helpful in understanding these, and to come up with workable solutions.

References for Chapter 5

[1] K.Bane and R.Ruth, SLAC-PUB-4905(1989)

[2] ATF Design and Study Report, KEK Internal 95-4(1995), and references therein.

[3] SLAC ZDR.

[4] S. Sakanaka et al., Proceedings of the 1993 Particle Accelerator Conference, p. 1027.

[5] S. Sakanaka et al., Proceedings of the 1994 International Linac Conference, p. 281.

[6] S. Sakanaka et al., Proceedings of the 1995 Particle Accelerator Conference, p. 1788.

[7] S. Sakanaka et al., Proceedings of the Fifth European Particle Accelerator Conference, p. 2017.

[8] F. Hinode and S. Sakanaka, Proceedings of the 1995 Particle Accelerator Conference, p. 1756.

[9] S. Sakanaka et al., to be presented in the 1997 Particle Accelerator Conference, Vancouver, B.C.

Authors and Major Contributers of Chapter 5

- Shigeru Kuroda
- Junji Urakawa
- Nobuhiro Terunuma
- Shogo Sakanaka
- Yoshisato Funahashi

CHAPTER 6

Bunch Compressor and Pre-linac

Contents

6.1 Bunch Compressor

6.1.1 Introduction

With the given beam emittance a higher luminosity can be obtained generally by making the β function at the collision point smaller. However, when β becomes comparable or smaller than the bunch length, the luminosity is limited because of hourglass effects. Thus, at JLC a short bunch is needed to attain high luminosity. A short bunch length is also helpful for minimizing the adverse effects of short-range wake-field in the main linacs. From these considerations the proposed beam parameters of JLC require an RMS bunch length of 90 μm in the main linacs.

The bunch length expected out of the 1.98 GeV damping ring (DR) is 4.85 mm with an energy spread of 0.862×10^{-3}. Thus, a compression of bunch length by a factor of 1/53.9 is required. Due to preservation of the emittance in the longitudinal phase space, this process causes an increase in the energy spread by the inverse factor. Such a large energy spread cannot be accepted by the main linac without fatal emittance growth across the rest of the machine, and in the compressor, itself. It is therefore necessary to have a system that consists of two compressors, between which an intermediate linac (pre-linac) accelerates the beam to reduce the relative energy spread within the acceptable range.

In the following sections, the number of particles in a bunch and the number of bunches in a train are assumed to be 0.72×10^{10} and 85, respectively.

6.1.2 Basic Parameters

In this section we discuss the choice of the beam energy at the second compressor and the compression factors of the first and the second compressors. A key issue here is the energy spread at each stage in those steps. The multi-bunch beam-loading in DR, if not compensated within DR, brings about an equal, but reduced, equilibrium bunch spacing. Such deviations of the bunch longitudinal positions are mapped to different energies at the exit of the first compressor (referred to as BC1 hereafter). The BC1 performs a 90° phase rotation in the longitudinal phase space. The position deviation amounts up to 4.85 mm (one σ_z-equivalent of the DR bunch length). This position deviation is translated into an energy shift of one σ_ϵ at the cavity of BC1.

Figure 6.1 shows a schematic view of the bunch compressor system. This system consists of two bunch compressors and a pre-linac. The pre-linac reduces the energy spread to be seen by the second bunch compressor (BC2). There must be a trade-off between the cost of the pre-linac versus the difficulties of the transport in BC2 and in the first portion of the linacs. In the following we choose 10 GeV as the beam injection energy into the main linacs. The RMS energy spread at the entrance of pre-linac and main linac is approximately 1 %. The compression factors of BC1 and BC2 are 0.083 (1/12) and 0.200 (1/5), respectively. Table 6.1 shows the basic parameters of the bunch compressors with linear

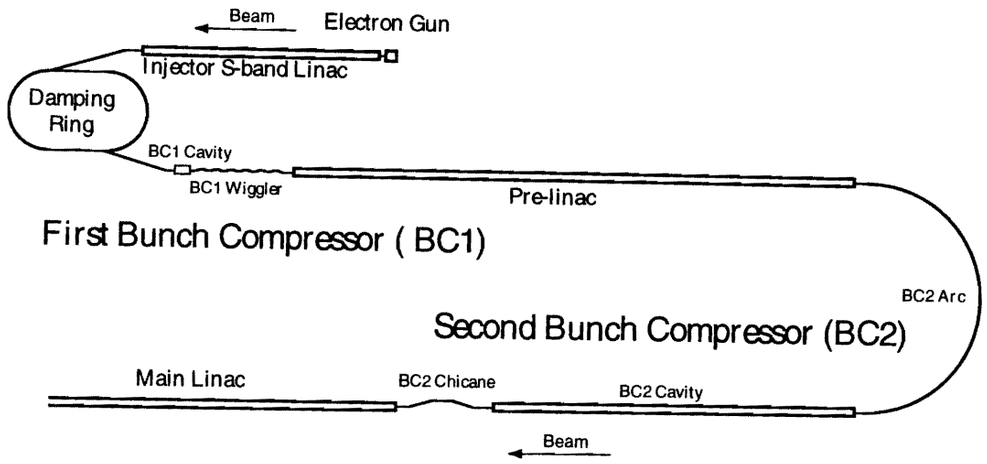

Figure 6.1: *Schematic view of the bunch compressor system.*

theory.

Location	Energy spread(1σ) (%)	Bunch length(mm)
exit of Damping Ring	0.0865	4.82
exit of BC1	1.042	0.400
exit of Pre-Linac	$1.042 \rightarrow 0.2084$	0.400
exit of BC2	1.042	0.080

Table 6.1: *Basic parameters of bunch compressors*

6.1.3 First Compressor (BC1)

There are two major issues which should be taken into consideration in the design of BC1.

One issue is a bunch-position shift that is generated in a damping ring. The beam-loading in the damping ring causes an equal, but reduced bunch spacing within a train. If the beam is directly injected to the linac without adequate treatment, this can result in unequal acceleration in the linac. Another issue is that, at the exit of the damping ring, the particle distribution in the longitudinal phase space has a large spread in z, rather than in δ (momentum deviation).

With those issues in mind, a 90° rotation system is adopted in BC1 (i.e., rotation in the longitudinal phase space). With such a phase space rotation, the relative position shifts of individual bunches at the entrance of BC1 are translated into a bunch-to-bunch energy spread at the BC1 exit. The extraneous energy spread can be reduced during acceleration in the pre-linac in terms of the relative energy deviation. Furthermore, the small energy spread at the damping ring exit is utilized for obtaining

Main Cavity Voltage	V_M	142.5	MV
Frequency	f_M	1428	MHz
Phase	ψ	-95	degrees
Length	L_M	9	m
Compensation Cavity Voltage	V_C	29.06	MV
Frequency	f_C	2856	MHz
Length	$L_{\pm M}$	1.5	m
Beat Frequency	Δf	1.084	MHz
Momentum Compaction of Wiggler	R_{56}	0.465	m

Table 6.2: *Parameters of the first bunch compressor*

a small bunch length at the exit of BC1 for the case of 90° rotation. The parameters of BC1 are summarized in Table 6.2.

Longitudinal Optics of BC1

The condition of 90° longitudinal phase rotation and that of the transfer matrix are given by:

$$M = \begin{pmatrix} 1 + kR_{56} & R_{56} \\ k & 1 \end{pmatrix} \tag{6.1}$$

$$\begin{aligned} \sigma_z^2 &= (1 + kR_{56})^2\sigma_{z0}^2 + 2R_{56}(1 + kR - 56) < \delta_0 z_0 > + R_{56}^2\sigma_{\delta 0}^2, \\ \sigma_\delta^2 &= k^2\sigma_{z0}^2 + 2k, < \delta_0 z_0 > + \sigma_{\delta 0}^2, \end{aligned} \tag{6.2}$$

where all of the parameters are defined in Table 6.2, except for k; k is the local slope of the RF voltage normalized to the nominal energy, which is defined by

$$k = -\frac{2\pi f_M}{c}\frac{V_M \sin(\psi)}{E_0 + V_M \cos(\psi)}. \tag{6.3}$$

Here, E_0 is the injection energy for an electron or positron beam to BC1 cavity, and c is the speed of light. In the present design, E_0 is 1.98 GeV.

When we impose the following condition to the beam transfer matrix of Equation 6.1, the longitudinal phase space is rotated by *roughly* 90° and a small energy spread is obtained at the exit of BC1,

$$1 + kR_{56} = 0 \tag{6.4}$$

Strictly speaking, the longitudinal phase space is not really rotated by $\pi/2$ in this case. However, since the correlation between the bunch length and energy spread is small, it is not considered to be a major problem here. The Twiss parameters in the BC1 system are shown in Figure 6.2.

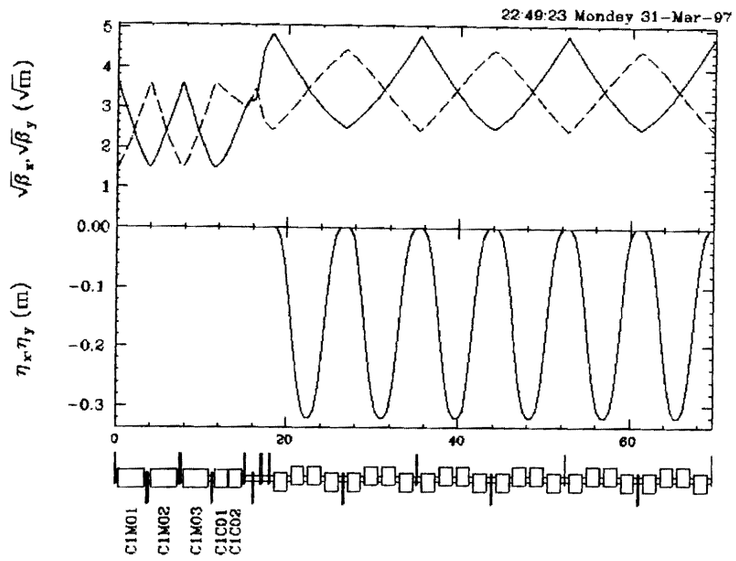

Figure 6.2: *β function and dispersion function in BC1*

Cavity Section of BC1

In this design, we primarily consider the L-band acceleration for the BC1 cavity system. This would require roughly a 9 m longitudinal beam line space for generating the peak accelerating voltage of 142.5 MeV. Another possibility is to use the S-band frequency for the BC1 cavities. The S-band cavities would occupy roughly a 3 m beam line length, and will need to generate a peak accelerating voltage of 71 MeV. However, the nonlinearity of S-band accelerating, relative to the injected bunch length, causes a nonlinearity in the longitudinal phase-space distribution of a single bunch. Such nonlinear components in the bunch distribution would cause the development of energy and position tails at the exit of the bunch compressor. For these reasons, L-band acceleration is chosen for the BC1 cavities.

Wiggler Section of BC1

The wiggler section, which generates the intended momentum compaction factor (R_{56}) in BC1 consists of 6 chicanes. Each chicanes consists of 4 rectangular-type dipole magnets, which has the length of 1.5 m and a magnetic field of 6.96 kG. Quadrupole magnets are arranged between the chicanes, and form the FODO cells, as shown in Figure 6.2.

Multibunch Beam-Loading Compensation in BC1

In the damping ring up to 5 (five) bunch trains are stored at one time. Each bunch in the damping ring feels a different accumulated wake-field of the fundamental mode. The trailing bunches feel a larger wake than the preceding bunches do. Since the energies of those bunches must be the same in the ring, different loaded voltages for individual bunches result in different equilibrium positions of the bunches. If only the fundamental mode is taken into account, the position shift is an almost linear function of the bunch number, and it amounts to 4.85 mm (roughly equal to the natural bunch length, itself). However, when the bunch train travels into BC1, the position shift is converted to an energy shift between bunches in the train.

If a multi-bunch energy shift is perfectly compensated at the exit of the BC1 cavity, a large amount of position shift is generated at the entrance of pre-linac (Figure 6.3(a)). However, if no beam-loading compensation is practiced, the transient beam-loading in the cavity of the bunch compressor, itself, produces an energy spread among bunches (Figure 6.3(b)). This brings about an incomplete rotation in the longitudinal phase space, that results in different longitudinal positions in the linacs. This will cause an energy spread again. Therefore, the beam-loading must be compensated for the amount of beam-loading in the BC1 cavity (Figure 6.3(c)).

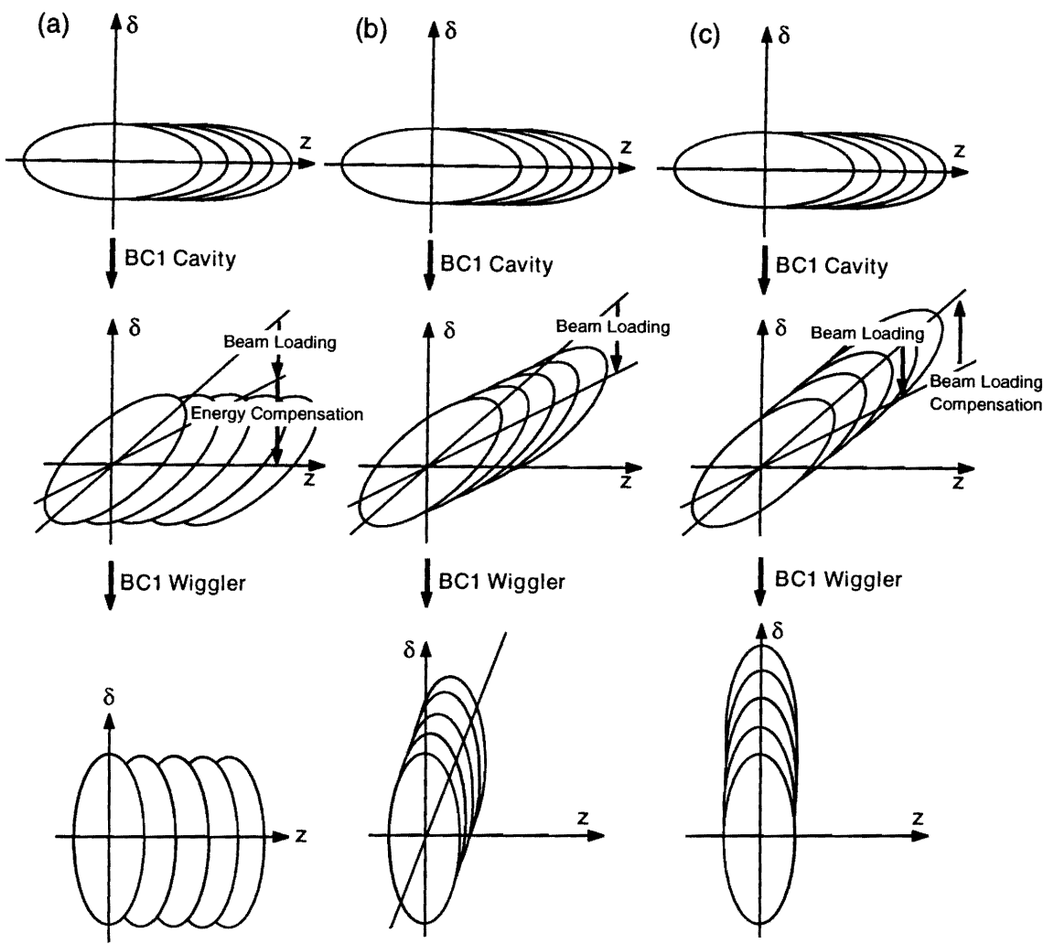

Figure 6.3: *Transformation of the longitudinal phase space (z,δ) in BC1. Effects of beam-loading are shown:*
(a) The case in which a multi-bunch energy shift is perfectly compensated
(b) The case in which no beam-loading compensation is practiced
(c) The case in which the beam-loading is compensated by the amount of loading in the BC1 cavity. This is the scheme adopted for this design study.

6.1.4 Issues Related to Pre-linac

The design of the pre-linac sections which bring the beam energy from 1.98 GeV of the damping ring exit to 10 GeV at the entrance of main linac is discussed in detail in Section 6.3. Here, we briefly comments on two issues related to the design of pre-linacs from the standpoint of operating the bunch compressor systems, namely, single-bunch beam-loading and multi-bunch beam-loading compensations.

Single-bunch Beam-Loading in Pre-linac

The empirical formula for single-bunch beam-loading was derived by K. Yokoya for short bunches as follows[1]:

$$W_L(s) = \frac{cZ_{vac}}{\pi a^2}(W_{L0} + W_{L1}\sqrt{\zeta} + W_{L2}\zeta) \tag{6.5}$$

$$W_{L0} = 0.988r^{0.078} \quad W_{L1} = -1.474r^{0.371} \quad W_{L2} = 0.702r^{0.784}$$

$$\begin{aligned} \zeta &= Ls/a^2 \\ r &= a/0.42L \\ L &= (\text{ cavity cell period }) \\ \lambda &= (\text{ RF wave length }) \\ a &= (\text{ structure iris aperture }) \\ Z_{vac} &= (\text{ vacuum impedance }) = 377\Omega. \end{aligned}$$

From comparison with a rigorous theoretical treatment of the problem, Equation 6.5 is known to be valid under the following conditions:

$$\begin{aligned} 0.10 \;\leq\; a/\lambda \;&\leq\; 0.18 \\ 0 \;\leq\; s/L \;&\leq\; 0.1 \end{aligned}$$

The longitudinal phase space is modulated by a short-range wake-field. For a given choice of the RF phase of the pre-linac, because of the beam-loading effects, each bunch becomes subject to a certain rotation in the longitudinal phase space. This results in a specific single-bunch energy spread at the exit of the pre-linac. Figure 6.4 shows the longitudinal phase-space distribution for four pre-linac phases: $-6°$, $-4°$, $-2°$, and $0°$. In this figure, the longitudinal Twiss parameter α_L is defined in a way similar to that of the transverse Twiss parameter $\alpha_{x,y}$, meaning to characterize the rotation of the longitudinal phase ellipse.

In addition to the phase-space rotation, for a given RF phase choice, a certain growth in the longitudinal phase space also occurs. Its magnitude has been calculated. Figure 6.5 shows the estimated longitudinal emittance growth, together with the expected longitudinal Twiss parameter, as functions of the pre-linac RF phase. In our design, the pre-linac RF phase was chosen to be $-1°$.

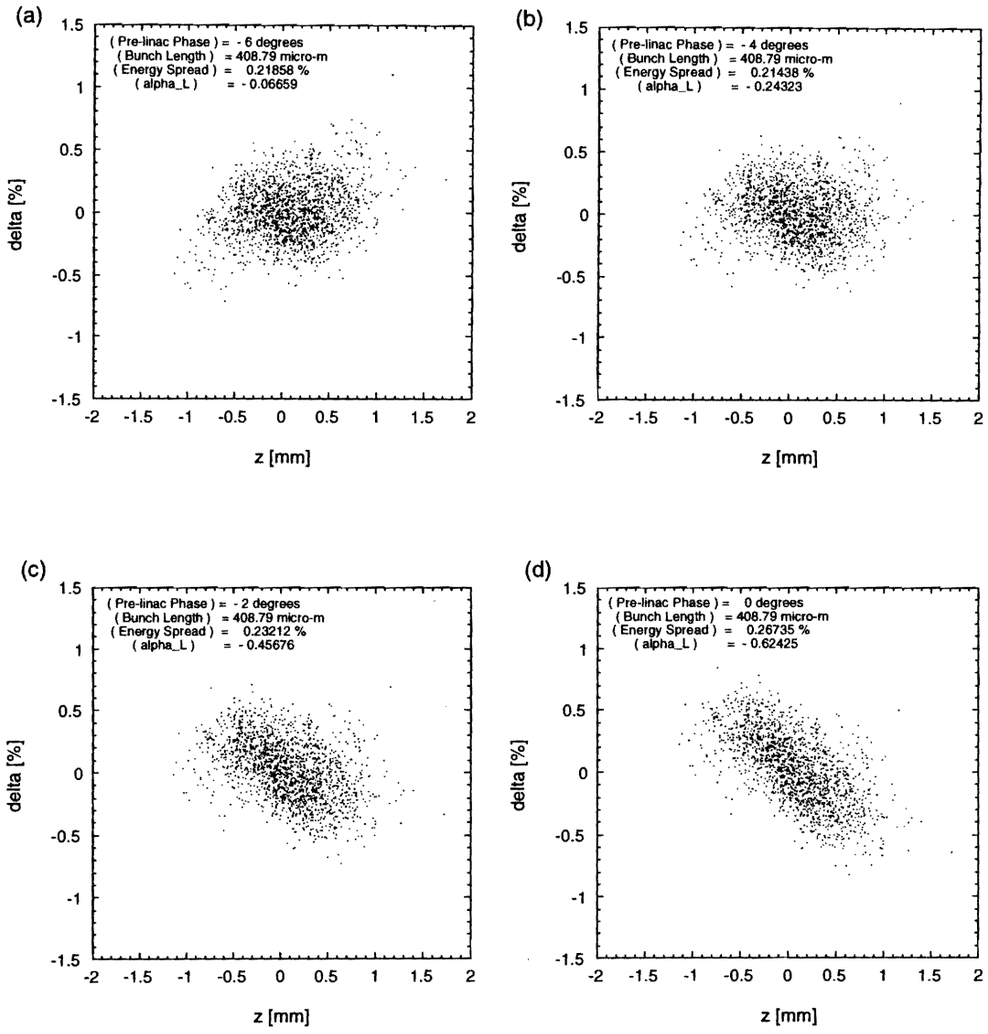

Figure 6.4: *Longitudinal phase-space distributions at the exit of the pre-linac*

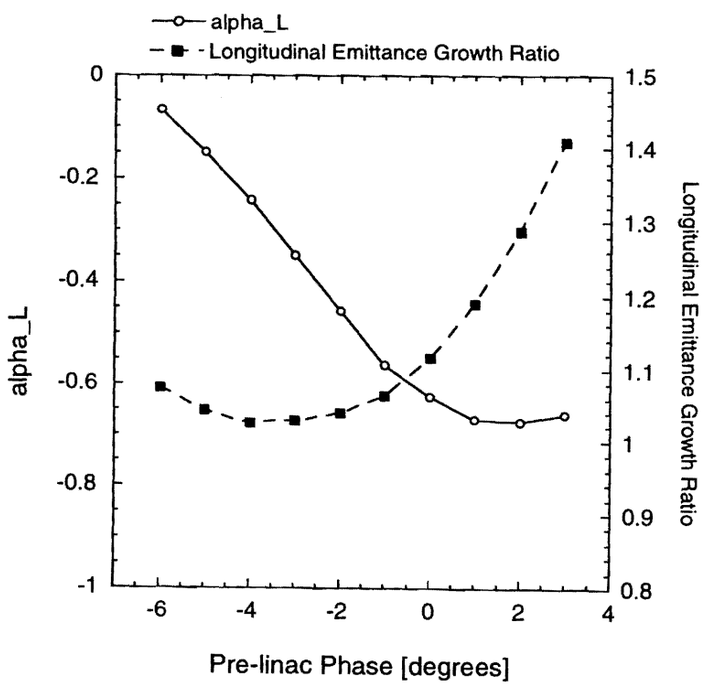

Figure 6.5: *Dependence of α_L and expected longitudinal emittance growth ratio on the pre-linac RF phase.*

Multi-bunch Beam-loading Compensation Method in the Pre-linac

There are at least two methods that are considered possible for compensating multi-bunch beam-loading effects:

1) ΔF Method (The method with slightly different RF frequency)
2) ΔT Method (The method with input RF modulation)

The longitudinal phase space is sensitive to an accelerating RF phase. If the leading and the trailing bunches are accelerated with different RF phases, the bunches will have different bunch lengths at the exit of the bunch compressor system. This means that the energy of bunches in a train should be not only be compensated, but the accelerating RF phase should also be kept in mind in bunch compressor system.

The ΔF method has an advantage in that it can compensate the beam-induced field, irrespective of the main RF field, since it utilizes other external RF fields with different frequencies.

On the other hand, the ΔT method utilizes the main RF field for the purpose of compensating the beam-induced field. Therefore, the phases of the effective field (the sum of RF field and beam-induced field) for the leading bunch and trailing bunch are different when the RF field and beam-induced field don't have a parallel phase.

It should be noted that the BC1 and BC2 cavities have an RF accelerating phase of $-95°$. Thus, the RF field of the BC1 or BC2 cavities and the beam-induced field have a relative phase difference of roughly 90°. Therefore, it is impractical to compensate for the beam-induced field by using RF modulation in the BC1 and BC2 cavities. On the other hand, the phase of the RF field and that of the beam-induced voltage are different from around 180° in the pre-linac. Therefore, both compensation methods are possible to use in pre-linac.

6.1.5 Second Compressor (BC2)

Figure 6.6 schematically shows the shape of the longitudinal phase space in each stage of the second bunch compressor (BC2). It illustrates how the phase space is transfered. In BC2, we adopt an overall 0°-phase rotation in longitudinal phase space. The bending sections (arc and chicane) are arranged at both sides of the BC2 cavities. The parameters of BC2 are given in Table 6.3.

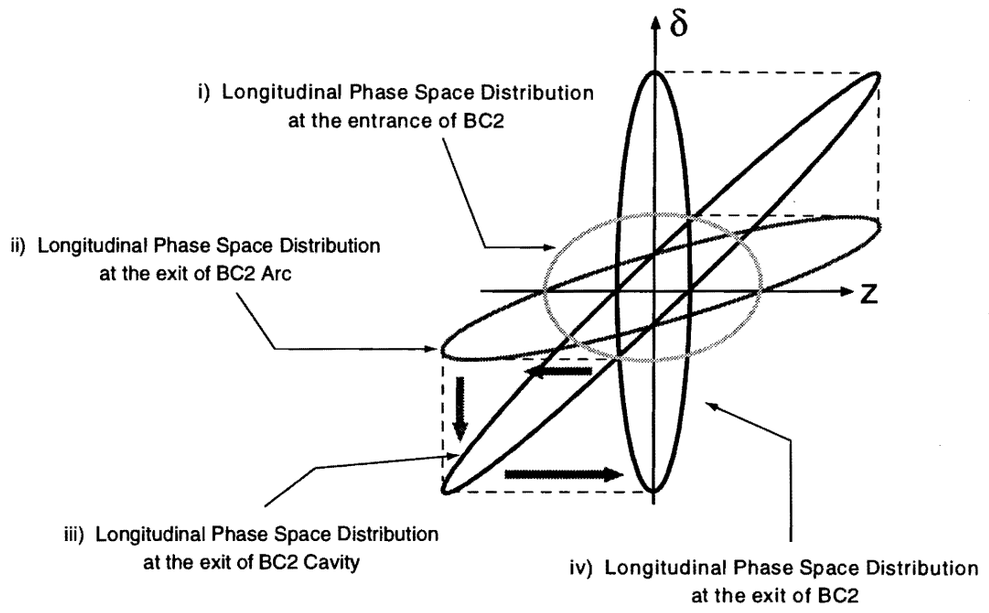

Figure 6.6: *Longitudinal phase space of a bunch in each stage of the second bunch compressor, BC2. Transformation of the phase space is illustrated.*

Main Cavity Voltage	V_M	3705	MV
Frequency	f_M	2856	MHz
Phase	ψ	-95	degrees
Length	L_M	150	m
Compensation Cavity Voltage	$V_{\pm C}$	467.5	MV
Frequency	f_C	2856	MHz
Length	$L_{\pm C}$	21	m
Beat Frequency	Δf	1.082	MHz
Momentum Compaction of Arc Section	R_{561}	-0.187	m
Momentum Compaction of Chicane Section	R_{562}	0.036	m

Table 6.3: *Parameters of the second bunch compressor*

Longitudinal Optics in BC2

The transfer matrix of the longitudinal phase space across BC2 is given by

$$\begin{aligned} M &= \begin{pmatrix} M_{11} & M_{12} \\ M_{21} & M_{22} \end{pmatrix} \\ &= \begin{pmatrix} 1 & R_{562} \\ 0 & 1 \end{pmatrix} \begin{pmatrix} 1 & 0 \\ k & 1 \end{pmatrix} \begin{pmatrix} 1 & R_{561} \\ 0 & 1 \end{pmatrix} \\ &= \begin{pmatrix} 1+kR_{562} & R_{561}+R_{562}+kR_{561}R_{562} \\ k & 1+kR_{561} \end{pmatrix}, \end{aligned} \tag{6.6}$$

where all of parameters are defined in Table 6.3. Twiss parameter for the longitudinal phase space is transferred according to the following relation:

$$\begin{pmatrix} \alpha_L \\ \beta_L \\ \gamma_L \end{pmatrix} = \begin{pmatrix} M_{11}M_{22} + M_{12}M_{21} & -M_{11}M_{21} & -M_{12}M_{22} \\ -2M_{11}M_{12} & M_{11}^2 & M_{12}^2 \\ -2M_{21}M_{22} & M_{21}^2 & M_{22}^2 \end{pmatrix} \begin{pmatrix} \alpha_{L0} \\ \beta_{L0} \\ \gamma_{L0} \end{pmatrix} \tag{6.7}$$

There are two conditions to be met by the longitudinal Twiss parameters at the exit of the bunch compressor system. One condition is that longitudinal β function should be 7.68×10^{-3} to obtain a 80μm bunch length with linear theory; second condition is that α_L must be zero for minimizing the energy spread. There are two adjustable parameters in BC2. One parameter is a momentum compaction factor in the arc section; the other is a peak voltage of the BC2 cavity. The two conditions of the longitudinal Twiss parameters at the exit of bunch compressor system are realized by suitably choosing these two adjustable parameters.

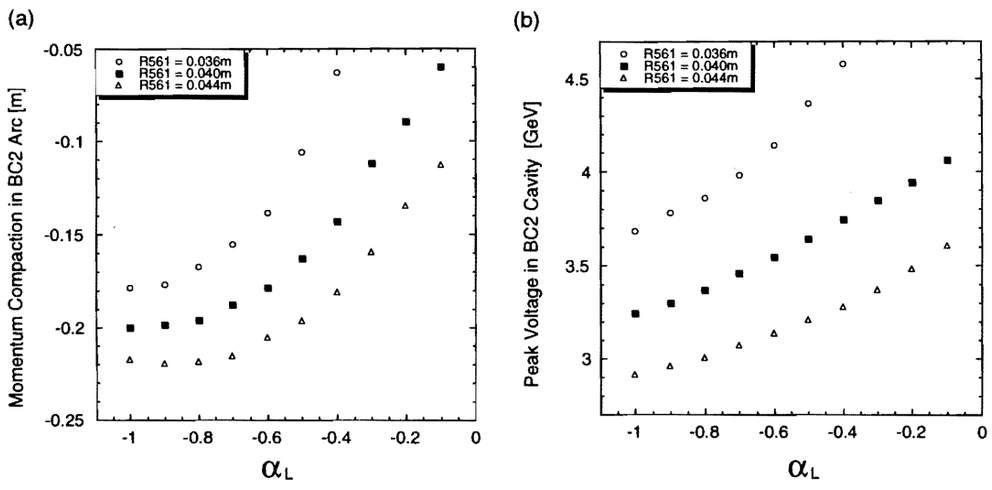

Figure 6.7: *Required momentum compaction factor and peak voltage for various α_L*

The relationship between the required momentum compaction factor in BC2 arc and the peak voltage in the BC2 cavity to α_L is shown in Figure 6.7. The large α_L require a low peak voltage in the BC2 cavity, and the large momentum compaction factor in the BC2 arc. The low peak voltage will relax the requirement of the accelerating voltage for BC2 cavity and the large momentum compaction factor requires the reduction in the number of cells in the BC2 arc. When the pre-linac phase is around on-crest, a large α_L is generated. Therefore, the pre-linac phase has been chosen to be around on-crest. The parameters listed in Table 6.3 were chosen based on a more detailed simulation which included nonlinear terms. For this reason the parameters in Table 6.3 are slightly different from those shown in Figure 6.7.

Arc Section in BC2

The arc section consists of 68 FODO cells. Each cell consists of 2 dipole magnets, which has a length of 1.2 m with a magnetic field of 6.3 kG and quadrupole magnets, which has a thickness of 0.45 m and a pole-tip field of 7.1 kG.

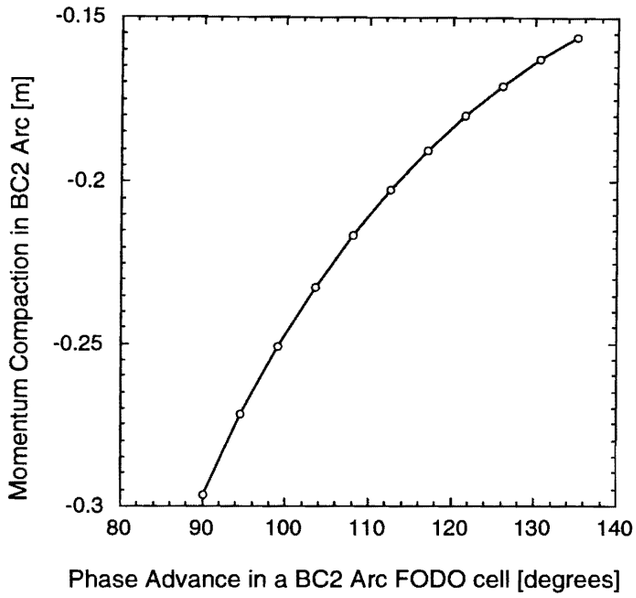

Figure 6.8: *Dependence of momentum compaction on the phase advances per cell of the FODO cell in BC2 arc.*

In this arc, the momentum compaction is easily adjusted by varying the horizontal phase advance of the FODO cells. The variation in the horizontal phase advance per cell from 90° to 135° changes the momentum compaction factor from -0.272 to -0.156 m, as shown in Figure 6.8.

Cavity Section of BC2

The cavity section of BC2 is driven at an S-band frequency of 2856 MHz. In this design study we have adopted a scheme where the multi-bunch beam-loading compensation is accomplished by using the ΔF method.

The design peak voltage of the BC2 cavity is 3.83 GeV and the accelerating gradient of the cavity is 25.4 MV/m. However, the maximum peak voltage can be increased up to 4.2 GeV for flexibility of initial longitudinal phase-space errors.

Chicane (Wiggler) Section in BC2

The chicane section of BC2 consists of 16 rectangular-type dipole magnets, which has a length of 2.5 m and the magnetic field of 0.99 kG. The quadrupole magnets are arranged between the chicanes and form FODO cells, as shown in Figure 6.9. The field strength of dipole magnets has been chosen so as to stay within the cut-off condition of coherent synchrotron radiation.

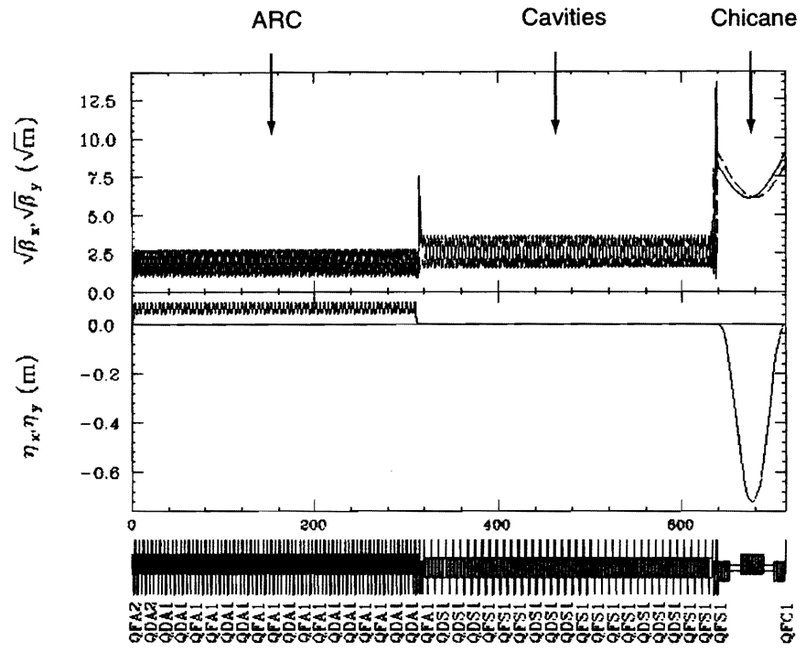

Figure 6.9: β Function and Dispersion Function in BC2

6.1.6 Simulation Studies

Some simulation studies have been conducted by tracking particles of a multi-bunch train through the designed bunch compressor system. Some of the results are discussed here.

Simulation Results in Longitudinal Phase Space

The parameters used in the simulation are shown in Table 6.4. The beam is accelerated without SLED cavities in the BC1 and BC2 cavity sections. However, the use of SLED cavities in the pre-linac is assumed to obtain the higher peak RF voltage. Furthermore, the phase of the pre-linac is fixed at

$-1°$ for optimizing the peak voltage in the BC2 cavity and the longitudinal emittance growth at the exit of the pre-linac.

BC1	Peak Voltage	142.5	MV
Main Cavity	Frequency	1428	MHz
	Phase	-95	degrees
	Length	9	m
	Peak Voltage	29.06	MV
Compensation Cavity	Frequency	2856±1.082	MHz
	Length	1.5	m
Wiggler	Momentum Compaction	0.465	m
Pre-linac	Peak Voltage (at SLED peak)	9223.5	MV
Main Cavity	Frequency	2856	MHz
	Phase	-1	degrees
	Length	330	m
	Peak Voltage	612.63	MV
Compensation Cavity	Frequency	2856±1.082	MHz
	Length	27	m
BC2	Peak Voltage	3705	MV
Main Cavity	Frequency	2856	MHz
	Phase	-95	degrees
	Length	150	m
	Peak Voltage	467.5	MV
Compensation Cavity	Frequency	2856±1.082	MHz
	Length	21	m
Arc	Momentum Compaction	-0.187	m
Chicane	Momentum Compaction	0.036	m

Table 6.4: *Parameters used in simulation*

The result of the simulation is shown in Figure 6.10. Figure 6.10(a) shows the longitudinal phase-space distribution for the 1st bunch in the bunch train. Figure 6.10(b) and (c) show the longitudinal phase-space distributions for the 43th and 85th bunches, respectively. Furthermore, Figure 6.10(d) shows an overlay of the longitudinal phase space distributions of from all of the 85 bunches in a train.

The RMS bunch length and its center position are shown in Figure 6.11(a), and the RMS energy spread and its center position are shown in Figure 6.11(b). It is found that all bunches have a bunch length of less than 90μm and a bunch-to-bunch position shift of about 20μm. The energy spread is roughly 1 %, and the bunch-to-bunch energy shift is 0.25 %.

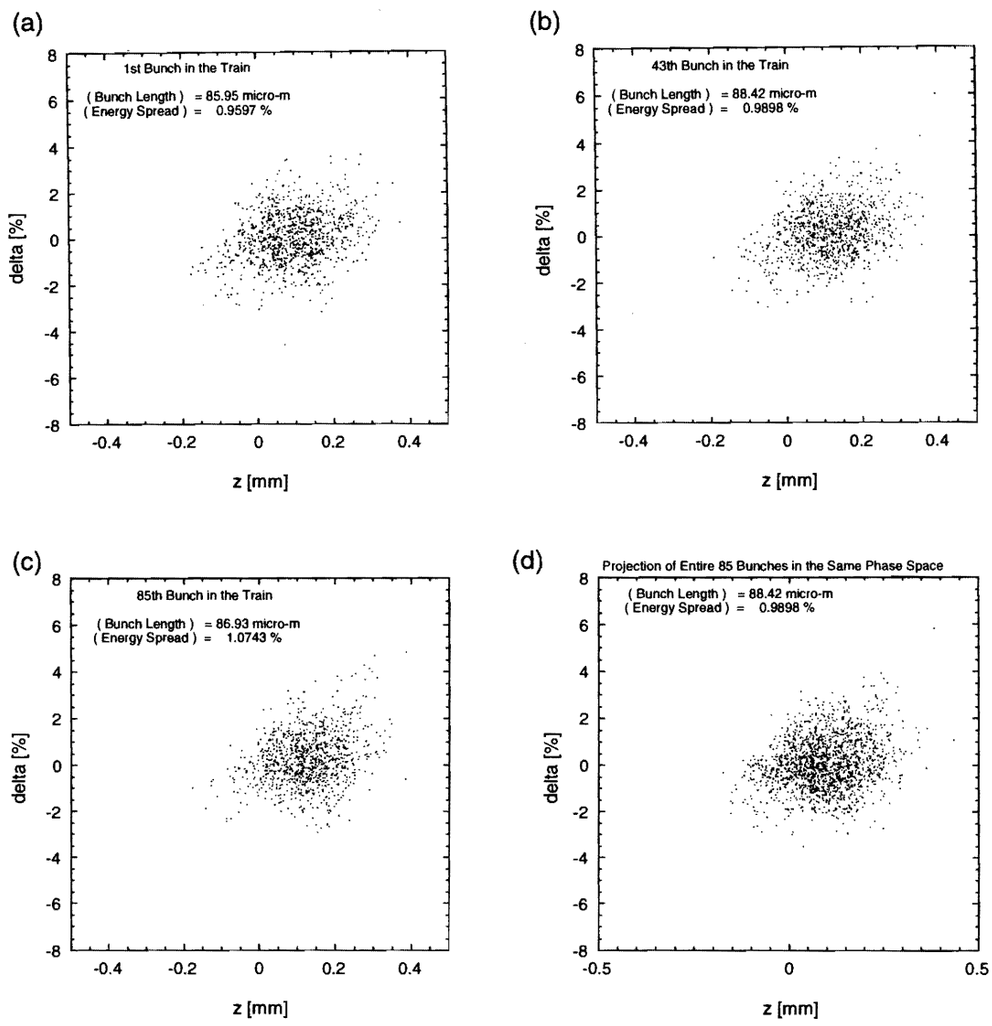

Figure 6.10: *Results of a simulation of the longitudinal phase space*

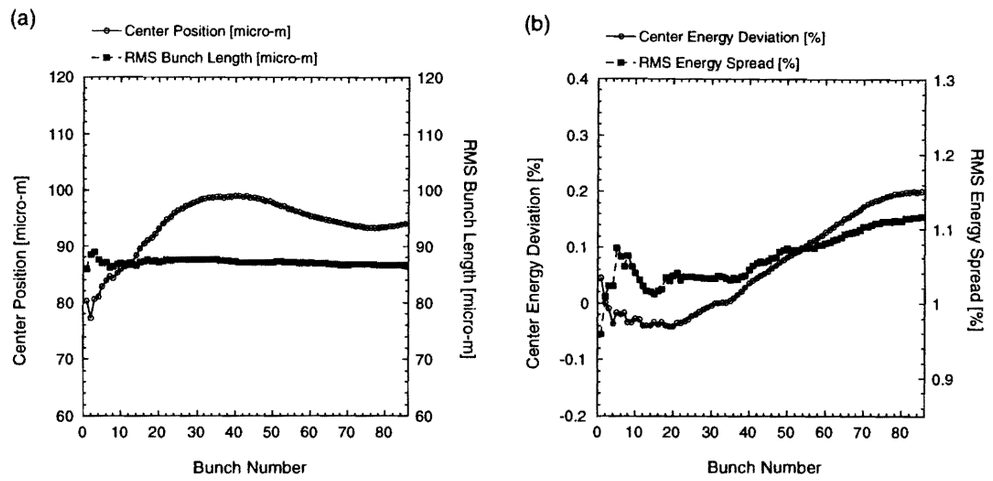

Figure 6.11: *Results of a simulation of the longitudinal phase-space distributions of bunches out of the bunch compressor system. RMS bunch length and the longitudinal bunch position as function of the bunch number (left). RMS energy spread and the energy centroid as a function of the bunch number (right).*

Flexibility of Initial Longitudinal Phase-Space Errors

This bunch compressor system is designed with flexibilities for the initial bunch length and energy spread errors. The basic design of the bunch compressor system is the initial beam with a bunch length of 4.85mm and an energy spread of 0.0862%.

Due to the characteristics of the design, in BC1, the final energy spread of a bunch is very sensitive to the initial bunch length. However, the final bunch length is not so sensitive to the initial bunch length. BC2 possesses the same characteristics. When the initial bunch length is different from 4.85 mm RMS, the energy spread is changed at the exit of the bunch compressor system, as shown in Figure 6.12. It is seen that the initial bunch length is correctly converted to the energy spread at the exit of bunch compressor system.

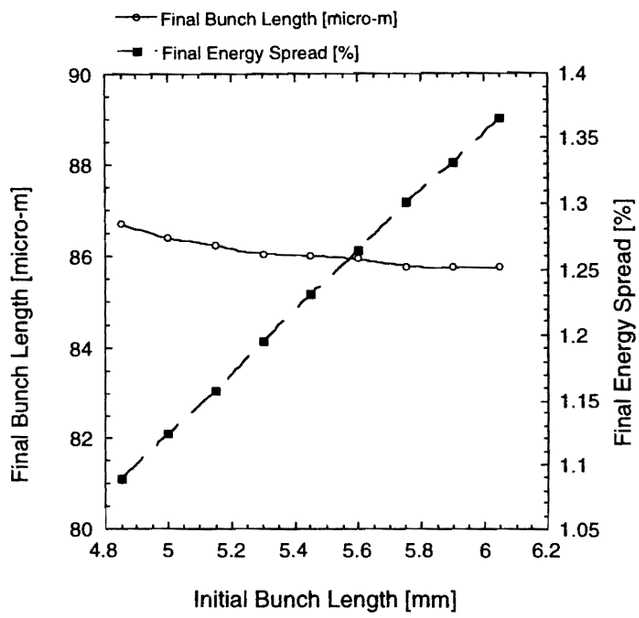

Figure 6.12: *Final bunch length and energy spread as functions of the initial bunch length error*

On the other hand, when the initial energy spread is different from 0.0862% RMS, the bunch length is changed at the exit of the bunch compressor from the design value. However, it can be compensated by adjusting the momentum compaction factor in the BC2 arc by changing the dispersion, and by changing the peak voltage in the BC2 cavities. This allows us to obtain a bunch length of 80μm and an α_L of zero at the exit of the bunch compressor system with linear theory, as shown in Figure 6.13.

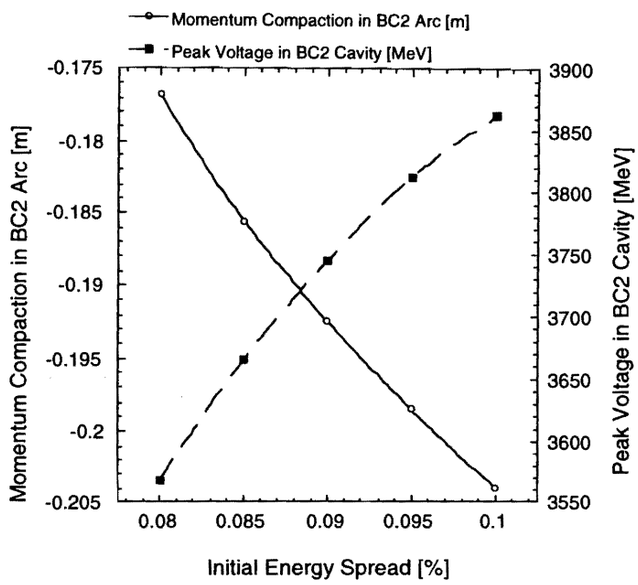

Figure 6.13: *When the initial energy spread of the beam deviates from the nominal 0.0862% RMS, the desired final bunch length 80μm is still available by adjusting the momentum compaction factor of the BC2 arc, and by adjusting the BC2 cavity voltage. This plot shows the appropriate momentum compaction factor and the BC2 cavity voltage to use, as functions of the initial energy spread.*

Effects of Momentum Compaction, Phase and Accelerating Voltage Errors

When the accelerating system has errors in the phase or peak voltage errors, or the bending system has momentum compaction errors, the bunch length and energy spread at the exit of bunch compressor system are affected. Figure 6.14 shows the effect of the momentum compaction error on the final bunch length and energy spread.

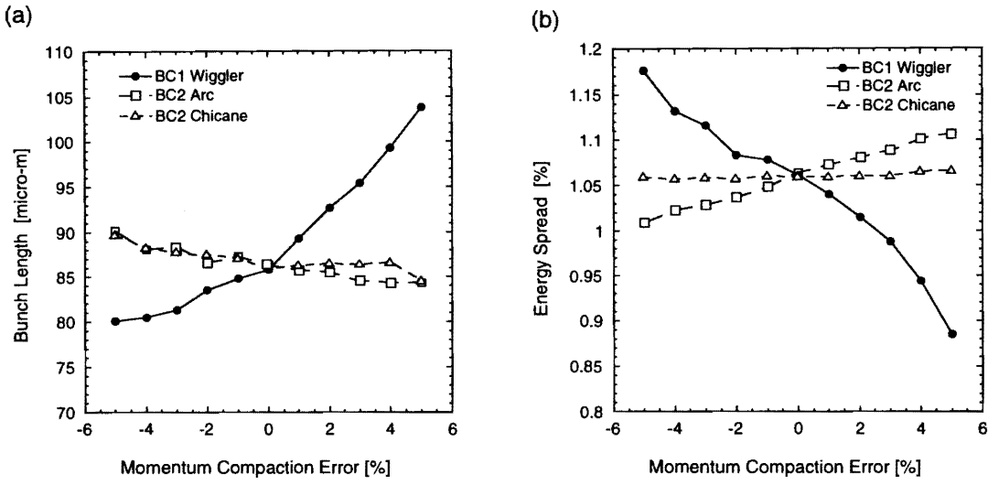

Figure 6.14: *Effects of the momentum compaction errors on the bunch length and energy spread at the bunch compressor exit.*

Figure 6.15 shows the effect of the peak RF voltage errors for various RF systems in bunch compressor system. It shows that the peak voltage error in the pre-linac main cavity has strong effects on the bunch length at the exit of the bunch compressor.

Figure 6.16 shows the effects of the phase errors for various RF systems in the bunch compressor system. It shows that the phase error in the BC1 main cavity has strong effects on the bunch length at the exit of the bunch compressor.

6.1.7 Emittance Growth and the Other Problems

Emittance Growth in the Bending System

There are two potential sources for the transverse emittance growth in the arc and wiggler sections of the bunch compressor system. One of them is a chromatic effect, which affects both the horizontal and vertical planes in the arc section. However, this effect is not significant here, since the energy spread at the BC2 arc is very small. Another effect is a dispersive effect from synchrotron radiation. This effect generates horizontal emittance growth in all of the BC1 and BC2 bending system. The

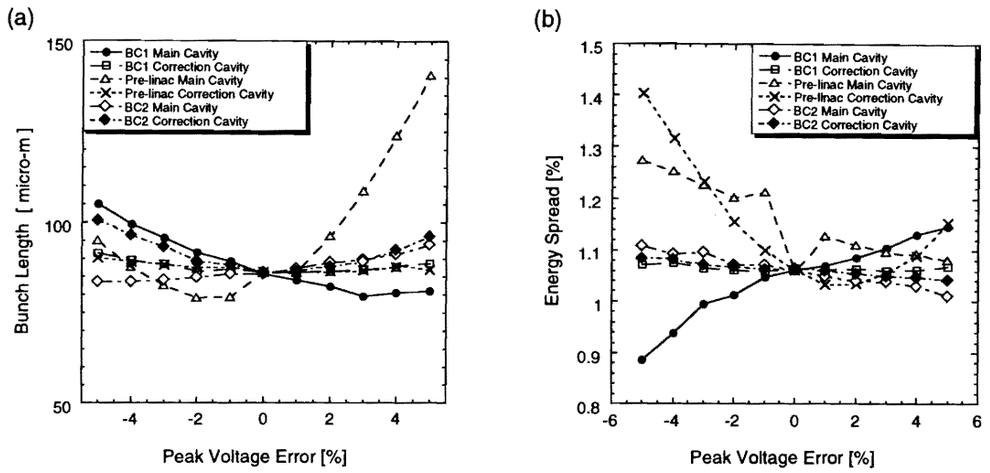

Figure 6.15: *Effects of RF voltage errors on the bunch length and energy spread of beams at the bunch compressor exit. RF voltage errors that can occur in various stages in the bunch compressor system are considered, i.e. BC1 main cavity, BC1 correction cavity, pre-linac main cavity, pre-linac correction cavity, BC2 main cavity and BC2 correction cavity.*

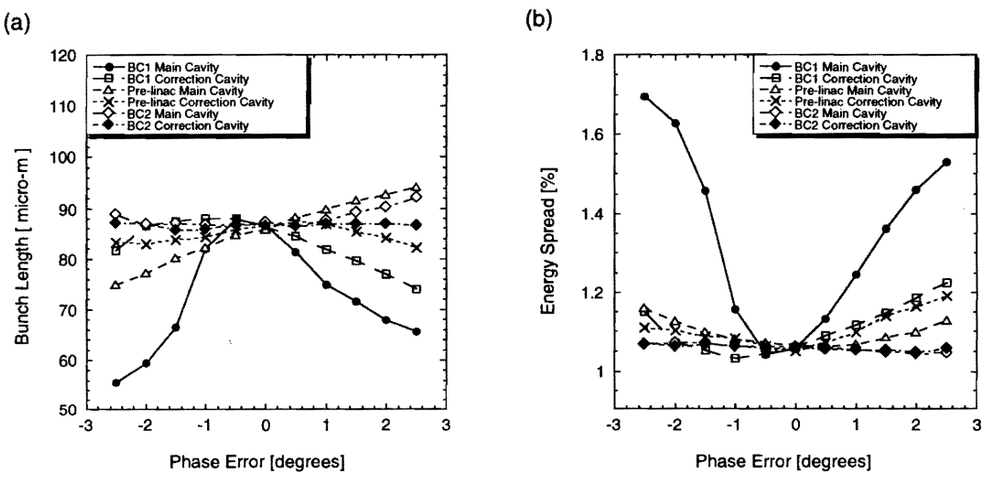

Figure 6.16: *Effects of RF phase errors on the bunch length and energy spread of beams at the bunch compressor exit. RF phase errors that can occur in various stages in the bunch compressor system are considered, i.e. BC1 main cavity, BC1 correction cavity, pre-linac main cavity, pre-linac correction cavity, BC2 main cavity and BC2 correction cavity.*

emittance growth was simulated with SAD.

The results are shown in Table 6.5. From Table 6.5, it is found that the emittance growth of the entire bunch compressor system is 8 % horizontally and less than 1 - 2 % vertically in the bending system, respectively.

	Vertical Emittance Growth	Horizontal Emittance Growth
BC1 Wiggler	$\leq$ 1%	1.32%
BC2 Arc	$\leq$ 1%	5.42%
BC2 Chicane	$\leq$ 1%	1.24%
Total	$\leq$ 1-2%	7.89%

Table 6.5: *Emittance growth in the BC1 and BC2 bending system*

Effect of Alignment Errors

The tolerances on the vibration errors in the BC1 wiggler and the BC2 chicane section are not tight. In this section, only the transverse vibration errors in the BC2 arc section for the quadrupole magnets are discussed.

The tolerance values are calculated as an error for each individual magnet which, by itself, can create an emittance growth of 5 %. The results of alignment tolerances in the BC1 and BC2 bending systems are listed for each element in Table 6.6.

Element		No. of Elements	Roll	Δx	Δy	ΔK
BC2 Arc	QF	73	0.152mrad	2.11μm	0.915μm	0.351%
	QD	72	0.375mrad	13.96μm	7.06μm	0.806%

Table 6.6: *Single element alignment tolerances (Defined by 5% emittance growth)*

Coherent Radiation [2]

The transverse effects of space-charge fields can be categorized into a centrifugal space-charge force and a coherent radiation force. It has been known some time that the coherent-radiation force is significant, while the centrifugal space-charge force is not so important in the bunch compressor system. The longitudinal electric field of the coherent synchrotron radiation induces an energy variation along the bunch. It especially acts on the leading particles in the bunch. This is to be contrasted with the familiar longitudinal wake-field.

In the wiggler or chicane sections of the BC1 and BC2, this field breaks down the achromaticity, thereby

causing a horizontal emittance growth. However, the emission of radiation with long wavelength is suppressed by the boundary conditions imposed by the vacuum chamber. The shielding condition is written as follows:

$$\sigma_z \geq \sqrt{\frac{h^2 w}{\pi^2 R}} \tag{6.8}$$

h : full height of vacuum chamber,
w : fill width of vacuum chamber,
R : bending radius of the beam trajectory.

	Full height	Full width	Bending radius	Bunch length
BC1 Wiggler	20mm	35mm	9.34m	$\geq 390\mu$m
BC2 Wiggler	16mm	80mm	334m	$\geq 78.9\mu$m

Table 6.7: *Shielding wavelength from the coherent-radiation force*

The horizontal aperture of the vacuum chambers is designed to be 10 or more times larger than the RMS horizontal beam size, and the vertical aperture is designed as 20 mm and 16 mm in the BC1 wiggler and BC2 chicane, respectively. The chamber aperture, bending radius and upper limits of the shielding bunch length are listed in Table 6.7. The design bunch length within BC1 is between 4 mm and 400 μm. The design bunch length within BC2 is between 400 μm and 80 μm. It can be seen from Table 6.7 that the vacuum chambers designs satisfy the shielding condition against coherent radiation.

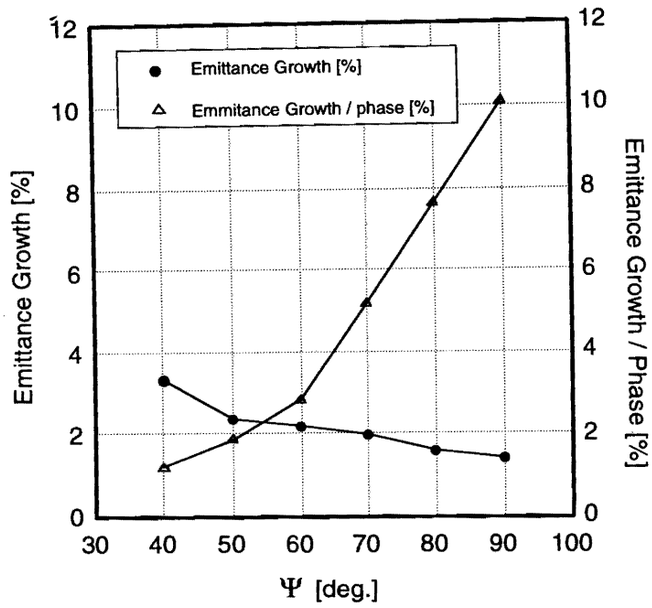

Figure 6.24: *The phase advance per cell (Ψ) versus the emittance growth due to the quadrupole magnets and the accelerating structure misalignment with respect to the beam. The quadrupole magnets and the accelerating structures are assumed to have rms 30 μm misalignment.*

For example, one module of ΔF ECS for pre-linac is shown in Figure 6.25. The quadrupole magnets must be located at the point where the bunch-to-bunch energy deviation is minimum. However, in this case still a sizeable single-bunch energy spread will remain at the quadrupole magnets, particularly when the regular accelerator stations are operated around the rf crest. This can lead to chromatic emittance growth of individual bunches. For this reason, the alignment tolerance of the structures and the quadrupole magnets will be tighter in the case of the ΔF compensation method than in the case of the ΔT compensation method.

All of the quadrupole magnets should be associated with high-resolution BPMs for beam handling, and each quadrupole magnet will be mounted on an active stage equipped with a remotely-controllable mover mechanism. The relations between the electrical centers of the BPMs and the magnetic centers of the quadrupole magnets will be determined by using the beam and internal BPMs, and the quadrupole magnets can be aligned by adjusting the stages. To align the accelerating structures with respect to the beam, all of the accelerating structures will have rf BPMs at their head and tail ends. An accelerating structure will also be mounted on a girder which can be remotely aligned.

magnet and the influence of dipole wake-fields in the accelerating structure[1].

In the case of ΔT ECS, the length of the FODO cell is 6.8 m in order to accommodate the 3-m long S-band accelerating structure and the steering magnet for orbit corrections. The quadrupole magnets are 20 cm in length and have an aperture of a 16 mm radius. Their pole-tip field strength is smaller than 1.5 kG.

The lattice, β functions, and beam size are shown in Figure 6.23. In this case the horizontal and vertical phase advances are both 55 degrees per cell. This value was determined from evaluations of the emittance dilution due to a misalignment of the quadrupole magnets and accelerating structures. Figure 6.24 shows the emittance growth due to a misalignment of the quadrupole magnets and the accelerating structure with respect to the beam vs. the phase advance per cell, Ψ. In this case, each random misalignment of the quadrupole magnets and the accelerating structure is rms 30 μm. Finally, the horizontal and vertical phase advances are separated by roughly a few percent to avoid x-y resonances.

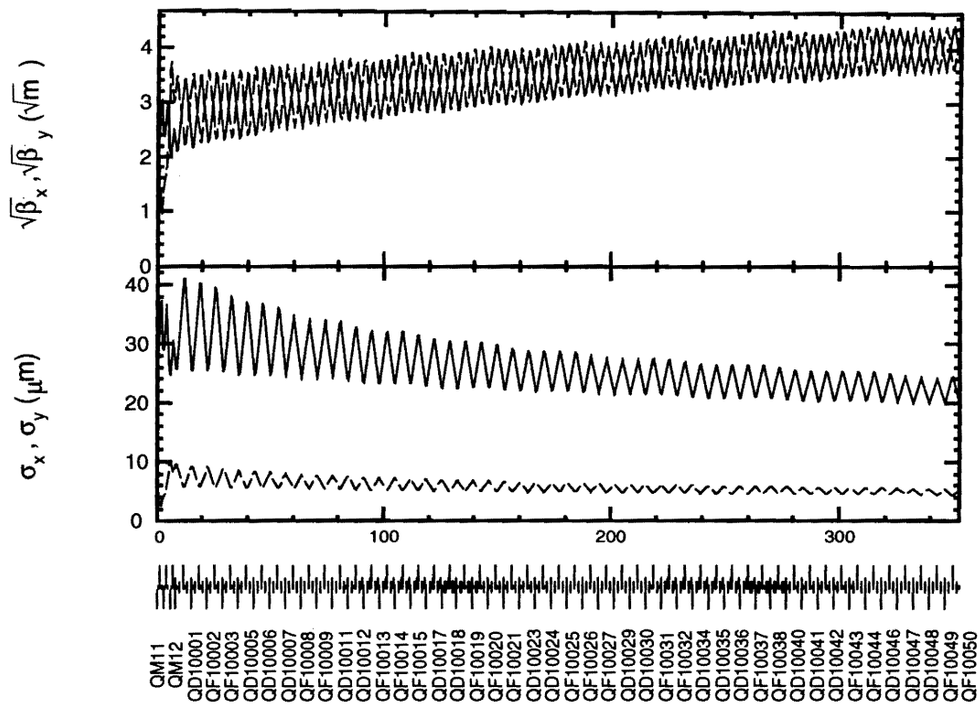

Figure 6.23: *Beta functions and beam size for the pre-linac which assumes that multi-bunch energy compensation would be made with the ΔT method.*

In the case of ΔF ECS, it is very important to suppress the emittance growth due to any chromaticity of the lattice. Especially, in the low-energy part, each section of ΔF should be made short, since the relative beam energy grows rapidly. This means that many small ΔF sections will be needed there.

180 degrees. If the phase change of the klystron is controlled in an rf pulse to obtain the optimum rf waveform for producing the same energy gain for individual bunches in the bunch train, the SLED cavities would be a compact rf pulse compression system for multi-bunch acceleration.

In the present design study, the possibilities of the ΔT ECS and ΔF ECS have been investigated for a low-energy linac which accelerates a train of 85 bunches with a 1.4 ns bunch separation.

6.3.2 Optics of the Pre-linac

Lattice design

The pre-linac should accelerate multi-bunch beams from 2 GeV to 10 GeV without causing a large energy spread, nor emittance growth, in either a single-bunch or in a multi-bunch sense. The emittance growth is mainly caused by the energy difference within the beam and the wake-field in the structure. When beam particles with different energies go through the magnetic field, particles get kicks with different angles. Therefore, the trajectories of particles with deferent energies are different, and the emittance would grow.

Another effect is that when the beam particles go through the accelerating structure, they are kicked by dipole wake-fields. The strength of this dipole wake-field is proportional to the transverse offset of the leading bunch. Due to this kick in the structure, the trajectories of the particles would start deviating, depending of their longitudinal positions, and the emittance growth will result. These sources of the emittance growth in combination determine the alignment tolerance of the quadrupole magnets and accelerating structures.

The optical design of the pre-linac consists of simple FODO cells. The cell length would differ, depending on the choice of the beam-loading compensation method. When multi-bunch beam-loading is compensated using the ΔT ECS method (Amplitude Modulation and Injection timing), the multi-bunch energy difference is corrected locally in each accelerating structure, so that any emittance growth due to dispersive and chromatic effects is minimized. On the other hand, the ΔF ECS method can also suppress any emittance growth due to a chromatic or dispersive effect, by placing the quadrupole magnets at the locations where the multi-bunch energy-spread is minimum.

Assuming that the β functions in the pre-linac varies as

$$\beta = \beta_0 \sqrt{\frac{E}{E_0}}, \tag{6.19}$$

where β_0 = 6 m at E_0=2 GeV, the total phase ϕ through the pre-linac as

$$\phi = \frac{2\sqrt{E_0}}{\beta_0 (dE/ds)} (\sqrt{E} - \sqrt{E_0}). \tag{6.20}$$

Form 6.19 is adopted, based on studies by Yokoya on the alignment tolerance of the quadrupole

6.3 8 GeV Pre-linac

6.3.1 Introduction

The pre-linac section is arranged between two bunch compressor systems for the intermediate linac. The mission of the pre-linac is to reduce an energy spread, and to adjust the longitudinal Twiss parameters at the entrance of BC2. The total accelerating voltage of the pre-linac is required to be roughly 8 GeV. With an accelerating gradient of $\sim 30\,\mathrm{MV/m}$, the total length of the pre-linac would be approximately 400 m.

The design of the pre-linac sections described here is based on the accelerator scheme extended from the ATF linac using the proven S-band rf technology. The rf unit consists of the conventional components, such as the conventional S-band traveling-wave constant-gradient accelerating structures (3 m long), an 80 MW klystron and SLED cavities for rf pulse compression. The machine parameters should be optimized by both the rf configuration and computer simulations, such as the beam optics, beam instabilities and energy compensation of the multi-bunch.

The rf pulse compression system is the key technology for reducing the total number of klystrons and klystron modulators for the low-energy linac. It also helps to reduce the total cost of the linac. The linac design should take into account of the tight relation of the rf compression system and the multi-bunch energy-compensation system, as follows:

First, if a staggered timing energy compensation is chosen, the rectangular rf pulse is required from the rf compression system. DLDS (Delay Line Distribution System), BPC (Binary Pulse Compression system) and SLED-II are suitable to produce a rectangular rf pulse. Those three rf compression systems have delay lines with a relatively long length, which is determined by the filling time of the accelerating structure and the beam pulse width. An application to the S-band linac is difficult, since the filling time would be 400–900 ns and the delays would have to be very long.

The second method of energy compensation is the ΔF ECS which has been applied to the 1.54 GeV ATF linac. The linac is completely separated into a normal acceleration section and a compensation section. In the normal acceleration section, the accelerating structures are driven at the full rf power from SLED cavities. Then, the multi-bunch energy spread is corrected in the ECS section of a relatively short length. This system has an advantage of higher flexibility for the bunch intensity than the ΔT ECS system, which is described below. On the other hand, the design of the optics is relatively complicated for the lower energy section compared to that of the ΔT ECS system.

Third, the beam-loading of the multi-bunch can be compensated in an accelerating structure, if the phase and amplitude from the rf compression system can be controlled to obtain the same energy gain in the multi-bunch. This system is called ΔT or $\Delta\phi$ ECS. The conventional SLED cavity produces an rf pulse waveform with a fast decay if the phase of the input rf pulse is simultaneously changed to

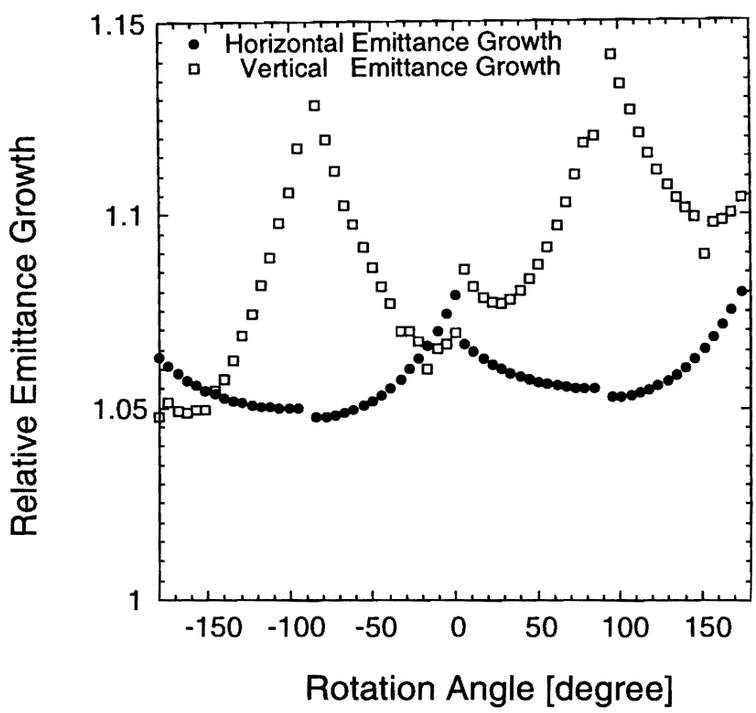

Figure 6.22: *Relative emittance growth for various spin rotation angles*

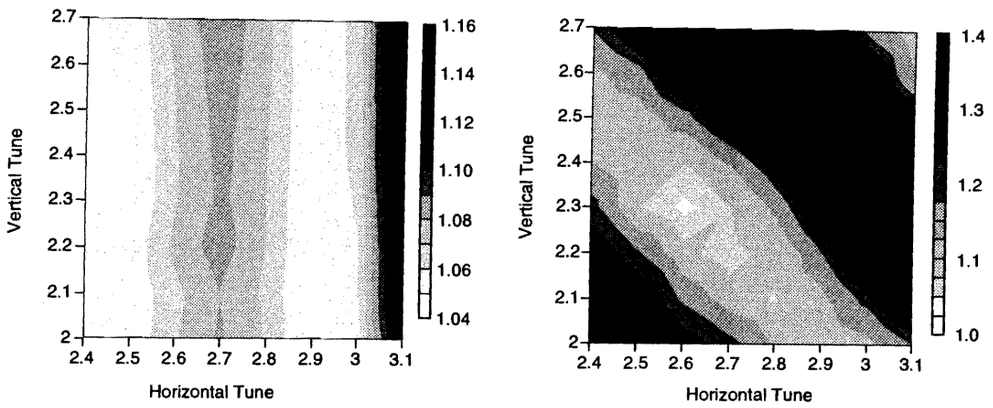

Figure 6.21: *Contour diagrams of the relative emittance growth in the horizontal vs. vertical tune space:*

(a) Relative growth of the horizontal emittance

(b) Relative growth of the vertical emittance

are shown in Figure 6.22 for the case of a 0.5% energy spread. The horizontal axis shows the rotation angle in the horizontal plane, and vertical axis shows relative dispersive emittance growth through all of spin manipulation-system. The rotation angles in Figure 6.22 are defined with reference to beam trajectory. At rotation angles from -180 degrees to -90 degrees and from 0 degree to 90 degrees, the rotation angles for first and second manipulators have like-sign polarities, and the other rotation angles have opposite polarities. The simulation results indicate that the dispersive vertical emittance growth is reduced to 15% for a beam with a 0.5% energy spread.

electron. This emittance growth has been simulated using the SAD code [4], the results of which are shown in Figure 6.20. Figure 6.20(a) shows a dispersive emittance growth ratio on the energy spread. Figure 6.20(b) shows this dispersive emittance growth ratio as a function of the energy offset.

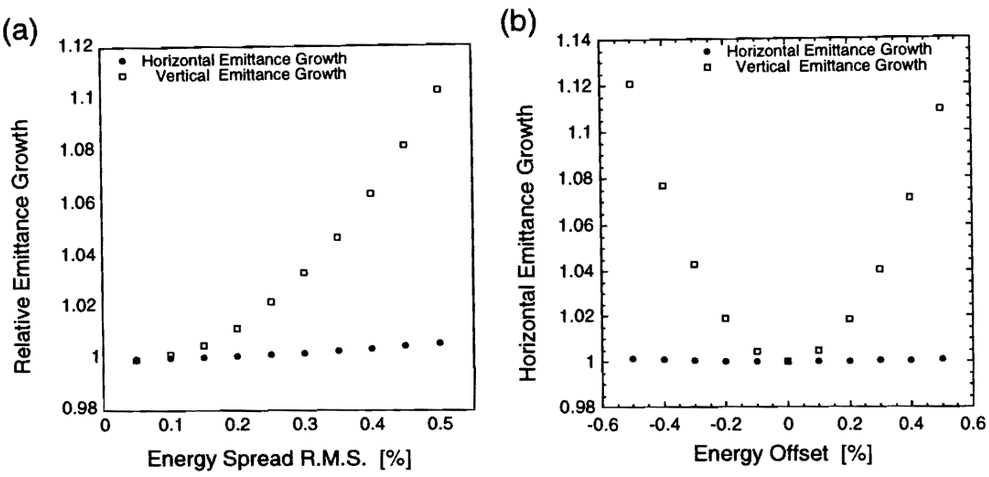

Figure 6.20: *Relative dispersive emittance growth:*
(a) as function of the energy spread.
(b) as function of the energy offset.

Suppression of the Dispersive Emittance Growth

In the design of the JLC spin-manipulation system, solenoid manipulators are arranged as outlined in the previous section. Furthermore, a matching section with six quadrupole magnets is inserted between the solenoid manipulators and the arc section. The six degrees of freedom are available for matching the Twiss parameters and tunes between the two solenoid manipulators. With this design the emittance growth for various tunes in the horizontal and vertical planes has been evaluated. The results are shown in Figure 6.21. In these calculations, a $+\pi/2$ spin rotation angle was assumed. It can be read from Figure 6.21 that the best reduction of vertical emittance growth is obtained when a horizontal tune of 2.6 and a vertical tune of 2.3 are chosen in the matching section. At these tunes, the dispersive emittance growth generated within the two solenoid manipulators shown in Figure 6.20 cancel each other.

To achieve all spin directions in the horizontal plane out of the spin-manipulator system into a linear accelerator, both like-sign and opposite-sign spin rotation angles are used for the first and second solenoid manipulators; the simulation has found that the best vertical emittance condition is obtained by choosing a horizontal tune of 2.9 and a vertical tune of 2.5. This happens to be the worst operation point if like-sign rotation angles are used in the two solenoid manipulators.

The emittance growth throughout this spin-manipulation system was simulated with SAD; the results

$$M_{mani}(\psi_s) = \begin{pmatrix} C^2 & SC/k & SC & S^2/k \\ -kSC & C^2 & -kS^2 & SC \\ -SC & -S^2/k & C^2 & C^2 \\ kS^2 & -SC & -kSC & C^2 \end{pmatrix}, \tag{6.15}$$

where C and S are $\cos(\psi_s/2)$ and $\sin(\psi_s/2)$, respectively, and

$$k \equiv \frac{\psi_s}{2L_{sol}} = \frac{B_z}{2(B_0)\rho}. \tag{6.16}$$

Equation 6.15 indicates that when an electron beam passes through a solenoid magnet a large x-y coupling is introduced. The projected vertical emittance at the exit of solenoid coil is given by

$$\epsilon_y^2 = \epsilon_{x_0}^2 S^4 + \epsilon_{y_0}^2 C^4 + \epsilon_{x_0}\epsilon_{y_0} C^2 S^2 (\beta_x\gamma_y - \alpha_x\alpha_y + \gamma_x\beta_y), \tag{6.17}$$

where ϵ_{x_0}, ϵ_{y_0}, α_x, β_x, γ_x, α_y, β_y and γ_y are the emittances and Twiss parameters at the entrance of the solenoid coil, respectively. The x-y coupling in a solenoid field quickly deteriorates the small vertical emittance. Since the expected emittance ratio of the JLC damping ring is roughly 100, with a $\pi/2$ spin rotation, the vertical emittance is multiplied 50 times in this system. Although this emittance growth cannot be recovered later, a low vertical beam emittance is critical for achieving high luminosity at a linear collider.

To reduce the emittance growth due to the x-y solenoid coupling, a spin manipulation system comprising 1.5 m-long paired solenoid magnets with a strength of 3.46T has been adopted here. The solenoid magnets are separated by a $+I$ transform in horizontal and a $-I$ transform in the vertical plane. The transfer matrix between the two solenoid magnets is formed with four FODO cells which have a betatron phase advance per cell of 90 degrees in the horizontal and 45 degrees in the vertical plane. The total transfer matrix through one solenoid manipulation system is given by

$$\begin{aligned} M_{mani} &= M_{sol2}(\psi_s/2) \begin{pmatrix} 1 & 0 & 0 & 0 \\ 0 & 1 & 0 & 0 \\ 0 & 0 & -1 & 0 \\ 0 & 0 & 0 & -1 \end{pmatrix} M_{sol1}(\psi_s/2) \\ &= \begin{pmatrix} C & S/k & 0 & 0 \\ -kS & C & 0 & 0 \\ 0 & 0 & -C & -S/k \\ 0 & 0 & kS & -C \end{pmatrix}. \end{aligned} \tag{6.18}$$

Equation 6.18 shows that the x-y coupling at the exit of the solenoid manipulator system is canceled exactly in the case that the transfer matrix in between a pair of solenoid magnets is $+I$ transform in horizontal and a $-I$ transform in vertical plane, exactly. However, in practice, there will remain a vertical emittance growth caused by the x-y coupling of off-momentum particles, since the transfer matrix in between a pair of solenoid magnets is slightly different from ideal one for the off-momentum

Optics Design of Downstream Spin-Manipulation System

The optics design of the downstream spin-manipulation system is shown in Figure 6.19. The downstream spin-manipulation system comprises two solenoid sections with an arc section in between. The arc section comprises six horizontal bend dipole magnets and four FODO cells. We assume that the arc section has an orbit angle of 20 degrees so that the 1.98 GeV electron beam is subjected to a 90 degree spin rotation therein. If the first and second solenoid manipulators are set up so that the electron spin is rotated by θ_1 and θ_2 around the longitudinal axis there, the total spin rotation will given by a matrix, as follows:

$$\begin{aligned} R_{mani} &= R_{sol2}(z;\theta_2)\, R_{arc}(y;90^\circ)\, R_{sol1}(z;\theta_1) \\ &= \begin{pmatrix} \cos\theta_2 & -\sin\theta_2 & 0 \\ \sin\theta_2 & \cos\theta_2 & 0 \\ 0 & 0 & 1 \end{pmatrix} \begin{pmatrix} 0 & 0 & 1 \\ 0 & 1 & 0 \\ -1 & 0 & 0 \end{pmatrix} \begin{pmatrix} \cos\theta_1 & -\sin\theta_1 & 0 \\ \sin\theta_1 & \cos\theta_1 & 0 \\ 0 & 0 & 1 \end{pmatrix} \\ &= \begin{pmatrix} -\sin\theta_1\sin\theta_2 & -\cos\theta_1\sin\theta_2 & \cos\theta_2 \\ \sin\theta_1\cos\theta_2 & \cos\theta_1\cos\theta_2 & \sin\theta_2 \\ -\cos\theta_1 & \sin\theta_1 & 0 \end{pmatrix}. \end{aligned} \tag{6.13}$$

If the spin is completely vertically aligned at the exit of the damping ring, the spin vector after going through the spin-manipulation system is given by

$$R_{mani} \begin{pmatrix} 0 \\ 1 \\ 0 \end{pmatrix} = \begin{pmatrix} -\cos\theta_1\sin\theta_2 \\ \cos\theta_1\cos\theta_2 \\ \sin\theta_1 \end{pmatrix} \tag{6.14}$$

Therefore, by choosing an appropriate rotation angle in the two solenoid manipulators in the range from $-\pi/2$ to $+\pi/2$, an arbitrary spin vector at the rotation angle exit can be obtained. For practical purposes, the experiments at the collision point would be only interested in spin polarization with the same or the opposite direction of its trajectory direction. The spin direction is varied in the horizontal plane when an electron beam is transported in the beam-line with some of dipole magnetic fields from the spin-manipulation system to the interaction point. To adjust to the required electron spin for any magnetic fields, it is necessary to adjust the spin direction to an arbitrary horizontal direction. In this case, the rotation angle of the second solenoid manipulator may be fixed at $+\pi/2$ or $-\pi/2$.

Coupling Compensation in the Paired Solenoid manipulator

The 4-dimensional transfer matrix due to a solenoid coil is given by

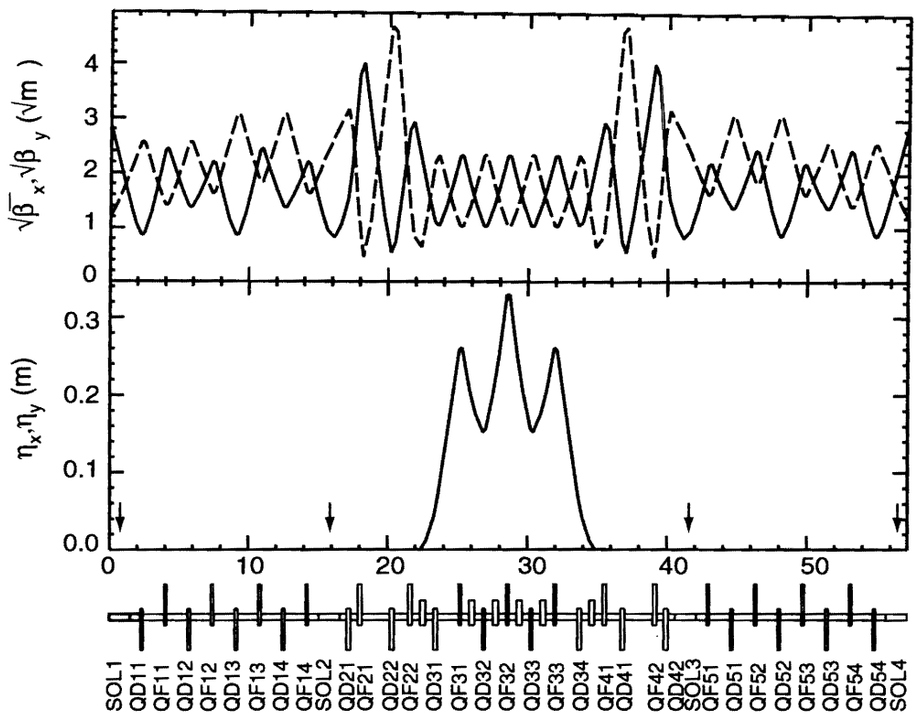

Figure 6.19: *β function and dispersion function in the downstream spin manipulator. Locations of four spin rotator solenoid magnets are indicated by arrows.*

Optics Design of the Upstream Spin-Manipulation System

The optics design of the upstream spin-manipulation system is illustrated in Figure 6.18. The upstream spin-manipulation system consists of a bending section and a solenoid coil with a spin-rotation angle of 90 degrees. The bending section consists of six horizontal bend dipole magnets and four FODO cells. To produce a spin-rotation angle of 90 degrees in the solenoid coil, the strength of the solenoid field has to be 3.46 T, if the coil length is 3 m. In this manipulator, the spin transfer matrix is given by:

$$
\begin{aligned}
R_{mani} &= R_{sol2}\,(z;\theta_s = 90°)\,R_{arc}\,(y;\theta_b = 90°) \\
&= \begin{pmatrix} \cos\theta_s & -\sin\theta_s & 0 \\ \sin\theta_s & \cos\theta_s & 0 \\ 0 & 0 & 1 \end{pmatrix} \begin{pmatrix} \cos\theta_b & 0 & \sin\theta_b \\ 0 & 1 & 0 \\ -\sin\theta_b & 0 & \cos\theta_b \end{pmatrix} \\
&= \begin{pmatrix} 0 & -1 & 0 \\ 1 & 0 & 0 \\ 0 & 0 & 1 \end{pmatrix} \begin{pmatrix} 0 & 0 & 1 \\ 0 & 1 & 0 \\ -1 & 0 & 0 \end{pmatrix} \\
&= \begin{pmatrix} 0 & -1 & 0 \\ 0 & 0 & 1 \\ -1 & 0 & 0 \end{pmatrix}
\end{aligned}
\tag{6.11}
$$

If the spin is completely azimuthally aligned at the entrance of the upstream spin manipulator, the spin vector after going through the spin manipulation system is given by

$$
R_{mani} \begin{pmatrix} 0 \\ 0 \\ 1 \end{pmatrix} = \begin{pmatrix} 0 \\ 1 \\ 0 \end{pmatrix}. \tag{6.12}
$$

6.2.4 Downstream Spin-Manipulation System

A downstream spin-manipulation system, which is based on a pair of solenoid manipulators and a bending manipulator in between, has been proposed by P. Emma et al. of SLAC [3]. Its schematic layout is shown in Figure 6.17.

Spin-manipulation systems at both the entrance and the exit of the damping ring are required for the purpose of avoiding spin destruction in the damping ring and tuning the helicity of the beam in experimental facility. However, the requirement for reducing the vertical emittance growth in spin-manipulator system located downstream of damping ring is tight, and that at the upstream of damping ring is not. We thus discuss here the reduction in the vertical emittance growth in the downstream spin manipulator system, mainly.

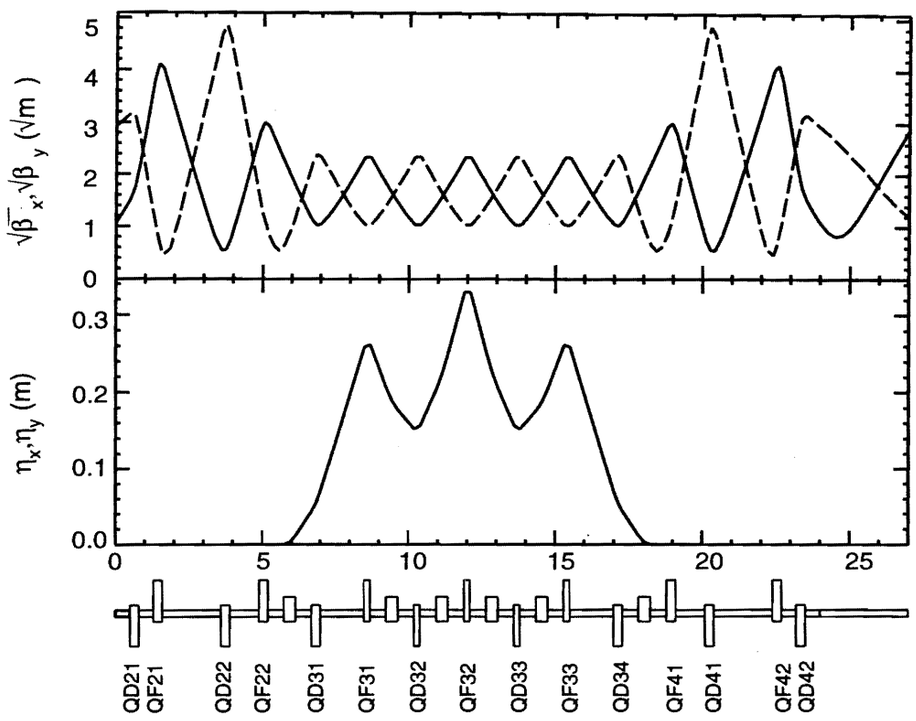

Figure 6.18: *β function and dispersion function in the upstream spin manipulator.*

6.2.2 Variation of the Spin Direction

The spin-manipulation systems located at the entrance and exit of the damping ring are based on spin rotators with solenoid coils and dipole bend magnets. The rotations of the electron spin with each manipulator are described in the following sections.

Variation of the Electron Spin in the Solenoid Magnetic Field

When an electron passes through a longitudinal solenoid magnetic field, its spin is rotated around the magnetic field axis. The rotation angle is approximately twice the rotation angle of the electron trajectory. The longitudinal rotation angle in the electron rest flame is given by

$$\psi_{sz} = \left[1 - \left(\frac{g-2}{2}\right)\right] \frac{B_z L_{sol}}{B_0 \rho} \approx \frac{B_z L_{sol}}{B_0 \rho} = 2\psi_{bz}, \tag{6.9}$$

where $\psi_{sz}, \psi_{bz}, B_0\rho, B_z, L_{sol}$ are the spin rotation angle, trajectory rotation angle, magnetic rigidity, field strength of the solenoid magnet at its center and its coil length, respectively. At JLC the spin-manipulation system is to be located immediately downstream of the damping ring, which operates at a beam energy of 1.98 GeV. Consequently, to produce a spin rotation angle of 90 degrees, the strength of the solenoid field has to be 3.46 T, if the coil length is 3 m.

Variation of the Electron Spin in a Dipole Magnetic Field

When an electron goes through a dipole magnetic field, its spin is rotated around the axis of the magnetic field. The rotation angle of the electron spin component that is perpendicular to the dipole field is given by

$$\psi_{sy} = \frac{g-2}{2} \frac{E_b}{m_e c^2} \frac{B_y L_{bend}}{B_0 \rho} \approx \frac{E_b\,[GeV]}{0.440652} \psi_{by}, \tag{6.10}$$

where $\psi_{sy}, \psi_{by}, B_0\rho, B_y, L_{bend}$ are the spin-rotation angle in the electron rest flame, the trajectory bend angle, the magnetic rigidity, the field strength of the dipole magnet and the effective length of the dipole magnet, respectively. E_b in Equation 6.10 denotes the electron energy. For a 1.98 GeV electron, the spin-rotation angle is about 4.5 times the bend angle of the trajectory. Hence, to produce a 90-degree spin rotation, a 20-degree orbit bending is required.

6.2.3 Upstream Spin-Manipulation System

An upstream spin-manipulation system is located upstream of the injection point of the damping ring. Its purpose is to rotate the spin of the longitudinally polarized electrons from the gun so that the spin is oriented in the vertical direction.

6.2 Spin-Manipulation System

6.2.1 Introduction

The availability of polarized electron beams is an important requirement at next-generation linear colliders, including JLC. There, longitudinally polarized electrons are to be produced by a gun with a special photocathode, such as those made of GaAs, accelerated, then delivered to the collision point with an experimental facility whose primary scientific interests are on the collisions of electrons with helicity eigenstates. However, beam storage in the damping ring will quickly destroy the overall longitudinal polarization of an electron bunch. Consequently, a spin-manipulation system has to be introduced whereby the electron spin can be aligned with the bend dipole fields of the damping ring prior to injection. Then, after extraction from the damping ring, the electron spin needs to be rotated back so that it produces the desired longitudinal polarization at the interaction point in an arbitrary way.

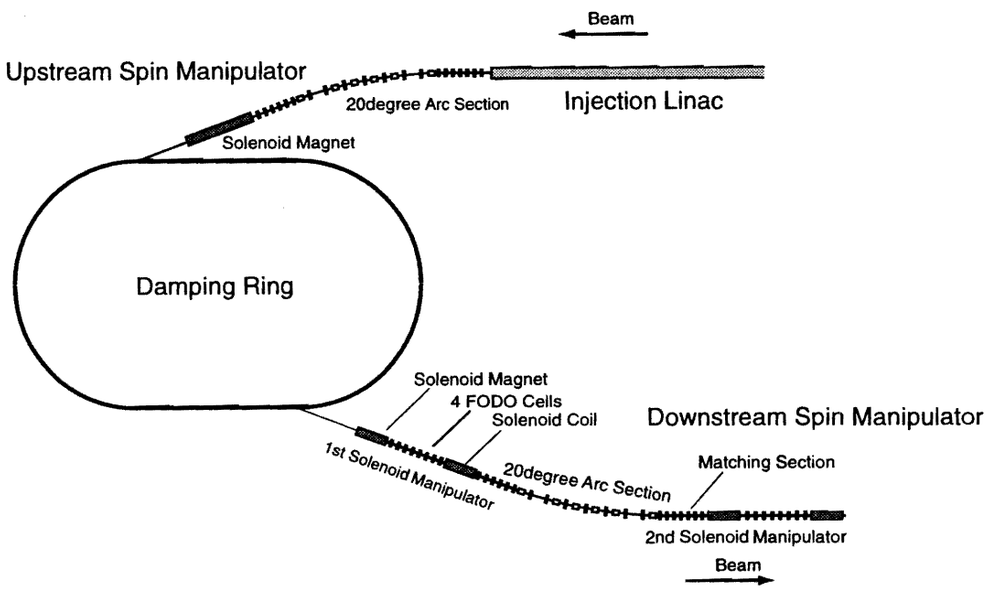

Figure 6.17: *Layout of the spin manipulation system*

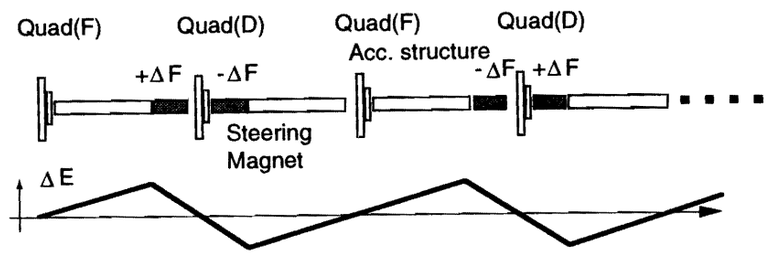

Figure 6.25: *Schematic illustration of how the layout of FODO cells would be, if the ΔF beam-loading compensation is adopted for bunch-to-bunch energy deviation, instead of the ΔT method.*

Simulation of Emittance Preservation

This section presents the results of a simulation of the emittance dilution due to a misalignment of the quadrupole magnet and accelerating structure with an orbit correction using the BPMs. Here, tolerance numbers are quoted for only the vertical direction. Since the design value of the vertical emittance of the incoming beam is two orders of magnitude smaller than that of the horizontal ones, the alignment tolerance of the components for the vertical direction will be much tighter. Here, the coupling between the horizontal and vertical directions is not considered. The parameters that characterize the condition of the simulation studies are listed in the following table.

Table 6.8: *Parameters of the simulation for the pre-linac.*

Particles/bunch	7.2×10^{9}
Number of bunches per pulse	85
Bunch spacing	1.4 ns
Incoming emittance;$\gamma\epsilon_y$	3.0×10^{-8}
Initial energy spread	1.25 %
Accelerating gradient	27 MV/m
Energy-compensation method	ΔT method

The wake-functions of the accelerating structure used here are a short-range and long-range longitudinal, short-range dipole and a long-range dipole. The optics design of the pre-linac assumes that the ΔT beam-loading compensation method is adopted.

Alignment of the quadrupole magnet In Figure 6.26, the horizontal axis represents the r.m.s. value of the misalignment of the quadrupole magnet. The misalignment is assumed to have a Gaussian distribution truncated at 3-σ. The vertical axis gives the emittance growth ratio. A 1.25 % initial energy spread, a 10 micron misalignment of the BPMs with respect to the quadrupole magnet, and a 10 micron misalignment of accelerating structures with respect to the beam are assumed. We

applied the simplest orbit correction, which simply sets the beam at the center of the BPMs. The BPM resolution is assumed to be 2 μm. From this result of the tracking simulation, the acceptable random motion of the quadrupole magnets is roughly estimated to be about 70 μm. This tolerance was estimated for a 20 % increase in the emittance.

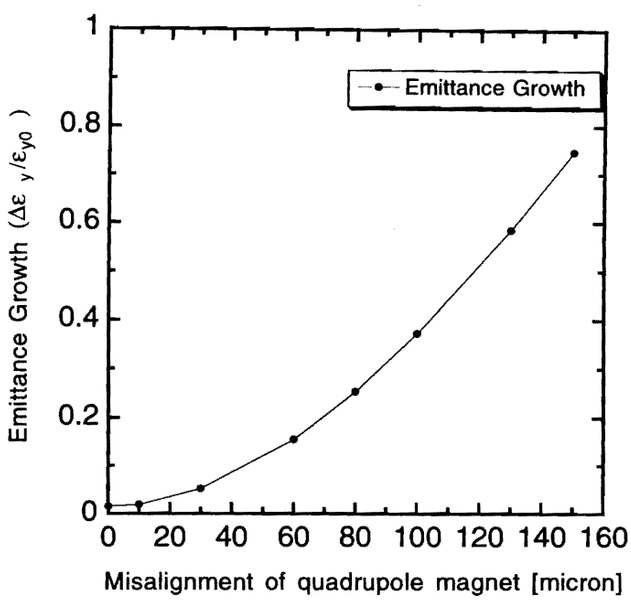

Figure 6.26: *Vertical emittance growth, $\Delta\epsilon_y$ / $\Delta\epsilon_{y0}$, as a function of the r.m.s. quadrupole misalignment. The optics design that is compatible with the ΔT energy-compensation method is considered (see Figure 6.23).*

Alignment of the Accelerating Structure

Figure 6.27 shows the vertical emittance growth in the pre-linac as a function of the misalignment of the accelerating structures. The initial energy spread is 1.2 %, and a 10 μm misalignment of BPMs with respect to the quadrupole magnets, a 30 μm misalignment of the quadrupole with respect to the design orbit are assumed. The accelerating structures align with respect to the beam using the rf BPMs at structure head, and any cell-to-cell misalignment within each accelerating structure is not considered here. In this simulation, we assumed that the alignment of the structure with respect to the beam is determined by the resolution of the rf BPMs at the structure head. A simulation of the emittance growth ($\Delta\epsilon_y$ / $\Delta\epsilon_{y0}$=20 %) due to a transverse dipole wake-field of the structures shows that a structure misalignment of less than 80 micron r.m.s. would not cause a serious problem once a simple orbit correction is performed.

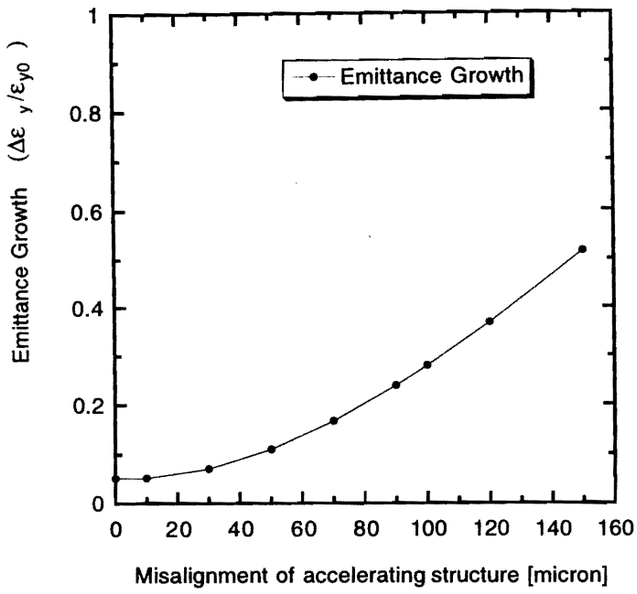

Figure 6.27: *Vertical emittance growth, $\Delta\epsilon_y$ / $\Delta\epsilon_{y0}$, as a function of the r.m.s. accelerating structure misalignment. The optics design that is compatible with the ΔT energy-compensation method is considered (see Figure 6.23).*

6.3.3 Accelerating Structure

The design of the S-band accelerating structure is closely related to the beam-emittance preservation and the required RF power, and, consequently, the wall-plug power. In terms of suppressing emittance dilutions due to a misalignment of the accelerating structures, the most harmful wake-field in the S-band accelerating structure to attack is the dipole wake-fields in the first passband . In addition to the accelerating gradient being high, the efficiency of the energy from rf to the beam within the accelerating structure should also be high. For this purpose, the shunt impedance of the structure should be as high as possible, and the a/λ should be as small as possible, while maintaining the realistically achievable alignment tolerance against single-bunch transverse emittance preservation.

A variety of structure schemes have recently been developed in order to reduce (i.e., detune or damp) the effect of dipole wake-fields [5]. One is the detuned structure (DS), in which the dipole modes will be canceled by spreading the frequencies of the relevant modes in the structure. Another possibility is the damped-detuned structure (DDS), which have been studied at SLAC [6]. The DDS scheme has an advantage in that it can measure the beam position in the structure through the damping port. Heavily damped or medium damped structures based on the choke mode scheme has also been developed recently [7]. In the choke-mode cavity structure, all of the higher-order modes are heavily damped. Therefore, the multi-bunch wake-field and associated instabilities are by and large absent. However, a short-range wake-field is not reduced by using the radial line damper and the

choke structure.

On the other hand, the conventional S-band structure, such as those used at the SLAC 2-mile accelerator, is good for mass production.[1] If the beam emittance is not diluted by the transverse wake-fields, there is a possibility that we would only modify this simple disk-loaded structure and apply it to the S-band pre-linac for JLC. Some studies have been made concerning the possibility in which a conventional (traditional) S-band structure of short filling time is considered in conjunction with the ΔT compensation method.

Parameters of the Accelerating Structure

As an example, the parameters of the ATF S-band linac structure are given in Table 6.9. Figure 6.28 shows the size of the half-iris aperture and the cell radius for two types of structures with different filling times.

Operating frequency	2856 MHz
Phase shift/cell	$2\pi/3$
Electric-field distribution	Constant gradient
Structure length	3 m
Number of cell	84 cells + 2 couplers
Quality factor	13,000
Shunt impedance	60 MΩ/m
Attenuation parameter	0.57
Group velocity	$0.0204 \sim 0.0065\ c$
Filling time	0.83 μs

Table 6.9: *Main parameters of the accelerating structures.*

Wake-Field of the Transverse Mode

The kick factors of all modes in the passband from the lowest to the 8'th were calculated using the "open mode expansion" for an S-band simple disk-loaded structure. This result is shown in Fig 6.29. The wake-field can be calculated from this result as the sum of all modes as [8]

$$W_\tau(t) = \sum_m 2k_T^m \sin(\omega_m t), \tag{6.21}$$

where k_T^m is the kick factor of mode m. The transverse wake-field of the conventional S-band structure is plotted in Figure 6.30. In this case, we assumed that the Q-values for all of the modes are infinite. If we suppose the Q-values of all the modes, without manifold damping, the Q-values are pretty much

[1] This is likely to be the case with the detuned structure, DS, also.

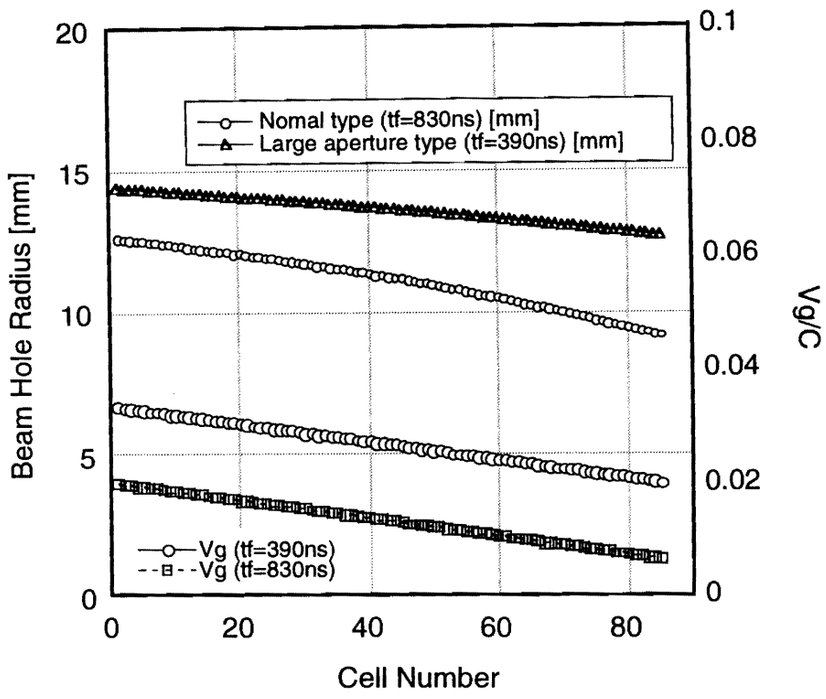

Figure 6.28: *The half iris aperture and the group velocity as function of the cell number.*

the same for all of the modes (about 13000 in S-band structure). We can thus estimate the reduction at the end of a train by multiplying each mode by $\exp(-\omega_m s/2Qc)$.

Transverse Emittance Growth

As will be presented in Chapter 8 [9], the transverse emittance dilution due to a random misalignment A_{rms} of the structures with respect to the beam is estimated to be

$$\langle \Delta\epsilon \rangle = \frac{e^2 A_{rms}^2 S_{rms}^2 \beta_0 L_a (E_f^a - E_0^a)}{2\alpha E_f E_0^a g} = \frac{e^2 A_{rms}^2 S_{rms}^2 \beta_0 N_a L_a^2 (E_f^a - E_0^a)}{2\alpha E_f E_0^a (E_f - E_0)} \tag{6.22}$$

where N_a, L_a, g and e are the total number of structures, the structure length, the accelerating gradient and the magnitude of the electron charge. Here, we assume that the beta-function is smooth (continuous focusing), and depends on beam energy as

$$\beta = \beta_0 (E/E_0)^\alpha, \tag{6.23}$$

where E_0 and β_0 are the beam energy and beta-function at the beginning of the linac.

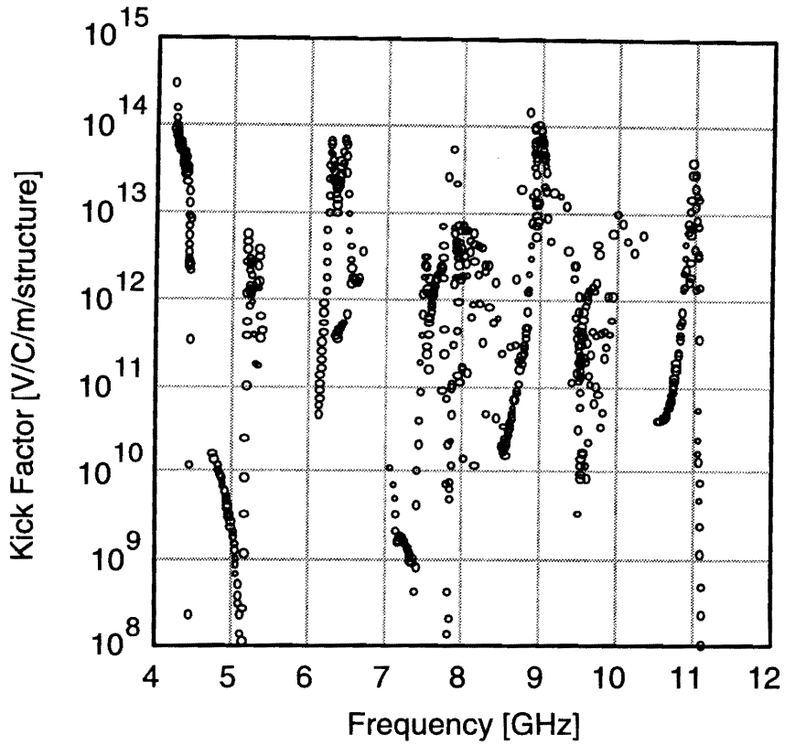

Figure 6.29: *Calculated kick factors of the modes in the 84-cell simple disk-loaded S-band structure. The calculations were performed by an open mode expansion method.*

The value of A_{rms} is determined by the accuracy of the structure fabrication and the beam-position monitor.

6.3.4 Beam-loading Compensation

Energy Gain and Transient Beam-loading

In a constant-gradient structure the accelerating gradient along the structure is constant at the cost of reducing the group velocity. The energy gain of the multi-bunch in the accelerating structures was evaluated. The multi-bunch should be injected into the structure before the rf power is completely supplied in the structure in order to avoid an energy spread due to the dispersive effect of the accelerating structure. For this case, the unloaded energy gain of the bunches gradually increases from the first bunch to the last bunch.

The beam energy of the bunches gradually decreases from the first bunch to the last bunch due to

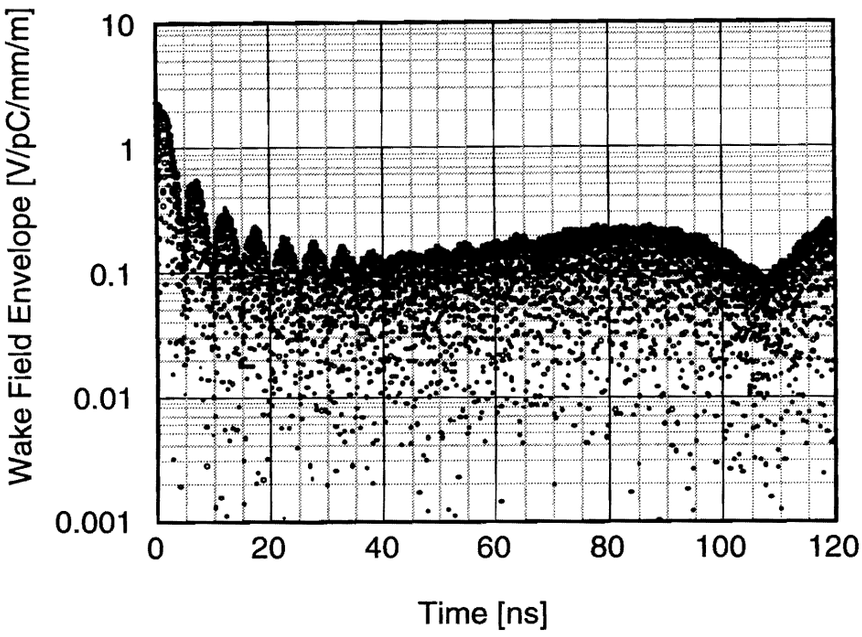

Figure 6.30: *Wake-field for the simple disk-loaded S-band structure.*

beam-loading in the accelerating structure. The energy loss (E_{bl}) at time t after beam injection is

$$E_{bl}(t) = \frac{r_0 i_0 L}{2}\left[\frac{2\tau^{-2\tau}}{(1-e^{-2\tau})}\frac{(t-T_f)}{T_f} - \frac{1-e^{-2\tau(t-T_f)/T_f}}{1-e^{-2\tau}}\right], \tag{6.24}$$

where i_0, r_0, τ, T_f are the instantaneous current of the beam and the shunt impedance, the attenuation parameter and the filling time of the accelerating structures, respectively. Since this equation is applicable to transient beam-loading,

$$T_b \leq T_f, \tag{6.25}$$

where T_b is the pulse length of the beam and t_f is the filling time of the structure.

In the JLC linac the pulse length of the beam was evaluated to be about 120 ns, since the total number of bunches and the bunch separation are 85 and 1.4 ns, respectively. The pulse length of the beam is much shorter than the filling time (830 ns). The instantaneous beam current is expressed as

$$i_0 = \frac{eN_b}{t_b}, \tag{6.26}$$

where e, N_b and t_b are 1.6×10^{-19}C, the total number of electrons per bunch and the bunch separation, respectively. The instantaneous beam current of the JLC linac was evaluated to be 0.823 A at

N_b=7.2×10^9 electrons per bunch. The energy loss of the last bunch in a 3 m-long structure was evaluated to be 10.6 MeV.

The energy distribution of the bunches accelerated in a 3 m-long accelerating structure is shown in Figure 6.31. An energy-compensation system should be required for the JLC linac.

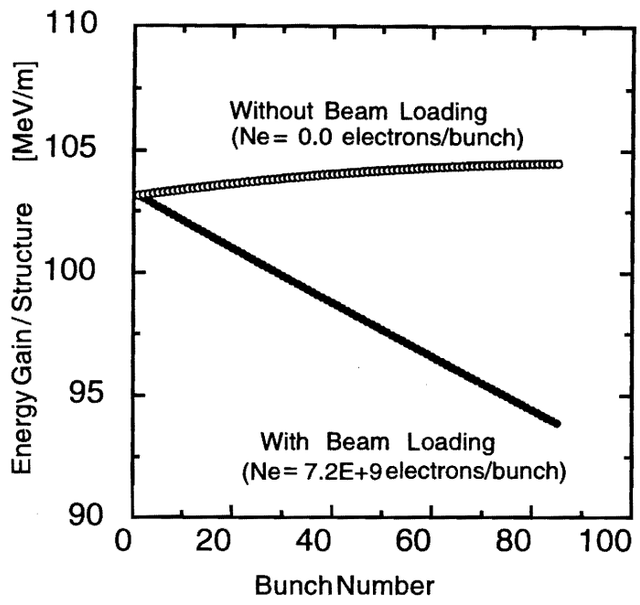

Figure 6.31: *Energy gain of multi-bunches accelerated in a 3 m-long accelerating structure with beam-loading.*

ΔT Energy-Compensation System

First-order compensation of the beam-loading can be done by injecting the beam before the rf pulse has filled the accelerating structure. The way that the ΔT compensation principle works is shown in Figure 6.32, in which the voltage $V(t)$ produced by a square rf pulse is plotted as a function of time for a traveling-wave structure. The beam-loading voltage $V_b(t)$ is also plotted as a function time. The resultant sum of $V(t)$ and $V_b(t)$ is shown as the dashed line. The optimum injection time is determined by the $V(t)$ and $V_b(t)$ slope.

If we use such a simple early-injection method, the beam current at which the energy-compensation can be comfortably performed is limited, and the power efficiency will be poor. We apply thus the amplitude modulation on the input rf pulse for pulse compression. Therefore, in the case of using the SLED system, we can obtain the desirable slope of the unloaded voltage $V(t)$ by changing the input rf wave form for the SLED cavity.

However, it is not a good idea to directly modulate the amplitude of the driving rf power to the

klystron. To stably operate the klystrons, they usually need to be used in the saturation mode. Thus, modulating the klystron drive RF phase would be a better method. To modulate the amplitude of rf pulse for the SLED cavity at a constant phase, two klystrons are needed. They run in saturation, keeping the input rf level constant. Then, we control their phases and combine the rf power from two klystrons by using a 3-dB hybrid combiner. Figure 6.33 shows a scheme in which the rf phases of two klystrons are rotated into opposite directions relative to each other. The sum of two vectors is delivered to the SLED cavity. The phase modulation of the two klystrons effectively realizes amplitude modulation using this method.

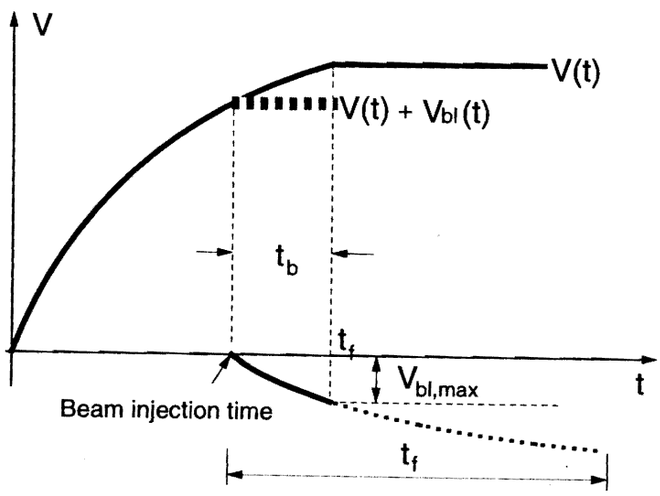

Figure 6.32: *Principle of the ΔT beam-loading compensation.*

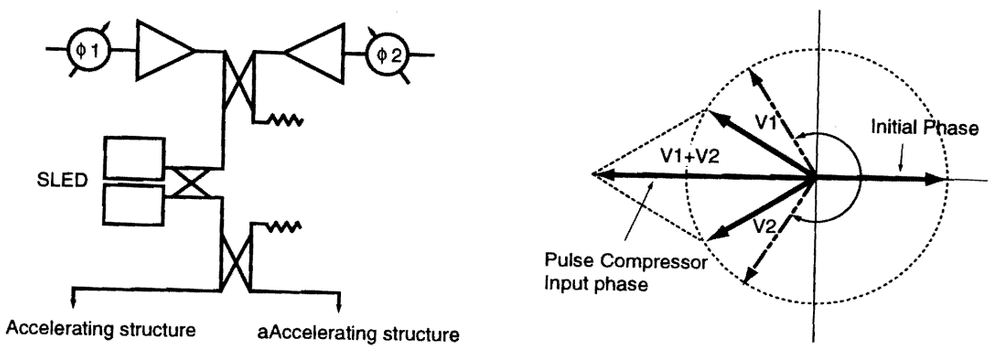

Figure 6.33: *Principle of phase modulation to amplitude modulation.*

ΔF Energy-Compensation System

The ΔF compensation method compensates for the multi-bunch energy spread by keeping a bunch separation synchronized with the rf frequency. In this compensation method, compensating structures are installed between the regular accelerating structures. When a bunch train goes through the compensating structures driven at an rf frequency which is slightly higher and lower than the fundamental accelerating frequency, successive bunches of the train ride on a different phase of the accelerating field (Figure 6.34). Due to this phase difference, the energy gain of the successive bunches is different. As a result, the multi-bunch energy spread is compressed to a small value. The compensating voltage $V_b(t)$ of the beam in ΔF compensation sections operating at a frequency $F_0 \pm \Delta F$ is plotted in Figure 6.35.

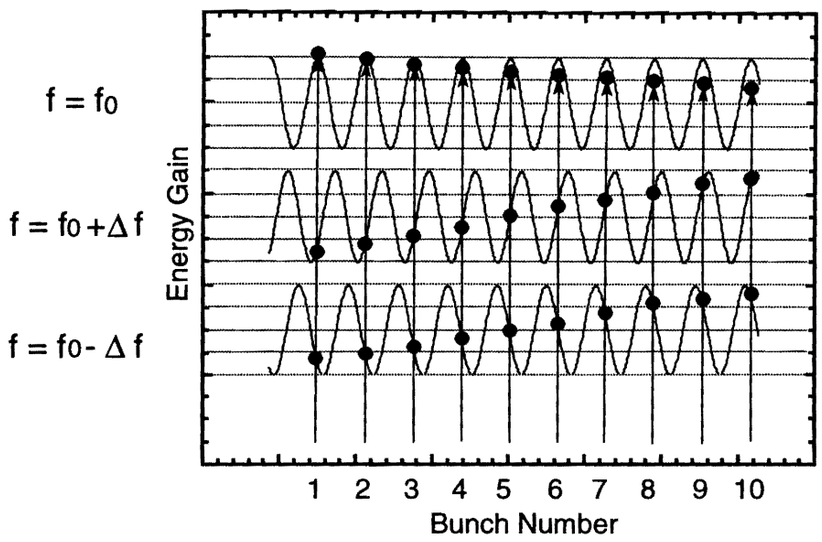

Figure 6.34: *Principle of the ΔF beam-loading compensation method. By adding two sets of accelerating structures with slightly different frequencies from the majority of the structures in the linac, the multi-bunch energy spread due to beam-loading can be compensated, without increasing the single-bunch energy spread.*

Two frequencies, $F_0 + \Delta F$ and $F_0 - \Delta F$, are required to maintain the desired single-bunch energy spread, while performing the multi-bunch energy compensation at the same time. When the bunch population changes, the amount of compensation can be controlled by changing the amount of input rf power to the compensating structure. Thus, this compensation method has a nice flexibility.

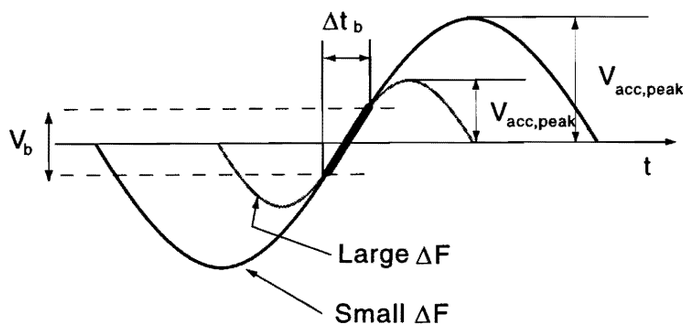

Figure 6.35: *Compensating voltage $V_b(t)$ of a beam in the ΔF compensation sections operating at a frequency of $F_0 \pm \Delta F$.*

6.3.5 Pre-linac RF System

The design of the rf system has been examined for the ΔT and ΔF energy-compensation systems. The klystron, klystron modulator and SLED as an rf pulse compression system are common for two energy-compensation systems.

S-band Klystron

The high-power S-band klystron, model E3712, was developed for the 1.54 GeV ATF linac. The designed maximum peak power is 100 MW in 1 μs and 80 MW in 4.5 μs pulse duration. The diode voltage is 450 kV at 100 MW and 400 kV at 85 MW peak power. The maximum repetition rate is 50 pps, which is limited by the cooling limit of the beam collector. For the low-energy linac, the E3712 klystron would be modified for a repetition rate of 150 pps with larger beam collector.

Modulator

The klystrons need a 400 kV pulsed-beam voltage with a 4.5 μs flat top to operate at the 80 MW peak power. A line-type modulator has been chosen due to the high efficiency, relatively low cost and high reliability. A conventional line-type modulator consists of 14 sections of pulse-forming network (PFN), and is resonantly charged and discharged by a single thyratron switch at a repetition rate of 150 pps, synchronized with a three-phase electric power line.

High efficiency must be achieved in order to reduce the wall-plug power. To reduce the energy loss in the circuit, a de-Q'ing circuit should be eliminated. This appears to be possible and about a 5% reduction in the wall-plug power from the pre-linac section can be expected. A 50-kV Inverter HV power supply is applied for charging the PFN. The charging voltage of the PFN is fed-back to the inverter in order to obtain pulse-to-pulse charging stability with an accuracy of $\pm 0.1\%$.

The rise and fall times of the pulse are mainly affected by the number of PFN sections, and the

characteristics of the pulse transformer. In order to produce a square pulse, the number of PFN sections must be increased and a pulse transformer with a low leakage inductance must be developed. On the other hand, an increasing number of PFN sections would increase the construction cost of the PFN and makes the modulator large.

A self-healing-type capacitor with a long lifetime has been developed to obtain a compact PFN. This capacitor consists of a metalized film with thin Zn-electrodes (300 Å in thickness), which form a series of microscopic capacitors. The case volume is less than half of the conventional type of capacitor. The components in the modulator cabinet have been arranged in consideration of compact size and easy maintenance, so that the size of the cabinet is 2.8 m in width, 1.8 m in depth, 2.2 m in height.

The specifications of the modulators are listed in Table 6.10. Approximately a 5 % positive mismatch is used at full voltage for a proper operation of the thyratron and the load impedance is about 5 % higher than the output impedance of the modulator. The charging efficiency of the PFN has been estimated to be 95 %.

Klystron Modulator	
Peak power output	198 MW
Average power output	210 kW
Transformer ratio	1:18
Output pulse voltage	22.0 kV
Load impedance	2.5 Ω
PFN impedance	2.4 Ω
Thyratron anode voltage	45.6 kV
Thyratron current	8982 A
Pulse flat top	4.5 μs
Rise time	0.8 μs
Pulse height deviation from flatness	1.0 % (p-p)
Pulse amplitude drift in short term	< 0.1 % (p-p)
Pulse amplitude drift in long term	< 0.3 % (p-p)
Repetition rates	150 pps
Efficiency of energy transfer	~ 85 %
Wall plug power of a modulator	243 kW
Wall plug power of modulator peripheral	
Low level and control	4.5 kW
Klystron focusing coil	8 kW
Klystron heater power	0.5 kW
Klystron driver	1 kW
The others	5 kW
Total wall plug power/rf unit	262 kW

Table 6.10: *Specifications of the S-band klystron modulator.*

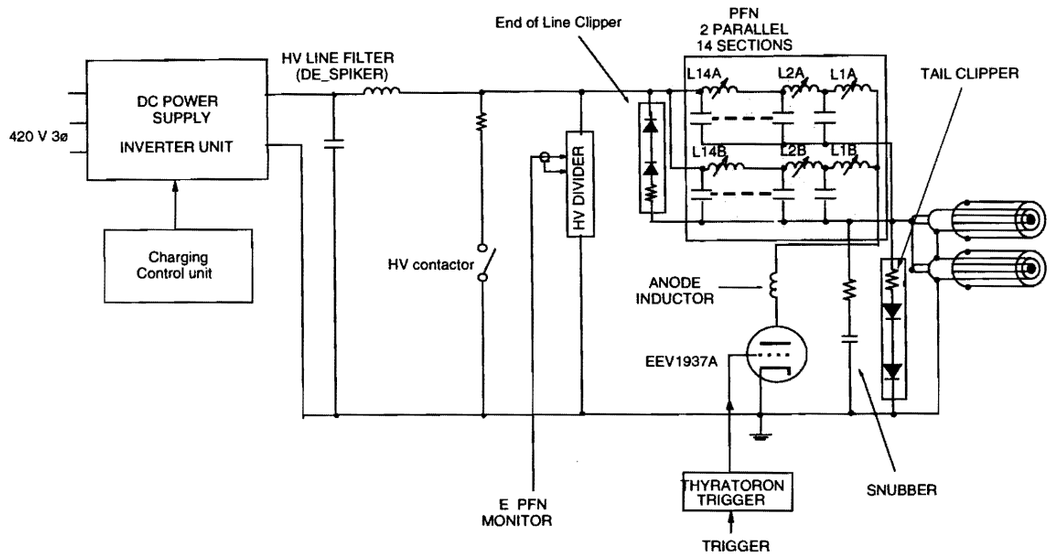

Figure 6.36: *Block diagram of the modulator circuit.*

RF Pulse Compression System (SLED)

The SLED pulse-compression scheme and associated SLED cavity ideas were invented and established at SLAC. This is a standard RF compression system at S-band frequencies, and are utilized for SLC, LEP injector, LAL at ORSAY, PLS linac and ATF linac. The RF energy from the klystron is stored in two TE_{015} high-Q cavities. Then the power is released through the coupling iris into the waveguide to feed the accelerating structure during the tail part of the same pulse by changing the phase of the RF input pulse from zero to π rapidly.

The parameters of the SLED cavity designed for the ATF linac are given in Table 6.11.

RF System for the Pre-linac Using ΔT ECS

The rf system of the pre-linac with the ΔT-ECS has been designed. The system is shown in Figure 6.37.

A klystron produces an rf pulse with 60 MW of peak power and 4.5 μs of pulse duration. The rf power is fed into a SLED cavity. At 3.5 μs after the feed of rf pulse into the SLED cavity, the rf phase would be reversed. A saw tooth-like waveform with instantaneous peak power of < 300 MW and pulse duration of 1.0 μs is extracted from the SLED cavity. The rf power is divided into two rf waveguides to feed rf peak power of < 150 MW into a 3 m-long accelerating structure. The multi-bunch should be accelerated before the rf front reaches the end of the accelerating structure in order to avoid the energy spread due to the dispersive effect of the structure itself. The net accelerating gain per unit

Operation frequency		2856 MHz
Cavity length	L	33.59 cm
Cavity diameter	$2a$	20.51 cm
Groove width	W_g	1.0 cm
Groove depth	d_g	0.9 cm
Iris diameter	D	2.98 cm
Iris thickness	t_w	1.2 cm
Quality factor	Q	10^5
Coupling coefficient	β	4.8
SLED filling time	$T_c = 2Q_0/\omega(1+\beta)$	1.92 μs
Klystron pulse width	t_{rfk}	4.5 μs
SLED input pulse width	t_{in}	3.5 μs
SLED output pulse width	t_{rf}	1.0 μs
Mode separation between TE_{015} and TM_{115}		20 MHz

Table 6.11: *Main parameters of the dual-iris SLED system.*

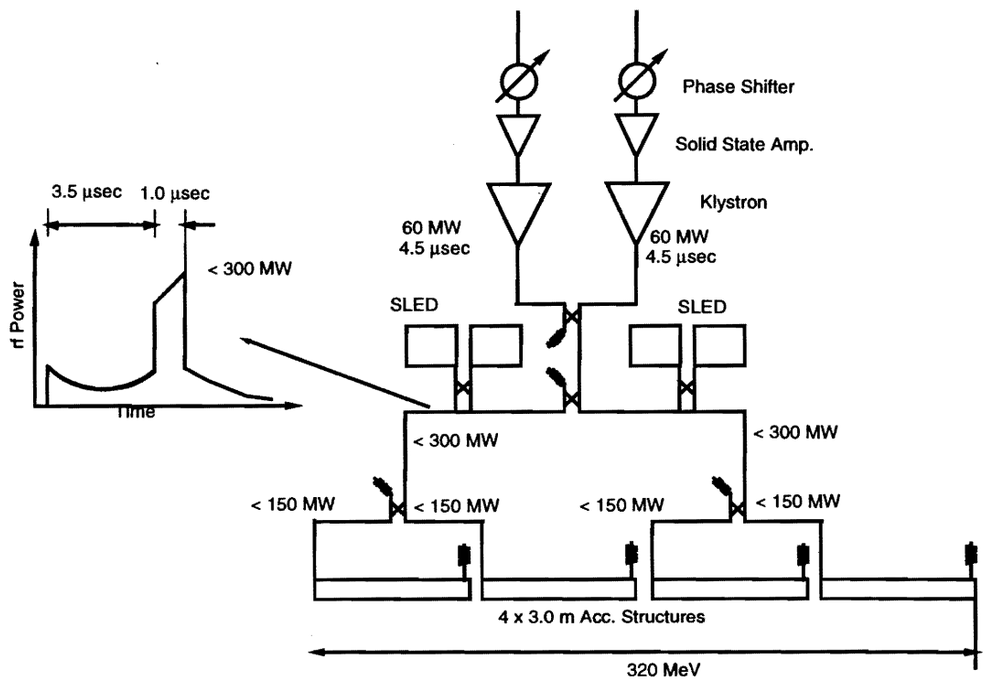

Figure 6.37: *Unit of linac for ΔT ECS.*

length would be reduced by beam-loading. Table 6.12 gives the parameters relevant to the pre-linac RF system when the ΔT ECS is adopted. Using those parameters, the total wall-plug power is roughly estimated to be 15 MW per pre-linac.

		Maximum specifications
Klystron		E3712-II
Klystron peak power	MW	60
Klystron voltage	kV	365
Klystron current	A	428
RF pulse width	μs	4.5
Micro-perveance		1.94
Efficiency	%	38
Number of modulators		60
Output pulse voltage	kV	20.3
Peak output power	MW	182.7
Average power output	kW	205
Repetition rate	pps	150
Thyratron anode voltage	kV	40.6
Thyratron anode peak current	kA	8.4
Pulse transformer ratio		1:18
Pulse width	μs	7.5
Nominal PFN impedance	Ω	2.4
Total PFN capacitance	μF	1.4

Table 6.12: *Parameters related to the klystron modulators for 8 GeV low-energy linac, when the ΔT ECS scheme is adopted.*

RF system for the Pre-linac Using ΔF-ECS

The rf system of the low-energy linac with the ΔF-ECS has been designed based on the ATF S-band linac. The configuration of the system is basically identical to that of the ATF linac. See Figure 6.38. The parameters relevant to the RF system, when ΔF-ECS is adopted, are given in Table 6.13.

A klystron produces an rf pulse with 60 MW of peak power and 4.5 μs of pulse duration. The rf power is fed into a SLED cavity. At 3.5 μs after feeding rf pulse into the SLED cavity, the rf phase would be reversed. The saw tooth-like waveform with an instantaneous peak power of 300 MW and a pulse duration of 1.0 μs is extracted from the SLED cavity. The rf power is divided into two rf waveguides to feed the rf power of 200 MW (peak) into a 3 m-long accelerating structure. Since the rf pulse front reaches to the end of accelerating structure, the accelerating field in the structure is distributed from 34 MV/m to 52 MV/m along the accelerating structure. The multi-bunch should be accelerated before the rf front reaches the end of accelerating structure in order to avoid an energy spread due to the dispersive effect of the structure, itself. The net accelerating gain per unit length would be reduced by the effects of beam-loading. ΔF-ECS section is installed before an individual quadrupole magnet, so that the energy spread of the multi-bunch is compressed before passing through the optics.

		8 GeV Accelerator Section	Energy Compensation System
Klystron		E3712-II	E3712-II
Klystron peak power	MW	60	50
Klystron voltage	kV	365	350
Klystron current	A	428	401
RF pulse width	μs	4.5	1.0
Micro-perveance		1.94	1.94
Efficiency	%	38	38
Number of modulators		52	26
Output pulse voltage	kV	20.3	19.4
Peak output power	MW	183	174
Average power output	kW	205	78.3
Maximum repetition rate	pps	150	150
Thyratron anode voltage	kV	40.6	38.9
Thyratron anode current	kA	8.4	8.08
Pulse transformer ratio		1:18	1:18
Pulse width	μs	7.5	3.0
Nominal PFN impedance	Ω	2.4	2.4
Total PFN capacitance	μF	1.4	1.4

Table 6.13: *RF system parameters (maximum specifications) for the JLC pre-linac, when the ΔF ECS scheme is adopted.*

Two such systems (with an RF frequency slightly higher and lower than the standard 2856 MHz), as shown in Figure 6.38, will be paired to form a complete unit energy-compensation system. In order to simplify the timing system, the rf frequency deviation was chosen to be 1.082 MHz, which is just the damping ring revolution frequency, and is also the 2640th subharmonic frequency of the 2856 MHz fundamental frequency. Therefore, one accelerating structure is driven at 2856+1.082 MHz, while another accelerating structure is driven at 2856−1.082 MHz. The peak power from the klystron is 50 MW at a 1.0μs pulse duration. One unit of the system can compensate a 40 MeV energy difference among the multi-bunch. Therefore, the system can compensate an energy difference of 80 MeV at the maximum among the multi-bunch.

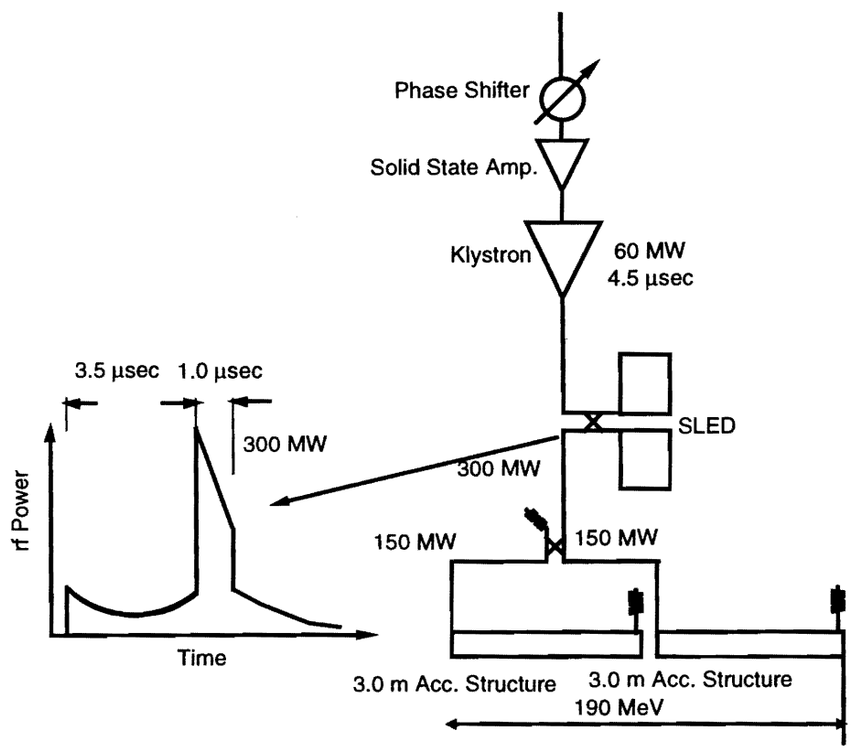

Figure 6.38: *A regular RF unit of the JLC pre-linac when the ΔF ECS scheme is adopted.*

References for Chapter 6

[1] K. Yokoya, private communication.

[2] Zeroth-Order Design Report for the Next Linear Collider, LBNL-PUB-5424, also SLAC Report 474 or UCRL-ID-124161, May 1996.

[3] P. Emma, "A spin Rotator System for the NLC," NLC-NOTE-7 (1994)

[4] K. Oide, Nucl. Instr. Meth. **A335, 1 (1989)**

[5] M. Yamamoto, "Study of Long-Range Wake Field in Accelerating Structure of Linac," KEK Report 94-9, 1995

[6] H. Deruyer et al., "Damped and Detuned Accelerator Structures," Int. Linear Accelerator Conf. Albuquerque, USA, 1990, and SLAC-PUB-5322, 1990

[7] See Chapter 12 of this report. Also, see T. Shintake et. al., "HOM-Free Linear Accelerating Structure for e+e- Linear Collider at C-Band," Proc. Part. Accel. Conf. and Int. Conf. High Energy Accel., Dallas, USA, 1995 and KEK Pre-print 95-48.

[8] M. Yamamoto et al., "Analysis of Detuned Structure by Open Mode Expansion," 17th Int. Linac Conf. (Linac94) Tsukuba, August (1994)

[9] Also, see K. Kubo et al., "Methods to estimate emittance dilutions due to misalignment of accelerating structures without tracking," NLC-Note 13 (1995)

Authors and Major Contributers of Chapter 6

- Seishi Takeda
- Shigeru Kashiwagi
- Toshiyuki Okugi
- Kiyoshi Kubo
- Mitsuo Kikuchi
- Toshiyasu Higo

CHAPTER 7

X-band Main Linacs: Design Overview

Contents

7.1 Basic Design Requirements

General idea

The basic purpose of the main linac is to accelerate multi-bunches from the injection energy to the final one. The nominal center-of-mass energy $E_{c.m.}$ is set to be 1 TeV, and all of the linac parameters are being first set at this energy. However, the linac is designed to be capable of operating at a lower energy, such as the center-of-mass energy of 250 GeV. Also, the present scheme should be technically applicable to an energy upgrade to the range of $E_{c.m.} = 1.5$ TeV without essential modifications of the RF system.

A length of about 20 km for the two linacs is considered to be reasonable at present. Acceleration at a level of 50 MV/m will be required to reach the nominal energy. The length and accelerating field should be optimized in the engineering design stage from stability, reliability and cost points of view. To realize this high field with a limited wall-plug power for the linac, a high frequency of 11.424GHz was chosen as compromise, by considering the merits obtained from the higher frequency and the difficulties concerning higher frequency structures.

The basic optical configuration of the linac is described in Chapter 8. The requirements on the various hardwares along the linac, such as the alignment tolerance and tolerable wake-field, are discussed there. The requirements on the beam instrumentation along with the strategy from the initial step to the feedback performance are given following the discussion in that section.

RF power-related issues to be established to realize this high-frequency design include the generation of a high RF peak power with a short pulse length, while maintaining a high efficiency from the wall-plug power to the beam. The RF system configuration, which realizes these requirements, is discussed in Chapter 10.

Another important issue concerning the high frequency design arises from the existence of structures near to the beam, which results in high longitudinal and transverse wake-fields.

The short-range longitudinal wake-field results in an energy distribution within a bunch. This distribution will be corrected by setting the bunch off crest to the RF phase along the whole linac with respect to the beam by about 17°. On the other hand, the short-range transverse wake-field should first be minimized by aligning the structures well with respect to the beam. The residual wake-field will be compensated by using a BNS damping scheme at the low-energy part of the main linac. These issues are described in Chapter 8 in detail.

As for the long-range longitudinal wake-field, one of the biggest concern is that of the accelerating mode. This wake-field, fundamental beam loading, causes an inter-bunch energy variation. To suppress this variation, various schemes, such as a staggered-timing scheme, an amplitude- or phase-ramping scheme and a passive-correction cavity scheme, are being studied. On the other hand, the

long-range transverse wake-field causes a transverse multi-bunch emittance growth. In order to suppress this, the wake-field is designed to be canceled among the modes in the four interleaved structures, which are aligned well. However, this cancellation cannot be realized perfectly. This is because of a misalignment of the cells in a structure or a relative misalignment among the four interleaved structures in addition to some residual wake-field which exists, even in the perfectly aligned case as intrinsic residual components and that due to fabrication errors. The requirements from a beam dynamics point of view are described in Chapter 8. The alignment of the structure or the cells in a structure should be made with respect to the beam within several microns, which tolerates the residual wake-field after cancellation. In order to make this cancellation method work, and also to realize a good alignment among the four structures, a high-precision fabrication technique becomes one of the key technologies. The issues related to the design and fabrication of such an accelerating structure are described in Chapter 9.

The philosophy of this high-precision fabrication should be applied to all components along the linac, such as the quadrupole magnets and the beam position monitors, in order to make the accuracy of their alignments good. It is also good to keep the wake-fields originating from those beam environments small. It should be noted that once high-precision fabrication and alignment techniques are established, they should naturally be extended to the mass production of a huge number of components in an inexpensive way.

Typical parameters of the main linac

The main-linac parameters are given based on a consideration of the whole linear collider system, while keeping reasonable operational values of such components as the klystrons, modulators and structures in mind. The parameters relevant to the main linac are listed in Table 7.1.

The bunch spacing of 1.4 nsec is now fixed as a nominal value. The possibility of a longer bunch spacing, such as 2.1 or even 2.8 nsec was studied, in order to ease the needed damping or cancellation of the long-range transverse wake-field in the accelerating structures. In the case of a heavily damped structure, the damping scheme still needs fairly heavy damping, even if we take such a long bunch spacing except for a margin in a fast cancellation of the wake-field. On the other hand, a constant-gradient structure already has a natural spread in the dipole-mode frequency, which almost meets the requirements for the case of a 1.4 nsec bunch spacing. In this sense, we do not have a large merit due to the longer bunch spacing. On the other hand, we cannot expect a gain in luminosity by going into a longer bunch spacing with a larger charge in a bunch.

The RF pulse width required for the structure is the sum of the rise and fall time of the RF pulse, the filling time of the structure and the width of the bunch train. It is estimated that the rise and fall time of the RF pulse is each 10 nsec. Thus, the total width is 250 nsec.

The repetition rate of the linac is limited due to the upper limit of the wall-plug power to around 200 MW.

Parameter	Symbol	Value	Unit
—— Energy ——			
Collision energy	E_{cm}	1000	GeV
Beam energy	E_{final}	500	GeV
Injection energy	E_{inj}	10	GeV
—— Beam parameters ——			
Number of particles per bunch	N	0.70×10^{10}	
Number of bunches per pulse	m_b	85	
Bunch spacing	t_b	1.4	ns
Repetition frequency	f_{rep}	150	Hz
Normalized emittance at the exit of damping ring	$\gamma\epsilon_x/\gamma\epsilon_y$	3×10^{-6} / 3×10^{-8}	m
R.m.s. bunch length	σ_z	90	μm
Single-bunch full-energy spread		0.3	%
Multi-bunch full-energy spread		0.1	%
—— RF basic parameters ——			
Main accelerating frequency	f_{rf}	11.424	GHz
Nominal accelerating gradient	G_0	73.0	MV/m
Effective accelerating gradient[1]	G_{eff}	55.6	MV/m
RF unit (number of modulator / klystron / structure)		4 / 8 / 12	
Peak power input to structure		130	MW
Off-crest angle for single-bunch energy compensation[2]	ϕ_{rf}	17.2	deg
Single-bunch extraction efficiency	η_1	1.97∼1.47	%
—— Structure parameters ——			
Structure type		Detuned	
Configuration		4-fold interleaved	
Accelerating mode		$2\pi/3$	
Number of cells in a structure[3]		150	
Structure length		1.31	m
Average iris radius in unit of wave length[4]	a/λ	0.166	
range (entrance - exit)		0.20∼0.14	
Filling time[5]	T_f	106.4	ns
Attenuation parameter[5]	τ	0.609	
Beam hole radius	a	5.23∼3.67	mm
Disk thickness	t	1.2∼2.4	mm
Group velocity	v_g/c	0.098∼0.02	
Q value[5]	Q	6800∼6050	
Shunt impedance[5,6]	r/Q	10.2∼13.6	kΩ/m
Shunt impedance[5,6]	r	70∼82	MΩ/m

Loss parameter	k_1	2.44~1.83×10^{14}	V/C/m
Average power loss per structure[7]		3.4	kW
—— Dipole mode frequency ——			
Gaussian spread (sigma) of 1st passband	$\sigma f_{d1}/f_{d1}$	2.24	%
full spread of 1st passband	$\Delta f_{d1}/f_{d1}$	11.2	%
frequency tolerance	$\delta f_{d1}/f_{d1}$	$< 10^{-4}$	
Gaussian spread (sigma) of 6'th passband	$\sigma f_{d6}/f_{d6}$	0.716	%
full spread of 6'th passband	$\Delta f_{d6}/f_{d6}$	3.58	%
—— Klystron parameters ——			
Peak power	P_{kly}	67	MW
Pulse length[7]	T_{kly}	750	ns
Cathode voltage	V_k	430	kV
Cathode current	I_k	338	A
Estimated efficiency	η_{kly}	45	%
Focusing		PPM	
—— Pulse compression ——			
Pulse compression scheme		4/3 DLDS	
Transmission mode		TE_{01}	
Delay line diameter		118.1	mm
Delay line length (long / short)		79.4 / 39.7	m
—— Modulator ——			
Number of klystrons to drive		2	
Modulator configuration		Blumlein	
Number of stages		24×2	
Pulse transformer ratio		1:5	
Charging voltage		86	kV
Current[9]		1696×2	A
Switching device		Thyratron	
—— Tolerances and acceptances[10] ——			
Injection energy spread (acceptance)		2	%
Structure misalignment tolerance[11]			
cell-to-cell		9	μm
structure-to-structure		6	μm
minimum (at wave length ~60m)		3	μm
Quadrupole magnet (random)			
between successive beam based alignments		2	μm
transverse position jitter tolerance		10	nm
field strength jitter tolerance		0.5	%

— Linac —			
Number of DLDS units		561	
Number of klystrons / beam		4485	
Number of structures / beam		6727	
Number of DLDS units per DLDS period		6	
Active length of main linac / beam	L_{acc}	8.81	km
Packing factor		79.2	%
Total length / 2 linacs		22.3	km
Average beam power / beam		7.14	MW
Assumed efficiency from AC to structure input		28	%
Wall-plug power / 2 linacs		234	MW

1: net accelerating gradient including single-bunch and multi-bunch energy compensation
2: average over the whole linac
3: including input and output coupler
4: averaged being weighted by $a^{-3.5}$
5: assuming 95% of the theoretical Q value
6: accelerator definition
7: at the nominal gradient without beam
8: including switching time of DLDS; (10+230+10)×3
9: driving two klystrons
10: based on the criteria of 25% emittance growth in the linac
11: based on the random offset which is constant over each alignment length

Table 7.1: *500 GeV X-band main linac parameters.*

7.2 RF System Configuration

A possible view of the linac is schematically shown in Figure 7.1. The basic RF system configuration, consisting of the above-mentioned system, is shown in Figure 7.3.

One RF system unit, called a DLDS unit, consists of eight klystrons with Blumlein pulse-forming networks and pulse transformers, delay lines and twelve 1.3m-long accelerating structures. Each klystron produces a peak power of 67 MW with 750 nsec in width. The power from the klystrons is

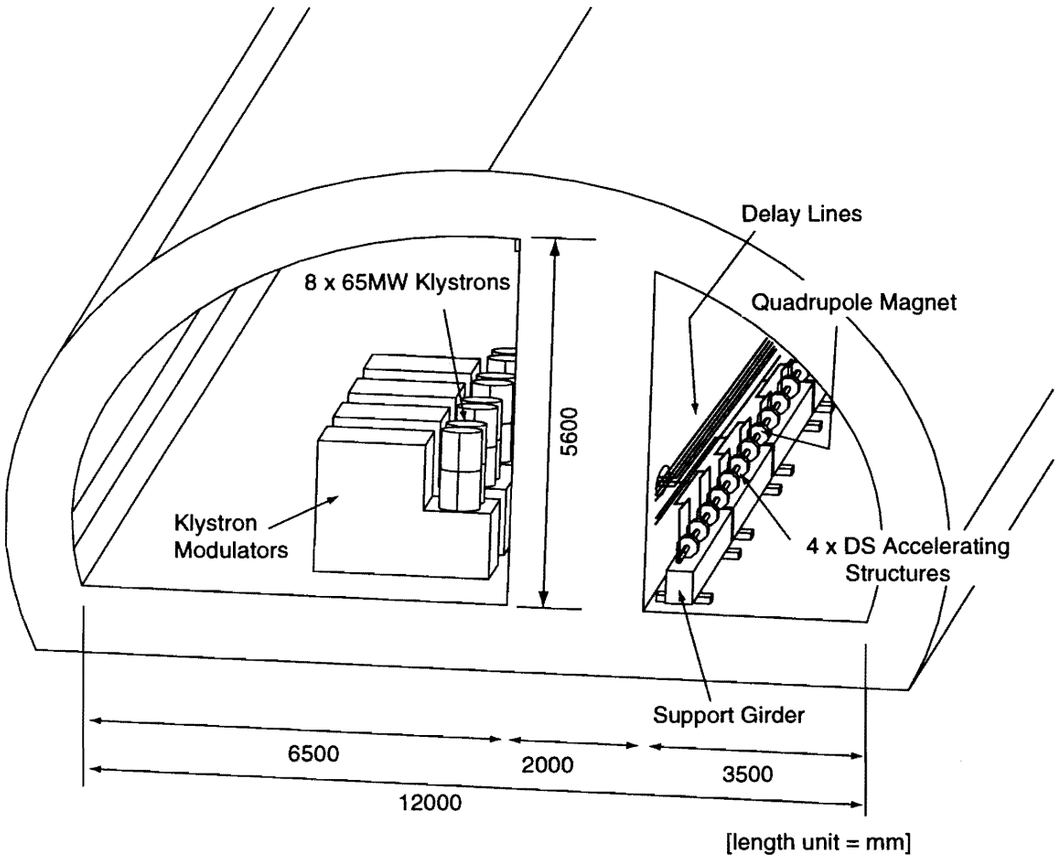

Figure 7.1: *A possible schematic view of the inside of X-band linac tunnel.*

chopped in time into three time bins. Each bin is combined with those from the other klystrons to make the power four-times higher than that of a pair of klystrons. This power is transported to the structure at a proper location, and is again divided into four wave guides to feed four structures. This system gives a peak power of 130MW for each structure with a duration of 230 nsec.

One of the key issues to operate the main linac and to reach a very high energy with reasonable luminosity is to keep the total wall-plug power within a reasonable limit. Concerning this aim, the efficiency of the energy transformation in the system should be sufficiently high. Therefore, each component should be designed to have a reasonably high efficiency. The adoption of the DLDS system is actually one of the ways to realize high efficiency. However, in this case, it should be noted that such RF characteristics as the phase stability between a long distance and so on should be carefully studied from the view point of beam dynamics.

To realize this high efficiency, the Blumlein PFN is aiming at a fast rise and fall time of the high-voltage pulse by increasing the effective voltage in PFN and reducing the pulse transformer winding

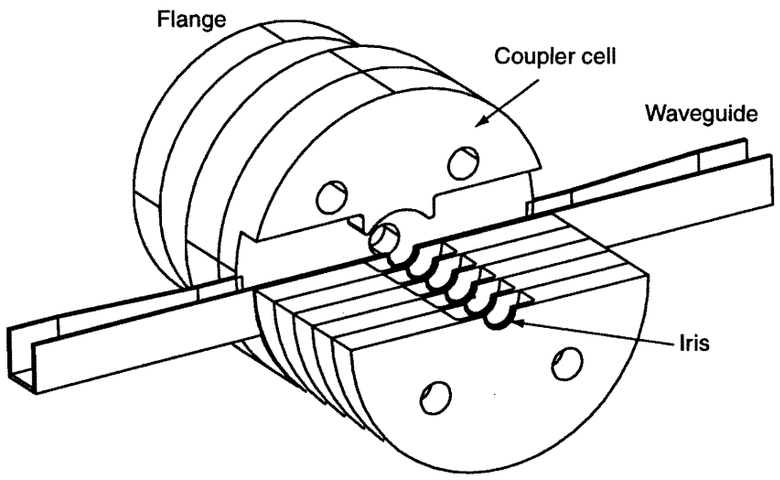

Figure 7.2: *Schematic view of detuned structure for JLC.*

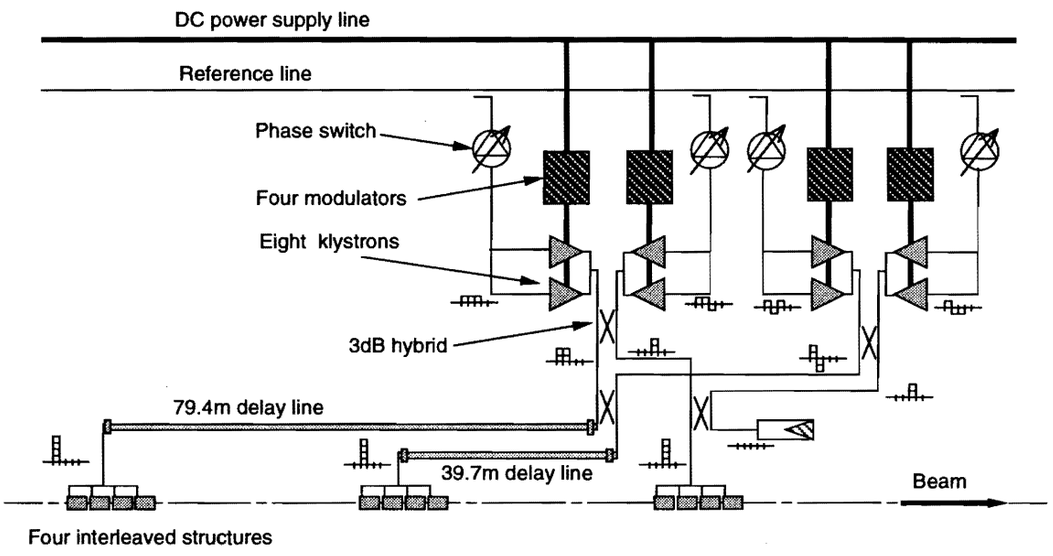

X-band RF system 4/3-DLDS

Figure 7.3: *Schematic diagram of a DLDS system.*

ratio. The klystron is designed to make an electric efficiency larger than 45% with beam focusing by a device, such as a periodic permanent magnet. Chopping of the RF pulse length is performed by simply dividing the produced long pulse by a 3 dB coupler circuit, and delivering it to a different place so that the loss is limited to only the transmission loss, and, thus, the loss can be kept fairly small.

As an accelerating structure, a simple disk-loaded structure was adopted in order to realize the stable operation at a high field with a careful control of the frequencies of the higher modes. Although the shape is evident, it is schematically shown in Figure 7.2. Due to the requirement on the cancellation of the dipole wake-field, four similar structures are located near by in space. In this sense, the four structures are aligned among each other to a fairly good precision. In a practical design, some sort of BPM's should be integrated into the accelerating structure. In some case, although those BPM's are independent structures, they are mechanically connected to the accelerating structure, while maintaining a good alignment among them. In another case the BPM's might be the accelerating structure itself equipped with some pickups for the BPM action. The design following these ideas should be studied in detail.

The period between the four structures which belong to the same DLDS unit is 39.7m. Then, six sets of four structures becomes a good number if we consider the space for the components, other than the net acceleration. In this case, the space other than the acceleration amounts to about 20%.

7.3 Energy Upgrade toward 1TeV

The essential parameters of the linac are determined at a nominal energy of 1 TeV c.m. energy. However, the initial operation of the linac will be at a considerably lower energy due to a requirement based on the strategy of physics experiment as well as the unfinished mass production of the components for the whole linac.

It is not necessary to change the configuration of the RF unit in order to change the energy of the linac. To operate at a lower energy mode, the simplest method is to operate the RF sections at the full specifications for 1 TeV c.m. energy while reducing the active length of the linac. This means that we need to transport the beam for the rest of the linac through a very large beam pipe with a very large beta function by installing large quadrupole magnets. On the other hand, it is also possible to operate the linac at a somewhat lower gradient to realize a lower energy. In this case, there is a lower limit of the gradient due to a heavy beam-loading behavior. The determination, such as the percentage of filling in the linac with the accelerating structures, and the choice of feeding or idling for the installed accelerating structures, should be determined while practically considering the status.

The extendibility to even higher energies can be considered in several strategies, such as increasing the RF peak power by increasing the klystron output power, or increasing the length of the linac while keeping the RF system the same. In any case, it should be inevitable to increase the wall-plug power, unless some advanced RF technologies make the electric efficiency much higher, or by admitting

the lower luminosity by adjusting the repetition rate of the linac. However, a detailed study of this extendibility is outside the scope of the present study.

7.4 Controlling the Emittance

There are a number of important issues to consider concerning the preservation of the ultra-low emittance of the beams through the main linacs.

- Energy spread

  The single-bunch energy spread can be compensated by the RF slope to within 0.3%.

  The multi-bunch energy spread becomes on the order of 20% due to fundamental beam-loading for the last bunch in a train, unless a correction is made. The energy distribution among the bunches can be reduced to within 0.1% by various methods. To find a proper method of compensation which meets this requirement, some beam-loading compensation schemes are being studied, such as a staggered-timing scheme, a ΔF scheme, an RF amplitude or phase modulation scheme, a scheme with correction cavities, etc. From a beam-dynamics point of view, local compensation should be used. Otherwise, the bunch-to-bunch difference of the focusing strength could be fairly large especially in a low-energy part of the linac, until passing through more than several structures and the compensation is completely finished. The choice should be made while considering the beam dynamics stability, the complexity of the system in the whole linac and so on.

- Transverse emittance

  The BNS damping scheme is used for suppressing the transverse single-bunch emittance growth.

  In addition to this damping scheme, a good alignment of the structures is very essential to suppress the transverse single-bunch emittance within a tolerable level. Each structure or each bunch of four structures is equipped with two beam-position monitors which are aligned well mechanically with respect to the structures. The measured beam position is fed back to the alignment of the structures via precise active movers.

  The multi-bunch emittance, that is the scattering of the multi-bunches in transverse phase space, should also be preserved along the linac so as to be smaller than the size of the single-bunch. This is so as to realize high luminosity in multi-bunch operation.

  Firstly, the long-range transverse wake-field is designed to be canceled out among the higher modes by distributing the frequencies of the relevant dipole modes in a truncated Gaussian manner, so that the wake-function in the time domain will also fall in a Gaussian manner. The spread of the Gaussian distribution in frequency is designed to be sufficiently wide so that the falling time is fast enough to make the wake-field decrease by two orders of magnitude at the time of the next bunch arrival (1.4 nsec).

In this design, a slow, but large, growth of the wake-field within a bunch train is inevitable because of the finite number of modes to be distributed within a structure. One of the methods used to overcome this is to design four structures interleaved so that the effective mode spacing becomes four-times smaller, and the resulting recurrence time becomes four-times later than before. Then, the wake-field will stay within a tolerable level during the bunch train. In the present report, this interleaved DS method is extensively mentioned. However, there might be a better way of avoiding this recurrence, by introducing a medium damping for the higher modes. This method is now being studied at SLAC in a damped-detuned structure, DDS. We keep in touch with this activity as an option until the final decision is made concerning the structure types. Another possible candidate for a heavily-damped structure, HDS, is now also being studied as an optional configuration of the linac structures to study practical optimization. A study of the structure based on the choke-mode idea has just started.

- Alignment

  In addition to the cancellation of the wake-field, the alignment of the structures and that of the cells in a structure are very important, because the wake-field is proportional to the offset of the beam. A practical estimation of the tolerance based on the calculated wake-field is under way. Especially, the coherent cancellation among four interleaved structures near to the injection area is not self-evident because the length of four interleaved structures becomes a large fraction of the betatron wave-length. The cell alignment in a structure is also very essential in the cancellation of the wake-field within a structure. The estimated cancellation of the wake-field is usually performed by assuming that all of the cells in the structure are perfectly aligned. However, a better approximation method should be developed to practically deal with a cell misalignment in a structure. A trial simulation which takes a misalignment of the structures into account is described in Chapter 8.

  The beam position with respect to a structure is measured and used to feed back to the position adjustment. A beam-based alignment should be applied as a final step to align the structures.

  The short-range wake-field, or even a long-range one, due to such steps as the connection point of various components along the linac or from side holes for the evacuation if existing, BPM's, etc. should be within a tolerable level.

  The alignment of such components as the quadrupole magnets, beam position monitors and the structures are very essential for preserving low emittance.

- Instrumentation and feedback

  The BPM is the most basic and important device used to align the quadrupole magnets and structures to the beam. They are located very close to those components. The accuracies and resolutions needed for those BPM's are described in Chapter 8. In several special beam-diagnostic sections along the linac, the single-bunch and bunch-to-bunch emittance of the beam is measured in order to globally compensate the emittance degradation. Such a non-local compensation should be considered after the practical configuration of the linac is fixed. This compensation might relax various tolerances as a result. However, this type of compensation should be designed as a safety margin of the linac to reach the required quality.

- Vacuum

  The vacuum pressure should be kept below the tolerance determined by the ion effect for multi-bunch emittance preservation. In the DS case, the vacuum conductance is limited because the evacuation is only through the beam hole in the disk. To make the vacuum low, the out-gassing rate, especially for the high-Z molecules, should be small. A study of the out-gassing rate is now under way, as described in Chapter 9.

Author of Chapter 7

- Toshiyasu Higo

CHAPTER 8

X-band Main Linacs: Beam Dynamics

Contents

8.1 Introduction

8.1.1 Issues with Emittance Dilution

In an ideal linac, the normalized transverse emittances $\gamma\epsilon_x$ and $\gamma\epsilon_y$ and the absolute energy spread ΔE are conserved quantities. In real linacs, some increases occur in these values due to a variety of phase-space dilution mechanisms. This chapter treats those issues related to the preservation of the transverse emittance of the beams along the main linacs.

It is well known that various construction and operational errors in the linacs can cause emittance dilution. It should be noted that since the design value of the vertical emittance of the beams extracted from the damping rings is smaller than that of the horizontal emittance by two orders of magnitude, the tolerable magnitudes of machine errors in the vertical direction will generally be much tighter than that of the horizontal ones. Consequently, in this chapter, various tolerance values for the main linacs are quoted only for the vertical direction.

Under usual operation, the acceptable energy spread at the end of the main linacs is determined by the calculated acceptance of the final focus system, which is $\pm 1\,\%$ in our design.

As for the transverse beam emittance, the nominal emittance values quoted for describing the "JLC design parameters" in Chapter 2 are 3×10^{-6} m and 3×10^{-8} m for the horizontal and vertical directions, respectively. The design of the current final focus section can accept the normalized beam emittance up to a horizontal value of 4×10^{-6} m and a vertical value of 9×10^{-8} m (See Chapter 13). These are to be compared with the design value of the equilibrium horizontal emittance (normalized) of 2.52×10^{-6} m from the damping rings (See Chapter 5).

It is seen from above that there are some design and operational margins in quoting the ideal, design and acceptable emittance values. However, of course, it is neither very safe nor particularly scientific to declare certain values of the emittance budget or emittance blow-up allowances, unless quantitative studies on specific causes of emittance dilution are conducted. In this chapter, for each error source that can cause emittance dilution, its tolerance is estimated for a $< 25\,\%$ increase of the emittance. The total increase in the emittance will be approximately a linear sum of increases due to each of these effects, if they are small compared with the nominal emittance.

At this moment, the effects of coupling between the horizontal and vertical phase spaces are not considered. However, the longitudinal dynamics is examined here. Because of the extremely relativistic beam energy in the main linacs, and because of the small transverse momentum of particles compared to the longitudinal momentum, we assume that the relative longitudinal positions of particles in the beams do not change along the linacs. In longitudinal dynamics, only changes in the particle energies are considered. The dependence of the transverse motions on the particle energy is an important issue. On the other hand, the dependence of the particle energies on their transverse motions will be

very small. These effects are ignored here.

8.1.2 Sources of Emittance Dilution

There are two major sources of emittance increase: dispersive effects and wake-field effects:

- Beam particles having different energies obtain different magnitudes of transverse kicks in magnetic fields. This effect leads to different trajectories for particles with different energies, and eventually causes an emittance increase. This is called the dispersive effect.
- When charged particles pass through accelerating structures, wake-fields are induced. Dipole-mode wake-fields are the most important in the main linacs when considering the transverse motions of particles. The amplitude of the dipole-mode wake-field is proportional to the transverse offset of the leading particle. Because of the wake-field, the following particles are kicked in the direction of the offset. This effect causes different trajectories of particles at different longitudinal positions, and it will eventually increases the emittance. This is the wake-field effect.

The dispersive effect mainly determines the misalignment tolerance of the quadrupole magnets that constitute the linac beam lattice, and the wake-field effect determines a tolerance of misalignment of the accelerating structures.

Jitters of the transverse beam positions can also reduce the luminosity, since they introduce transverse offsets of electron and positron beams at the interaction point. This effect needs to be considered in addition to the emittance dilution effects. A reduction in the luminosity that takes the position-jitter effects into account can be expressed by a quantity called, the "effective emittance." It is defined as

$$\epsilon_{\rm eff} = \sqrt{< x^2 >< x'^2 > - < xx' >^2}, \tag{8.1}$$

where x and x' are particle offset and angle. The symbol <> means to take an average of all particles in many pulses.

Note that the emittance is defined by

$$\epsilon = \sqrt{< (x- < x >)^2 >< (x'- < x' >)^2 > -(< xx' > - < x >< x' >)^2}, \tag{8.2}$$

where <> means the average of all particles in a pulse.

The "effective emittance" is a measure of the beam quality with position jitter, and the emittance is a measure of the beam quality when the centers of the two beams can be well-controlled.

8.2 Lattice Design

The approximate emittance growth of the beam in the linac is given by an analytical formula,

$$< \gamma\Delta\epsilon > \approx \frac{e^2 A_{rms}^2 S_{\rm rms}^2 \beta_0 L_a (E_f^\alpha - E_0^\alpha)}{2\alpha mc^2 E_0^\alpha g}. \tag{8.3}$$

Here, the beta function is assumed to be smooth along the linacs (continuous focusing), and is assumed to be given by,

$$\beta = \beta_0 (E/E_0)^\alpha. \tag{8.4}$$

In Equation 8.3, A_{rms} is the rms of misalignment, β_0 the beta function at the beginning of the linac, L_a the length of a unit accelerating structure, g the accelerating gradient, and mc^2 the electron rest mass.

$S_{\rm rms}$ is a quantity that is determined by the wake-function and distribution of the bunch charge. Suppose that we divide a bunch into longitudinal slices and let q_m be the charge of the m-th slice, and z_m the longitudinal position of the slice m. Then the "sum wake" of a structure is defined as

$$S_m(\lambda) \equiv \sum_k q_k W(\lambda, z_m - z_k). \tag{8.5}$$

Here, λ is an index for specifying an accelerating structure along the linac. $S_{\rm rms}(\lambda)$ is defined for structure - λ as

$$S_{\rm rms}^2(\lambda) = \sum_m q_m S_{a,m}^2(\lambda) / \sum_k q_k, \tag{8.6}$$

where

$$S_{a,m}(\lambda) \equiv S_m(\lambda) - \sum_m q_m S_m(\lambda) / \sum_k q_k. \tag{8.7}$$

We consider here a concept which we call "alignment unit." Each alignment unit is assumed to consist of either (a) M structures or (b) $1/M$ structure ($M = 1, 2, 3, ...$), and is considered to be aligned as one *inseparable* object. Assuming that all of the alignment unit have the same rms as that of the misalignment magnitude, the same wake-function and the same length, the arguments for $S_{\rm rms}$ can be omitted. More on the effects of the accelerating structure will be discussed in section 8.7.

The above expression shows that the energy dependence of the growth of the normalized emittance is given by $(E_f^\alpha - E_0^\alpha)$. The emittance growth per unit length at the point where the beam energy equals E is proportional to β/E,

$$g\frac{d}{dE} < \gamma\Delta\epsilon > \approx \frac{e^2 A_{rms}^2 S_{\rm rms}^2 \beta_0 L_a}{2mc^2 E_o^\alpha} \frac{1}{E^{1-\alpha}} \approx \frac{e^2 A_{rms}^2 S_{\rm rms}^2 L_a}{2mc^2} \frac{\beta}{E}. \tag{8.8}$$

The length of an accelerator segment that corresponds to a unit phase advance is β. It is equivalent to $\beta_0 (E/E_0)^\alpha$. Therefore, the increase in the normalized emittance per unit phase advance is given by

$$g\beta\frac{d}{dE} < \gamma\Delta\epsilon > \approx \frac{e^2 A_{rms}^2 S_{\rm rms}^2 \beta_0^2 L_a}{2mc^2 E_0^{2\alpha}} \frac{1}{E^{1-2\alpha}} \approx \frac{e^2 A_{rms}^2 S_{\rm rms}^2 L_a}{2mc^2} \frac{\beta^2}{E}. \tag{8.9}$$

This indicates that if $\alpha = 1/2$, the emittance growth rate per unit phase advance will be a constant quantity along the linac.

As the optical lattice for the main linacs, we consider FoDo cells. Two accelerating structures are placed between quadrupole magnets in the low-energy region. The number of structures between the quadrupole magnets is gradually increased as the beam energy increases. The expected increase in the normalized emittance in unit length caused by wake-field effects due to a misalignment of the accelerating structures is approximately proportional to β/E. Since the alignment accuracy of the structures will be at a fixed quality along the linac, this means that the beta-function value should increase as the beam energy increases. We have adopted a design in which beta is proportional to the square root of the beam energy. This will make the expected emittance increase per betatron period to be a constant along the linac.

We now turn to the emittance increase caused by dispersive effects due to a misalignment of the quadrupole magnets in the lattice. The emittance increase in this case depends on the phase advance per FoDo cell. It should be noted that the length of a unit FoDo cell along the linac changes only when the number of the structures between quadrupole magnets is stepped up. Consequently, the phase advance cannot be arranged so as to keep the beta function to be perfectly proportional to the square root of the beam energy.

In practice, in our design each linac is divided into 7 sections, where the number of accelerating structures between quadrupole magnets is 2, 4, 6, ..., 12 and 14, respectively. We choose 90 degrees per cell phase advance at the beginning of each section. Then, within each section the phase advance per cell is decreased as the beam energy increases. When the beam energy becomes n^2 of the initial energy, the n-th section is started.

The phase advance at the beginning of the sections, which determine the initial value of the beta function (because the length of the FODO cells is determined by the number of accelerating structures), should be determined by compromising both effects: a small beta function reduces the wake-field effect, and a large beta function reduces the dispersive effects. We chose 90 degree so that the estimated tolerances of both the accelerating structures and the quadrupole magnets are not too tight.

Figure 8.1 shows the resultant vertical beta function along the linac. Because we did not consider coupling between both coordinates, the horizontal beta function is almost the same as the vertical one in this design.

It should be noticed that the present choices of the parameters are not well optimized, and that some of the parameters will have flexibilities, even after all of the hardware is constructed. Here, we use the parameters as one possible model to evaluate the tolerances etc.

Tracking simulations were performed to study the beam dynamics. The model linac comprises quadrupole magnets and accelerating structures as the main elements. At each quadrupole magnet, a beam position monitor and a steering magnet are placed for orbit corrections.

In an actual linac, although there should be several beam-diagnostic regions to measure the beam energy and emittance etc., we have not designed these areas yet.

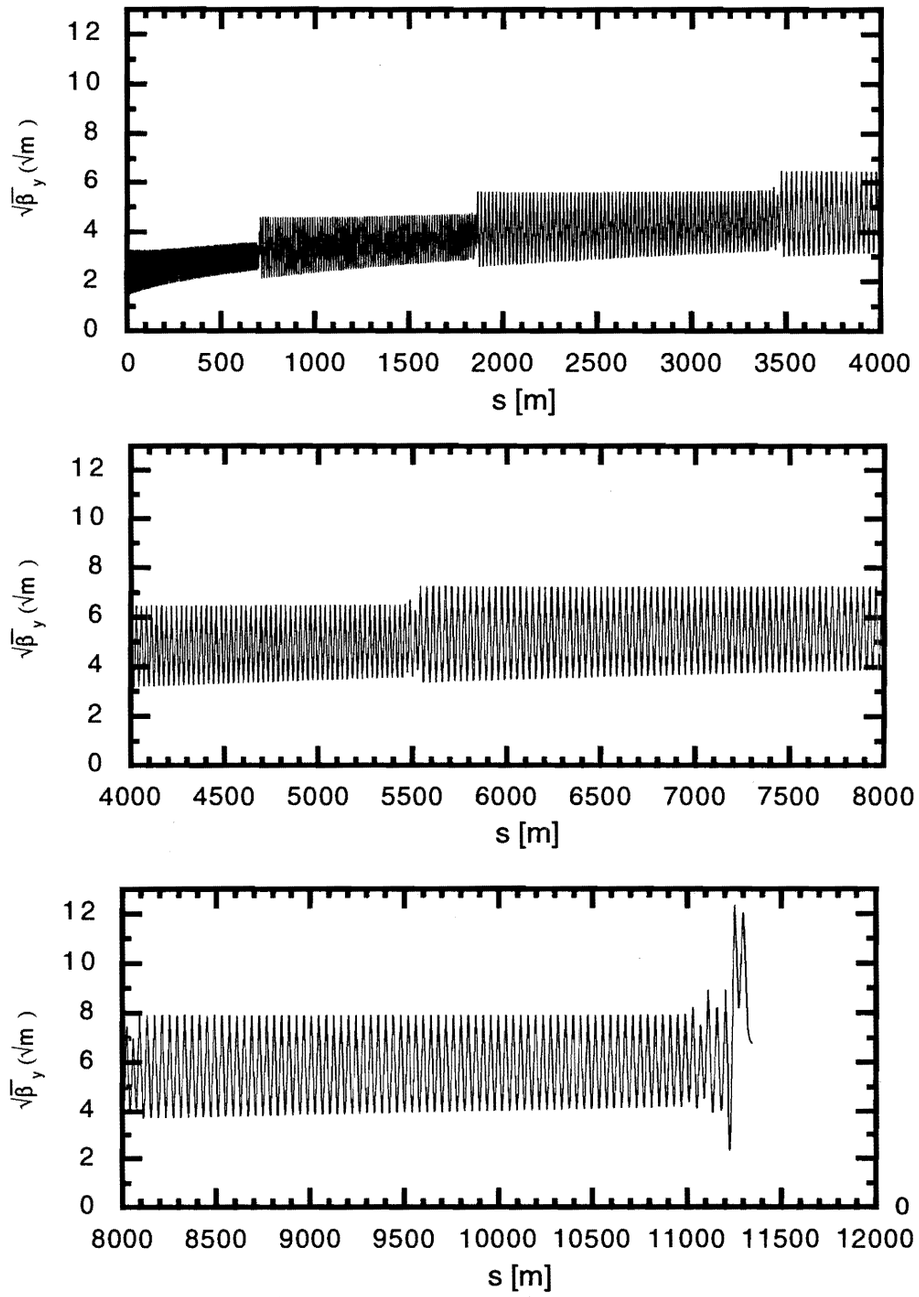

Figure 8.1: *Design vertical beta function along the linac.*

8.3 Wake-field Calculation

8.3.1 Short-range Wake-field

Short-range wake-functions of the accelerating structures were calculated from formulae as follows [16]. For the longitudinal wake,

$$W_L(s) = \frac{cZ_{\rm vac}}{\pi a^2}(W_{L0} + W_{L1}\sqrt{\zeta} + W_{L2}\zeta), \tag{8.10}$$

and for transverse wake,

$$W_T(s) = \frac{cZ_{\rm vac}}{\pi a^4}(W_{T0} + W_{T1}\sqrt{\zeta} + W_{T2}\zeta), \tag{8.11}$$

where

$$\begin{aligned}
\zeta &= \frac{Ls}{a^2}, \\
L &= \text{cavity cell period}, \\
\lambda &= \text{wave length}, \\
a &= \text{iris aperture}, \\
r &= \frac{a}{\lambda}\frac{1}{0.14}, \\
Z_{\rm vac} &= \text{vacuum impedance},
\end{aligned}$$

and

$$\begin{aligned}
W_{L0} &= 0.998r^{0.078}, \\
W_{L1} &= -1.474r^{0.371}, \\
W_{L2} &= 0.702r^{0.784}, \\
W_{T0} &= 1.550r^{0.179}, \\
W_{T1} &= -1.378r^{0.411}, \\
W_{T2} &= 0.433r^{0.762}.
\end{aligned}$$

Equations 8.11 and 8.10 are valid when the following conditions are satisfied

$$\begin{aligned}
0.10 &\leq \frac{a}{\lambda} < 0.18, \quad \text{and} \\
0 &\leq \frac{s}{L} \leq 0.1.
\end{aligned}$$

The formula was obtained for infinite constant-impedance pill-box cell structures, where all of the cells have the same dimensions and the wake-function depends on the aperture of the cells. Because the cells of our structure have different dimensions, we take the average of wake-functions of constant-impedance structures with the same aperture of cells of our structure.

In Figures 8.2 and 8.3, the obtained longitudinal and transverse wake-functions are shown, respectively. The straight line in Figure 8.3 shows the linear approximation used in our tracking simulations.

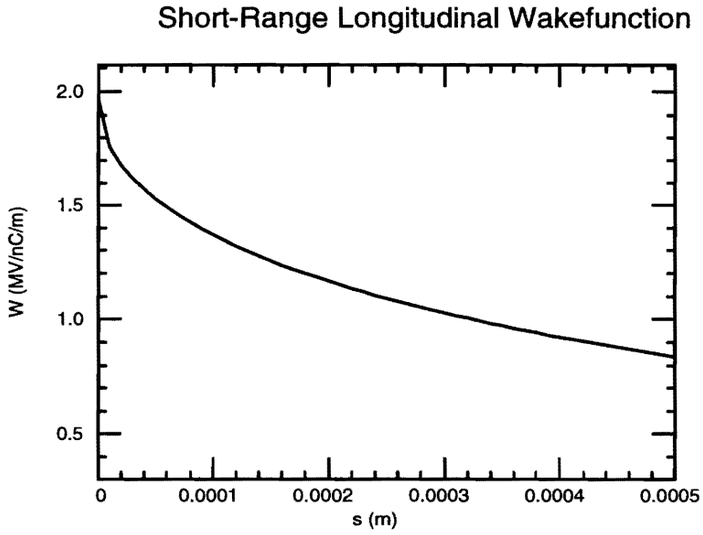

Figure 8.2: *Short-range longitudinal wake-function.*

8.3.2 Long-range Wake-field

The long-range longitudinal wake-field was not studied here. The bunch-by-bunch energy difference has not yet been studied in detail.

The long-range transverse wake-field of a detuned structure was calculated using the "Open mode expansion" [15]. The frequencies, kick factors and field distribution of the modes of the lowest 8 pass bands of the detuned structure were obtained by this method.

Figure 8.4 shows the wake-functions at the distance between bunches for 4 different types of structures. Figure 8.5 shows a summation of the wake-functions of the 4 types of structures. The designed cancellation of wake-functions of 4 types is shown here. Note that the actual cancellation is effective only within a length comparable to or shorter than the beta function. At the low-energy region, the beta function is small, and the cancellation is not as effective as suggested in these figures.

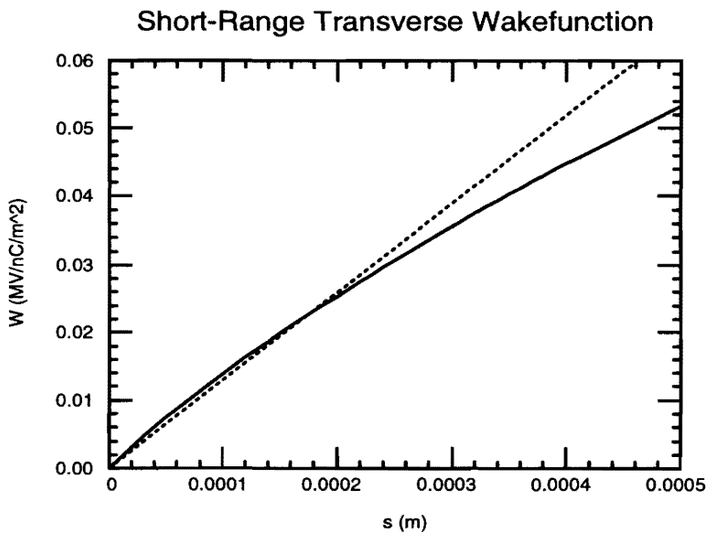

Figure 8.3: *Short-range transverse wake-function. The straight line shows the linear approximation used in our tracking simulations.*

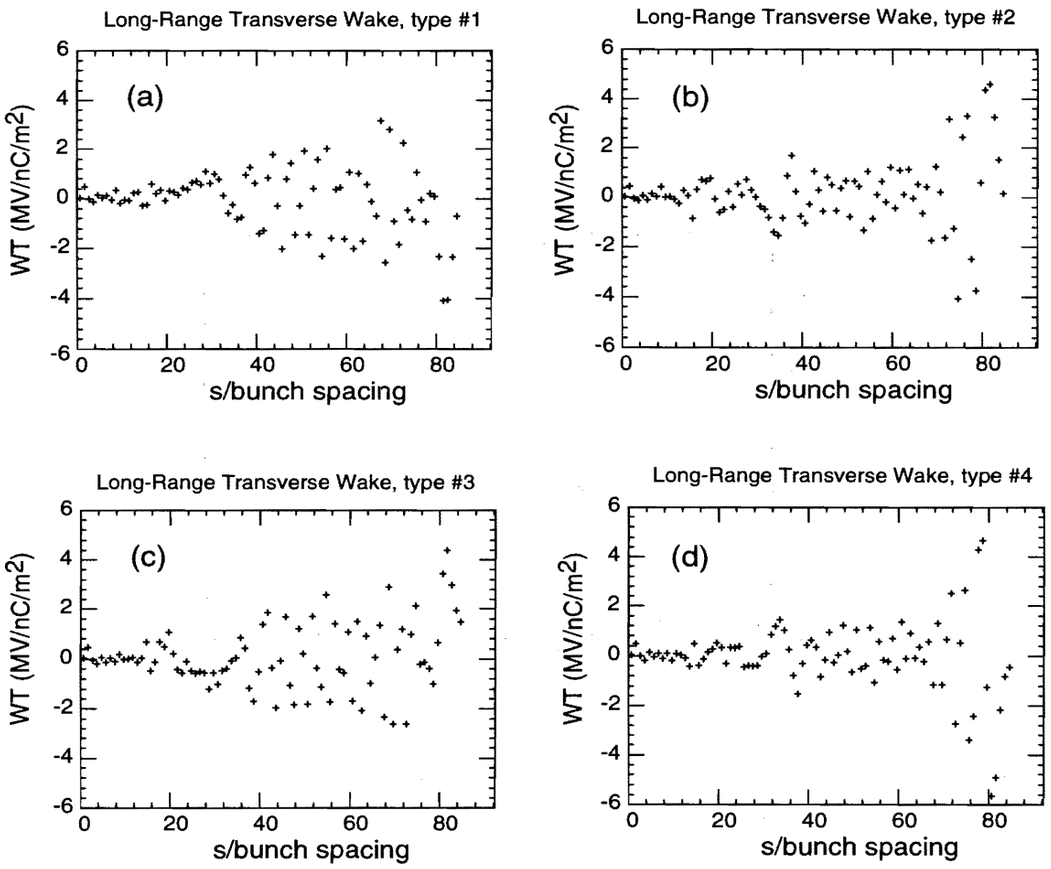

Figure 8.4: *Wake-functions at the distance between bunches for 4 different types of structures, respectively.*

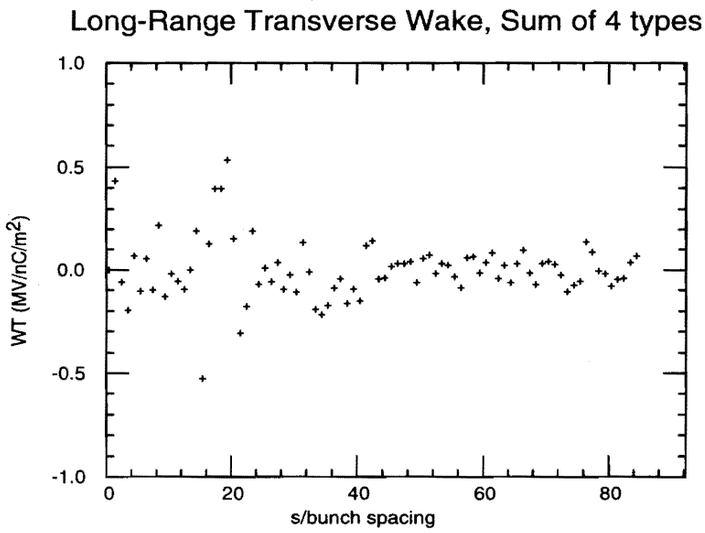

Figure 8.5: *Summation of the wake-functions at the distance between bunches of the 4 types of structures.*

8.4 Energy Distribution

The longitudinal position dependence of the energy of particles in the beam and the uncorrelated energy spread are described in this section. For simplicity, the longitudinal charge distribution is assumed to be semi-Gaussian, truncated by 3-σ, with $\sigma = 90$ μm.

The energy distributions of the beam depend on:

1. Initial distribution at injection,
2. Longitudinal wake-field,
3. Amplitude and phase of accelerating RF field.

The initial distribution is given by the design of the bunch compressor and the pre-linac. The tolerable energy spread was estimated by tracking simulations. Figure 8.6 shows the emittance increase vs. initial energy spread. To simplify the study, the distribution is assumed to be Gaussian and the

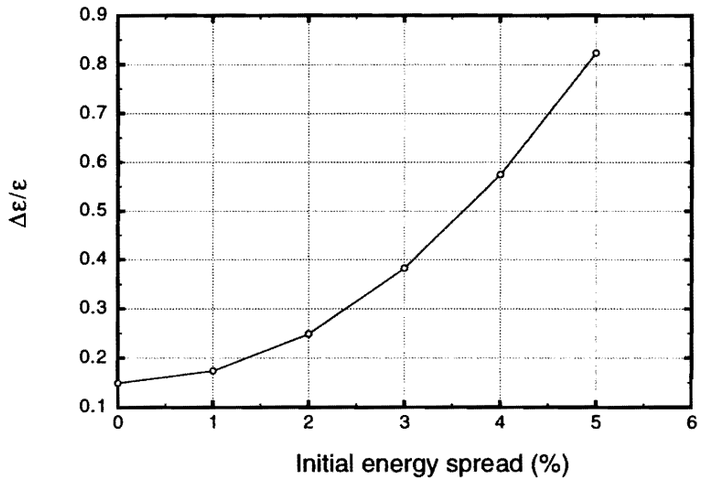

Figure 8.6: *Relative emittance increase vs. initial energy spread. A 2 micron misalignment of the quadrupole magnets, an orbit correction using BPMs 2 micron maligned with respect to quadrupole magnets, and a 5 micron misalignment of the accelerating structures with respect to the beam are assumed.*

particle energy to not depend on the positions in a beam. A 2 μm misalignment of the quadrupole magnets, an orbit correction using BPMs 2 μm maligned with respect to the quadrupole magnets, a 5 μm misalignment of the accelerating structures with respect to the beam are assumed.

In our design of the bunch compressor and pre-linacs, the initial energy spread at the beginning of the main linacs is estimated to be less than 2 %, including both single-bunch and multi-bunch effects. This spread (2 %) is acceptable, and is assumed in other simulations in this chapter.

The energy loss due to the longitudinal wake-field was calculated based on the short-range wake-function of the accelerating structures and the longitudinal charge distribution in a bunch. This energy loss strongly depends on the longitudinal position in a bunch.

In this beam-dynamics study, the long-range wake-field was not considered explicitly. All bunches are assumed to have exactly the same energy distribution. The bunch-to-bunch energy difference due to long-range wake-fields, or beam-loading, and the compensation of the difference are other important issues and should be studied more.

The only free parameter that we can change to control the energy distribution is the phase of the RF field. To make the average beam energy gain maximum, the bunch center is on the crest of the RF field, defined as the zero off-rest angle. However, because the short-range wake-field decelerates later particles, the position-correlated energy spread becomes too large. In order to compensate for this, bunches should put on a slope of the RF field, or off-crest. We chose an averaged RF phase with respect to the bunch center of 17 degrees, making the final energy spread minimum, 0.2 % (r.m.s.).

On the other hand, also known as "BNS damping" [14], it is better that the tail part of a bunch should have a slightly lower energy than the head part in order to damp coherent transverse oscillations. As a measure of the correlation, the "energy-z correlation" is defined as

$$\frac{1}{E\sigma_z q}\int E(z)z\rho(z)dz, \tag{8.12}$$

where E is the averaged energy of the bunch, σ_z the bunch length, q the bunch charge, $E(z)$ the averaged energy at the longitudinal position z and $\rho(z)$ the charge density at z. It is noted that the r.m.s. energy spread is always larger than this value. The optimum energy-z correlation is roughly estimated to be

$$eq\beta^2 W(2\sigma_z)/4E, \tag{8.13}$$

which is 0.02 in our case and approximately constant along the linac, because the beta function is proportional to the square root of the energy. It is not acceptable to set the RF phase to match this condition all along the linac, because it makes the final energy spread too large. It may be beyond the acceptance of the final focus system.

It was found that it is better to set different RF phases at different beam energies. The energy-z correlation could be made large, based on Equation 8.13, at the low-energy part where the effect of the wake-field is strong; then it could be gradually reduced in the high-energy part to make the final energy spread small. It should also be considered that to a much change of the RF phase causes a loss in the energy gain from the same RF peak voltages.

However, for simplicity's sake, we only studied cases in which the linac is divided into two parts having different RF phases. Keeping the final energy spread as small as 0.2 %, there are two parameters. One is the beam energy at which the RF phase changes. The other is the relative acceleration loss compared

with the case of a constant RF phase while keeping the final energy spread minimum (17 degrees off crest in our case). Maintaining a large energy-z in a large part of the linac leads to a larger amount of acceleration loss. In the case that the energy at which the RF phase change takes place is low, energy-z correlation becomes large only at the beginning part of the linac. In the case that the energy at which the RF phase changes is high, an energy-z correlation becomes large at most part of the linac, though the amount is small for the same acceleration loss.

The emittance increase with an injection error and with a misalignment is estimated by tracking simulations of a single-bunch beam. Figures 8.7 and 8.8 show the emittance increase vs. the relative loss of energy gain for different energies at which the RF phase changes. In Figure 8.7 the injection

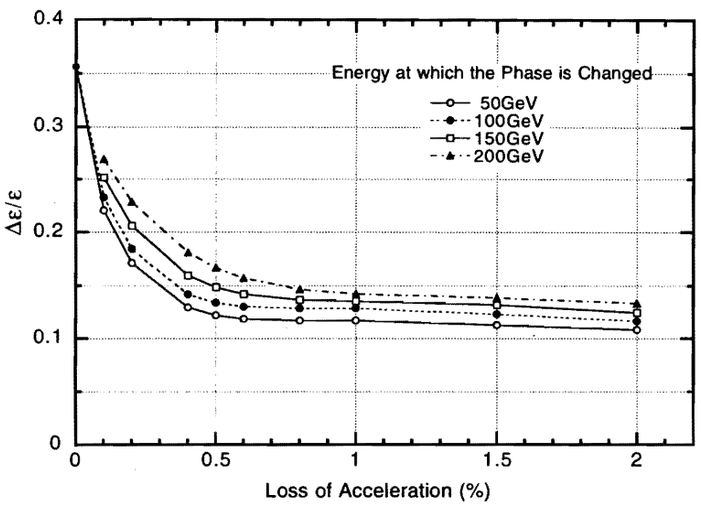

Figure 8.7: *Emittance increase vs. relative loss of energy gain due to phase change, for different energies at which RF phase changes. Injection offset of a half of the beam size was assumed.*

offset of half of the beam size was assumed, and no other errors were included. In Figure 8.8, a 2 μm misalignment of the quadrupole magnets is introduced, and an orbit correction was applied by using signals BPMs which are randomly misaligned by r.m.s. 2 μm with respect to quadrupole magnets. A 5 μm (r.m.s.) misalignment of accelerating structures with respect to the beam are assumed also in Figure 8.8. In both cases, the initial energy spread was assumed to be 2 %.

Figure 8.7 shows that effect of an injection error rapidly decreases, as the loss of acceleration increases up to about 0.5 %, beyond which it becomes almost constant. This reduction is due to the effect of "BNS damping". On the other hand, Figure 8.8 shows that effect due to an alignment error slowly increases, as the loss of acceleration increases. This is due to a dispersive effect, because "BNS damping" does not help reduce the dispersive effect caused by a misalignment.

Also, the effect of injection error and the effect of a misalignment have an opposite dependence on the energy at which the RF phase changes.

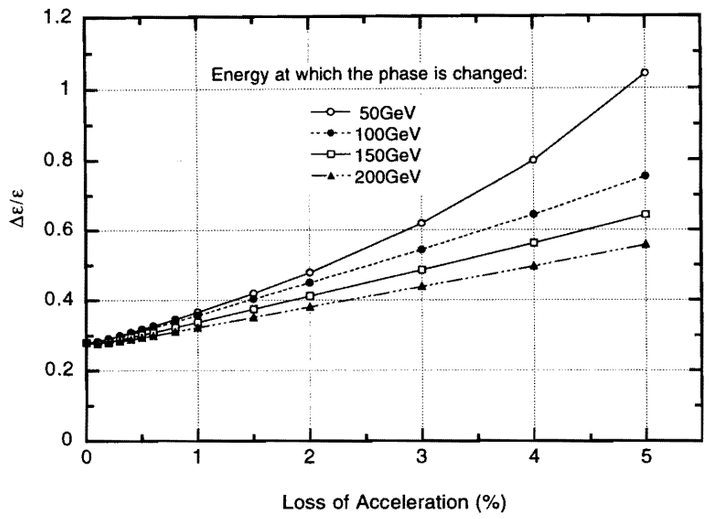

Figure 8.8: *Emittance increase vs. relative loss of energy gain due to a phase change for different energies at which the RF phase changes. A 2 micron misalignment of the quadrupole magnets, an orbit correction using BPMs misaligned by 2 microns (r.m.s.) with respect to the quadrupole magnets, a 5 micron misalignment of the accelerating structures with respect to the beam are assumed.*

From these results, an acceleration loss of 0.5 % and an energy 150 GeV were chosen as the point at which to change the RF phase. For this case, the energy spread (r.m.s.) and energy-z correlation vs. beam energy are shown in Figure 8.9.

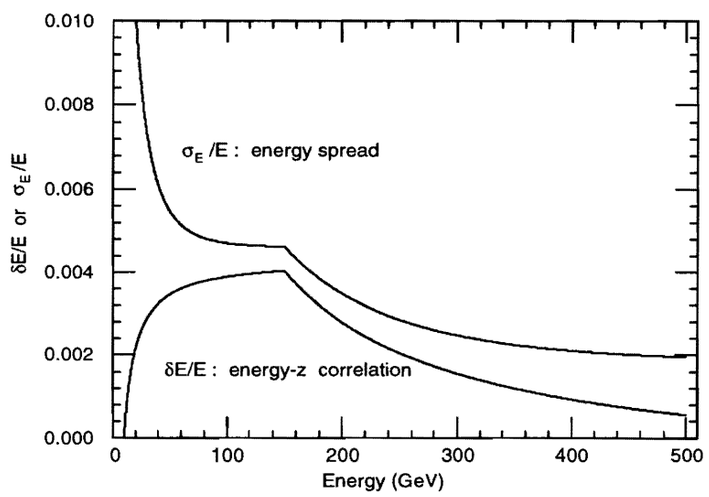

Figure 8.9: *Energy spread (r.m.s.) and energy-z correlation vs. beam energy.*

It should be noted that the present choice of phases is not necessarily optimum, because we studied only those cases involving two different phases. The RF phase may change many times along the linac during actual operation.

8.5 Vibration and Jitter of Quadrupole Magnets

Vibration of the quadrupole magnets cause a fluctuation in the beam trajectories and transverse position jitters at the interaction point, which cause a luminosity reduction. Also, strength jitters of the quadrupole magnets have a similar effect, because the beam will have some offset with respect to each field center of the magnet.

Figure 8.10 shows the emittance increase vs. misalignment of the quadrupole magnets without any orbit corrections. The lower line shows the usual emittance, and the upper line shows the "effective emittance" with respect to the center line. These are averages from 100 seeds of random numbers. The upper line gives the tolerance of vibration of the quadrupole magnets, or their motion faster than the orbit-correction feed back. The amplitude of vibration, σ_y, should be less than 8 nm for a 25 % "effective emittance" increase if the motion is totally random. Figure 8.11 shows an example of an emittance increase along the linac in the case that the rms random misalignment of the quadrupole magnets is 10 nm. A typical value of an additional kick due to the offset of a quadrupole magnet is

$$\sigma\theta_{\mathrm{vibration}} = \sigma_y k, \tag{8.14}$$

where σ_y is the offset of the magnet and k the k-value of the magnet.

It should be noted that the tolerance of the correlated motions over a longer range than the beta function will be looser. Additional effort is necessary to estimate the tolerances for realistic ground motions.

The tolerance for jitters of the strength of the quadrupole magnets is related to the typical trajectory error, or offset of the beam with respect to the center of the quadrupole magnets, Δy.

A typical value of an additional kick due to an error in the field strength of a quadrupole magnet is

$$\sigma\theta_{\mathrm{strength}} = \Delta y \sigma_k, \tag{8.15}$$

where σ_k is the error of the k-value of the magnet.

By comparing this equation with Equation 8.14, the tolerance of strength jitters is related to the tolerance of vibration as

$$\mathrm{Tolerance}(\sigma_k/k) = \mathrm{Tolerance}(\sigma_y/\Delta y). \tag{8.16}$$

Δy is equal to the typical misalignment of the BPMs with respect to the center of the quadrupole magnets, because orbit corrections will be applied by using these BPMs. We assume that it is 2 μm,

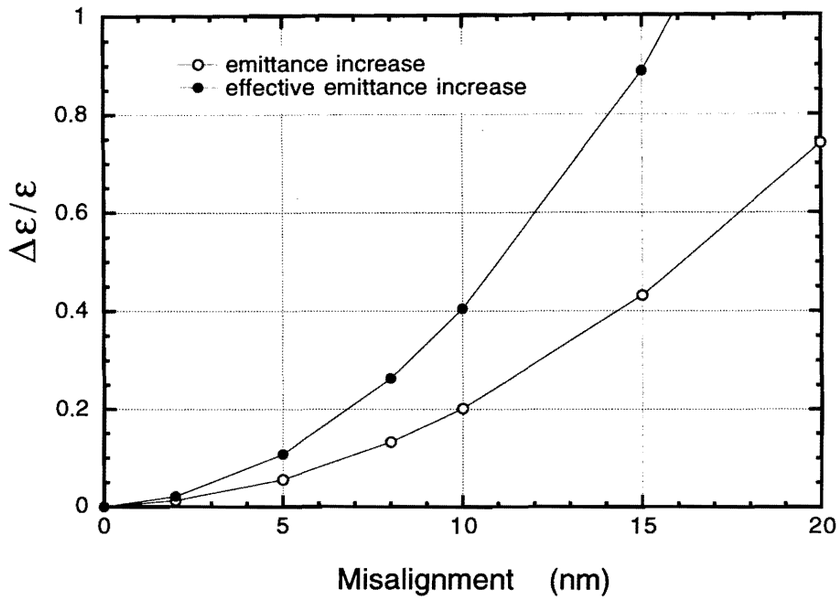

Figure 8.10: *Emittance increase vs. misalignment of the quadrupole magnets without any orbit corrections. The lower line shows the usual emittance and the upper line shows the "effective emittance" with respect to the center line. These are averages from 100 seeds of random numbers.*

and that the tolerance of the relative jitters of the k-value of each magnet is estimated to be 0.005 (this is 10 nm / 2 μm).

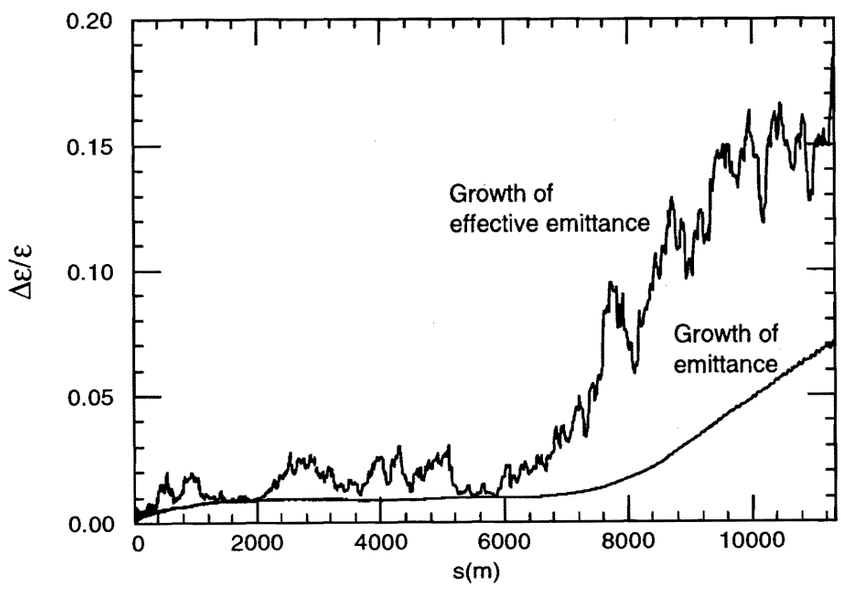

Figure 8.11: *Example of emittance increase along the linac in the case that the r.m.s. of the random misalignment of quadrupole magnets is 10 nm. No orbit corrections are applied.*

8.6 Alignment of the Quadrupole Magnets

Figure 8.12 shows the emittance increase vs. misalignment of the quadrupole magnets. A 2 % initial energy spread, a 2 μm misalignment of the BPMs with respect to the quadrupole magnets, and a 5 μm misalignment of the accelerating structures with respect to the beam are assumed. Orbit corrections using steering magnets are assumed with a BPM resolution of 1 μm, and it is also assumed that there are no other jitters source. This is an average from 100 seeds of random numbers. Figure 8.13 shows an example of the emittance increase along the linac in the case that the misalignment is 2 μm.

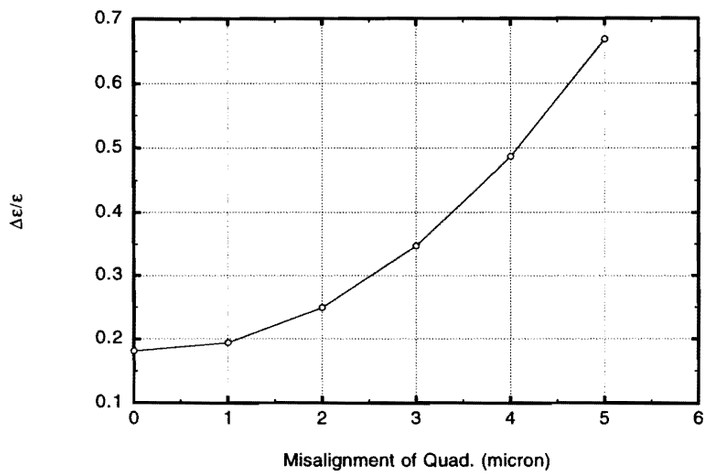

Figure 8.12: *Emittance increase vs. misalignment of the quadrupole magnets. A 2 % initial energy spread, a 2 micron misalignment of the BPMs with respect to the quadrupole magnets, and a 5 micron misalignment of the accelerating structures with respect to the beam are assumed. An orbit correction using steering magnets is assumed with a BPM resolution of 1 micron. This is an average from 100 seeds of random numbers.*

It is not expected that the initial alignment accuracy will be as small as a few microns. A beam-based alignment (see later section) will be needed to preserve the small emittance. From this result of the tracking simulation, the acceptable random motion of the magnets from the last beam-based alignment is roughly estimated to be about 2 μm.

In order to study techniques for a beam-based alignment of the quadrupole magnets, tracking simulations were performed. The initial distribution of the misalignment is assumed to be Gaussian. In the correction, the beam positions are measured at the BPM attached to every quadrupole magnet. The quadrupole magnets are moved in a transverse direction to make the beam go though the center of the BPMs. To decide how much of a move is necessary, a transfer matrix from all of the quadrupole magnets to the all the BPMs used. It is taken into account that each BPM is attached to a quadrupole

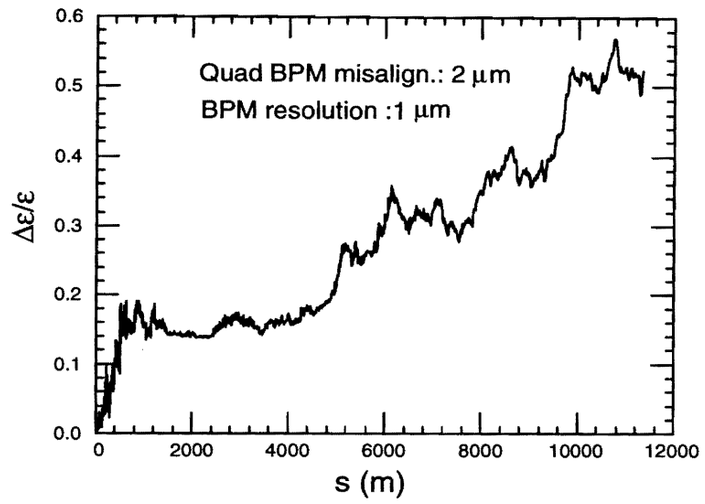

Figure 8.13: *Example of the emittance increase along the linac in the case that the misalignment of the quadrupole magnet is 2 microns. A 2 percent initial energy spread, a 2 micron misalignment of the BPMs with respect to the quadrupole magnets, and a 5 micron misalignment of the accelerating structures with respect to the beam are assumed. An orbit correction using steering magnets are assumed with BPM resolution of 1 micron.*

magnet and moves together with the magnet.

Figure 8.14 shows the emittance increase vs. the BPM misalignment with respect to the quadrupole magnet (or BPM- Quad ambiguity, how accurately we know the center of magnet). The four lines are for different initial misalignments of the magnets. The BPM resolution (measurement-to-measurement fluctuation) was assumed to be 1 μm. These are averages from 100 seeds of random numbers. The emittance increase strongly depends on the BPM-Quad ambiguity, or the accuracy of information concerning the magnetic field center.

It is also shown that the initial alignment accuracy is not very important. Figures 8.15 and 8.16 show an example of the offset of the quadrupole magnets before and after a beam-based alignment, respectively, in the case of an initial misalignment of 50 μm. These figures show the data only for the first 3.4 km of the main linacs. The behaviors in the rest of the linacs are very similar.

Figures 8.17 and 8.18 show an example for the case in which the initial misalignment is 100 μm. The same random seed was used for both simulation and a 2 μm BPM- Quad ambiguity in both cases. It is noted that the final offsets are scaled with the initial offset. However, in both cases the offsets change slowly along the linac. This slow change dose not affect the emittance very strongly. The figures show the data only for the first 3.4 km of the main linacs. The behaviors in the rest of the linacs are very similar.

The field center of the quadrupole magnets will also be determined using beams. The technique

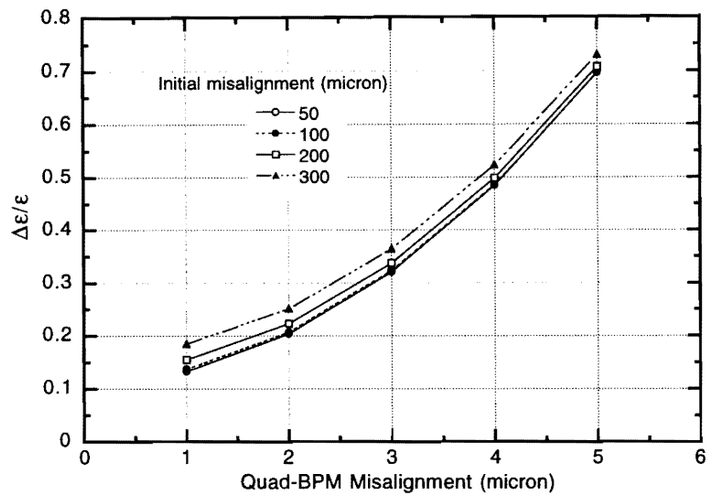

Figure 8.14: *Emittance increase vs. BPM misalignment with respect to the quadrupole magnet (or BPM- Quad ambiguity, how accurately we know the center of magnet) for different initial misalignments of the magnets. The BPM resolution (measurement-to-measurement fluctuation) was assumed to be 1 micron. These are averages from 100 seeds of random numbers.*

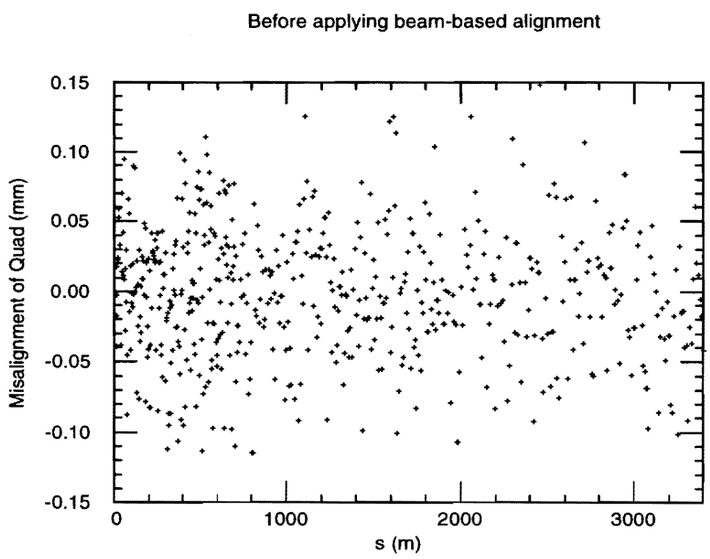

Figure 8.15: *Example of the offset of the quadrupole magnets before the beam-based alignment, in the case of an initial misalignment of 50 microns.*

involves a measurement of the changes of the orbit by downstream BPMs while the strength of an upstream quadrupole magnet is intentionally changed. It is expected that BPM-Quad ambiguities of

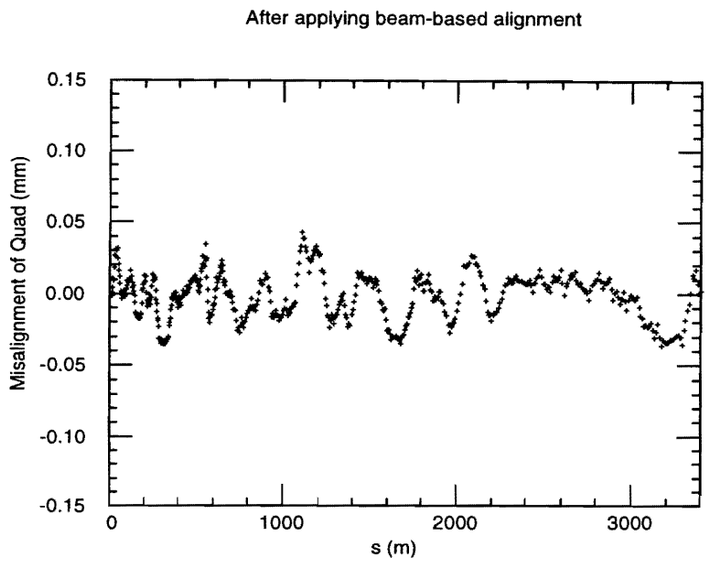

Figure 8.16: *Example of the offset of the quadrupole magnets after a beam-based alignment, in the case of an initial misalignment of 50 microns.*

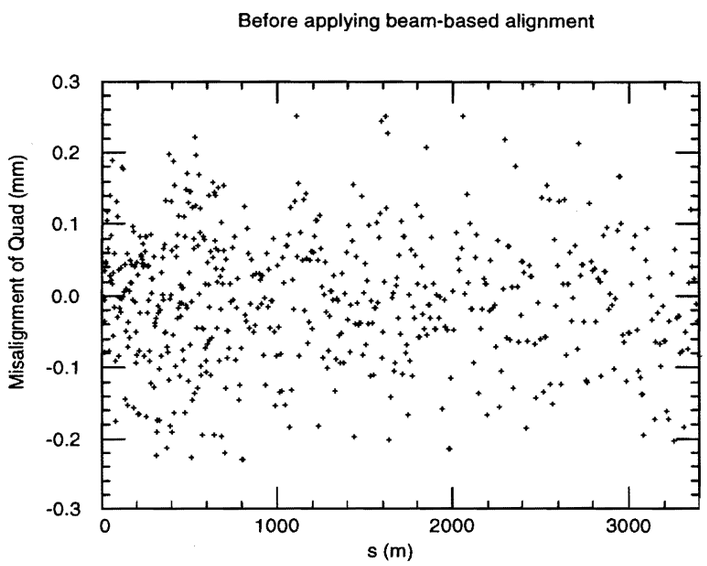

Figure 8.17: *Example of offset of quadrupole magnets before the beam-based alignment, in the case of an initial misalignment of 100 microns.*

the order of a few times the BPM resolution can be resolved. The BPM resolution is assumed to be

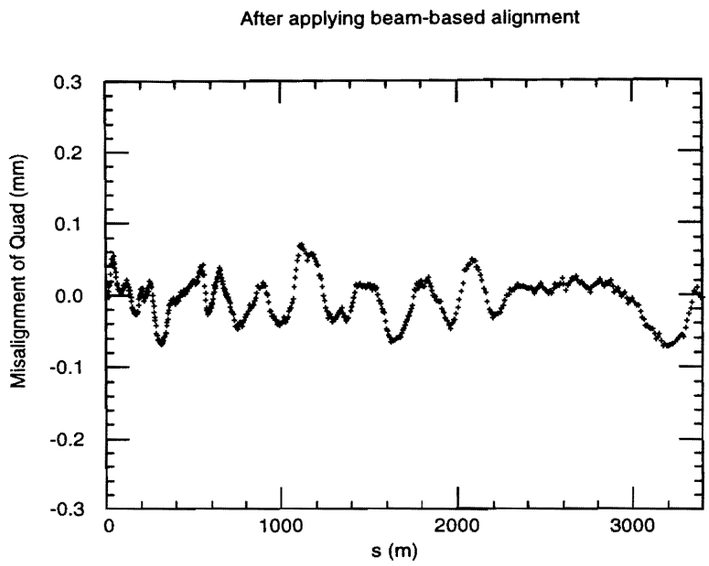

Figure 8.18: *Example of the offset of the quadrupole magnets after the beam-based alignment, in the case of an initial misalignment of 100 microns.*

1 μm and BPM-Quad ambiguity is assumed to be 2 μm in our design study.

8.7 Errors of the Accelerating Structures

To estimate the tolerance of the misalignment of the accelerating structures, tracking simulations were performed[3].

To simulate single-bunch effects, each bunch is divided into five slices and each slice has five macro-particles with different initial energies. For multi-bunch simulations without single-bunch effects, each bunch is treated as being rigid.

The accelerating structures are randomly misaligned and the average of the emittance growth of 100 seeds of random numbers is used to estimate the alignment tolerance. The tolerance depends on the length of an "alignment unit," which is aligned independently. Each alignment unit is assumed to consist of either (a) M structures or (b) $1/M$ structure ($M = 1, 2, 3, ...$). A long-scale misalignment is simulated in Case (a). The alignment of girders can also be simulated in this case where M structures are on an alignment girder and each girder is aligned independently and randomly while the structures are perfectly aligned on each girder. The fabrication errors of each structure are simulated in Case (b). Each structure is divided into M pieces and each piece is "aligned" independently. The situation corresponds to, for example, each structure consisting of M pieces brazed together with random errors, with each piece being fabricated error-free. Each slice of the beam is kicked by wake-fields at the center of each structure in Case (a) and at the center of each piece of the structures in Case (b).

The transverse short-range wake-function was assumed to be a linear function. Though the shape of the cells changes along a structure, only averages over a structure were used for both the longitudinal and transverse short range wake-functions.

The frequencies, kick factors and field distribution of the modes of the lowest 8 pass bands of the "detuned structure" were used to obtain the long-range transverse wake-field[15]. Because there will be four different types of structures and each structure has 150 cells, a total of 4800 modes are used to calculate the inter-bunch effect. In the case of simulations for fabrication errors (a structure is divided into pieces), the field distribution of each mode is assumed to be unchanged by the fabrication error. The wake-function is calculated for each cell of a structure. The amplitude and phase of a certain mode exited by a charged particle at a certain cell is proportional to the offset of the particle with respect to the cell center, and the coefficient is calculated from the field distribution of the mode in the structure. The wake-function of the cell is the summation of the coefficients of all modes. The wake-function is the summation of the contributions from all cells. This wake-field calculation method is a good approximation when the length of each structure is smaller than the beta function, which is the case of our main linacs.

One-to-one trajectory steering is assumed to be always performed so that the beam centroid goes through the center of every focusing quadrupole magnet. Because all quadrupole magnets are perfectly aligned in this simulation, the alignment tolerances obtained here should be regarded as being alignment tolerances with respect to the beam or required accuracy of a beam-based alignment of the

accelerating structures.

Figure 8.19 shows the alignment tolerances for an averaged emittance growth of less than 25 % as a function of the alignment unit length. The lowest line shows tolerances considering both multi-bunch and single-bunch effects. The tolerances for a single-bunch and a multi-bunch without a single-bunch effect are also shown here.

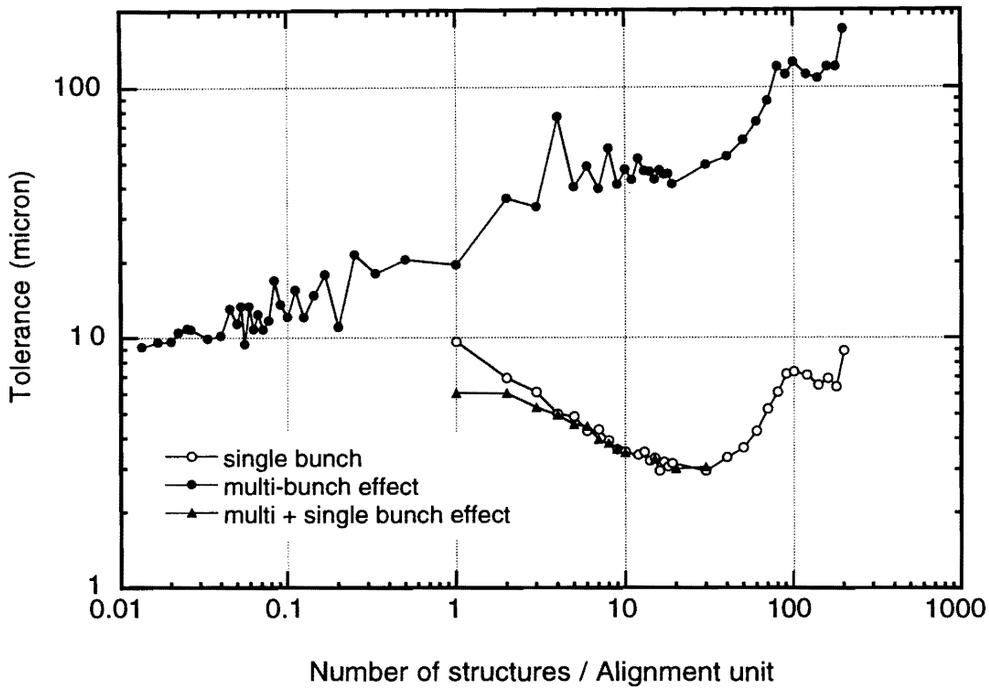

Figure 8.19: *Alignment tolerances for an averaged emittance growth of less than 25 % as a function of the alignment unit length. The calculation is for a 500 GeV linac. The lowest line shows tolerances considering both multi-bunch and single-bunch effects. The tolerances for a single-bunch, and a multi-bunch without single-bunch effects are also shown. It is seen that if individual accelerating structure (i.e. 1.3 m-long detuned structure) can be individually aligned with respect to the beam, its alignment tolerance is 6 μm for a 25 % emittance growth.*

The curves have a minimum at an alignment length of about 20 structures, or 30 m, which is about the betatron wavelength at the beginning of the linac; it increases with the alignment length until 80 structures, or 160 m which is the betatron wavelength at the end of the linac. This is expected, because, if the beam offset from the structure center is constant, the effects of the wake-field will be canceled out along a betatron cycle. The single-bunch curve decreases for a short alignment length according to the -1/2 power up to a length of about 16 structures. This is because the effect of a kick by the wake-field depends only on the average offset of the beam with respect to the structure center over a length comparable to the beta function. However, the multi-bunch curve drops for an

alignment length less than four structures. This is because, with a misalignment between four different types of structures, the designed cancellation of the dipole modes of the four structures is disturbed. Also, with a misalignment (fabrication error) of pieces in a structure, the designed cancellation of the dipole modes of each structure is disturbed. Combining both the single- and multi-bunch effects, the single-bunch effect is dominant for a longer alignment length, and the multi-bunch effect is important only for pieces in each structure.

The fabrication error, or misalignment of pieces in each structure, was also studied using a numerical method[1]. The curve in Figure 8.20 shows the tolerances as functions of the alignment length, and number of cells per piece. In this figure, the results of tracking simulations are also plotted as makers. The results of the numerical method agree well in the region of short pieces.

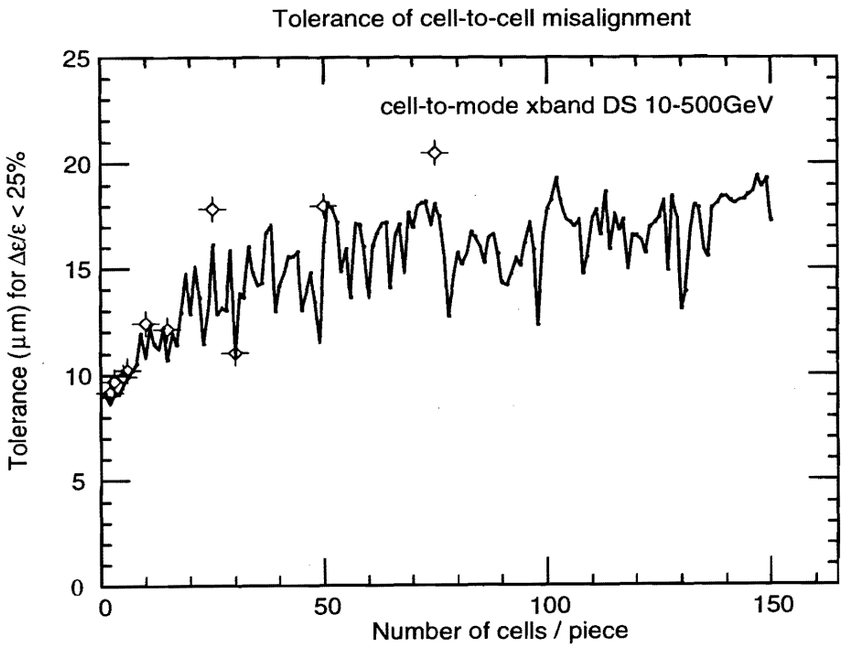

Figure 8.20: *Tolerance of the fabrication of detuned structures for 25 % emittance growth as a function of the alignment length and number of cells, considering only multi-bunch effects from the numerical method. The curve is from the numerical method and the marks are from tracking simulations.*

As a conclusion, we estimated the tolerances as follows:

- The minimum alignment tolerance is 3 μm for an alignment unit length of about 30 m.
- The tolerance for each structure is 6 μm.
- The minimum tolerance for short pieces (fabrication) is about 9 μm in the case of short pieces

per structure.

In the above estimations, even with fabrication errors, the wake-functions of the transverse modes are assumed to be unchanged. Only the transverse offset of the structure was changed. The error of each mode caused by machining errors and a deformation after machining will also disturb the designed cancellation of the dipole modes of our detuned structures. The tolerance of the mode-frequency error was studied by tracking simulations. Figure 8.21 shows the emittance increase vs. relative r.m.s. error of the mode frequencies. It was assumed that each mode has a random and independent errors. For the upper curve, the structures of the same type are assumed to have the same errors, simulating systematic errors. The lower curve shows the case of random errors. To simulate random errors, the wake-function of each structure is assumed to have one of 100 different sets of mode-frequency errors. The sets are created randomly and the selection of sets is also random. In the simulation, each accelerating structure is randomly misaligned with an r.m.s. of 5 μm, and all quadrupole magnets are perfectly aligned.

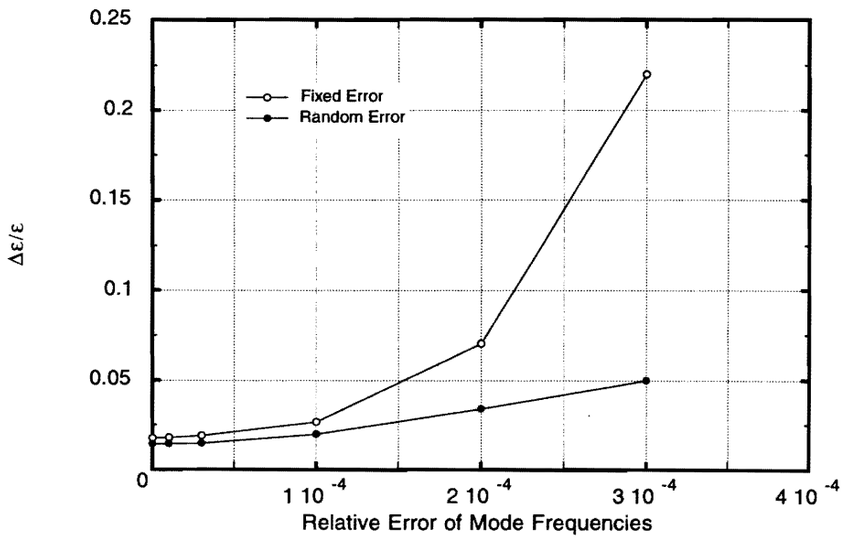

Figure 8.21: *Emittance increase vs. relative r.m.s. error of the mode frequencies. Each mode has random and independent errors. The upper curve is for structures of the same type, and are assumed to have the same errors. The lower curve is for random errors.*

The tolerance for mode frequencies is roughly estimated to be 10^{-4} from the result. It should be noted that it will be necessary to study how realistic errors of machining and deformations cause frequency errors, and to input the information to the simulations.

8.8 Corrections and Feedbacks

An orbit correction using the BPMs and steering magnets was assumed in most of the simulations discussed in this chapter. This correction steers the beam thorough each BPM center. The BPM resolution is assumed to be 1 μm. Because this correction is simple and fast, it will be used as a fast feed back.

When the simple orbit feed-back becomes insufficient, due to a too large change in the conditions, more sophisticated corrections need to be performed. Several techniques have been proposed in which the strength of the quadrupole magnets are changed and the beam positions are measured using BPMs[5] [8] [9] [10].

It should not be very difficult to achieve the required alignment by precise movers and measurements of the beam position relative to the structure axes using cavity-type BPMs. To improve the accuracy of alignment measurements, some additional techniques are available. For example, it has been suggested [11],[4] to detect the dependence of trajectories on the bunch and current and/or bunch length. However, this method may have some difficulties. A more practical approach may be to use a combination of the following two techniques :

1. Trajectory bumps or moving structures, tuned by emittance measurements with a single-bunch beam and
2. fast kickers for a multi-bunch[5], tuned by bunch-by-bunch position measurements with a multi-bunch beam. The emittance and bunch-by-bunch positions will be measured at several locations in the linac.

In technique 1, the beam offset with respect to the beam is intentionally produced at some short parts of the linac in order to compensate for the effects of the wake-field due to a misalignment of the other part. In method 2, the beam is kicked bunch-by-bunch, so that all bunches have the same trajectory. Tracking simulations of these techniques were reported in [6] and [7].

When the ground motion becomes too large, a re-alignment of magnets and/or accelerating structures will be necessary.

References for Chapter 8

[1] Methods to estimate emittance dilutions due to misalignment of accelerating structures without tracking, NLC-Note 13 (1995)

[2] K.Kubo et. al., "Alignment tolerance of accelerating structures and corrections for future linear colliders, PAC95, SLAC-PUB-95-6884

[3] K. Kubo et. al., "A simulation program for Phase Space Dynamics in Future Linear Colliders," NLCNote 14 (1995)

[4] K. Kubo and T. Raubenheimer, "A Beam-Based Alignment Technique for Correction of Accelerator Structure Misalignments", LINAC94, SLAC-PUB-6608 (1994)

[5] T. Raubenheimer and R. Ruth, Nucl. Instr. and Meth. A302 (1991) 191.

[6] T. Raubenheimer and K. Kubo, "Proc. of 5th International Workshop on Next Generation Linear Colliders", SLAC-Report-436, p275 (1993)

[7] T. Raubenheimer and K. Kubo, "LC95", KEK Proceedings 95-5, p1280 (1995)

[8] C. Adolphsen, et al., "Beam-based alignment technique for the SLC linac", Proc. 1989 IEEE Particle Accelerator Conf.

[9] G. Guidnard, "Treatment of nonlinearities in achromatic trajectory correction for future linacs, Proc. 1992 EPAC.

[10] V. Balakin, Proc. LC91. Int. Workshop on Linear Colliders, (1991) p302.

[11] T. Raubenheimer and K. Kubo "A technique of measuring and correcting emittance dilutions due to accelerator structure misalignment", Nuclear Instruments and Methods, A370 (1996) 303-311

[12] K.L.F. Bane et. al., "Issues in Multi Bunch Emittance Preservation in the NLC", EPAC'94, SLAC-PUB-6581 (1994)

[13] C. Adolphsen, Proc. of Fifth International Workshop on Next-Generation Linear Colliders, SLAC-436 (1993) p265

[14] V. Balakin, A. Novokhatsky and V. Smirnov, "VLEPP: Transverse Beam Dynamics",Proc. of 12th Int. Conf. on High Energy Accelerators, Fermilab, 119 (1983)

[15] M. Yamamoto, "Study of Long-Range Wake-Field in Accelerating Structure of Linac", KEK Report 94-9

[16] K. Yokoya, Private Communication

Author of Chapter 8

- Kiyoshi Kubo

CHAPTER 9

X-band Main Linacs: Accelerating Structure

Contents

9.1 Structure Design Overview

9.1.1 Outline of the Structure Design

The accelerating structure should be operated stably at an accelerating gradient higher than 50 MV/m. To satisfy this requirement within a limited peak power, the shunt impedance of the accelerating mode should be reasonably large. For this purpose, a/λ is likely to be small while keeping the alignment tolerance not too tight against single-bunch transverse-emittance blow-up and making the length of the structure not too short. An a/λ value of 0.16 is proposed as a compromise[1].

In addition to the high field, the efficiency of the energy transfer from the RF to the beam within the structure should be sufficiently high so that the total wall-plug power is within a reasonable limit. For this purpose, the Q value of the structure should be as high as possible, and, thus, the shape of the simple disk-loaded structure was adopted. It can be further optimized by modifying the shape of the cell. This simple disk-loaded structure is also good for mass production.

In return for these good features in the accelerating mode, this simple structure suffers from a severe transverse multi-bunch emittance growth unless some suppression mechanism is introduced. The most severe dipole-mode passband, which is responsible for the main part of the long range wake-field, can be canceled among the modes of the passband by distributing the frequencies of those modes in a Gaussian manner. The structure using this method is called "a detuned structure" (DS[3]) in the present report.

The number of modes in a Gaussian distribution is finite. Therefore, the wake-field will re-cohere after a certain period. In the present design, the recurrence will take place within the period of the linac bunch train. Therefore, four types of structures have been designed to be interleaved in the lowest dipole-mode frequencies so that the recurrence will occur four times later than the period of the bunch train[4].

This cancellation mechanism needs a well-controlled distribution of frequencies of the higher modes. This means that the structure should have precise dimensions. To make this scheme function as intended, it is necessary to make the structure parts precisely, and to maintain the precision of such cells through the fabrication process.

The possibilities of citing other types of structures which introduce a medium, or even heavy, damping scheme are also to be studied before a final decision is made concerning the structure type. The structures, such as the DDS[2], which is being studied at SLAC, has the merit of being capable of measuring the beam position through the damping port as a function of the position in the structure, in addition to making the recurrence amplitude less. However, the cell shape is slightly complicated and may require more care in machining. A heavily-damped structure (HDS) or possibly a medium-damped structure, based on the choke-mode structure[5], has also recently been started.

In the present report, the main focus is on the design based on the DS, because this type of structure has been extensively studied in recent years, while the others have been studied only briefly up to now by our group. A discussion concerning which type of structure, or what kind of configuration among the available types is the best optimized, should be made in the near future, before going into a series of study activities on prototype fabrication and tests for the engineering design.

The alignment of the structure with respect to the beam is very critical for controlling the transverse emittance. For this purpose, the beam-position monitor should be tightly integrated in the structure body in the transverse position with a high precision. The active alignment of the structure on a μm order is probably inevitable. Therefore, the above-mentioned BPM signal is used for correcting the positions of the accelerating structures.

Typical parameters of the DS are summarized in Table 9.1.

9.1.2 Electrical Design

The basic parameters that characterize the detuned structure are shown in Figure 9.1. The cell period is determined from the choice of the $2\pi/3$ mode. The "a" and "t" are varied along the structure in order to distribute the higher modes, as designed. The "b" is adjusted to make the frequency of the $2\pi/3$ mode at the correct operation frequency.

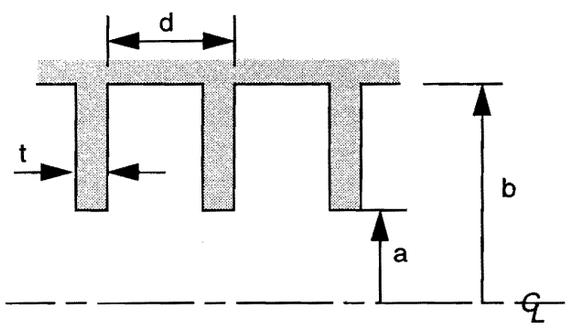

Figure 9.1: *Schematic cross-sectional view of an accelerating structure. The dot-dash line indicates the symmetry axis. The* **a** *denotes the half iris aperture,* **b** *the cell radius size,* **t** *the iris thickness and* **d** *the cell period.*

Frequency Distribution of the Dipole Modes

The wake-field due to the lowest passband is higher than the others by more than several times. Therefore, the frequencies of this band are designed to be distributed in a truncated Gaussian manner. However, it is not straightforward to make the frequencies of the modes as designed, due to the coupling between the cells. Practically, the frequencies of the periodic structure with the phase velocity being

Item	Symbol	Unit	Value
Frequency	f	GHz	11.424
Operation mode			$2\pi/3$
Number of cells			150
Length		m	1.31
Beam hole radius	a	mm	$5.23 \sim 3.67$
	a/λ		$0.20 \sim 0.14$
	$< a/\lambda > \#$		~ 0.166
Disk thickness	t	mm	$1.2 \sim 2.4$
Group velocity	v_g/c		$0.098 \sim 0.02$
Q value *	Q		$6800 \sim 6050$
Shunt impedance	r/Q	kΩ/m	$10.2 \sim 13.6$
Shunt impedance *	r	MΩ/m	$70 \sim 82$
Filling time *	T_f	nsec	106.4
Total attenuation *	τ		0.609
Peak power input	P_{IN}	MW	130
Pulse length		nsec	230
Unloaded gradient	E_{NL}	MV/m	73
Loaded gradient **	E_{LD}	MV/m	58
Repetition rate	f_{rep}	Hz	150
Average power loss		kW/m	2.6
Dipole mode	Q_{ex}		∞
Gaussian Sigma of 1st mode	$\sigma f_{d1}/f_{d1}$	%	2.24
Total distribution of 1st mode	Δf_d	%	11.2
Tolerance* of 1st mode	$\delta f_d/f_d$		$< 10^{-4}$
Cell misalignment tolerance		μm	9
Four-cavity misalignment tolerance		μm	4
Cavity misalignment tolerance †		μm	3

Weighted in $a^{-3.5}$. * Assuming 95% of theoretical Q value.

* Assuming the beam on the crest of RF phase.

† Most severe is the tolerance for the betatron wave length of 30m at the beginning of the linac.

Table 9.1: *Representative parameters of the JLC Detuned Structure. *For tolerance concerning the 6'th mode, see Chapter 7.*

the same as that of the beam are to be distributed as designed. This procedure ensures at least the initial damping of the wake-field. The method to distribute the frequencies physically is to vary the beam hole radius ("a") along the structure.

On the other hand, the wake-field due to the 6'th passband is lower by an order of magnitude than the lowest, but stays longer, due to the tiny spread of the frequencies, even in the presence of a variation of the beam-hole radius[6]. Since this mode has a node in the z-component of the electric field, the thickness of the disk is varied so as to distribute the mode frequencies.

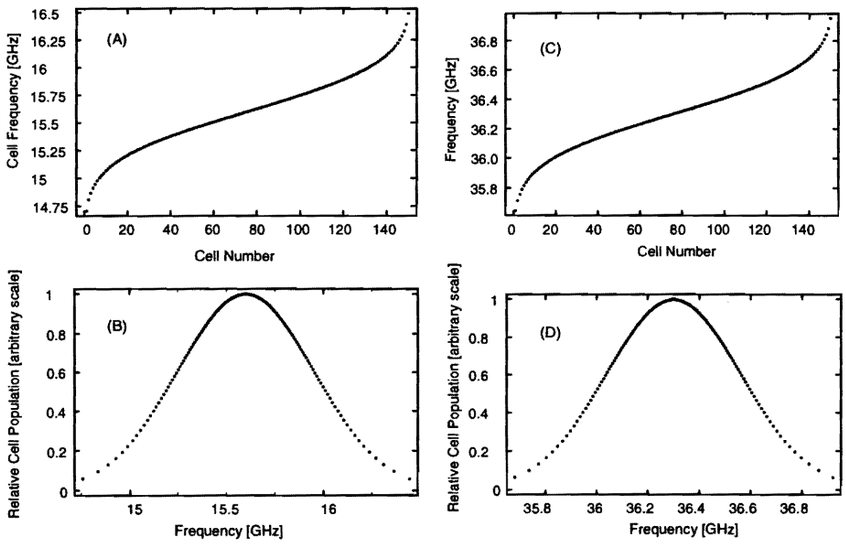

Figure 9.2: *(A),(C): Distribution of frequencies f_1 and f_6, the frequencies of the lowest and 6'th dipole modes of each cell synchronous to the beam as a function of the cell number. (B),(D): Population of the frequency distributions of f_1 and f_6.*

In practice, the population of the modes in the two pass-bands is designed to be distributed as a truncated Gaussian, as shown in Figure 9.2. The parameters, center frequencies, sigmas and full widths are listed in Table 9.2.

		First passband		6'th passband
Center	f_1	15.6 GHz	f_6	36.3 GHz
Sigma	σ_{f_1}	0.35 GHz	σ_{f_6}	0.26 GHz
(Relative	σ_{f_1}/f_1	2.24 %)	(σ_{f_6}/f_6	0.716 %)
Full width	Δ_{f_1}	1.75 GHz	Δ_{f_6}	0.30 GHz
(Relative	Δ_{f_1}/f_1	11.2 %)	(Δ_{f_6}/f_6	3.58 %)

Table 9.2: *Parameters that characterize the uncoupled frequency distributions of the detuned structure.*

Obtaining Beam Hole Radius a and Disk Thickness t

In order to obtain the cell dimensions, the functional forms of the frequencies of the first and the 6'th passband as functions of a and t are obtained. Here, the frequency of the accelerating mode is kept by adjusting the cell inner radius b. The functional forms were presently deduced from a calculation using "TRANSVERSE-II" [7]. This code was made following "TRANSVRS" by B. Zotter and K. Bane [8]. It is assumed that the beam hole is flat, which means that the beam hole is cut in a disk as a simple cylinder. Therefore, there is a small change compared to the actual beam hole with a round shape.

Seven equi-frequency lines are plotted in Figure 9.3 in the (a,t) parameter space. These lines pass through cell numbers 1, 25, 50, 75, 100, 125 and 150. As the cell number increases, the lines for f_1 shift from larger a to smaller a, where frequency f_1 increases, while those of f_6 shift from smaller t toward larger t, where frequency f_6 also increases. Parameters (a,t) at the crossing points are used as the design values. Since the increasing order naturally follows the characteristics of the constant-gradient structure, but not in the reverse order, it is not practical to choose the decreasing order in frequency f_1. The increasing order of f_6 is necessary to make the crossing points within a reasonable range, as shown in the figure.

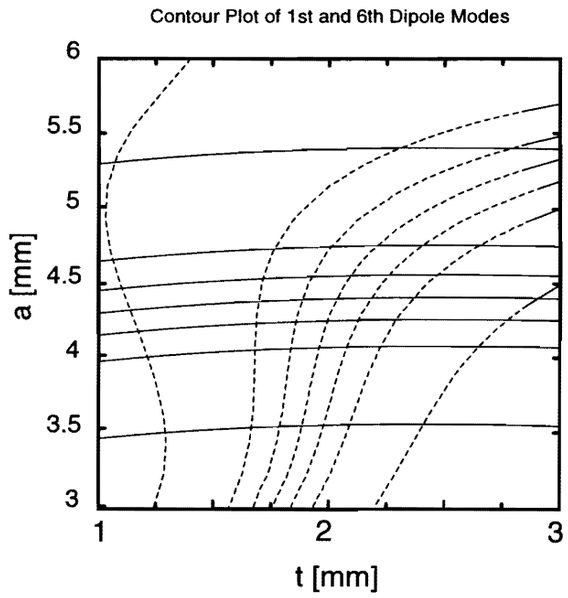

Figure 9.3: *Equi-frequency lines of the two modes, f_1 and f_6, in the (a,t) plane. The solid lines, f_1, are those of the modes in the lowest passband, while dashed lines, f_6 are those of the 6'th passband. The f_1 is low at large a, while f_6 is low at large a and small t.*

From the previous procedures, parameters (a,t) were determined as a function of the cell number (n),

where n is integer. In order to ensure the smoothness of the cell dimensions as a function of the cell number, functions $a(n)$ and $t(n)$ are fitted in n to obtain the actually required parameters for the disk, where n is half integer. The obtained parameters (a, t) as function of the cell number (n) are shown in Figure 9.4.

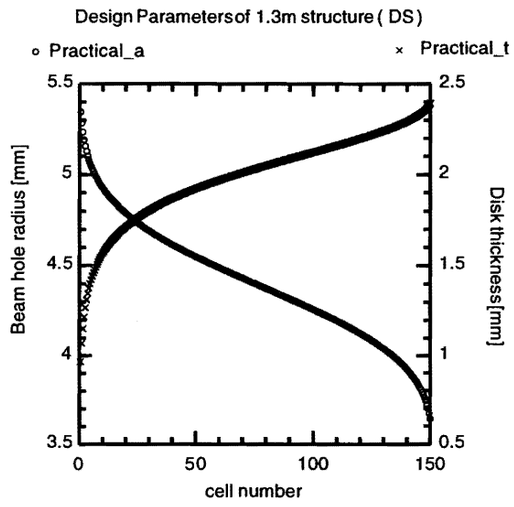

Figure 9.4: *Design parameters of the 150-cell detuned structure as a function of the cell number. The value* **a** *is the beam-hole radius and* **t** *is the disk thickness.*

Wake-field of the Transverse Mode

Based on the above-obtained parameters, the kick factors of all the modes in the passband from the lowest to the 8'th were calculated using the "open-mode expansion" code; here, we call it the OM code [7]. The result is shown in Figure 9.5; eight pass-bands can be clearly seen. The modes in the first and 6'th bands are found to be distributed in a good shape.

The resultant wake-field ($W_T(t)$) can be calculated as the sum of all the mode, as

$$W_T(t) = \sum_m^{all} 2\, k_T^m \, \sin(\omega_m t)\,, \tag{9.1}$$

where k_T^m is the kick factor of mode m, and ω_m is the angular frequency of mode m.

It is worthwhile seeing how the kick factors of the severest first passband distribute. Figure 9.6 shows the kick factors weighted by the mode density. As shown in this figure, the Gaussian distribution is quite clear.

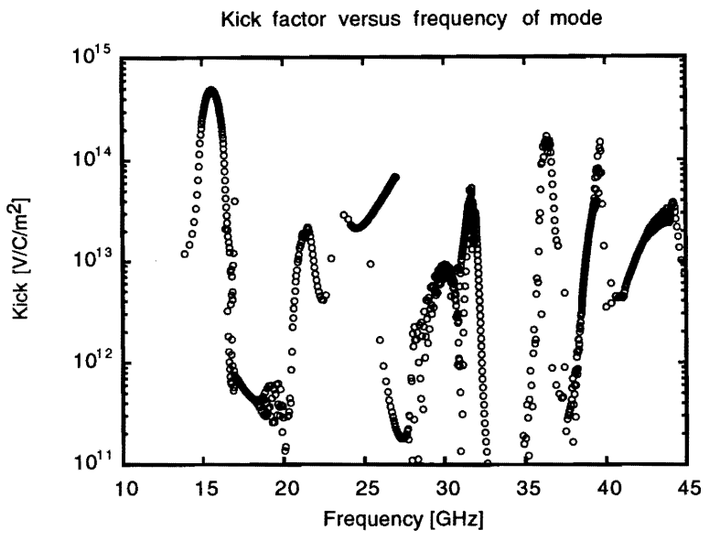

Figure 9.5: *Calculated kick factors of the modes in the 150-cell detuned structure. The calculation was performed by an open-mode expansion code taking up to the 8'th mode in the cell as the base of the expansion.*

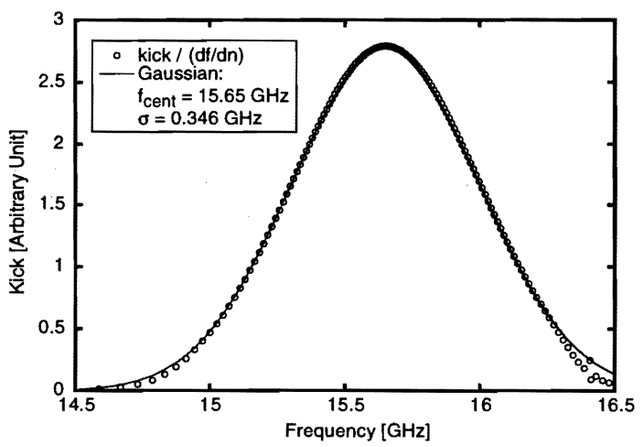

Figure 9.6: *Effective kick factors in the lowest dipole passband region calculated by an open-mode expansion. The circles indicate the kick factors divided by the mode spacing as a function of the mode frequency. The solid line shows a Gaussian fitting with the parameters shown in the box.*

Figure 9.7 shows the envelope of the wake-fields calculated by the OM code. They were obtained by assuming the Q values for all of the modes to be infinite. As shown in the figure, the wake-field re-coheres significantly in the case of one structure, as shown in (A). This can be explained by a detailed view of the kick factors, as shown in Figure 9.8. For a structure, the kick factors of the lowest

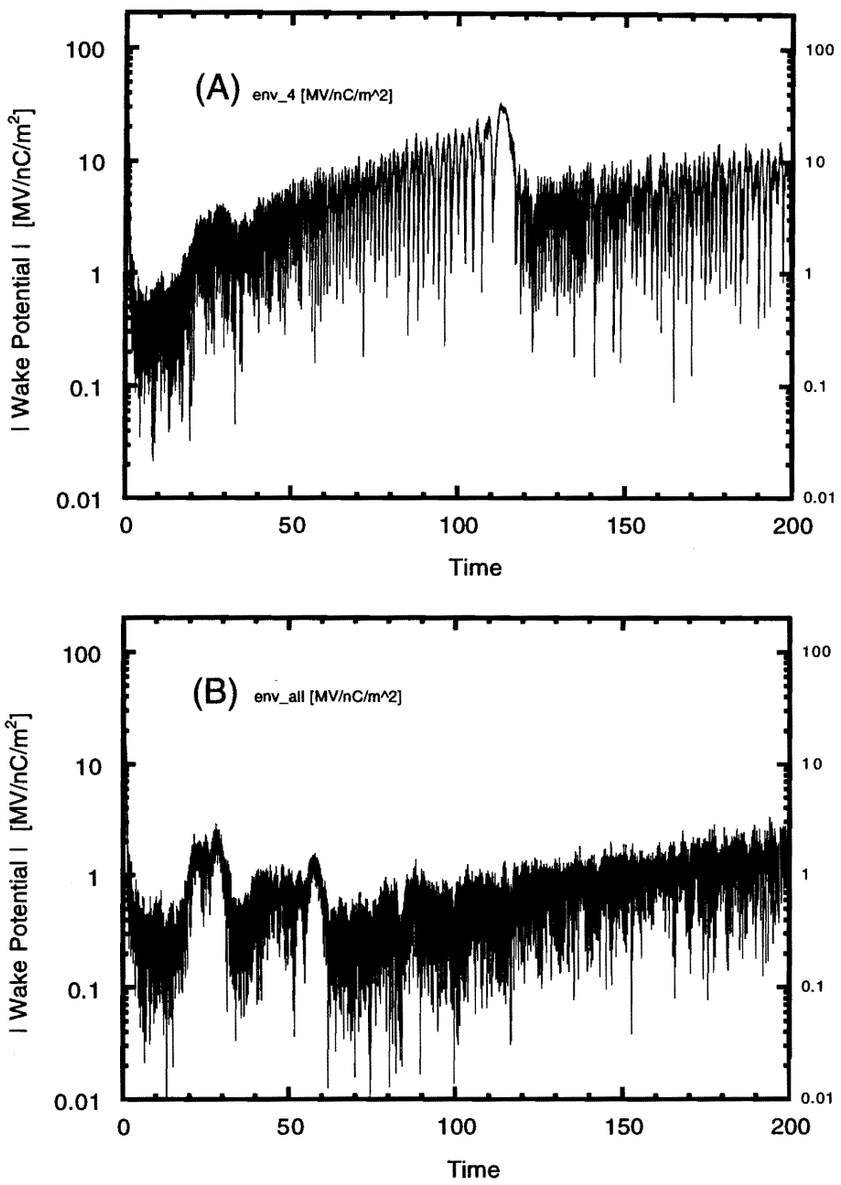

Figure 9.7: *Envelope of the wake-field calculated by the open-mode expansion code for the 150-cell detuned structure. The upper figure shows the wake-field of one structure. The lower figure shows that of the four-interleaved structures. In both cases it is assumed that the Q values of all of the modes are infinity.*

and severest passband are spaced by about 9 MHz. Therefore, 110 nsec later, the contribution from almost all of the relevant modes re-cohere. If it is designed to distribute the kick factors as that shown

in the same figure, but to include all of the points, the spacing becomes 2 MHz and the recurrence occurs four times later, ie. about 500 nsec later, which is well beyond the bunch trains. As a result, the wake-field within the bunch train stays at around 1%, which is comparable to the desired level, as shown in Figure (B). It should be pointed out that the intrinsic Q values are considerably important in the later part of the wake-field. At the last part of the bunch trains, the damping due to the intrinsic Q value is simply estimated to be $1/e$ as a reasonable estimate of $Q = 6000$ for the lowest passband.

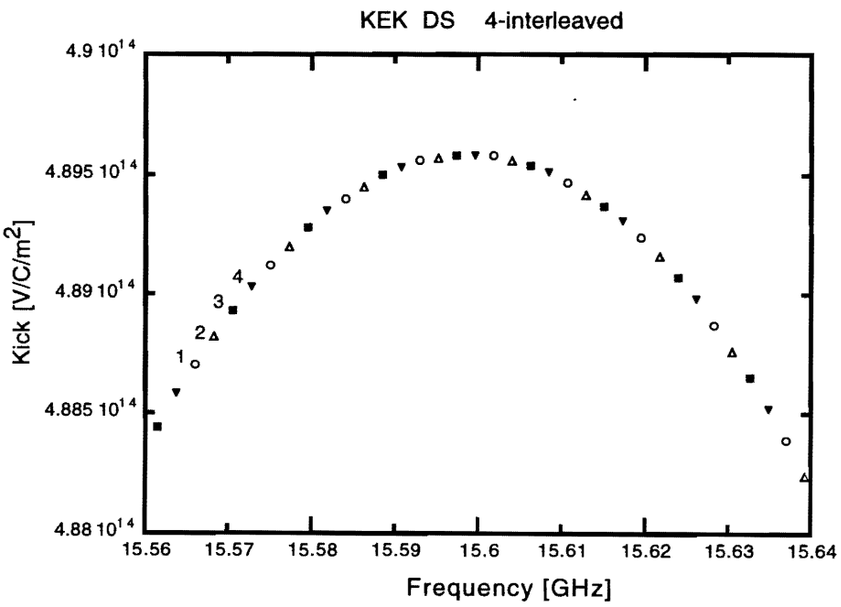

Figure 9.8: *Calculated kick factors in the frequency region near to 15.6 GHz. The same symbols attribute to those of the same detuned structure among the four interleaved ones.*

Final Determination of Parameter b

While keeping the above-obtained (a, t) values, the beam hole is rounded by a radius of $t/2$. Then, the cell radius "b" should be tuned to make the accelerating mode correct. Since the relative frequency tolerance of the accelerating mode is a few times the 10^{-5} level, the determination of parameter "b" should be very accurate.

For this purpose, the frequency of the $2\pi/3$ accelerating mode is calculated with using a finite-element code, PISCES-II[9] [10], in a periodic boundary condition. The convergence of the calculation was proven to be within ± 0.1 MHz for the typical three cells along the structure, as shown in Figure 9.9.

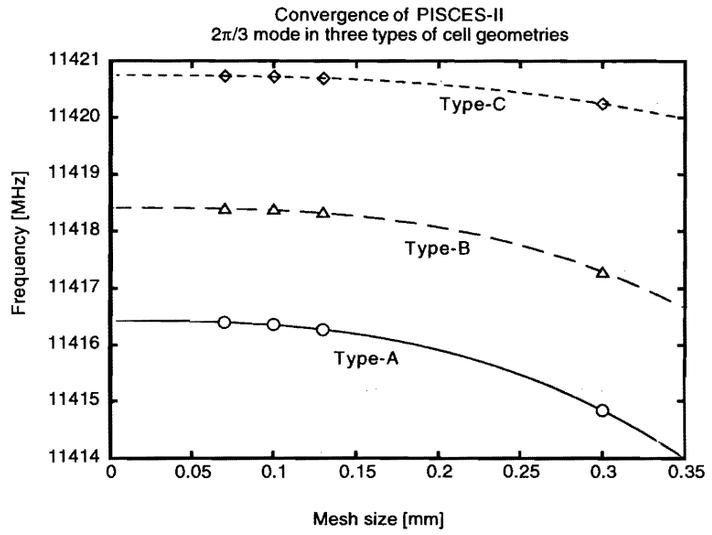

Figure 9.9: *Frequency-convergence characteristics of the PISCES-II. The calculations are for three different cell shapes along the detuned structure as a function of the nominal size of the mesh.*

It is still not practical to design the cell dimensions based simply on the above estimation, even though the accuracy of the calculation is sufficiently good. This is because the fabricated cells are different in dimensions and shape from the design, and we do not know the difference based on the mechanical checking on the order of 0.1 MHz, or, in other words, the order of as low as 0.1μm in dimensions. Therefore, we decided to make three reference cells to obtain the difference of the frequency between the calculation and the fabricated cells.

The $2\pi/3$ mode frequencies of the three types of cells were measured. Three cases with 2, 5 and 8 regular cells were measured, while sandwiched with half end cells at both ends. The measured frequencies were analyzed in a so-called $1/N$ plot, as shown in Figure 9.10, where N is the number of the regular cells plus one. The frequency in the periodic structure can be obtained from this figure with a precision of ± 0.1 MHz at $N \to \infty$.

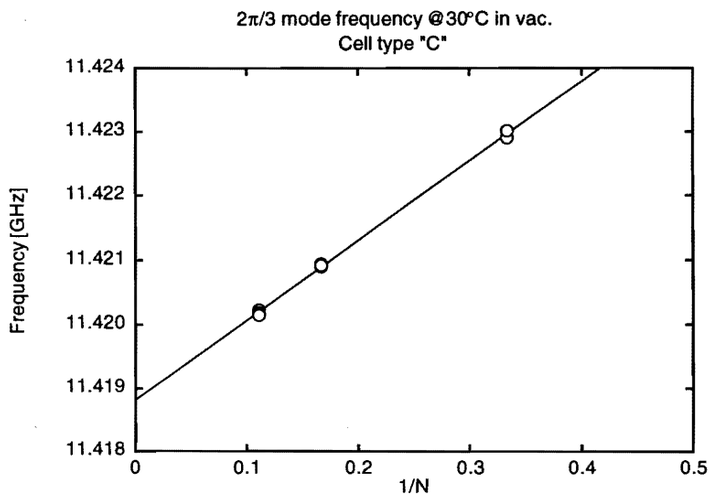

Figure 9.10: *Measured frequencies versus $1/N$, where N is the number of cells for the measurement setup. If the frequency error comes from an irregularity due to the end half cell, it is proportional to $1/N$, because the weight of the effect is reduced inversely proportional to the stored energy at the end cell compared to that of the total.*

These measured frequencies were compared to those calculated. The measured values were found lower than those calculated by 0.5 MHz for all three cases. It was concluded that this calibration value could be applied for all cells along the structure. Based on the calculation, and using this calibration value, parameters b was finally determined.

Consideration of the Tolerances of the Frequencies and Dimensions

Accelerating mode: If the accelerating-mode frequency deviates from the nominal value, the corresponding phase error along the i'th cell is described as

$$\delta\phi_i = \frac{120}{v_{gi}/c}\frac{\delta f_i}{f}, \tag{9.2}$$

and the total phase slip along the structure becomes

$$\Delta\Phi = \sum_{i=1}^{N} \delta\phi_i \,. \tag{9.3}$$

The group velocity of the DS structure is shown in Figure 9.12. The corresponding integrated phase slip measured from the input coupler side is also shown in Figure 9.11 in the case of a +1MHz offset above the nominal frequency for all cells.

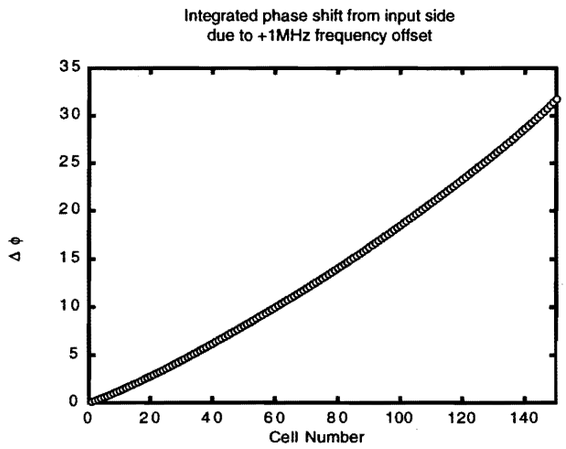

Figure 9.11: *Integrated phase slip as measured from the input coupler side in the case of a +1 MHz offset above the nominal frequency for the case of a detuned structure.*

The average slope of this curve gives the sensitivity of the phase slip, and is 32°/structure/MHz or 0.211°/cell/MHz. (This value corresponds to an average group velocity of $v_g/c = 0.0498$.)

Systematic error: The integrated phase slip along the structure becomes as large as 9.6° if there is a systematic error of 0.3MHz. In order to decrease the phase slip by a factor of 10, the relative frequency error needs to be on the order of 10^{-6}, which is very difficult to realize.

A ±0.3 MHz systematic error corresponds to a temperature change of ±1.5°C. This offset can be corrected by controlling the temperature of the input cooling water, because this value is comparable to the change of the average temperature of the structure, on the order of 1°C. A feedback system to

control the water temperature should be made based on parameters such as the difference between the input and output RF phase, or the monitored temperature of the structure body.

Random error: If the error is purely random, the integrated effect is reduced by a factor of $\sqrt{150}$. Therefore, a random error should be less than 3.7 MHz.

Tolerance on $2b$, $2a$, t: The typical dimensions used to define the shape of the cell is the cell diameter ($2b$), the beam-hole diameter ($2a$), and the disk thickness (t). The sensitivity of these dimensions to the accelerating-mode frequency is shown in Table 9.3. As shown in this table, the most sensitive parameters for the accelerating mode is "$2b$". If the deviations of all three dimensions occur in a random manner, the estimated error in the accelerating-mode frequency (δf) is described as

$$\delta f^2 = \left(\frac{\partial f}{\partial b}\delta b\right)^2 + \left(\frac{\partial f}{\partial a}\delta a\right)^2 + \left(\frac{\partial f}{\partial t}\delta t\right)^2 . \tag{9.4}$$

If the tolerance given in Table 9.3 is applied, the estimated frequency error becomes 0.34 MHz, which almost satisfies the above tolerance. If the cutting method, as proposed in the next section, is applied, the deviation of dimension "$2a$" should be almost the same as that of "$2b$". In this case, the error from "$2b$" partly cancels that from "$2a$", and the resultant error in frequency becomes ever smaller to be 0.20 MHz with the same tolerance.

Based on this estimation, we set this tolerance for the accelerating mode. They are summarized in Table 9.3. The consideration of the tolerances for higher modes is described in the following discussion.

Dimension	Sensitivity from input to output	Unit	Tolerance	Unit
$2b$	$-0.596 \sim -0.585$	MHz/μm	± 0.5	μm
$2a$	$+0.31 \sim 0.21$	MHz/μm	± 0.5	μm
t	$+0.08 \sim 0.15$	MHz/μm	± 1	μm

Table 9.3: *Estimated tolerance of the dimensional parameters of the JLC Detuned Structure.*

Dipole (TM110-like) mode: Figure 9.8 that appeared earlier shows a plot of the kick-factor distribution near to the peak as a function of the mode frequency. The mode-frequency spacing in this region is 2.2 MHz in the case of four interleaved structures. As for the crude estimation of the frequency tolerance of these modes, we can cite a value of 0.2 MHz, one order of magnitude smaller than the mode spacing. The validity of this rough estimation should be confirmed.

Random error: The modes, which have a significant contribution to the wake-field, spread over a few tens of cells. Then, the tolerance of the random-frequency error of each cell is

$$0.2\text{MHz} \times \sqrt{20} = 0.9\text{MHz}. \tag{9.5}$$

This means a relative frequency tolerance of 6×10^{-5}. This corresponds to 0.7 MHz in the tolerance of the accelerating-mode frequency, if we consider that the mode pattern is similar to that of the accelerating one. This tolerance level is looser than that of the accelerating mode stated above.

Systematic error: The systematic error within a few tens of cells in one of the four structures should be less than 0.2 MHz, compared to the frequency of the same mode in another interleaved structure in the four structures. The 0.2MHz corresponds to a relative error of 1×10^{-5}. Such a relative frequency tolerance is slightly tighter than that of the accelerating mode. However, the tolerance in 0.2μm for "$2b$" and the systematic error should be controlled among the four interleaved structures.

Characteristics of the Accelerating Mode

Based on the parameters of the cells along the structure, the characteristics of the accelerating mode were calculated. The basic parameters of the accelerating mode as a function of the cell number are shown in Figure 9.12. Here, the Q value is assumed to be 95% of the theoretical value at 20°C. This factor is considered to be a reasonable number, based on experience at KEK. If the nominal operation temperature is different from 20°C, the additional decrease in the Q value due to this temperature rise is about 2%/°C, though this decrease is not taken into into account in the present study.

It should be noted that in the case of a choke-mode structure designed for the C-band [5], the degradation of the Q and R/Q values amounts to 10% and 15%, respectively, as listed in Table 9.4. This degradation comes from the finite amount of stored energy in the choke.

Let us estimate the excess power for this case, compared to that of the DS case, in order to obtain the same accelerating field. For this purpose, we consider a constant-gradient structure (CG), which is cited as a reference and is equivalent to the detuned structure (DS), as in the following. The shunt impedance (R_0) is assumed to be the same as the average value of the DS, while total attenuation parameter (τ) is adjusted to have the same average accelerating field with beam loading, as that of DS. The beam-loaded accelerating field (E_{NL}) is expressed as

$$E_{NL} = \sqrt{P_0 R_0 \frac{1 - e^{-2\tau}}{L_s}}, \tag{9.6}$$

where P_0 is the input power to the structure and L_s is the structure length.

If the beam-loading field is included, the accelerating field with beam loading, (E_{LD}), is expressed as

$$E_{LD} = E_{NL} - i_0 R_0 \left(\frac{1}{2} - \frac{\tau e^{-2\tau}}{1 - e^{-2\tau}} \right), \tag{9.7}$$

where i_0 is the average beam current (here, 0.7 A). The required power for obtaining the same beam-loaded accelerating field is given in Table 9.4. As can be seen in the table, the peak power per structure is the same, but the structure length (L_s) decreases by 20%, resulting in an extra power per unit length of about 20% to maintain the same beam-loaded accelerating field.

In order to reduce the required RF power, and to make the structure length longer, it should be noted that the simple DS structure described in the present paper can be further optimized.

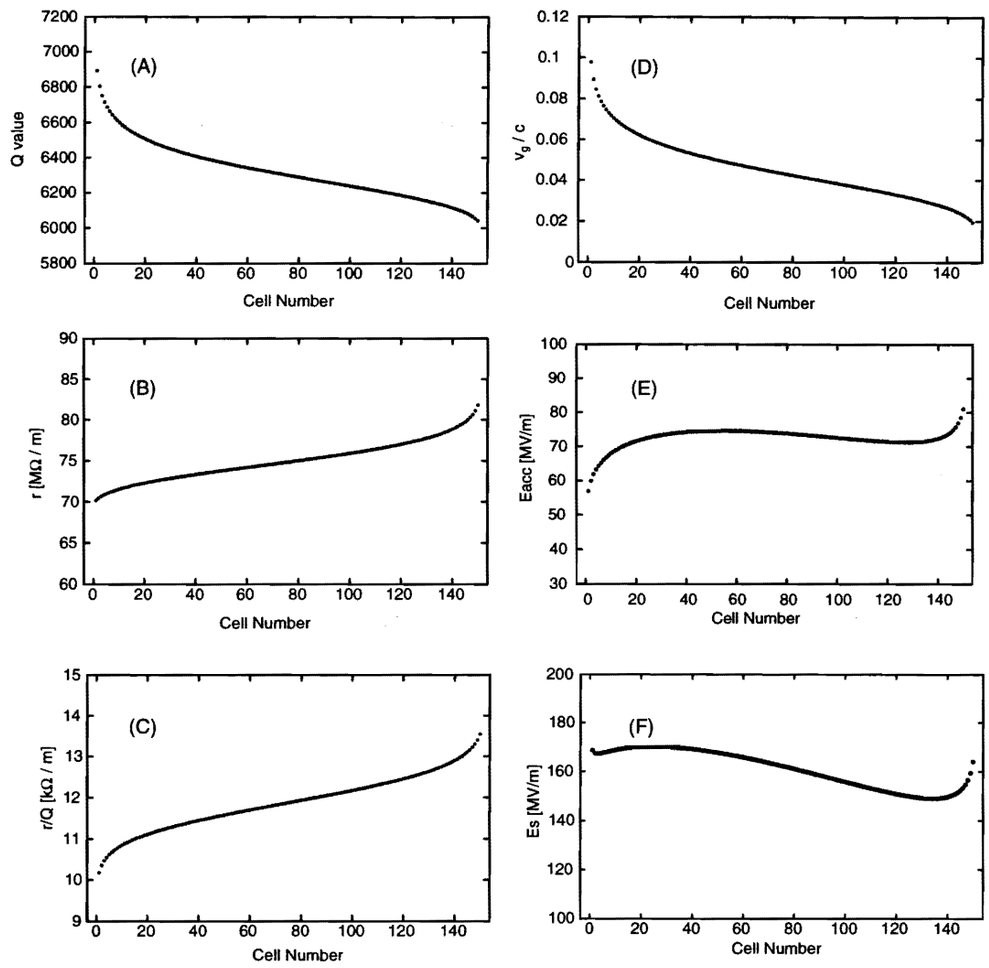

Figure 9.12: *Characteristics of the accelerating mode of the detuned structure. (A): Q-value of each cell. Assuming a realistic value to be 95% of the ideal copper case at 20°C. (B): Shunt impedance (R) while assuming the above Q-value. (C): R/Q value. (D): Group velocity (v_g) normalized by the velocity of light. (E): Average accelerating field in a structure, (E_{acc}). A nominal input power of 130 MW/structure is applied. No beam loading is included. (F): Maximum surface field in the structure (E_p/E_{acc}) as a function of the cell number. A nominal input power of 130 MW/structure is applied. The calculation assumes that the beam is absent.*

Item		Unit	DS	CS
Shunt impedance	R_0	MΩ/m	79	60.4
Degradation of Q	$\delta Q/Q_0$	%	0	15
Degradation of R/Q	$\delta(R/Q)/(R/Q)_0$	%	0	10
Attenuation parameter	τ		0.609	0.569
Structure length	L_s	m	1.31	1.11
Nominal accel. field	E_{NL}	MV/m	73.0	70.0
Beam loaded accel. field	E_{LD}	MV/m	60.2	60.2
Power / structure	P_0	MW/struct.	130	133
Power / unit length	P_0/L_s	MW/m	99	119

Table 9.4: *Estimation of the excess power needed to keep the beam-loaded accelerating field the same during the existence of a degradation in the Q value and the R/Q value. The calculation assumes a constant-gradient structure. DS in the table stands for a constant-gradient structure equivalent to a detuned structure, while CS stands for that of a low-Q and a low-R/Q structure.*

9.1.3 Mechanical Design

One of the greatest concerns about the mechanical design of the structure is the alignment of the cells along the structure. The cells are aligned by aligning the outer surface of each cell to a straight line, possibly by pressing the cells against a precise vee block and keeping the alignment through a bonding process. The alignment of the cells is assured by the good concentricity among the outer surface of the cell, beam-hole aperture and the cell inner cylinder. For this purpose, the cell is made by cutting from a copper block without re-chucking, especially for the machining of such important surfaces, so that the concentricity is very tightly controlled. The typical cross section of the regular cell is shown in Figure 9.13. The outer diameter, almost four-times larger than the electrical cell diameter, was chosen from the intuitive consideration on the process of stacking the cells to 1.3 m high.

The coupler cells should also be aligned well with respect to the regular cells. Therefore, the diameter of the coupler cells are designed to be the same as that of the regular cell. These cells are thus aligned at the same time as the regular cell alignment. A schematic drawing around the coupler cell is shown in Figure 9.14.

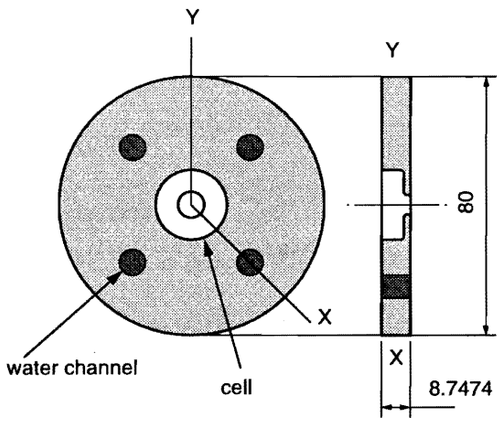

Figure 9.13: *Schematic view of a regular cell. Four water channels are integrated.*

Tolerances in Dimensions

Typical tolerances in dimensions are listed in Table 9.5 in addition to those in Table 9.3.

The outer diameter is essential to obtain a straight structure, as stated above. In order to reach an alignment precision of one micron, the tolerance of the OD is set to be $\pm 0.5\mu$m.

Even if the OD is precisely machined, and all of the cells are aligned against a reference straight line, the present bonding method goes through the process for all of the cells to be stacked vertically and sitting on a plate in a furnace at a high temperature, being sustained with an axial compressing pressure. In this stage, the tracing line of the centers of the cells can be rather freely bent transversely

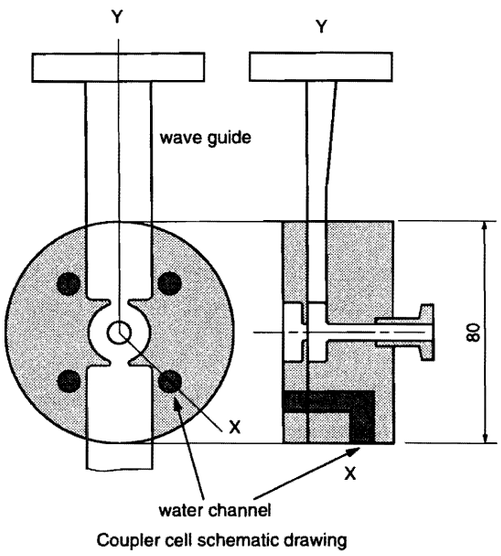

Figure 9.14: *Schematic view of the coupler cell. Water connectors are radially extruded. The vacuum connection port for the beam pipe can be as small as 20mm in diameter. Two wave guides with their height tapered down from the normal one for the rectangular wave guide to fit to the gap of the coupler cell are attached. In a future design, the BPM block may be directly connected to this coupler block.*

Dimension	Unit	Tolerance
OD	μm	$\pm$0.5
parallelicity	μm/80mm	$\pm$1
concentricity	μm	0.2
flatness	μm	0.3
d	μm	$\pm$1

Table 9.5: *Estimated tolerance (continued) of the dimensional parameters of the Detuned Structure.*

due to the imperfect parallelicity of the cells. Suppose the parallelicity is 0.1μm/80 mm, and that the direction of the inclination is the same for all of the cells. Then, the quadratic increase in the transverse deviation from the vertical axis becomes fairly large. In this case, the cell deviation from the line connecting both end cells is as large as 30μm/1.3 m. However, the practical amount of bending is much smaller than this value, because of the random direction of the inclination, by such an order as $\sqrt{150} \sim 10$. In addition, the boundary condition of the end cells during the bonding process will make the deviation small through the force to try to keep the two end cells parallel. Based on these considerations, the required tolerance for parallelicity is presently set at 1 μm/80mm.

The required tolerance on the concentricity of the cell inner radius and the beam hole is set at 0.2μm, which can be easily obtained.

The flatness of the cells is important for reliable diffusion bonding with vacuum tightness and a good alignment of the cells. The presently available level of 0.3μm is set as the tolerance. Within this level, the alignment of a structure became within 10μm in one of the two prototype structures, indicating that this value can be a realistic tolerance.

The error in the cell length ("*d*") does not very severely perturb the acceleration until the deviation becomes a considerable fraction of the wavelength, say 0.15 mm/1.3 m, ie. 2°/structure at 11.4GHz. This sets a systematic error of 1μm.

Another characteristic of the design is the integration of the water-cooling channels into the cell body. This is a challenge regarding vacuum tightness because many intermittent cutting is inevitable on the bonding surface. However, if this design works, the temperature distribution in a cell can be more uniform, and the fabrication process will become much simpler. This design should be studied in parallel with the feasibility study for the extraction of the water channels towards the outside, while maintaining a good alignment of the cells.

Eliminating the water channels from inside the cell body will make the outer radius of the cell smaller, so that the machining area would become fairly small, and thus making the machining time much shorter. However, a small outer diameter might cause difficulties in the cell-aligning process before bonding or in the slippage of the cells during bonding. Therefore, an outer diameter of 80 mm is considered to be a reasonable size at present for a structure having a total length of 1.3 m.

Since the copper material used for the structure body is soft, the structure can be easily bent with a fairly small external force. The self weight makes the structure to bend on the order of 60 μms. Keeping this magnitude in mind, the structure body should be designed to be held tightly by pressing it to a rigid block, such as a vee-block. Once the structure is held tightly, it is resistive against many perturbations until installation, as well as against various vibrations during operation. Also it can be physically moved in transverse directions, driven by a fast actuator, in such cases as the position feedback and the beam-based alignment.

9.1.4 Thermal Design

Typical thermal characteristics of copper are listed in Table 9.6 for the following discussions.

Item	Symbol	Value	Unit
Density	ρ	8.93	g / cm^3
Young's modulus	E	1.32×10^4	kg / mm^2
Poisson ratio	σ	0.343	
Heat capacitance	c	0.0919	cal / °C / g
Thermal conductivity	κ	386	W / m / °C
Thermal expansion coefficient	α	1.65×10^{-5}	

Table 9.6: *Some mechanical and thermal characteristics of copper.*

Loss Distribution

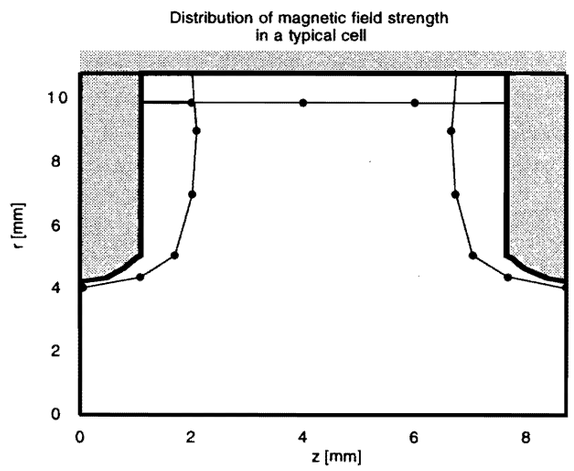

Figure 9.15: *Typical distribution of the magnetic field in a cell when operated in the $2\pi/3$ mode. The calculation was performed using MAFIA. The distance from the thick curve along the cell surface to the thin lines in the cell is proportional to the strength of the magnetic field. The power loss per unit area is proportional to the square of the magnetic field.*

The wall loss per unit area is proportional to the square of the magnetic field. A typical distribution of the magnetic field in a cell is shown in Figure 9.15, which was calculated by MAFIA in the $2\pi/3$ mode[11]. The partition of the wall loss in a cell into that on the disk and that on the wall at $r =$ maximum was calculated for the following estimation. The ratio of the loss in the disk to the total loss in a cell was calculated to be smoothly varying from 0.54 for the cells near to the input coupler to 0.59 for the cells near to the output coupler.

The wall-loss distribution along a structure in the case without a beam was calculated, and is shown in Figure 9.16. Here, the total wall loss is 3.4 kW / structure.

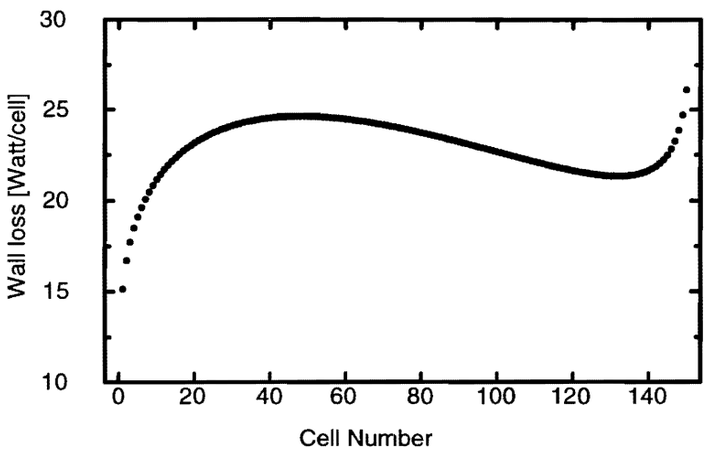

Figure 9.16: *Wall loss per cell along the structure operated at a nominal input power of 130 MW, but without a beam.*

Temperature Distribution in a Cell

Since the wall loss in a cell is cooled by water running outside of the cell, the highest temperature in a cell is at the beam hole. Judging from the above magnetic-field distribution, the temperature rise in the disk can be estimated by assuming that the wall loss per unit area is constant on the flat surface of the disk, where the beam hole is approximated as being flat with a radius that is the same as the real one. In addition to this approximation, the temperature in the disk at the same radial position is assumed to be the same throughout the disk body. In this approximation, the disk temperature as a function of the radius (r) is estimated to be

$$\Delta T_d(r) = \frac{q_0}{t \cdot \kappa}\left(\frac{r^2}{2} - a^2 \ln(r)\right) + C\,, \tag{9.8}$$

where q_0 is the power loss per unit area on a disk, a and t the disk aperture and thickness, κ the heat-transfer constant of copper and C an integration constant.

Based on information concerning the loss in the cells along the structure, and using the above equation, the temperature rise in the disk was calculated, and shown as in the middle curve of Figure 9.17. In the

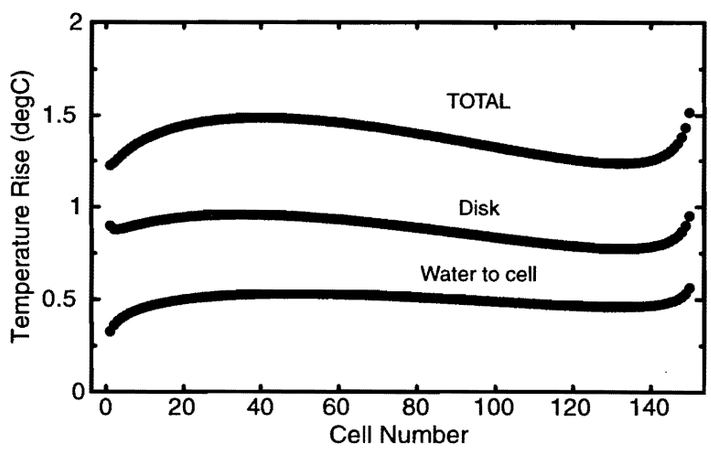

Figure 9.17: *Rough estimation of the temperature rise in a cell. Top: total temperature rise from the water channel to the disk tip. Middle: temperature rise in the disk. Bottom: temperature rise between the water channel and the cell outer surface.*

lowest curve in the same figure, the temperature rise from the water channel to the cell surface, (ΔT_{wc}), is estimated to be the temperature rise from a water channel of 4 mm in radius (r_w) surrounded by a cylinder whose outer surface is 25 mm in radius (r_{wc}), apart from the center of the water channel. All of the power is assumed to be uniformly deposited in this outer surface. Here, the temperature rise is simply written as

$$\Delta T_{wc}(r) = \frac{q}{2 \cdot \pi \cdot d \cdot \kappa} \ln\left(\frac{r_{wc}}{r_w}\right) , \tag{9.9}$$

where q is the total power loss per cell and d is the cell length. Temperature rise at the boundary between the copper body and the water should be included in the actual temperature rise with respect to the water temperature. The estimation of this temperature difference at the boundary depends on the surface condition, and should be evaluated experimentally. The water temperature can be set and controlled by monitoring a typical temperature in the structure.

The effect of a temperature change on the accelerating mode has been estimated. Here, we approximate very simply that the cell is uniformly expanded due to a temperature rise of 3°C, which is estimated from Figure 9.17, and a temperature rise of the water by 2°C. The change of 3°C gives a 0.57 MHz change in frequency. This frequency shift should mainly be compensated by the temperature of the input water. This correction is performed by measuring the phase shift of the output RF, or even by simply measuring a typical temperature of the structure.

The effect on frequency detuning for the higher modes should be estimated in addition to an analysis of the accelerating mode. In this case, such a deformation as a bending of the disk should be carefully analyzed. However, a temperature rise on the order of 1°C corresponds to a relative thermal expansion of copper on the order of 10^{-5}, and should only perturb the higher modes within a relative-frequency tolerance of less than 10^{-4} if the temperature of the four interleaved structures change in phase.

A detailed estimation of the deformation of the cell and the structure is to be studied from now. The deformation not only changes the frequency, but also puts stress on the structure, or even bends the body. A careful thermal-distortion analysis should be performed.

RF Load

The RF power transmitted through the structure to outside, due both to the fed RF power and the beam-excited power, is absorbed in an RF dummy load made of magnetic stainless steel, which can be cooled by spent water from the structure.

Cooling Water

The heat generated in the cells is cooled by water. The total water flow rate for a structure is designed to be 23 l/min to keep the average water temperature rise within 2°C for the case of nominal operation without a beam. Four pipes of 8 mm in diameter for flowing the water are located 25 mm from the beam axis, being equally spaced in the azimuthal angle. These channels run through the total structure length and come out radially at the coupler cells through a 90° deflection. The flow direction is reversed from a channel to the adjacent one, located at 90° in the azimuthal angle. This counter-flow method makes a difference in the water temperatures among the four channels in a cell. It becomes 4°C, which is maximum and twice the average water temperature rise existing at input and output coupler cells.

The water-flow speed is 1.9 m/sec. Assuming that each cooling channel is a simple round pipe, the Reynolds number (R) is vd/ν, and becomes 19080; this value is in between the two estimated values of the minimum critical Reynolds number (2320) and that of the maximum (5×10^4) [15]. This means that the flow must be in a turbulent regime. Many discontinuities due to the chamfering at all of junctions between the cells may help the flow to become turbulent.

Assuming a smooth round pipe of 8 mm in diameter and 1.3 m in length, the pressure drop (Δp) along the structure is estimated to be

$$\Delta P = \gamma \lambda \frac{l}{d} \frac{v^2}{2g}, \tag{9.10}$$

where l and d are the length and diameter of the pipe, g the gravitational acceleration, v the flow speed, γ the density of water and λ a constant, which is estimated by a formula[15],

$$\frac{1}{\sqrt{\lambda}} = 2 \cdot \log_{10}(Re \cdot \sqrt{\lambda}) - 0.8\,. \tag{9.11}$$

The pressure drop due to this simple pipe becomes less than 0.1 kg/cm^2. The pressure drop arising from discontinuities due to chamfering at the junction of the cells, and also the 90° bending and the connectors for the tube fitting at both ends, should cause the main part of the pressure drop. These unknown contributions should be evaluated experimentally.

As an example, the temperature control of the water should be within ±0.3°C in order to keep the total phase shift along a structure less than ±3°. The practical tolerance of the temperature control should be evaluated based on a consideration of the beam dynamics, such as the accelerating field or BNS damping phase through the whole linac, including both the systematic- and random-error components.

Thermal Response

The time response of the temperature rise from no RF to nominal operation without a beam is roughly estimated in the following way. It is assumed that the wall loss in a cell changes by W at time $t = 0$. Then, the temperature rise of the structure (T) follows the equation

$$M(dT/dt) = W - TS\,, \tag{9.12}$$

where M is the heat mass of the structure and S the coefficient of heat removal by water. These parameters are calculated as

$$M = 155 \ \text{Joule/°C}, \tag{9.13}$$

$$S = \kappa A/\delta = 23.3 \ \text{W/°C}, \tag{9.14}$$

where the gradient of the temperature is assumed to be within a distance of d through area A. Here, we assume intuitively that $A = 12$ cm^2 and $d = 2$ cm. Integration of this formula gives

$$T = \exp\left(-\frac{t}{M/S}\right) + W/S, \tag{9.15}$$

where M/S measures the response of the system. For the present case, this becomes 7 sec.

9.1.5 Vacuum Design

General

The average vacuum pressure along the main linac should be less than 10^{-8} Torr as for the CO-equivalent gas[2].

In the DS structure, we assume that the pumping of the structure is performed through the wave guide, the iris aperture to the coupler cell and the beam hole in the disks between the regular cells. If there is any pumping mechanism in the beam pipe side or running along the structure, the vacuum will become better than the following estimation.

Calculation of the Vacuum Conductances

At first, the vacuum conductances of various components were estimated using simplified analytical formula in a reference book [30]. The calculated vacuum conductances between the input coupler cell and the pumping port in the wave guide and that for the same in the output side were estimated as given in Table 9.7.

Item	Input side		Output side	
	Dimension	Conductance	Dimension	Conductance
	mm	liter/sec	mm	liter/sec
iris width	9.75		7.60	
iris height	7.60	}16.3	6.36	}10.3
iris effective thickness	2		2	
iris to taper	30	12.2	30	9.1
taper length	48	9.86	48	8.77
wave guide **	100	5.88	100	5.88
vac port		22.9		22.9
Total conductance C		2.18		1.87

Table 9.7: *Calculated vacuum conductance between the input or output coupler cell and the pumping port. * The vacuum port is equipped with 74 holes of 1.5 mm in diameter and 2.57 mm in thickness located at both H-planes. ** The waveguide is 10.16 mm in height and 22.86 mm in width.*

Estimation of the Pressure along the Structure

The pressure along the structure was estimated assuming that all of the out-gas comes from the inner surface of the structure. The evacuation is performed by ion pumps having a pumping speed of 10 liter/sec. The base pressure at the coupler cell can be estimated to be

$$p_1 = p_0(1 + S/C), \tag{9.16}$$

where p_0 and p_1 are the pressure at the ion pump and coupler cell, respectively, S is the pumping speed of the ion pump and C is the vacuum conductance from the coupler cell to the ion pump. Since the conductance (C) is fairly small compared to S, the pressure in the coupler cell is already more than a factor of 5 larger compared to that at the ion-pump head. It can be estimated to be about 7×10^{-9} Torr, assuming a pump-head pressure (p_0) of 10^{-9} Torr.

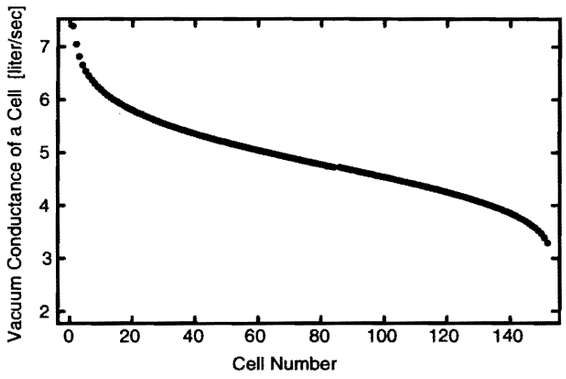

Figure 9.18: *Calculated vacuum conductance as function of the cell number.*

The pressure in the cells can be calculated using a simple analytical form of the vacuum conductance and the out-gassing from the inner side of the cells. The beam hole is approximated to be flat with the same diameter as that of the actual round case. The conductance of each cell is shown in Figure 9.18, and the calculated pressure is shown in Figure 9.19. In this case, the out-gassing rate is assumed to be 1×10^{-12} Torr l / sec/ cm^2. Here, the average pressure along the structure becomes 1.1×10^{-8} Torr.

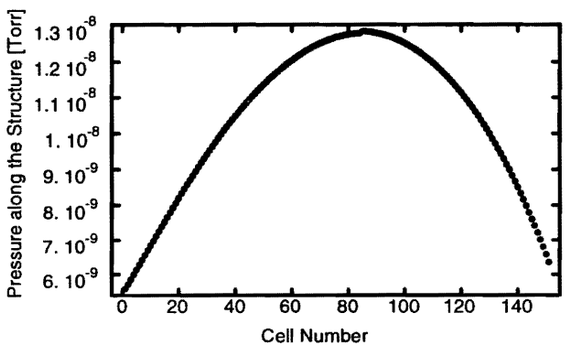

Figure 9.19: *Calculated pressure along the detuned structure. The step in the middle is due to the calculation method and is not physical. The out-gassing rate is assumed to be* 10^{-12} *Torr* l */sec/cm*^{2}.

Outgassing Rate

From the above result, it is essential to reduce the out gassing rate to less than 10^{-12} Torr l / sec/ cm^2 in order to realize the required pressure level.

The material, itself, of a typical oxygen-free copper of class 1, such as Hitachi copper, shows the required out gassing rate after a moderate temperature-baking process [31]. Because the cells for the structure are made of such a material, the inclusion or absorption of various materials in the fabrication process should be suppressed well to obtain the characteristics of the material, itself. The greatest concern is the final cutting process, which uses a diamond tool with kerosene oil as a cutting fluid. This may inevitably take the kerosene oil into the surface. The amount of these effects should be studied experimentally. It is to be noted again that the vacuum requirement depends on the atomic charge number of the gas in connection to the beam dynamics. Any high-Z material should be avoided with great care.

Possibility of Other Pumping Channels

If it is impossible to reduce the out gassing rate below the above tolerable level, such an idea as drilling a few small holes into each cell connected between the cells and the vacuum manifold would be needed. This can be realized in such a design as the cells for one of the prototype structures (M1), shown in Figure 9.33 of Section 9.2, though the connection for the cells to the manifold can be simpler. However, this still makes the fabrication of the cells complex, and should be avoided for mass production.

9.2 Structure Manufacturing

9.2.1 Cell Fabrication

To maintain the machining tolerances of a, b, t and d in Figure 9.20 is very important for realizing the electric design of an accelerating structure, as described in the previous section. From the view point of the thin, sub-micron skin depth of microwaves and the utilization of copper-copper diffusion bonding, the cells should be machined with good flatness and roughness and with the least thickness of the layer where the usual crystal structure of copper is considerably disturbed by defects, stress and chemicals, etc. due to machining. The ultra-fine machining now widely used in many engineering fields becomes a very essential technique.

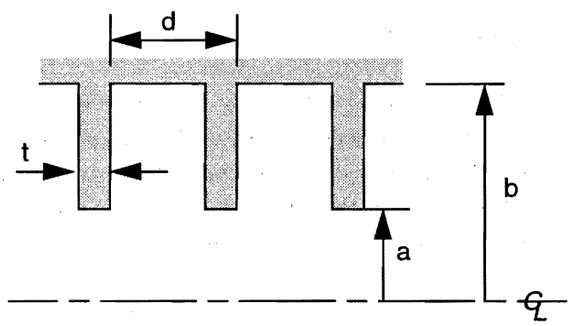

Figure 9.20: *Schematic cross-sectional view of an accelerating structure. The dot-dash line indicates the symmetry axis. The a denotes the half iris aperture, b the cell radius size, t the iris thickness and d the cell period. This figure is a reproduction of Figure 9.1.*

Precise machines and circumferences

Before considering a machining study, the status of high-precision machining in Japan is surveyed. Firstly, a chronological advance in the accuracy of material processing is shown in Figure 9.21 [16]. Secondly, typical tolerances for the present-day mechanical, electrical and optical products are shown in Table 9.8 [16]. As can be seen in these examples, the cell machining tolerance is considered (in principle) to be within the present technology of high-precision machining. Keeping these situations in mind, a high-precision machining laboratory was made in 1993 at KEK as a key station for fabrication studies dedicated to the X-band accelerating structure.

The principle of the cutting mechanism is that the cutting depth should be uniform and the tool shape should be exactly transfered to the work surface. For this purpose, natural diamond is the best

Tolerance (accuracy)	Mechanical parts	Electronics parts	Optical parts
200μm	Normal machine and homeware parts	General purpose electric parts (switch, motor, connector)	Camera and telescope bodies
50μm	General-purpose mechanical parts (gear,thread), typewriter parts, engine	Package (electronic parts) micromotor, transistor, diode, magnetic head parts	Camera shutter, lens holder (camera, microscope) (tape recorder)
5μm	Mechanical watch parts accurate gears, threads machine tool bearings ball screw, rotary compresser parts, shaver blade	Electric relay, resistor, condenser, disk memory, silicon wafer, TV color mask, video head and cylinder	Lens, prism, optical fiber and connector
0.5μm	Ball and roller bearings precision drawing wire flapper servo valve, gyrobearing, air bearing, precision die, roll thread die, ink jet nozzle	Magnetic head (video cassette recorder), magnetic scale, CCD, quartz oscillator, magnetic bubble memory, IC, magnetron, thin film-pressure transducer, thermal printer head	Precision lens and prism optical scale, IC exposure mask (photo, x-ray), laser polygon mirror, x-ray mirror, elastic detection mirror
0.05μm	Block gauge, diamond indenter, high-precision XY table, high-precision stamper and die, microtome cutter (diamond)	IC memory, electronic video disk, large scale IC, microvaccum tube, TFT-LCD	Optical flat, precision Fresnel lens, optical diffraction grating, optical video disk (CD)
0.005μm (5nm)	Ultraprecision parts (plane ball, roller,	VLSI, super lattice (synthesis) thin film	Ultraprecision diffraction grating
Special feature	thread) Shape (3-D) preciseness	Pattern (2-D) fineness	Mirror surface roughness grating (1-D) accuracy

Table 9.8: *Tolerance or allowable errors of products.*

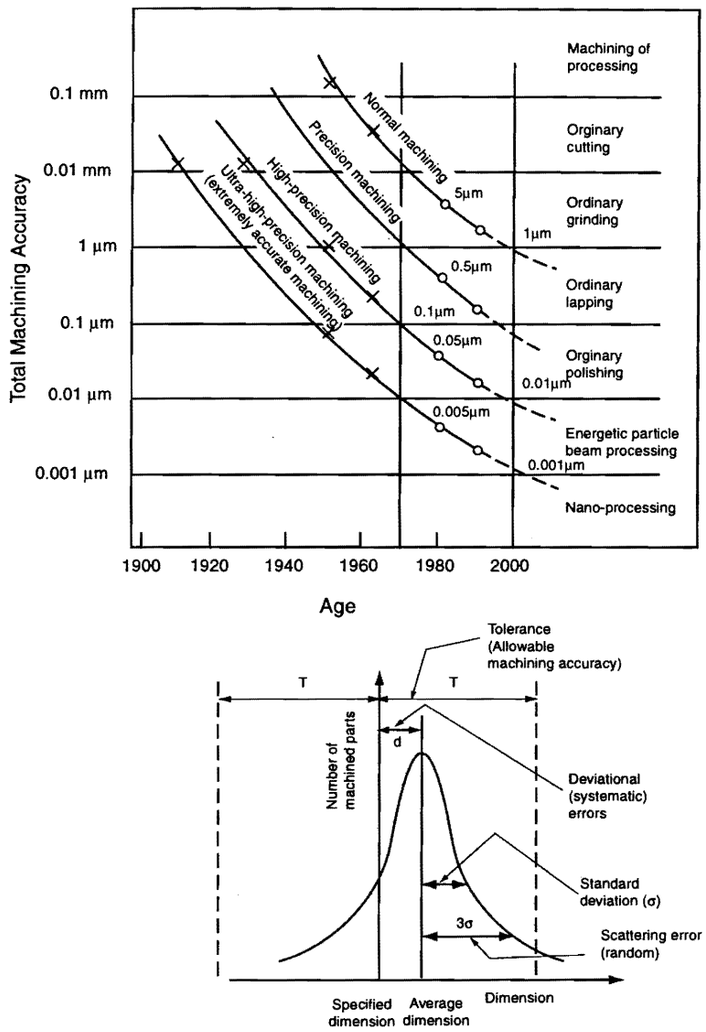

Figure 9.21: *Achieved machining accuracy in the respective age. Processing error=difference between the specified and processed dimensions. Machining accuracy e=systematic error $\epsilon d(d)$+random error $\epsilon s(3\sigma)$. Accuracy in a narrow sense= systematic error or deviational error(d). Precision in a narrow sense = random error or scattering error(3σ). Precision in a wide sense = high accuracy. Standard variance = σ^2.*

material for machining an OFC copper material, because of the small tool wear and small chemical reaction between the tool and the material. In addition to these cutting characteristics, the cutting tool and the work spindle, or the tool spindle, should be precisely rotated geometrically to make high-precision cutting.

Any error propagation should be carefully analyzed for the machine to reach such a tight tolerance,

	Preparation room	Machining room	Inspection room
area ($m \times m$)	3.6×1.9	6.6×3.6	6.6×4.7
cleanness class	no control	10000	1000
temperature ($°C$)	no control	$23\,(\pm 1) \pm 0.2$	$23\,(\pm 1) \pm 0.2$

Table 9.9: *Specifications of rooms for a high-precision machining laboratory. The numbers in the parentheses are those of the long-term drift, where + is in summer and - in winter.*

especially concerning some absolute dimensions. The machining error (dE (r.m.s)) is expressed as follows, if each error source is independent on each other:

$$dE = \sqrt{(\frac{\partial D}{\partial t})^2\, dT^2 + dP^2 + (\frac{\partial P}{\partial t})^2\, dT^2 + (\frac{\partial M}{\partial t})^2\, dT^2 + dR^2 + (\frac{\partial R}{\partial t})^2\, dT^2}, \tag{9.17}$$

where T is the circumferential temperature, P the individual tool positioning error, D the size of the material under machining, M the machine deformation and R the shift in the rotation axis of the work spindle. The thermal expansion coefficients of copper and glass scale for tool positioning are 1.6×10^{-5} and 8×10^{-6}, respectively. Considering the preliminary study of the machine, the positioning error of the tool, the difference between the specified and processed dimensions (dE) becomes on the order of 0.5μm if the dT is assumed to be ± 0.2°C. This error already exceeds the tolerance. In addition, this value does not include such errors as dP and dR, which are inherent to the machine. From this very rough estimation, it was found that one of the most important conditions when designing a high-precision engineering laboratory is to make the temperature of the room stable for machining and the measurement of dimensions. Another important condition is cleanness.

Two clean rooms of constant temperature were built, one for installing two high-precision diamond turning machines and a milling machine, and the other for microwave and mechanical measuring systems. A smaller, less clean room for preparation work was attached. The specifications of the rooms are listed in Table 9.9.

Two diamond turning machines and a precision milling machine were installed. Each machine is set in an independent booth with air flow from the top. These machines are commercially available CNC high-precision turning and milling machines, which are capable of producing various optical components through 2-axis and 3-axis simultaneous control, respectively. The bed is supported by air mounts to isolate the machine from any external vibrations. Figures 9.22 and 9.23 show the precise turning lathe and milling machine installed at KEK. Table 9.10 shows the major specifications of the machines.

A work spindle is especially made of super invar and rotates while being sustained by a hydro-static air bearing. The heat from the servo motors is removed by circulating temperature-controlled water in order to prevent any change in the temperature distribution in the machine. The unbalance of the spindle caused by the attached vacuum chuck was measured, and then corrected.

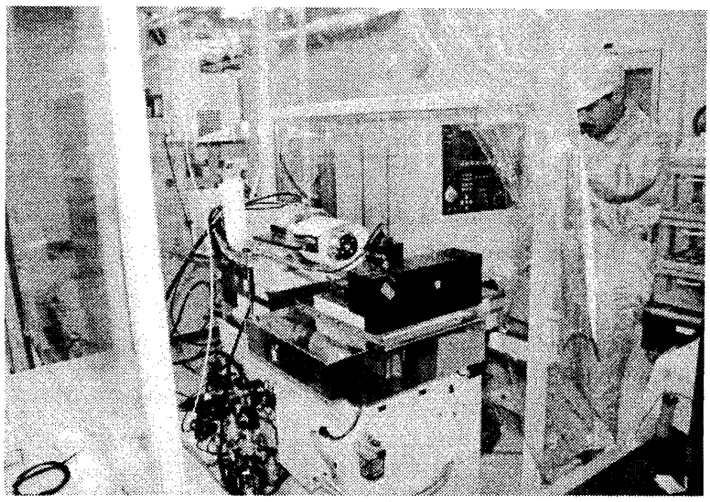

Figure 9.22: *One of the precise lathes installed at KEK.*

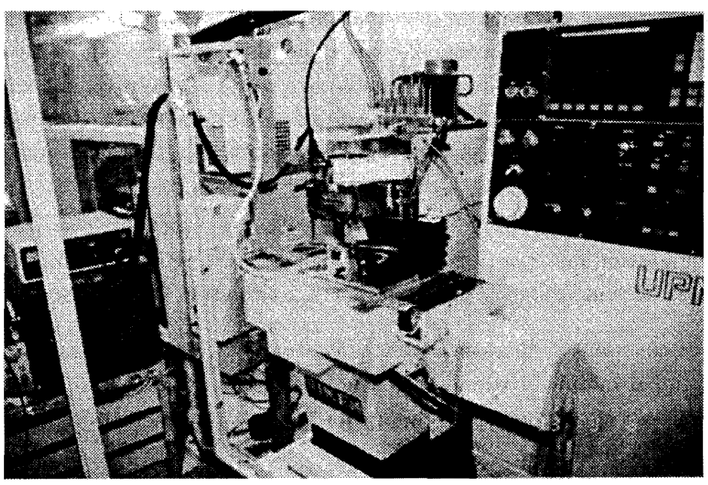

Figure 9.23: *Precise milling machine installed at KEK.*

Cell Machining

A schematic drawing of the regular cell is shown in Figure 9.24. This shape is common for all of the cells used for detuned structures.

Regular cells are machined according to the following procedure:

1. Slicing a round plate from a 0.5m-long copper bar of ϕ82 mm in diameter.

Machine type Company	Units	Turning machine Nihon Seiki Lab.	Turning machine Toshiba machine Co.	Milling machine Riken Seiko Co.
Max workpiece diameter(mm)	mm	ϕ 100	ϕ 100	150×200
Work spindle revolution speed#	r.p.m.	300-3000	300-3000	200-8000
X-axis stroke	mm	150	150	200
Y-axis stroke	mm			150
Z-axis stroke	mm	100	100	100
Positioning resolution	μm	0.1 †	0.01 †	0.1 ‡
Positioning accuracy	μm	0.2	0.1	<1

† in (X,Z) ‡ in (X,Y,Z) # all air spindle

Table 9.10: *Three machines installed at KEK.*

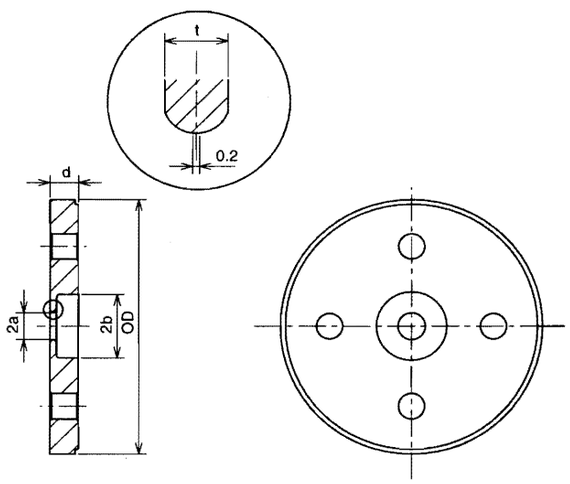

Figure 9.24: *Schematic drawing for the regular cell. The shape for the detuned structure is essentially the same. OD is 80mm and d 8.7474mm. In the middle of the beam hole, the shape is flat in the cross-sectional view. This is to make sure that the connection from the curved section to this flat, 0.2mm-long section can be with a finite angle so that the burrs etc. can be minimized.*

2. Cutting with oversize dimensions by 100μm using ordinal CNC turning machines.
3. Drilling water-channel holes.
4. Annealing in a vacuum at 500°C for 1 hour.
5. Hand lapping of one side.
6. Cutting with oversize dimensions by 50μm using a turning lathe in the high-precision machining lab.
7. Annealing in a vacuum (500°C for 1 hour).

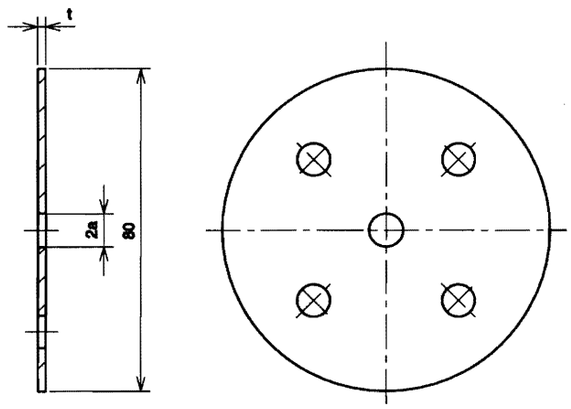

Figure 9.25: *Schematic drawing for the disk for a detuned structure.*

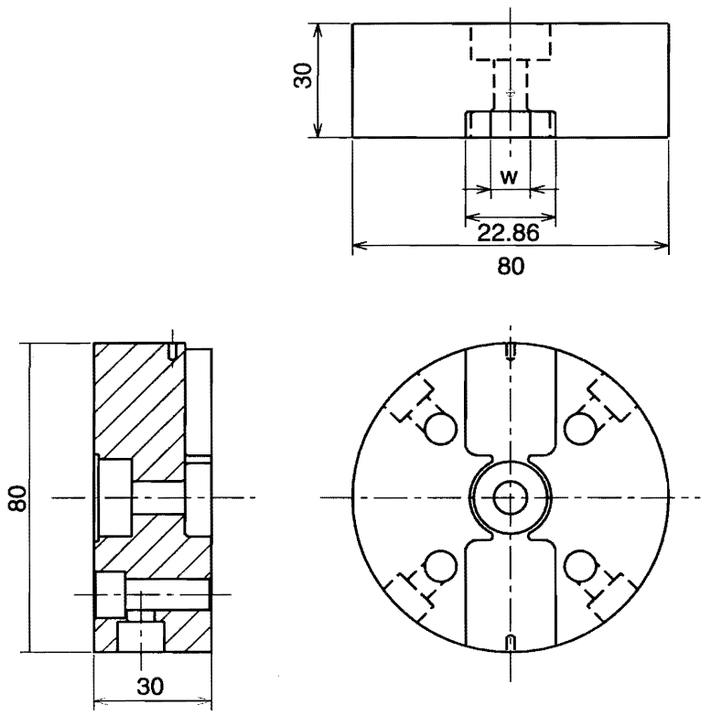

Figure 9.26: *Schematic drawing of a coupler cell for a detuned structure.*

8. Test cut a similar dummy cell targeting the same outer diameter and compare the OD with the reference cell.

9. Based on the above comparison, adjust the tool positioning if necessary.

Measurement item	Company	Type	Resolution
Surface interferometer	Zygo	Mark-II	0.01 μm/ϕ 100 mm
Roundness tester	Tokyo Seimitu		0.05 μm/ϕ100 mm
Roughness	Rank Taylor Hobson Inc.	Talystep	vertical 0.5 nm
			horizontal 0.2 μm
CCD camera	Keyense		magnification $\times$1000
			resolution 1μm
Gap distance	A.D.E.	Microsense	0.03 μm

Table 9.11: *Specifications of the measuring machines commercially obtained at KEK.*

10. Final turning.

11. Frequency checking using the choke mode set up (Figure 9.42).

In the procedure of cell machining, flatness is very important for achieving good diffusion bonding. Therefore, the heat-treatment process is performed twice in order to eliminate any stress acquired when the cell is roughly machined. The flatness of a roughly machined cell is on the order of 1μm for 80mm in diameter. This flatness is corrected by hand-lapping on an optical flat. The shape of the vacuum chuck has been carefully designed, because even a lapped surface is not sufficiently flat for the following machining. After various trials, the deformation of the cells due to vacuum chucking was reduced by using a chuck where the contact area was reduced by only keeping the groove at the outer most circle.

While cutting cells, the operator is outside of the constant-temperature booth. However, the temperature of the cell on the machine changes due to the exposure of the cell to the cutting oil. This was studied. The tool-positioning error due to the warming-up time of the turning machine was also studied. By carefully checking the temperature of the cells and making a comparison of the OD's, these temperature effects can be practically compensated.

A schematic drawing of the coupler cell is shown in Figure 9.26. Machining of coupler-cells requires almost the same procedure as that of regular cell processing, except for the iris region. The iris is machined by using a milling machine with an artificial diamond tool. The use of an artificial diamond is due to the long tool needed to meet the height of the wave guide and the associated expensive cost when applying a natural diamond there.

Dimension measurement

In order to verify the machining accuracy, non-contacting instruments for measuring the dimensions (a, b, d and OD) of the machined cells have been developed. A picture of the field-emission ultra-micrometer is shown in Figure 9.27. The specifications of the measuring machines commercially available are given in Table 9.11.

The d is simply measured by setting the cell on and removing it from the flat base and comparing the height with and without the cell by measuring the height by a *Microsense*.

The OD is measured as follows: First the cell is moved between two *Microsenses* facing each other, and the sum of the two gaps between the cell and the *Microsenses* is measured. Then, the same measurement is performed for a reference cell. The difference of the two measurements becomes the relative measurement of OD.

On the other hand, the inner diameter, such as a and b, is measured by moving a small metallic ball inside the cell. By applying several volts between the ball and the cell the field-emission current between them can be detected when they almost touch. The maximum position is recorded for both sides of the cell. The difference of the recorded values plus the diameter of the ball becomes the inner diameter of the cell. The dimension of the ball is calibrated by measuring the length of the known precision block gauges using the same system. The typical resolution of this kind of tool, which is called "Field Emission Ultlramicrometer"[17], is 10 nm. The accuracy of the system is limited by the accuracy of the block gauges, and is about $\pm 0.2\mu$m.

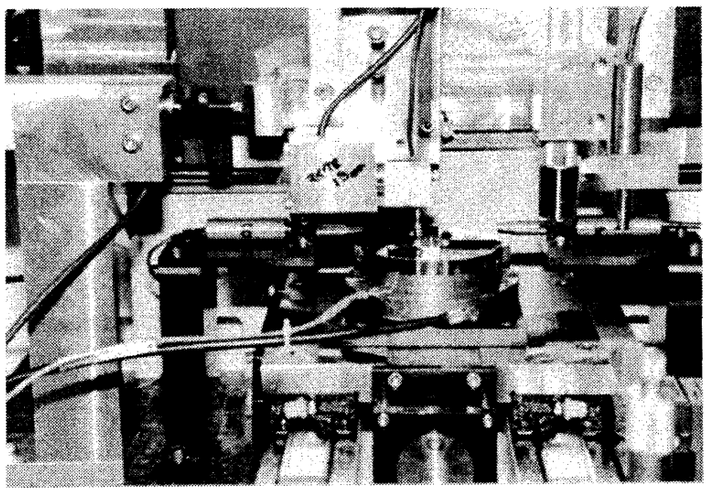

Figure 9.27: *Field-emission micrometer developed at KEK with a metallic ball sensor in a cell to measure "2a" and "2b". The "OD" is measured with two microsenses facing each other. The cell length ("d") is measured with a microsense facing downward.*

For studying the surface quality, a surface interferometer, a roundness tester and a roughness measuring machine were used. These machines are commercially available, and are listed in Table 9.11.

The width of the irises is measured by using a milling machine. A high-resolution CCD camera is attached to the head and optically determines the position in the (X,Y) plane. This measurement is also used for determining the diameter of the tool.

Confirmation of Machining Method

The diameter (OD) is the dimension used as a reference which determines the tool positioning. In this sense, it is the key parameter for the dimension control in machining. The dependence of OD on the temperature during machining has been tested. Figure 9.28 shows the measured relation between

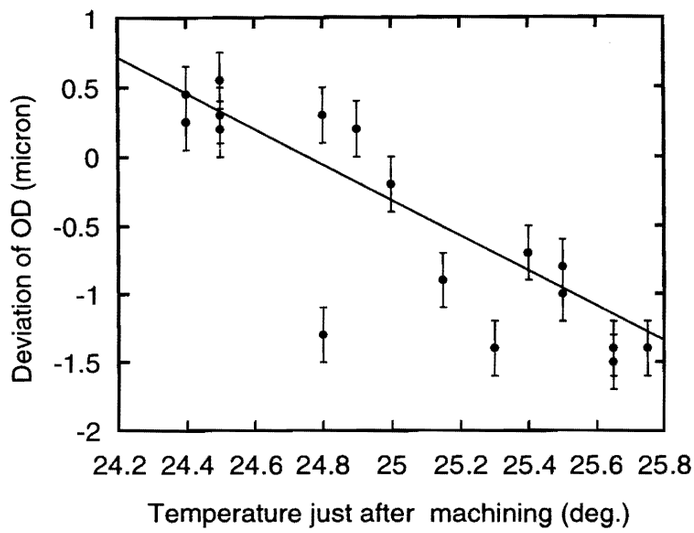

Figure 9.28: *Measured OD versus the temperature of the cell just after machining. The solid line shows the thermal-expansion coefficient of copper. Note: The data were taken during an early stage of the machining study. Therefore, the points largely deviated from the line are believed to be due to some other effects than the thermal expansion of the cell, itself. Such effects were controlled in the actual machining stage, as is described by the examples shown in the present paper.*

the temperature and the OD's of the machined cells. The error includes the machining errors and tool-positioning error. Even if there are some exceptions, a monotonic decrease as a function of the cell temperature can be clearly seen. The average slope of -1.3μm/°C is just the same as the thermal-expansion coefficient of copper. This effect can be corrected in advance by estimating the temperature of the cells under machining if the cause has a slowly varying origin, such as the variation in the ambient temperature change within one day.

In order to prove the reliability of the accurate relative movement of the turning machine, four cells were machined while varying the $2b$ dimension in 0.1μm steps. The $2b$ of these cells was measured using the field-emission micrometer, and the frequencies of these cells were also measured using a network analyzer and the set up shown in Figure 9.42 (to be discussed more in later sections). The results are given in Figure 9.29. From the relationship of these measured values, the relative controllability of $2b$ in the system was found to be about $\pm$0.1μm.

Several hundred cells were machined using one of the two turning machines, and the error character-

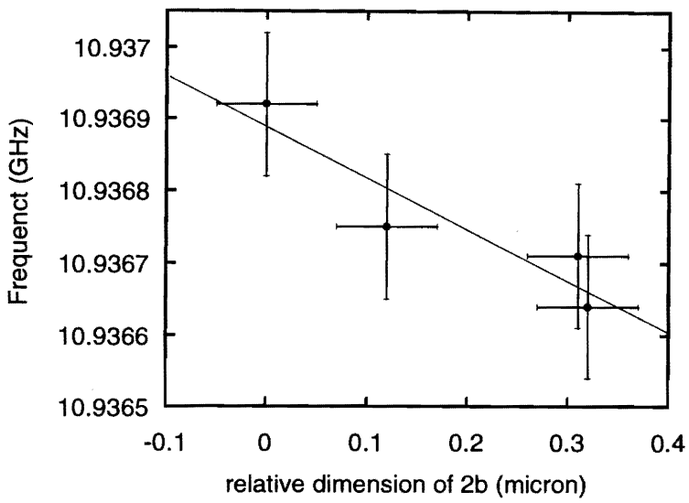

Figure 9.29: *Frequency change due to a change of "2b". The cutting was performed to vary only dimension "2b" in 0.1μm steps. The data were found to be consistent with a sensitivity of df/d2b=-0.6MHz/μm.*

Turning machine	Nihon Seiki Lab. Co.
Spindle revolution freq. (r.p.m)	1400
Feed speed (mm / min)	11.2
Cutting tool	natural single crystal diamond (R=0.4mm)
Cutting oil	temperature controlled pure kerosene
Material	OFC HITACHI class 1
Pre-treatment	500°C 1hour stress release

Table 9.12: *Conditions of test machining.*

istics of the machining using the machine was investigated. The test-machining conditions are listed in Table 9.12, and the results are listed in Table 9.13. All of the tolerances were cleared, except for the flatness. The flatness is possibly affected by such issues of the machining configuration as the material stability against stress release, the effects of the hole at the center of the cell and so on.

	Units	Tolerance	Obtained
Surface roughness Rmax	μm	0.02	0.03
Flatness over ϕ80 mm	μm	0.1	0.3(mean average)
Roundness	μm	<0.1	0.1
Absolute dimension at ϕ20 mm	μm	<0.2	0.4(mean average)
Relative error in $OD(\phi 80$ mm)	μm	<0.5	$\pm$0.5

Table 9.13: *Results of the test machining of cells.*

Cell fabrication for a 30cm constant-impedance structure

In order to establish the basic machining technologies in cell machining and to study the bonding characteristics, three 30cm-long accelerating structures were fabricated. Figure 9.30 shows a schematic drawing of the structure. The structure consists of 32 regular cells, a disk, an input and an output coupler cell with two taper wave guides, two beam holes and four cooling channels.

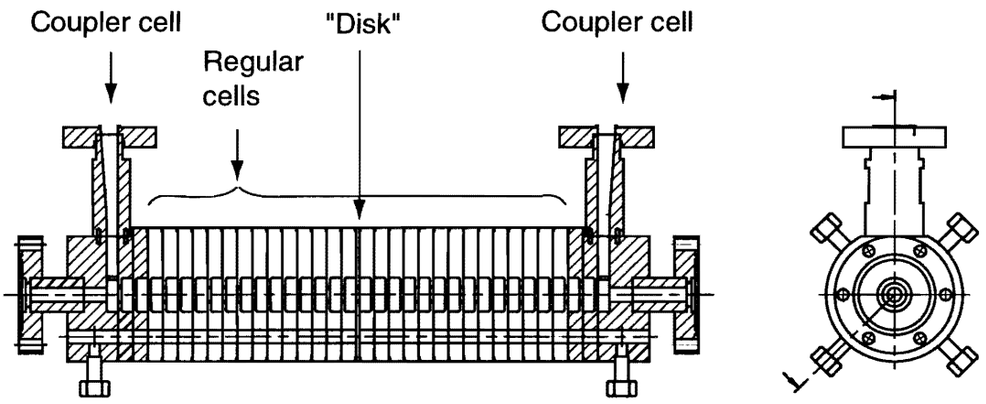

Figure 9.30: *Drawing of a constant-impedance accelerating structure with a 30 cm length.*

Schematic drawings of the regular cell, the coupler cell and the disk are shown in Figures 9.24, 9.25 and 9.26.

As shown in Figure 9.30, disk in the middle is necessary for reverting the direction of the regular cell in the z-direction so that the same type of coupler can be adopted.

In one of three structures, the outer diameters and the cell frequencies of all of the cells were measured. The results are shown in the histogram in Figure 9.31. The full width of OD was $\pm 0.6 \mu$m and the full width of the frequency was ± 0.2 MHz. The characteristics of the machining for the other structures showed almost the same machining-error distribution. From these cell fabrications, it was found that the most important issue in machining is the thermal stiffness of the machine.

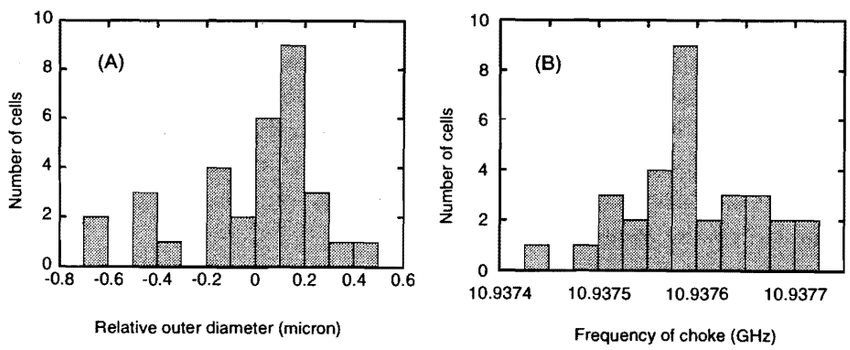

Figure 9.31: *Histogram of (A): outer diameter of cells and (B): frequencies of cells.*

Cell fabrication for 1.3 m DS structures, (M2 and IH1)

A schematic view of a 1.3 m detuned structure is shown in Figure 9.32. The structure mainly consists of 148 regular cells , one disk and an input and output coupler. Each cell in a structure has a different dimension of "a","b"and "t". Based on the procedure that was established in the fabrication of the 30 cm structures, three full-size structures were machined. The cutting conditions were the same as that for the 30cm structures, except for that the dimension of the cell was different from cell to cell. A system has been developed where a computer supplies all the information necessary for each cell.

Rough machining with the 100 μm over-sized dimensions was performed utilizing an ordinary machining center; a batch of 50 regular cells were mounted on a working table of the machining center. Then, these cells were machined one after the other.

The final machining accuracy can be seen indirectly in Figures 9.49 and 9.50 of Section 9.3. From Figure 9.49, the deviation in the frequency of the $2b$-sensitive measurement can be observed; the shape of deviation is like a sine wave as a function of the cell number. Since almost all of the cells were machined in the order of cell number, the deviation pattern shows a daily variation throughout several days. Cell machining is interrupted during the night, and then every morning much time should be devoted for the idling of the machine and setting the tool position again. From time to time, during the machining in one day, outer diameter of the newly machined cell was measured. This value was used to compensate the change of the cell size and machine distortions arising from the temperature change. As a result of machining, uncontrollable dimension were about ± 0.5 μm by using present turning machine and present environment conditions.

Cell Fabrication for 1.3m DS with Shallow Channels, (M1)

Before making the above DS structures, a full-size structure, called M1, with the regular cells shown in Figure 9.33 was fabricated. As shown in the figure, the cell has four coupling slits for higher modes connected to the four independent manifolds. This type of structure gave us some experience concerning the machining of the slots. The iris facing the cell is cut in a μm tolerance to keep the accelerating mode frequency under control. This shape can be applied to the DS if the vacuum level is poor in the simple DS and additional pumping channels are needed. Through the production of these cells, it was studied how to adjust the position of the slots with respect to the cell. This technique is applied in a straightforward way to the machining of the DDS cells mentioned below.

Cell fabrication for DDS for SLAC

Under the collaboration between KEK and SLAC, an opportunity to conduct fabrication studies for the DDS structure was presented. KEK has made two DDS structures for SLAC. Figure 9.34 shows a schematic drawing of the cells for the DDS structure. The most essential difference from that of the DS is that there are four radial slots which meet the accelerating cell. Required the machining tolerance of the slots was relatively relaxed at ± 20 μm.

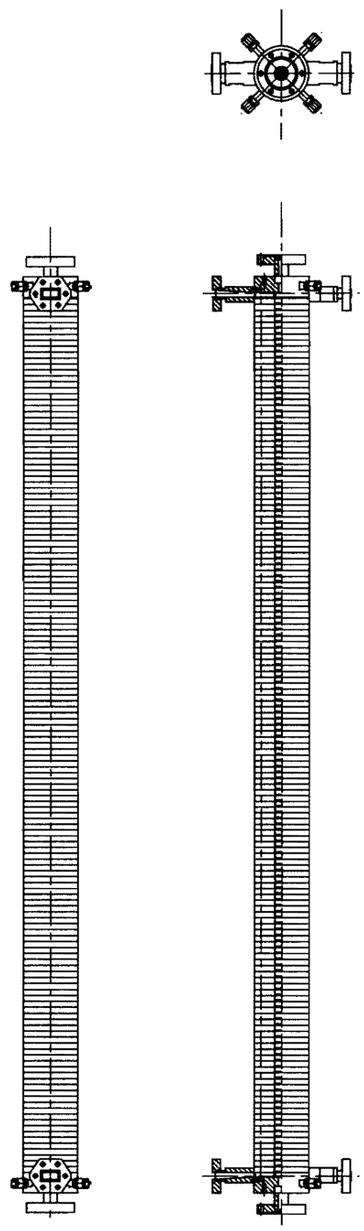

Figure 9.32: *Configuration of 1.3m detuned structures, 'M2' and 'IH1'.*

The milling of the four slots was performed after rough machining and a heat treatment at 500°C for one hour. A horizontal-type CNC milling machine was used with a turn table which mounted a hexagonal block. Six palettes were attached to each six surfaces. On each palette 12 cells were set. Because the slots of each cell have different dimensions from cell to cell, a personal computer was

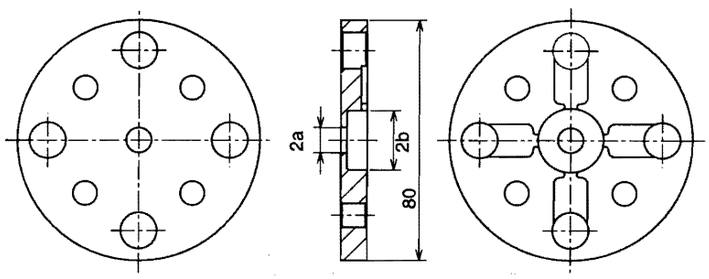

Figure 9.33: *Schematic drawing of the regular cell for "M1".*

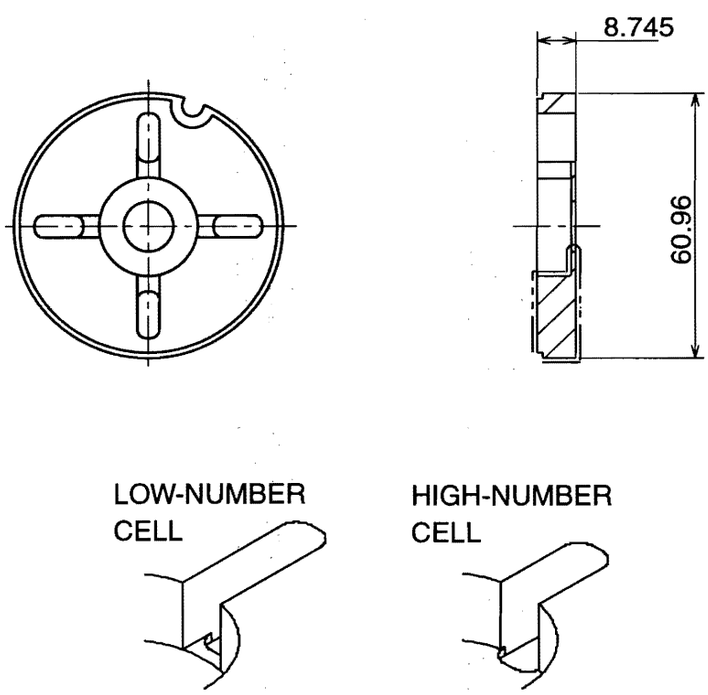

Figure 9.34: *Schematic drawing of the DDS cell.*

utilized for automatically generating the machining data. Figure 9.35 shows a conceptual drawing of such equipment.

Through the machining of two DDS structures at KEK, it was found that a fairly large amount of burrs remained at the edge of the slots. Since there is a possibility for them to drop into the accelerating cavity, it is necessary to remove all of the burrs before bonding. At KEK, the burrs were initially remove by hand using a knife. However, a plastic deformation around the slots was formed. It is not good for such processes as stacking and bonding.

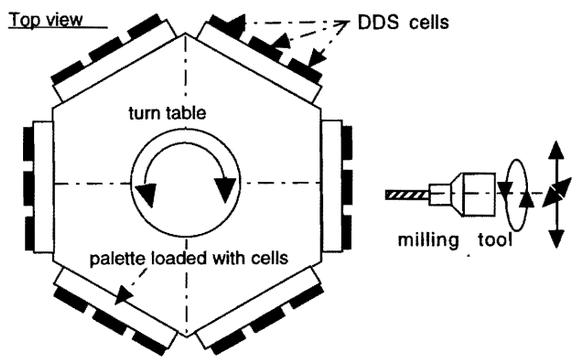

Figure 9.35: *Conceptual drawing of the slot-machining technique for the DDS cells.*

Condition	Chemical polishing	Electrical polishing	Water jet
Reaction fluid	Top Gruppe Cu8-M †	chromic acid anhydride 115 g/l	pure water
	phosphoric acid 22%	phosphoric acid 724 ml/l	
		water 232 ml/l	
Current density		350 mA/cm^2	
Processing time	4 minutes	4 minutes	2 minutes
Pressure			75 Kg/cm^2
Etching depth‡	10 μm	10 μm	

† Commercial name supplied by Okuno Drug Co.
‡ Measured experimentally.

Table 9.14: *Various processing methods studied for removing burrs.*

Three methods have been studied to remove burrs: chemical polishing (CP), electrical polishing (EP) and mechanical removing by using a water jet (WJ). The test conditions are listed in Table 9.14. In the cases of the CP and EP, some of the burrs still remained. In addition, many etching pits were generated. These two chemical process were found not to be suitable for burr removal.

On the other hand, high-pressure water-rinsing removed the burrs almost completely. Figure 9.36 shows a conceptual drawing of water-jet processing. This system was originally built for super conducting cavities. The surfaces of the cells were covered by masking with a film except for the burr region, in order to protect the other surfaces than that of the area of the burrs. This pure water jet is not only effective for removing burrs, but is also good for surface cleaning of cells[19]. The exposure point to a water jet should be controlled this time by hand.

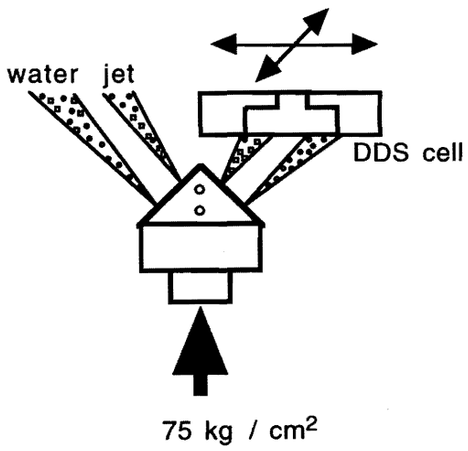

Figure 9.36: *Water-jet processing to remove burrs.*

9.2.2 Design consideration for the mass production of cells

The technique of cell fabrication for an X-band accelerating structure has already proved to be at a realistic level to meet the present machining tolerances. Beyond the currently studied fabrication programs, the important items to be further developed are such as "quality control" and "cost reduction". To realize these, a completely automated factory for the final machining of cells should be built. Therefore, it is necessary to develop some new techniques, as follows:

- Auto-loading techniques in each process of cells.
- On-machine measurement of the required dimensions.
- Diagnostic system for diamond tool conditions.

In such a factory, a number of high-precision diamond-turning machines are needed. Therefore, such developments as

- Inexpensive CNC
- A small diamond turning machine dedicated to cell machining

should be developed.

Let us consider the requirements for the cutting speed. The number of cells necessary for 7000 structures at E_{cm}=500GeV is more than 1 million. Suppose that this number of cells must be machined within 3 years. If we assume 250 working days per year, the number of cells to be machined in one day amounts to 1400, or 1cell/minute.

On the other hand, the present machining time for the final machining of a cell is about 35 minutes, including the time for chucking, concentricity adjustment and re-chucking. It also includes a fairly large amount of the positioning time of the diamond tool on the slide table due to the present poor servo system for positioning. If a linear movement guided by double V-grooves with a hydro-static bearing or a needle bearing is applied, the tool-positioning time can be extremely reduced. In the present turning machine one minute is needed as the tool-positioning time every time the direction of the movement is changed.

Another factor is the cutting speed. The theoretical limitation of the cutting speed for the copper material is 100~200 m/sec. Although the present work spindle rotates at 2800 *r.p.m.* the revolution speed of 3500 *r.p.m.* is considered to be reasonable for the current spindle technique. If this high speed rotation is adopted and the feed speed of the cutting tool is chosen to be 34 mm/min, the time and cost will be greatly reduced compared to the present condition. Here, the theoretical roughness is still kept at an peak-to-valley value of 30 nm.

In this case, the net cutting time of one cell can be reduced down to 10 minutes. If an auto-loading system and auto alignment of the cell on the vacuum chucking is developed, the total time for a cell is estimated to be 15 minutes.

Since 15 cells should be made in one minute, the number of high-precision diamond turning machines should be 15. A few spare machines will be needed, estimating a working efficiency of 85% in one day. The loss time is for the tool-exchanging time, cleaning time on the vacuum chuck and so on. A few milling machines should also be installed.

The rough and medium machining of the cells are not technically critical, because ordinary CNC turning machines already satisfy the required machining accuracy. Thus, many companies worldwide can perform the task within a fairly short time, inexpensively.

Finally, but not the least, the initial shaping of the OFC copper material should be discussed. The original shape of the copper material usually supplied at present is a bar or sheet. A bar has an advantage that the stress and strain distribution are in the radius direction. However, the slicing process is not a reasonable technique for mass production due to the following reasons. The present method of slicing is sawing. It takes much time and the cut surface has a low quality, especially regarding flatness. Therefore, a fast slicing technique which makes a flat surface should be developed.

On the contrary, the shaping of the cell from a sheet material by a stamping method might be a quick and good method for later precise machining.

However, a shaping from a sheet has disadvantages concerning the stress and strain distributions, which are not in a radial direction. When shaping a sheet from an ingot of copper material, the material should be extruded several times through rolls. The orientation of the stress and strain is determined by the rolling process. Therefore, there is a possibility of uncontrollable deformation to remain due to the rolling process, even after the final machining of the cell. Considering these issues, the machining of the cells from a sheet material should be studied. A press-shaping technique has already been briefly studied. Although it seems to be very hopeful, the pros and cons of this processing are not yet clear. Therefore, the technique should also be studied.

9.2.3 Cell-handling and -cleaning Process

The machining oil should be removed before the subsequent process. Especially before the bonding process, the surface should be cleaned to realize the copper-to-copper contact as easily as possible. Chemical cleaning using a weak acid, for example rinsing in a bath of 3% H_2SO_4, is used at present. The cleanness in the drying process is important, after such a chemical wet process to make it dust free. The dependence or tolerance of the cleanness on the performance of bonding and vacuum characteristics should be studied quantitatively, before going into mass production.

Since the outer diameter is used for a precise alignment of the cells, the surface should be preserved well. The automated process is inevitable not to introduce scratches and bumps, which would result in a bonding failure.

9.2.4 Structure Assembly

Cell Stacking

It is possible to make a Vee-block with a straightness of a few μm over a 2m length. The possible deviation from a straight line is usually a smooth function. If the cells can be aligned with respect to this V-block and if the cell-to-cell slippage during the bonding process is not significantly large, the structure becomes straight, or can be straightened at the last step of fabrication, or even during the alignment after installation. Considering these points, the present stacking is performed by pushing the cells against a Vee-block.

Two stacking methods have been tried for studying the stacking technique; one stacking vertically and the other horizontally. These were applied for the two structures, M2 and IH1, described in the following section. The vertical stacking method is shown schematically in Figure 9.37, while the horizontal one is shown in Figure 9.38.

The Vee-block was placed on a precise granite plate in a horizontal stacking method. The granite plane and one of the side walls of the Vee-block was used to make a reference line to measure the alignment of the stacking.

It is very important to measure the alignment of the cells along the structure in order to study the feasibility of these alignment techniques. However, the present level of measurement needs an improvement, because the measurement reproducibility and the accuracy were limited as follows:

- reproducibility $\pm$ 0.5 μm
- accuracy $\pm$ several μm or more.

These should be improved by a factor of 2$\sim$3, especially the latter (the accuracy). A better alignment mechanism should be developed for improved alignment accuracies. For this work, it is highly desirable to build an additional few more test structures.

Cell Moving and Setting in a Furnace

After stacking, the assembly should be moved to a furnace where a high-temperature bonding process takes place. The stacked cells are held with some moderate axial pressure, so that the slippage of individual cells during subsequent works is avoided.

9.2.5 Bonding

It is very essential to maintain the design distribution of the dipole-mode frequencies of the detuned structure. The cells can be accurately machined as described in the previous section. Then, they are

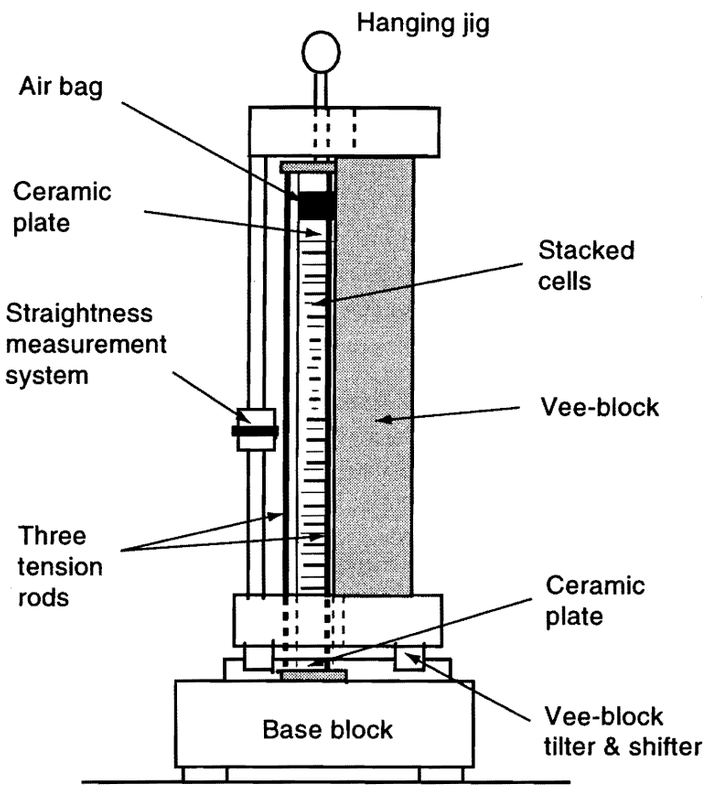

Figure 9.37: *System for the vertical stacking of the cells for 'M1' and 'M2'. The cells are aligned against a vertical vee-block. The alignment of the cells is measured by two microsenses set on a plate which runs along the two air slides. After stacking, the cells are axially pushed by an air bag. Then, the vee-block is tilted away from the cells and the cell assembly is hung up.*

to be bonded to form a vacuum-tight RF structure. This process usually requires a high-temperature process, so that the frequency distribution can easily be perturbed unless the process is carefully controlled.

In the early stage of the study, our usual silver-brazing technique, BAg-8 at slightly above 800°C, was studied in order to investigate whether brazing is feasible or not. From a series of test brazing operations of a few to several cells, it was concluded that the brazing technique which we had in our hands then did not satisfy the requirements for the DS[18]. Some of the potential difficulties of the brazing method are discussed below:

- Gap or groove for the brazing material, sheet or wire, makes the deformation large.
- Brazing material may run into the cell.
- There needs to be a procedure for setting the brazing material.

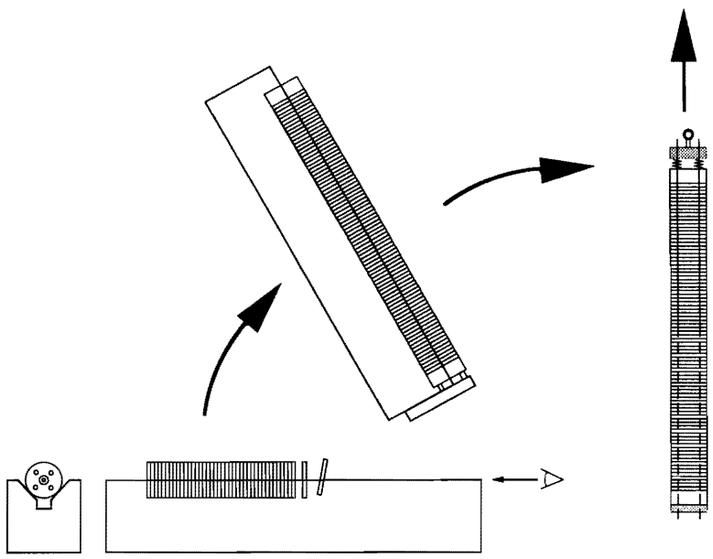

Figure 9.38: *System of the horizontal stacking of the cells for 'IH1'. The cells are aligned on the horizontal vee-block. The alignment of the cells is measured by a microsense guided along the two surfaces in the vee-block and the granite plate. After stacking, the cells are axially pushed by ceramic springs. Then, on the base of the furnace, the cells are rotated with the vee-block to almost the vertical position. and extracted up from the vee-block. The assembly is hung up in the furnace.*

- It should pass the liquid phase, which might make the cells floating and slipping.
- A very smooth surface may not be good for reliable brazing.

To overcome all of these points, direct diffusion bonding between the flat surfaces became a reasonable research direction.

To study the feasibility of this technique, a series of bonding tests were performed. Bonding parameters, such as the temperature, contact pressure, surface flatness, surface cleanness and period at high temperature, were considered to be important.

Consider that two copper bodies contact each other. If the facing surfaces are flat on the atomic order, and if the surfaces are neither oxidized nor contaminated with some other chemicals, the two surfaces naturally disappear as soon as the distance between them becomes within the Van der Waals force, resulting in an almost perfect bonding of the two bodies. It should be noted, however, that the actual copper material is polycrystal. Therefore, the directions of the crystal axes change from crystal to crystal between the bonding surface. In this sense, many defects concentrate over the bonded surface. The bonding cannot be practical without removing those defects.

More seriously, the actual surface of the machined cell is oxidized in addition to having the surface contaminations and many defects. This oxidized layer will become disintegrated by making the temperature high and the surrounded vacuum level low. The latter method is not very adequate after stacking, because the vacuum conductance through the gap between the two cells is very small. However, the oxidized copper disintegrates and the dissociated oxygen at the surface migrates into the copper body. This mechanism makes it possible to make a copper-to-copper diffusion bonding.

If some diffusion process starts from contacting points, which are scattered on the two surfaces, the external axial pressure makes the plastic deformation of the non perfect flat surface. High temperature and high pressure are expected to promote diffusion. However, they tend to induce deformation of the cells during the bonding process. Flatter surface makes the bonding quicker and with less deformation. Clean surfaces make the copper atoms easier to diffuse into the other side.

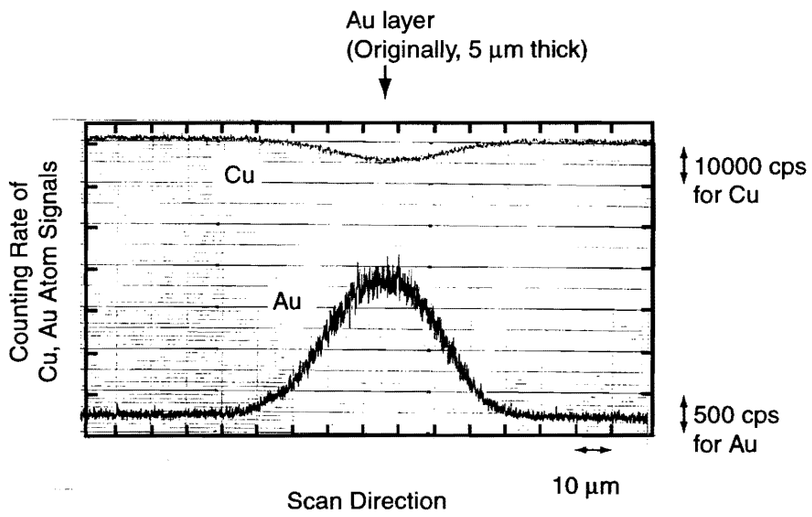

Figure 9.39: *Evidence for the diffusion of gold atoms into a copper material through a 890°C 30 min diffusion process between a copper surface and a gold-evaporated copper surface. The original thickness of the gold film on the copper body was 5μm. The scanning was performed by an X-ray micro analyzer EPMA at an electron energy of 20 kV. The beam spot size is a few μm. The upper and lower curves show the signal counts for copper and gold atoms, respectively (arbitrary scale).*

Such a plating as gold or silver is preferred for the dissociation of the oxygen atoms from the surface if the free energy of the chemical reaction is considered. However, as stated above, it was finally found that the copper-to-copper direct diffusion bonding works fairly well. As a byproduct of the early studies on the diffusion bonding between gold-plated copper surfaces, an evidence of mutual diffusion of atoms crossing the junction was observed. An evidence of the diffusion of gold atoms into the both copper body is clearly seen in the X-ray micro analysis shown in Figure 9.39. The diffusion proceeded symmetrically into both sides, even though the gold film originally existed on only one of the two copper surfaces. The amount of diffusion was found to be roughly consistent to that expected from

the diffusion length (x(m)), as in the following formula:

$$x = 3.6\sqrt{D_0 \exp(-\frac{\epsilon}{kT})\, t}, \tag{9.18}$$

where D_0 is the diffusion constant (3.1×10^{-6} m^2/sec), ϵ the activation energy (1.8 eV), T the absolute temperature, k the Boltzmann constant and t the period at a high temperature in seconds. The estimated diffusion length as a function of the period at a high temperature is shown in Figure 9.40.

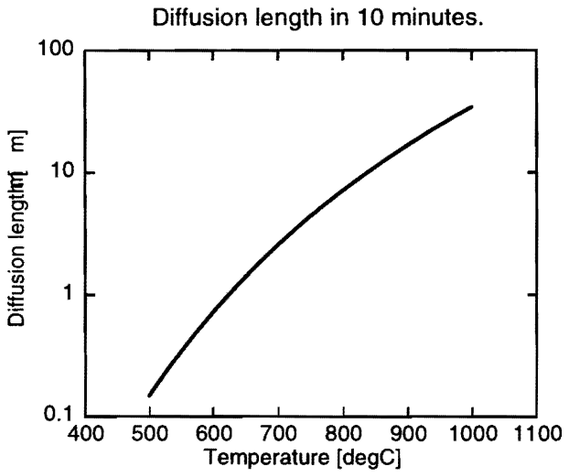

Figure 9.40: *Estimation of the diffusion length in 10 minutes. The estimation was performed by equation 9.18.*

The bonding temperature was chosen, temporally, based on the following consideration.

Generally, if the flatness of the cells is in the range of a few tenths of a micron in our usual cell-machining quality, the diffusion bonding at the temperature of 700°C or higher is required to achieve reliable vacuum tightness.

However, a higher temperature results in a larger deformation; thus, for a smaller deformation a lower temperature is preferred.

The example shown in Figure 9.41 shows the case where the bonding was done at 750°C. The observed deformation was on the order of a few tenths of one MHz. This deformation is much smaller than in the cases of bonding at 800~900°C or higher, which usually results a frequency change on the order of a half to one MHz.

However, it should be noted that the machining of the cells for the structure of Figure 9.41 was carefully performed, the cell flatness was better than 0.5μm and the surface roughness was better than that in our more typical cases of 0.05μm. Thus, we cannot exclude the possibility that this good cell quality is mainly responsible for the good result.

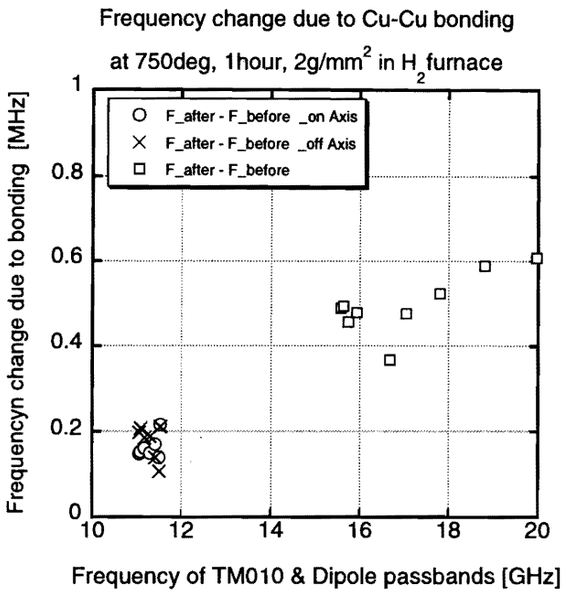

Figure 9.41: *Change of frequencies in a 5-cell stack due to diffusion bonding at 750°C, 1 hour. The data lower than 12GHz are those are for the modes in the TM110 passband. Those from 15 to 20 GHz are those of the modes in the first and second dipole pass-bands.*

In short, we have not yet established a solid set of preferred parameters at present for cases with temperatures lower than 800°C. Through a series of bonding experience on short accelerating-structure models, we set what we conceive is a reasonable temperature of the diffusion bonding at 800~900°C. Based on this temperature parameter, three full-scale prototypes have been built. However, still, it may be possible to lower the bonding temperature, so that the deformation due to the bonding will become still lower. This is one of the near-future study items.

9.2.6 Electrical Checking during Manufacturing

It is important to check the characteristics of the parts or assemblies in several stages of the fabrication. This is so as to ensure that fatal problems during the manufacturing process would not stay undetected until much later stages of work.

The first check-up is the "individual-cell checking" of the machined cells, because their quality, especially in their precision in dimensions, is essential to obtain a high-precision structure through the following processes.

The cells are stacked then on a straight vee with a moderate axial pressure. This assembly can be checked using such devices as plunger or bead. This measurement gives us the information on the quality of the assembling in addition to the individual-cell characteristics. The assembled cells can be checked right before the bonding, and the assembly can also be checked after bonding in just the same way. Therefore, the study on the bonding-related process can be studied in detail. The measurement with bead is good in the sense that the perturbation on the electrical properties is small comparing to that by plunger, where complete detuning in necessary for the cell with a plunger. The measurement with bead has not been studied experimentally at KEK but will be tried from the next structure fabrication. The measurement with plunger is preferred in some study cases, especially in the studies of individual cells or individual modes trapped in the mid-structure.

Final checking of the structure as a whole is performed by measuring the S-parameter from the input coupler to the output. These tools are described below in detail.

Individual Cell Checking

The cells just after being machined should be checked electrically for the purpose of confirming the machining and excluding any cells with defects due to mis-operation in machining.

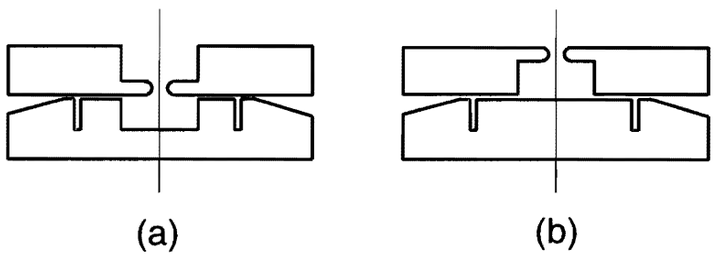

Figure 9.42: *Schematic cross-section views of the choke stand that is used to measure the characteristic frequency of individual cells.*

Since the greatest interest is in the accuracy of the accelerating mode, the mode with a similar field pattern as that of the accelerating mode should be measured. A choke stand, as shown in Figure 9.42, is used for this purpose. In this stand, the measurement in set-up (b) is mainly sensitive to parameter

"b", where that in (a) is sensitive to "a". The measured cell sits on three Teflon posts outside of the choke structure, and there is no metal-to-metal contact between the test stand and the cell, keeping a gap of 0.5 mm. It might be better to have a detuning cell on top of these assemblies, because of a large leakage of power through a large beam hole for the cells near to the input and output coupler cell.

Measurement with Two Plungers

For the purpose of studying the fabrication characteristics, it is useful to measure the pseudo-$\pi/2$ mode by using two plungers. Two plunger heads, each equipped with an antenna, sit at the cells adjacent to the cell of concern to excite the middle cell while detuning the adjacent cells. The S-parameter from an antenna to the other was measured to determine the frequency and the Q values. The position of the plunger is referenced from the mechanical reference of the cells in order to compare those before and after the bonding. This procedure has a precision of about 0.1 MHz.

Measurement with One Plunger

It is difficult to measure the cells with the above-mentioned method if the structure length becomes more than a meter. In this case, a plunger is used to measure the RF wave originally input through the coupler cell, but reflected by the plunger. A stainless pipe of 5 mm in diameter and 0.5 mm in thickness is used. The system can be set horizontal. It is bent upwards before setting horizontally, and its transverse positioning was checked by moving through some dummy cells. This procedure ensures a stable plunger movement through the gap between the plunger and the smallest beam hole without touching.

The plunger is moved by a stepping motor and the position is measured by a ready-made linear scale with μm precision.

A typical measurement of the reflection phase versus the plunger position is shown in Figure 9.43. The dwelling point is obtained by fitting these curves as the point where the phase shift / movement of the plunger becomes minimum. The measured dwelling points were shifted from the mechanical cell pitch due to the varying ration of the plunger to the beam hole as a function of the position in the structure. The deviation from a simple linear line is shown in Figure 9.44. Since the deviation is fairly large, the mechanically determined points cannot be used as a reference to perform an electrical measurement. This behavior was reproduced by a simulation using an S-matrix formulation [20], as shown by the solid line in the same figure. All of the data used to measure the structure characteristics were deduced from the dwelling point determined as stated above.

It is thus difficult to measure the characteristics of the accelerating mode, such as the absolute frequency (or phase advance per cell), through this method. However, the measurement can be used to study the relative frequency change, etc. Once a reference data is taken from a known good structure, this system can be used for the final checking of the stacked cells before bonding.

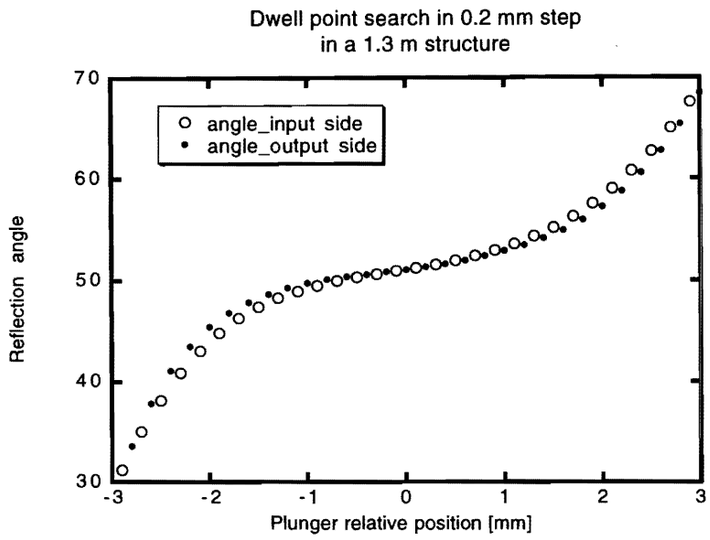

Figure 9.43: *Typical measurement result of the reflection phase versus the plunger position. The open (solid) circles are those of the case when the plunger is near to the input (output) coupler side.*

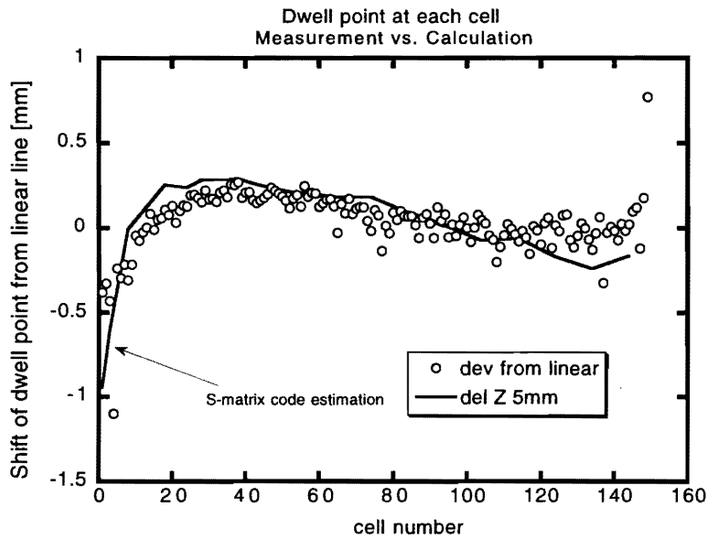

Figure 9.44: *Deviation from a simple linear-fit line of the data points in Figure 9.43. The open circles are those measured. The solid line is an estimation calculated by an S-matrix formalism.*

Because the RF power is almost completely reflected by the plunger, this measurement method sensitive to the geometry of the reflecting objects including the plunger and the surrounding-cell structures. Since the ratio between the plunger diameter and the structure beam hole diameter varies along the

structure, the reflection condition also varies. To overcome this difficulty, such a measurement as bead pulling should be performed to evaluate various characteristics. It is now being planned.

Bead Measurement

In order to measure the absolute frequency of each cell, a bead-pulling measurement should be performed. This gives at least information concerning the accelerating mode. A system is now planned to be built at KEK.

Even in the mass-production stage, the measurement on the accelerating mode is useful to finally check the stacked cells. It should be carefully performed to make the thread for the bead installed through the structure without allowing any dust to fall.

Although the system can also be used to measure the dipole modes, it is in the standing-wave mode by measuring the frequency shift due to the bead perturbation. If this works, the direct comparison of the calculation of the dipole mode can be compared to the experimental results. This should be tried until some method is established which is precise enough to estimate the wake-field within the required precision.

S-parameter Measurement

A simple checking of the characteristics of the structure as a whole is to measure the S-parameters, the reflection and transmission, of the accelerating mode through the input and output waveguide. This measurement is usually the final, but gross, check of the fabrication. However, this measurement can be performed even before the bonding, and can be used for checking as a whole in parallel to the measurement with a plunger or with a bead, as stated above.

9.3 Studies with Prototype Models

After studying a diffusion-bonding technique through test bonding of a few cells to a 17-cell stack, the basic parameter range of the bonding was determined. Several 30cm-structures of a constant-impedance type were made following this technique for establishing and evaluating the practical fabrication technique. The basic features of the bonding were studied through these fabrications, and are described in the following section.

After studying the fabrication technique in the 30cm-structures, three full-scale detuned structures were fabricated in order to investigate the issues related to the application to the full-scale ones. The structure has 150 cells. The first, called "M1", was designed to have four medium damping slits from the accelerating cell toward outside for the damping of the higher modes, as shown in Figure 9.33. After encountering severe problems in vacuum sealing, we gave up on this type of structure, and are now focusing on a purely detuned structure with regular cells, as shown in Figure 9.13 or 9.24. These detuned structures, called "M2" and "IH1", were made for the purpose of extending the present technology in aligning and bonding to the full-scale case. The wake-field of "M2" was measured at SLAC. The results are described in section 9.4.4. The structure is now waiting there for a high-power test in addition to a bead measurement of the accelerating mode. The out-gassing rate of "IH1" has been measured, and is described in section 9.5. The structure will be tested at KEK in a high power soon.

9.3.1 30 cm Constant-Impedance Structure

The typical parameters of the 30 cm structure are listed in Table 9.15. The value $a/\lambda = 0.16$ is set to be almost the same as that of the full-scale detuned structure.

Five structures were made for studies of various ideas concerning the bonding method. Some of the conditions and the results of the fabrication are listed in Table 9.16.

The Q values were obtained from the measured total-attenuation parameters. In the present technology, reliable diffusion bonding should be made at a temperature higher than 800°C. The necessity or advantage of coating a gold film is not clear. At least, the copper-to-copper bonding seems to work well. The reason why the Q value of the #1 case is not good is not yet understood.

The frequencies ($\delta F_\pi/2$) of the monopole pseudo-$\pi/2$ mode, which has a similar field pattern as that of the accelerating mode, were measured by inserting two plungers from both ends to study the frequency change due to bonding. The change is as large as a few MHz in only four cells out of the 112 measured cells. Almost all of them except for those cells, were fairly stable within 1 MHz. Especially the low temperature trial, such as #4, showed an excellent stability of the frequency. This indicates the preference of low temperature bonding if it gives a reliable vacuum seal. This characteristic was discussed in the preliminary test bonding described in Section 9.2. As a typical example, the measured

Geometry	Symbol	Value	Unit
Beam hole radius	a	4.199	mm
Disk thickness	t	2.0	mm
Effective length (34 cells)	L	0.2974	m
Group velocity	v_g/c	0.038245	
Impedance	r/Q	12.218	kΩ/m
Shunt impedance	r	81.3	MΩ/m
Q value	Q	6657	
Attenuation parameter	α	0.470	neper/m
Total attenuation	$\tau = \alpha L$	0.140	neper
Filling time	T_f	25.9	ns
Surface field enhancement	E_p/E_{acc}	2.15	

Table 9.15: *Design parameters of the 30 cm constant impedance accelerating structure. (Assumed 100 % Q value.)*

Item	Unit	#1	#2	#3	#4	#5
Insertion		Au 2 μm	Cu-Cu	Au 1 μm	Cu-Cu	Ag
Temperature	°C	890	800	800	750 + ...	700
Period	min	10	60	10	60	60
Pressure	g / mm^2	10	3	5	3	3
Vacuum		OK	OK	OK	leaked	leaked
Δf (bonding)	MHz	$-0.5 \sim -1.0$	~ 0			
$\delta F_{\pi/2}$	±MHz	0.5***	0.7#	0.5**	0.4	
$\exp(-\tau)$	dB	-1.494	-1.273	-1.31		-1.42*
Q/Q_{cal}	%	81	95	93	82	86*
Delay	nsec	26.4	26.6	26.4		26.2
Q_{ex}	coupler	58	59	58		
$\delta\phi$	± deg		1 deg	1.2 deg		
VSWR		1.29	< 1.05	1.15		2†

† Due to the frequency change by the inflow of brazing material into a coupler cell.

\# The scattering around a linear dependence along z is ±0.4MHz.
Just after diffusion bonding

* Two exceptional cells (+2 MHz, −4 MHz) out of 28 cells.

** Two exceptional cells (< +1.5 MHz) out of 28 cells.

Table 9.16: *Characteristics of several 30cm structures made by using the diffusion bonding technique, but under various bonding conditions.*

frequencies for the case of #2 are shown in Figure 9.45. The figure also indicates the possibility of a gradual change in the frequency as a function of the vertical position in a high-temperature furnace.

However, in no other cases was such a systematic change observed as the cell number. This effect should be examined in the full-scale structure.

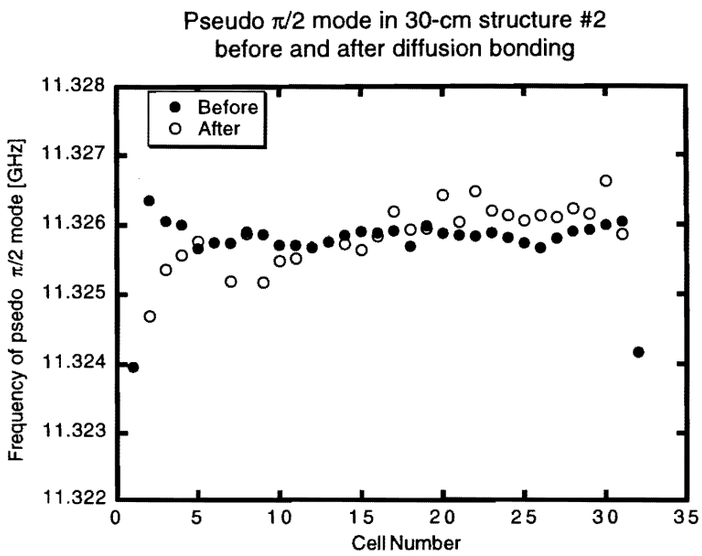

Figure 9.45: *Frequency of the pseudo-$\pi/2$ mode of a 30 cm structure. The crosses are those just after machining and the open circles after diffusion bonding and the final brazing.*

Structure #2 has been tested at high power up to 50 MV/m as of now without any troublesome features. It is still waiting for further conditioning.

9.3.2 1.3 m Detuned Structure

Based on the technology obtained in the 30cm structures, three full-scale structures were fabricated. Detailed descriptions of the fabrication procedures for three structures are listed in Table 9.17. In Table 9.18 are listed typical characteristics obtained in the three structures.

Item	M1	M2	IH1
Shape	Fig. 9.32	Fig. 9.27	Fig. 9.27
bonding	diffusion	diffusion	diffusion
temperature	800°C	850°C	890°C
period	1 hour	4 hours	10 min.
weight on top	16 kg	16 kg	40 kg
pressure at top cell	$3\,g/mm^2$	$3\,g/mm^2$	$10\,g/mm^2$
cell shape	four slots	DS	DS
cell / coupler machining	KEK / KEK	KEK / KEK	IHI / KEK
cell cleaning†	acetone in US	acetone in US	acetone in US
cell flatness	$< 0.5\mu m$	$< 0.5\mu m$	$0.4\sim1.2\ \mu m$
cell roughness	$0.05\ \mu m$	$0.05\ \mu m$	$0.05\sim0.1\mu m$
cell cleaning ‡	alkali soak	alkali soak	acetone
	H_2SO_4 3%	H_2SO_4 3%	HCl 3.5%
	pure water	pure water	pure water
	acetone→N_2 blow	acetone→N_2 blow	acetone 40°C
reference vee	vertical	vertical	horizontal
cell inclination check	none	none	autocollimator
fixing air gap	none	20 kg load	none
move to furnace	in-house 10m	in-house 10m	by truck ~30km
stacked situation	free in vertical	free in vertical	on horizontal vee
axial constraint	bolts, 16 kg	air spring, ~100 kg	ceramic spring, 40 kg
furnace	vacuum#	vacuum#	vacuum ##
position	vert. hang	vert. hang	vert. hang
hanging rods	four*	three**	four*
heater in furnace	carbon	carbon	carbon
temp. ramping rate	usual	slow$	slow$
diffusion bonding			
1st	800°C, 2 hrs, 16 kg	850°C, 4 hr, 16 kg	890°C ~10 min, 1 hr, 40 kg
2nd	850°C, 1hr, 16 kg		890°C, 1 hr, 40kg
3rd	820°C, 4 hrs, 60 kg		
4th	820°C, >10 hr, 60kg		
final vacuum seal	leaky	OK	OK
brazing	BAg-8	BAg-8	BAg-8

* Through the cooling pipes. ** Running outside OD. † US: in ultra sonic bath. ‡Just before bonding. $ Ramping rate at slow mode is set about 100°C/hr. # Furnace dedicated for the vacuum components for accelerator. ## Furnace for many types of heat treatments.

Table 9.17: *List of detailed parameters that characterize the prototype 1.3 m structures.*

Parameter	Unit	M1	M2	IH1
$\mid S_{11} \mid$	dB	-26	-29	-25
$\mid S_{21} \mid$*	dB	-8.37	-8.27	-8.13
ΔFreq†	MHz	0.7	0.7	0.6
σFreq‡	MHz	1.9#	0.74	2.3@
Alignment	μm	∼300	∼40	∼10
Shrinkage/cell	μm	3.3	0.87	1.0

* Transmission from both sides of the input to one side of the output wave guide.
† Frequency change due to first diffusion bonding.
‡ Standard deviation assuming a random scattering.
\# 0.74 if removing a slope of 0.8 MHz / 150 cells.
@ Almost all came from the first diffusion bonding.

Table 9.18: *Table of characteristic parameters related to the bonding process of prototype structures)*

The structure "M1" was the first trial of the full-scale structures. It came out badly with severe vacuum leakage and a large bending of a few hundred μm. From the former result, we learned about the difficulties in bonding between surfaces with many slits. Although the latter result was miserable, experience involving high-precision alignment was obtained through the process of aligning the cells vertically and keeping it through the following processes. Based on these experiences, the next two structures, "M2" and "IH1", were designed to target the purely detuned structures by removing the troublesome slit structure from the bonding surface of the regular cell. In these structures, the stability of the frequency and a good alignment along the structure were targeted. The following describes various key characteristics obtained in the fabrication processes to discuss the feasibility and near future studies.

Cells for the 1.3m Structure

Each cell in a structure has different dimensions. The precise control of these dimensions is maintained by comparing the OD with the reference cell using a setup with microsense and sliding stage (Figure 9.27). Figure 9.46 shows the differences from the target values. These cells were electrically checked in the choke stand shown in Figure 9.42. The measured result for "M2" is shown in Figures 9.47 and 9.48. The difference from a smooth curve is shown in Figures 9.49 and 9.50. These deviations are to be considered in a later analysis.

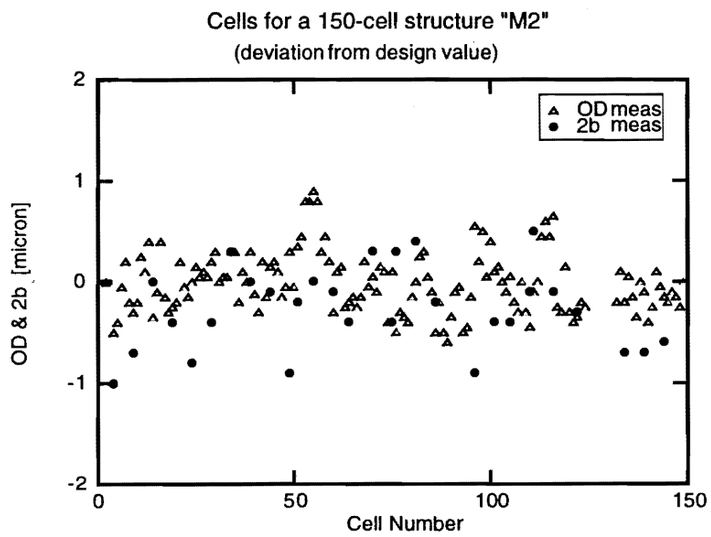

Figure 9.46: *Typical results of the machining of 150 cells for a detuned structure. The triangles are the deviations of the outer diameters from 80 mm. The solid circles are the deviations of the inner diameters of the cells from the design values.*

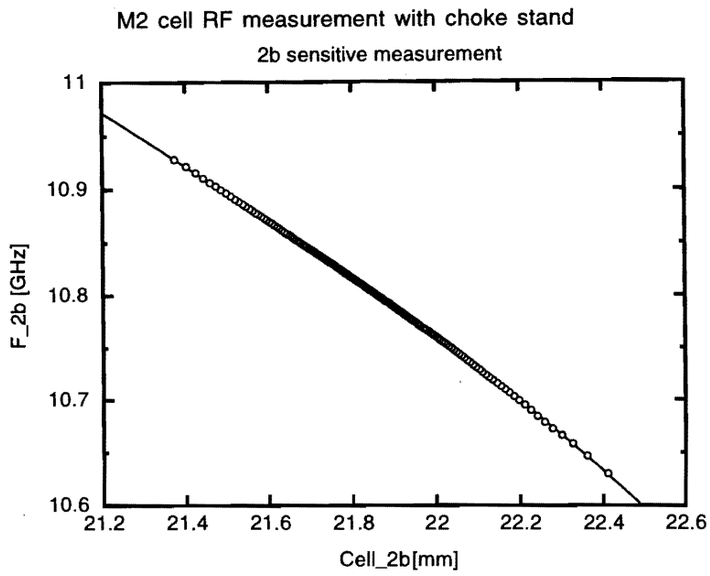

Figure 9.47: *Observed correlation between the measured cavity size (2b) and the cell frequency, as measured with setup in Figure 9.42(b).*

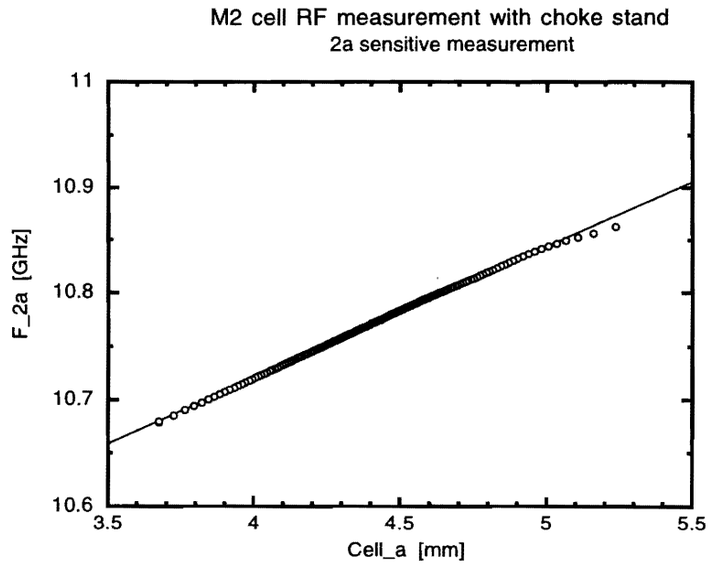

Figure 9.48: *Observed correlation between the measured beam hole size (a) and the cell frequency, as measured with the setup shown in Figure 9.42(a).*

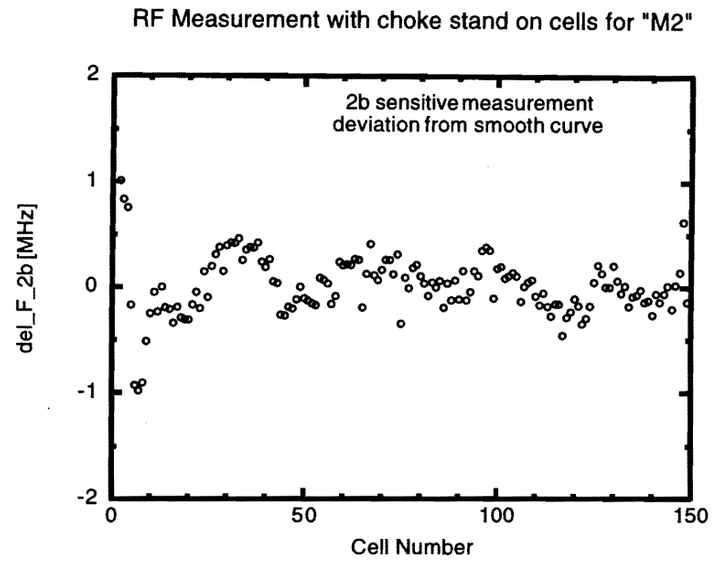

Figure 9.49: *Deviations of the measured frequencies from a smooth fitting curve in Figure 9.47.*

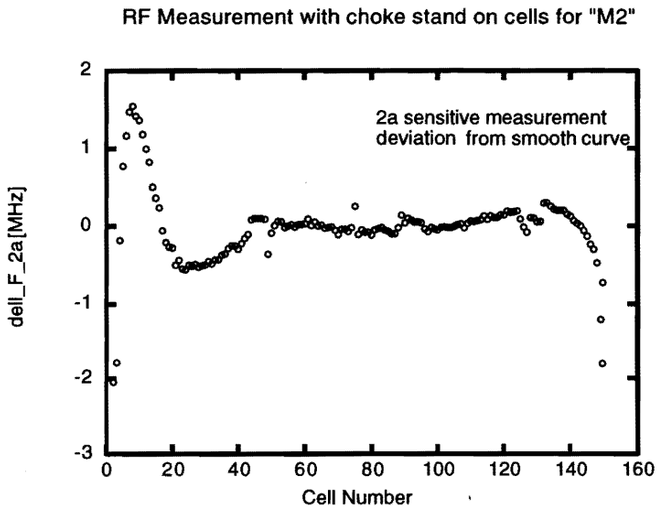

Figure 9.50: *Deviations of the measured frequencies from a smooth fitting curve in Figure 9.48.*

Electric Characteristics before and after Bonding

In order to confirm the stability of the frequency due to the bonding process, the reflection phase seen from the input coupler side was measured by varying the position of the plunger. The results for "M2" are shown in Figure 9.51.

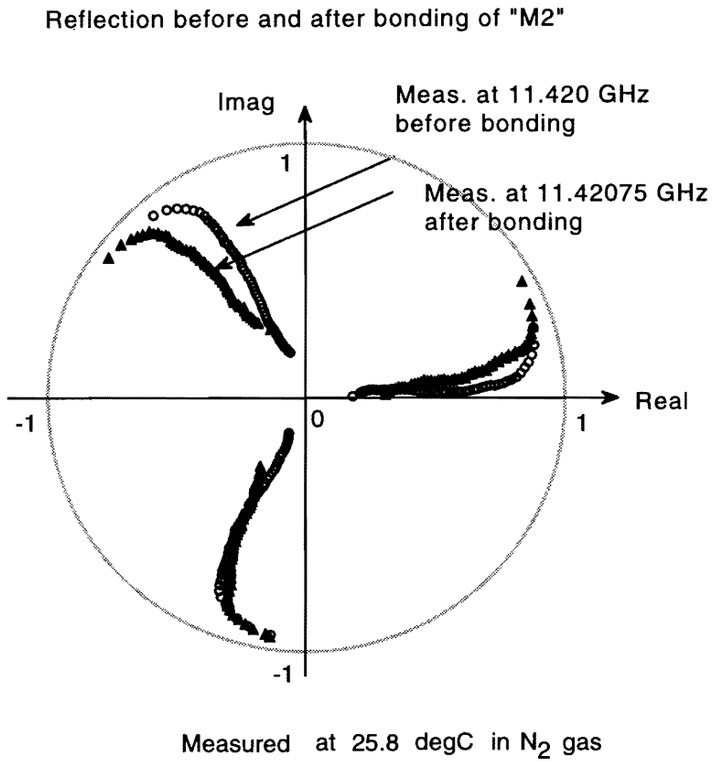

Figure 9.51: *Measured reflection coefficient versus the plunger position. The open circles are those before diffusion bonding, while the solid circles are those after. The measurement frequency is adjusted arbitrarily to obtain a smooth curve for the region with a low group velocity.*

The changes in the accelerating-mode frequencies of all the cells were deduced from this result. To make the comparison robust against possible reflections in such a part as the input coupler cell, the phase difference between those with a plunger at the n'th cell and $(n+1)$'th cell was used. The changes in the phase were converted into the average frequency shift of the three cells. The result is shown in Figure 9.52. Those in almost all of the cells were within ± 1 MHz. The scattering was almost random, and the standard deviation of the scattering was 0.74 MHz. The average shift of frequency was +0.6 MHz, which should be corrected in the stage of cell machining.

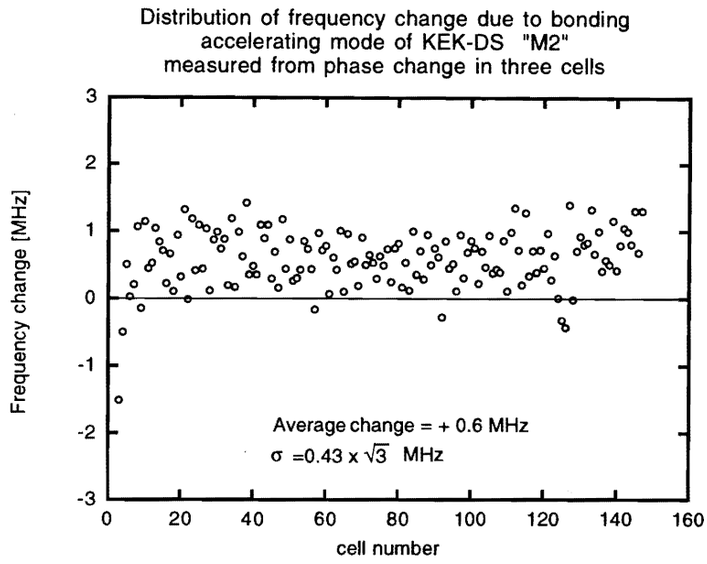

Figure 9.52: *Frequency change of the accelerating mode averaged in each three cells along the structure.*

Structure Assembly of Full-scale Structure

The alignment of the cells in the 30cm-structures was successful and some structure showed a misalignment of several μm level along the structure. Although this experience was very encouraging, a 30cm-structure has only 34 cells and it is further necessary to study the stacking technique for full-size structures, because the number of cells in the full-size one is 150.

As shown in Table 9.17, the alignment of the cells was performed on the vee-block. Essentially two methods were studied: one with vertical stacking, and the other with horizontal stacking. The former can stay in the vertical form after stacking until setting in the furnace. The latter should be stable during the stacking process. However,it has to pass through an process of rotating it into a vertical position.

The definitions of the alignment measurement in both cases, such as A, B, TOP and BOTTOM, are shown in Figure 9.53.

- Vertical stacking for "M2"

The Vee-block was installed in a clean room whose specification is class 1000. Workers are dressed in dust-free clothes and wear a mask. The straightness of the Vee-block has been checked to be less than 5μm/1500mm. Cell stacking was performed on a ceramic plate sitting on a stainless-steel plate set at the bottom of the Vee-block. The cells were set, while pushing against the Vee-block. The ceramic plate and stainless-steel plate were set on the stacked cells in just the same way as the bottom. After

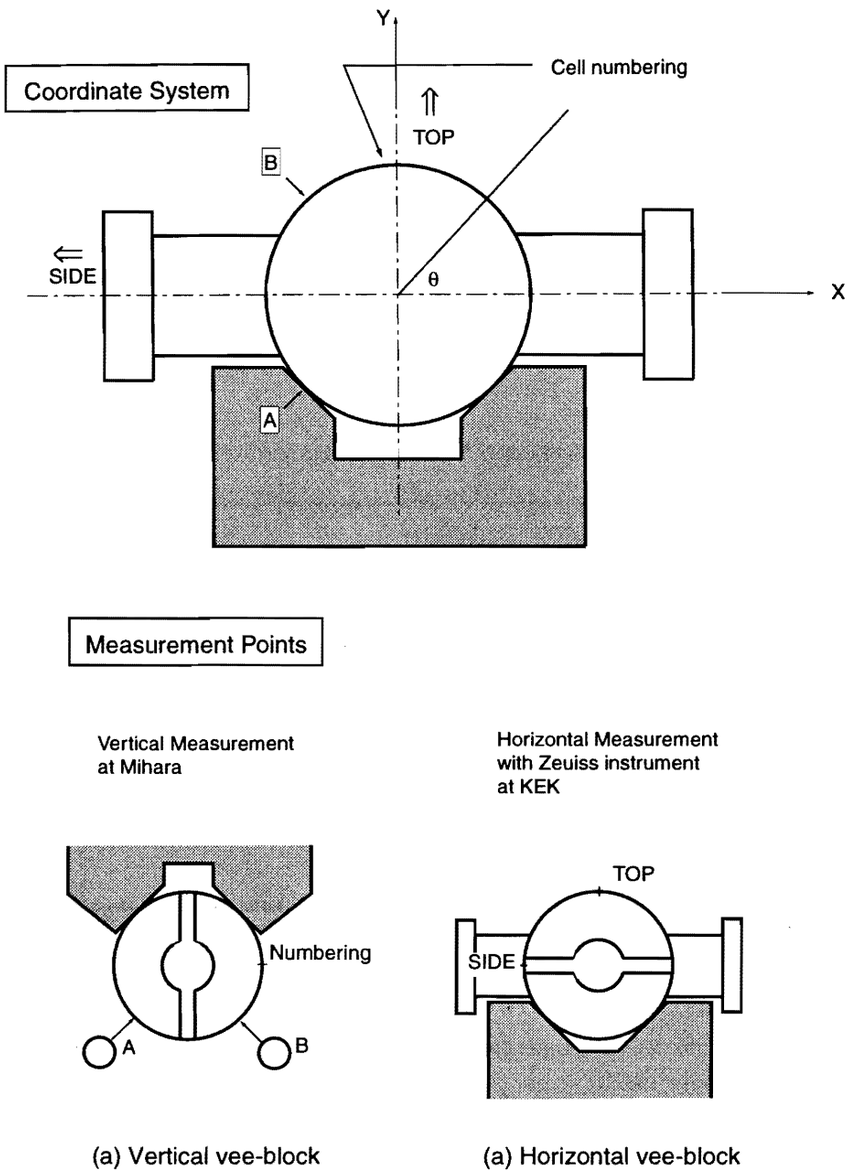

Figure 9.53: *Top: Definition of the parameters to describe the cell alignment. Bottom: Schematic diagram of the set up for the measurement. (a): Cells are stacked against a vertical V-block. The alignment is measured by two capacitive-gap sensors sitting on a plate running along the two parallel cylinders. (b): Cells are stacked on a horizontal V-block. The alignment measurement is performed by a capacitive gap sensor running parallel to two planes, one on the side wall of the V-block and the other on the plate where the V-block is sitting.*

stacking the cells, the straightness of the stacked cells was checked by using two capacitance gauges. Before moving the stacked cells into the furnace for diffusion-bonding process, the stacked cells were loaded using 100kg by an air cylinder mounted on the top of the jig and compressing the cells by using the three stretched-bars between both ends of the stack. Then, the Vee-block was taken off from the structure using a sophisticated moving mechanism. A conceptual drawing is shown in Figure 9.37 that appeared in section 9.2.

During the cell stacking against the vertical vee, the cells were pressed by a 20kg weight after each 30-cell stacking in order to reduce the air film between the cells, and to stabilize the whole stacked column. The alignment measurement was performed in the vertical position compared with the reference of a straight edge running parallel to the Vee-block. The result of the alignment measurement is shown in Figure 9.54.

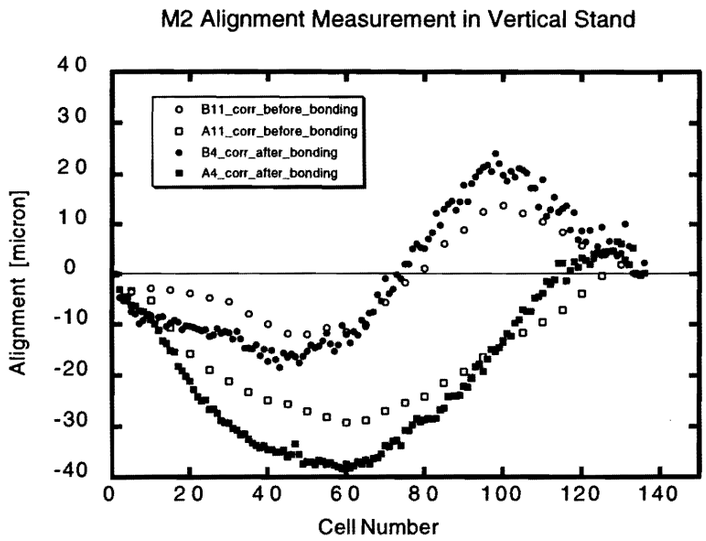

Figure 9.54: *Measured alignment of a detuned structure (M2). The assembly was performed against a vertical V-block. The open (solid) symbols are those before (after) bonding.*

• Horizontal stacking for "IH1"

On the other hand, the cell stacking for "IH1" was performed on a horizontal Vee-block. The inclination of the stacked cell was checked by a laser beam of an auto collimator in order to check any insertion, such as dust, between the cells. The alignment was measured with the reference defined by two flat planes running along the vee-block.

The stacked cells were transported by truck to a furnace 30km away from the stacking place. On the truck the cells were sitting on the same vee-block where the stacking was performed. After reaching the furnace company, the stacked cells were rotated from the horizontal to the vertical on the base of the furnace and hung there.

The results of the alignment just after the stacking and that after bonding are shown in Figure 9.55.

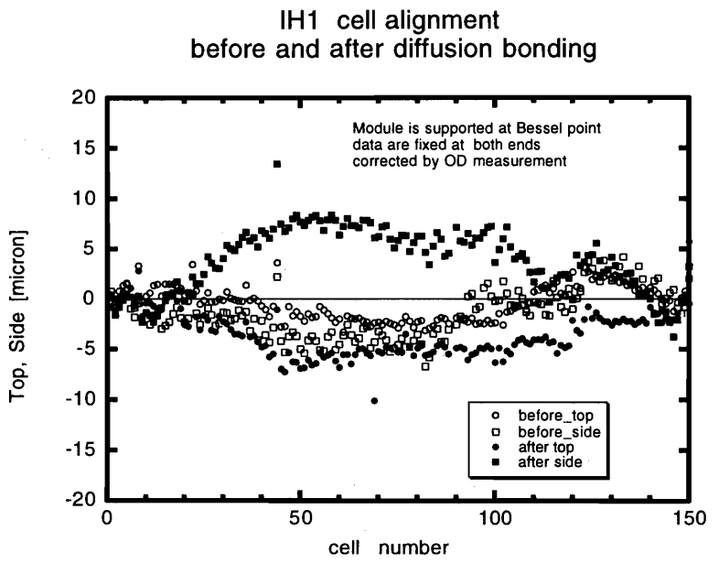

Figure 9.55: *Measured alignment of a detuned structure (IH1). The assembly was performed on a horizontal V-block. The open (solid) symbols are those before (after) bonding.*

Cell Shrinkage

It was found that the cells were shrunk through the diffusion-bonding process. Figure 9.56 shows the cell shrinkage due to diffusion bonding for the case of 'M2', while Figure 9.57 shows that for "IH1". It was found through the bonding of "M2" and "IH1" that diffusion bonding gave almost the same shrinkage of about 1μm/cell. In both cases the structure experienced a temperature higher than 800°C for a long period. The silver brazing cycle (BAg-8 at about 810°C) was short, which gave a fairly small amount of shrinkage.

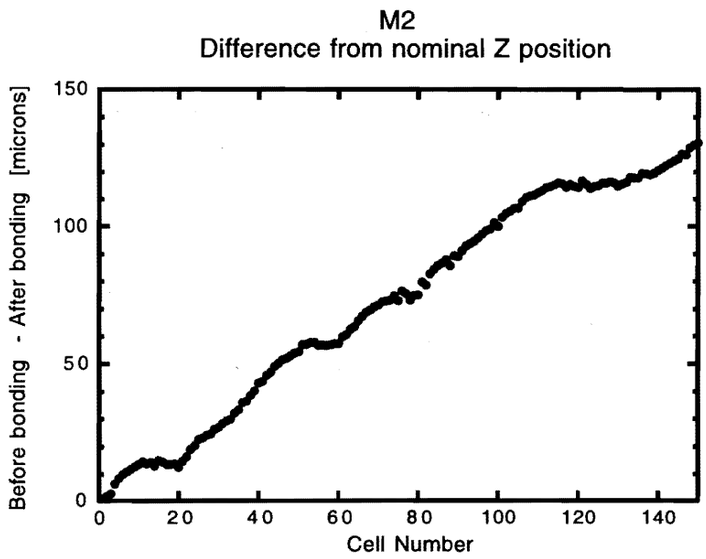

Figure 9.56: *Deviation of the cell position in M2 from the design value measured from the input coupler side.*

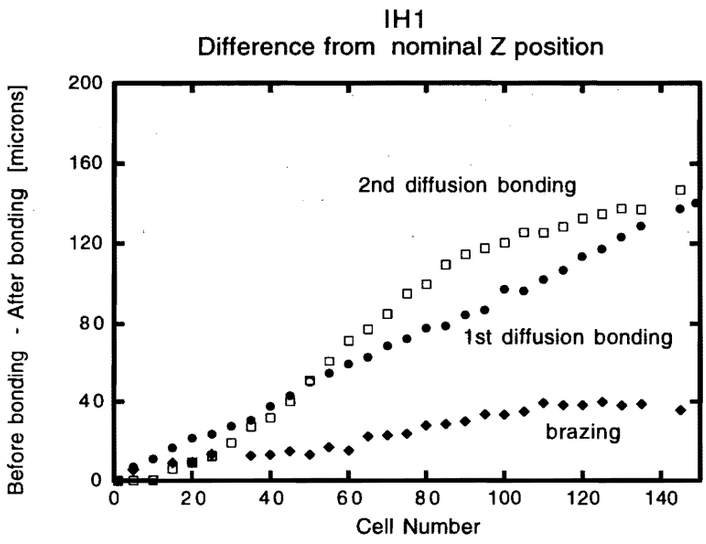

Figure 9.57: *Deviation of the cell position in IH1 measured from the input coupler side.*

9.3.3 Future Study on Full-scale Structure Fabrication

From the fabrication of the two detuned structures, "M2" and "IH1", the level of frequency control has almost been cleared. However, since this level has been still barely achieved, a series of similar structures should be built in order to optimize the cell tolerances, surface quality and the bonding parameters.

The alignment of the cells in a structure has been proven to be within the 10μm level, which is almost within the tolerance. However, more reliable and accurate measurement techniques should be developed in order to identify any mechanism that creates a misalignment, and to keep the alignment level always within the tolerance, or better. These studies should also be included in the fabrication and assembly studies of the following full-scale structures.

Considering these points, a few structures should be made in order to establish the present fabrication and assembly technology. Furthermore, a set of DS with four structures interleaved should be made at once to confirm that the present fabrication level can be extended for the interleaving case, where a better "relative" control of the frequencies between the structures should be realized.

9.4 Wake-field Control

It is important to precisely estimate the dipole wake-field in a structure so that the cancellation between the modes in it, or even among four interleaved structures, is confirmed. The evaluation code should be tested experimentally, because the treatment of the wake-field in a multi-cell structure is a complicated problem, and many approximations should be applied. For this purpose, the wake-field test setup ASSET at SLAC [21], was used. The following describes the present status of the codes, a comparison with the experiment and future study items.

9.4.1 Wake-field Calculation

Longitudinal Mode

An evaluation of the short-range wake-field is discussed in the section of beam dynamics. The magnitude of this wake-field is almost entirely determined by the choice of the beam-hole radius.

The severest long-range longitudinal wake-field is the one due to the accelerating mode. This effect results in the multi-bunch energy distribution. It will be compensated by manipulating the RF phase, amplitude and timing. These estimations are under study[13]. Another long-range longitudinal wake-field due to higher modes, which might cause a complex bunch-to-bunch energy distribution, will not put severe requirements on the detuned structure, because the detuned structure is expected to have a given-spread of the higher longitudinal mode. This is similar to that estimated for the ATF injector linac[12]. The estimation of the multi-bunch energy distribution using an equivalent-circuit model, which takes the higher modes into account separately for each passband, is being studied[14]. The energy distribution from the TM_{011} mode was calculated to be within $\pm 0.1\%$.

Dipole Mode: Equivalent-circuit Model to an Open-mode Expansion

In this section, a calculation of the long-range transverse wake-field is described in detail. In the detuned structure for the linear collider, the modes in the lowest dipole passband mainly contribute. However, those in the second lowest should be taken into account at the same time, because the coupling between those two passband is very large. An equivalent model analysis based on an assumption of the shape, as in Figure 9.1, consisted of a chain of pill-box cavities, and took these two modes into account (K. Bane and R. Gluckstern[25]). This mode is referred to here as the EQC code. This analysis gives the basic characteristics of the severest modes. However, it was pointed out that modes such as the 6'th passband, should also be taken into account[6].

In order to treat the dipole modes, with the higher modes at the same time, a code has been developed, based on the expansion of the modes in a cell into the modes with the electric open boundary condition at both ends of the cell. This code is called here the "open-mode-expansion" code, OM code. The

expansion into the open modes is expressed as

$$E = \sum_{k=1}^{N} \sum_{m=1}^{M} e_{km} \,, \tag{9.19}$$

where E is the field of the whole structure, k the cell number from 1 to N, m the mode number in a cell from *1* to M and e_{km} the field of the m'th open mode in the k'th cell. If the modes up to the 8'th are taken into account, this representation should better reproduce the characteristics of the structure. However, the realistic detuned structure has some features which are not represented in the OM code. One of them is a treatment of the round beam-hole shape, now treated as a flat shape with the same radius. Another one is the assumption of symmetry with respect to the mid-plane. This assumption contradicts the basic nature of the detuned structure, especially on a rapidly changing part of the structure, such as near to the input and output coupler region.

Dipole: Finite-element Code

As an attempt for making a very realistic calculation of the wake-field in a detuned structure, a finite-element code (FE code) was developed[24]. In this code, all of the modes in a passband can be calculated for a CPU time of one hour or so by utilizing massively parallel processors.

Figure 9.58 compares the kick factors calculated by two codes, the OM code and the FE code. As shown in this figure, the two calculations give fairly similar results. A notable difference in the lowest passband is due to an approximation of flat beam hole in the OM code, while in FE a realistic nose shape is taken. The disagreement in the 8'th passband is due to a truncation at the 8'th passband in the OM code. With these limitations in mind, the OM code can be used to evaluate the wake-field, especially for design optimization, because the CPU-time requirement of the OM code for 8 pass-bands is only a quarter of an hour using the usual workstation available today.

Future Developments

Although the FE code is fairly precise, there are still some features to be included even in the FE code. Examples of these are the inclusion of a 3D shape of the coupler cell and the coupling to the waveguide in addition to the coupling to the beam pipe. These effects are supposed to be on the order of one percent, because the ratio of number of the coupler cells to the total is such an amount. For the final design of the detuned structure, the code should be revised so as to give the required precision to discuss the beam-dynamics issues.

9.4.2 Wake-field Evaluation without a Beam

It is straightforward to compare the calculation results to the measurements in a standing-wave mode. A trial was performed for the 28-cell model detuned structure. Figure 9.59 shows the measured

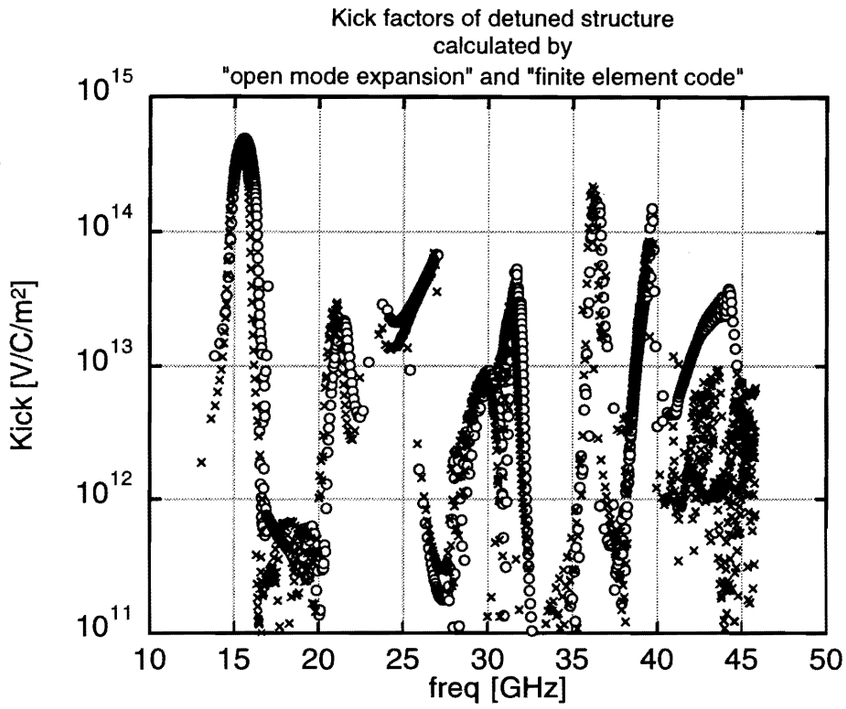

Figure 9.58: *Comparison of the kick factors of the detuned structure. The open circles are those calculated by the OM code, while the crosses are those by the FE code.*

frequencies and the calculated ones by the OM code. The agreement is quite nice. However, the measurement of the field, ie. the measurement of the kick factor of the mode, was difficult, though a field measurement is essential to estimate the wake-field. Feasibility study of the measurement of the field in an X-band structure is being planned.

This approach is especially important for understanding the modes coupled to the input or output coupler cell so as to understand the difference between theoretical estimate and the experiment to a precision of one percent.

9.4.3 Wake-field Measurement with a Beam and a Comparison with the Calculation

ASSET Condition

In ASSET [22],[21] at SLAC, the momentum kick received by the electron bunch was measured by the BPM's in the downstream linac for a varying offset of the driving positron bunch with respect to

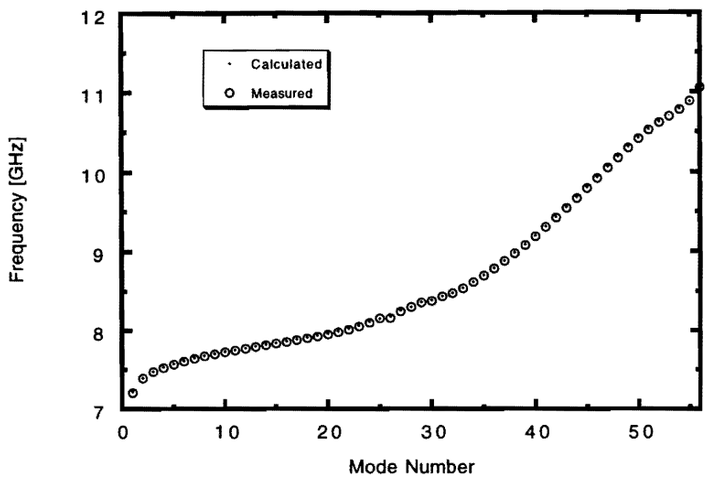

Figure 9.59: *Frequencies of the modes in the lowest two pass-bands of a test 28-cell detuned structure scaled by a factor of 2 from the X-band structure. The open circles are those measured, while the dots are those calculated by the open-mode expansion code.*

the structure. Therefore, the wake-function (W_t) is deduced from the slope of the following formula:

$$W_t(t) \sim \frac{\partial}{\partial y_d} \frac{\delta P_t}{P} \frac{1}{Q_d}, \tag{9.20}$$

where δP_t, is the transverse momentum received by the witness bunch of its momentum (P), Q_d the drive bunch intensity, and y_d the offset of the drive bunch. The parameters that characterize the experiment are listed in Table 9.19.

In Figures 9.60, 9.61 and 9.62, the measured wake-fields are shown in various time ranges.

It was confirmed that the cancellation of a factor of 100 at the next bunch arrival was realized as shown in Figure 9.60. The solid line is an estimation by the OM code.

Energy E_d, E_w	GeV	1.2
Drive bunch intensity Q_d	$\times 10^{10}$	$2 \sim 3$
Witness bunch intensity Q_w	$\times 10^{10}$	1.5
Drive bunch length σ_z	mm	0.6
Emittance ϵ_x / ϵ_y	μm	30 / 3
Beam size σ_x / σ_y	μm	110 / 65
BPM resolution in NRTL	μm	25
BPM resolution in downstream linac	μm	7

Table 9.19: *Typical parameters of the ASSET experiment. NRTL stands for the injection line to the setup, while the linac functions as a detector of the kick.*

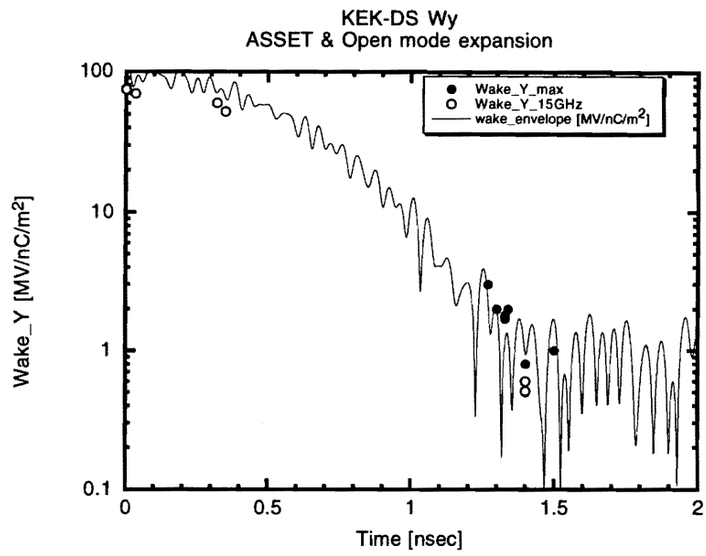

Figure 9.60: *Wake-field of a detuned structure, '"M2", measured using ASSET at the SLC. The open circles are the 15 GHz component deduced from the fitting within each measured time span. The solid circles are the maximum value obtained by eye. The solid line is a calculation using open-mode expansion code.*

The estimations by EQC, OM and FE all underestimate the wake-field in the region after 1.4 nsec until 10 nsec. The inclusion of higher modes above the second passband, such as in the OM and FE, or the simple inclusion of fabrication error, as examined in the case of EQC, do not explain the difference. This time range should be examined more carefully in the light of a design with four interleaving structures.

The wake-field at a longer time range is shown in Figures 9.62 and 9.63. Again, the solid line is an estimation by the OM code and the EQC code. The agreement between the experiment and the code prediction is fairly good. The longer recurrence time in the OM code result comes from an approximation of the flat beam-hole shape. If the nose radius is appropriately taken into account as an effective beam hole radius, the recurrence time should agree with the experimental result. This is shown in the result by the EQC analysis by K. Bane[23], shown in Figure 9.63.

In the region from 10 to 100 nsec, the experimental data appeared below both theoretical estimates. One of the reasons is that the data points are on the slope of the envelope of the wake-field with an oscillatory behavior. However, the probability of the data appearing lower than the maximum of the theoretical envelope seems still to be larger than a simple random appearance.

The existence of high-frequency components in the wake-field is clearly seen in such data as shown in Figure 9.64, about 25.4 nsec later than the drive bunch. In this example the same amount of the frequency components is assumed for both 18 and 40 GHz, though in reality more than two higher

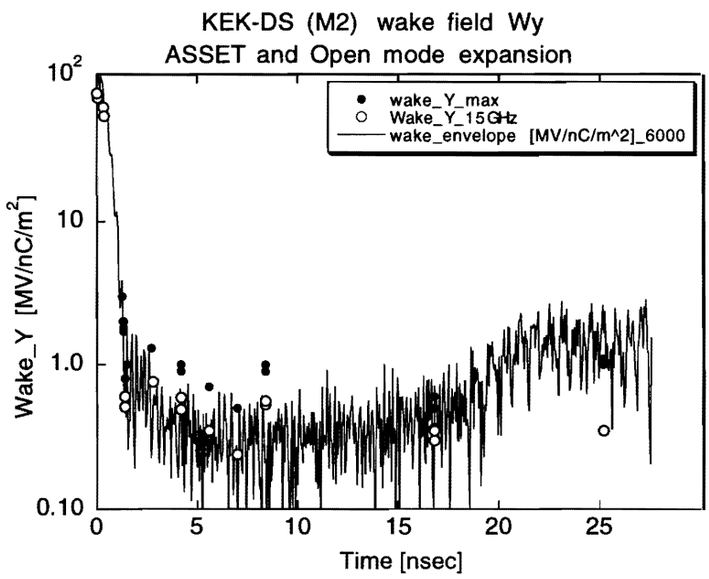

Figure 9.61: *Wake-field of a detuned structure, "M2", measured using ASSET at the SLC. The open circles are the 15GHz component deduced from the fitting within each measured time span. The solid circles are the maximum values obtained by eye. The solid line is a calculation using the open-mode expansion code.*

modes should contribute. Since the level of a few percent appears in the wake-field, this also should be reproduced in an estimation to design the structure based on some calculation.

Figure 9.65 shows the 15GHz component of the measured wake-field of DS in the x-y plane. They are almost the same as each other in almost all of the time ranges measured, except for the region from a few nsec to a few tens of nsec. Since the structure is circularly symmetric, except for the coupler cells, this difference should originate from the coupler cells. The coupling of the structure to the outer waveguide or the frequency deviation from the nominal value due to the coupling iris should be responsible. These effects should be understood before the final design.

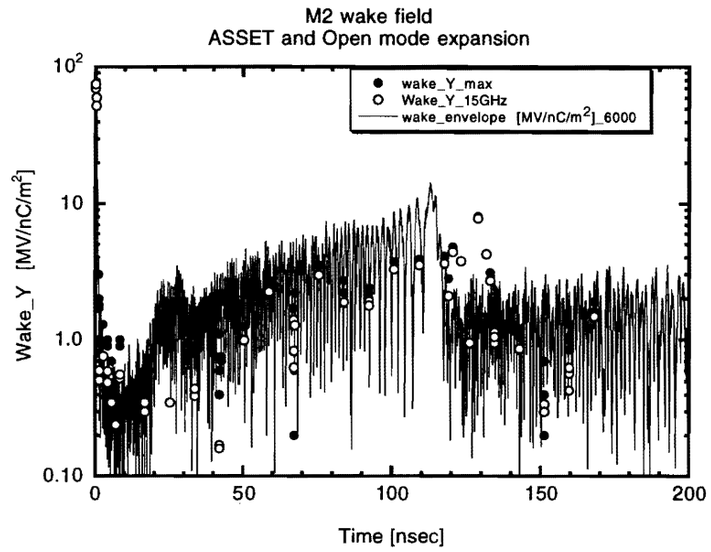

Figure 9.62: *Wake-field of a detuned structure, "M2", measured at ASSET of the SLC. The solid circles are those points depicted as the maximum by eye, while the open circles are those of the 15 GHz component. The line is an estimation of open-mode expansion. The Q values of all of the modes in the calculation are assumed to be 6000.*

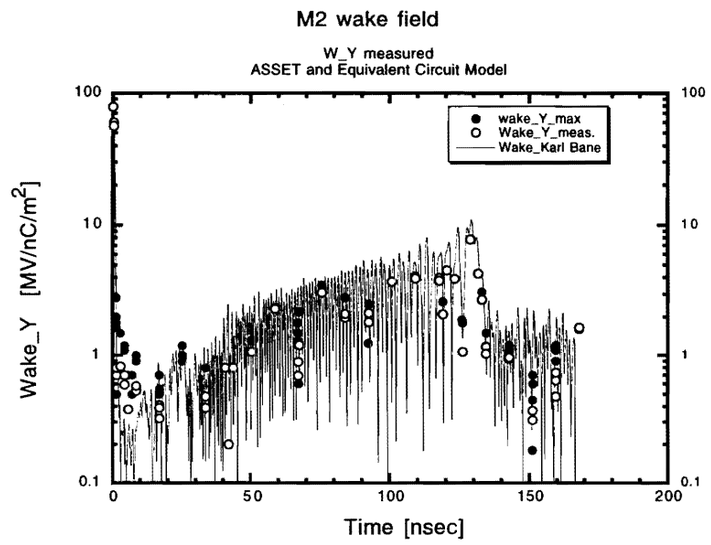

Figure 9.63: *Wake-field of of a detuned structure, 'M2', measured at ASSET of the SLC. The solid circles are those points depicted as the maximum by eye, while the open circles are those of the 15GHz component. The line is an estimation by the EQC code. The Q values of all the modes in the calculation are assumed to be 6000.*

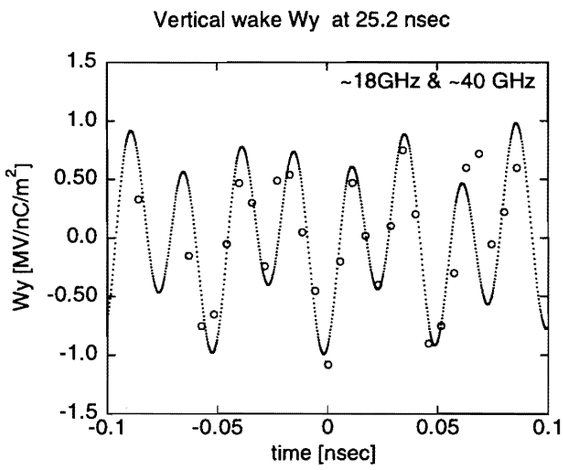

Figure 9.64: *The solid circles are the vertical wake-field measured at time 25.2 nsec. The horizontal axis is measured with respect to 25.2 nsec. The dotted line is an example fitting with two frequency components at 18 GHz and 40 GHz, showing the contribution of the frequency components higher than the lowest dipole passband.*

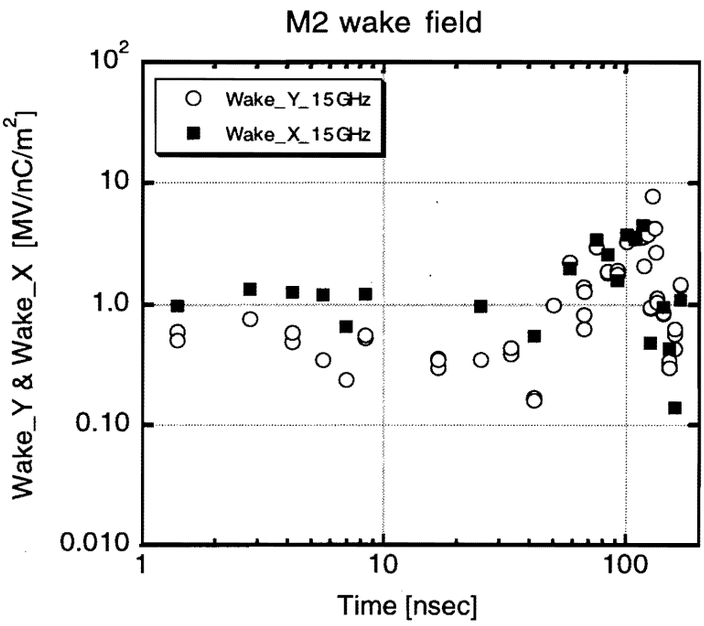

Figure 9.65: *Wake-field of the detuned structure measured at ASSET of the SLC. The open (solid) symbols are those of the vertical (horizontal) wake-field at a frequency of 15 GHz.*

9.4.4 Future Plan for Further Precise Measurements

If the beam is passing through a structure being parallel to it, the wake-field to be induced in it can be calculated, and can also be measured at ASSET.

To make a design based on this analysis, the cell-to-cell misalignment within a structure should be much smaller than the offset of the beam with respect to the structure. If this is not the case, the effect of the cell misalignment in the structure should be included rigorously. The effective kick from the misaligned cells might be estimated as

$$\Delta P_t \approx \sum_m^{\text{mode}} \sum_i^{\text{cell}} \frac{1}{U_m} \left(\int_i dz \cdot e^{ik_m z} \frac{\partial}{\partial y} E_{zi}(z) \delta y_i \right), \tag{9.21}$$

where m is the mode number, i the cell number, U_m the stored energy in the mode m, $E_{zi}(z)$ the z-component of the electric field, and δy_i the misalignment of the i'th cell; the integration is performed in the i'th cell. In order to confirm the precision of this approximation, some experimental studies should be performed. For this purpose, the structure should be well aligned to the beam, and the residual wake-field which still remains is deduced.

In order to complete the engineering design, such effects as the structure inclination, rotation in the x-y plane and cell misalignment, should be practically studied. In addition to this study, a system with four interleaving structures should be proved to work experimentally from a beam dynamics point of view while using the beam.

9.5 Vacuum Characteristics of the Accelerating Structure

The out-gassing rate from the inner area of the accelerating structure should be within 1.3×10^{-9} Pa m^3/sec/m^2 in order to keep the average pressure inside the structure at less than 1.3×10^{-6}Pa. The out-gassing rate from the oxygen-free copper (OFC) material is easily reduced down to less than the above-mentioned criteria if the surface is properly prepared[31]. Although the structure is made of OFC copper, it can be contaminated through various fabrication processes, such as a diamond machining using oil, high-temperature bonding in a furnace and various inspections performed in the air with slowly purging nitrogen gas, but with some of the flanges open. Therefore, it should be studied whether a structure made through the present method meets the above-mentioned requirement.

9.5.1 Measurement of the Out-gassing Rate

The out-gassing rate of one of the 1.3 m structures, "IH1", has been measured. The total inner-surface area of copper in the structure is 1972 cm^2, mainly consisting of the accelerating cells, but also including an extra area of 242 cm^2 for the beam pipe and wave guide. The layout of the test setup is shown in Figure 9.66. The system is baked at 150°C for one day before testing the structure. The base out-gassing rate of the system is less than 1×10^{-10} Pa m^3/sec/m^2 if baked. Since the inner area of the system is roughly the same as that being tested, the present system can measure the out-gassing rate down to the critical value of the detuned structure, which is 10-times larger than that of the system background. The total pressure was measured by two extractor gauges located at both sides of the orifice. The partial pressure was measured by a quadrupole-based residual-gas analyzer (RGA) being set at the structure side of the orifice.

The structure was fabricated through such processes as an RF measurement and a mechanical-alignment measurement, performed while being purged by nitrogen gas. Just before the present vacuum test, this structure was evacuated for one day and then exposed to air for one hour to establish the initial condition of the test.

Figure 9.67 shows the total pressure versus the pumping time. As can be seen in the figure, the pressure in the upstream chamber is always 20-times higher than that in the downstream chamber. Therefore, the out-gassing rate can be estimated by neglecting the pressure at the pumping side of the orifice. This process overestimates by less than 5%. Also seen from the figure is that the system background pressure is about 10% or less compared to the pressure in the system with the cavity connected. Therefore, the out-gassing rate can be estimated again by neglecting the system background. This approximation overestimates by 10% or less.

The partial pressures were measured by a quadrupole-based residual-gas analyzer in parallel with the total pressure measurement. Several main components are shown in Figure 9.68. As can be seen in this figure, the main components are the gas molecules with mass numbers 18, 28 and 44, indicating water and carbon-related molecules.

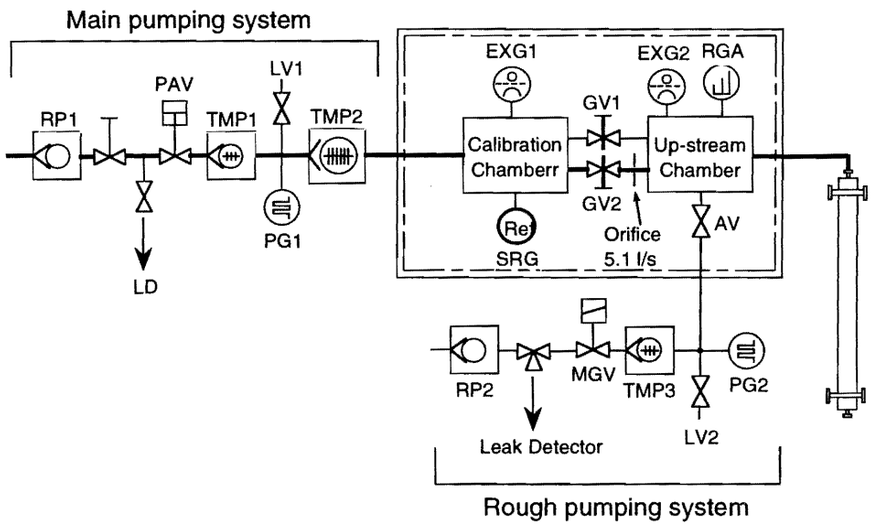

Figure 9.66: *Schematic diagram of the set up for measuring the outgas-sing rate. The structure being tested was connected to the up-stream chamber, which was evacuated through the orifice and the calibration chamber. The conductance of the orifice was 5 l/sec. The total vacuum pressures at both sides of the orifice were measured using extractor gauges, EXG1 and EXG2. The gas pressure at the up-stream chamber connected to the structure was analyzed by a residual-gas analyzer (RGA). The temperatures of the two chambers were at about 21°C. Base pressure in the calibration chamber was on the order of 10^{-9} Pa. Purging by nitrogen gas and air was performed through a filter and value LV2. The area closed with a solid line and a dot-dashed line was baked before the present study.*

A typical mass spectrum near to the end of the measurement is shown in Figure 9.69. The water is the main component, as shown in the figure. This can be considerably reduced by baking at around 200°C. Even if the water content is baked out, the other components, such as the mass numbers 28 and 44, probably in such molecules as CO and CO_2, cannot be reduced so easily under medium-temperature baking. The pressure level should be reduced by more than 10 times, compared to the amount at the last moment of the present measurement. If necessary, high-temperature baking at such a high temperature as 500°C, or more, like that the klystron tube fabrication process, should be studied. The contribution of such a low-Z gas as H_2 is less harmful.

Before considering high-temperature baking, it should be studied in which mechanism the copper surface is contaminated by such carbon-related materials. Such processes should be studied as the cell machining, itself, where kerosene oil is used as a cutting fluid. The diffusion-bonding process, which is performed in a vacuum furnace, may also contaminate the surface, because the furnace used

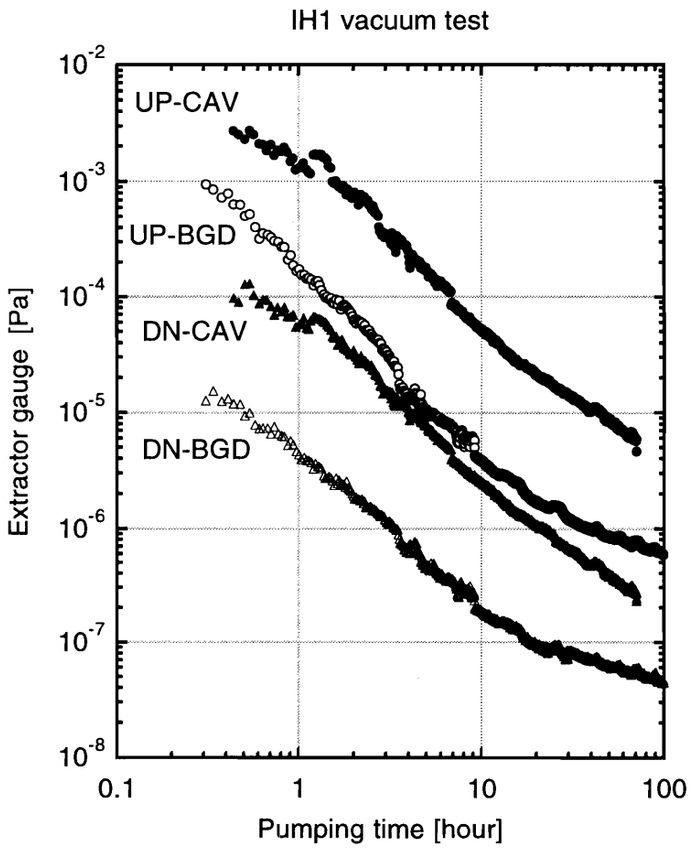

Figure 9.67: *Out-gassing rate of the detuned structure measured by the setup shown in Figure 9.66. The solid circles and triangles with the name 'CAV' are those obtained with the structure connected, while the open symbols with name 'BGD' are those without the structure, showing the system background. Those with 'UP' and 'DN' are the pressures at the upstream and the downstream chamber, respectively.*

for "IH1" is at a fairly high pressure, $\sim 10^{-2}$Pa during high-temperature bonding. Thus, those gas components can possibly be reduced throughout the fabrication processes.

These surface-related studies are to be performed through the fabrication of several structures from now on.

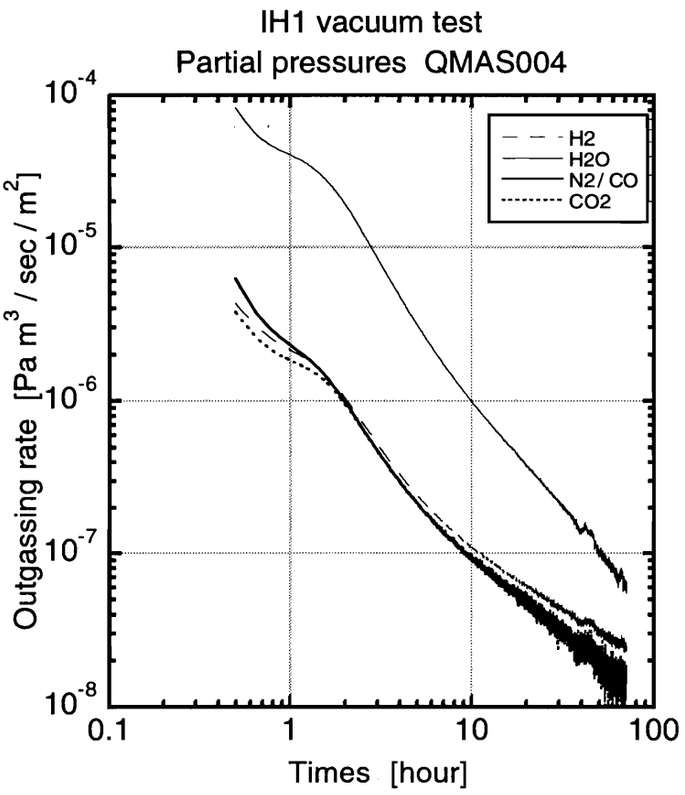

Figure 9.68: *Partial pressure of typical residual gases as a function of the pumping time.*

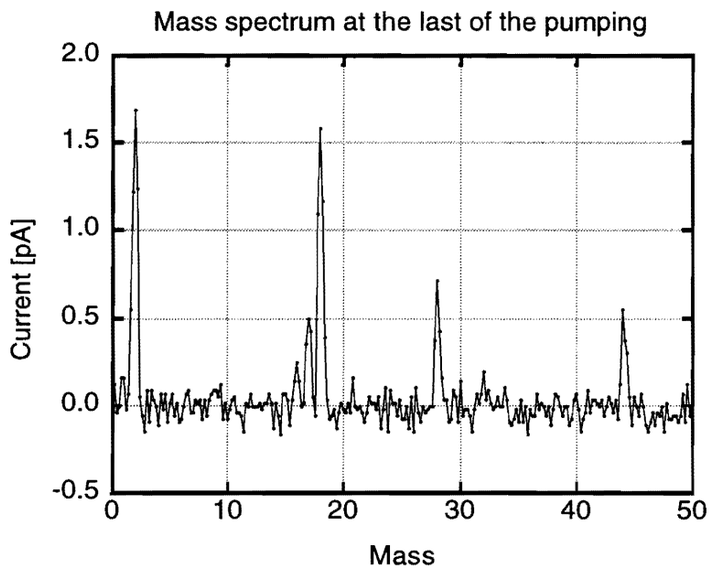

Figure 9.69: *Typical residual-gas spectrum near to the end of the measurement.*

9.6 High-Field Issues

High-field experiments were performed in two stages before studying realistic prototype structures. Tests on 20cm structures were performed at first to study the high-field characteristics with a limited power of a few tens of MW. Two structures were tested. These structures were made by silver-brazing technique to bond the cells. Thereafter, 30 cm structures were made using the diffusion bonding, the same technique as that for the full-scale structure. Therefore, high-field test on these structures will be used to check whether any inherent difficulties exist or not, related to the unique fabrication technique. A test on a full-scale structure is, of course, the most practical study. It is scheduled to be performed soon.

9.6.1 20cm Constant-impedance Structure

It is necessary to stably operate the structure at a high-field level of well more than 70 MV/m. To investigate the feasibility, two 20cm-long constant-impedance structures of the same electrical design were first studied at high power[26, 27]. These structures were designed to have a high field with a relatively small input power by reducing the beam-hole diameter as small as 6mm, while the disk thickness was 2mm. One of the structures was made by KEK by utilizing an industrial-fabrication technique of commercial accelerating structures for medical applications. Another one was made at CERN based on cells made using an ultra-precise diamond tool, followed by the fabrication process at CERN. Both structures were made by a silver-brazing technique for joining the cells.

Figure 9.70 gives the history of the conditioning for the CERN structure. The nominal pulse width was 100 nsec, and the repetition rate was typically 50Hz. It was found that a 100 MV/m level can be obtained without difficulty. On the contrary, the KEK structure was conditioned for a period of almost one order of magnitude longer, but reached only 70 MV/m. This means that in some cases a field level more than 70 MV/m is not easily obtained. It should be clarified how to reliably obtain a level over 70 MV/m. The conditioning was performed at a nominal pulse width of 100 nsec, though the actual structure was designed to be under a high field during an RF period of 230 nsec. To investigate the characteristics on the pulse width, the maximum pulse width just before the breakdown was recorded by keeping the peak power constant. The result is shown in Figure 9.71. As can be seen in this figure, it is usually difficult to maintain a high-field level for a longer pulse duration. In this figure, the CERN structure shows a much better performance compared to the KEK one, indicating again the importance of the fabrication method on the obtainable field level and pulse length.

A small amount of dark current is preferable against various bad effects, speculated to be appeared in the beam position monitor, the background production for the physics detector, etc. As shown in Figure 9.72, the dark current of the KEK structure is very large compared to that of CERN. The amount rapidly increases as the field increases. Therefore, it is in principle better to make it small so as to operate the structure at a high-field level. This stresses again the importance of the

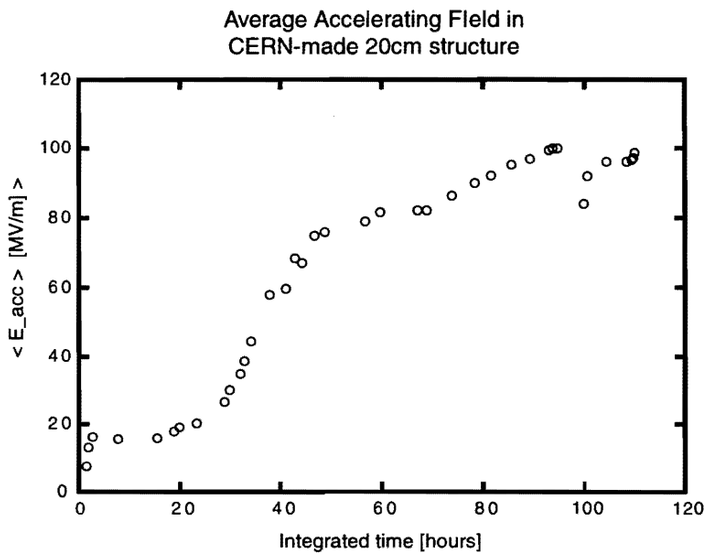

Figure 9.70: *Conditioning curve of a CERN-made 20 cm structure. The vertical axis is the average accelerating field along the structure, while the horizontal axis is the integrated conditioning time. The conditioning was typically performed at 50 Hz.*

fabrication process. This data was also analyzed using the modified Fowler-Northeim formula shown in Figure 9.73. It was found that even if the amount of dark current, as well as the reached maximum field are very different between the two structures, the surface field-enhancement factor is similar. It should be noted that the dependence of these characteristics of the dark current on the fabrication method, especially on how well the fabrication processes maintain cleanness, were also observed in the S-band case[28]. The momentum spectra of the dark current for the two structures are shown in Figure 9.74. As shown in this figure, the KEK structure has a large contribution in the low-energy part. This low-energy part remains at the pulse duration of 40 nsec, shorter than the filling time of the structure, 50 nsec.

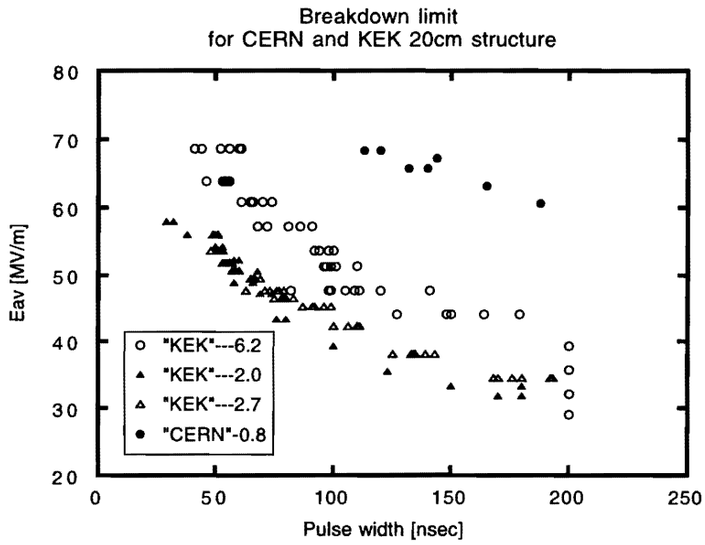

Figure 9.71: *Break-down limit of the two 20 cm structures, KEK-made and CERN-made. The data points are the maximum pulse length observed in the lengthening at each power level. The triangles and open circles are those of the KEK-made structure at the beginning and final stage of the conditioning, respectively. The solid circles are those of the CERN-made structure at a fairly early stage. The numbers in the box are the integrated number of RF pulses until then in units of* 10^6.

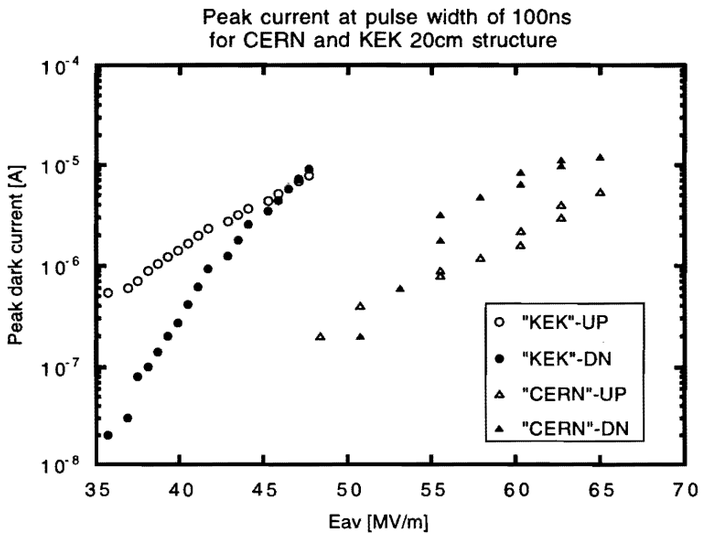

Figure 9.72: *Peak dark current measured at Faraday cups during an RF pulse of 100 nsec. Notes, "UP" and "DN", in the figure are the directions of the dark current towards upstream side and downstream side of the structure considering the direction of the beam acceleration.*

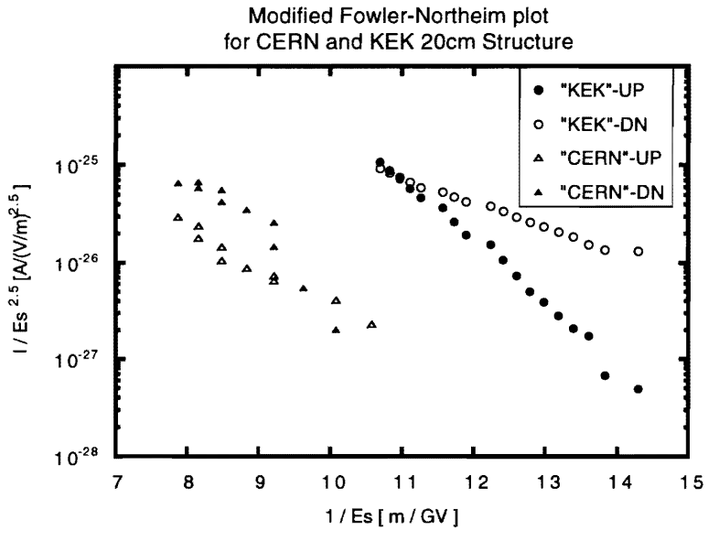

Figure 9.73: *Modified Fowler-Northeim plot of the data of Figure 9.72. Notes, "UP" and "DN", in the figure are the directions of the dark current towards upstream side and downstream side of the structure considering the direction of the beam acceleration.*

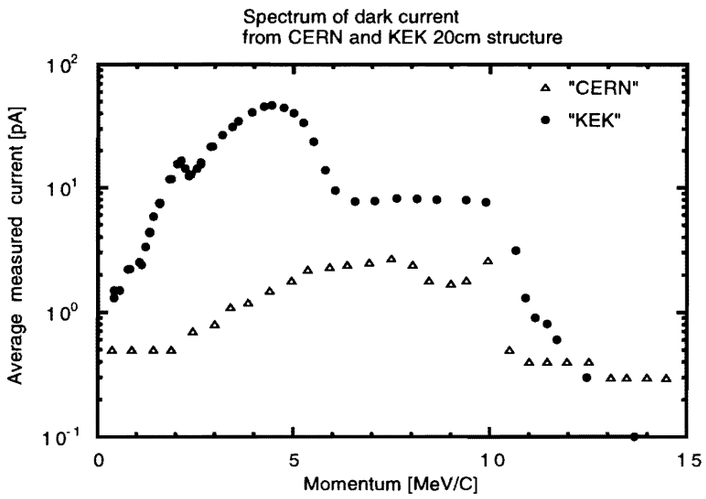

Figure 9.74: *Momentum spectrum of the dark current measured at the downstream analyzer magnet. The pulse length was 80 nsec. The solid circles are those from the KEK-made structure at an accelerating field of 56 MV/m, while the open triangles are those from the CERN-made one at 59 MV/m. The momentum acceptance of the analyzer magnet was set 4.3%.*

9.6.2 30cm Constant-impedance Structure

A schematic drawings of the 30 cm structure was shown in Figure 9.30. The beam-hole aperture (a) is 4.2mm, and the disk thickness (t) is 2 mm. These values were adopted to make the structure similar to the full-scale DS structure. From these parameters, the average accelerating field along the structure is given by

$$< E_{NL} >= E_{in} F(\tau), \tag{9.22}$$

where

$$E_{in}\ [\mathrm{MV/m}] = \sqrt{2\alpha r P_{in}} = 8.742 \times \sqrt{P_{in}\ [\mathrm{MW}]} \tag{9.23}$$

$$F(\tau) = \frac{1 - \exp(\tau)}{\tau} = 0.933. \tag{9.24}$$

Actual detuned structures will be fabricated using cells machined by a diamond tool and by utilizing the diffusion-bonding method, which was used for the 30cm structures. This type of structure is made from a new fabrication technique, and its characteristics at high fields should be studied. As a test of the fabrication technique, several 30cm long structures were made, as shown in Table 9.16. One of them (#2), which was made by a technique considered to be suitable for the full-scale structure, was tested at high power. The conditioning curve is shown in Figure 9.75. A level of 50 MV/m is easily obtained. It is now being tested at higher fields.

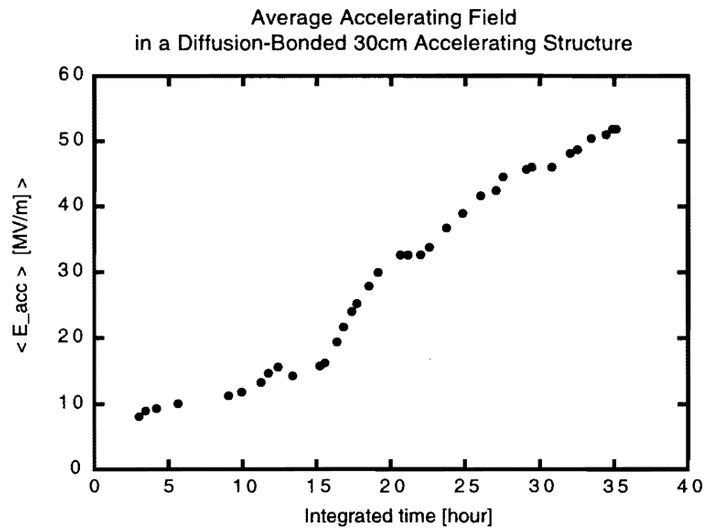

Figure 9.75: *Conditioning curve of a 30 cm structure made by diffusion bonding. The vertical axis is the average accelerating field along the structure, while the horizontal the integrated conditioning time. The conditioning was typically performed at 100 nsec and 50 Hz.*

An attempt was made to measure the field-emission currents. The peak current to the Faraday cup upstream of the beam pipe was about 1 μA at the highest field over a pulse-width range of 30 to 130

nsec. That towards the downstream one could not be measured. The dependence on the field level will also be measured in the future.

9.6.3 Full-scale 1.3m Prototypes

The full-scale detuned structure is 1.3 m in length. High filed experiment on the full-scale structures has not been performed yet. However, the amount of dark current is estimated to be fairly large compared to that of the short structures[29]. In addition to the length, the beam-hole aperture changes from larger size to smaller size so that more field-emitted electrons can hit the downstream disk than in the case of the constant-impedance structure, and that they may produce more secondary particles and photons in a cascade manner. These secondary particles cause many effects. A multiplication mechanism from a structure to the downstream one will also enhance such a behavior originating from field-emitted electrons. These should be studied in a practical configuration.

One of the structures, M2, will be tested at SLAC using RF power compressed by SLED-II with a 150 nsec duration. Another one, IH1, will be tested at KEK using the combined power from XB-72K, possibly reaching over than 100 MW with a variable-pulse length in order to study the characteristics at 80 MV/m or higher.

In order to study and prove high-field operation in a practical configuration, it should be studied in such a configuration that two to four structures are driven at once with some focusing elements as the quadrupole magnet. In this configuration, the stability of the operation, and such characteristics as the field-emitted electrons, the performance of the beam position monitors, the fault rate, and the vacuum level, should be studied before establishing the engineering design. Also, a realistic multi-bunch beam should be injected in order to observe the behavior on the beam.

9.7 Structure BPM for Alignment

An estimation of the alignment tolerance of the accelerating structure is discussed in Chapter 7. The structures should be aligned with respect to the beam within several micrometers. To this aim, the beam position with respect to the structure is measured and fed-back to the structure positioning.

The requirements on these BPM's are a resolution of 1μm and an accuracy of 3μm. The relative alignment of the electrical center of the BPM to that of the relevant modes in the accelerating structure should be within this accuracy.

The simplest method is to measure the beam position is to detect the dipole modes excited in the structure. Because this BPM performance depends on the mode characteristics and the structure straightness, a realistic electrical system should be designed based on the understanding of the modes excited in the structure. On the other hand, two BPM's electrically isolated from the accelerating structure serve as a beam-position monitor for the structure if they are attached at both ends while being mechanically aligned well with respect to the structure axis. It should be noted again that in both cases good straightness of the cells along the structure is one of the most basic requirements to be kept for these BPM to work for the purpose of structure alignment.

The actual beam consists of 85 bunches in a train, each containing 0.7×10^{10} electrons or positrons. The BPM should be safe against such multi bunches in full single-bunch intensity, but should be possible to measure the position of a single bunch of less intensity, such as 1×10^{9} particles per bunch.

This section briefly describes an idea concerning the feasibility of these two types of BPM's for the alignment of detuned structures.

9.7.1 Independent BPM

Cavity-type BPM's have been studied to reach a position resolution of well less than a micrometer[32, 33, 34, 35] and in Chapter 16. All of the BPM's use the TM_{110} mode in a pillbox-type cavity with frequencies comparable to that of the accelerating one. Therefore, the mechanical outer diameter of the BPM can be within ϕ80mm, that of the accelerating cells. Therefore, it can be integrated in a mechanically well-aligned structure. A resolution of 1μm is fairly easily obtained. The electrical center of the mode in the BPM cavity should be kept the same as that of the mechanical center of the BPM cavity. For this purpose, high-precision machining of the BPM cavity with a concentricity much better than 1μm should be realized.

The long-range wake-field coming from the modes excited in the BPM cavity, including the mode for the BPM function, should be less than the wake-field tolerance.

Three identical prototype BPM cavities and their electric circuits should be made, and, especially, the accuracy should be checked. This study requires a beam without big transverse tails.

9.7.2 Structure Modes

It is straightforward to measure the beam position using the excited modes in the structure. If the cells are aligned well, the electrical axes of many relevant modes are in the same position and one of those will be used for the BPM action. In a detuned structure, some modes are trapped in a fairly small region of the structure, so that the dipole mode localized there can serve the beam-position information averaged around those cells.

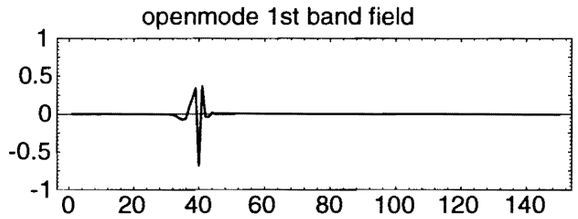

Figure 9.76: *Electric-field strength of the 38'th mode in frequency of the dipole modes calculated by "OM" code. This mode is a candidate for the measurement of the beam position with respect to the input-coupler side of the structure. The BPM might be attached at the 40'th cell.*

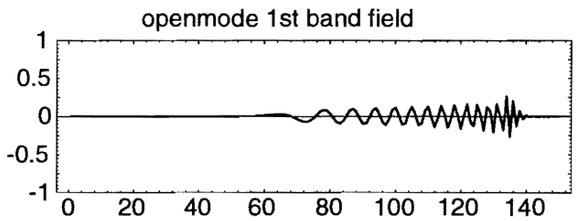

Figure 9.77: *Electric-field strength of the 108'th mode in frequency of the dipole modes calculated by "OM" code. This mode is a candidate for the measurement of the beam position with respect to the output-coupler side of the structure. The BPM might be attached at the 110'th cell.*

The field patterns of the lowest dipole modes for the two candidate modes are shown in Figures 9.76 and 9.77. From this pattern, the BPM cell will be at the 40'th cell for the 38'th mode and at around the 110'th cell for the 108'th cell. The BPM will take the position of the beam averaged in the region where stored energy exists. However, it should be noted that the thus-obtained position information has meaning only down to the length of the misalignment of the cells located there. The dipole-mode signal will be extracted and picked up by a simple antenna or loop. The dipole-mode frequency of such a cell should not be perturbed much by such an external-coupling circuit in order to maintain the design distribution of the dipole modes. Since the frequency spacing of the mode in a detuned structure is at least 9 MHz, a frequency filter of a few MHz can be used.

The performance of these BPM's should be confirmed by experiments with a beam which is aligned to the structure with some other measuring tools, such as the signal from the input and output coupler cells, where the outputs from left and right should be combined differentially or by installing two independent BPM's, as in the previous section.

References for Chapter 9

[1] JLC-I, KEK Report 92-16, December, 1992.

[2] Zeroth-Order Design Report for the Next Linear Collider, LBNL-PUB-5424, also SLAC Report 474 or UCRL-ID-124161, May 1996.

[3] H. Deruyer et al., "Damped and Detuned Accelerator Structures", Int. Linear Accelerator Conf. Albuquerque, USA, 1990, and SLAC-PUB-5322, 1990.

[4] K. A. Thompson et al., "Design and Simulation of Accelerating Structures for Future Linear Colliders", SLAC-PUB-6032, 1993.

[5] T. Shintake, et al., HOM-Free Linear Accelerating Structure for e+e- Linear Collider at C-Band, Proc. Part. Accel. Conf. and Intn'l Conf. High Energy Accel., Dallas, USA, 1995 and KEK Pre-print 95-48.

[6] K. L. F. Bane et al., Issues in Multi-Bunch Emittance Preservation in the NLC, Proc. European Part. Accel. Conf. London, 1994 and SLAC-PUB-6581.

[7] M. Yamamoto, Thesis in Japanese, Study of Long-Range Wake Field in Accelerating Structure of Linac, KEK report 94-9, 1995.

[8] B. Zotter and K. Bane, Transverse Resonances of Periodically Widened Cylindrical Tubes with Circular Cross Section, PEP-NOTE 308, 1979.

[9] T. Higo et al., Practical Application of Very Precise Frequency Calculation to a Disk-Loaded Structure, Proc. of the 20th Linear Accelerator Meeting in Japan, Osaka, 1995.

[10] Y. Iwashita, "PISCES II : 2.5-D RF CAVITY CODE, AN EXTENSION OF SUPERFISH", Proc. of the 1994 International Linear Accelerator Conf., Tsukuba, Japan, p239-241, 1994.

[11] K. Klatt et al., Proc. of the 1986 Linear Accelerator Conf., SLAC-Report-303, 1986, p276-278.

[12] M. Yamamoto et al., Multi-bunch Energy Distribution due to Higher Order Modes in a Traveling-wave Constant Gradient Structure, Proc. 18th Linear Accelerator Meeting in Japan, Tsukuba, Japan, 1993, in Japanese.

[13] I. V. Syrachev and T. Higo, Numerical Investigation of Transient Beam Loading Compensation in JLC X-band Main Linac, KEK Report 96-8, 1996.

[14] I. Syrachev, private communication.

[15] Kikai kogaku binran, in Japanese.

[16] N. Taniguchi, "The State of the Art of Nanotechnology for Processing of Ultraprecision and Ultrafine Products", ASPE Jan., 1994, vol 16, No. 1.

[17] R. D. Young, 'Field Emission Micrometer', RSI vol.37, Num.3, Mar. 1966, p275 278.

[18] T. Higo et al., Precise Fabrication of X-band Accelerating Structure, 9th Symposium on Accelerator Science and Technology, Tsukuba, Japan, 1993, KEK Preprint 93-57.

[19] K. Saito et at, water jet rinsing on SCC cavity

[20] V. A. Dolgashev et al., 'Application of Scattering Matrix Formulation for simulation of Accelerating Structures', JLC-Note No. 64, 1995, and the following progress in private communications.

[21] C. Adolphsen et al., Measurement of Wakefield Suppression in a Detuned X-band Accelerator structure, Proc. of LINAC94, 17th Int. Linac Conf., Tsukuba, Japan, 1994.

[22] C. Adolphsen et al., Measurement of Wake-Field Suppression in a Detuned X-Band Accelerator Structure, Phys. Rev. Lett. 27(1995) p2475.

[23] K. L. F. Bane, private communication.

[24] Xiaowei Zhan, Presented in SLAC/KEK workshop on Linear Collider, SLAC, Nov. 1996.

[25] K. L. F. Bane and R. L. Gluckstern, The Transverse Wake Field of a Detuned X-band Accelerator Structure, Part. Accel., p123, vol 42, 1993.

[26] T. Higo et al., High Gradient Performance of X-band Accelerating Sections for Linear Colliders, Particle Accelerators, 1994, Vol 48, pp.43-59.

[27] T. Higo et al., High-gradient Experiment on X-Band Disk-Loaded Structure, KEK Report 93-9, 1993.

[28] H. Matsumoto et al., High Gradient Experiment at the Accelerator Test Facility, Contrib. XVth International Conf. High Energy Accelerators, Hamburg, Germany, 1992, KEK-Preprint 92-84.

[29] J. Wang et al., High Gradient Experiments on NLC Accelerator Structures, Proc. XVIII Int'l Linear Accel. Conf. Geneva, 1996, p656.

[30] A. Roth, Vacuum technology, North Holland Publishing Co., 1976.

[31] Y. Suetsugu et al., Proceedings of International Workshop on B-factory, KEK, Tsukuba, Japan, 1992 and KEK Proceedings, 93-7, p189, 1993.

[32] H. Hayano et al., Submicron Beam Position Monitors for Japan Linear Collider, Submit. 16th. International Linac Conference, Ontario, Canada, 1992, and KEK Preprint 92-118.

[33] V. Vogel et al., Beam Position Monitor with Nano Meter Resolution for VLEPP, Proc. International Workshop on Emittance Preservation in Linear Collider, KEK, Tsukuba, Japan, 1993, KEK Proceedings 93-13, p664.

[34] T. Shintake et al., High Resolution RF-BPM Experiment at SLAC-FFTB, Presented in SLAC/KEK Workshop for Linear Collider, SLAC, USA, Nov. 1996.

[35] I. Wilson, Fifth International Workshop on Next-Generation Linear Collider, SLAC, 1993, SLAC-436, p352.

Authors of Chapter 9

- Toshiyasu Higo
- Yasuo Higashi

Main contributors to Chapter 9

- Toshikazu Takatomi (cell machining etc.)
- Shigeaki Koike (cell machining etc.)
- Susumu Koizumi (precision machining)
- Toshikazu Suzuki (assembly process etc.)
- Masashi Yamamoto ("OM" code, Ishikawajima-Harima Heavy Industry Co. at present)
- Keiko Tsukamoto (outgassing-rate measurement)
- Shigeki Kato (outgassing-rate measurement)

Thanks are due to the following colleagues outside the JLC design study group, who have made important contributions to the work presented in this report:

Karl Bane (SLAC) for wake-field evaluation using equivalent circuit, Chris Adolphsen (SLAC), David Whittum (SLAC), and Mike Seidel (SLAC) for the ASSET experiment, Juwen Wang (SLAC), Harry Hoag (SLAC), and Rodd Pope for collaborative work concerning DDS and more in general, Samy Hanna (SLAC) for the bead-pull measurement, Kwok Ko (SLAC), Xiaowei Zhang (SLAC) for various numerical evaluations, and many other people (SLAC) in various helps and discussions, Igor Syrachev (BINP, Protvino) for discussions on multi-bunch energy distribution, Valery Dolgashev (INP, Novosibirsk) for S-matrix analysis on multi-cell structure, Ian Wilson (CERN) and Walter Wuensche (CERN) for fabrication of a short structure and a high-field test, Meili Gao (IHEP, China) for building X-ray detection system for high-field test, Yuzheng Lin (Tsinghua Univ.) for analysis on damped structure and also in general, Liling Xiao (Tsinghua Univ.) for code development, and Peter Hülsmann (Fankfurt Univ.) for conducting HOM measurements.

CHAPTER 10

X-band Main Linacs: RF Power Generation and Delivery

Contents

10.1 Introduction

Through discussions on the next-generation linear colliders during the past decade, several major proposals concerning conventional-type electron-positron linear colliders emerged at accelerator laboratories world-wide[1]. A variety of main linac designs were surveyed, ranging from L-band superconducting linacs to the 14 GHz normal conducting linac; also, more ambitious schemes, such as two beam-type electron-positron linear accelerators that utilize a 30 GHz-class RF frequency were considered. The specifications of such linac designs are summarized in Table 10.1[1]. At this moment, it is widely felt that the next electron-positron linear collider at an energy range of 500 GeV center of mass can be based on an ordinary linac-type collider, that is driven by pulsed RF power sources of somewhere between the S-band and X-band frequencies.

	TESLA	SBLC	JLC	NLC	VLEPP	CLIC
Energy (C.M) (GeV)	500	500	500	500	500	500
RF Frequency (GHz)	1.3	3	11.4	11.4	14	30
Nominal Luminosity (10^{33} cm^{-2}/sec)	2.6	2.2	5.1	5.3	12	$0.7 \sim 3.4$
Linac rep. rate (Hz)	10	50	150	180	300	2530~1210
Particles/bunch(10^{10})	5.2	2.9	0.63	0.65	20	0.8
Bunches/pulse	800	125	85	90	1	1-10
Bunch separation (ns)	1000	16	1.4	1.4	—	0.67
Beam power/beam (MW)	16.5	7.26	3.2	4.2	2.4	0.8~3.9
Damping ring energy (GeV)	4.0	3.15	2.0	2.0	3.0	2.15
Total AC power to make rf (MW)	164	139	114	103	57	100

Table 10.1: *General parameters of the existing LC designs world-wide, which were presented in the TRC report 10.1[1].*

At KEK since 1988, among other possibilities, a version of the X-band (11.424 GHz) collider has been most intensively studied under close collaboration with SLAC[3, 2] and, more recently, with BINP, Protvino.

The general parameters of several linear colliders, including the JLC are summarized in Table 10.1. These elementary parameters are almost common to the two X-band linear colliders, JLC and NLC[4]. The critical aspects of these linear-collider designs are:

- These collider have a single-pass collision process instead of a multi-pass collision process in ordinary ring colliders,
- Consequently, they need to focus the colliding bunches to an extremely small cross section, such as several hundred square nano-meters, to deliver the required luminosity.

To satisfy this requirement, in the first stage of acceleration, a train of very low-emittance bunches

that are prepared by the damping ring are injected to the main linac. The main linacs are then required to sustain the high accelerating gradient to accomplish a high center-of-mass energy in beam collisions at the interaction point within a laboratory site with a realistic length. Of course, the main linacs need to preserve the low emittance of bunches by carefully controlling the deflecting wake-fields within the accelerating structure due to preceding bunches. The main linacs also have to include a mechanism to compensate for beam-loading effects. Extensive discussions on these requirements appear in [1, 3, 4].

The total electric power required for operating the linear colliders is quite high; it can amount to 200 MW. Consequently, efficient beam acceleration is of paramount importance. The energy-conversion efficiency starting from the wall-plug power to the beam, must be as high as possible. This must be achieved while the beam quality, such as the emittance and the energy spread, is kept within the limit to maintain a small beam size at the colliding point. Therefore, the beam-loading of the accelerating structure must be lower than the limit which is determined by the limit on the bunch energy spread, or the energy variation among bunches in a train. Thus, the beam-loading of the accelerating structure has an upper limit. Therefore, the total energy-conversion efficiency of a linear collider is basically determined only by the energy-conversion efficiency from the wall-plug power to the RF driving power at the input of the accelerating structure.

10.2 General Description of the X-band RF Power Source System

To achieve an accelerating field gradient of $\sim$ 70 MV/m or greater in an accelerating structure with a shunt impedance of $\sim$ 80 MΩ/m, the RF power fed per unit length of the linear collider should be around 100 MW/m or higher. The duration of the RF pulse should be 250 nsec, which is the sum of the filling time (106 ns) of the structure and the time-length of the multi-bunch train which consists of $\sim$ 85 bunches, each separated by 1.4 nsec.

These are absolute requirements for building a collider with $E_{\rm CM} \sim$ 500 GeV within a reasonable site length of 20 $\sim$ 30 km. In Table 10.2, the X-band linac parameters of the JLC main linac are presented. The most notable feature of this X-band linac is the shorter and higher pulsed RF driving power compared to that of the present S-band electron linacs, such as the SLAC 2-mile linear accelerator or the PF/KEKB injector linac at KEK [5, 6, 7].

In the JLC design, to provide a peak power of up to 130 MW to a unit 1.3 m-long accelerating structure, klystrons that are distributed every 4 - 5 m must feed a set of accelerating structures with an RF power totaling 390 MW. Clearly, such a high peak power is out of reach for a single klystron, even with the most advanced modern klystron technologies. In addition, the required RF pulse duration of 250 ns is too short to efficiently drive klystrons. The present high-voltage pulse-forming network with step-up pulse transformers that are used to drive klystrons can never create pulses with a rise time much shorter than 100 ns. Thus, the klystron modulator systems will suffer from poor efficiency if it were to drive klystrons with output pulses of 250 ns.

As techniques to simultaneously solve the issues of the high-peak power requirements and the use of a short-pulse length at accelerating structures, a series of RF pulse-compression schemes have been invented. The SLED (SLAC Energy Doubler) is a pioneering example [28, 31, 29]. The klystron driving pulse is set to about 4-5 times longer than the linac driving pulse. Then, the RF pulse is compressed so as to excite the accelerating structure with the required high peak power for a short period of time.

Parameter	Symbol	Value	Unit
— Energy —			
Collision energy	E_{cm}	1000	GeV
Beam energy	E_{final}	500	GeV
Injection energy	E_{inj}	10	GeV
— Beam parameters —			
Number of particles per bunch	N	0.70×10^{10}	
Number of bunches per pulse	m_b	85	
Bunch spacing	t_b	1.4	ns
Repetition frequency	f_{rep}	150	Hz
Normalized emittance at the exit of damping ring	$\gamma\epsilon_x/\gamma\epsilon_y$	3×10^{-6} / 3×10^{-8}	m
R.m.s. bunch length	σ_z	90	μm
Single-bunch full-energy spread		0.3	%
Multi-bunch full-energy spread		0.1	%
— RF basic parameters —			
Main accelerating frequency	f_{rf}	11.424	GHz
Nominal accelerating gradient	G_0	73.0	MV/m
Effective accelerating gradient[1]	G_{eff}	55.6	MV/m
RF unit (number of modulator / klystron / structure)		4 / 8 / 12	
Peak power input to structure		130	MW
Off-crest angle for single-bunch energy compensation[2]	ϕ_{rf}	17.2	deg
Single-bunch extraction efficiency	η_1	1.97~1.47	%
— Structure parameters —			
Structure type		Detuned	
Configuration		4-fold interleaved	
Accelerating mode		$2\pi/3$	
Number of cells in a structure[3]		150	
Structure length		1.31	m
Average iris radius in unit of wave length[4]	a/λ	0.166	
range (entrance - exit)		0.20~0.14	
Filling time[5]	T_f	106.4	ns
Attenuation parameter[5]	τ	0.609	
Beam hole radius	a	5.23~3.67	mm
Disk thickness	t	1.2~2.4	mm
Group velocity	v_g/c	0.098~0.02	
Q value[5]	Q	6800~6050	
Shunt impedance[5,6]	r/Q	10.2~13.6	kΩ/m
Shunt impedance[5,6]	r	70~82	MΩ/m

Loss parameter	k_1	2.44~1.83×10^{14}	V/C/m
Average power loss per structure[7]		3.4	kW
—— Dipole mode frequency ——			
Gaussian spread (sigma) of 1st passband	$\sigma f_{d1}/f_{d1}$	2.24	%
full spread of 1st passband	$\Delta f_{d1}/f_{d1}$	11.2	%
frequency tolerance	$\delta f_{d1}/f_{d1}$	$< 10^{-4}$	
Gaussian spread (sigma) of 6'th passband	$\sigma f_{d6}/f_{d6}$	0.716	%
full spread of 6'th passband	$\Delta f_{d6}/f_{d6}$	3.58	%
—— Klystron parameters ——			
Peak power	P_{kly}	67	MW
Pulse length[7]	T_{kly}	750	ns
Cathode voltage	V_k	430	kV
Cathode current	I_k	338	A
Estimated efficiency	η_{kly}	45	%
Focusing		PPM	
—— Pulse compression ——			
Pulse compression scheme		4/3 DLDS	
Transmission mode		TE_{01}	
Delay line diameter		118.1	mm
Delay line length (long / short)		79.4 / 39.7	m
—— Modulator ——			
Number of klystrons to drive		2	
Modulator configuration		Blumlein	
Number of stages		24×2	
Pulse transformer ratio		1:5	
Charging voltage		86	kV
Current[9]		1696×2	A
Switching device		Thyratron	
—— Tolerances and acceptances[10] ——			
Injection energy spread (acceptance)		2	%
Structure misalignment tolerance[11]			
cell-to-cell		9	μm
structure-to-structure		6	μm
minimum (at wave length ~60m)		3	μm
Quadrupole magnet (random)			
between successive beam based alignments		2	μm
transverse position jitter tolerance		10	nm
field strength jitter tolerance		0.5	%

— Linac —			
Number of DLDS units		561	
Number of klystrons / beam		4485	
Number of structures / beam		6727	
Number of DLDS units per DLDS period		6	
Active length of main linac / beam	L_{acc}	8.81	km
Packing factor		79.2	%
Total length / 2 linacs		22.3	km
Average beam power / beam		7.14	MW
Assumed efficiency from AC to structure input		28	%
Wall-plug power / 2 linacs		234	MW

1: net accelerating gradient including single-bunch and multi-bunch energy compensation
2: average over the whole linac
3: including input and output coupler
4: averaged being weighted by $a^{-3.5}$
5: assuming 95% of the theoretical Q value
6: accelerator definition
7: at the nominal gradient without beam
8: including switching time of DLDS; (10+230+10)×3
9: driving two klystrons
10: based on the criteria of 25% emittance growth in the linac
11: based on the random offset which is constant over each alignment length

Table 10.2: *500GeV X-band JLC main linac parameter.*

Considering these conditions, the most probable X-band RF power system that is presently believed to be a good RF power source for the next generation of linear colliders has a block-diagram as illustrated in Figure 10.1.

In these X-band RF power-source systems, there are several important differences from a traditional S-band electron linac RF power source.

The most significant difference is clearly the higher accelerating gradient of 50 MV/m in these X-band linear colliders. To achieve this higher gradient, the X-band RF power system is required to supply shorter and higher peak RF pulses compared with those of the S-band system. This requirement imposes a notable change in the RF power system of the X-band linear colliders [20]. Since the energy consumption of a future collider is considered to reach several hundred MW, as noted above, it is

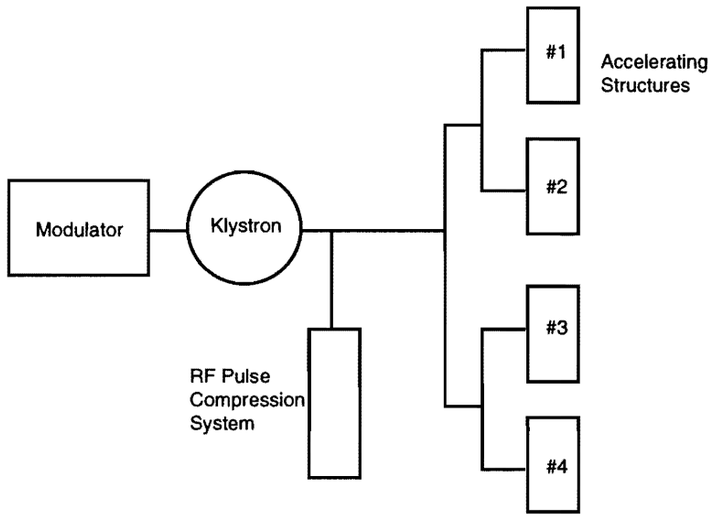

Figure 10.1: *Block diagram of the X-band RF power-source system. A conventional configuration with a modulator, a klystron and an RF pulse-compression system.*

quite important to supply these RF power with a high conversion efficiency. Thus, two major features were introduced to the X-band RF power system for JLC:

First, the introduction of the RF pulse-compression stage. This is to compress the klystron RF output pulse to be shorter by about a factor 4. This is due to the fact that the X-band RF power system has to deliver about a factor of 4 shorter RF pulse than the S-band system.

Second is the introduction of a Blumlein-type pulse-forming network as the driving pulser of the klystron [9, 10]. In the following sections, these design aspects of the X-band RF power source system of the X-band linear colliders are described in more detail.

10.3 X-band RF Power Source System for the JLC Main Linacs

10.3.1 Energy-Conservation Issues

In modern large-scale accelerators for high energy physics experiments, the electric power-consumption problem sometimes limits the scale of the machine. Even in the TRISTAN e^-e^+storage ring at a moderate energy of 30 GeV per beam, more than 50 MW of electricity was used in total, and most

of that was consumed to produce the RF accelerating power to compensate the beam energy loss due to synchrotron radiation from the beam.

As shown in Tables 10.1 and 10.2 the total electric power of a typical 500 GeV center-of-mass linear collider exceeds 100 MW, and at or over 1 TeV center-of-mass energy, overall electric power required for the main linac RF power system will be larger than 200 MW. This magnitude of electric power could support a modern city having a population of several hundred thousand people. Therefore, considering this problem from social points of view, one of the most important issues in the design of the RF power system for a linear collider in the sub-TeV to TeV energy region is the energy-conversion efficiency from the wall-plug to useful RF power (see Figure 10.2). In each stage of the RF power system from the wall-plug to the linac input, the energy conversion process necessarily has some energy loss, and this loss should be suppressed to be as low as possible.

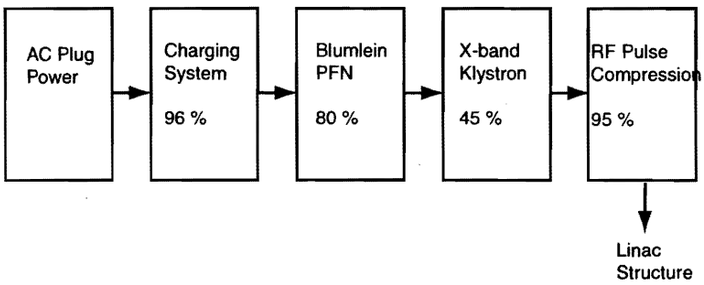

Figure 10.2: *Energy conversion efficiencies at each stage in an RF power system.*

The proposed X-band RF power-source system for the JLC main linac is sketched in Figure 10.3; its energy conversion efficiency in each stage is also summarized in this figure. The main parts which determine the overall efficiency are considered to be as follows:

1. A modulator consisting of a pulse-forming network and a step-up pulse transformer,

2. A klystron, and

3. An RF pulse-compression system.

In the sections below, energy-efficiency characteristics of these 3 stages mentioned above are discussed, since these three stages mostly determine the overall energy conversion efficiency of the system and furthermore, other stages, such as the DC charging system and RF power-transfer stage, already have a rather high conversion efficiency of over 90 %, and, consequently, could have only a minor contribution on the overall efficiency. Thus, relatively and practically they have no room for the possibility of further improvements.

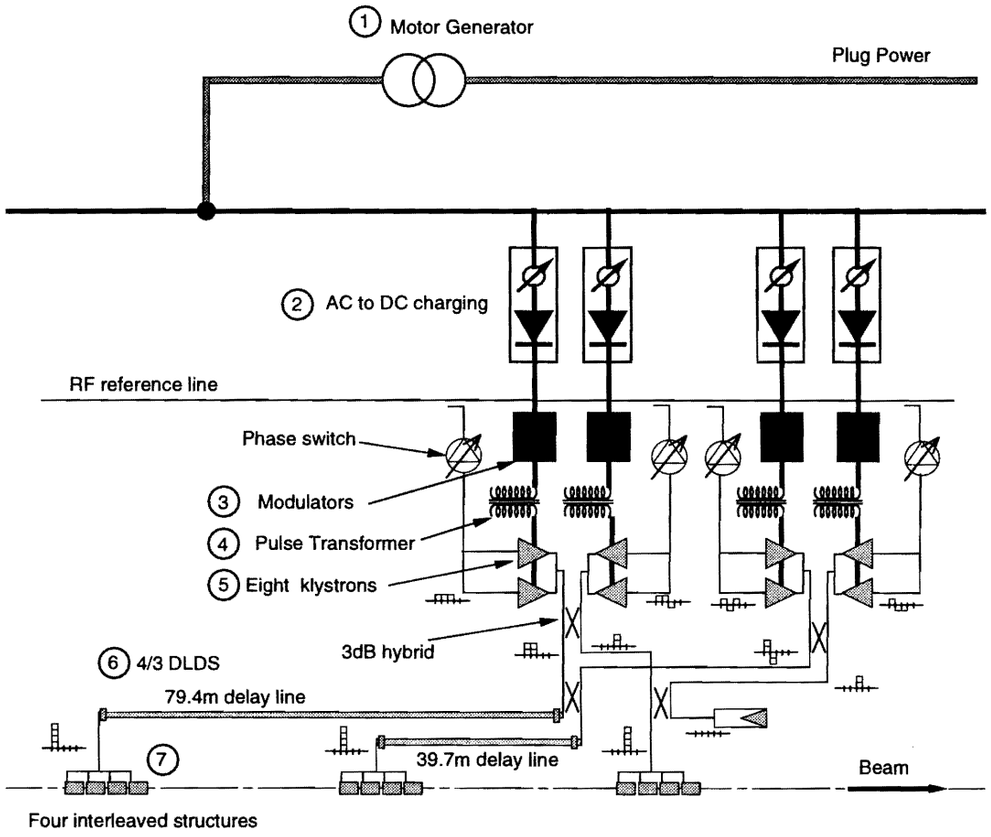

Figure 10.3: *JLC RF power-source system configuration (1) Stabilized Motor Generator (300 Hz, 10 MW/unit, 84 kV, 0.2% stability). (2) AC charging system (Direct AC charging, IVR(50(?)-105%), Command Charging System (Also as a Protection system)). (3) Pulse Forming Network (Blumlein type PFN) (86 kV, 900 ns, 150 pps, Thyratron SW. tube, 2-klystrons/1-PFN). (4) Pulse Transformer (Step-up ratio 1-5, 2nd Vout 430kV, 150pps. 2-klystrons/1-P.T.). (5) X-band Klystron (1.2 micro-P, 65 MW, 45%). (6) RF pulse-compression system (4/3-DLDS system, 250 ns output pulse, 80 m and 40 m Delay Lines). (7) RF Power distribution system (3 dB hybrid, waveguide and mode converters, RF monitor system)*

10.3.2 Issues with the X-band RF Power System

As briefly described in the preceding sections, it is widely believed that the next generation of electron-positron linear colliders could be constructed as the conventional-type linacs.

The high-power RF technologies applied to these X-band colliders should be designed as a natural extension of a present S-band RF power source, which is essentially based on the currently available pulsed high-power RF technologies. These S-band high-power RF technologies have been well estab-

lished through their long histories since the start of electron linacs and still has the potential to satisfy the specifications required for the X-band linear colliders.

However, the X-band RF power system necessarily has many different characteristics compared with these present S-band technologies, which may need some important change on its technology. As already described in the preceding sections, one of the most distinguished and also important point concerning these differences is the fact that at X-band the RF pulse duration, which covers the sum of the structure filling time and the bunch train duration is at most one fourth of that of ordinary S-band linacs. Therefore, this shorter pulse requires some significant changes in the X-band high power pulse system, especially in a klystron driver and an RF power-distribution system from a klystron to the linac accelerating structures.

10.4 DC Charging System for Modulators

The charging circuit of the modulator, which charges up the pulse-forming network, is usually the resonant charging circuit [6]. To stabilize the charging voltage within the necessary range for a stable operation of the linac, a de-Q'ing circuit is usually applied. This circuit bypasses the charging current when the charged voltage of the capacitance reaches a specific voltage. A typical charging-circuit for a line-type pulser consists of an AC DC power supply, a capacitor bank, a charging chalk, a charging diode or a command charging SCR controller, and, finally, the de-Q'ing circuit that regulates the charging voltage of the PFN capacitors. This kind of charging system has a long history, and is considered to be a possible choice of the charging system for future colliders. This charging and voltage-stabilizing system can be designed as a rather independent stage from the rest of the RF power system, and several schemes could be considered as possible candidates that could fulfill the specifications for klystron drive [9].

One possible example of a stabilized DC-charging system for the klystron driver, such as a PFN, is a simple AC charging system [9]. In this system the AC power line at a frequency of 300 Hz is supplied by a motor generator system that is stabilized by a large fly-wheel which can absorb a load-current change. This kind of stabilized AC power supply has once been widely used as the magnet power supply for rapid-cycle ring accelerators, such as synchrotrons. Figure 10.4 shows a conceptual illustration of the charging circuit with the 300 Hz IVR voltage adjuster.

The technologies required for this AC charging system are well established. The high stability of the fly-wheel system simplifies the charging system by eliminating the voltage stabilizer system, such as the de-Q'ing system [6, 9]. The energy efficiency of this charging system is excellent; it is typically higher than that of the ordinary DC power supply and a resonant charging system with the de-Q'ing circuit. At frequencies higher than 300 Hz, all electric power systems can be designed in more compact ways than that for an ordinary 50 Hz power line. The following are the distinctive points of this AC charging system:

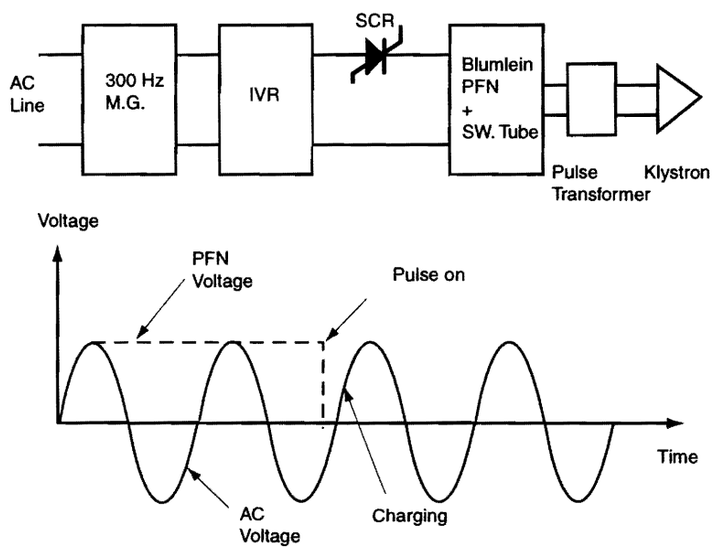

Figure 10.4: *Simplified diagram of a charging circuit.*

1. For 150 pps operation of the main linac, the lowest frequency of the fly-wheel system should be 300 Hz.

2. The power, which is adequate to be handled by a unit power system, is around 10 MW. Each system will handle about 1 km of the main linac.

3. Each RF power unit consisting of 8 klystrons should have an adjustable cathode voltage in the range of 100 - 30 %. This is to cope with situations where a power-unit swap is made, or conditioning procedures are being made.

4. The linac system can be controlled in synchronization with the power supply frequency of 300 Hz.

5. To provide uninterrupted service in the case of a faulty unit or scheduled maintenance, the system must include one or two reserve units.

6. A command-charging system driven by a thyrister switching device can be applied, instead of the usual charging diode. This circuit can also work as a protection system in case of faults of switching-tubes.

7. Stability of the output voltage. As pointed out earlier, since the fly-wheel system is sufficiently stable, the de-Q'ing system can be eliminated.

8. Choice of frequency. Probably between 300-1000 Hz. The choice of the core material of the transformers for the selected frequency needs to be examined.

This AC charging system is relatively simple, and all technologies necessary for it are presently well established; therefore, in this report further details are not presented.

10.5 Klystron Modulators

10.5.1 Introduction

A high-power pulsed klystron at the S-band is usually driven by the combination of a Pulse-Forming Network (PFN) and a step-up pulse transformer [6, 9]. This klystron-driver system has a long history since an S-band electron linac was constructed as a tool for high-energy physics experiments [5]. Since then, as a driver of a klystron, this combination has been practically utilized in all high energy electron linacs at the S-band [6, 7, 41].

Although, this combination guarantees very reliable and stable operation as a pulsed klystron driver, in the JLC X-band RF systems, several improvements are necessary. As described in the previous sections, an X-band linear collider requires a far shorter RF pulse duration than that of any existing S-band electron linacs. Most S-band pulsed RF power sources are operated with a modulator pulse duration of several micro-seconds. On the other hand, the klystron driving pulse at X-band linacs must be as short as a quarter of such S-band driving pulses, and must be as short as, or sometimes even shorter than, 1 μs. This short pulse prevents a straightforward application of the conventional type PFN with a step-up pulse transformer, since its rise and fall times can not be made short enough to sustain high efficiency.

In the light of increasing the power efficiency, it is desirable to entirely eliminate the modulator and to drive the klystron by means of anode modulation, a gridded cathode gun, or also by means of direct switching tubes (Hard Tube Pulser). They could all achieve faster rise and fall times than an ordinary modulator based on a step-up pulse transformer [36, 37, 40]. These technologies have a long history, and, in some cases, were very successful [9].

At present, a hard tube pulser which drives a 20 MW class klystron is being tested at DESY for their S-band linear collider [40]. Although this pilot study has been successful, this kind of klystron driver still has difficulties in switching high-voltage tubes and the development of a 500 kV-class switching tube may require a rather long lead-time.

A gridded-cathode type klystron has been under development at BINP since the early 1980's [36, 37]. It could achieve a peak output power of 80 MW at 14 GHz. However, again, this new technology faces many challenges, such as a lifetime problem of the gun and the cathode configuration. This gun configuration especially has difficulty concerning its grid, which, by requirement, is positioned close to the cathode surface. There, issues of grid contamination by evaporation of the cathode materiel and an inevitable high-voltage insulation problem still remain to be solved.

10.5.2 Conventional PFN modulator

A conventional modulator having a pulse-forming network with a step-up pulse transformer has a long history of driving high-power pulsed klystrons since the start of the pulsed RF power technology. Even in modern electron linacs, this configuration is the standard method as a klystron driver [8]. Therefore, it is widely believed that this conventional modulator with a pulse transformer is the most promising system if its efficiency could reach an acceptable level, such as 70-80 %, in terms of the klystron beam power made available for RF pulse with respect to the wall-plug power.

A modern standard modulator usually consists of two main components: a pulse-forming network (PFN) with a switching tube, and a step-up pulse transformer [7]. Naturally, it is desirable to directly connect a klystron to the output of the pulse-forming network, without going through a step-up pulse transformer. Unfortunately, current high voltage pulse technology can not produce such a high-voltage pulse directly. Thus, a pulse transformer with a 1:15 step-up ratio is usually inserted between PFN and a klystron that requires cathode pulses of 400 - 600 kV.

It is well known that in this configuration, the rise and fall times of the klystron cathode voltage are mainly determined by the time constant of the pulse transformer [7]. The losses in this area can be discussed in two portions. The first one is the efficiency from the wall-plug to the stored energy in the PFN through the high voltage transformer and a rectifier. The second one, which is very dependent on the circuit design, is the energy-transfer efficiency from the stored PFN energy to the flat top portion that is available as the klystron pulse.

Figure 10.5 shows a simplified equivalent-circuit diagram for a step-up pulse transformer and a klystron. In this circuit, the klystron is represented by a resister R_k and a capacitance C_k. Although the resistance of the klystron generally changes according to the cathode voltage, in this chapter it is simply represented by a constant resistance at the fixed operating voltage of the klystron [8].

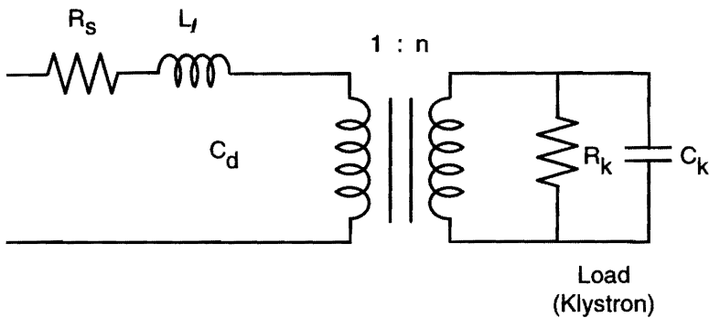

Figure 10.5: *Equivalent circuit for a pulse transformer and a klystron.*

The rise time T_r of this circuit is limited by the time constant determined by the leakage inductance L_l and the distributed capacitance C_d, as follows:

$$T_r \propto \sqrt{L_l \times C_d}. \tag{10.1}$$

In turn, the leakage inductance and the distributed capacitance of the pulse transformer are both determined by the geometry of the transformer. The secondary winding is separated by a gap of d in order to assure the insulation, since the secondary winding is raised to the high potential of the klystron cathode. To decrease the volume between the two windings, the secondary winding is usually tapered from the bottom to the top of the winding in proportion to the voltage difference. The leakage inductance is determined by the magnetic flux which is induced in the volume between the primary and secondary windings. The magnetic field between the primary and secondary can be approximated by an infinitely long solenoid field for the present discussion. Then, the leakage inductance is represented by

$$L_l \propto n^2 ad/l_w, \tag{10.2}$$

where l_w is the winding length and n the step-up ratio of the pulse transformer, a is the circumference of the coil, and d is the distance between the primary and secondary windings. The distributed capacitance is proportional to the winding surface area, and is inversely proportional to the distance d:

$$C_d \propto al_w\epsilon/d \tag{10.3}$$

The high-voltage pulse transformer is usually immersed in the insulation oil with a dielectric constant of ϵ.

Substituting C_d and L_l into the previous equation, the time constant of the pulse transformer is given by

$$T_r \propto na\sqrt{\epsilon}. \tag{10.4}$$

Thus, the time constant T_r is directly proportional to the step-up ratio n, if the rest of the circuit elements, other than that of the pulse transformer, is neglected. In a real system the capacitance of the klystron C_k should be taken into account. Capacitance C_d in the equation above should be replaced by $(C_d + C_k n^2)$. Since C_k is determined by the gun geometry of the klystron and the potential distribution of its surroundings, such as an oil tank, and shielding electrodes, this capacitance C_k is independent of the choice of the step-up ratio n.

Another factor which affects the time constant is the inductance of the klystron, itself, which should be added to the inductance L_l. While it may increase the time constant, when compared to the capacitance of the klystron, this inductance generally has a smaller effect on T_r, and can be mostly neglected in these considerations. [1]

On the other hand, the capacitance of the klystron is first determined by its perveance, and second by the dimensions of the gun-support structure, including the insulation ceramics and their geometrical configuration relative to the surrounding ground-potential parts such as the tank wall. Therefore, this parasitic capacitance of the klystron usually can not be negligibly small compared with the

[1] When the pulse transformer is driven by a pulse, an electro-magnetic wave propagates in the TEM mode along the secondary winding conductor. This propagation time determines the rise time of the transformer. By comparing the order of the length of the wiring from the pulse transformer to the klystron with the length of this secondary winding, it is readily seen that the effect of the length of the connection from the secondary to the klystron can be considered to be much smaller than this secondary-winding effect. This picture is valid as long as the propagation of the TEM mode wave is concerned.

stray capacitance of the pulse transformer, and must be included in the above discussions. However, following conclusion is still valid.

The time constant of the transformer is directly related to the step-up ratio of the pulse transformer, and is proportional to the step-up ratio n. It is quite simple that the energy efficiency of the klystron driver is improved by decreasing the step-up ratio of the pulse transformer. To realize this condition, the most important point to note is the fact that high-voltage circuit elements, especially the thyratron switching tube and capacitors, are vital parts of the PFN, and their high-voltage limit is the most important (and difficult) issue to overcome. Therefore, the application of the Blumlein circuit is an effective improvement measure, since this circuit configuration can double the output voltage of the PFN with the same charging voltage at its capacitances. A brief consideration of the application of this circuit to the modulator is discussed in the next section.

10.5.3 Blumlein PFN modulator

As briefly discussed in the previous section, the rise and fall times of a modulator are mainly determined by the stray capacitance and leakage inductance of the pulse transformer between the pulse-forming network (PFN) and the klystron. It was also concluded that to shorten the rise and fall times, and, consequently, to increase the modulator efficiency, it is effective to raise the primary voltage of the transformer, thus relaxing the step-up ratio of the pulse transformer [6, 10, 2, 11].

The Blumlein-type configuration is an arrangement where two identical PFN's are connected to each other through the output load. In our case the load is the pulse transformer, whose secondary winding is connected to the klystron load [8]. As stated in circuit theory, a PFN is a cascaded chain of low-pass filters.

It is well known that this Blumlein configuration can double the output voltage compared to the ordinary single-stage PFN [8]. This type of PFN has the advantage of introducing no new high-voltage components such as a thyratron and a capacitor, for doubling the output voltage. The rise and fall times of the PFN are determined by the delay time per stage, and usually the rise time of the PFN is chosen to be about 2-3 times the stage delay time to achieve a moderate rise time without any harmful overshoot at the head of the pulse. The parameters are given in Table 10.3 for the case of a PFN comprising 24 stages. The main parameters, such as capacitance and inductance, are all within the reach of the commercially available parts, and no significant problems are expected concerning this PFN. All circuits, including the switching tube and the charging chalk, are to be set in one large oil tank, so as to compactify the construct of the modulator while maintaining good high-voltage insulation.

A circuit diagram of the 100 MW-class Blumlein modulator is shown in Figure 10.6. The primary winding of the pulse transformer is connected at the potential of the charging voltage while charging the PFN capacitors. In a standard Blumlein-type PFN, the primary winding of the pulse transformer is usually kept at the ground potential during the charge-up period. This circuit configuration was chosen because the capacitance and inductance shown in Table 10.3 are rather small, and stray

Klystrons	XB72k×2	XB72k×1
Charging voltage	113.2 kV	113.2 kV
Current	5110 A	2555 A
Impedance	11.0 Ω	22.15 Ω
Inductance	2.305×10^{-7} H	4.61×10^{-7} H
Capacitance	1.88×10^{-9} F	0.939×10^{-9} F
Stage number	24 × 2	24 × 2
Total capacitance	90.24×10^{-9} F	25.1×10^{-9} F
Delay time / Stage	20.8 ns	20.8 ns
Total delay	1000 ns	1000 ns
Pulse energy	578 J	289 J
Rise time (3 stages)	60 ns	60 ns

Table 10.3: *Blumlein PFN parameters.*

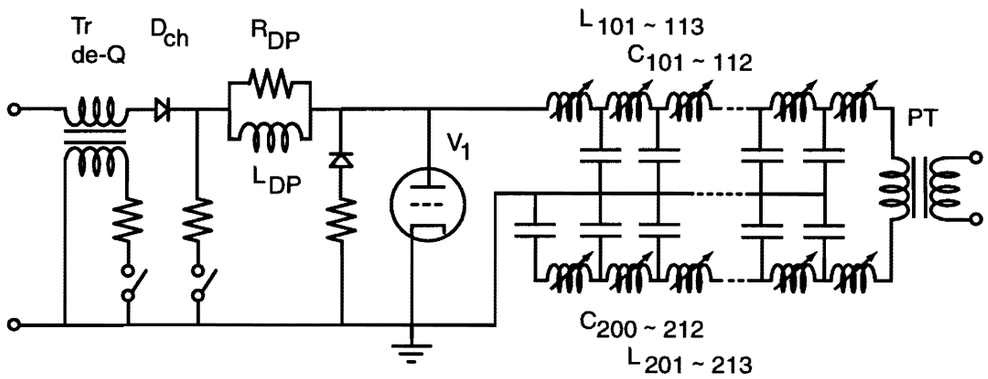

Figure 10.6: *Blumlein pulse-forming network (circuit diagram).*

capacitance and the stray inductance caused by the wiring and their geometrical size effects are large in comparison. In this circuit configuration the primary winding of the pulse transformer is kept at the charging potential. All of the ground line can be kept at the ground potential through the whole period of its pulse operation.

On the other hand, in the standard configuration of the Blumlein circuit, the primary winding of the transformer, which is kept at ground potential during the charging period, inevitably changes its potential once the pulsing operation begins. Thus, the standard-circuit configuration is apparently more sensitive to stray capacitance and inductance of the ground line, itself, because these values can not be made as negligibly small compared with those of the circuits constant. This circuit configuration requires that the primary winding of the pulse transformer should be insulated from the iron core by the potential of the charging voltage. However, since this insulation distance is far shorter than that of the secondary winding, this constraint introduces no significant difficulties, such as an increase in

the stray capacitance and the leakage inductance.

10.5.4 Pulse transformer

The pulse transformer for the system usually limits the rise and fall times of the driving pulse. As described in an earlier part, the rise time of the PFN, itself, is determined by its number of stages; it is relatively easy to shorten this rise time by increasing the number of stages so as to make the delay time per stage shorter. Thus, the rise time of the PFN, itself, could be shorter than 60 ns, as shown in Table 10.3, without any substantial difficulty. On the other hand, the rise and fall times of the pulse-transformer are determined by several parameters of the pulse-transformer design, and also by the additional capacitance and inductance of the loads in the secondary circuit, i.e. in this case the capacitance and inductance that are added by the klystron and its socket configuration. Therefore, choosing the parameters of the pulse transformer is a rather cumbersome and empirical process. Figure 10.7 shows a photograph of a 1:7 pulse transformer for vers. 1 and 2 Blumlein prototype modulators. The primary winding is set to be floating. In this section, an outline of the design of the pulse transformers is presented.

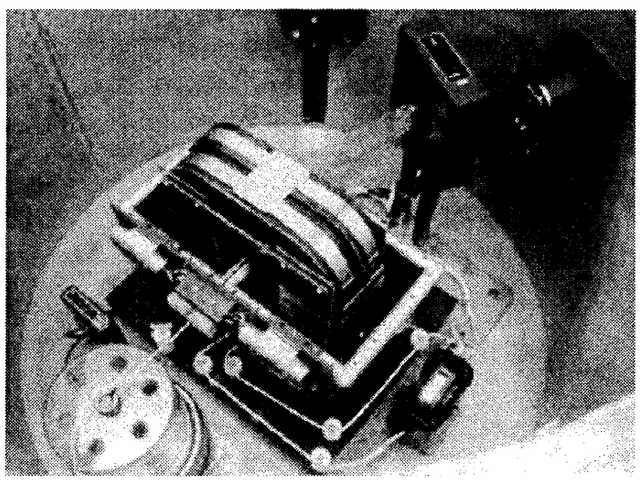

Figure 10.7: *A 1:7 pulse transformer for vers. 1 and 2 Blumlein prototype modulators. The primary winding is set to be floating.*

As mentioned earlier, the primary winding of this pulse transformer is kept at the charging voltage during the charging period in order to keep the ground line potential throughout the pulsing operation. This rather specific feature does not introduce any new restriction to the design. No degradation, such as an increase in the leakage inductance or stray capacitance in the transformer, is expected to be introduced by the constraint of the primary potential. Thus, the pulse transformer of the JLC X-band RF power system can be designed as a conventional-type without requiring any new technology or development of a new material. One example of the design is shown in Table 10.4. As

shown in this Table, a commercially available core material, 1 mil-thick Si-Fe sheet, has a satisfactory quality to achieve a pulse rise time of 160 ns with sagging of 2 % due to the pulse transformer. This sagging is well within the limit that can be easily compensated by the tapering technique of the pulse-forming network circuits. Other parameters, such as several kinds of losses and size, are all set within a practically satisfactory range. In general, pulse transformers are one of the parts that can be constructed without requiring any new technology. Therefore, no further detailed discussion of the pulse transformer is presented.

Rep. Rate	150 pps
Secondary output	430 kV
Flat top	800 ns
Sagging	2.2 %
Impedance(Pri.)	25.5 Ω
Impedance	636 Ω
Step-up ratio	1 - 5 (3 - 15 turns)
Rise time	160 ns
Fe core cross section	144 cm^2
ΔB (w. Bias I)	17.2 kG
Fe-Si sheet	25 μm
Bias Current	(25 A)?
Primary Inductance	460 μH
Capacitance	4 nF(total in primary)
Leakage Inductance	897 nH
Hysteresis Loss	—
Joule Loss	—
Eddy Current Loss	—

Table 10.4: *Parameters of the 1-5 pulse transformer for driving two units of 65 MW klystrons. The hysteresis loss, Joule loss and Eddy current loss have not been fully examined.*

10.5.5 Prototype Blumlein modulator, Vers. 1

The vers.1 Blumlein modulator was the first test model to be built [12, 13]. The general set-up of this Blumlein is very similar to that of a standard single-stage PFN, which is widely used in S-band linacs. The PFN circuit components of the vers.1 Blumlein are operated under atmospheric condition, while the pulse transformer is located inside of an oil tank.

In the initial configuration the PFN of this modulator consisted of a 9-stage ordinary PFN network (case 1). Testing under this condition was performed with a HV up to 500 kV, while being loaded with high-voltage resistors. After this initial test, the number of PFN stages was increased to 13 so as to produce longer pulses (case 2). Under this condition, testing was again performed with HV up

to 500 kV, but loaded with a XB72K klystron tube. In the following, the results from these tests are presented.

Case 1: With a Resistor Load

The PFN circuit parameters and the parameters of a 1:7 step-up transformer are given in Table 10.5. A test operation was made with this 1:7 step-up transformer.

PFN parameters		
	Impedance	23 Ω(11.5 Ω×2 lines)
	Charging voltage	80 kV
	Pulse width	700 ns (full width)
	Number of stages	9 stages × 2-lines
	Inductance / stage	460 nH
	Capacitance / stage	3.5 nF
Pulse transformers		
	Step-up ratio	1:7
	Leakage inductance	830 nH
	Stray capacitance	4 nF (including klystron)
	Hysteresis loss	100 W (at 200 pps)
	Eddy current loss	1 kW (at 200 pps)
	Rise time	~100 ns
	Fall time	~200 ns
	Sagging	2.0 % (500 ns flat top)
	Core material	25 μm Si-Fe sheet

Table 10.5: *Parameters of the PFN and the pulse transformer for the case 1 testing of the vers.1 Blumlein modulator. The values correspond to the measurement as shown in Figure 10.9 (A).*

Capacitors from two vendors (one Japanese; the other, Maxwell of U.S.) were tried in the PFN circuit. The Maxwell capacitors allowed a faster rise time of 280 ns; with Japanese capacitors the measured rise time was about 330 ns. This difference is considered to have originated from the smaller inductance of the American capacitors. Figure 10.8 shows a photograph of the installation work of the HV capacitor bank for the Blumlein modulator prototype.

Figure 10.9 shows the wave form from this test, indicating a rise time of 280 ns. It shows a light sagging on its flat-top portion and a light overshoot at the head of the pulse. However, regarding the rise time, the measured wave form was found to be in good agreement with a simulation obtained from the SPICE code, which is shown in Figure 10.10.

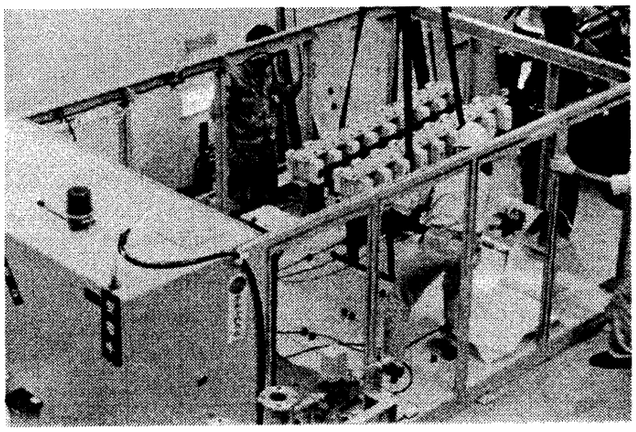

Figure 10.8: *Installation of the HV capacitor bank for the Blumlein modulator prototype.*

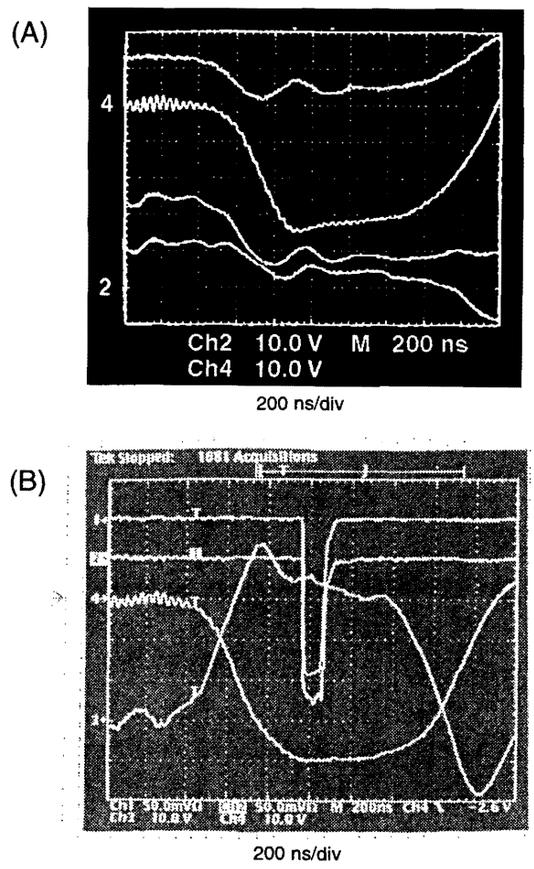

Figure 10.9: *Observed output pulse in a high-power test of the vers.1 Blumlein modulator. (a) A 1:7 pulse transformer is used with a 1 kW high-voltage resister load. (b) A 1:8 pulse transformer with a XB72K klystron as the load.*

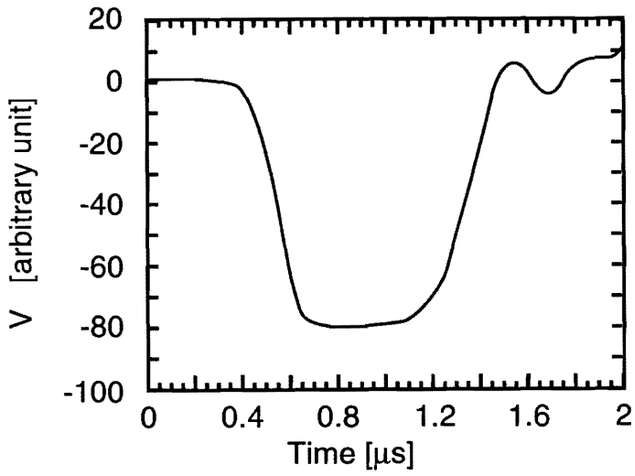

Figure 10.10: *Simulated output pulse shape according to a simulation using the "SPICE" code for the 1-7 pulse transformer case. This calculation is to be compared with the measurement shown in Figure 10.9 (A).*

Case 2: With a Klystron Load

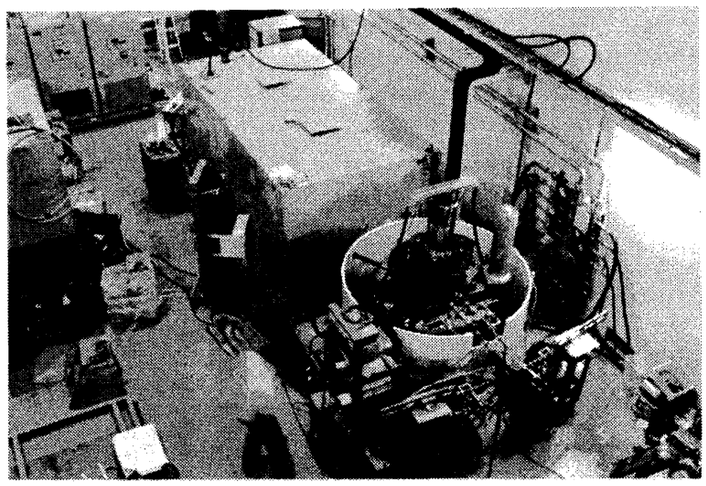

Figure 10.11: *Version-1 Blumlein modulator during testing, loaded with an XB72K klystron.*

Loaded with a XB72K klystron, a high-voltage test of the vers.1 Blumlein modulator was performed with a HV up to 530 kV. To provide a longer flat-top pulse to drive the klystron, the pulse transformer was rewound so as to have a 1:8 step-up ratio; the number of stages was increased from 9 to 13. The PFN impedance was adjusted so as to cope with this revision by changing the circuit inductance. In a test with XB72K #6 and #7 tubes as the load, a rise time of 300 ns was achieved, exceeding the performance of other conventional-type PFN's. Figure 10.11 shows the version-1 Blumlein modulator during testing, loaded with an XB72K klystron.

Figure 10.9(B) shows the output pulse shape from this test, loaded with a XB72K klystron. The shoulder of the pulse is somewhat dull. This is probably due to stray capacitance of the klystron and transformer. Apparently, the choice of the step-up ratio of the transformer is quite important to achieve a rise time of 200 ns or less. An additional careful investigation of the stray capacitance of the klystron and transformer is also necessary.

Vers.1 Blumlein: Present and Future

The vers.1 Blumlein presently serves in the test station for XB72K-series klystrons. It is typically operated within an output voltage range of 300 - 530 kV at 10 - 50 pps. Operation during the past year (1996) was successful, except for a minor annoyance due to a mis-operation of the interlock circuit due to thyratron noise. This is being treated.

10.5.6 Prototype Blumlein modulator, Vers. 2

Based on the operational experience with the vers.1 Blumlein modulator, a new oil-tank version of the Blumlein modulator (vers.2) was designed and built. The charging chalk, PFN's and thyratron switching circuits are all located inside of one big oil tank. This allows the circuit components to be made significantly smaller than in the case of the vers.1 Blumlein modulator. It also makes it much easier to control the stray capacitance, parasitic inductance and coupling between the coils that usually degrade the performance of the PFN circuits. A picture of the vers.2 Blumlein is shown in Figure 10.12. Its basic parameters are listed in Table 10.6.

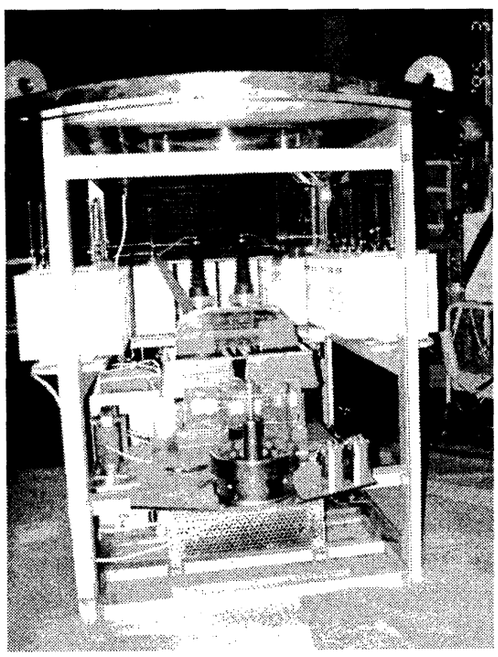

Figure 10.12: *A picture of the vers.2 Blumlein modulator.*

PFN parameters		
	Impedance	23 Ω(11.5 Ω×2 lines)
	Charging voltage	80 kV
	Pulse width	700 ns (full width)
	Number of stages	16 stages × 2-lines
	Inductance / stage	252 nH
	Capacitance / stage	1.9 nF
Pulse transformers		
	Primary voltage	80 kV (while charging) ±40 kV (operation)
	Primary current	3478 A (peak)
	Secondary voltage	560 kV
	Secondary current	497 A
	Step-up ratio	1:7
	Primary impedance	23 Ω
	Repetition rage	50 pps
	Pulse width	400 ns (flat top)
	Rise time	110 ns
	Fall time	150 ns
	Primary inductance	560 μH
	Sagging	< 2.0 % (with 25 A bias current)
	Leakage inductance	< 1.2 μH
	Stray capacitance	0.434 nF (Primary-secondary)
	Hysteresis loss	100 W (at 200 pps)
	Core material	25 μm Si-Fe sheet
	Bias current	max 30 A (2-turns)

Table 10.6: *Parameters of the PFN and the pulse transformer for the case-1 testing of the vers.2 Blumlein modulator.*

Preliminary Results from the vers.2 Blumlein Testing

Low-voltage testing of the vers.2 Blumlein modulator was conducted by using an FET switching circuit, instead of a thyratron. A load resister was attached to the secondary terminal of the 1:7 setup-up pulse transformer. In these tests the inductance coil in the PFN was changed to the double-parallel type for improved inductance trimming. All low-voltage test operations were performed in an atmospheric environment.

A high-voltage test of this vers.2 Blumlein modulator was also conducted, but without using oil. For this test, the load resister was replaced by a high-voltage resister built by Tokai-Konetsu Co. A charging voltage of around 5 kV was applied, resulting in about 35 kV at the secondary. The rise time of the output pulse in this condition was measured to be 200 ns (10 - 90 %). After conducting a few more similar tests and trimming of the PFN for an improved flat-top width and faster rise time, a full-voltage test of this modulator in the oil tank is scheduled for Spring, 1997.

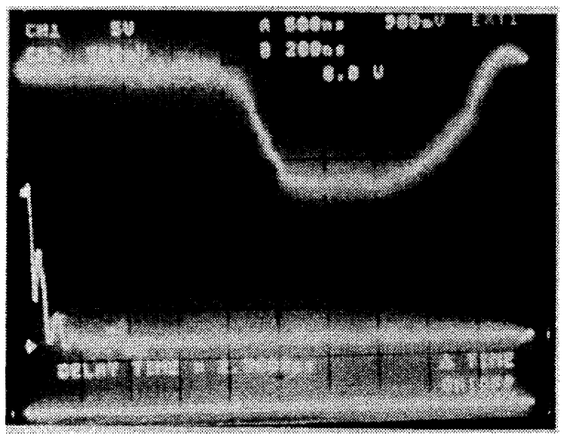

Figure 10.13: *Output pulse shape from the vers.2 Blumlein modulator (oil-tank type) in a low-voltage test. This test was performed in the atmospheric environment. Switching was done by a thyratron. The charging voltage was 8.8 kV. The horizontal axis gives the time with 200 ns/div scale.*

Figure 10.13 shows the output pulse shape in the low-voltage test. The best measured rise-time was 180 ns (10 - 90 %). The pulse shape was fairly flat. All low-voltage test operations were performed in an atmospheric environment. Overall, the results obtained in the low-voltage condition were quite satisfactory, and no further low-voltage measurements are considered to be necessary. It should be noticed, however, that these tests were performed in an atmospheric environment. Therefore, the rise time obtained here should be considered to be the fastest limit, due to the relatively small stray capacitance in the system compared to that in an oil environment.

10.5.7 R&D on Blumlein Modulators in the Immediate Future

As described in the preceding sections, the Blumlein-type PFN was proved to be a promising technology for the JLC klystron drivers. In the R&D plan for the future, the following issues are to be considered:

1. Attempts should be made to reduce the step-up ratio of the pulse transformer. This requires an increase in the charging voltage. A charging voltage of 120 kV is considered the practical limit of the currently available commercial thyratrons. The results obtained in our experiments with vers.1 and vers.2 Blumlein modulators indicate that charging with 120 kV is sufficient for accomplishing an adequate rise-time performance. In this case, the step-up ratio of the pulse transfer would be 1:5. Going beyond a charging voltage of 120 kV will require new R&D work on the thyratron itself; this is considered to be somewhat out of reach.

2. A further inspection of the stray inductance and capacitances at the secondary of the pulse transformer should be made. An improved trimming of the stray capacitance needs to be incorporated into the design, while taking the klystron cathode configuration into account. Within the klystron the size of the bottom portion near to the heater transformer should be reduced. This can be done by applying a direct feed without using a transformer.

3. Parallel driving of the 2-klystrons by a single modulator should be considered for the final design of the JLC. This arrangement is likely to allow a saving of the construction cost, and to relax the space problem within the accelerator housing. Due to the lower impedance of the PFN in this case, a shorter rise time can be expected.

   Since the 4/3-DLDS requires 8 klystrons, which should be located at the same position, this double-drive configuration is especially suitable for the 4/3-DLDS.

Considering these factors, the next step is to design and fabricate a JLC prototype Blumlein with a 1:5 pulse transformer that drives two 65 MW klystrons. We will proceed with this stage after completing high-voltage tests of the present oil-tank type Blumlein (vers.2).

10.6 X-Band Klystron

10.6.1 X-band Klystrons as the Main Linac Power Source

X-band klystron is the most vital part of the RF power system that drives linacs. The history of the high-power pulsed klystron parallels that of electron linacs. The basic technologies of pulsed high-power klystrons at the S to X-band, 3 $\sim$ 10 cm wave range, have seen significant progress during the past decade. The X-band klystrons, which can fulfill the minimum requirements as the RF power source for a linear collider, are currently believed to be within reach of the present klystron technology. A typical operational result of the SLAC XL4 klystron is shown in Figure 10.14 [4] (also, see [14, 15, 16, 17]).

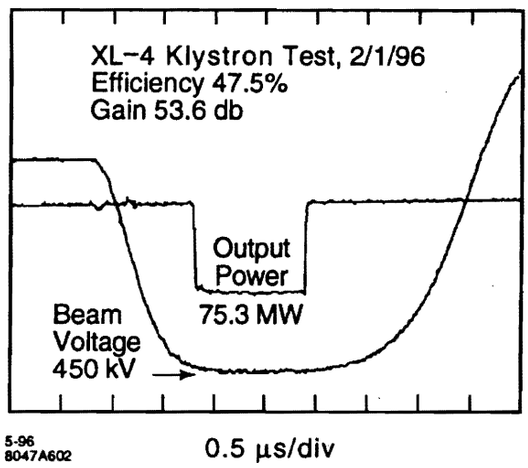

Figure 10.14: *High-powered test of the SLAC XL-4 klystron. Output power, 75.3 MW. Pulse duration, 1.1 μsec.*

For the first-phase operation of JLC main linacs, the primary candidate for use as its power source is 80 MW-class X-band klystrons driven at 65 MW peak output power with a pulse length of 800 ns. The parameters required to be achieved by these klystrons are summarized in Table 10.7.

The current R&D efforts for the X-band klystrons are thus focused on 80 MW-class tubes. Specifically:

1. High-power klystrons with an output peak power of 65 MW, first with conventional focusing solenoid, and eventually with PPM (periodic permanent magnet) focusing. This is the highest priority item.

Operating frequency	11.424 GHz
RF pulse width	800 ns
Repetition rate	150 pps
Peak power output	65 MW
RF efficiency	45 %
Cathode heater power	500 W
Beam voltage	430 kV
Beam current	338 A
Beam Impedance	1271 ohm
Focusing field	6.5 kG(Max.)
Solenoid power	1.5 kW (SCM)
Microperveance	1.2 micro perveance
Peak drive power	1 kW(?)
Gain	> 53 dB
Ceramic windows	1 or 2-"Otake" TE11 windows
Output Cavity	5 or 7 cell TW

Table 10.7: *Specifications of the 65 MW X-band klystrons for the current JLC design.*

2. Design studies of the tubes as part of the RF power source system, including matching aspects with the PFN and pulse transformers. Efforts need to be made to reduce the capacitance of the gun structure so as to achieve a faster rise time of the power pulse for better operational efficiency.

3. Development of a super-conducting solenoid coil based on a high-T_c material as the strong focusing of electron beams within the tube.

4. R&D on a VLEPP-type gridded gun structure.

Efforts are under way at KEK for R&D of an 80 MW-class X-band klystron, named XB72K [22, 21, 24, 23]. Its specifications are summarized in Table 10.8. The test results that have been obtained in high-voltage tests since 1992 are also given in the same table in the far right column.

10.6.2 Gun Design of XB72K

The gun of the XB72K was designed, based on past experience involving several 60 MW-class S-band klystrons, including model 5045 (SLAC), and the KEK 30 MW-class klystron (XB50K) [18, 19]. The XB50K was tested once up to 480 kV. The experience obtained with the 80 MW-class S-band klystron, built by Toshiba Co., was also taken into account. The basic parameters, such as the cathode loading, maximum surface field stress on the anode and beam-area compression factor, were all designed to stay within a factor of 1.5 of the existing S-band klystrons. Table 10.8 summarizes basic gun parameters. The values of these parameters are considered to be a natural technological extension of the present

Item	Design value	Achieved
Frequency	11.424 GHz	
Beam voltage	550 kV	620 kV
Beam Current	490 A	550 A
Max. surface field(Gun)	273 kV/cm	
Beam area compression	110^{-1}	
Cathode diameter	72 mm	
Cathode loading(Max.)	17 A/cm^2	
Focusing field(Max.)	6.5 kG	
Number of cavities	5	
RF output	120 MW	95 MW (70 ns pulse)
Efficiency	47 %	36 %(at 50 MW)
Max. surface gradient (Output gap)	720 kV/cm	Serious damage at 50 MW RF out
Gain	53-56 dB	

Table 10.8: *Initial design target and achieved parameters of XB72K klystrons.*

state-of-the-art in high-power pulse technologies and high-power pulsed klystrons.

Figure 10.15 shows a result of simulation with EGUN in the vicinity of the gun that shows the electric equi-potential lines and electron trajectories. Figure 10.16 shows a photographic view of the gun cathode of the XB72K.

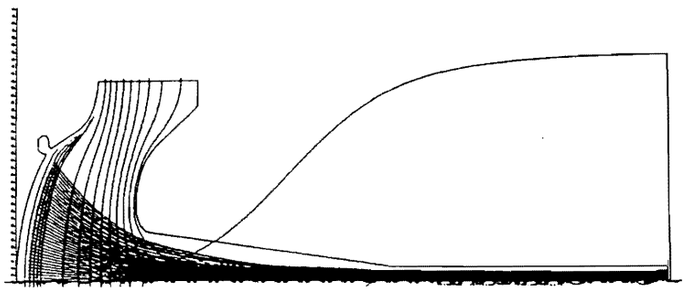

Figure 10.15: *Simulation result of the gun design for the XB72K, indicating the electric field and electron trajectories at a cathode voltage of 550 kV with a current of 490 A.*

The gun portion of the XB72K has repeatedly demonstrated its operation as a 600 kV - 1.2 μperveance gun with a pulse length of 2 μs. Operational experience with the # 1 through # 5 prototype XB72K tubes have shown that this gun design essentially has sufficient performance to be used in a 100 MW-class klystron. Up to 330 MW of beam power has been successfully obtained. No beam-interception problems have been experienced in the gun during operation or in post-mortem analyses of the tubes.

Figure 10.16: *Photograph of the gun of an XB72K tube that was retrieved after high-voltage testing.*

10.6.3 RF Structure of XB72K

Bunching System

Figure 10.17 shows a schematic view of the bunching system of the XB72K klystrons. The results

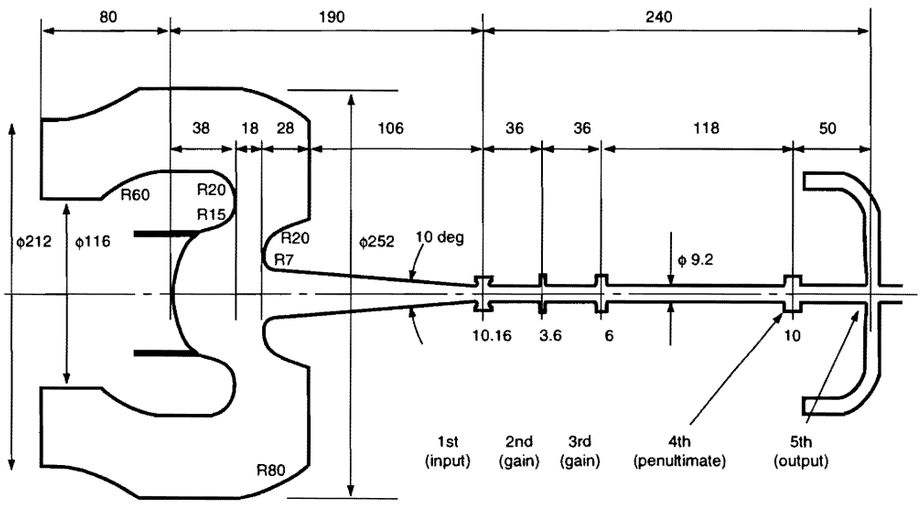

Figure 10.17: *Schematic view of the bunching system in XB72K.*

obtained with the # 1 through # 5 prototype XB72K indicate that its bunching system is capable of producing an RF current that corresponds to an RF power of 50 MW with an efficiency of 36 % at the output structure. The observed gain of $\sim$ 53 dB is in good agreement with simulation results from the FCI [24].

It is considered that some modifications to the bunching section are necessary in order to improve the RF conversion efficiency. Possible measures include the application of a second harmonic cavity. This will be surveyed in the near future.

Output Cavities

The prototype # 2 through # 4 XB72K tubes employed a single-gap output structure. In these tubes, serious damage was induced by RF discharging in the output cavity repeatedly. This discharge was the limiting factor for the magnitude of the output RF power. This problem also limited the output pulse duration to at most about 100 ns at 90 MW, even after a long conditioning period (or 200 ns with 30 MW output power).

Several improvements in the design near to output cavities have been considered. First, the surface stress of the output cavity needs to be reduced. Second, the bore size of the output gap needs to be increased. For this purpose, a traveling-wave-type multi-gap output structure has been developed at BINP, Russia and has been adopted starting with the #6 prototype[25].

The TW output circuit of the #7 XB72K is shown in Figure 10.18. The maximum surface field strength has been reduced to about 700 kV/cm at an output power of 120 MW. Figure 10.19 shows the field distribution along the TW structure obtained by the "DISKLY" code. Thus, the discharge limit of the output cavity was expected to be significantly relaxed compared to that of the single-gap klystrons up to #5.

So far, two tubes of this type (#6 and #7) have been built and tested.

Figure 10.20 shows a photo of the test set-up with the XB72K. Figure 10.21 shows a schematic drawing of the XB72K with a multi-gap output structure.

Figure 10.22 shows the obtained output power as a function of the cathode voltage. Measured RF output power for operation with a pulse length of 100 ns, and prediction based on a simulation using the DISKLY code are shown. The current issues involving these tubes are the following:

1. While an output pulse of 30 MW with 300 ns duration has been obtained after 10 hours of conditioning, behavior indicative of RF discharges has still been observed.
2. The RF power conversion efficiency is low (26 %). This is due to the design which maintains a low surface stress in the output gap (700 kV/cm at 120 MW).
3. The output RF output is unstable for pulses longer than 100 - 200 ns. The exact cause of this behavior needs to be investigated.

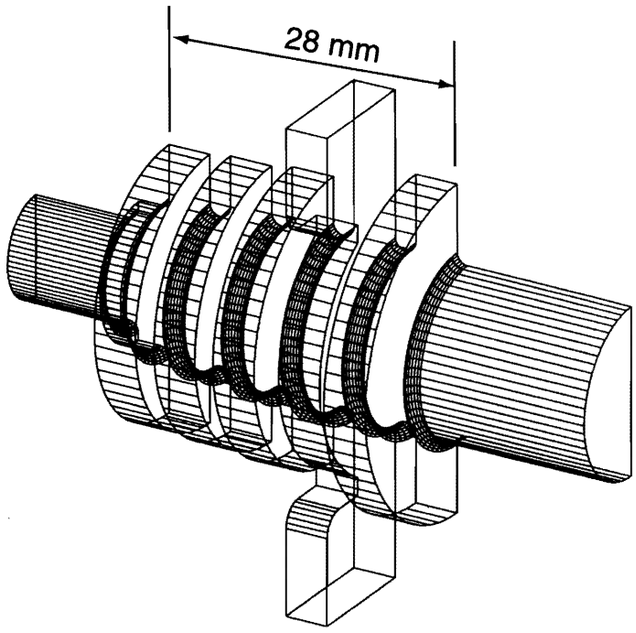

Figure 10.18: *Three-dimensional view in the vicinity of the 5-cell output cavity of the XB72K.*

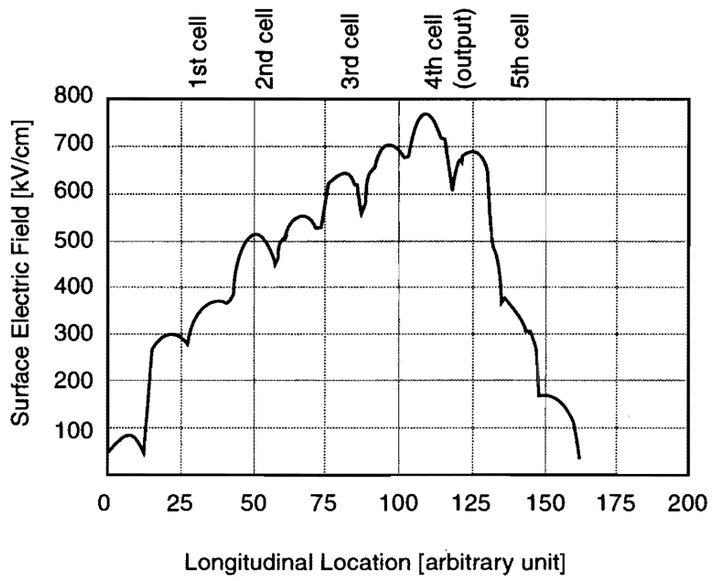

Figure 10.19: *Calculated surface field in the region of the 5-cell TW output cavities of the XB72K when the klystron is operated at 120 MW output power.*

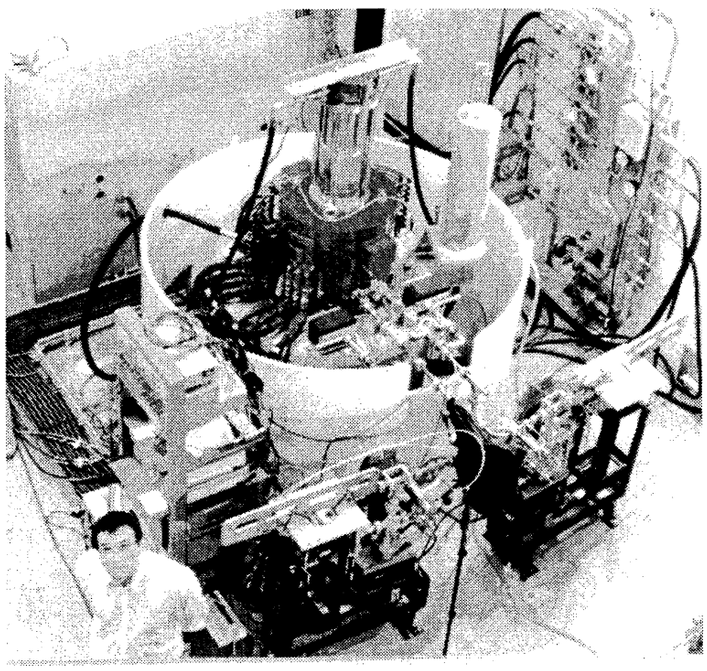

Figure 10.20: *The XB72K klystron in the test set-up.*

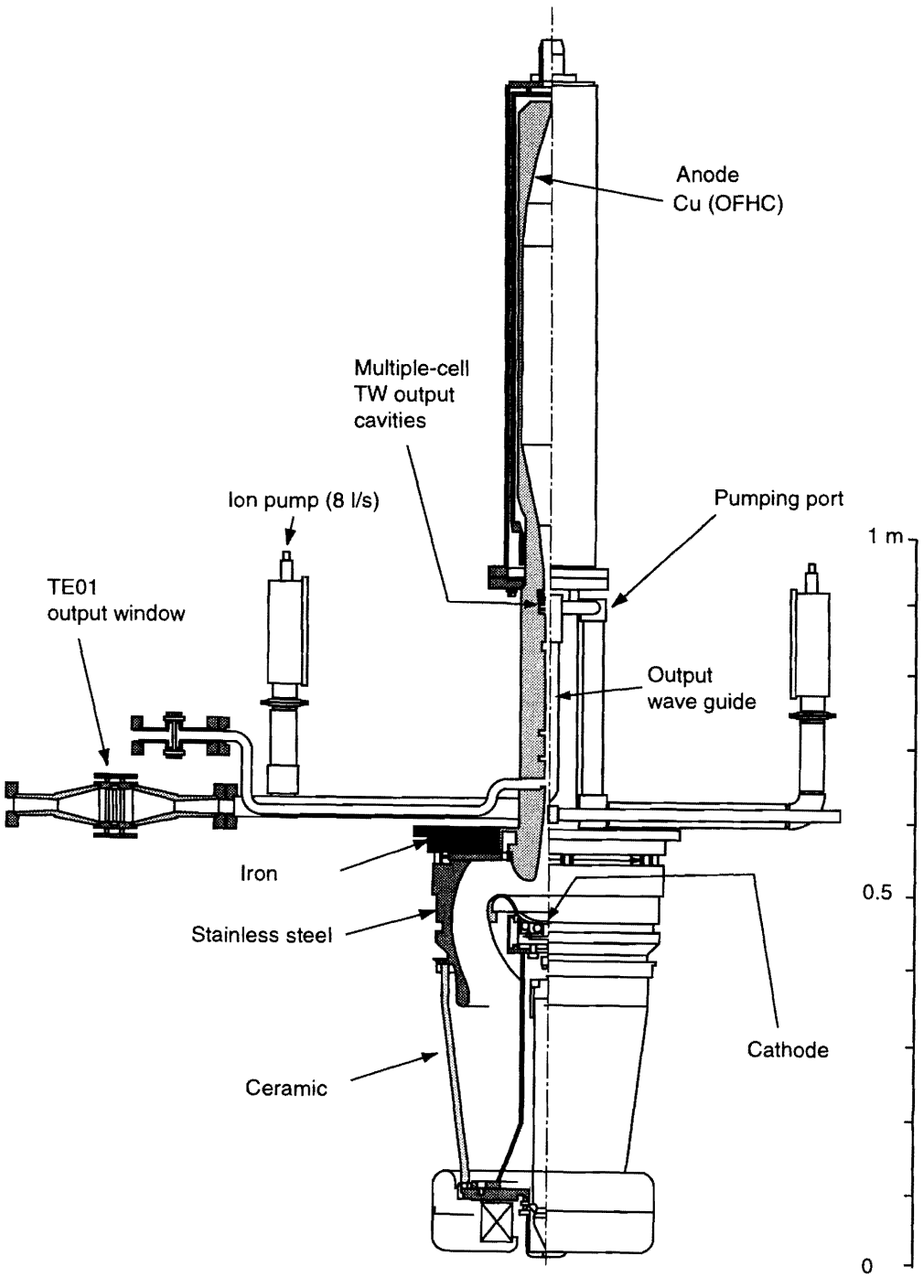

Figure 10.21: *Schematic diagram of an X-band klystron model XB72K #7.*

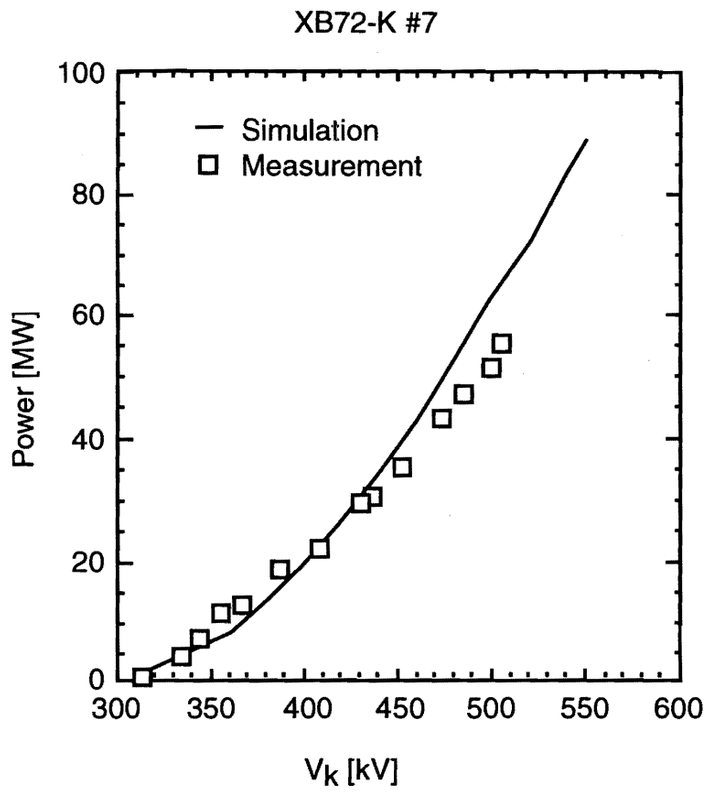

Figure 10.22: *Result from high-power testing of the XB72K klystron, prototype # 7. The output power as a function of the cathode voltage. Measured RF output power for operation with a pulse length of 100 ns, and prediction based on a simulation using the DISKLY code are shown.*

10.6.4 RF Windows for the XB72K

The ceramic windows are one of the vital parts of a high-power pulsed klystron system for any frequency. At the X-band the power-handling capability of the ceramic window is more serious than that of S-band high-power klystrons. This is because the RF power density to be handled at the X-band is more than 10-times the case with the S-band. The development of X-band windows has been initiated since the first stage of X-band R&D at KEK [26, 27]. High-power testing and development work has been carried out for the following types of RF windows:

1. $1/2\lambda_g$ rectangular type,
2. pill-box type,
3. TE11 $1/2\lambda_g$ type.

The best RF window obtained at KEK was developed by Y.Otake[27]. This window employs the TE11 $1/2\lambda_g$ mode at the ceramic. To reduce the RF power density through the ceramic, a 51 mm-diameter ceramic was applied, and careful dimension trimming was surveyed in order to reduce the surface field on the ceramic surface. Figure 10.23 shows a schematic view of the Otake window. Figure 10.24 shows a photograph of the completed window assembly.

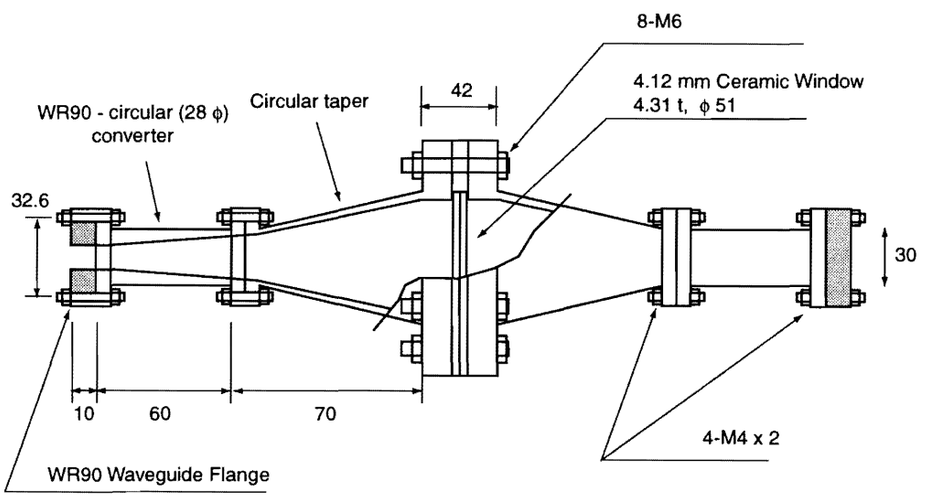

Figure 10.23: *Schematic drawing of the TE11-type window developed at KEK.*

Several windows of this type were tested in a resonant ring. A maximum pulse power of 130 MW with a 300 ns duration of the resonant ring was applied; at this power level this window with high-purity ceramics was successfully operated. After reaching this power level, the input RF power was set at 70 MW and the pulse length was increased up to 800 ns. The RF discharge on the ceramic surface stayed at a reasonable level, and the window operated stably. A further attempt to increase the pulse

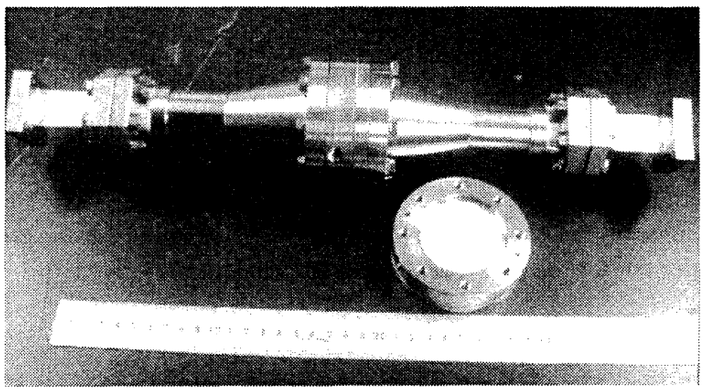

Figure 10.24: *Photograph of a completed window assembly.*

length eventually resulted in hard RF discharge which destroyed the ceramic. Figure 10.25 shows the experimental setup of the TE11 window in the resonant ring.

These TE11-mode windows are presently being used as the standard ceramic window of the XB72K series klystrons. This is also employed as the standard window for the X-band accelerating structure test station at KEK. Figure 10.26 shows the RF pulse shape while testing in a resonant ring.

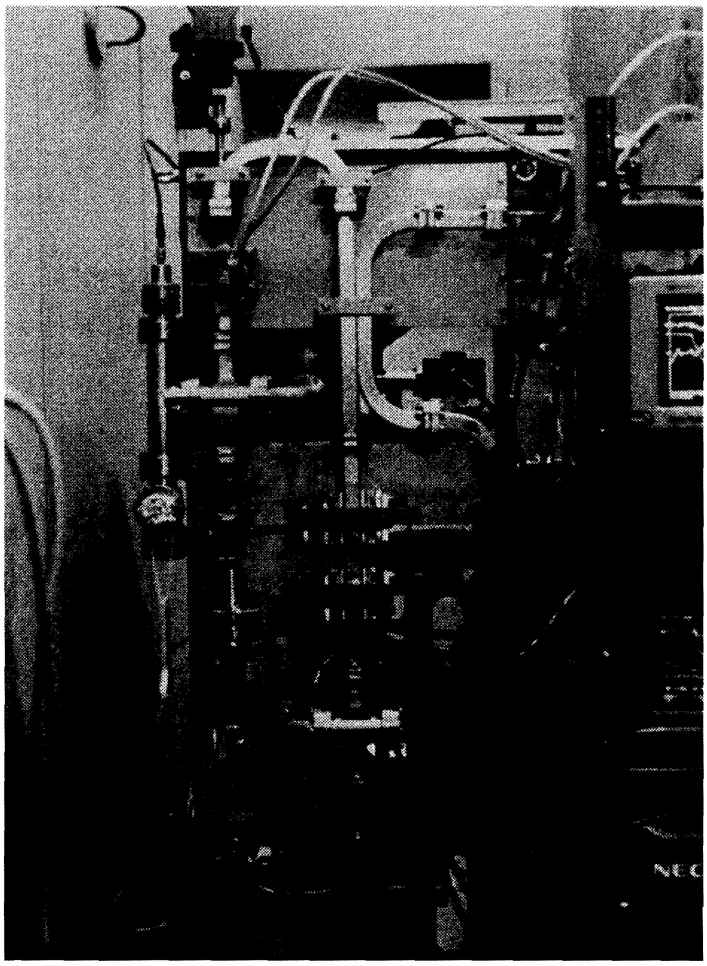

Figure 10.25: *Setup with an X-band resonant ring that has been built and used for conducting high-power tests of klystron windows.*

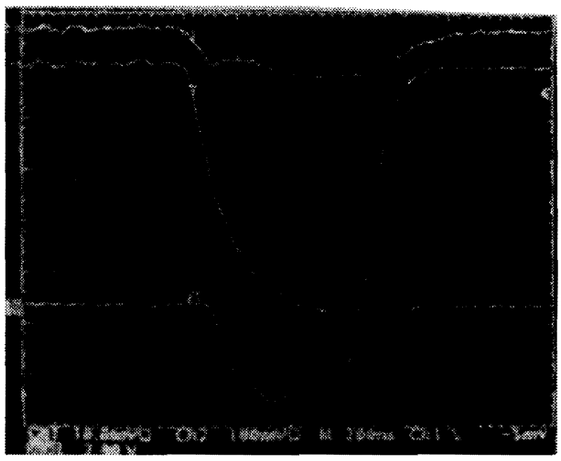

Figure 10.26: *TE11 window high-power test in the resonant ring. A 700ns input pulse was built up to 70 MW of circulating RF power in the ring.*

10.6.5 Latest Analysis of Issues with XB72K

As stated in Section 10.6.3, the RF discharging problem near to the output cavities is being addressed by using traveling-wave multi-cell output cavities. Also, recent progress involving X-band klystrons at SLAC has proven the real feasibility of high-power X-band klystrons as an RF power source for the 500 GeV class electron-positron linear colliders. However, at KEK, the cause of problems in high-power operation of XB72K # 7 tube (i.e. the one with TW multiple-cell output cavity) has not been fully understood. In particular, an unstable behavior of the RF output pulse shape found during conditioning is quite enigmatic. Some factors that can cause this behavior are:

1. RF discharge in the output gap or in the penultimate cavity.
2. RF discharge in the waveguide system, including the matched load.
3. Beam interception and discharge therein, especially in the vicinity of the output circuit.
4. Gun oscillation.

Out of these possibilities, gun oscillation is considered to be quite unlikely. This is because the instability behavior shows some bi-stable RF output pulse shape. The gun operation without RF input power was observed to be quite stable at the cathode voltage in the range of 300-500kV. Generally, the gun oscillation shows unstable diode operation without any RF input.

Problems with the waveguide system are also considered unlikely. This is because no indication of a discharge, such as bursting of the vacuum pressure, has been observed. Another evidence against a waveguide problem is the absence of a swing in the output RF signal from near zero to 100 %.

To explore the cause of the instability, scans have been made by changing the focusing field strength, mostly by varying the backing coil current. This allows us to change the magnetic field on the cathode surface over the range of 50 - 130 % of the design value. While the changes in the backing coil current had effects on the RF output power, the behavior of the instability was not affected. This suggests that the solenoid focusing system was functioning normally, including the geometrical configuration of the klystron and the magnet.

At this moment, a more plausible cause of the output instability is a combined effect of beam interception and the resulting RF discharge in the output cavities or their neighborhood. RF aging processing has been found to be somewhat effective in improving the operational stability at 30 MW output power with a 100 ns to 300 ns pulse length. This is indicative of the existence of discharging. However, as stated earlier, no vacuum bursting, which is a direct signature of discharging, has been observed. Thus, it must be concluded that at this moment the definitive cause of the instability in high-power operation of the # 7 XB72K is not yet understood.

The fundamental design concept and the parameters of the XB72K are quite similar to those of the SLAC XL4 klystron (1.2 μperveance) that has successfully produced 65 MW output power for 1 μs [14, 15, 16, 17]. Table 10.9 compares the parameters of the XB72K and XL4, which are related to discharging issues. As can be seen there, no essential difference exists in the two designs. More

diagnostic testing and further analysis of the design, including that of the gun, are likely to be necessary.

	SLAC XL-series	KEK XB72K #7
Window	TE01 TW-mode × 1	TE11 $1/2\lambda_g \times 2$
Gun	1.2 μP	1.2 μP
Conversion ratio	1/100	1/110
Drift tube diameter	10.8 mmϕ	9.6 mmϕ
Output cavity	6 + 1 cells	4 + 1 cells
Input and gain cavities	single cell	single cell
Penultimate cavity	2 cells or single cell	single cell
Surface field	51 MV/m at 50 MW	56 MV/m at 65 MW

Table 10.9: *Comparison of parameters for XB72K and XL4 that are related to discharging issues.*

10.6.6 Perspective on X-band Klystron R&D

Obviously, the highest priority task concerning the current X-band klystron R&D is to demonstrate the production of 65 MW peak power for the required 800 ns pulse duration with our own system. For this goal, continued R&D on the traveling-wave (TW) output structure of a few variations is necessary. At this stage, ideally, several test tubes need to be built in succession.

In the next step of testing of the XB72K tubes, the immediate plan is to build the # 8 klystron with, again, a 5-cell output structure, but with an improved design over the # 7. Specifically, a relatively high surface stress is employed to achieve a higher RF conversion efficiency of 45 %, as compared to 35 % of # 7. The # 8 klystron has been delivered in April, 1997. For subsequent test klystrons, the adoption of a new 7-cell TW structure, whose design has been already completed at BINP, Russia, is being considered.

During the past 5 years, the development of the XB72K has been conducted at a rate of one or two test tubes to be built every year. This rather slow pace has been governed by the limitation on the funding and manpower available at KEK. To conduct the full testing of two to three tubes per year at KEK, at least one full-time-equivalent (FTP) senior staff and one FTE engineer are necessary.

It is widely known that the issue concerning the DC power to be consumed by the focusing magnets of the klystrons is a rather serious one. The PPM (periodic permanent magnet) focusing method is an excellent solution to this problem [36, 15, 17, 38]. Since 1995, KEK has had a formal collaboration program with BINP laboratory in Russia on PPM klystrons. The first diode gun with a multi-stage ceramic insulator was completed in Spring of 1997.

The first BINP-KEK PPM klystron is being designed at BINP. It will be built as a completely Russian-made tube under the direction of the BINP group. The perveance of this PPM klystron was chosen to be $\sim$ 0.8 μperveance, based on considerations on the focusing-magnetic field and a better RF

efficiency. The completion of the # 1 PPM klystron with full RF structures is scheduled for the end of October, 1997. The RF structures are to be designed, pending the high-power measurement results of the ongoing and coming XB72K with TW multi-cell output structures (i.e. XB72K # 7 and # 8).

10.7 RF Power Distribution

Some sort of an RF pulse-compression stage is an absolutely necessary element if a conventional RF power source system with a pulsed klystron is to be considered as the driver of an X-band linear collider.

In most S-band linac power source systems, the RF pulse-compression system is usually applied in cases where it is necessary to achieve a higher accelerating gradient at the cost of sacrificing the RF power efficiency. An example of this kind of application was SLED in the SLAC 2-mile electron linac. In SLC, the existing 2-mile linac was upgraded to almost twice its beam energy by upgrading the klystron, and, at the same time, by installing a new RF pulse-compression system, SLED (SLAC Linac Energy Doubler)[28]. This original RF pulse-compression scheme successfully achieved an energy upgrade of about 1.8 times higher than the accelerating gradient which was achieved without this system, with an energy efficiency of about 65 %.

Since the introduction of SLED, several successors have been investigated. However, although these schemes were sometimes successfully utilized in electron linacs, and also tested as a prototype of a linear collider power source, there is still great room for improvement. In the following, detailed discussions of this RF pulse-compression stage and a possible new RF power distribution scheme, having a better energy efficiency, are presented.

10.7.1 Conventional RF Pulse-compression Systems

As mentioned in the previous section, the klystron driver can not supply short pulses that the linac operation requires. Therefore, some RF pulse-compression scheme which can compress the pulse length, and, at the same time, increase the pulse height while conserving the total pulse energy is necessarily required. Such an RF pulse-compression system is already being successfully utilized in the S-band electron linacs of several laboratories [7, 32]. In the design of the X-band linear accelerators, such an RF pulse-compression system i.e. SLED (SLAC Energy Doubler) or its developed version, such as SLED-II [31, 33] and VPM (VLEPP Pulse Multiplier) [36, 39], are considered to be the RF pulse-compression system of future linear colliders, and are under R&D in several laboratories.

SLED, SLED-II and VPM

The schemes called SLED, SLED-II and VPM (VLEPP Pulse Multiplier), are all based on the same operational principle. The operational principle of SLED is illustrated in Figure 10.27. The RF output power from the klystron is stored once in the resonant cavity, or a long delay line, which build up the incoming RF energy. After this build up period, the stored energy is released from this storage cavity or its equivalent system, such as delay lines (SLED-II), by reversing the phase of the incoming pulse. Thus, a longer RF pulse from a klystron or klystrons is compressed into a shorter pulse with a higher amplitude [34]. Another type of the RF pulse-compression system is the so-called BPC (Binary

pulse-compression) proposed by D.Farkas in 1986 [29]. This BPC is based on a different operational principle from SLED family, and is discussed later in next section.

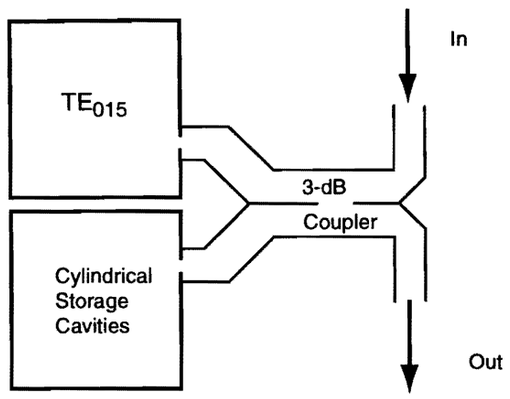

Figure 10.27: *Principle of operation of SLED.*

The resonant cavities or delay lines used in these pulse-compression schemes and the necessity of the time to build up RF energy are the main factors that determine the system energy efficiency. The energy losses consist of following two categories:

1. Wall loss on the inner surface of the energy-storage cavity,

2. RF reflection during the storage period.

Although a careful shaping of the RF input pulse could eliminate the reflection loss during the build-up period, this pulse shaping, itself, inevitably decreases the RF conversion efficiency of the klystron as long as the klystron is driven by a flat pulse. This also decreases the efficiency by prolonging the build-up period. Therefore, the system efficiency in the case of a loss-less cavity or a delay line is determined by this so-called intrinsic loss of about 80%. With this intrinsic loss and the resistive wall loss in the cavity, an efficiency of the RF pulse-compression system of around 75% maximum is expected in the factor 5 X-band RF pulse-compression system for linear colliders [4, 33, 34].

Another RF pulse-compression system is the VPM (VLEPP Pulse Multiplier). This system has an advantage in that there is only one storage cavity, instead of two cavities in SLED family, by utilizing a directional coupler and the traveling-wave mode for the energy storage in a special resonator, called an "open cavity". Although this system has several different points compared with the SLED family, its overall performance, especially its energy efficiency, is almost same the as that of other systems. Therefore the detailed description of this system is left for another occasion.

Binary Pulse-compression (BPC)

An RF pulse-compression system based on a different operational principle from these energy storage-type pulse-compression of the SLED family is the BPC (Binary pulse-compression). This pulse-compression system was proposed by D.Farkas, and the first high-power test was successfully achieved in SLAC [29, 34, 35].

The operation principle of the BPC is illustrated in Figure 10.28 in the case of a compression factor of $4(= 2^n)$. This system is driven by two independently operated klystrons, and their output pulse are divided into four short pulses in the time domain.

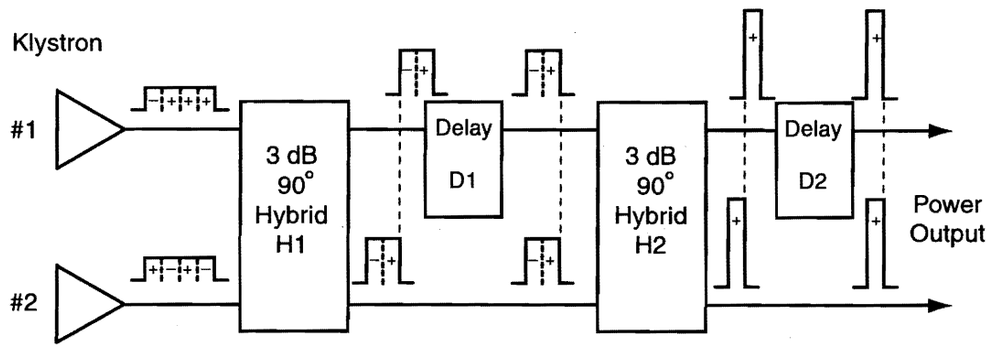

Figure 10.28: *Operation principle of the BPC.*

In this system, the head parts of the RF pulse are guided by 3 dB couplers to several delay lines connected to one port of 3 dB-couplers. As shown in the figure, this delay line system gives the necessary delay periods in turn to each part of the divided RF pulses, which can later meet the last part of the RF pulse at the end of each delay-line system. This stage is repeated, and at each stage the RF pulse height is doubled; at the same time the pulse duration is shortened to half. Finally, they are combined through 3 dB hybrid modules to give a 2^n times higher peak power a the shorter pulse duration of $1/2^n$ of the original pulse.

If the wall loss of the delay lines is neglected, it is quite easy to find that the n-stage of the BPC system can give a factor 2^n times higher pulse with a 2^n'th pulse duration. It is also easy to recognize that in this BPC pulse-compression system the intrinsic energy efficiency could reach 100 % in case of loss-less delay lines. However, this BPC system requires far longer delay lines compared to other pulse-compression schemes, and, consequently, needs a long space to arrange these delay lines. The longest delay line in the BPC for a round trip of the first stage is expressed as

$$L_{max} = 2^{n-1} T_p v_g, \tag{10.5}$$

where n is the multiplication factor of the BPC, T_p is the length of the linac driving pulse, and v_g is the group velocity of the RF propagating in the delay lines.

However, due to a rather involved configuration of the system, the BPC may face challenges to

overcome in many practical aspects, when a massive number of units needs to be built. Thus, its application in a large linear accelerator requires a careful analysis of its construction, even if it can achieve a better energy efficiency of close to or more than 90% in the case of compression factor 4 [4, 34, 30].

10.7.2 Delay Line Distribution System (DLDS)

Recently, a new RF power distribution system named, DLDS (Delay Line Distribution System), which works as a replacement of an ordinary RF pulse-compression system, and its energy efficiency could be improved up to 98%, was proposed by the authors [44, 42, 43]. This system is based on a new operational principle that is completely different from any other existing RF pulse-compression systems, such as SLED, SLED-II and VPM.

Like BPC, in the DLDS a long pulse from the klystrons are divided into short pulse trains, and these short pulse trains are led to different parts of the linac. The most distinct point concerning the DLDS is that the divided RF pulses are never compiled again, like in the case of BPC. In this new system, the flight pass of the beam, itself, works as a delay line in the BPC; thus, half of the delay time necessary for the divided short RF pulse trains is given by the beam, itself. In this new system, the length of the delay lines, and, consequently, their losses can be decreased by about a factor of 1/2 compared to the BPC system. The operation principle of this new system DLDS is described in some detail below.

Basic Factor-2 DLDS

In the linear collider RF power system, the main difficulty exists in the fact that the RF output pulse length is always longer than the necessary pulse length of the linear accelerator driving pulse, which should cover the sum of the structure filling time and the 85-bunch train duration. Usually, the klystron operation pulse is set at 2 - 8 times longer than this driving pulse in order to achieve the high RF power-conversion efficiency in the klystron driving system, which consists of a Blumlein PFN and a step-up pulse transformer.

As shown in Figure 10.29, the RF power from two klystrons which are independently phase-controlled are combined together through a 3-dB coupler. Figure 10.30 shows the "train diagram" of the factor-2 DLDS, illustrating the delivery of RF power and its encounter with the beam that is being accelerated.

One output port of the 3 dB hybrid is connected to the upstream of the linac at about one half of the linac operating time apart from the klystron location through a low-loss waveguide; the other port is connected to a structure located close to the klystron position. The first half of the RF pulse, which is equal to the sum of the filling time and the bunch train, is sent upstream of the linac through the delay line shown in the figure. The second part of the RF pulse is fed to a structure close to the klystron without any delay. The delay line gives a delay time of $T_d = L/v_g$, and the beam flight time

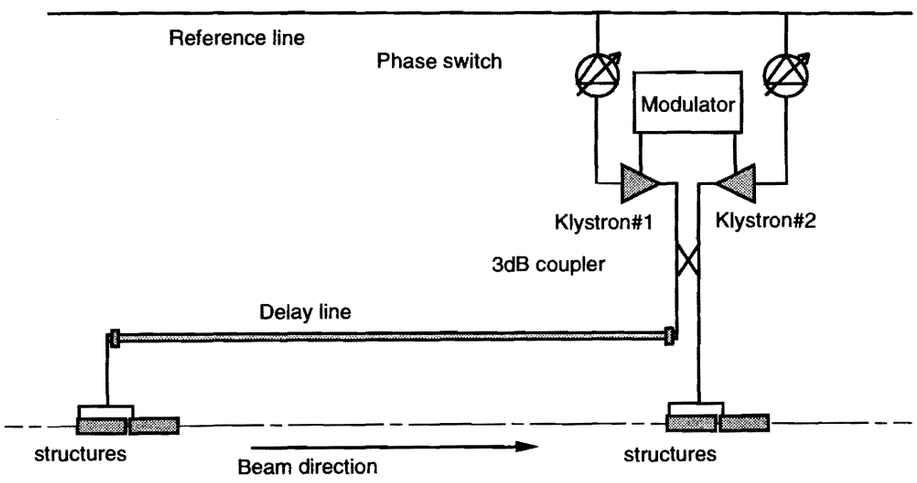

Figure 10.29: *Schematic diagram of the simplest factor-2 delay-line distribution system*

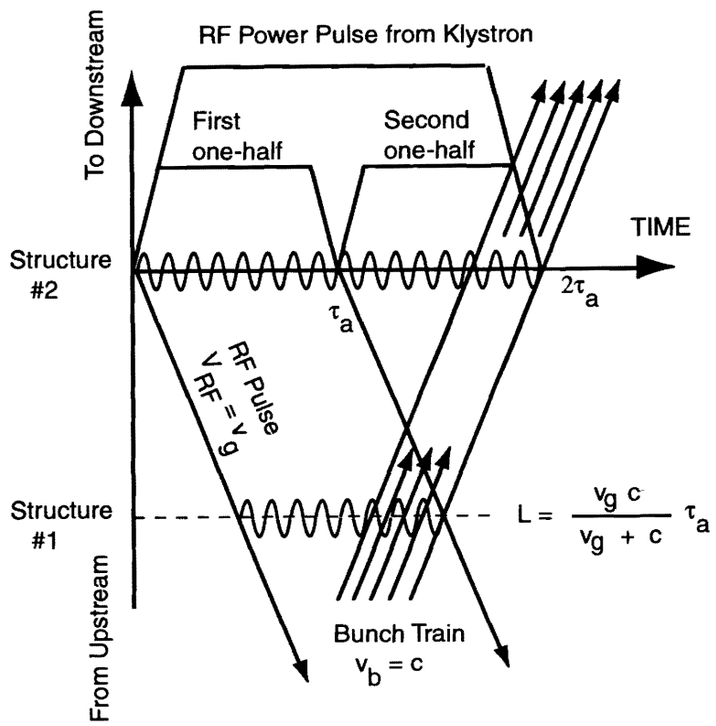

Figure 10.30: *Train diagram of a factor-2 DLDS.*

between the two structures is $T_b = L/c$. If these time delays satisfy the next relation, neglecting the delay time in the other RF transport system, such as the 3 dB hybrid etc.,

$$T_d + T_b = \frac{L}{v_g} + \frac{L}{c} = t_a. \tag{10.6}$$

Here, t_a is the pulse length of the linac operation, which is just the sum of the structure filling time and the duration of the bunch train. It is easily recognized that the timing of the bunch train and the RF pulse is adjusted to accelerate the beam, and that the beam is accelerated just as in the ordinary linac configuration. The timing relation of this delay line scheme is illustrated in the "train diagram" shown in Figure 10.30 in the case that the RF pulse from the klystrons is divided into two consecutive RF pulses. Thus, the factor-2 DLDS (Delay Line Distribution System), which works equivalently to the factor-2 RF-compression system, can be constructed.

Factor-$2^n/m$ DLDS

In general, the DLDS scheme can be extended to the factor 2^n combined pulse height as follows. Each of the 2 klystrons in the factor-2 scheme mentioned in the previous section can be replaced by a pair of 2-klystrons combined through a 3 dB hybrid coupler; thus, this new system also works as a factor-2 system, and the remaining 2 output ports of the 2 hybrid couplers can be connected to one more 3 dB hybrid coupler, which serves as an additional factor-2 DLDS. Thus, a factor-2^2 system can be constructed as illustrated in Figure 10.31. The timing chart of this factor-4 DLDS is easily extended from the factor-2 DLDS case.

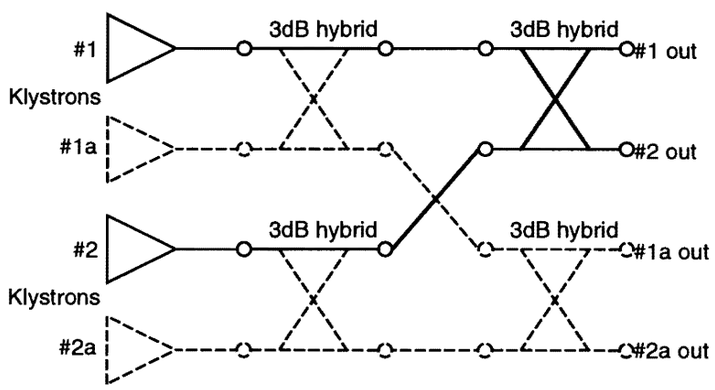

Figure 10.31: *A factor-4 DLDS built from factor-2 DLDS blocks.*

By applying this scheme to the factor 2^n system, a factor 2^{n+1} system can also be constructed, as shown in Figure 10.32 with the train diagram of the factor 2^n case. In this scheme the time-domain compression-equivalent factor, i.e. the klystron pulse length, can be chosen from 1 to 2^n times longer than the linac operational RF pulse length. This system is generally noted to be a factor $2^n/m$ delay-line distribution system ($2^n/m$ DLDS); 2^n represents the multiplication factor of the RF power and

m represents the time-domain compression-equivalent factor. In this case, the $(2^n - m)$ ports left disconnected are terminated with matched loads. A graphical representation and a train diagram of this factor-$2^n/m$ DLDS system can be constructed as a natural and easy extension of the previous cases; therefore, these figures are omitted here. The cases of $n = 2$ and $m = 3$ (4/3-DLDS) are discussed in some detail in the following section.

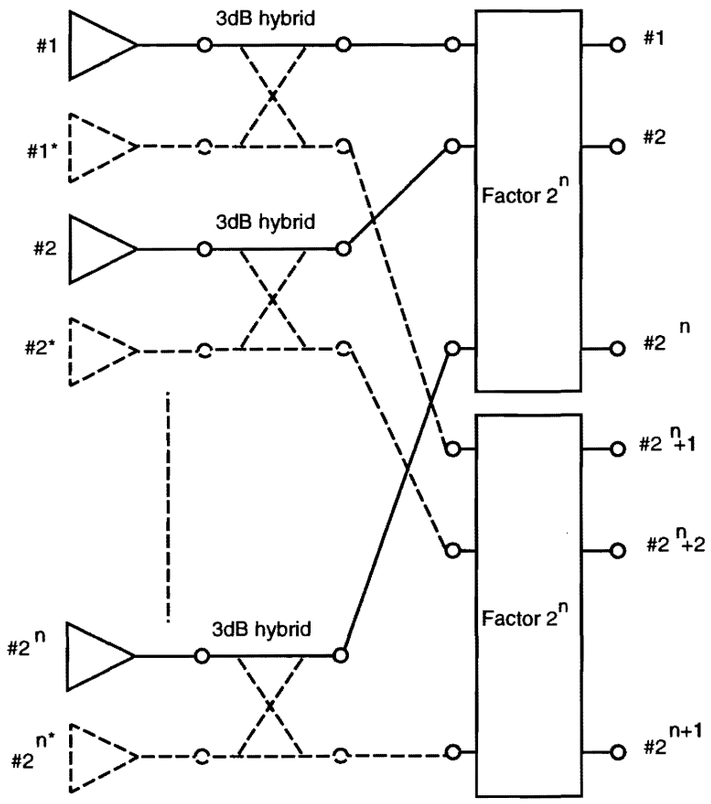

Figure 10.32: *Factor-2^{n+1} DLDS built from factor-2^n DLDS blocks.*

To adjust the timing of the bunches relative to the RF driving pulse in each acceleration unit, the distance L_m between the m-th acceleration units and the position of the klystron RF power unit must be determined by the relation

$$L_m = \frac{(m-1)T_a c v_g}{v_g + c}, \tag{10.7}$$

where, T_a is the pulse duration of the RF driving pulse covering the sum of the filling time and the bunch train, c the velocity of the light (velocity of the accelerated electrons), and v_g the group velocity of the RF driving pulse propagating in the delay line, respectively.

The energy loss of this system is due only to the wall loss in the waveguide. As described in the previous sections, the DLDS has no intrinsic energy loss associated with the power build-up process

in resonant cavities, since such elements are non-existent. This situation is similar to the case of BPC.

The losses calculated for the several sizes of waveguides are summarized in Table 10.10. As shown in this table, practically, the losses in the guide are small enough in all cases. The latter half of the RF pulse is fed directly to the accelerating structure located close to the klystrons; thus, the total loss of this system is one half that shown in Table 10.10. This distribution system has no narrow-band components, such as a storage cavity; therefore, this system can be as flexible as an ordinary RF power system in a conventional linac system. This advantage is preferable for controlling the RF power system related to the beam dynamics, such as beam-loading compensation.

1) TE01 mode					
Waveguide	Loss	v_g/c	Line length	$\Delta\phi$ (°/m/K)	
(Diameter)	(dB/m)		(270 ns)	s-invar (10^{-7}/K)	Cu (165×10^{-7})
51 mm	1.276×10^{-2}	0.7785	35.431 m	3.407×10^{-3}	5.621×10^{-1}
69 mm	4.528×10^{-3}	0.8859	38.022 m	2.203×10^{-3}	3.635×10^{-1}
118.1mm	8.311×10^{-4}	0.9626	39.700 m	1.216×10^{-3}	2.006×10^{-1}

2) TE11 mode					
Waveguide	Loss	v_g/c	Line length	$\Delta\phi$ (°/m/K)	
(Diameter)	(dB/m)		(270 ns)	s-invar (10^{-7}/K)	Cu (165×10^{-7})
51 mm	1.347×10^{-2}	0.9535	39.508 m	1.668×10^{-3}	2.752×10^{-1}
69 mm	8.95×10^{-3}	0.9749	39.957 m	1.525×10^{-3}	2.516×10^{-1}
118.1 mm	4.78×10^{-3}	0.9915	40.298 m	1.422×10^{-3}	2.347×10^{-1}

Table 10.10: *Values of the transfer loss and phase-shift in waveguides.*

10.7.3 Design of a 4/3-DLDS for the JLC X-band Main Linacs

It is quite easily seen that the sum of the delay lines in the DLDS increases in proportion to the square of the factor m:

$$L_{sum} = \frac{m(m-1)}{2}. \tag{10.8}$$

On the other hand, in BPC, the total length of the lines is

$$L_{sum} = 2^n - 1, \tag{10.9}$$

where 2^n is the multiplication factor of the BPC. Thus, the length of the delay lines required in DLDS will exceed that at other competitive system, such as SLED-II or BPC, when the compression factor m increases. Figure 10.33 shows the "train diagram" for the 4/3-DLDS scheme. Figure 10.34 shows a schematic view of a 4/3-DLDS, which means RF power from four power source clusters are distributed onto three groups of accelerating structures.

Considering the energy-compression ratio and the technical feasibility of the total length of the DLDS system, the highest practical compression ratio is 4. In Table 10.11 the required wave-guide length

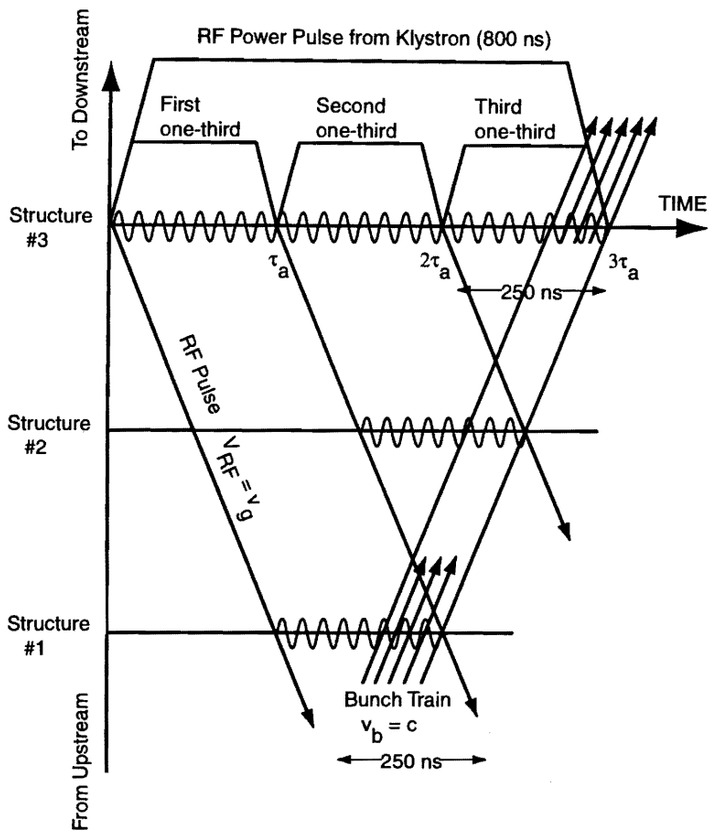

Figure 10.33: *Train diagram of 4/3-DLDS*

per power unit is summarized in case of factor-4/4 and 4/3 DLDS, along with the value in the case of the SLED-II pulse-compression system from NLC-ZDR[4] and a representative ×4 BPC.

	SLED-II	×4 BPC	4/3-DLDS	4/4-DLDS
Klystron pulse width	1.25μs	1.0μs	0.75μs	1.0μs
Length of delay line	1.0T	3T	1.5T	3T

Table 10.11: *The required delay line length for various types of pulse-compression / power-distribution systems. Listed here are SLED-II in NLC-ZDR [4], a representative ×4 BPC, 4/3-DLDS and 4/4-DLDS. The delay line lengths are shown in the unit of the RF pulse length (T) at the accelerating structure input.*

Thus, considering the total length of the system and the number of waveguide parts such as the mode converter and the 3 dB hybrid, the 4/3 DLDS system was chosen as the pulse-compression system of the RF power source for the JLC X-band RF power-source system. Table 10.12 gives the

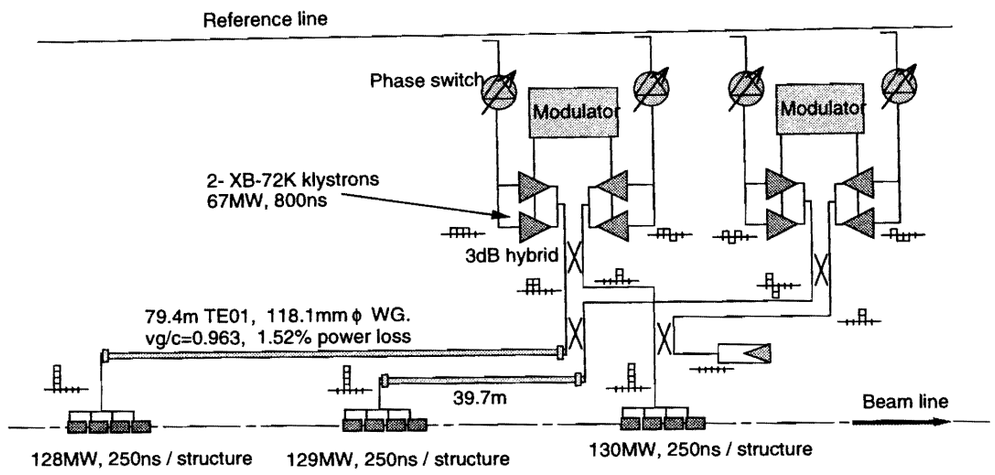

Figure 10.34: *Block diagram of a 4/3-DLDS for JLC main linacs.*

Output RF power	(65 + 65) MW×4	
RF pulse length	790 ns = 3 × 250 ns + 40 ns (for phase flip)	
Delay line mode	TE01	TE01
Waveguide Diameter	69 mm	118.1 mm
Group velocity (v_g/c)	0.8859	0.9626
Delay Length		
for 135 ns	35.431 m	39.700 m
for 270 ns	70.862 m	79.400 m
Delay line loss	4.528×10^{-3} dB/m	8.311×10^{-4} dB/m
Delay Line Efficiency	96.37%	99.24%
Phase var. for 270 ns line		
s-invar	0.156°/K	0.128°/K
copper	25.7°/K	21.1°/K
Switching time*		
low level	< 5 ns	
Klystron out	< 20 ns	
Linac input	< 20 ns	

Table 10.12: *Parameters of the 4/3-DLDS. *Temporary values are quoted for the items under "Switching time."*

specific parameters of the 4/3-DLDS system that are considered for JLC. Two sets of parameters are presented. They correspond to two cases where delay lines with inner diameter 69 mm and 118.1 mm are used.

Packing Factor and the Configuration along the Linac

As mentioned earlier, one RF power unit of the 4/3-DLDS has 3 groups of 4 accelerating structure units which are about 40 m apart from each other. Therefore, this 1-group of structure occupies roughly 6 m in length including the required drift spaces between the structures. As illustrated in Figure 10.34, the accelerating structures occupy only 12 times a 1.3 m section within the total length of an 80 m DLDS system. Thus, it is necessary to interleave several DLDS units in order to fulfill the whole length of the linac space. One example of this interleaved configuration is illustrated in Figure 10.35. As shown in this figure, six 4/3-DLDS units are interleaved with each other, and

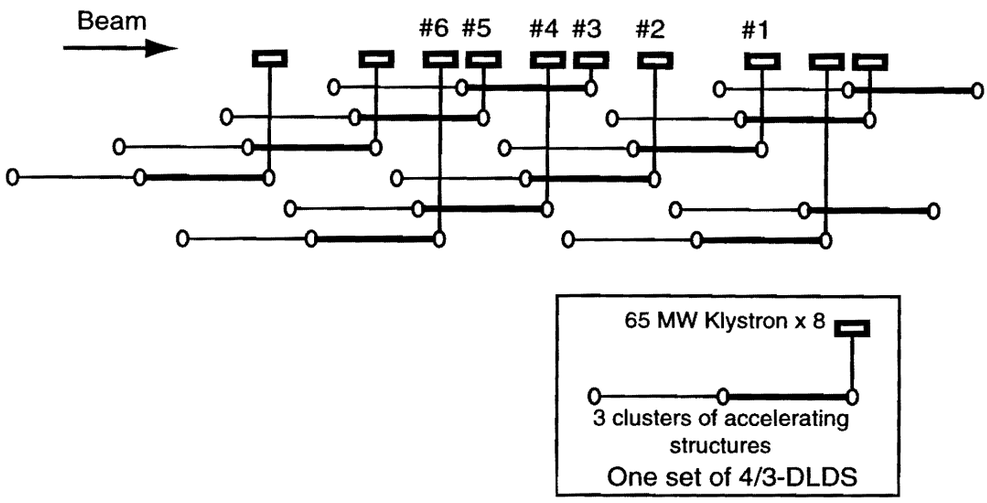

Figure 10.35: *Configuration of six units of 4/3-DLDS systems along the main linac.*

could achieve a packing factor of 75-80 % which is equal to that of an ordinary linear-accelerator configuration. Figure 10.36 shows how this arrangement may look like for a section of the main linac tunnel.

Figure 10.37 shows a schematic perspective view of a cross section of the main linac tunnel.

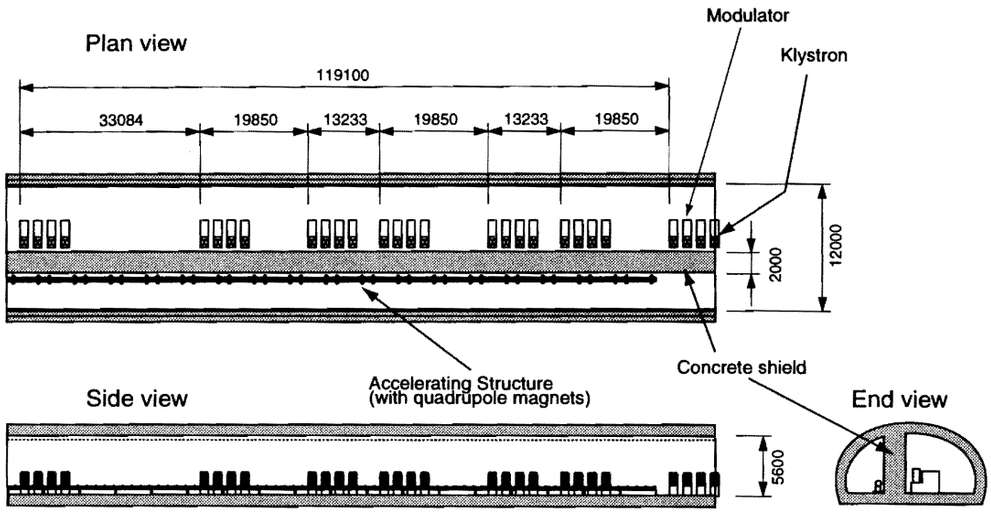

Figure 10.36: *Schematic layout of the interleaved DLDS configuration in the accelerator tunnel.*

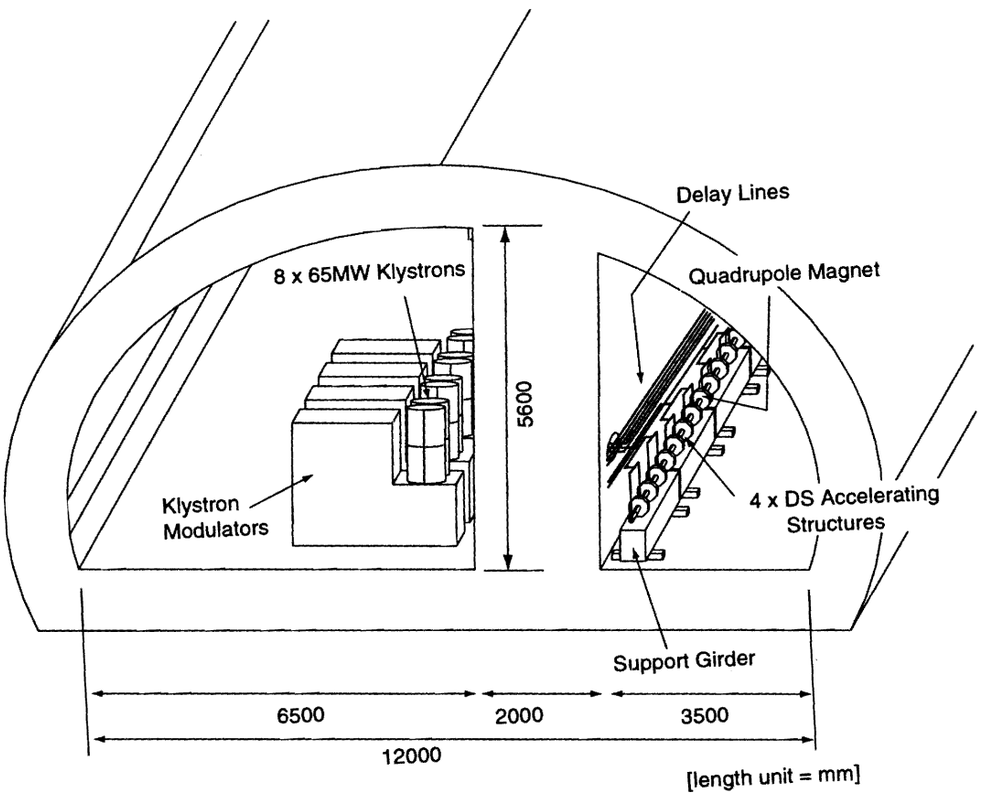

Figure 10.37: *Perspective view of the layout of the interleaved DLDS configuration in the accelerator tunnel.*

10.7.4 Comparison of DLDS and other RF Pulse-compression Systems

Energy Efficiency

The advantage of this new DLDS pulse-compression equivalent system is, first, its high energy efficiency; based on the discussion in the previous section, this efficiency could reach more than 99 %. Table 10.13 summarizes the overall energy efficiency of the 4/3 and 4/4-DLDS systems and the factor 5 SLED-II for the NLC 1st phase [4]. The efficiency of the DLDS is better than that of the SLED-II by 20 %, due mainly to the absence of resonant components in the system.

			SLED-II	4/3-DLDS	4/4-DLDS	×4 BPC
Klystron pulse width		(μs)	1.25	0.75	1.0	1.0
Linac pulse width		(μs)	0.25	0.25	0.25	0.25
Intrinsic efficiency	η_0	(%)	80.4	100	100	100
Intrinsic compression ratio	R_1		(4.02)	(3.00)	(4.00)	(4.00)
Efficiency of components	η_1	(%)	95	95	95	95
Compression ratio	$R_1 \times \eta_1$		3.8	(2.85)	(3.8)	3.8
Efficiency of RF distribution	η_2	(%)	95	95	95	95
Net power gain	$R_1 \times \eta_1 \times \eta_2$		3.6	(2.71)	(3.61)	3.61
Total efficiency	$\eta_0 \times \eta_1 \times \eta_2$	(%)	72	90	90	90

Table 10.13: *Power efficiencies of the SLED-II, DLDS and BPC systems. As is well known, the intrinsic compression ratio of SLED-II is determined by the pulse width compression ratio (5), multiplied by the intrinsic efficiency of the system (80.4 %). In the case of DLDS, strictly speaking, the term "Compression ratio" does not really apply, since the RF pulse is never compressed in time. Rather, when the klystron pulse is divided into three pieces as in the 4/3-DLDS, the beam receives acceleration by the same power-source three times, from accelerating structures situated at three separate locations. Thus, this number "3" is quoted within parentheses as the number to be compared with the "RF compression gain" of SLED-II. A similar argument goes for the 4/4-DLDS. Intrinsic efficiencies for DLDS and BPC are taken as 100 %. However, the loss during power transmission is assumed to be 95 % for purposes of comparison with SLED-II.*

Number of Components

RF pulse-compression systems need several components, such as 3 dB couplers, delay lines, and mode converters. The required numbers of these components per power unit (i.e. a cluster of a varying number of 50 $\sim$ 65 MW klystrons, depending on the scheme) are summarized in Table 10.14.

As shown in Table 10.14, all four RF-compression systems require the same number of 3 dB hybrid modules per klystron. In terms of the component count per klystron, SLED-II and DLDS are similar. They are within a 50% difference.

	SLED-II	×4 BPC	4/3-DLDS	4/4-DLDS
Number of klystrons[a]	2	2	8	8
Klystron pulse width	1.25μs	1.0μs	0.75μs	1.0μs
Number of 3dB hybrid	2	2	8	8
Number of mode converters	2	8	4	6
Length of delay line[b]	1.0T*	3T	1.5T	3T
Peak power at output port	~8	8	8	8
Number of accelerating units[c]	4	4	12	16

Table 10.14: *Number of components per power unit that are required for various types of pulse-compression / power-distribution systems. Listed here are SLED-II in NLC-ZDR [4], a representative ×4 BPC, 4/3-DLDS and 4/4-DLDS.*

[a] The RF power from a klystron is ~50 MW for SLED-II (NLC-ZDR) and 65 MW for JLC.

[b] T is the length of the RF pulse at the accelerating structure input.

[c] Typical accelerating gradient is 50 ~ 70MV/m (unloaded); a unit structure length is 1.3 ~ 1.8 m. A fair comparison of "linac system efficiency," normalized by the component count, is a very non-trivial task, since it depends on many factors. Readers are encouraged to consult original references of SLED-II and BPC to develop their own informed judgment.

A major difference lies in the required length of the delay line. BPC system requires delay lines that are two- or three-times longer than that of the DLDS and SLED-II, respectively. Remembering that in BPC the RF pulse must complete a round trip and in the DLDS only a one way trip is necessary, this line length difference is simply the result of this difference.

Counting the number of components is relatively straightforward. However, to make a fair comparison of "the linac system efficiency," normalized by the klystron count, of various pulse-compression / power-delivery schemes is a very non-trivial task. This is because it involves many design-specific factors, such as the choice of the accelerating structure, pulse length and others. We encourage the readers to consult original references of SLED-II and BPC to develop their own informed opinion. However, it should be safe to conclude that for a given RF power from a klystron, the DLDS scheme tends to be capable of driving more high-gradient structures with a relatively small component count, when normalized by the number of klystrons.

Operational Flexibility as the Linac Power Source

Another important advantage of the DLDS pulse-compression equivalent system is flexibility of the pulse-compression and power-distribution system. The frequency band width of the DLDS system, as the RF power transport system, is wider than the klystron itself, due to the absence of resonant

components. Therefore, no restriction is expected in the DLDS pulse-compression equivalent system. In the DLDS system, 3 or 4 groups of the acceleration structures can be operated with independent parameters, such as phase, amplitude and pulse shape; on the other hand no other RF pulse-compression scheme can ever have this flexibility because of the pulse-compression process, itself.

One more advantageous aspect of this DLDS pulse-compression system is that the choice of the compression ratio is not related to the intrinsic energy efficiency of the system. It should be noted that in DLDS, the pulse-compression ratio is the number of the divided RF pulses at the input of the accelerating structures. On the other hand, the conventional RF pulse-compression schemes, such as that of the SLED family and the VPM change their intrinsic energy efficiency as the compression factor is changed due to the choice of the compression factor. This is because of the required change in the coupling coefficient to the storage cavities in the case of SLED or VPM, or to the energy-storage delay lines in the case of the SLED-II system. This condition limits the range of the compression factor of the SLED-family-type RF pulse-compression systems. This efficiency change in SLED-II is relatively large for a compression ratio less than a factor of 3; also,recent progress in the technology of short-pulse modulators has shown the possibility that the RF pulse-compression factor can be decreased down to 2-4 without sacrificing the modulator efficiency.

10.7.5 Practical Issues with the DLDS Scheme

As described in the preceding sections, the operational principle and the construction of the DLDS is relatively simple, and only the high power parts that have already been verified in SLED family and the BPC are necessary.

However, this DLDS necessarily has to distribute RF pulses to different points along the linac. This distance, much longer than that of the usual linac power system, may create some new technological problems. One of them is an RF phase change due to a thermal expansion of the delay lines in the system.

Stability of RF Phases

In the 4/3-DLDS system, one power-source unit that is made of 8 klystrons must feed 3 groups of accelerating structures, which are located 40 m apart from each other. The thermal expansion of the delay-line waveguide changes its physical length, and also changes the guide wave-length. This causes a phase shift at the input of the linac accelerating structures separated, by 40 and 80 m from the position of the klystron power unit.

As shown in Table 10.10, this phase shift reaches 30°/K in the case of the ordinary copper TE01-mode waveguides. To suppress this phase shift within the 0.5 degree required for the linear-collider operation (see Chapter 7 and [2]), the temperature of the waveguide should be kept within 17 mK throughout the whole length of 80/40 m.

Such a tight temperature stability requirement is practically impossible to satisfy when a scale of the

delay line waveguide having a 120 mm diameter and 80 m length is considered. Instead of a copper waveguide, waveguides made of Super Invar with a Cu-plated surface is considered to be much more suitable for this purpose.

Super Invar has extremely low thermal-expansion coefficient compared to that of any other material, and is likely to be the only candidate material for this waveguide. As shown in Table 10.10, the use of this material relaxes the temperature-stability requirement to a moderate level of 4 K (increase by a factor of 160), compared to that of a Cu-waveguide. Since the required thickness of the plated copper is 10 micron or less, the mechanical stress caused by the thermal-expansion difference between the base Super invar and the plated copper should be sufficiently small.

Since the Joule loss in the waveguide is at most 10 W/m, the temperature of the wave guide in the DLDS can easily be stabilized without any significant auxiliary power.

Phase Measurement and Control

In order to control the driving RF phase at the input of the accelerating structure of X-band linear-collider main linacs, it is necessary to measure the length of the long TE01-mode delay lines of 40-80 m. A new measurement scheme that utilizes a low-frequency resonant mode of the TE01-mode delay line has been proposed [45]. Since the delay lines have a tapered guide on both ends, the low-frequency resonant mode at around 2 GHz can be a measure of the delay-line dimensions. The operational principle and elementary characteristics of this measurement method, such as the sensitivity, S/N ratio and other basic design parameters, are presented here.

A conceptual illustration of this phase-measurement method is shown in Figure 10.38.

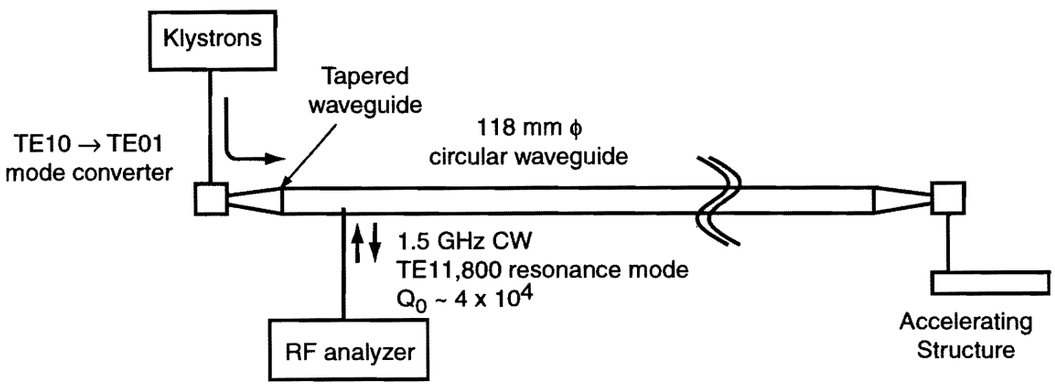

Figure 10.38: *Conceptual illustration of the phase-measurement method using a low-frequency resonance mode of a delay line. The tapered parts on both ends of the delay line work as a long high Q resonator at a lower frequency than that of the X-band.*

The sensitivity of this method is determined by the loaded Q-value of the resonant mode. The

calculation of the sensitivity is shown in Figures 10.39 and 10.40 when the 2 GHz TE11,800 mode of a 118 mm circular delay line is used. It is seen that the X-band phase shift in the DLDS delay line can be deduced from the observed phase shift at the low frequency, TE11,800 mode, with good accuracy. The sensitivity varies as function of coupling β. To choose a suitable coupling, the strength of the reflected power signal needs to be taken into account. It is considered that $\beta \simeq 0.5$ would be appropriate. This will be experimentally tested later this year (1997).

Once the phase error is detected, the correction can easily be carried out by controlling the output of the klystron phase. No phase-control system, such as a phase shifter, is necessary in the delay line, itself. This allows us to treat the delay-line system as a simple waveguide without any phase shifters.

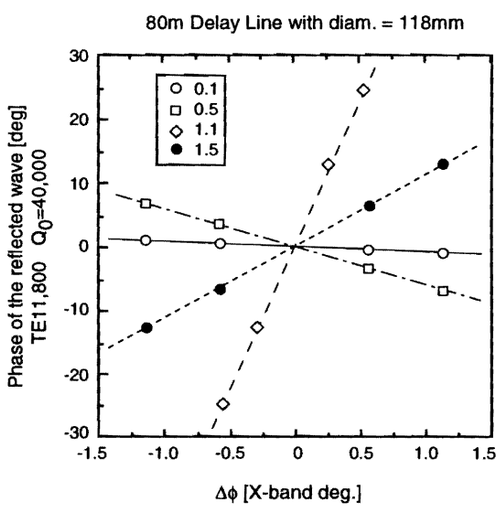

Figure 10.39: *Relationship between the phase shift of the DLDS delay line, as seen at the X-band frequency and at the TE11,800 mode frequency. The sensitivity would vary as function of the coupling β. The calculated results are shown for β = 0.1, 0.5, 1.1 and 1.5.*

Amplitude and Phase of the Combined Power through 3 dB Hybrid

As described in the preceding chapters, the DLDS operation is quite simple, and has no important problem if a group of klystrons work exactly in phase and at the same amplitude. However, in the actual DLDS operation, klystrons may find a different performance, especially their relative phase and output power.

Since the DLDS has 3 dB hybrid couplers, the phase and amplitude difference of two klystrons may cause a power loss of the combined power at the output port of each 3 dB hybrid. The combined amplitude and phase changes at the output port of a hybrid is graphically illustrated in Figure 10.41. It is clearly illustrated in the figure that the amplitude difference has only a smaller effect to the

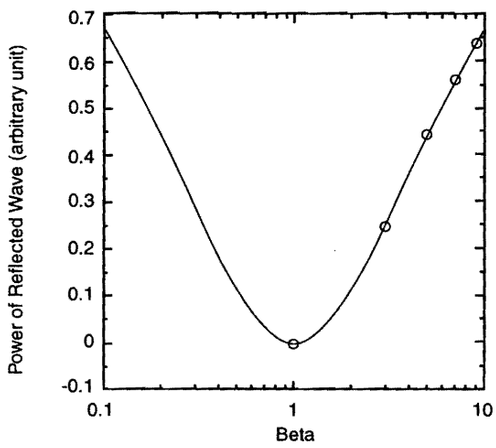

Figure 10.40: *The ratio of the input and reflected powers as function of the coupling β. Since it would be difficult to measure the phase when the reflected power is too small, the coupling will be chosen to be* ~ 0.5.

combined amplitude due to the characteristics of a 3 dB hybrid. Figure 10.41(A) shows that if the amplitude difference of two klystron is less than 10 %, the power loss to be seen at the other output port of the 3 dB hybrid would be less than 0.5 %. It is safely concluded that this amplitude difference has practically no effect on the operation and control of DLDS.

Figure 10.41 (B) illustrates the effect of the phase difference of the power from two klystrons. Since the output phase stability that is required for the operation of linac must be better than 1 degree to satisfy the specifications of the main linacs related to the beam energy spread. As shown in the figure, a 1 % loss in the combined power corresponds to a relative phase difference of 11 degrees; thus, the power loss due to this phase unbalance is negligibly small in the operation of linear colliders.

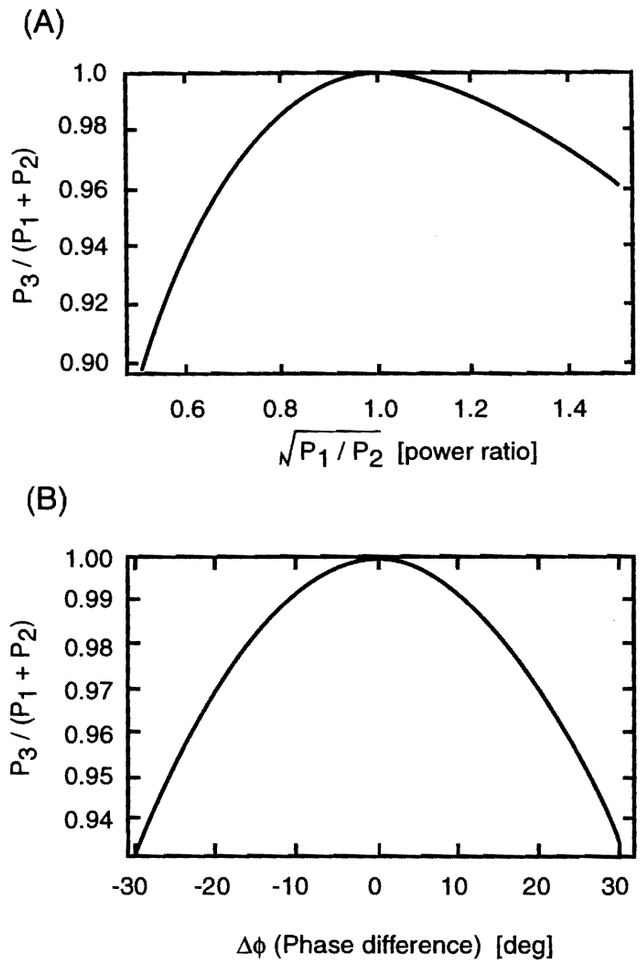

Figure 10.41: *Characteristics of 3 dB hybrid modules. A) Combined power change due to input power difference B) Combined power change due to input phase difference*

References for Chapter 10

[1] "International linear collider technical review committee report 1995"; SLAC. Technical Publications Department. Stanford University. :P.O. Box4349, Stanford, CA94309, USA

[2] "JLC-1"; KEK report 92-16, December 1992 A/H/M.

[3] K.Yokoya:"JLC Status"; "Sixth International Workshop on Linear Colliders(LC95)2; March 27-31, 1995 Tsukuba Japan.; KEK Proceedings 95-5 August 1995 A. P-61

[4] "Zeroth-order Design Report for the Next Linear collider"; SLAC Report 474. May, 1966.

[5] M.Chodorow et.al ;"Stanford High-Energy Linear Electron Accelerator (Mark3)": The Review of Scientific Instruments, Vol. 26, No. 2, 134-204, February, 1955

[6] R.B.Neal ;"The Stanford Two-Mile Accelerator" Chapter-13 ;W.A.Benjamin,Inc. New York

[7] "Design report on PF injector linac upgrade for KEKB" (in Japanese); KEK Report 95-18 March 1996 A.

[8] G.N.Glasoe and J.V.Lebacqz; "Pulse generators"; M.I.T. Radiation Laboratory Series:New York nd London, McGraw-Hill Book Company,INC. 1948

[9] G.N.Glasoe and J.V.Lebacqz; "Pulse generators"; M.I.T. Radiation Laboratory Series:New York nd London, McGraw-Hill Book Company,INC. 1948

[10] H.Mizuno;"PFN type klystron modulators for 100MW X-band Klystron"; Proceedings of the 3rd international workshop on linear colliders(LC91). September 17-27, 1991 BINP, Protvino, USSR. Volume 3. P172.

[11] R.F.Koontz et al; "Pulse Modulator Developments in Support of Klystron Testing at SLAC": Proc. 1993 Particle Accelerator Conf., Washington, D.C., U.S.A., May 17-20, 1993, p.1318.

[12] H.Mizuno, T.Majima, S.Sakamoto and Y Kobayashi; "A Blumlein type modulator for 100MW class X-band klystron"; Proceedings of the 1993 Particle Accelerator Conference, Washington, D.C., U.S.A., May 17-20, 1993: P-1321.

[13] H.Mizuno, T.Majima, S.Sakamoto and Y Kobayashi; "A.Blumlein type modulator for 100MW class X-band klystron"; Proceedings of the 4th European Particle Accelerator Conference(EPAC94), London, U.K., June27-July 1, 1994: P-2538.

[14] G.C.Caryotakis et al; "Development of multi-megawatt klystrons for linear colliders"; Proc. 1993 Particle Accelerator Conference, Washington, D.C., U.S.A., May 17-20, 1993: p1106.

[15] G.C.Caryotakis et al; "50-MW X-band klystron sources for the next generation of linear colliders"; Proc. 4th European Particle Accelerator Conf. (EPAC94), London, U.K., June 27 - July 1, 1994: p.1921.

[16] W.Wright et al; "Design of a 50-MW Klystron at X-band": AIP Conference Proc. 337 (Pulsed RF Sources for Linear Colliders), Montauk, NY 1994, p.58.

[17] K.R.Eppley; "A RPM-Focused Klystron at X-band with a Traveling-Wave Output Structure": AIP Conference Proc. 337 (Pulsed RF Sources for Linear Colliders), Montauk, NY 1994, p.67.

[18] H.Mizuno, J.Odagiri and T.Higo;"X-band klystron diode test for Japan Linear Collider" :Proc. 14th International Conference on High Energy Accelerators Part-4. 1989 P-1125

[19] H.Mizuno, J.Odagiri, T.Higo, M.Akemoto and H.Sakai;"X-band klystron for Japan Linear Collider": Proceedings of the 1990 Linear Accelerator Conference September 10-14, 1990 Albuquerque, New Mexico P-168.

[20] H.Mizuno;"X-band klystrons as a power source of the next linear collider"; The ICFA Seminar on "Future Perspectives in High Energy Physics" DESY, Hamburg, Germany, May 3-7, 1993:KEK preprint 93-200 February 1994 A.

[21] H.Mizuno, J.Odagiri, T.Higo and M,Akemoto;"X-band klystrons for Japan Linear Collider": Proceedings of the 15-th International Conference on High Energy Accelerators July 20-24, 1992 Hamburg Germany.: P-921.

[22] H.Mizuno, J.Odagiri, T.Higo, H.Yonezawa and N.Yamaguchi;"X-band klystron for Japan Linear Collider": Proceedings of the 1992 Linear Accelerator Conference. 1992 August 24-28 Ottawa, Ontario, Canada.;P-127.

[23] H.Mizuno, J.Odagiri, T.Higo and H.Yonezawa; "X-band Klystrons for Japan Linear Collider": Proceedings of the 4th European Particle Accelerator Conference(EPAC94), London, U.K., June27-July 1, 1994: P-1918.

[24] J.Odagiri, H.Mizuno, T.Shintake and K.Takata;"FCI Simulation on 100MW class klystron at X-band": Proceedings of the 17th International Linac Conference, Tsukuba, Japan, August 21-16 1994: P-469.

[25] V. Balakin, S. Kazakov and V. Teryaev, communication.

[26] S.Michizono, Y.Saito, H.Mizuno and S.Yu.Kazakov;"High-power tests of pill-box and TW-in-CERAMIC type S-band RF windows": Proceedings of the 17th International Linac Conference, Tsukuba, Japan, August 21-16 1994: P-457.

[27] Y.Otake, S Tokumoto and H.Mizuno;"Design and high power test of a TE11 mode X-band RF window with the taper transitions": Proceedings of the 1995 Particle Accelerator Conference and International Conference on High -Energy Accelerators, May 1-5, 1995, Dallas,Texas, U.S.A.: KEK preprint 95-30 May 1995 A.

[28] Z.D.Farkas et al. "SLED: A method of doubling SLAC's Energy"; Proc. 9th Int. Conf. High Energy Accelerators, SLAC. Stanford. 1974. P576.

[29] Z.D.Farkas et al.; "Binary Peak Power Multiplier and its Application to Linear Collider design"; IEEE Trans. MTT-34(1986), P1036.

[30] T.L.Lavine, Z.D,Farkas et al.; "High Power RF Binary Pulse Compression Experiments at SLAC"; Proc. of the IEEE Particle Accelerator Conference May 1991. San Francisco. California. USA. P652.

[31] P.B.Wilson, et al. "Progress at SLAC on High Power RF Pulse Compression"; Proc. of 15th Int. Conf. High Energy Accelerators, Hamburg Germany, July 1992, World Scientific, Singapore, 1992. P824.

[32] H.Matsumoto et al.;"High power test of a SLED system with dual side wall coupling irises for linear colliders"; KEK preprint 92-179.

[33] P.B.Wilson, et al. "Progress at SLAC on High Power RF Pulse Compression"; Proc. of 15th Int. Conf. High Energy Accelerators, Hamburg Germany, July 1992, World Scientific, Singapore, 1992. P824.

[34] C.D.Nantista; "Radio frequency pulse compression for linear accelerators" Thesis, University of California 1994.

[35] S.G.Tantawi et al; "The Next Linear Collider Test Accelerator's RF Pulse Compression and Transmission Systems": Proc. 5th European Particle Accelerator Conf. Sitges (Barcelona), Jun 10-14, 1996, p.2062.

[36] V.E.Balakin.;"Pulsed power RF sources for linear colliders" ;(REF 1-6)

[37] V.E.Balakin et al..;"14 GHz VLEPP Klystron" ;Proc. of the 3rd. EPAC Berlin, Germany, 1992.

[38] L.N.Arapov et al; "High Power Sources for VLEPP": AIP Conference Proc. 337 (Pulsed RF Sources for Linear Colliders), Montauk, NY 1994, p.118.

[39] I.Syrachev, V.Vogel, H.Mizuno, J.Odagiri, Y Otake and S Tokumoto; "The results of RF high power tests of X-band open cavity RF pulse compression system VPM(JLC)": Proceedings of the 17th International Linac Conference, Tsukuba, Japan, August 21-16 1994: P-475.

[40] M.Bieler et al.;"Commissioning of the hard tube pulsar experiment at DESY"; Proceedings of the 4th European Particle Accelerator Conference (EPAC94), London, U.K., June27-July 1, 1994: P-1993.

[41] M.Bieler et al; "Modulators for the S-band Test Linac at DESY": AIP Conf. Proceedings 337 (Pulsed RF Sources for Linear Colliders), Montauk, NY 1994, p.332.

[42] H.Mizuno and Y.Otake: "A New RF Power Distribution System for X-band Linac Equivalent to an RF Pulse Compression Scheme of Factor 2": Proc. 19th Linear Accelerator Meeting in Japan, July 20-24, 1994, Japan Atomic Energy Research Institute, Tokai, Japan, p.90 (in Japanese).

[43] H.Mizuno; "A Prototype RF Power Source System for the X-band Linear Collider"; AIP Conf. Prof. 337 (Pulsed RF Sources for Linear Colliders), Montauk, NY 1994, p.89.

[44] H.Mizuno and Y.Otake;"A new RF power distribution system for X-band linac equivalent to an RF Pulse compression scheme of Factor 2^n"; Proceedings of the 17th International Linac Conference, Tsukuba, Japan, August 21-16 1994: P-463.

[45] F.Tamura and H.Mizuno; "A new measurement method of the delay line length in the X-band Delay Line Distribution System (DLDS)" to be submitted to PAC 1997.

Authors and Major Contributers of Chapter 10

- H. Mizuno
- T. Higo
- F. Tamura
- S. Anami
- S. Fukuda
- Y. Saito
- S. Tokumoto
- Y. Otake
- J. Odagiri
- E. Takasaki

We would like to express our gratitude to many colleagues from abroad, in particular, scientists and engineers from SLAC (U.S.A.) and BINP, Protvino (Russia), for many useful discussions and collaborative R&D work on the RF power source systems. Special thanks go to Prof. V. Balakin, Dr.S. Kazakov and V. Teryaev of BINP, Protvino for their design work of X-band high-power klystrons which is the basis of our XB-72K #7 klystron, and for providing a site for conducting prototype tests of a DLDS system.

CHAPTER 11

X-band Main Linacs: Installation and Alignment

Contents

11.1 Introduction

Systematic studies related to the installation and alignment of the main linac components have just recently started within the JLC accelerator group. The purpose of the studies is to establish a method for making the condition in which the BBA (beam based alignment) method can work. At present, we adopt detuned structures (DS), as presented in Chapter 9. Issues related to linac alignment may be classified into two categories. One is local alignment; the other is global alignment. Local alignment means aligning components over several meters within a required accuracy. Global alignment means alignment over a whole linac.

For local alignment, a feasibility study concerning the support girder is in progress. For suppressing the long-range wake-field, four successive DS units, 1.3 m-long each, must be aligned within a tight tolerance on a common girder. Based on simulations of the beam dynamics, the alignment tolerance of the components, which are accelerating structures and quadrupole magnets, is currently understood to be several microns. The goal of the study here is to develop an alignment system on a girder with an accuracy of sub microns.

The construction of a test alignment system has begun within the JLC group, and is currently on-going. An outline of this system will be given at the end of this chapter. One of the purposes of this experiment is to find out whether the girder can be considered to be a rigid body or not at the frequency of interest. If a girder can be built that is sufficiently rigid, we can use the girder as a base of alignment for the successive four structures. Then, the girders will be aligned along a standard line. If, on the other hand, a long girder cannot be assumed to be sufficiently rigid, each structure have to be held on separate girders, and be aligned according to an external reference line.

For global alignment, one of the important issues is to establish a standard of alignment. The current focus of our study is on investigations of some fundamental features of suspended wire and a light beam. We will investigate other methods for a global reference, such as using astrophysical sources, a satellite system and so on. At the present, no proper method to construct a standard of alignment for the whole linac has been established. An experimental study has started for the test system. The range of the distance is about several meters. We will gradually expand the range of the experiment. It may be possible to perform experiments up to about 1 km at the site of KEK. To realize test experiments up to 4 km, collaboration may be required with a project involving a large interferometric gravitational-wave detector, such as LIGO.[1]

Once a global standard is established, the components of linac will have access to the standard for aligning. We may regard this process as the extraction of information from the standard. The standard works as a sort of path for transmitting information. The degree of freedom for accession may be on the order of 10^5 over the entire linac. A flow of information on the standard will be studied for optimizing the signal-to-noise ratio of each degree of freedom.

Since our studies are at a very preliminary stage, this chapter describes our plan for test experiments

concerning the support and alignment systems and a few results. No definitive conclusions about the full engineering scope of the system are given.

11.2 Standard of Alignment

In order to align the components at their proper positions, one needs a standard line. The standard should be studied from the viewpoint of the limit of length coverage and the limit of accuracy. Although there are some candidates for a standard, we have not studied yet all of them.

11.2.1 Suspended Wire

A suspended wire is one of the commonly used standards of positioning, because it is a simple and a convenient way to obtain a reference line in space. What is necessary for the wire as a standard of alignment is to have a well-defined shape between the suspension points. Any component of the linac can determine its certain position by measuring the relative position to the wire. Therefore, a limit of measurement has to be considered in order to know the accuracy of alignment. In the following, some basic features are discussed based on a simple model of a wire. After defining the model, we consider a static problem in order to understand the shape of the wire. Also, some discussion concerning the accuracy of the position is given.

We consider a wire to be a single fiber with a Young's modulus E, a mass density ρ, a cross sectional area A and an area moment of inertia I. The wire is fixed at both ends. There is a tension on the suspended wire, which causes a stress in the wire. For a stable suspension of the wire, the stress caused by the tension should be less than the yield stress of the material. The value of the yield stress is much smaller than the elastic modulus of the wire. For example, the yield stress of steel is on the orders of $10^8\,\mathrm{N/m^2}$. Then, the Young's modulus is on the order of $10^{11}\,\mathrm{N/m^2}$, and the shear modulus is on the order of $10^{10}\,\mathrm{N/m^2}$. Thus, compared to a transverse deformation, neither the longitudinal nor shearing deformation can be negligible on the wire. Thus, the transverse deformation of the wire is be considered. Any torsional motion is neglected along the wire.

We define the Cartesian coordinate system (x, y, z) according to a right-handed oriented set, such that the x-axis points in the horizontal direction, the y-axis points up, and the yz-plane contains two suspension points of the wire. We assume a uniform gravitational acceleration g in the y-direction. Due to the symmetry of the problem, the wire should be in the yz-plane when it is in equilibrium. The shape of the wire is described as a function of $y(z,t)$ for $z \in [z_1, z_2]$. A displacement of $x(z,t)$ becomes important only for a vibration problem. It may be sufficient to treat it as a small perturbation around the equilibrium position.

Based on these assumptions, the kinetic energy of the wire is given by

$$K = \int_{z_1}^{z_2} \frac{1}{2}\rho A \dot{y}^2 \, dz, \tag{11.1}$$

where the dot indicates the time derivative. The potential energy consists of the gravitational energy, the work due to the initial tension and the potential energy of elastic bending, as

$$U = U_{grav} + U_F + U_{elas} \ , \tag{11.2}$$

where

$$U_{grav} = \int_{z_1}^{z_2} \rho A g \, y\sqrt{1+y'^2} \, dz \ , \tag{11.3}$$

$$U_F = \int_{z_1}^{z_2} \frac{1}{2} F \, y'^2 \, dz \ , \tag{11.4}$$

$$U_{elas} = \int_{z_1}^{z_2} \frac{1}{2} EI \, y''^2 \, dz \, . \tag{11.5}$$

Here, F is the tension and the prime indicates $\frac{\partial}{\partial z}$. During a deformation of the wire, it is assumed that Young's modulus E, the mass density ρ, the cross-sectional area A and the area moment of inertia I are kept constant along the wire. A small displacement is assumed for U_F and U_{elas}.

The equation of motion is obtained by varying the action,

$$S = \int (K - U) \, dt, \tag{11.6}$$

with respect to $y(z,t)$. The Euler equation 11.6 requires four boundary conditions. In the case of the wire being hinged at the suspension point, the boundary conditions are given by

$$y(z_i,t) = y''(z_i,t) = 0 \ \ (i = 1,2). \tag{11.7}$$

It can be appropriate to avoid any influence of the rigidity of the wire near to the suspension points. For a practical setup, there could be a mechanism that controls the tension of the wire, at least at one suspension point. A schematic illustration shows an example in Figure 11.1.

The Euler equation 11.6 represents a transverse motion of a uniform beam under tension in a constant gravitational field. In the case of a thin wire, the contribution of U_{elas} becomes smaller than the other terms in Equation 11.2, because the area moment of inertia depends on the fourth power of the thickness of the wire. For example, the parameters of an actual wire-alignment system used in the Accelerator Test Facility(ATF) of KEK have been evaluated. The parameters are shown in Table 11.1. From Equation 11.5, the ratios of U_F and U_{elas} to U_{grav} have approximate values of

$$U_F/U_{grav} \approx 0.3 \ , \tag{11.8}$$

$$U_{elas}/U_{grav} \approx 7 \times 10^{-10} \ , \tag{11.9}$$

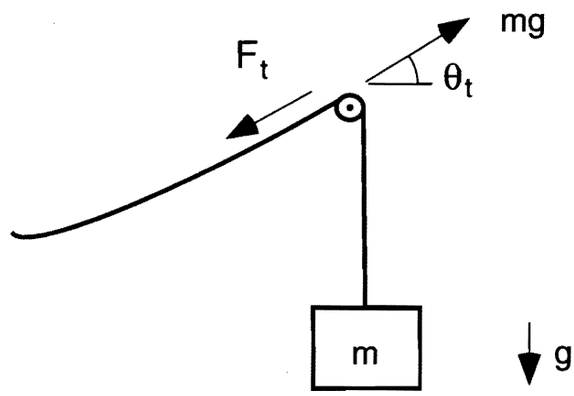

Figure 11.1: *An example of the tension controller. The wire bends smoothly on the wheel to balance the tension with a weight. The wire is equivalently hinged if the radius of the wheel is much larger than the diameter of the wire.*

	symbol	value	unit
diameter	d	0.6	mm
span	l	91	m
tension weight	m	33.5	kg
maximum sag	y_{sag}	$\approx$90	mm
Young's modulus	E	2.1×10^{11}	N/m^2
density	ρ	7.9×10^{3}	kg/m^3
area moment of inertia	I	6.4×10^{-15}	m^4
cross sectional area	A	2.8×10^{-7}	m^2
supplied tension	mg	3.3×10^{2}	N

Table 11.1: *Parameters of wire-alignment system of the ATF*

where the following approximations were used: $y \approx y_{max}$, $y' \approx y_{max}/(\frac{l}{2})$, $y'' \approx y_{max}/(\frac{l}{2})^2$ and $\int dz \rightarrow \times(\frac{l}{2})$. Compared with the dominant term of U_{grav}, we could neglect U_{elas}, but had to keep U_F in this case.

Any stress caused by the tension must be smaller than the yield stress of the material of the wire. Thus, an applicable tension has an upper limit of $\sigma_Y A$, where σ_Y is the yield stress of the material and A is the cross-sectional area of the wire. By the same approximation in Equation 11.9, the ratio of U_F/U_{grav} is limited by

$$\frac{U_F}{U_{grav}} \lesssim \frac{\sigma_Y}{\rho g l}\frac{2y_{max}/l}{\sqrt{1+(2y_{max}/l)^2}}, \tag{11.10}$$

where y_{max} is the maximum sag and l is the span of the wire. The ratio U_F/U_{grav} becomes small in the case of a long span, although the maximum sag is large. From the above discussion, we could

take the action of a thin wire as

$$S = \int (K - U_{grav} - U_F)\, dt \,. \tag{11.11}$$

Substituting $g = 0$ into Equation 11.11, we obtain the action of a straight string under tension F. If U_F is neglected in Equation 11.11, the solution of $\delta S_{tw} = 0$ would give the motion of a catenary. In the following sections, we will discuss some static and dynamical problems based on Equation 11.11.

11.2.2 Catenary

In this section we consider the stationary shape of a suspended wire. From Equation 11.11, a solution $y(z)$ is determined by varying the potential energy with respect to z. We first focus only on U_{grav}. It will be discussed later for the case of $U_{grav} + U_F$.

The Euler equation is obtained by

$$\delta U_{grav} = 0 \,. \tag{11.12}$$

The solution, which is known as catenary, is obtained as

$$y(z) = y_0 + h \cosh \frac{z - z_0}{h} \,, \tag{11.13}$$

$$h \equiv \frac{H}{\rho A g} \,, \tag{11.14}$$

where H denotes a constant of the first integral of the Euler equation. Three constants y_0, z_0 and h are determined from two boundary conditions $y_1 = y(z_1)$ and $y_2 = y(z_2)$, when the length of the wire is given. In the case of $z_1 = -l/2$, $z_2 = l/2$ and $y_1 = y_2 = 0$, the shape of the wire is given by

$$y(z) = h \left(\cosh \frac{z}{h} - \cosh \frac{l}{2h} \right) \,, \tag{11.15}$$

where l denotes a span of two suspension points.

Figure 11.2 shows the function of Equation 11.15. To determine h, one needs the length of the wire, which is given by

$$L_w = 2h \sinh \frac{l}{2h} \,. \tag{11.16}$$

The constant H corresponds to the horizontal component of the tension. The horizontal component of the tension should be constant along the wire, because any horizontal plane is an equipotential surface of a uniform gravitational field. Thus, the vertical component is given by $F_v = F_h y'(z)$ on the wire, where F_v denotes the vertical component and F_h denotes the horizontal component. Using (11.15), we obtain

$$F_v = F_h \sinh \frac{l}{2h} \tag{11.17}$$

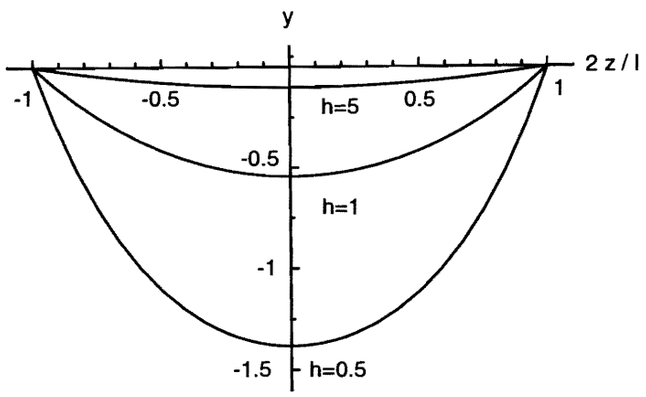

Figure 11.2: *This plot shows catenaries for $h = 0.5, h = 1$ and $h = 5$. Coordinate z is normalized by $l/2$. The larger h becomes, the shallower the curve becomes.*

at the end of the wire. In the case of h tending to zero, F_v goes to an asymptotic form, as

$$F_v \sim \frac{F_h}{2} \exp \frac{l}{2h} \quad (h \to 0). \tag{11.18}$$

On the other hand, the F_v asymptotically equals half of the weight of the wire, because L_w becomes much longer than l. By using Equations 11.14 and 11.16, F_v is expressed as

$$F_v \sim \frac{h}{2}\rho A g \exp \frac{l}{2h} \quad (h \to 0) \tag{11.19}$$

$$= \frac{H}{2} \exp \frac{l}{2h}. \tag{11.20}$$

Equating Equation 11.18 to 11.20, we obtain $F_h = H$.

One obtains an expression of the tension as

$$F_t(z) = \sqrt{F_v^2 + F_h^2}\,, \tag{11.21}$$

$$= H \cosh(z/h)\ . \tag{11.22}$$

$F_t(z)$ takes a maximum, which balances the weight, as shown in the Figure 11.1, at $z = \pm l/2$. In order to maintain a fixed shape of the wire, any stress caused by the maximum tension of $F_t(\pm l/2)$ has to be less than any yield stress of the material of the wire:

$$\frac{H}{A} \cosh \frac{l}{2h} < \sigma_Y\,. \tag{11.23}$$

Here, σ_Y is the yield stress of the material of the wire. From Equation 11.23, an upper limit of a span is obtained by

$$l_{ul} = 2h \cosh^{-1} \frac{\sigma_Y}{\rho g h}\,. \tag{11.24}$$

where the definition of $h \equiv H/\rho A g$ is used. A span shorter than l_{ul} is allowed. Optimizing the right hand side of Equation 11.24 with respect to h, one may estimate the attainable span of the wire.

material	σ_Y $[10^8\,Pa]$	ρ $[10^3\,kg/m^3]$	$2\phi_{max}\frac{\sigma_Y}{\rho g}$ $[km]$
steel	≈6.0	7.9	10
brass	≈3.0	8.6	4.7
Be-Cu	≈	8.3	
Be	≈4.1	1.84	30
Ti	≈4.9	4.54	15
W	≈?	19.1	
fused silica	≈10	2.2	61
carbon fibre	≈29	1.77	220
poly acethal	≈10	1.42	95

Table 11.2: *Attainable spans of a wire listed in the right-hand column. The values of σ_Y in this table are rough numbers for estimating the upper limit of the span. For the non-metallic materials listed here, the tensile strengths are used instead of the yield stress. The value of ϕ_{max} is of 0.6627, which is the maximum of $\cosh^{-1}(s)/s$ in $s \in (1,\infty)$.*

Table 11.2 lists the attainable spans of some materials, together with σ_Y and ρ. Regarding Table 11.2, it appears to be possible to suspend a wire over a distance of a few ten kilometers. We, however, have to consider about a sag of the wire. Substituting $z = 0$ into (11.15), we obtain the sag of the wire:

$$y_{sag} = h\left(\cosh\frac{l}{2h} - 1\right) . \tag{11.25}$$

When one substitutes $l = 2\phi_{max}\sigma_Y/\rho g$ into the right hand side of 11.25, the sag becomes comparable to the attainable span, as

$$y_{sag} = 0.338 \times 2\phi_{max}\frac{\sigma_Y}{\rho g} . \tag{11.26}$$

According to the right-hand column of Table 11.2, a wire with fully attainable span is not suitable to be a standard of positioning. Thus, a wire alignment method may be applicable for a short span, compared with the length of the main linac.

From a practical point of view, a small sag of the wire is preferable. At least, the sag must be smaller than the radius of the tunnel in which a linac is installed. According to Equation 11.25, the sag becomes smaller by making h larger. It is equivalent to supplying a large tension to the wire. Simultaneously, the span of the wire is restricted by Equation 11.24. From this and Equation 11.25, l_{lu} is expressed by

$$l_{lu} = \sqrt{\frac{8\sigma_Y y_{sag}}{\rho g}}\left[1 - \frac{7}{12}\left(\frac{\rho g y_{sag}}{\sigma_Y}\right) - \frac{71}{480}\left(\frac{\rho g y_{sag}}{\sigma_Y}\right)^2 - \frac{319}{4480}\left(\frac{\rho g y_{sag}}{\sigma_Y}\right)^3 \cdots\right] \tag{11.27}$$

as a series of y_{sag}, where $(\rho g y_{sag}/\sigma_Y) < 1$ is assumed.

11.2.3 Static Solution (General Case)

From Equation 11.11, a static solution of a suspended wire is given as

$$\delta\left(U_{grav}+U_F\right) = 0 . \tag{11.28}$$

Substituting $g = 0$ into Equation 11.28, we obtain a straight line as the solution. The existence of U_F might be reasonable due to this fact.

The solution of Equation 11.28 is represented by a parameter, p:

$$z = \left(\frac{1}{4}f+h\right)\log(p+\sqrt{1+p^2})+\frac{3}{4}f\sqrt{1+p^2} , \tag{11.29}$$

$$y = h\sqrt{1+p^2}+\frac{1}{2}fp^2\sqrt{1+p^2} , \tag{11.30}$$

where $h \equiv H/\rho Ag$, $f \equiv F/\rho Ag$ and H denotes a constant of the first integral of the Euler equation. The parameter p is just the tangent of the curve. Obviously solution 11.30 contains catenary as the case of $f = 0$. We may determine how the solution 11.30 is relevant for representing a real wire by some experiments.

11.2.4 Accuracy of a Measurement

When we use a suspended wire as a standard of the alignment procedure, any vibration problem is important in concerning the accuracy of the measurement. For our interest concerning the accuracy of a measurement, it is sufficient to consider a small vibration . We may assume that the local tension as well as the local density of the wire are determined by only the gravitational sag of the wire. A small vibration could be considered to be a ripple on the static solution. If the static solution is given by catenary, we may obtain a equation of motion:

$$\frac{\partial}{\partial s}\left(F(s)\frac{\partial u}{\partial s}\right) = \rho A\frac{\partial^2 u}{\partial t^2} , \tag{11.31}$$

where s denotes the length along the wire, $F(s)$ the local tension and u the transverse displacement from a catenary. Transferring the independent variable from s to z, we obtain

$$\frac{1}{\cosh(z/a)}\frac{\partial}{\partial z}\left(H\frac{\partial u}{\partial z}\right) = \rho A\frac{\partial^2 u}{\partial t^2} , \tag{11.32}$$

where H is the horizontal component of the tension. We may regard Equation 11.32 as being the motion of a wire with a constant tension and with a z-dependent density. Under a proper boundary condition, Equation 11.32 has eigenmodes $\{\ \xi_n\ \}$ that satisfy

$$\frac{d^2\xi_n}{dz^2}+\frac{\omega_n^2}{ag}\cosh\frac{z}{a}\cdot\xi_n = 0 , \tag{11.33}$$

where ω_n is the eigen-frequency and $a \equiv H/\rho Ag$.

Many external forces excite a vibration of the wire. These forces could be, in principle, isolated by some appropriate apparatus. After decreasing these disturbances, thermal noise appears as a fundamental limit of a measurement. The square mean of the thermal fluctuation of the wire is obtained in the following.

An arbitrary deformation $\xi(z)$ can be expanded by a generalized Fourier series as

$$\xi(z) = \sum_n^\infty c_n \xi_n \ , \tag{11.34}$$

where c_n denotes the coefficient of expansion and a normalized condition,

$$\int \xi_m \xi_n \cosh \frac{z}{a} dz = \delta_{mn}, \tag{11.35}$$

is established. The potential energy U is given by

$$U = \frac{H}{2} \int \left(\frac{d\xi}{dz}\right)^2 dz \tag{11.36}$$

$$= \frac{H}{2ag} \sum_n^\infty \omega_n^2 c_n^2 \ . \tag{11.37}$$

Consider a wire contacting a thermal bath at temperature T. Regarding $\{c_n\}$ as a generalized coordinate, the thermal fluctuation is given by

$$< c_m c_n > = \frac{\prod_j^\infty \int dc_j \, c_m c_n \exp\left(-\frac{U}{k_B T}\right)}{\prod_j^\infty \int dc_j \exp\left(-\frac{U}{k_B T}\right)} \tag{11.38}$$

$$= \frac{k_B T}{H} \frac{ag}{\omega_n^2} \delta_{mn} \ , \tag{11.39}$$

where k_B denotes Boltzmann's constant. The square mean of a the thermal fluctuation of the wire is given by

$$< \xi^2 > = \sum_m \sum_n < c_m c_n > \xi_m \xi_n \tag{11.40}$$

$$= \frac{k_B T}{H} \sum_n \frac{ag}{\omega_n^2} \xi_n^2 \ . \tag{11.41}$$

The most important purpose of the wire as a standard of alignment is to make a line as straight as possible. This is realized by a large tension on the wire over a short span. It is equivalent to put $\cosh(z/a) \approx 1$ in Equation 11.33. We may treat the wire in such cases as a straight wire. In this case, the eigen-frequency and eigen-function are given by

$$\frac{\omega_n^2}{ag} = \left(\frac{n\pi}{L}\right)^2 \ , \tag{11.42}$$

$$\xi_n = \sqrt{\frac{2}{L}} \sin \frac{n\pi z}{L} \ , \tag{11.43}$$

where L denotes the length of the wire. In Equation 11.43, we assume that the wire is hinged at both $z = 0$ and $z = L$. The last sum of Equation 11.41 is calculated in the case of Equation 11.43 as

$$< \xi^2 > \;=\; \frac{k_B T}{HL} z \cdot (L - z) \;, \tag{11.44}$$

where we use the formula of $\sum_{n=1}^{\infty} \sin^2 nz/n^2 = z(\pi - z)/2$ in $z \in [0, \pi]$. [2]

For example, upon substituting T=300 K, H=328 N and L=91 m into Equation 11.44, we obtain the maximum root mean square of the thermal fluctuation,

$$\sqrt{< \xi^2 >_{max}} \;=\; 1.7 \times 10^{-11}\,\mathrm{m} \;, \tag{11.45}$$

at $z = L/2$. This value may be much smaller than the practical limit of measurements.

11.2.5 Light Beam

The velocity of particles ($e^{\pm}$) in the beam is practically equal to the speed of light. According to this fact, a ray of light in a vacuum is a natural standard of alignment. An actual beam of light has a finite size. This causes some diffraction of the beam. Also, a beam in the atmosphere is affected by any inhomogeneity of refractive index due to hydrodynamic motions and thermodynamic fluctuation. From the viewpoint of alignment, the features of a light beam will be studied in a prototype experiment.

11.3 Environmental Noise

There are many quantities that determine the environment of the tunnel of the linac. Any fluctuation of those quantities can appear as noise in the alignment of the linac. In this section, a brief description is given concerning possible noise sources in the tunnel. A study about such environmental noise has also just started for an X-band linac. The structure of the tunnel for a linac, including power sources, should be considered from the viewpoint of optimizing it. Most investigations will go further.

11.3.1 Temperature

The variation of temperature affects the physical properties of matter. An example is thermal expansion. A typical value of the coefficient of linear thermal expansion is $\alpha \sim 10^{-5}$ 1/K. A simple way to reduce the effect of thermal expansion is to use a material with a small coefficient of linear thermal expansion. Some materials having a small expansion coefficient are listed in Table 11.3. Invar alloy may be used as a structural material instead of stainless steel when thermal stability is required. However, it should be noted that Invar is not corrosion-resistant. Also, this alloy is ferromagnetic. We measured the forced magnetostriction of Invar by interferometry at room temperature. A preliminary result shows $\frac{1}{L}\frac{\partial L}{\partial H} = 7 \times 10^{-10}$[1/(A/m)] under a change of magnetic field H=0 - 9300[A/m].

material	α [1/K]	
Invar	7 - 9 $\times 10^{-7}$	283K - 323K
Fused silica	5×10^{-7}	273K - 323K
Clearceram-z	8 $\times 10^{-8}$	273K - 323K
Zerodure	5 $\times 10^{-8}$	293K - 573K
ULE	3 $\times 10^{-8}$	273K - 473K

Table 11.3: *Materials with a small coefficient of linear thermal expansion. Invar is a steel-based alloy containing 36%Ni with small quantities of Mn, Si, and C, amounting to a total of less than 1%.[3] Clearceram[4], Zerodure[5] and ULE[6] are glasses with a controlled expansion.*

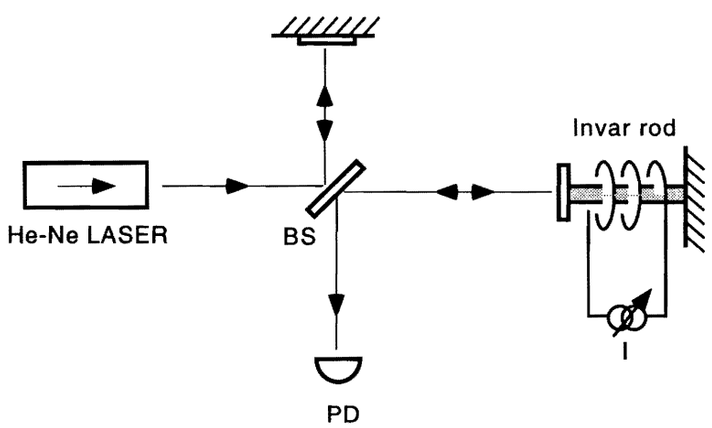

Figure 11.3: *Interferometric measurement of forced magnetostriction of Invar. The specimen is a 12 mm ϕ Invar rod that is supported in a solenoid of 14 mmϕ×100 mm with 1500 turns.*

We do not describe about any other effects of the temperature variation here. Even though the temperature is constant, it produces a thermodynamic fluctuation of the physical quantity in a system with a finite temperature. The thermodynamic fluctuation gives a fundamental limit of any measurement of a physical quantity.

11.3.2 Atmosphere

Any hydrodynamic motion of the air cause a mechanical motion of the apparatus due to momentum transfer. Also, a turbulent flow disturbs the propagation of light due to an irregularity in the refractive index. Even in static air, a light beam is scattered due to any thermodynamic fluctuation of the refractive index. Those noises will be studied in an experiment with a prototype local-alignment system, which is described in the last section of this chapter.

Acoustic noise also causes a mechanical vibration of the apparatus. This will be discussed in the section of vibration.

11.3.3 Mechanical Vibrations

There are many sources of mechanical vibrations, such as acoustic waves, human activities, the operation of equipment in the laboratory and ground motion. Roughly speaking, the former three sources cluster in characteristic frequency regions as follows:

- Acoustic noise is dominant above 100 Hz,
- The vibration of machines, such as pumps, distribute at 10 Hz $\sim$ 100 Hz,
- The intensity of the spectrum at 1 Hz $\sim$ 10 Hz has a difference in the daytime and nighttime,
- The resonances of buildings and floors of the laboratory exist at 1Hz $\sim$ 10Hz.

These sources distribute above 1 Hz. Therefore, it may be possible to isolate any sensitive apparatus from such noise if necessary.

An effective way to reduce the peak amplitude of the resonance is to use a low-Q material for constructing mechanical structures. There exist some low-Q alloys. A manganese alloy, called M2052, has a large damping capacity and workability[7]. The strength of the alloy is comparable with that of some aluminum alloys. It may be useful to suppress any vibration of the cooling-water tubes if they are corrosion-resistant. Also, it may be useful to apply such techniques for air conditioning ducts.

Ground Motion

The requirement on the ground motion is tightly coupled to the alignment strategy of the whole system. Results of early investigations regarding the effects of ground motions on the operation of JLC have been reported in [8]. More studies related to ground motion will be re-initiated soon.

Vibration Isolation

The isolation of an object from vibration is realized by putting a mechanical low-pass filter into the object and the source of vibration. The simplest way to do this is to construct a harmonic oscillator. A schematic diagram is shown in Figure 11.4. The transfer function of the system is given by

$$H_{x_g \to x}(\omega) = \frac{\omega_r^2 + \mathrm{i}\omega\omega_r/Q}{-\omega^2 + \omega_r^2 + \mathrm{i}\omega\omega_r/Q}\,, \tag{11.46}$$

$$\omega_r \equiv \sqrt{\frac{k}{m}}\,, \tag{11.47}$$

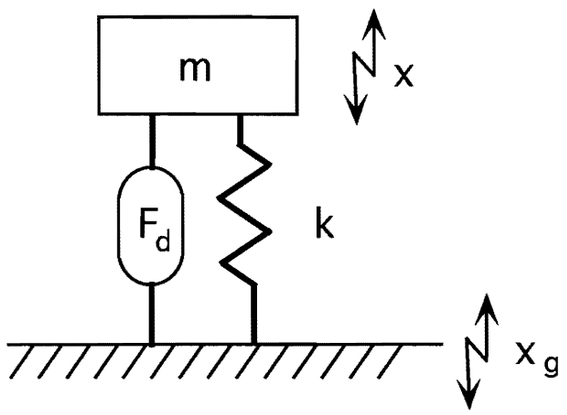

Figure 11.4: *A simple vibration isolator. A mass m and a spring with a spring constant of k construct a harmonic oscillator. A damping force F_d is introduced.*

where ω_r is the resonant frequency. We assume viscous damping, $F_d = \frac{m\omega_r}{Q}(\dot{x}-\dot{x}_g)$, in Equation 11.47. In the case that $\omega_r \gg \omega$ and $\omega/\omega_r \gg Q$, the transfer function works as a vibration isolator,

$$H_{x_g \to x}(\omega) \approx -\left(\frac{\omega_r}{\omega}\right)^2 . \tag{11.48}$$

According to Equation 11.48, we have to make ω_r sufficiently smaller than the planned frequency of ω. In order to realize a resonance frequency of ω_r by a simple mass-spring system in the Earth's gravitational acceleration g, the length of the spring is equivalent to the length of a pendulum with the same resonance,[1] $l_{equiv} = g/\omega_r^2$. From a practical point of view, it is hard to obtain a vibration isolator with a mechanical resonance below 0.1 Hz in the laboratory. One has to use a special design or active spring for isolating low frequencies.[9]

Active Vibration Isolator

As mentioned before, a resonance frequency of $\omega_r/2\pi$ =0.1 Hz is a practical lower limit of resonance in a passive vibration isolator. One can obtain effective isolation in the low-frequency region by an active isolator. Figure 11.6 shows the principle of an active isolator. The equation of motion of this system is given by

$$m\ddot{x} = -m\omega_r^2(x - x_s) - \frac{m\omega_r}{Q}(\dot{x} - \dot{x}_s) + f_n , \tag{11.49}$$

$$x_s = G(x - x_s + x_n) + x_g , \tag{11.50}$$

$$\tag{11.51}$$

[1] Assume that no offset stress exists.

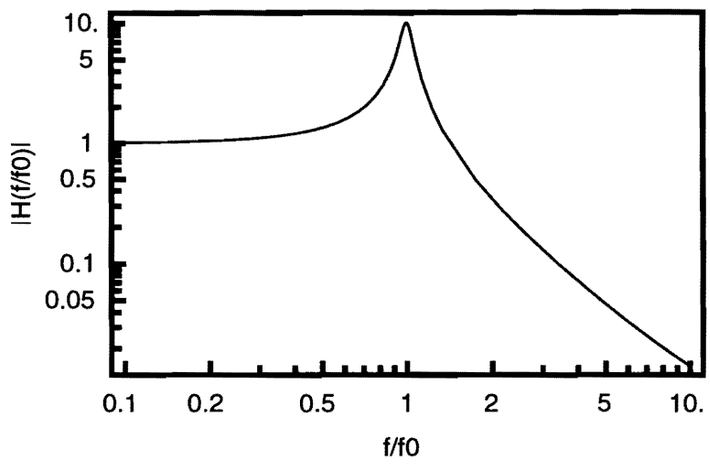

Figure 11.5: *Transfer function of a simple vibration isolator. A viscous damping force is assumed,* $F_d = \frac{m\omega_r}{Q} \cdot (\dot{x} - \dot{x_g})$. *The horizontal axis shows the frequency that is normalized by the resonant frequency. The plot shows the amplitude of the transfer function* $|H_{x_g \to x}|$ *with* $Q = 10$.

where G denotes the loop gain of the feed back, f_n the force noise and x_n the displacement noise. Upon solving Equation 11.51, we obtain

$$x(\omega) = \frac{\left(\frac{\omega_r^2}{1+G} + \frac{i\omega_r\omega}{Q(1+G)}\right)(x_g + Gx_n) + \frac{f_n}{m}}{-\omega^2 + \frac{\omega_r^2}{1+G} + \frac{i\omega_r\omega}{Q(1+G)}} . \tag{11.52}$$

The result corresponds to changing the system parameters as

$$\omega_r \to \frac{\omega_r}{\sqrt{1+G}}, \tag{11.53}$$

$$Q \to Q\sqrt{1+G}, \tag{11.54}$$

$$x_g \to x_g + Gx_n, \tag{11.55}$$

except for the effect of force noise. Therefore, we can improve the response of the vibration isolator if the gain G is sufficiently large. However, the noise performance has not been improved, even by a large G. Thus, a low noise electronics is required.

11.4 Test System of Local Alignment

A test system for local alignment was designed and fabricated. The accelerating structure is fixed on a v-block suspended by a link mechanism. The motion of the structure in the x-y plane is a pendulum-type motion without any rotation about the z axis. The laser beam is divided by the rectangle edge

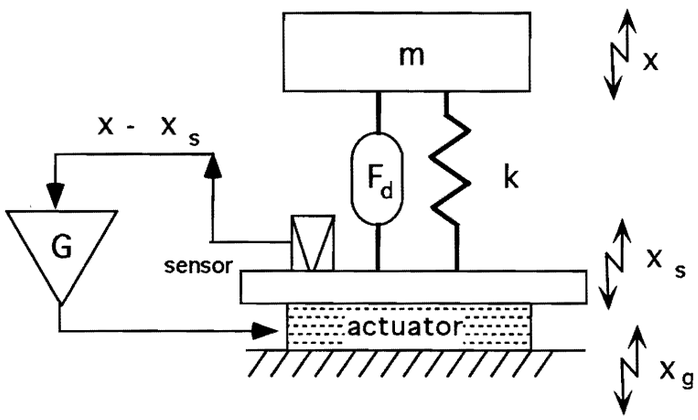

Figure 11.6: *Active vibration isolator. The relative displacement, $(x - x_s)$, is picked up by the sensor. Then, a loop filter feeds it back to an actuator.*

of a ring mirror. Any difference in the intensity detects the position of the structure. This error signal is fed back in order to keep the structure at the proper position.

References for Chapter 11

[1] B.Barish, LIGO Overview, *NFS Technical Review*, Oct., 1995.

[2] S.Moriguchi, K.Udagawa and S.Hitotumatu, Mathematical Formulas, vol.II, 1965.

[3] ASM International Committee ed., *Metals Handbook (10th ed.)*, vol.2, ASM International, 1990.

[4] *Catalogue of Ohara Co., Inc.*

[5] *Catalogue of Schott Co., Inc.*

[6] Code 7971,*Catalogue of Corning Glass Works Co., Inc.*

[7] K.Kawahara, N.Sakuma and Y.Nishizaki, J. Japan Inst. Metals, **57** (1993), 1089.

[8] JLC-I, KEK Report 92-16, December, 1992.

[9] M.A.Barton N.Kanda and K.Kuroda, A low-Frequency Vibration Isolation Table using Multiple Crossed-Wire Suspensions, ICRR-Report-371-96-22.

Authors of Chapter 11

- Toshikazu Suzuki
- Toshiyasu Higo

CHAPTER 12

C-band Main Linac Option

Contents

12.1 C-band Main Linac System Overview

12.1.1 Introduction

Hardware R&D for the C-band (5712 MHz) rf system for a linear collider started in 1996 at KEK as development of a back-up technology for the main linacs of JLC. An accelerating gradient of 32 MV/m (including beam-loading) will be generated by 50 MW C-band klystrons in combination with an rf-compression system. The klystron and its power supply can be fabricated by conventional technology. The straightness tolerance for the accelerating structures is 30 μm, which is also achievable with conventional fabrication processes. No critical new technology is required in a C-band system. Therefore, a reliable system can be constructed at low cost with a minimum of R&D studies. The first high-power test is scheduled for 1997.

The overall parameters are listed in Table 12.1 for 500-GeV and 1-TeV C.M. energy linear colliders. In the 500-GeV case, an accelerating gradient of 31.7 MV/m is generated by a 50-MW klystron in combination with rf pulse compression; thus, an active length of 7.3 + 7.3 km is required to reach 500 GeV C.M. energy. A luminosity of 7.2 $\times 10^{33}/\mathrm{cm}^2/\mathrm{s}$ (assuming that crab crossing is used) can be obtained using a 150 MW wall-plug power. The details are described in Chapter 2 and [3].

CM Energy	TeV	0.5	1.0
Number of electrons per bunch	$\times 10^{10}$	1.11	1.39
Number of bunches per pulse		72	
Bunch separation	nsec	2.8	
Repetition frequency	Hz	100	50
Bunch length	mm	0.2	
RF-parameters			
RF frequency	GHz	5.712	
Peak input power at cavity	MW	84.3	165
Nominal accelerating gradient	MV/m	40.0	56.0
Effective accelerating gradient	MV/m	31.9	46.4
Wall-plug power for RF (2 linacs)	MW	153	133
Accelerating Structure			
Number of structures per beam		4184	5864
Total length of cavities per beam	km	7.53	10.55
Structure Type		CG with choke-mode	
Unit length of structure	m	1.80	
Iris radius/wavelength		0.125 - 0.173	
Shunt-impedance	MW/m	53.1	
Pulse-compressor			
Compression Scheme		multi-cell coupled cavity	
Pulse compression ratio		5	
Pulse compression efficiency	%	70	
Klystron			
Klystron peak power	MW	50.3	98.6
Efficiency	%	45	70
Number of klystrons per beam		2092	2932
RF pulse length	msec	2.44	
Modulator			
Number of modulators per beam		2092	2932
Power efficiency from AC to pulse	%	75	
Beam Dynamics			
Injection energy	GeV	10	
Phase delay of rf-crest	deg	14.5	10.0
Structure straightness tolerance	μm	30	
Final focus			
Spot size at IP (horizontal)	nm	318	318
(vertical)	nm	4.4	3.1
Crossing angle (crab crossing)	mrad	8.0	8.0
Luminosity	$\times 10^{33}$	7.2	7.6

Table 12.1: C-band Parameters.

12.1.2 System Description

Figure 12.1 shows a schematic diagram of one unit of the main linac rf-system. Two 50 MW klystrons are driven by two high-voltage pulse modulators independently, followed by a 3dB hybrid power combiner and pulse compressor to generate 350 MW peak power, which drives four accelerating structures. The pulse-compression action is performed by rotating the phase of the input rf-signal in opposite directions in each klystron. By combining two powers at 3-dB hybrid, the phase modulation (PM) is converted to the amplitude modulation (AM) of the ramp-waveform, which compensates the beam-loading effect in the accelerating structure. The energy-storage cavity consists of three coupled cavities using a low-loss TE01n mode.

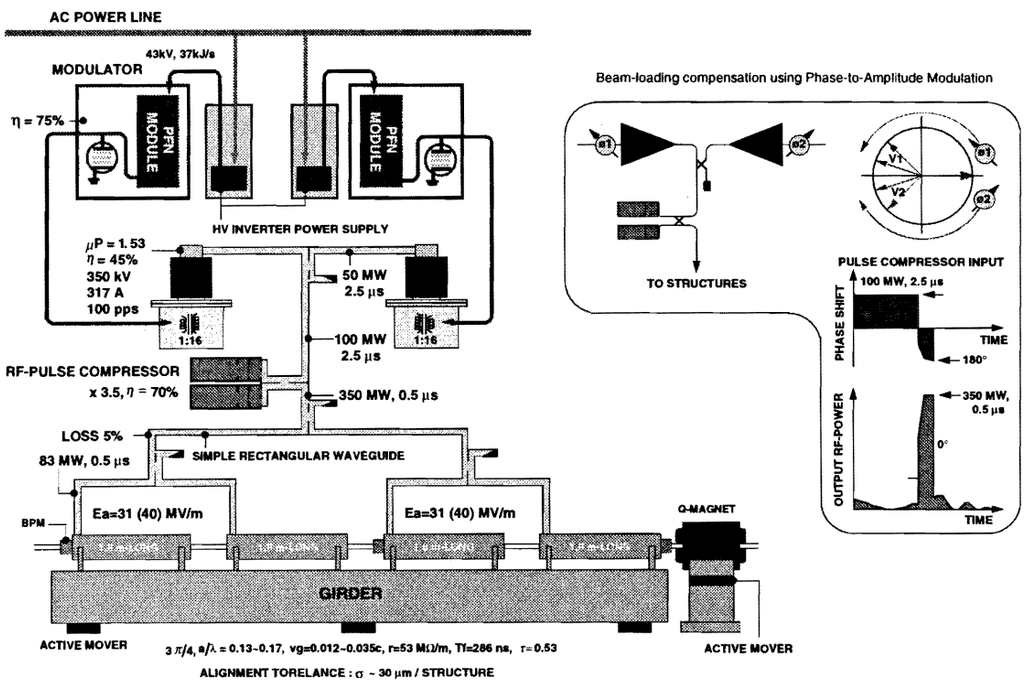

Figure 12.1: *Schematic view of one RF unit of the C-band main linac.*

We use a standard rectangular waveguide, EIA187 (47.55 mm × 22.15 mm, 3.95-5.85 GHz), whose attenuation constant is 0.03 dB/m (5% loss/m).

Figure 12.2 illustrates advantages of the C-band main linac scheme.

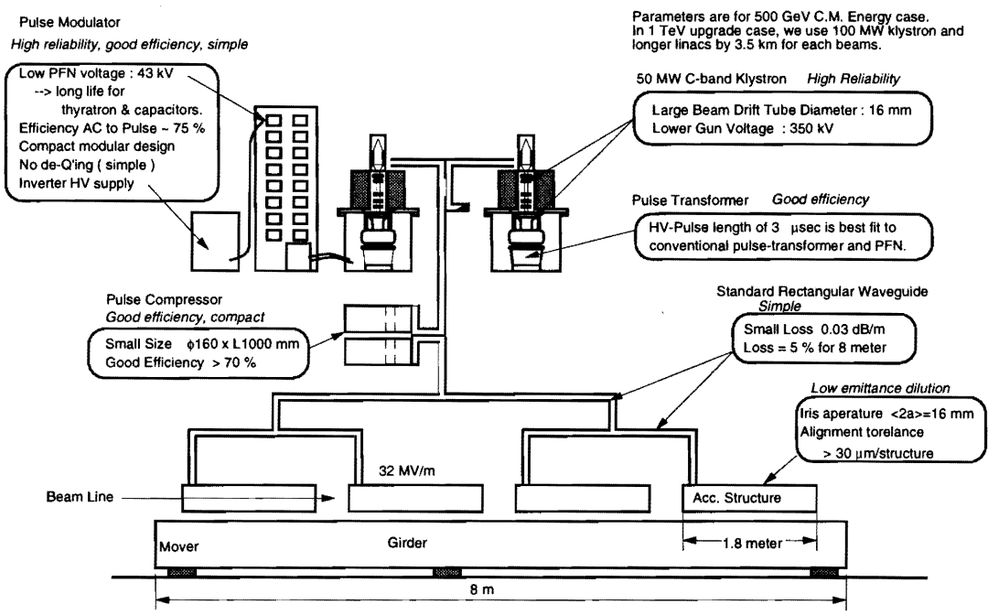

Figure 12.2: *Advantages in the C-band RF design.*

12.1.3 Klystron Power Supply & Pulse Transformer

The filling time of the accelerating structure scales as

$$\tau_F = \frac{2Q/}{\omega}\tau \propto \omega^{-3/2}. \tag{12.1}$$

At the C-band, it becomes 280 nsec. Including the pulse-length of the beam and a compression factor of five in the rf-compression system, the rf-pulse at the klystron becomes 2.44 μs. Including the rise- and fall-times, the pulse-length of the high-voltage applied to the electron-gun of the klystron becomes 3 μs or longer, which is quite suitable for the conventional power-supply consisting of a Pulse Forming Network (PFN) and a step-up pulse-transformer. This type of power supply has been used in many linear accelerators, owing to its high reliability and good efficiency.

To charge high-voltage into the PFN capacitors, we use an inverter power supply. Such a high-voltage power supply has been widely used to drive pulsed lasers for a long time. Modern technology for power-semiconductor devices (such as IGBT) has improved the power efficiency by better than 90 %. Using this power supply, we can simplify our modulator design, making it modular according to the required functions: the inverter power supply (DC block), the PFN module (pulse forming block), and the pulse-transformer tank (matching block to a klystron). With this approach, it becomes easier to reduce the cost, improve the reliability and ease maintenance. In the case of a failure, we simply replace any broken block with a new one and send the old one to a factory for repair.

12.1.4 C-band Klystron

Since the klystron drift-tube diameter is proportional to the rf wavelength, we can use an electron beam with a larger diameter than that of the higher frequency bands. It also makes it easier to design an electron gun with a larger cathode to extract a higher beam current. Therefore, we can design the beam voltage to be as low as 350 kV, which enables the PFN voltage to be as low as 43 kV. At this voltage level, it is easier to obtain suitable PFN-capacitors from the existing ranges of various manufacturers.

12.1.5 RF Pulse Compressor

We use a three-cell coupled-cavity pulse-compressor instead of a delay-line type pulse-compressor. The cavity is compact, having a length of 1 m, and its diameter is 160 mm. Therefore, it will be easier to fabricate at lower cost. A computer-simulation code was made to simulate the time response of the coupled-cavity system, which has shown a maximum efficiency of as high as 70 %. The details are reported in [5].

12.1.6 Accelerating Structure

We use a choke-mode cavity structure[6], in which all of the higher-order modes are heavily damped. Therefore, the multi-bunch wake-field and any associated instability will not harm the beam emittance. The only concern is the single-bunch emittance dilution due to the short-range wake-field, which is a strong function of the iris aperture. We use a relatively large iris-aperture: average $< 2a >= 16$ mm. As a result, the straightness tolerance for one structure becomes 30 μm or larger. This is a controllable level in conventional fabrication techniques of the disk-loaded structure. To eliminate any stress and make the structure straighter, a low-temperature brazing technique will be adopted[16].

To align the structure with a beam, we use an RF-BPM attached to the structure. This type of RF-BPM was tested using the FFTB beam line at SLAC in December, 1995[18]. It demonstrated a very high resolution of 44 nm for a single bunch. Three RF-BPM were assembled in one block, and the misalignment between them was measured with an electron beam. It was only 3 μm. This is a quite promising result for a structure-alignment procedure.

The dark-current problem due to field-emission under a high accelerating gradient has been studied using computer simulations[19], from which no serious contributions to the background in the detector at IP is expected at the C-band frequency.

12.1.7 Hardware R&D Program

In January, 1996, hardware R&D formally started at KEK as development of a backup technology for the main linacs of JLC. In 1997-1998, we will construct one unit of the rf-system. Since we use one

klystron, the input rf will be directly amplitude modulated to demonstrate the flat-top output from the compressor. The first klystron tube will be available in 1997.

12.2 C-band RF Pulse Compression

12.2.1 Introduction

Multi-bunch operation requires a flat-pulse output from the rf-compressor. For this purpose, the SLED-II was presented by A. Fiebig and C. Schieblich[7] in 1988, which was then developed at SLAC[8] as the X-band NLC component. The SLED-II stores the energy of the input rf into two delay lines, and compresses the pulse into a square-pulses by reversing the input rf phase. A unique idea, "DLDS" was proposed by H. Mizuno[9], in which a delay-time of the rf-power to propagate along a low-loss delay-line is utilized to cancel the traveling time of the electron beams to go down the beam-line. By overlapping two or four traveling-waves in hybrid combiners, we can multiply the rf-power by two or four times with sufficient efficiency. This is a candidate to solve the power-efficiency problem at the higher frequency bands.

One difficulty in using these schemes at lower frequencies arises from the physical length of the delay-line. The required rf-pulse length to fill the disk-loaded accelerating structure becomes longer at lower frequency bands. At the C-band (5.712 GHz) frequency, it becomes 500 nsec, including the beam pulse length, which requires a delay line 75 m long. This is very long, and such a system would be expensive, too.

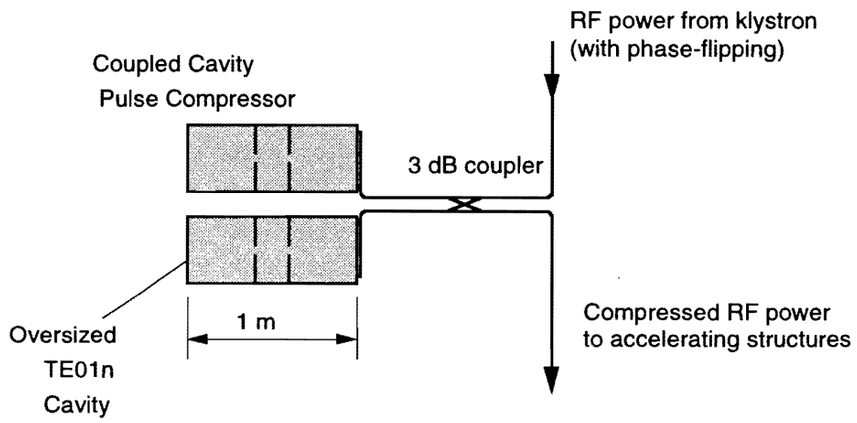

Figure 12.3: *Basic schematics of a three-cell coupled-cavity compressor, SLED-III.*

To solve this problem, a new method, which uses (1) a coupled-cavity comprising disk-loaded cells for

energy storage in the pulse-compressor and (2) an AM-modulation on the input rf-power to obtain a flat pulse, has been proposed. Figure 12.3 shows its schematic diagram. This scheme uses a 3-cell coupled cavity as an RF energy storage. After the filling time, when the input RF phase is flipped by 180 degrees, the compressed RF pulse is emitted into the output port. No reflection power goes back into the input port, because of the 3-dB hybrid coupler. This feature is similar to the case with original SLED. The difference lies in the use of coupling irises which limit the group velocity of the propagating wave inside the 3-cell cavity. Thus, the cavities act like a delay line. This allows to build the C-band pulse compression system in a very compact manner.

This section presents the design considerations and preliminary results from a cold-model testing of the RF pulse compression based on a 3-cell coupled cavity. We, hereafter, call this scheme SLED-III.

12.2.2 Coupled-Cavity Pulse Compressor

For SLED-III, we consider a coupled-cavity system with uniform impedance (each cavity has the same Q-factor, the resonance frequency and the cell-to-cell coupling constant). We consider the $\pi/2$-mode (the phase advance per cell is $\pi/2$). Since the $\pi/2$-mode stays in the middle of the passband, the rf phase does not deviate from zero during the transient time. To avoid field cancellation at the 1st cell, we can use only odd number for the total number of the cells, that is, $N = 1, 3, 5, 7, \ldots$

In the case of a uniform coupled-cavity pulse compressor, we can estimate the performance using SLED-II theory. We define a compression ratio as,

$$C_r = \frac{\text{Klystron pulse duration}}{\text{Compressed pulse duration}} = \frac{T_{in}}{T_{out}} \tag{12.2}$$

The compressed pulse duration is equal to the round-trip propagation time of rf-pulse in the coupled-cavity chain, which is given by

$$T_{out} = \frac{2(2N-1)}{k\omega}, \tag{12.3}$$

from which we can determine the coupling constant k. The one-way attenuation constant is given by

$$\tau = N/kQ. \tag{12.4}$$

The input voltage-reflection coefficient is

$$s = \frac{k - 2/Q_{L1}}{k + 2/Q_{L1}} \tag{12.5}$$

Where Q_{L1} is the loaded-Q of the 1st cavity. According to SLED-II theory[10], there is an optimum value of s to maximize the power gain (loss-less case),

$$s_{opt} \sim 1/[C_r - 1/2]^{-1/(C_r - 3/2)}. \tag{12.6}$$

Using Equations 12.5 and 12.6, we can determine Q_{L1}.

In order to study the pulse response of a coupled-cavity system, a computer simulation code has been written, which solves an equivalent-circuit model in the time-domain[11]. Figure 12.4 shows the

simulation result for a pulse-compressor using a 3-cell coupled-cavity, where the input rf-phase was flipped once in the same manner as in SLED-II. The expected pulse length compressor factor is 5. Thus, the effective power efficiency is 70 % (= 3.5 / 5).

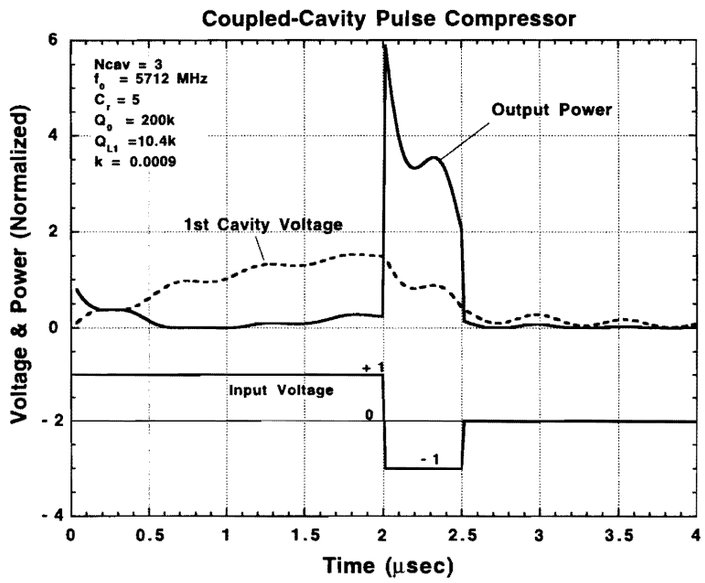

Figure 12.4: *Simulation result for a SLED-III RF pulse compressor with a simple phase-flip.*

The 1st cavity voltage shows a step-by-step build-up pattern. Each step corresponds to the round-trip rf propagation along the coupled-cavity chain. When the rf-phase flips, the compressor emits a sharp spike at the beginning, followed by a swing. This is a consequence the use of an energy-storage cavity with multiple cells. The existence of irises shortens the required length of the energy-storage cavity. However, it causes a frequency dispersion effect in the propagating wave, resulting in a large distortion in the output waveform. A solution to this issue is discussed in the next section.

12.2.3 Flat-Pulse Generation by PM-AM Modulation

The solution for controlling the output pulse shape of SLED-III at will is to introduce a means to modulate the amplitude of the input RF power. Figure 12.5 shows the pulse-compression system considered for a C-band version of the JLC main linac, including a solution.

Generally it is not a good idea to directly modulate the amplitude of the input rf power to the klystron, because the klystron has a non-linear input-output characteristic, and the power gain is quite sensitive to any change in the beam parameter. To stably operate a klystron, we usually use a saturation mode. In our system, we keep the input rf power at a constant level, but control the rf-phase and combine the rf-power from two klystrons by a 3-dB hybrid combiner. By rotating the phase into the opposite

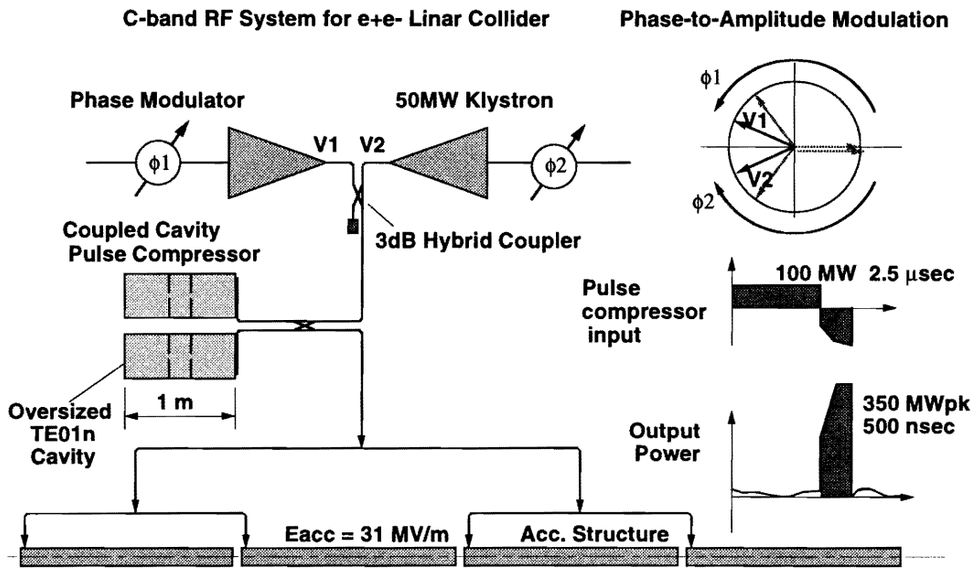

Figure 12.5: *Schematics of a SLED-III RF pulse compression system, considered for a C-band version of the main linacs of JLC.*

direction to each other, the phase modulation (PM) is converted to the amplitude modulation (AM). The vector sum goes to the pulse compressor, and the vector difference (quadrature component) goes to a dummy load attached to the hybrid.

Since the two vectors rotate in opposite directions, the vector sum always runs on the real axis, and no phase change is caused in the output sum vector. The amplitude of the two vectors is adjusted to be of the same value with the input RF power knob.

Figure 12.6 shows the simulated output waveform. A power gain of 3.5 and a nominal efficiency of 70 % are achieved. To obtain a high Q-factor of 200,000 at the C-band, we use a low-loss mode TE0,1,15 in a pill-box cavity having a diameter of 157 mm, a length of 400 mm. We use three pill-box cavities in series. Since the middle cavity stores less energy, we can reduce its length. The total length of the cavity is about 1 m. The details of the cavity are being designed.

Under multi-bunch beam operation, the accelerating gradient inside the structure decays exponentially due to a beam-loading effect. To compensate this, we slowly increase the power during the filling-time. When the wave front reaches the end of the structure, we start the beam pulse and keep the input power at the maximum level. In Figure 12.6, the input rf-power was controlled so as to follow a programmed waveform, which starts from 0.3 normalized power, and linearly increases up to a maximum power of 3.5 during a filling time of 280 nsec, then stays constant at the maximum.

Figure 12.7 shows the variation in the power gain as a function of the total number of cavities. In the case of a uniform coupled-cavity system, the power gain increases along with increasing the number

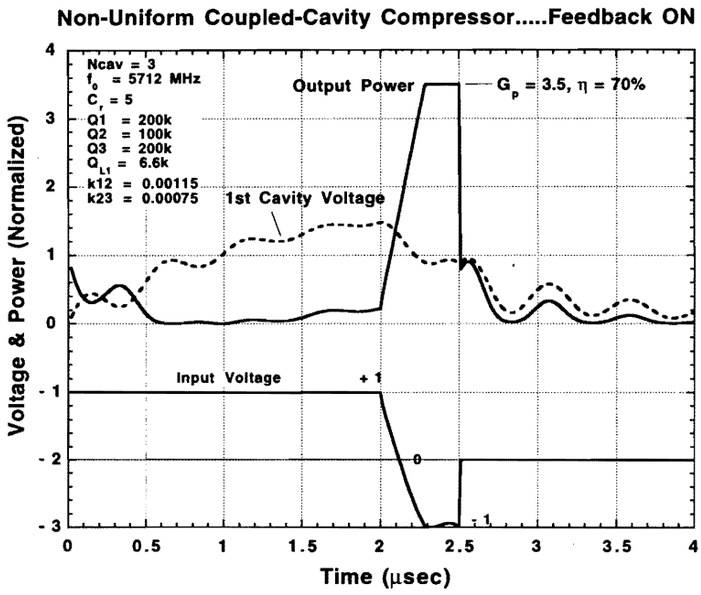

Figure 12.6: *Simulated output pulse shape from a SLED-III system with PM-AM modulation.*

of cavities, and slowly approaches a maximum value of 3.5, which is the optimum power gain of an ideal SLED II at $\tau = 0.02$. Therefore, there is no good reason to use a large number of cavities.

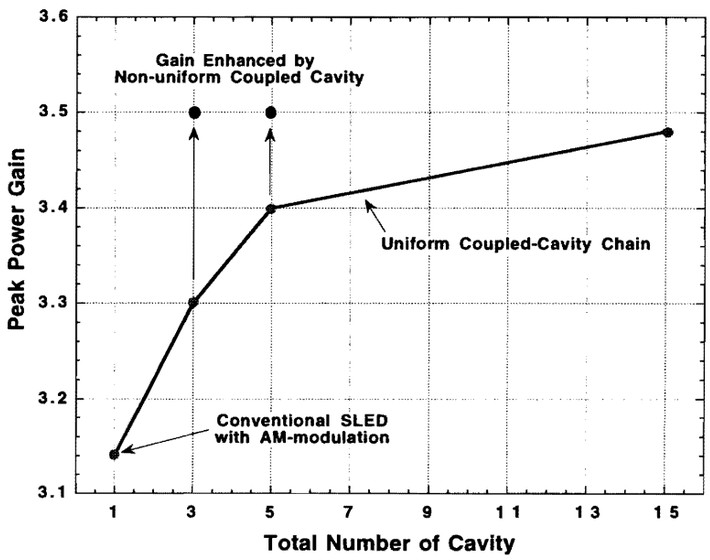

Figure 12.7: *RF power compression gain vs. the number of cells in the compressor cavity.*

The left-most point at cavity number 1 corresponds to the conventional SLED system. It is noticeable that by using the PM-AM modulation scheme, even a conventional SLED can generate a flat pulse with a sufficient power gain as high as 3.1. This feature will be useful for applying the scheme to existing linacs implemented with the SLED system.

The solid circles in the figure represent the non-uniform coupled-cavity case. Since the beam-loading compensation requires less power at the beginning of a pulse, it is better to store less energy in the first cell, and more energy in the 3rd cell. The middle cell acts as a transformer, which can be used to step-up or down the field intensity in the 1st and 3rd cells. The stored-energy ratio is proportional to the square of the coupling-constant ratio; in Figure 12.6 it is $U_3/U_1 = (k_{12}/k_{23}^2 = 2.4)$. As can be seen in Figure 12.7, using a non-uniform coupled-cavity system, three cells are sufficient to obtain a sufficient power gain of as high as 3.5.

12.2.4 Feedback Control for Beam-Loading Compensation

One problem of using the PM-AM modulation scheme in a practical rf-system is how to generate the modulation pattern. We can analytically solve the pulse response of the non-uniform coupled-cavity system for a simple input waveform case[12], which is very useful for optimizing the parameters. However, the actual waveform for energy compensation in the accelerating structure takes a complicated form. Additionally, the actual beam current is not a simple and perfect square waveform. As a result, the modulation pattern for the klystron input signal becomes quite a complicated form; it would thus be difficult to generate the modulation pattern from the theoretical equations.

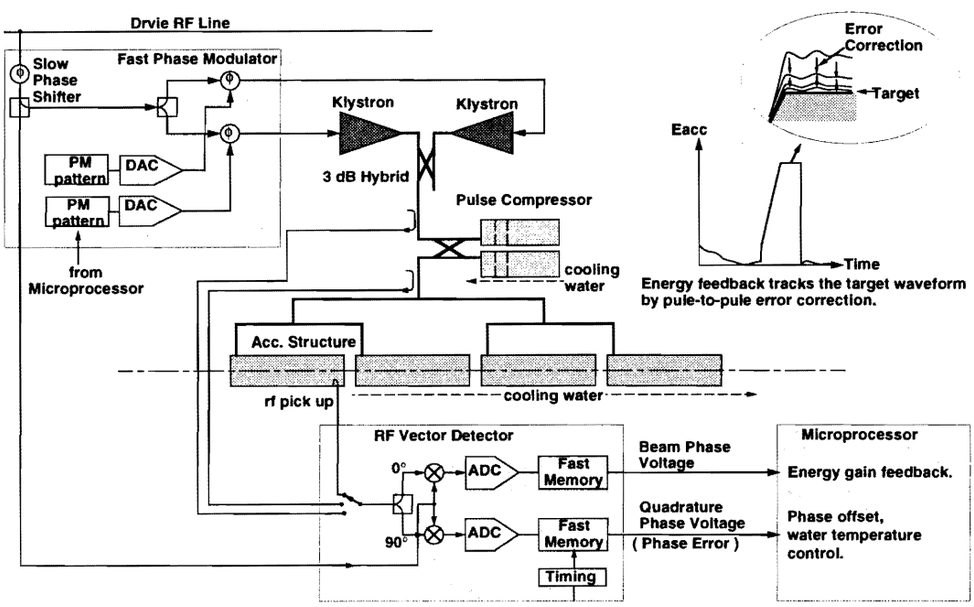

Figure 12.8: *Schematic diagram of the RF feedback system.*

To solve this problem, we use a practical method, which uses feedback-loops for:

1. A beam-to-rf phase adjustment,
2. An energy-gain adjustment, and
3. Water-temperature control.

The rf-vector-detector rectifies the rf signal using the phase reference from the rf drive line. The detected waveforms are sampled and digitized in the in-phase and quadrature-phase components. They are stored in fast memories in each pulse. The rf waveforms are also monitored at the klystron output and the pulse-compressor output. The microprocessor computes the error in the beam-phase voltage, and corrects the phase-modulation pattern in order to track the target waveform (target energy gain), which is directed from the main control computer. The quadrature-phase voltage gives the phase error, from which the phase-offset in the rf drive line is corrected and the cooling-water temperature is controlled.

Since the energy gain is always monitored and controlled by a microprocessor, a slow variation of the klystron output-power, or a fast, but repeatable, ripple on the klystron modulator output, will also be compensated. As shown in the schematic, since all feedback loops are closed in one unit of the rf-system, and isolated from the other units, beam operation becomes quite simple and easy. Every unit runs automatically to give a constant energy gain to the beam. In the case of a failure in one unit, the main computer directs other units located in the same sector to increase the energy gain. They follow the new target value within 10 pulses or less, that is, within 0.1 s.

12.2.5 Prototype Studies of SLED-III

Design of the Cold Model Energy-Storage Cavity

Figure 12.9 shows the cold-model of the RF compressor. One delay line is sufficient for studies of RF pulse compression by detecting the reflection wave using a directional coupler. The input power is fed through a rectangular waveguide, converted into circular TE01-mode in the newly developed mode converter. The RF power is, then, injected into the 3-cell energy storage cavity. The total cavity length is about 1 m.

The design and achieved parameters of the system are given in Table 12.2.

In order to obtain a high Q-value in the low-loss mode, a copper pipe with a large diameter needs to be used. We have chosen the pipe diameter to be 152.60 mm. This corresponds to $k_a = 9.12$. Since the operating frequency is much higher than the lower cutoff frequency, which is 1.1 GHz for TE11, a large number of unwanted modes come to exist, as shown in Figure 12.10. We use TE01n mode for the energy storage. To avoid mode-mixing, all of the structures in the energy-storage cavity was made cylindrically symmetric. This prevents any mode-coupling to the modes other than TE0n.

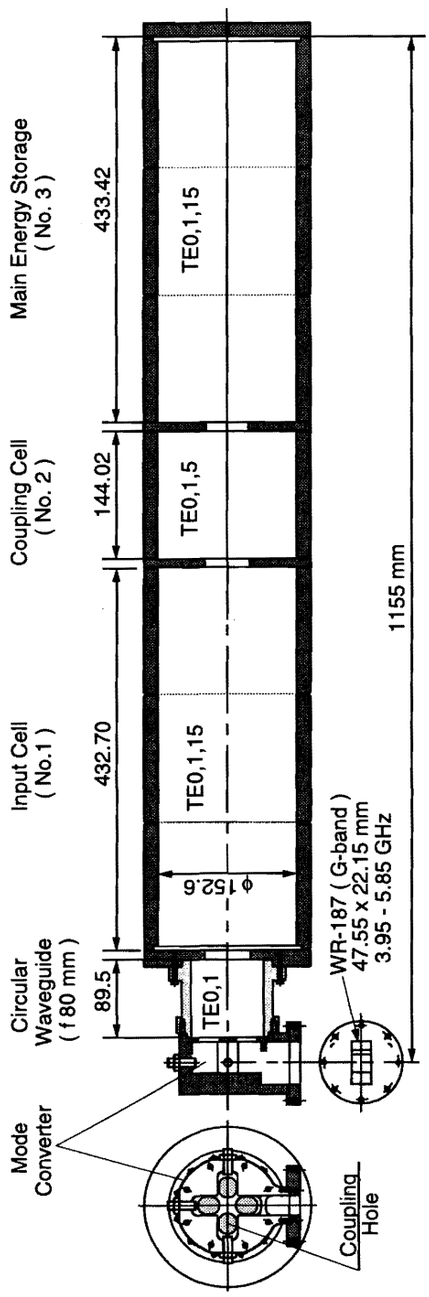

Figure 12.9: *Schematic figure of the cold-model of a energy-storage cavity and a mode converter.*

	1st cell	2nd cell	3rd cell
Diameter (mm)	152.60	152.60	152.60
Length (mm)	432.57	144.06	433.30
Mode	TE0,1,15	TE0,1,5,	TE0,1,15
Q (measured)	181,000	82,000	187,000

	1-2 cell	2-3 cell
Iris diameter (mm)	43.6	42.4
k (designed)	1.00	0.65
k (measured)	0.95	0.66

Table 12.2: *Parameters of the energy-storage cavities. The symbol k stands for the coupling constant between two neighboring cavities.*

Additionally, in order to avoid direct excitation of those modes from the external circuit, a mode converter is employed.

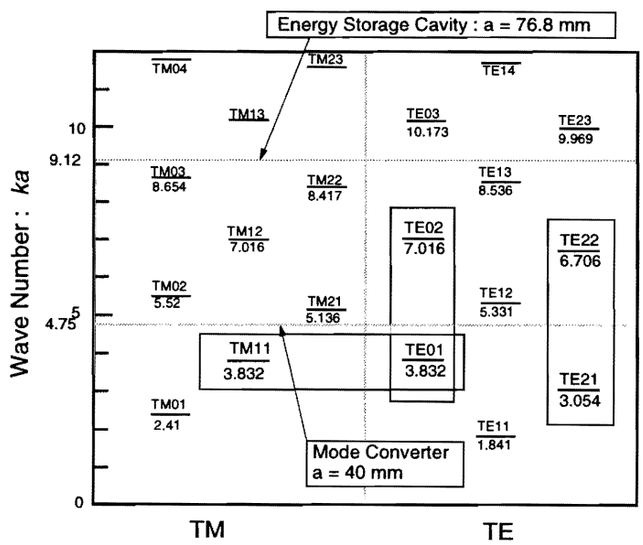

Figure 12.10: *Mode diagram of the 3-cell energy-storage cavity system.*

From a simulation with the measured coupling constants, the highest attainable power gain is 3.45.

Tuning of the Cavity

The $\pi/2$-mode pattern and its resonance frequency are exactly identical to the modes to be excited when those cavity cells are independently considered. Practically, cell-modes can be created by replacing the neighboring cells with detuned cavities. Since the dimensions of the detuned cavity are chosen not to resonate at the target frequency in any mode, no power can leak into the detuned cavity; all the fields are trapped within the test cell.

The cell-modes were measured by using detuned cavities. Based on the measurements, the lengths of the cells were carefully tuned by machining, so as to match the target frequency. All three cells were tuned to a high accuracy, with the maximum error being 100 KHz on the 2nd coupling cell.

Mode Converter

In order to limit the number of propagation modes inside the circular waveguide a relatively small diameter, 80 mm, was chosen for the mode converter. The four coupling irises generate rotationally-symmetric electric field. If the symmetry is exact, only TE01 mode would be excited. Residual imbalance, however, can generate a small amount of TE21 mode. Computer simulation using HFSS predicted the excitation power of unwanted mode is less than 1 %.

The RF performance of the mode converter was measured from the rectangular waveguide port, while attaching a matched load in the circular waveguide. The measured VSWR was 1.05 with a bandwidth of 5 MHz.

12.2.6 Results from the Cold-Model Test of SLED-III

The input pulse for this cold model measurement was generated by AM modulation with a double-balanced mixer. The modulation signal was provided by HP8175A Digital Signal Generator. The input signal was fed to the cavity, then the reflected signal was detected.

Fine trimming of the modulation pattern was performed to maximize the power gain and to make the top portion of the output pulse as flat as possible. The resultant output signal is shown in Figure 12.11. In the trace (A) of Figure 12.11 the entire output pulse shape is shown. The horizontal axis gives the time in the 500 ns/div scale. The trace (B) shows a magnified view of the flat-top of the output pulse. The horizontal axis gives the time in the 100 ns/div scale. At the flat-top, the output power is constant within 1 %. The measured power gain G_p is 3.25, which is 98 % of the expected value, 3.45. Further analysis on the power gain measurement is under way.

12.2.7 Discussion

The required tuning accuracy of SLED-III cavity cells was estimated by the coupled cavity analysis[13]. Thanks to the high stability of the $\pi/2$ mode, errors in the cell resonance frequency do not cause large

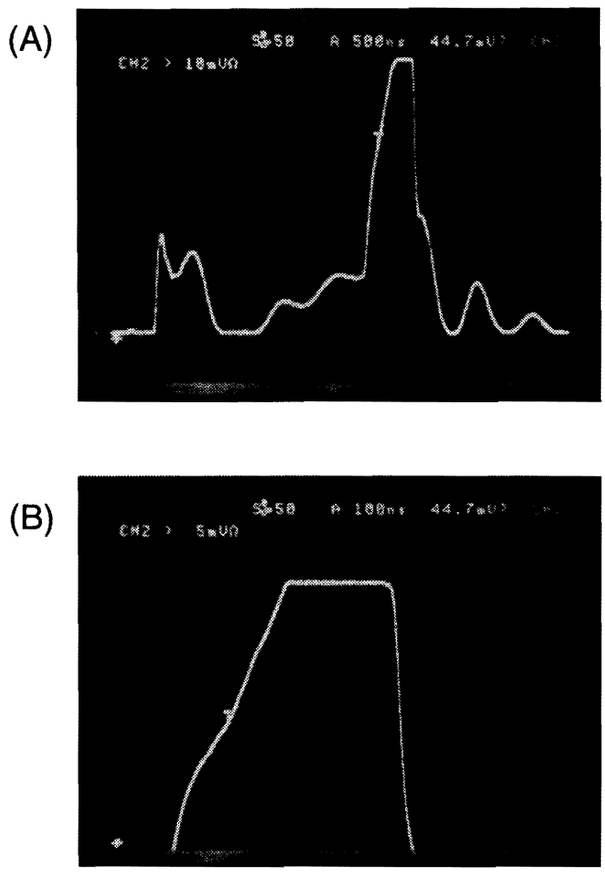

Figure 12.11: *Output pulse from the SLED-III cold-model testing. (A) shows the entire output pulse. (B) shows a zoom-in view of the flat-top.*

phase or voltage errors in the stored field. Therefore, tuning accuracy of the cell-to-cell frequency is not tight. For example, a 300 KHz frequency error (relative frequency error of 10^{-4}, which corresponds to dimensional error of 50 μm of cavity length, or 15 μm of cavity diameter) on the 3rd cavity causes only a 1 % amplitude error and a 0.06-degree phase error in the 3rd cavity voltage. The leakage power into the 2nd coupling cell is sensitive to the 3rd cavity error. However, deterioration in the total Q-factor due to this leakage is only 0.67 %. Dimensional accuracy in a practical machining of a cylindrical cavity on a turning lathe is much better than the error assumed above.

We need to study the error effect due to the brazing process. According to some experience in fabrication of the disk-loaded structure, the resonance frequency shift due to brazing is below 200 KHz at S-band (2856 MHz). Therefore, the brazing should not cause a difficulty.

After the brazing, we will measure the $\pi/2$-resonance using the detuned cavity mounted on the end plate of the 3rd cavity to bring its frequency to the right operation frequency of 5712 MHz. The $\pi/2$-mode resonance frequency is simply given by

$$\omega_{\pi/2} = \frac{U_1\omega_1 + U_3\omega_3}{U_1 + U_3}, \tag{12.7}$$

where U_n is the stored energy in the n-th cavity. Since a large energy is stored in the 3rd cavity, we can adjust the $\pi/2$-mode resonance by tuning the 3rd cavity frequency. To obtain phase stability of 3 degrees in the compressed RF pulse, the required frequency accuracy is 8 kHz. The temperature must be kept constant within 0.1 degrees C.

12.3 C-band Accelerating Structure

12.3.1 Introduction

Multi-bunch beam operation is essential for obtaining the high luminosity needed for physics experiments at JLC. It is also very important to accelerate a low-emittance beam in the main linac to achieve a nano-meter size beam at the collision point. However, this is not easy because of the wake-field power that accumulates in the structure.

Thus, R&D on HOM-free structures is one of the most important issues for the realization of a linear collider. There have been some ideas for HOM-free structures. However, some of the early concepts involved a rather complicated cell shape, leading to difficulty in the fabrication process of the accelerating structure. In 1992, T. Shintake proposed a simple HOM-free accelerating structure which combines a choke-mode cavity with rf absorbers.

A high-power model structure, 0.5 m-long, was built for the S-band (2856 MHz), and beam tested at KEK (July 1994) to confirm its performance[14]. The beam was accelerated with an energy gain of 26 MeV at an accelerating gradient of 52 MV/m. The main purpose of the first experiment was to confirm the high-power performance of this structure; it was very successful at that. However, at that time, HOM absorbers were not implemented.

The next step of the R&D program was started in 1996. Both an original and a modified C-band (5712 MHz) high-power choke-mode-type structure are now under development, as will be discussed in the following sections. The modified scheme of the structure is devised to avoid the need for providing a separate, outer vacuum chamber, and to introduce an in-line-type rf dummy load, which will be installed on few last cells of the structure.

SiC-ceramic is one of the best materials for a microwave absorber, and has been adopted for the high-power dummy load at the KEK-PF linac and the ATF injector linac[15]. SiC-ceramic will be used as the HOM absorber, and also for the in-line dummy load, which will be put in the last few cells to terminate the rf power.

This section describes the details of the choke structure and its fabrication problems.

12.3.2 Concept of the Choke-mode Cavity

One of the best solutions to damp the wake-field excited by an intense beam in an rf-structure is to allow the wake-field to exit out of the cavity [6]. In the choke-mode cavity this is done by making a cut in the cavity wall, which connects the cavity to a parallel plate radial line with a good rf absorber at the end of the line. The structure does not have a cutoff frequency from DC to high frequency.

Thus, the wake-field power at all frequencies propagates very smoothly out to the rf absorbers.

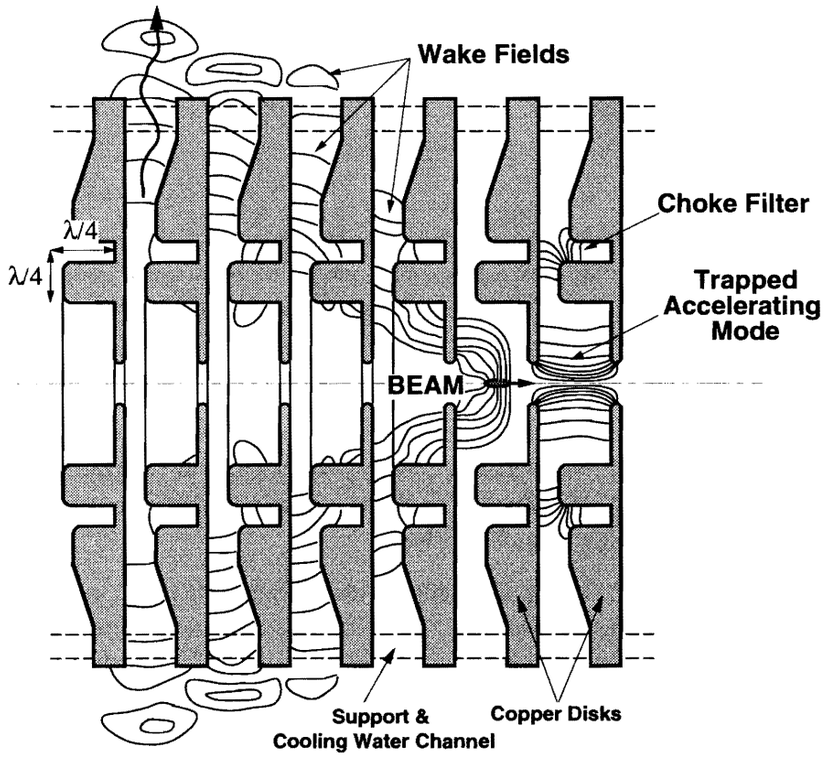

Figure 12.12: *Choke-mode-type accelerating structure*

However, if only this is done, the accelerating mode also propagates out and is dumped into the rf loads. Thus, it is necessary to cut off the accelerating mode; this can be done by inserting a choke filter between the accelerating cavity and the rf absorber. The choke filter has a very simple groove shape and surrounds the accelerating cavity, as shown in Figure 12.12. From the manufacturing point of view, the choke-mode-type cavity has a significant advantage over any slot-type HOM-free (or damped) structure.

12.3.3 Parameters of the Accelerating Structure

The structural parameters for JLC phase-1 (500 GeV at C.M.) are listed in Table 12.3. The sensitivity to alignment errors in a constant gradient structure is approximately proportional to $a^{-3.5}$, where a is the iris aperture radius. Thus, the iris diameter $2a$ is the most important parameter, which is determined to obtain a realistic alignment tolerance of 30 μm per cavity.

The structure was designed so as to obtain an unloaded electrical field gradient of 40 MV at 83 MW of rf input power. The required klystron peak power would be 50.3 MW at a 2.5 μsec pulse width and

Table 12.3: Main Parameters of the C-band accelerating structure.

Frequency	5712	MHz
Phase shift per cell	$3\pi/4$	
Field distribution	C. G.	
Number of cells	91	cell
Active length	180	cm
Iris aperture (2a) : up-stream	1.82	cm
: down-stream	1.31	cm
Cavity diameter : up-stream	4.47	cm
: down-stream	4.25	cm
Disk thickness: t	0.4	cm
Quality factor: Q	9950	
Group velocity : up-stream	0.035	c
: down-stream	0.012	c
Average shunt impedance: r_s	53.1	MΩ/m
Attenuation parameter	0.53	
Filling time: T_f	286	nsec

100 pps repetition rate, which should be available without major new R&D. The loaded electrical-field gradient will be 31.9 MV/m, with 1.11×10^{10} electrons per bunch and 72 multi-bunches. For the case under consideration, the active length is 14.7 km for the two linacs. The system is comprised of 4184 klystrons and their modulators, and 8368 accelerating structures. The wall-plug power requirement is 153 MW for the two linacs (Chapter 2).

12.3.4 Fabrication of the Choke-Mode Structure

An original choke-mode-type structure is shown in Figure 12.13. Each cell comprises an accelerating cavity with a choke, button-shaped HOM absorbers and cooling-water holes. From a manufacturing point of view, there is no special requirement for machining technique. Typical high-precision machines can deliver machine parts with less than 10 μm errors, which is sufficient for the C-band to work.

At this time, a limiting technology is the brazing process between the SiC-ceramic absorbers and the OFHC copper plates. In general, it is very difficult to join a SiC-ceramic to OFHC copper, because the thermal-expansion coefficients of the two materials are quite different: SiC-ceramic has $\sim 4.6 \times 10^{-6}$ and OFHC copper has $\sim 2 \times 10^{-5}$. Another problem is deformation arising during brazing at high temperatures. R&D work on these issues is in progress.

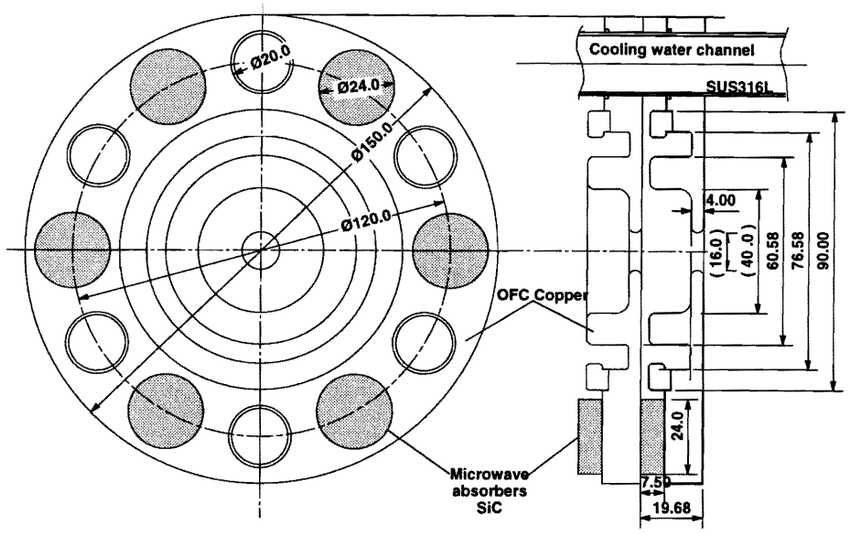

Figure 12.13: *Original version of the choke-mode structure.*

12.3.5 Modified Choke-Mode Cavity

The original choke-mode accelerating structure has open slots between the cells. Thus, the entire structure must be located inside a vacuum chamber. Also, an external rf-load must be attached for high-power operation. This tends to push up the cost of the system.

For reducing the cost, a modified choke-mode cavity is being considered in order to avoid an extra external vacuum chamber and to introduce an in-line rf dummy load, as shown in Figure 12.14. The structure is vacuum tight in itself, since it is closed by ring-shaped OFHC copper spacers. This is quite the same as conventional structures. There are two cell types. The first one is just a typical copper cell; the second type has two SiC-ceramic absorbers, one on each side of the cell. The two kinds of cells are stacked alternately with spacers, which are mounted between them. The SiC-ceramic absorber size will be $ID = 9.6$ cmϕ, $OD = 11.6$ cmϕ and $t = 1$ cm.

An external rf-load is not necessary, because the SiC-ceramic in the last few end cells can be used as an rf dummy load. The leak rf power from the accelerating cavity to the SiC-ceramic is controlled by de-tuning the choke cavity so as to equalize the loss along the axis.

Recently, the ring shaped SiC-ceramic of the size stated above was successfully joined to the C-band cavity by vacuum brazing with a special alloy at 710 deg C.

Thus, developing a low-temperature brazing method, such as is possible with Sn (Tin) alloys, which have a temperature range of 139 to 724 degC, was a priority issue. However, the now SiC-ceramic has now been successfully joined to OFHC copper by using a Sn+Au alloy low temperature brazing material.

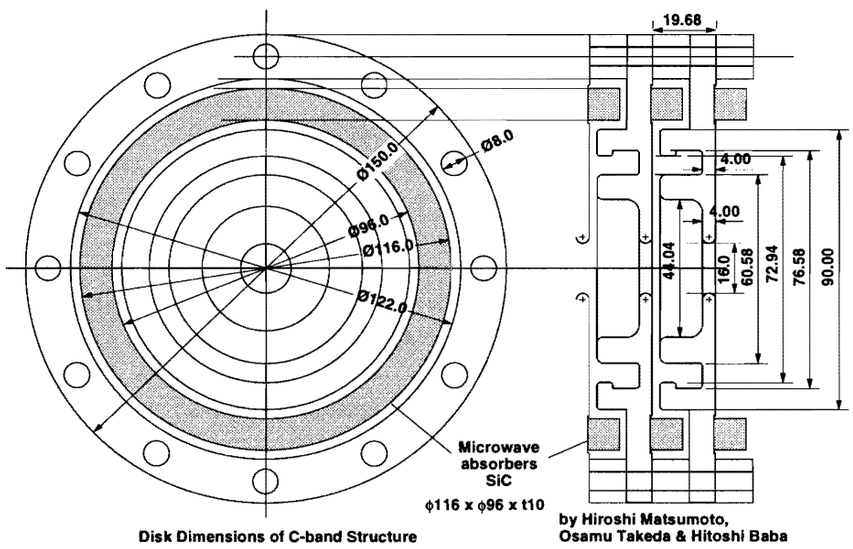

Figure 12.14: *Modified version of the choke-mode accelerating structure.*

12.4 C-band Main Linac Alignment Issues

12.4.1 Estimation of the Structure Alignment Tolerance

The alignment tolerances of the accelerating structures were estimated using tracking simulations and a numerical method[20], while taking into account short-range transverse wake-fields, which were assumed to be a linear function of the distance. Multi-bunch effects caused by long-range wake-fields were ignored, because we will chose choke-mode cavity structures in which higher order mode fields will be heavily damped by use of the choke-mode structure.

For short bunch beams, the alignment tolerance of the accelerating structures is proportional to the inverse of the slope of the short-range transverse wake-field, W', which was assumed to be constant (see Appendix). The short-range transverse wake-fields were calculated by Yokoya[21] for constant-impedance disc-loaded structures. The strength of the wake-fields depends on the aperture of the structures. Fixing the resonant frequency of the fundamental mode and the length of a cell, W' at a distance 400 μm, which is 2σ of the bunch length, is found to be approximately proportional to the aperture radius. Since our structures are designed to have a constant gradient with a different cell-to-cell aperture, we took the average of all cells to estimate the wake-fields. We used a(average)= 8.0mm or a/λ(average)= 0.152, where λ is the wave length of the fundamental mode, and obtained $W' = 1.0 \times 10^{19}$ V/C/m^3.

The injection energy and final beam energy were set to be 20 GeV and 250 GeV respectively.[1] The lattice was a FODO lattice with a beta function that varies approximately as the square root of the beam energy, in a manner similar to what is presented in Chapter 8 for the case of the X-band main linacs. Number of accelerating structures between the quadrupole magnets is an even number, and also varies approximately as the square root of the beam energy.

As discussed in [20], the tolerances depend on the length of the alignment unit. Assuming that the structures are perfectly straight in each unit, and that each unit is aligned with respect to the beam line with a random transverse offset, the alignment tolerance is proportional to the inverse of square root of the unit length if the length is small compared with the beta function. The reason for this is that the effects of the wake-fields can be averaged over a length comparable to the betatron wavelength. In the case that each 1.8 m long structure is an alignment unit, the estimated tolerance for the vertical displacement is 30 μm for 25% emittance growth.

[1] In the latest parameter set that is presented in Chapter 2, the injection energy to the C-band main linacs has been lowered to 10 GeV. Effects of this revision to consideration on the C-band alignment tolerance is considered to be a few percent.

12.4.2 Alignment of the Accelerating Structure

Since it will be necessary to align the accelerating structures with respect to the beam in rather tight tolerances, a cavity-type BPM will be attached at each end of the structures and the transverse positions will be adjusted by fine movers.

The accuracy of this kind of BPMs was tested in the FFTB facility at SLAC[18]. The test showed that the BPMs can be constructed and attached using usual machining and brazing techniques in accuracy of a few microns. This accuracy is small compared with the alignment tolerance of the structures assuming that each structure is constructed perfectly straight.

In practice, two or more structures will be set on an alignment girder which has fine movers. It is not necessary to adjust all BPMs on a girder to exact zero points because the effects of the wake-fields will depend only on the average of the misalignment. Thus, the number of structures required on a girder or the number of movers for one girder is not essentially important. The number of BPMs for a structure is important for measuring the average displacement of the structures (in length comparable to the beta function) on a girder.

12.4.3 Requirement for the Straightness

Assuming that both ends of each structure are placed precisely, the effects of wake-fields will be proportional to the average transverse displacement caused by the construction error of the structure. The tolerance of the cell-to-cell displacement will be much loser than the alignment tolerance of the whole structure, if the displacement of the cells is randomly distributed. In practice, the bow of each structure, which results from both the construction error and deformation after construction, will be most important. Assuming that the shape of a structure is sinusoidal, the transverse displacement at position z of a structure with length l is

$$\Delta y(z) = b\sin(\pi z/l), \tag{12.8}$$

and the average from 0 to l is

$$\overline{\Delta y} = \frac{2}{\pi}b = 0.64b, \tag{12.9}$$

where b is the peak of the deformation. This means that the tolerance for this kind of deformations is loser than that of the alignment of the whole structure by a factor of about 1/0.64 (i.e. 50 μm) for 25% emittance growth.

We expect that it is not difficult to satisfy this requirement. To make it easier, we will apply a low-temperature brazing technique[16] to assemble the structure. It will also be possible to make some mechanical correction while measuring the deformation after construction of the structure.

12.4.4 Quadrupole Magnets

The main source of emittance growth due to a misalignment of the quadrupole magnets is dispersion created from a non-straight orbit. The precise value of the tolerance depends on the energy spread, both the initial spread at injection and that created in the linac due to the position dependence of the accelerating field and longitudinal wake-fields.

In practical designs, the tolerance for the random displacement of magnets without any corrections (feedbacks) is about 50 nm. This gives requirements for the vibrations of magnets and ground motions faster than the feedback processes. The alignment tolerance of the quadrupole magnets with feedbacks, which means the tolerance for random displacements with respect to the beam, is a few microns.

Every quadrupole magnet will be set on an individual table having fine movers for the transverse alignment. Changing the strength of the quadrupole magnets, and measuring the beam positions by BPMs, the transverse displacement of the magnets with respect to the beam can be evaluated. The accuracy of the displacements will depend on the resolution of the BPMs, the measurement-to-measurement error. It will not depend on fixed errors, such as the alignment error of BPMs, which is usually much larger than the resolution. We expect that the resolution of BPMs and the accuracy of movers can be as small as 1 μm, which will give a better alignment than the requirements. After the initial alignment, to make the feedback faster, steering magnets will be used instead of movers. Only after large ground motions an alignment correction will be needed again[22].

It should be noticed that in general a stronger focusing lattice design (meaning a small beta function) gives a tighter tolerance for quadrupole magnets but a looser tolerance for accelerating structures. A weaker focusing has the opposite effect. There is a possibility to change the strength of focusing in order to ease the alignment requirement for either the quadrupole magnets or the accelerating structures if the requirement for the other can be tightened.

12.4.5 Summary

From our estimation, accelerating structures should be aligned with accuracy better than 30 μm and fabricated with straightness within 50 μm. Tolerance for the alignment of quadrupole magnets is a few microns. We expect that it is possible to satisfy those requirements using techniques which have been or being established.

Appendix

As discussed in references [20], [23] and [24], assuming that the beam oscillation is negligibly small compared to typical misalignment of the structures and that all of structures have the same shape of the wake-function, the expected increase in the emittance is proportional to the square of the "rms of wake-sum," defined as

$$S_{rms}^2 = \sum_m q_m S_{a,m}^2 / \sum_m q_m, \tag{12.10}$$

where m is index of particles, q_m the charge of the m'th particle and

$$S_{a,m} \equiv S_m - \sum_m q_m S_m / \sum_m q_m, \tag{12.11}$$

$$S_m \equiv \sum_k q_k W_1(z_m - z_k), \tag{12.12}$$

where z_m and z_k are the longitudinal positions of the m'th and k'th particles. The $W_1(z)$ wake-function and summations are taken for all particles in the beam. Introducing the longitudinal charge distribution $\rho(z)$,

$$S_{rms}^2 = \int_{-\infty}^{\infty} dz' \rho(z') S_a^2(z') / \int_{-\infty}^{\infty} dz' \rho(z'), \tag{12.13}$$

$$S_a(z) \equiv S(z) - \int_{-\infty}^{\infty} dz' \rho(z') S_a(z') / \int_{-\infty}^{\infty} dz', \tag{12.14}$$

$$S(z) \equiv \int_{-\infty}^{\infty} dz' \rho(z') W_1(z - z'). \tag{12.15}$$

In the case of a short single-bunch beam, since the wake-function is approximately linear,

$$W_1(z) = \begin{cases} zW' & (z > 0) \\ 0 & (z \leq 0), \end{cases} \tag{12.16}$$

$$S(z) = \int_{-\infty}^{z} dz' \rho(z')(z - z')W'. \tag{12.17}$$

For a Gaussian distribution with an r.m.s. of σ_z,

$$S_{rms}^2 \simeq \frac{0.91/}{\pi} \sigma_z^2 W'^2. \tag{12.18}$$

Since the expected increase in the emittance is also proportional to the square of the r.m.s., for any misalignment of the accelerating structures, the tolerance for some increase will be proportional to the bunch length σ_z and the slope of the wake-function W'.

References for Chapter 12

[1] JLC Group, "JLC-I", KEK Report 92 - 16, December 1992, A/H/M

[2] T. Shintake, et al., "C-Band Linac RF-System for e+e- Linear Collider", Proc. 1995 Particle Accelerator Conf. and Int. Conf. on High-energy Accelerators, May, 1995, Dallas, Texas, U.S.A., KEK Preprint 95-49

[3] K. Yokoya, et al., "C-band Linear Collider with C.M. Energy 500 GeV to 1 TeV", Proc. 5th European Particle Accelerator Conference (EPAC96), Sitges, Barcelona Spain, 10-14, June 1996, KEK Preprint 96-68, July 1996 A

[4] T. Shintake, et al., "C-band RF Main Linac System for e+e- Linear Colliders at 500 GeV to 1 TeV C.M. energy", Proc. 5th European Particle Accelerator Conference (EPAC96), Sitges, Barcelona Spain, 10-14, June 1996, KEK Preprint 96-69, July 1996 A

[5] T. Shintake and N. Akasaka, "A New RF Pulse-Compressor using Multi-Cell Coupled-Cavity System", Proc. 5th European Particle Accelerator Conference (EPAC96), Sitges, Barcelona Spain, 10-14, June 1996, KEK Preprint 96-71, July 1996 A

[6] H. Matsumoto, et al., "C-band Choke-Mode Accelerating Structure for the Linear Collider", Proc. 5th European Particle Accelerator Conference (EPAC96), Sitges, Barcelona Spain, 10-14, June 1996, KEK Preprint 96-70, July 1996 A T. Shintake, et al., "HOM Free Linear Accelerating Structure for e+e- Linear Collider at C-band", Proc. 1995 Particle Accelerator Conf. and Int. Conf. on High-energy Accelerators, May, 1995, Dallas, Texas, U.S.A., KEK Preprint 95-48 T. Shintake, "The Choke Mode Cavity", Jpn. J. Appl. Phys. Vol.31, pp.L1567-L1570, Part2, No.11A 1992

[7] A. Fiebig and C. Schlieblich, "A Radiofrequency Pulse Compressor for Square Output Pluses", presented at the European Particle Accelerator Conference, Rome, Italy, June 1988.

[8] P.B.Willson, Z.D.Farkas, and R.D.Ruth, "SLED II: A New Method of RF Pulse Compression", presented at the Linear Accelerator Conference, Albuquerque, New Mexico, September 1990, SLAC-PUB-5330.

[9] H. Mizuno and Y.Otake, "A New RF Power Distribution System for X-band Linac Equivalent to an RF Pulse Compression Scheme of Factor 2n", Proc. 17th Int. Linac Conference(LINAC94), Tsukuba Japan, August 21-26, 1994, KEK Preprint 94-112.

[10] P.B.Wilson et al., "Progress at SLAC on High-Power RF Pulse Compression", SLAC-PUB-5866.

[11] This is a similar code as that made by C.D.Nantista, "Radio-Frequency Pulse Compression for Linear Accelerators", SLAC-R-95-455.

[12] K. Akai et al., "Tuning Control and Transient Response of the ARES for KEKB", presented at EPAC, 1996.

[13] E. A. Knapp, B. C. Knapp and J. M. Potter, "Standing Wave High Energy Linear Accelerators," Review of Scientific Instruments, Vol. 39, No. 7, 1968, pp.979 - 991.

[14] "High Power Test of HOM-Free Choke-Mode Damped Accelerating Structure", by T. Shintake, H. Matsumoto and H. Hayano of KEK, published by Linear Accelerator Conference 1994, Tsukuba, Japan.

[15] "Development of the S-band High Power RF load", by H. Matsumoto of KEK, published by Accelerator Meeting in Japan, 1991

[16] H. Matsumoto, et al., "Low Temperature Brazing Technique for the Accelerators", Proc. 5th European Particle Accelerator Conference (EPAC96), Sitges, Barcelona Spain, 10-14, June 1996, KEK Preprint 96-67, July 1996 A

[17] K. Kubo, et al., "Alignment Issue for C-band Linear Collider", Proc. 5th European Particle Accelerator Conference (EPAC96), Sitges, Barcelona Spain, 10-14, June 1996, KEK Preprint 96-66, July 1996 A

[18] The experimental results on RF-BPM will be published soon.

[19] N. Akasaka, "Dark Current Simulation in High Gradient Accelerating Structure", Proc. 5th European Particle Accelerator Conference (EPAC96), Sitges, Barcelona Spain, 10-14, June 1996, KEK Preprint 96-65, July 1996 A

[20] K.Kubo, et. al., "Alignment tolerance of accelerating structures and corrections for future linear colliders", PAC96, SLAC-PUB-95-6884.

[21] K.Yokoya, Private communication.

[22] Shigeru Takeda, Private communication.

[23] Need to quote work by C. Adolphsen.

[24] Need to quote work by K. Bane.

Authors and Major Contributers of Chapter 12

- Tsumoru Shintake
- Hiroshi Matsumoto
- Nobumasa Akasaka
- Kiyoshi Kubo

CHAPTER 13

Beam Delivery System

Contents

13.1 Layout of Beam Delivery System

This chapter discusses the design of the beam delivery system that connects the exit of the main linacs and the interaction region, ending at the beam dumps. The beam delivery system consists of six (6) major sections:

- Collimation sections. Energy collimation is made in a dispersive area that is created by chicanes. Emittance collimation is achieved by using the nonlinear transverse collimation technique.
- A Beam switch yard which steers the beam into two separate final focus beam lines. This will allow the implementation of two interaction regions at JLC.
- "Big bend" sections with a total bending angle of about 8 mrad.
- Final Transformer with a chromaticity correction section that uses an asymmetric dispersion scheme.
- Interaction region that is associated with a finite beam-crossing angle of 8 mrad. It will optionally include crab cavities.
- Beam dump.

The design shown here does not present specifications for the beam switch yard and the beam dump. Between these sections some optical matching and beam-diagnostic regions may also be eventually introduced. However, their designs have not been fully developed, and they are not discussed in this study, either. A schematic layout of the final focus system is shown in Figure 13.1.

The layout of the beam delivery system was determined based on considerations of several important constraints:

- The crossing angle of two beams at the interaction point (IP) is set to be 8 mrad. This is so as to keep the luminosity reduction due to multi-bunch kicks near the IP at a manageable level. Also this magnitude of crossing angle is required to have the outgoing beams from the IP to safely pass through the pole-gap in the opposing final quadrupole magnet without hitting the pole pieces.
- The beam delivery system ought to be able to handle the conceived operational energies of JLC without requiring major reconstruction. Specifically, the length (1600 m/beam) and the bending angle (8 mrad) of the final transformer shall be common for energies of from 250 GeV up to 1.5 TeV C.M.
- It needs to allocate sufficient work-room in the two interaction region areas with minimum interference. For this reason, the transverse separation of two IPs should be larger than 20 m.

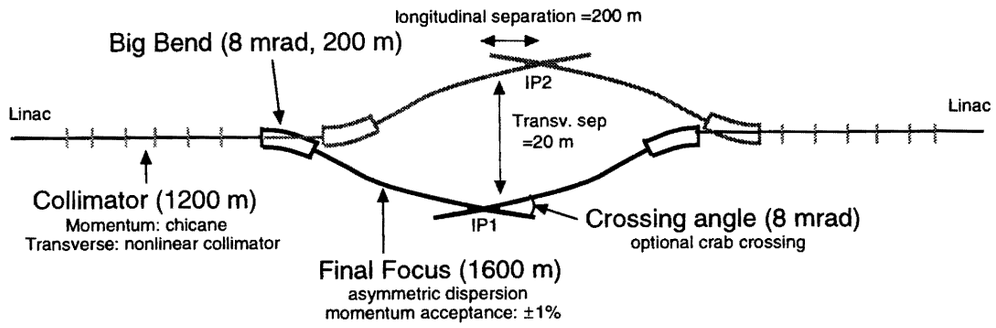

Figure 13.1: *Schematic layout of the beam delivery system. A common beam line will be used for collision energies of from 250 GeV up to 1.5 TeV C.M. An exception is the final quadrupole magnets, which need to be replaced as the beam energy is increased.*

- While the exact relative orientation of two main linacs may depend on the condition of the site, it appears natural to build the two linacs along a common straight line. Hence, this is assumed to be the case in this design study.

The JLC-I report presented a design of the beam delivery system for a 500 GeV C.M. collider. Its layout included eight big bend sections (i.e. two big bends / beam / IR. Hence, 8 big bends in total). At that time this layout was chosen mainly because of the short length of the transformer beam line (600 m), which was optimized for beam collisions at lower energies below 500 GeV.

For the present study the goal of the design was to have the entire final focus system capable of handling the whole future energy range of the collider up to 1.5 TeV, without major reconstruction. It has been found to be possible to arrive at such a design. In this new design, almost all magnetic components are commonly used with the strengths simply scaled with the beam energy, without requiring any physical relocation. The final doublets are the only exceptions. They are supposed to be replaced at least in three steps for beams energies of 250, 500, and 750 GeV. Also, in this latest design the number of big bend sections has been reduced to four (i.e. one big bend / beam / IR).

A large number of muons are generated at the collimation section when the tail particles hit the collimator material. If the IP is on the straight line extrapolated from the beam direction in the collimation section, it will result in a large flux of muon background tracks to traverse the detector facility. Therefore, a relative transverse offset needs to be introduced between the IP and linac axis. This requirement determines the minimum bending angle of the big bend, together with the bending angle of the final transformer.

In addition, it is preferable to have the two interaction regions (IRs) built with a longitudinal offset,

for instance, of about 200 m, in addition to the transverse offset. This will help reduce the interference in collision operation at one IR, while maintenance or construction work takes place in the other. A good spatial isolation of the two IRs is welcome in terms of reducing the vibration and environmental noise as well as ensuring radiation safety. Thus, in this design study a new optics design has been developed where the right and left switch yards are somewhat different and asymmetric in length, although the differences are small.

In summary, the optical system shown in this report serves to present an estimation of the maximum size of the beam delivery system for the next linear collider. This report leaves a large number of issues that have not yet studied or discussed. Major strategic decisions should be made concerning the maximum energy, common beam line system, and the crossing angle for the final design of the beam delivery system.

It should also be noted that the present design of the beam optics has not been fully optimized in detail. Many innovative ideas, such as Brinkmann's sextupole[3] or Taylor map analysis[2, 4, 5], have not yet been applied. The technical designs of each component are not given, except for the design of the final quadrupole magnets, which were presented in JLC-I. The details concerning the material, dimensions, mechanisms of the collimators are also left for near-future design work.

13.2 Collimator

The task of the collimator section is to clip the beam tails in five dimensions of phase space. The collimator section must collimate the beam so that it fits within the acceptance of the final transformer. The collimator section considered in this design study consists of two sections: a momentum collimation section with chicanes are placed first; then, nonlinear transverse collimators would follow.

13.2.1 Wake-field at the Collimators

We consider here the effects of the wake-field that is induced when the bunch particles go through the collimator jaws. If the beam has a transverse offset at a collimator, its tail is blown up by the transverse short-range wake-field. It magnifies the effective emittance of the beam. The magnitude of the blow-up has been given by K. Yokoya, as follows:

$$\Delta\varepsilon_y = (1+\epsilon)\Delta\varepsilon_{y0} \,, \tag{13.1}$$

$$\epsilon = \delta^2/2 \,, \tag{13.2}$$

$$\tag{13.3}$$

with

$$\delta = 0.3\frac{Nea_c^2cZ_0}{\pi m\gamma A_y}\left(\frac{L}{a^3}\sqrt{\frac{2\lambda}{\sigma_z}} + \frac{2\theta_{\rm opt}}{a\sigma_z}\right) \,, \tag{13.4}$$

where $\Delta\varepsilon_{y0}$ is the effective increase in the emittance due to the offset of the beam, γA_y is the invariant vertical acceptance of the collimator of an aperture radius a with length L.

The wake-field effect involves two terms:

- A term that represents the resistive wall wake, characterized by a conductivity parameter, $\lambda \equiv 1/\mu_0 c\sigma$, where σ is the conductivity.

- The second term, which represents the geometrical wake of the tapers around the collimator, is minimized at a slope angle $\theta_{\rm opt}$ of $(2\lambda\sigma_z/a^2)^{1/4}$.

Through the design of the collimator, we assume $\epsilon \leq 0.01$ for each collimator. Since this system has 6 collimators, the total emittance increase, due the entire collimation system, is 6%.

13.2.2 Momentum Collimator

Table 13.1 lists the parameters of the momentum collimator.

Beam energy	E	750	GeV
Particles/bunch	N	1	10^{10}
Bunch length	σ_z	80	μm
Momentum collimation width	Δ_p	± 2	%
Number of collimators	N_{cp}	2	
Radius of the collimator	a_p	200	μm
Collimator length	L_p	10	cm
Optimum taper angle	$\theta_{\rm opt}$	20	mrad
Transverse acceptance	$\gamma A_x \sim \gamma A_y$	1.5×10^{-4}	m
Horizontal dispersion at collimator	η_p	10	cm
Beta functions at collimator	$\beta_{xp} \sim \beta_{yp}$	400	m
Emittance blow up factor	$\epsilon_{px} \sim \epsilon_{py}$	0.01	

Table 13.1: *Parameters of the momentum collimator, for 750 GeV beam energy.*

Ideally, momentum collimation should be done so that it applies a suitable clipping at $\delta x + \eta\delta E/E$ and at $\delta x - \eta\delta E/E$. For this purpose, the collimation considered in this study is done in two steps, associated with the two chicanes, whose dispersion functions would have reversed signs. Although the betatron phases at two collimators are not identical in the current design, the difference is small enough so that it is acceptable to achieve effective momentum collimation.

13.2.3 Nonlinear Collimator

In transverse phase space, the requirement on how deeply the collimation should be done is determined by the hardware and optics configuration around the IP. The most stringent requirement comes from a consideration of the synchrotron radiation background to the detector. A large number of synchrotron photons are produced at the final quadrupole magnets. Its partial population that hits the pole of the quadrupole magnet at the opposite side of the IP is considered to be the most harmful; and thus must be controlled below a certain value, as discussed in Chapter 14. The invariant beam emittance envelope, that is allowed near the IP from these considerations, is estimated to be about

$$\gamma A_y \approx 7.2 \times 10^{-5} \tag{13.5}$$

for a beam energy of $E = 750$ GeV. Particles having a phase-space deviation larger than this value should be collimated away.

Naturally, the impacts of applying deep collimation needs to be quantitatively evaluated. Equation 13.4 indicates that the minimum wake-field would be obtained if the collimation aperture is given by the following equation:

$$a = a_{\rm opt} = \left(L(2\lambda\sigma_z)^{1/4}\right)^{2/3} . \tag{13.6}$$

Assuming that the surface material of the collimator is copper, if $L = 0.1$ m, we obtain $a_{\rm opt} = 0.95$ mm. The blow-up factor given by Equation 13.4 with this aperture meets the requirement of Equation 13.5, indeed. However, the β-function that is required to be compatible with this aperture $a_{\rm opt}$ and from the required acceptance of Equation 13.5 would be 16,000 m. While being not impossible, creating such a high-β section in a short length would result in huge chromaticity, which would require a chromaticity correction section that would inevitably introduce dispersions and sextupole magnets. Thus, a design of such a linear collimator would lead to a cascade of complications to the beam line design and a large number of optical elements to build it.

Another solution of a transverse collimator is to use nonlinear magnets (sextupole magnets) to selectively blow-up the tail part of the beam where it is collimated. Since a nonlinear magnet increases the phase-space amplitude ratio of the tail and the core, the effect of the wake-field to the core is relatively reduced. The nonlinear kick on the core can be compensated by another nonlinear magnet which is placed at an identical phase with respect to the first nonlinear magnet. In this design, two pairs of identical sextupole magnets and four collimators are introduced. The beam is collimated twice for each of (x, x', y, y'). Figure 13.2 illustrates the scheme of the nonlinear collimator.

The nonlinear collimation scheme allows a reduction of the aperture of the collimator, while keeping the effect of the wake-field on the beam core at a small level. Table 13.2 lists the parameters of a design for an $E = 750$ GeV beam. Figure 13.3 shows the lattice for the collimation section with a momentum collimator and a big bend.

The residual geometric aberration of the sextupole magnets, due to their finite thickness, is estimated to be less than 0.3% in amplitude. Here, we have assumed the beam parameters given in Table 13.1. The tolerance parameters of the sextupole magnets are listed in Table 13.2. Since these tolerance values are looser than what are required for the components in the final transformer, they are considered to

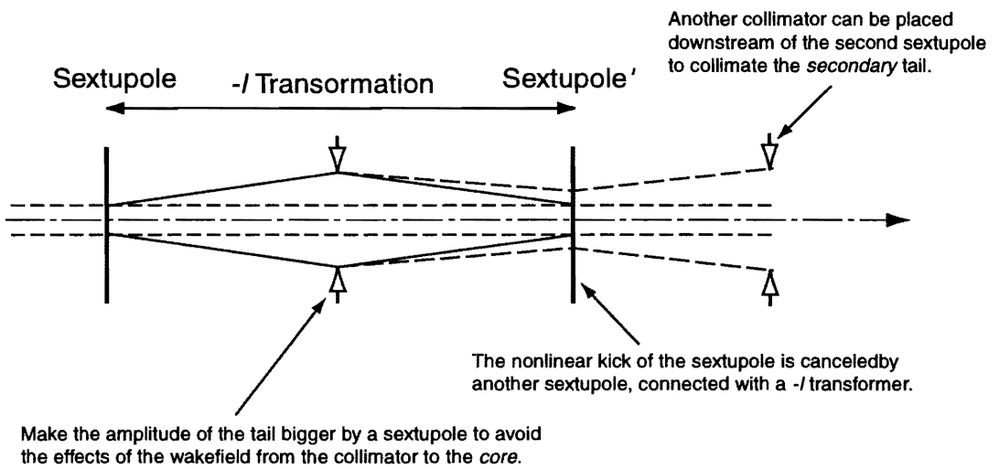

Circular collimator:

$$a^2 \geq \left(-\frac{k'}{2}(x^2 - y^2)R_{12}\right)^2 + (k'x\,yR_{34})^2$$

$$= \frac{k'^2R_{12}^2}{4}(x^2 + y^2)^2 + k'^2x^2y^2(R_{34}^2 - R_{12}^2)$$

$$= \frac{k'^2R_{12}^2}{4}(x^2 + y^2)^2 \qquad (\text{if } R_{12} = R_{34}),$$

then the collimation amplitude is given by

$$x^2 + y^2 \leq \frac{2a}{k'R_{12}}$$

Figure 13.2: *The nonlinear transverse collimator.*

be achievable with beam-based alignment techniques. The vertical phase advances from SG1.1 and SG1.3 to the IP are 12.7π and 11.2π, respectively.

sextupole	error	amount for $\Delta\sigma_y^*/\sigma_y^* = 2\%$	
SG1.{12}	$\Delta k'/k'$	36	%
	Δx	5.1	μm
	Δy	1.2	μm
SG1.{34}	$\Delta k'/k'$	37	%
	Δx	3.6	μm
	Δy	1.4	μm

Table 13.2: *Tolerance parameters of the sextupole magnets for the nonlinear collimator. Each number corresponds to an increase in the vertical spot size at the IP by 2%. The dependence is quadratic.*

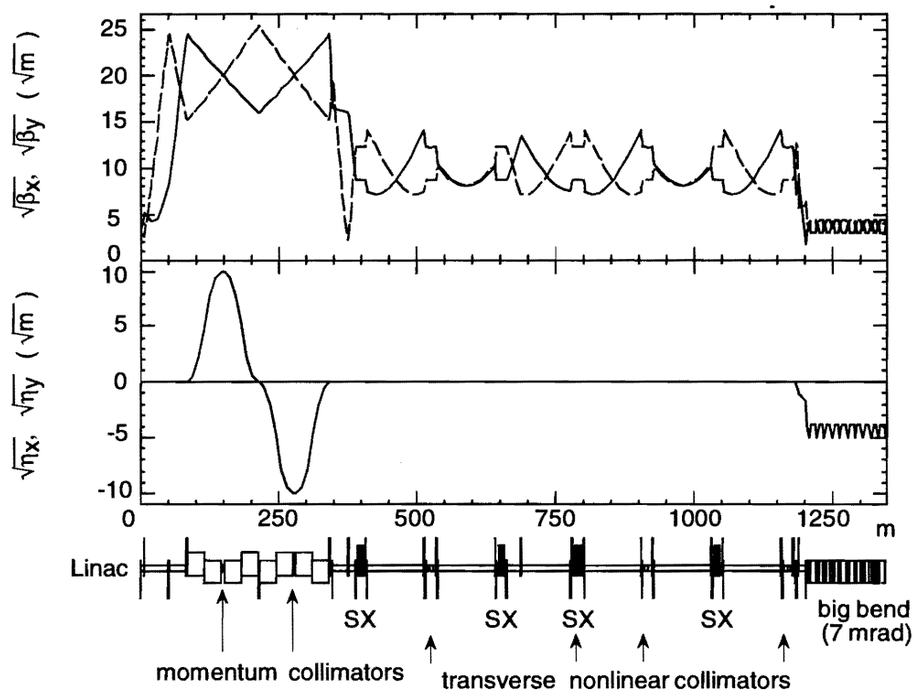

Figure 13.3: *Lattice of the collimator and the big bend. SX denotes the four identical sextupole magnets for the nonlinear transverse collimator.*

13.3 Big Bend

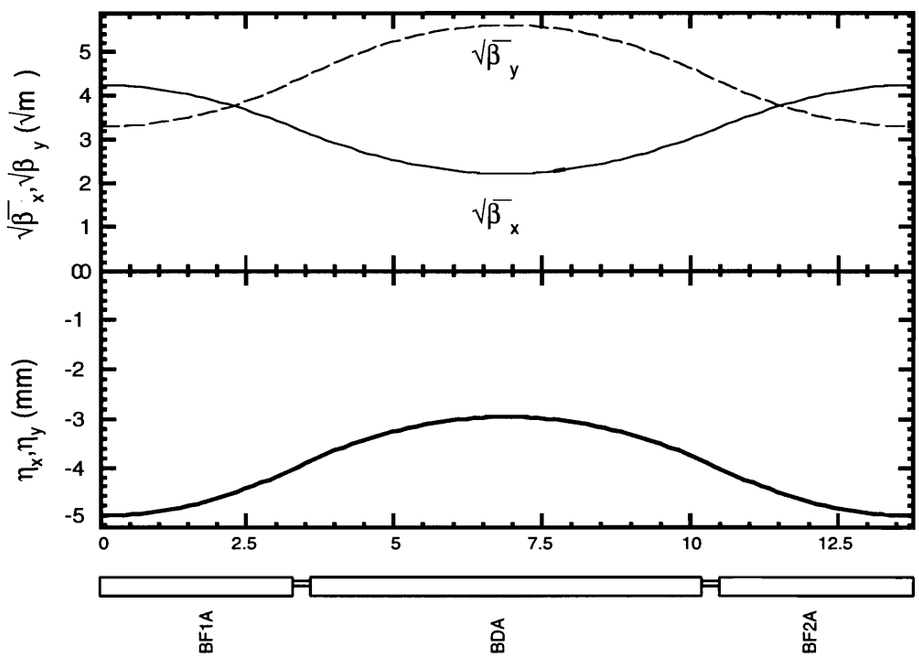

Figure 13.4: *Unit cell of the big bend, which consists of 12 cells.*

The big bend consists of 12 cells of the $B_F B_D$ structure, as shown in Figure 13.4. The parameters of the magnets are shown in Table 13.3.

		BF1A+BF1B	BDA	
Bending angle	θ_B	-0.31	-0.31	mrad
Orbit length	L_B	6.6	6.6	m
Focusing strength	$k = B'L_B/(B\rho)$	0.308	0.252	m^{-1}

Table 13.3: *Magnets for the big bend.*

The total bending angle of the big-bend section is 7.4 mrad. The phase advances per cell in the x- and y-planes are $\Delta\nu_x = \pi/2$, and $\Delta\nu_y = \pi/4$, respectively. The horizontal emittance growth due to synchrotron radiation is 6% for a 750 GeV beam energy.

13.4 Final Transformer

13.4.1 Parameters

Important machine parameters for designing the final transformer are listed in Table 13.4.

Beam Energy	E	250	500	750	GeV
Incoming emittances	$\gamma\varepsilon_x/\gamma\varepsilon_y$		4/0.09		μm
Momentum acceptance	$\Delta p/p$		$\pm$1.0		%
β-functions at IP	β_x^*/β_y^*	1/0.1	1/0.1	1/0.18	mm
Spot sizes at IP	σ_x^*/σ_y^*	300/4.7	240/3.7	250/4.1	nm
Emittances at IP	$\gamma\varepsilon_{x,\mathrm{IP}}/\gamma\varepsilon_{y,\mathrm{IP}}$	4.2/0.099	4.5/0.11	6/0.11	μm
Total bending angle/beam	θ_{FF}		3.5		mrad
Maximum bending field	$B_{\max}$	90	180	270	G
Length of free area at IP	ℓ^*		2		m
Pole-tip field	B_0		1.3		T
Lengths of final doublet (FD)	$L_{\mathrm{QC1}}/L_{\mathrm{QC2}}$	2.2/4	3.1/4.7	4/5.4	m
Aperture radius of FD	$a_{\mathrm{QC1}}/a_{\mathrm{QC2}}$	5.8/19	4.7/12.6	4.8/10.3	mm
Crossing angle	θ_x		$\pm$3.5		mrad
Length/beam	L		1600		m

Table 13.4: *Parameters of the final transformer.*

13.4.2 Design strategy

The final transformer consists of (1) two chromaticity-correction sections (CCSs) for x- and y- planes, (2) the final "telescope", and (3) matching sections between them. Each CCS comprises two identical sextupole magnets that are connected by a pseudo $-I$ transformer (*i.e.*, a π-section with identical magnification). The basic idea of this optical system is equivalent to that of the optics of FFTB.

One significant deviation from FFTB is the dispersions at the sextupole magnets. At FFTB, the dispersions of two sextupole of each family are designed to have equal magnitudes. The design presented here has a large dispersion at the second sextupole magnet, which is closer to the IP. However, at the other sextupole magnet the dispersion is nearly zero. The merit of this asymmetric dispersion is to concentrate the chromatic effect of the sextupole to the second one, and to reduce the inherent chromo-geometric aberration of the pseudo $-I$ transformer. The residual second-order dispersion arising from the asymmetry of the dispersion is canceled by another family of sextupole magnets.

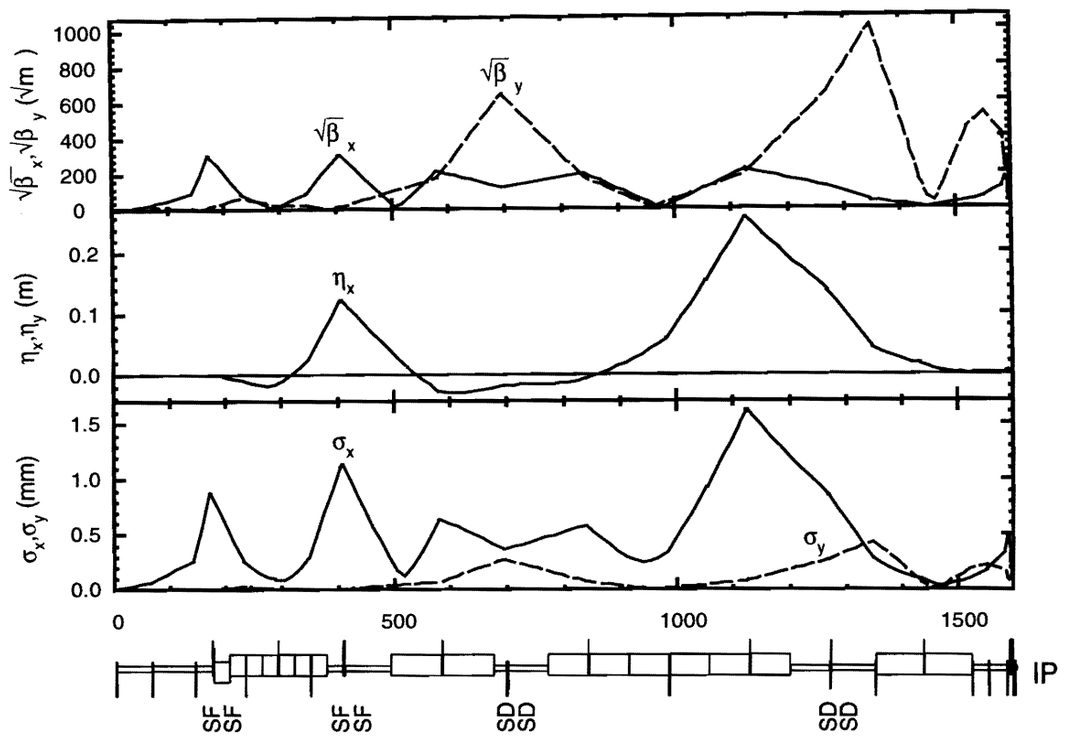

Figure 13.5: *Optical functions and linear beam sizes of the final transformer, with the parameters given in Table 13.4 and a beam energy E=750 GeV.*

This basic design scheme of the CCS has already been presented in the JLC-I report. It has been shown that there is no demerit in tolerances or tunability of the asymmetric scheme compared to a symmetric scheme.

The design of the final transformer is common for the entire energy range of JLC, namely, from $E_{\rm cm}$ = 300 GeV up to 1.5 TeV. An exception is the final doublet, which will be replaced at least twice according to the energy upgrade, as shown in Table 13.4. The excitation of other magnets would be basically scaled with energy, or trimmed only by a limited amount for optical matching.

The idea of the common beam line imposes a set of strict constraints on the optimization of the beam line. For a high-energy end of the operation, increased synchrotron radiation flux limits the allowed strength of focusing. To circumvent this limitation, the bending angle in the final focus line needs to be generally decreased. This will lead to a larger amount of optical aberrations for the low-energy end of operation. The design optimization under these constraints tend to make the total length of the transformer generally longer to avoid difficulties at both extreme energies. The resulting aberrations and effects from synchrotron radiation are shown in Figure 13.6. The total length, 1600 m, is longer than the design with single-energy operation in mind. For instance, 1100 m will be sufficient for

a final transformer that is dedicated to E_{cm} = 1.5 TeV. The length of a transformer dedicated to E_{cm} = 500 GeV is 500 m. The merits and demerits of the common beam line should be further investigated in the future.

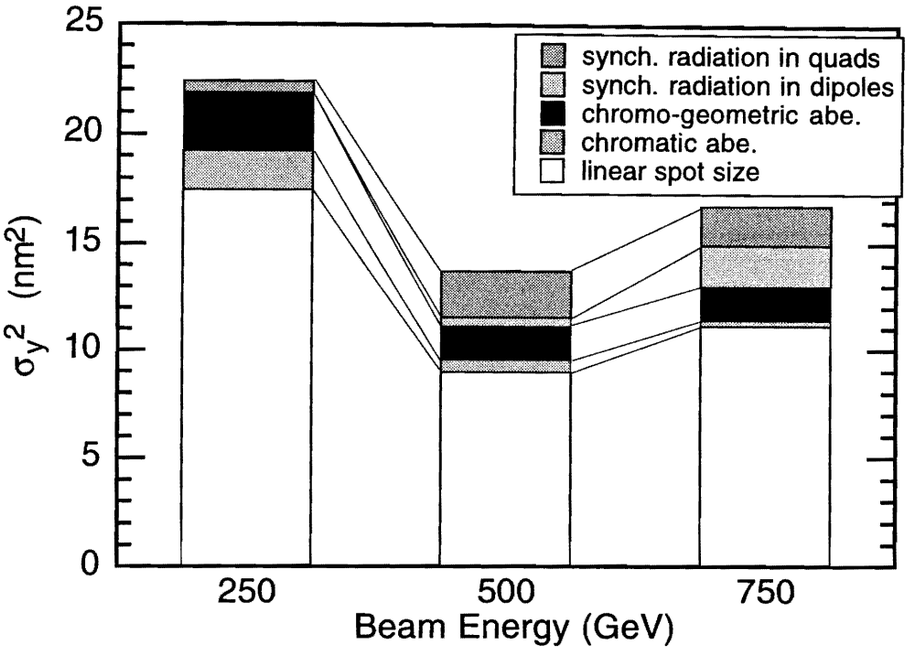

Figure 13.6: *Various kinds of aberrations in the vertical spot size (squared) at the IP for different beam energies. The optical aberrations dominate in the low-energy, while synchrotron radiation dominates at higher energies.*

Finally it should be pointed out that, generally, more optimization of the transformer should be possible with Brinkmann's multi-pole technique[3] or the Taylor-map approach[4, 5, 2]; however, they have not been applied to this design.

References for Chapter 13

[1] JLC-I, KEK Report 92-16, December, 1992.

[2] Zeroth-Order Design Report for the Next Linear Collider, LBNL-PUB-5424, also SLAC Report 474 or UCRL-ID-124161, May 1996.

[3] R. Brinkmann, DESY-M-90-14 (1990).

[4] J. Irwin, LC91 Proc. of Linear Colliders, 3rd International Workshop, Protvino, USSR.

[5] J. Irwin, SLAC-PUB-5315, published in Nucl. Instr. and Meth, **A298**, 460, (1980). (1989

Authors and Major Contributers of Chapter 13

- Noboru Yamamoto
- Toshiaki Tauchi
- Hisayoshi Nakayama
- Kaoru Yokoya
- Katsunobu Oide
- Yoshihito Namito

CHAPTER 14

Interaction Region and Detector Interface

Contents

14.1 Introduction

In this chapter, we examine aspects of experimentation that directly interacts with the accelerator design. Of particular concern in this area is the background to the physics experiments that are caused by the beams passing through the detector.

The characteristics of background events at JLC will be very different from those at typical e^+e^- colliders except the SLC. The features of the background strongly depend on numerous operational parameters of the accelerator, such as the beam aspect ratio (typically $\sigma_x^*/\sigma_y^* = 0(100)$), a high beam-intensity (10^{10}particles/bunch) and possible tails in the particle distribution that deviates from the Gaussian distribution. The population of low energy $e^{\pm}$ pairs that are created during collisions are directly related to the beam aspect ratio, while the tail is mostly responsible for synchrotron radiation and muon backgrounds. The optimization of machine operational parameters must be considered by taking this "interaction" between the experimentation and the machine into account. The highest-priority goal here is of course to maximize the luminosity while minimizing the background. With such motivation in mind, effects of $e^{\pm}$ pairs have been estimated by detailed Monte Carlo simulation with the proposed JLC-1 detector[1], in addition to simulation of masking of synchrotron radiation and attenuation of muon flux that are produced by interactions of the beams with upstream collimator materials.

Another important issue is the need for measurement of the distribution of the center-of-mass energy within each beam collision; hereafter called "luminosity spectrum." At TeV linear colliders, particles in the colliding beams loose a significant amount of energy before "collisions" take place. This is due to emission of synchrotron radiation in a strong electromagnetic field produced by the opposite beam, known as "beamstrahlung" phenomenon. Therefore, the effective luminosity at $\sqrt{s} = 2 \times E_{beam}$ is always smaller than the nominal value that does not take beamstrahlung into account. The luminosity spectrum as function of the center-of-mass energy depends on the magnitude of beamstrahlung. The knowledge on such issues is very important for conducting precision measurements, especially for studies of toponium physics[2] and detailed investigation of SUSY physics[3], which are the research opportunities unique to linear colliders. A method based on measurement of acollinearity angles in Bhabha scattering events is examined as a possible technique to measure the luminosity spectrum.

Detailed engineering design studies for the interaction region are not ready at this moment, and thus it will not be given in this chapter. No consideration on the support system of final focus quadrupole magnets and a heavy masking system are given. The designs of the extraction beam lines and measurements of electron polarizations are not discussed, either. These issues are left for subsequent design studies in the near future.

14.2 Background

To illustrate where the background particles can originate from, the beam line from the exit of the main linear accelerator (linac) to the interaction point (IP) is schematically shown in Figure 14.1. A +7 mrad bending magnet section (200 m long) downstream of the collimation section is needed in order to create a sufficient amount of separation for two experimental halls and to prevent the background from the upstream linac from directly hitting the detector. In the final focus system, beams are gradually deflected to have a horizontal beam crossing angle of ±4 mrad at the interaction point (IP).

There are two major sections for beam collimation (1200 m long) and a final focus system (1800m long) in the beam line to handle the beam energy up to 0.75 TeV. While their main purposes are to clip the beam tails, secondary particles are inevitably produced, namely, (1) muons and (2) synchrotron radiation photons, respectively. In addition at the IP, (3) e^+e^- pairs and (4) mini-jet are created through beam-beam interactions. They all cause background hits in the detector facility.

In subsequent sections the first three kinds of background are discussed together with a possible design of the interaction region.

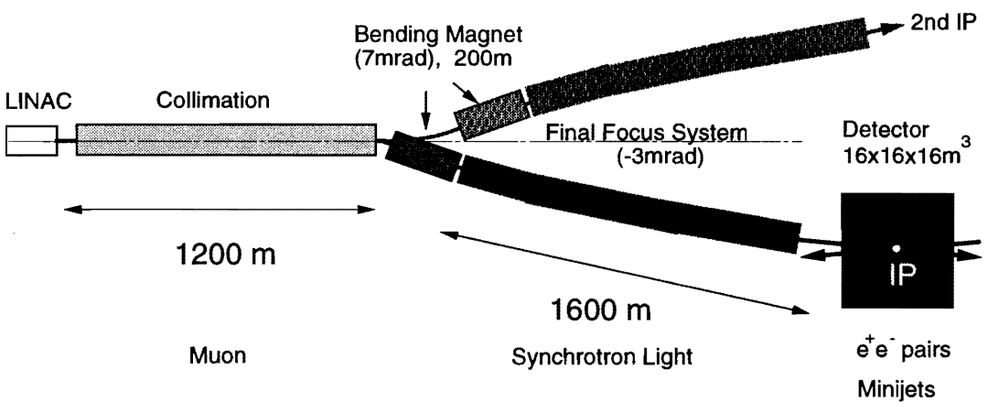

Figure 14.1: *Top view of the beam line from the exit of the main linac to the interaction point (IP) at* $E_{cm} = 0.5 - 1.5$ *TeV.*

14.2.1 Collimation and Muons

In this section we will discuss on production of muons through interaction of particles in the beam tails when they are collimated at upstream collimation sections.

Generally the transverse profile of the beam do not exactly follow a Gaussian distribution at linear

colliders. The beams can be accompanied by long tails according to experiences from experiments at SLC [4]. While the origin of these tails is not thoroughly understood at present, we shall conservatively assume that the beam has a flat tail beyond $\pm 3\sigma_{x(y)}$ both in the horizontal(x) and vertical(y) directions with a relative intensity of 1 %.

As it can be seen in the next section, the beam has to be collimated within $\pm 6\sigma_x$ and $\pm 40\sigma_y$ in order to keep the background due to synchrotron radiation at a manageable level. Since the typical size of the beam core is on the order of a few μm, collimating such beams is a seriously non-trivial task. A work-around is to expand only the tail part sufficiently by using a non-linear collimation technique as discussed in Chapter 13. This is part of the reason why a 1200 m-long collimator section is required for collimating a 0.75 TeV beam.

As stated in Chapter 2 and subsequent chapters, one RF pulse will accelerate a bunch train which contains up to 85 bunches separated by 1.4 nsec, at a repetition rate of 150Hz. Since each bunch consists of 6.45×10^9 electrons (or positrons) at the IP, about 10^8(1%tail)$\times 10^2$(bunches) electrons may hit collimators at 150 Hz. In the interactions of the beam tails with the collimators a large number of muons are produced through the Bethe-Heitler process, $e^{\pm}N \rightarrow e^{\pm}\mu^+\mu^-N$. Without suitable measures these muons would traverse through the tunnel and create a large amount energy deposit within the detector facility. They would cause serious background problems for conducting high-energy physics experiments.

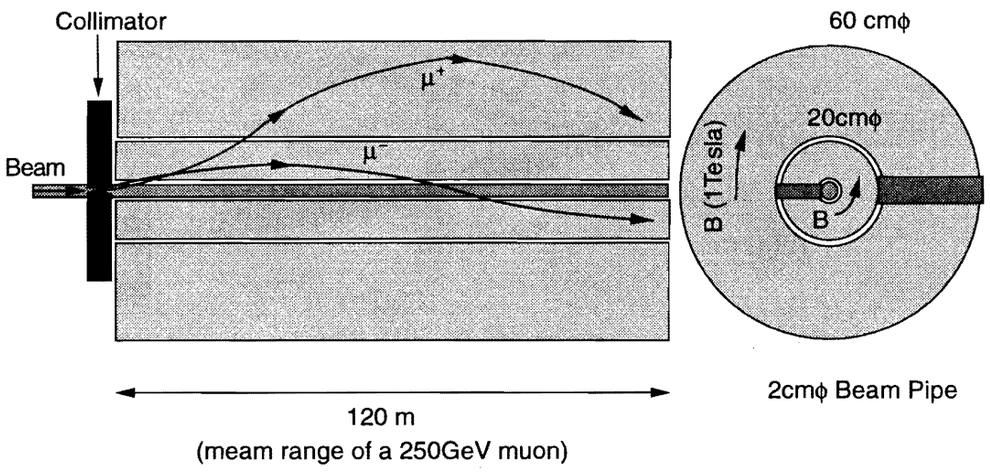

Figure 14.2: *Original idea of muon attenuator. Two iron pipes are magnetized axially in opposite directions for both charged muons which can be trapped, where the 120m length of the iron pipe corresponds to a mean range of 250GeV muons.*

Several techniques have been invented so far to reduce the muon background at linear colliders. The first of them is the "muon spoiler" idea that was implemented at SLC. There, a set of large iron toroid magnets are installed in the beam line to over-focus the muons, so that they are dispersed away from the detector.

In the design study here, another method which is called "muon attenuator" is considered. This idea was first proposed by by E.A.Kushnirenko [5]. The principle idea was to confine μ^+ and μ^- inside two iron pipes magnetized axially in opposite directions and to absorb the muons by the energy loss. The schematic diagram of this scheme is shown in Figure 14.2. We have performed a simulation study on the attenuation of muon flux onto the detector when this technique is applied. In the present JLC design there are six collimators in the collimation section between 1840 m and 2856 m as measured from the IP. Various effects of long iron pipe shield of the attenuator was investigated with and without magnetization. The best condition was found to be the case with no magnetization in the iron pipes.

The outer and inner radius of the iron pipe shield are 31 and 1 cm, respectively. The beam pipe is located inside the iron pipes. The beam line between 1721 m to 2856 m from the IP except for the collimators is assumed to be covered with the iron shield. Muons that penetrate through the collimation section are bent by the big bend (+7 mrad, see Figure 14.1) and go through the tunnel of 3.5 mϕ. In this study a second bending magnet(-3.28 mrad) is assumed to be located at 80 m from the IP. This is so to make the horizontal beam crossing, although the actual design has several bending magnets distributed in the final focus system. Sand stone is assumed to surround the tunnel. The cross section of the tunnel is shown in Figure 4.78 of Ref.[1].

Figure 14.3 shows the result of the simulation. The horizontal axis gives the locations of collimators as measured from the IP in meters. They correspond to the origins of muons. The vertical axis gives the number of electrons that are required to hit the collimators so that one muon produced out of these would to hit a detector of $16 \times 16 \times 16\text{m}^3$ volume size. The solid circle, solid triangle and open

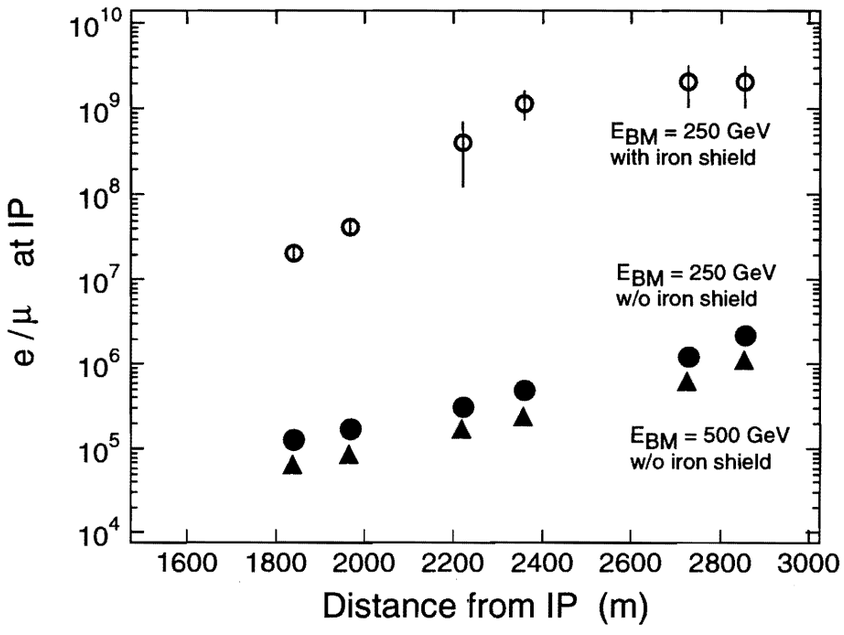

Figure 14.3: *Number of electron to produce one muon which reaches the IP.*

circle symbols correspond to cases of the beam energies of 250 GeV without the iron shield, 500 GeV without the shield and 250 GeV with the shield, respectively. The result of the simulation can be summarized below;

- The e/μ ratio is proportional to the inverse of beam energy.
- The long iron pipe shield reduces the muon background by 2 or 3 orders of magnitude.

The "first" two collimators that are the farthest from the IP are for momentum collimation, while the subsequent two sets would collimate elliptically the transverse beam profile ($6\sigma_x \times 40\sigma_y$) twice. A smearing effect, due to edge scattering off collimator jaws, has been calculated to be 10^{-4} beyond the edges of the ellipse by a single collimation. Consequently, from these results, we can estimate that at most 10 muons may traverse the detector at 150 Hz. Although this result looks to be acceptable for experiments, further reduction of factor of 10 should be pursued for an additional safety margin. This additional reduction will be realized if muon spoilers are implemented in the final focus system as studied in the NLC-ZDR[6].

14.2.2 Synchrotron Radiation

Since the intensity of synchrotron radiation is of the same order as the intensity of the beam itself, it would be very harmful to the experimentation if they are scattered at the pole tips of the nearest quadrupole magnet QC1. It is also very difficult to shield them near the IP. The amount of synchrotron radiation is determined by the maximum size and angular divergence of the beam profile. Both the maximum beam size (x, y) and the divergence (x', y') shall be well defined and controlled by the collimators.

The divergences can be expressed by $\sigma_{\theta_{x(y)}} = \sqrt{\epsilon_{x(y)}/\beta_{x(y)}}$, where $\beta_{x(y)}$ is a (optical) beta function in the final focus system and $\epsilon_{x(y)}$ is an emittance of beams. The beam size and the divergence are related by $\epsilon_{x(y)} = \sigma_{\theta_{x(y)}} \cdot \sigma_{x(y)}$. If we can not control them by some means, we must change the optics to enlarge $\beta_{x(y)}$ so that $\sigma_{\theta_{x(y)}}$ decreases. We may thus even have to sacrifice the luminosity because of $\sigma_{x(y)} = \sqrt{\epsilon_{x(y)} \cdot \beta_{x(y)}}$. A similar situation would likely occur at the beginning of operation with a larger emittance than the expected one, as happened in the SLC experiments.

Figure 14.4 shows the development of transverse beam envelops that correspond to $6\sigma_x \times 40\sigma_y$. Figure 14.4 covers the region from the IP up to the nearest dipole bend magnet. Here the smearing effect due to collimation is not taken into account, since it was estimated to be very small(10^{-8}) as mentioned earlier.

With a mask of 8 mmϕ radial aperture that is located at 30 m from the IP, synchrotron radiation from upstream magnets beyond the last bending magnet can be completely masked. Any synchrotron radiation that passes through the aperture of 8 mmϕ mask would pass through the final quadrupole magnet (QC1) without scattering. The half aperture of QC1 is chosen to be 6.85 mm. As can be clearly seen in Figure 14.4, the radiation from QC3 and QC2 provide the maximum divergence at the IP in the horizontal and vertical directions, respectively. The profiles of the radiation at the QC1 are

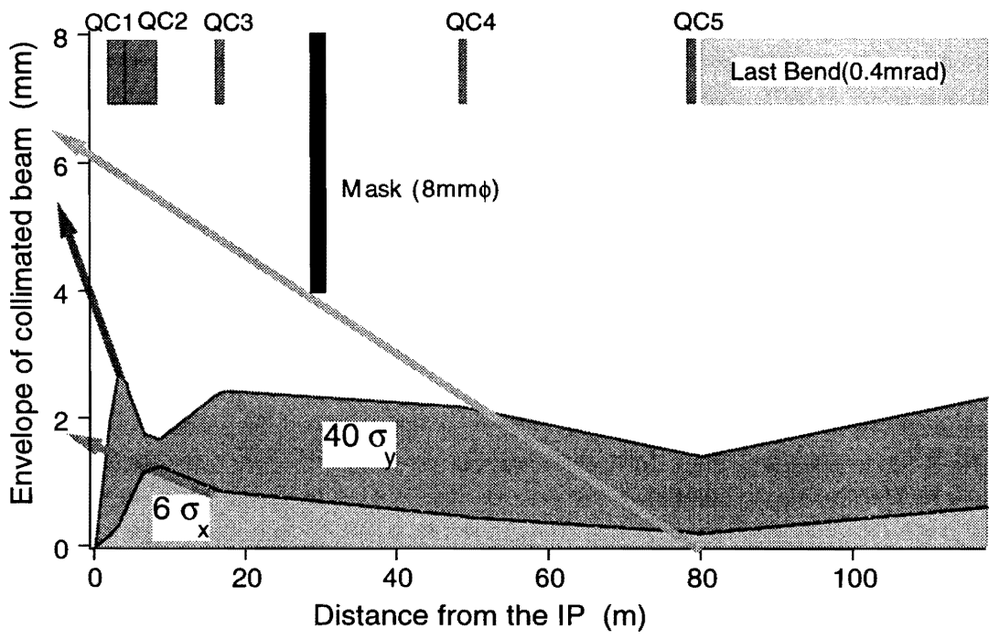

Figure 14.4: *Horizontal ($6\sigma_x$) and vertical ($40\sigma_y$) beam envelopes through the last bending magnet and five final focus quadrupole magnets(QC1,QC2,QC3,QC4 and QC5). The maximum divergences of the synchrotron radiation are also drawn by arrows.*

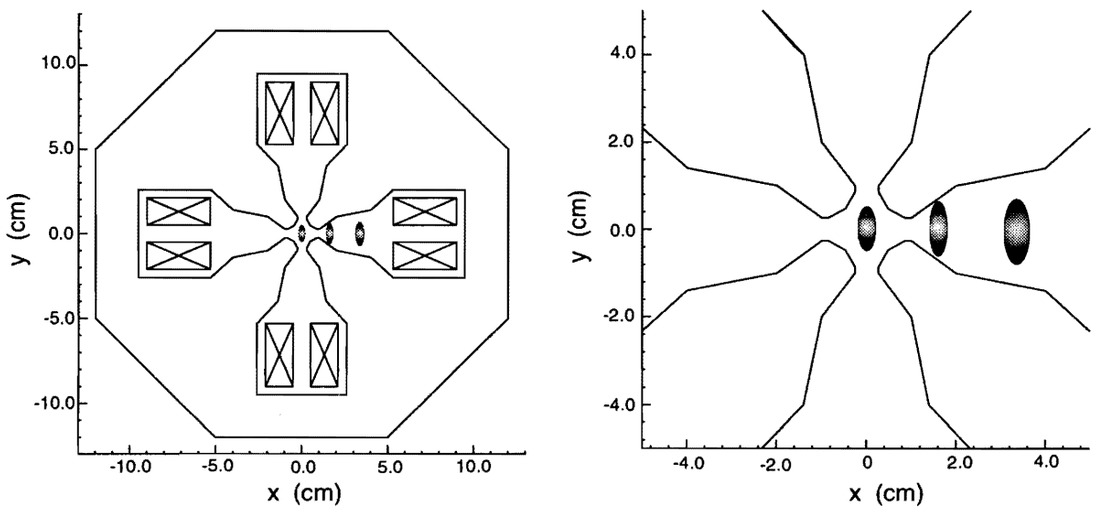

Figure 14.5: *Profiles of the synchrotron radiation at QC1;right figure shows the magnified view around the center of QC1. The profile at the center accompanies the in-coming beam. The two right-hand side ones are passing through QC1 of 2.2m long after a collision with a 8mrad horizontal crossing.*

shown in Figure 14.5. The length and inner aperture of QC1 are 2. 2m and 13.7 mmϕ, respectively. The front face of QC1 is located at 2.0 m from the IP. The in-coming radiation passes through the central axis of QC1. After making collision with the opposing beam at a horizontal crossing angle of 8 mrad, the out-going radiation passes off-axis through the QC1 magnet on the other side. The location of out-going radiation is depicted as two elliptic profiles at the right hand side in Figure 14.5.

As described above, it is expected that there should be no background problems due to the synchrotron radiation if we carefully optimize the collimation and the optics simultaneously.

14.2.3 e^+e^- pairs and Masking System

An enormous amount of e^+e^- pairs will be created during collisions, for instance a few times 10^5 pairs per a bunch crossing. While their vast majority are scattered into extremely forward angles, some can be greatly deflected by the strong magnetic field that is produced by the on-coming beam. In such cases they can enter the detector region and can create background noises to the detector facility. Figure 14.6 shows the angular distributions of pair-produced electrons and positrons after

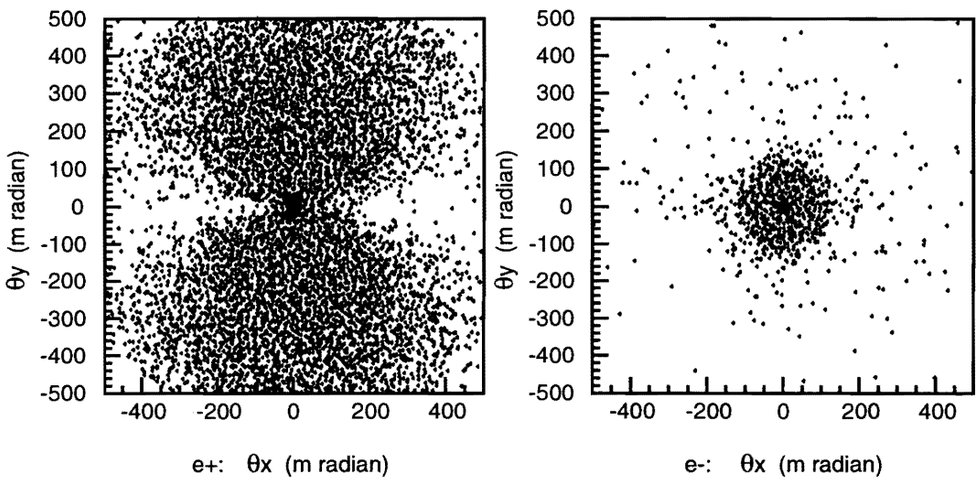

Figure 14.6: *Electrons and positrons scattered by beam-beam interaction at IP. The vertical and horizontal axes denote the scattering angles in vertical and horizontal directions, respectively. The left and right figures show distributions of the positrons and the electrons, respectively, downstream of the electron beam. Since the positrons have the same sign charge as the in-coming (positron) beam, they are scattered by larger angles than the electrons.*

the beam-beam interaction. The calculation was done by using ABEL[7]. Many particles (electrons or positrons) are scattered at large angles exceeding 200 mrad. We can also clearly see an asymmetry in their azimuthal distribution. More particles are deflected in the vertical direction than in the horizontal because of a very flat transverse beam profile ($\sigma_x^*/\sigma_y^* = 260\text{nm}/3.0\text{nm}$). Since the energies of the particles are relatively small, and are at a few hundreds MeV, most of these particles are confined

near the beam axis due to the detector solenoid magnetic field of 2 T. However, when they hit QC1 in the out-going side, many of secondary photons are back-scattered uniformly into the detector region. They can become serious background.

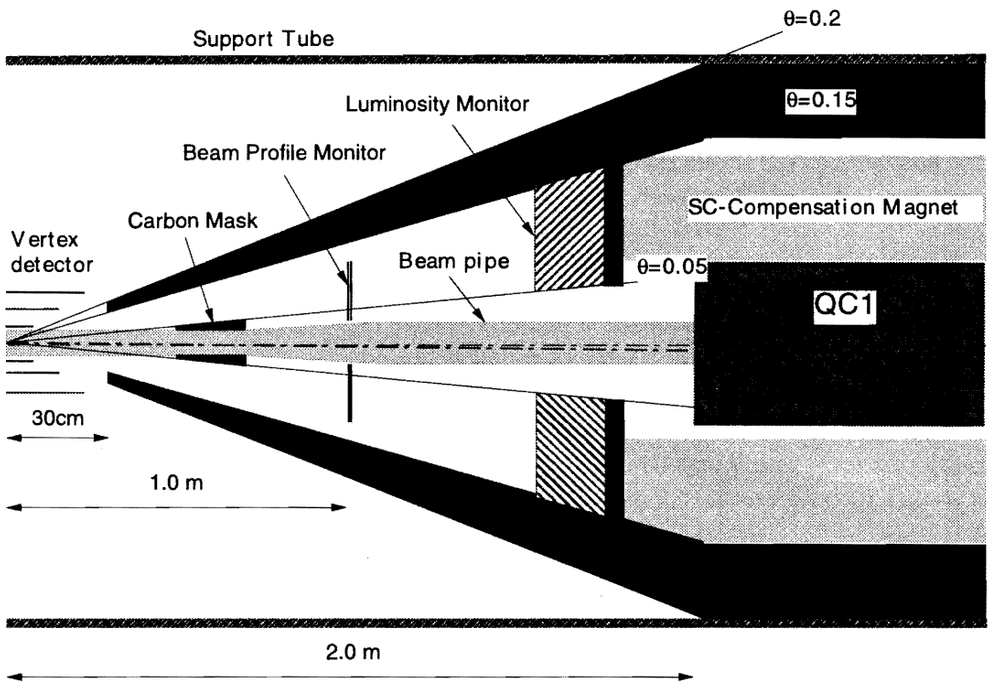

Figure 14.7: *Schematic view of the interaction region for E_{cm} =0.5TeV.*

A possible configuration of the interaction region is shown in Figure 14.7. A cone-shaped mask of heavy metal (tungsten) will be used to absorb the photons with a good efficiency. The mask occupies a polar angle region of $0.15< \theta <0.2$. The front aperture of the mask needs to be minimized in the light of reducing the background. However, it has to let the core part of the incoming beam pass through. An aperture size of $r = 4.5$ cm was chosen. The conical mask is mechanically connected to a 10.36 cm-thick cylindrical mask of the same material in a hermetic manner.. A doublet of final focus quadrupole magnets, QC1 and QC2, are implemented inside the mask. QC1 and QC2 are surrounded by a super-conducting solenoid magnet that compensates the detector solenoid field of 2 T.

Detailed engineering design of the compensating magnet is not complete yet. However, naturally, a sufficient space needs to be allocated to accommodate these magnets inside the mask. In addition, inside the conical mask, two kinds of detectors will be installed: a beam profile monitor (at 1 m from the IP, to be described in the next section), and a luminosity monitor of tungsten-scintillator sandwich type (at 1.63 m from the IP, covering $0.05 < \theta < 0.15$). A set of 20 cm-thick carbon mask is also implemented (0.5 m from the IP). The carbon mask is designed to absorb back-scattered low energy particles. The mask will be built as an "active" device which generates signals to veto scattered electrons/positrons at $\theta > 0.05$ in combination with with the luminosity monitor. They are considered

important detector elements for studies of SUSY physics[3].

In order to estimate the background due to low-energy electron-positron pairs in a detector, numerical simulations have been conducted. The pairs, which are generated by the ABEL code, were tracked by employing a Monte Carlo program based on GEANT3.21[8]. This simulation software is called JIM (Jlc detector sIMulator). The JIM takes the geometries of all detectors which have been described in the JLC-I[1] into account, except a few small revisions: The vertex detector is now assumed to have 3 layers instead of 2 as stated in JLC-I; The inner radius of the central drift chamber has been increased from 30 cm to 45 cm; And the arrangement of final focus quadrupole magnets QC1 and QC2 and the masks follow the geometry as shown in Figure 14.7 of section 14.4..

For an accurate estimation of backgrounds in the detectors, the threshold energies of electrons/positrons and photons, *i.e.* the minimum energies to be tracked in the JIM, have been set fairly low: 200 KeV and 10 KeV, respectively. The simulated statistics presented here corresponds to 10 bunch-crossings. The beam parameters used in this simulation are taken from the standard E_{cm} =500GeV operation. Values of major parameters are: 6.45×10^9 e's/bunch, 85 bunches/train, a repetition rate of 150Hz, σ_y/σ_x = 260/3nm and the horizontally crossing angle of ±4mrad. This corresponds to the luminosity of $8.1 \times 10^{33}\mathrm{cm}^{-2}\mathrm{s}^{-1}$ with a crab crossing. In this simulation the crab crossing was assumed to be perfect so that two beams collide head-on.

Figure 14.8 shows the pairs and the secondary (back-scattered) particles simulated with the JIM code. As can be clearly seen in the figure, most of them, appearing like a core of dark band in the figure, go through the front aperture(R_{mask}=4.5cm) of the mask. Particles outside the core are scattered by much larger angles than the deflected ones, which represent a possible background to be considered.

Number of hits detected in the detectors are plotted as function of the radial distance in Figure 14.9. Number of tracks that create those hits are similarly plotted in Figure 14.10. In these figures, contributions from secondary particles are also plotted by solid circles. Here, the secondary particles are simply defined as those having off-vertex positions, *i.e.* $r_{vtx} > 0.5$mm or $z_{vtx} > 0.5$mm. We note here that the vertex detector consists of $25 \times 25\mu\mathrm{m}^2$ pixels (CCDs) and that three layers are located at r=2.5(z=±7.5 cm), 5.0(z=±15 cm) and 7.5cm(z=±22.5 cm). With these geometry parameters the hit densities are calculated to be 3.6, 0.1 and 0.01 hits/mm^2 for one machine pulse that consists of 85 bunch crossings (at 150Hz), respectively. We have assumed here that the hits are distributed uniformly within each layer. It should be noted, however, that since the actual angular distribution of pair particles is asymmetric, as shown in Figure 14.11, the hit counts quoted here represent only the average numbers.

On the average, a single charged particle track which originates from the pair creation process will produce about 20 hits on the first layer of the vertex detector. This number is arrived at by comparing the two figures: 14.9 and 14.10. Except for the first layer, the hit rates in the vertex detector are well below 1 hit/mm^2, which is considered an empirical limit[9, 6].

About a half of the hits in the first layer as shown in Figure 14.9 are due to secondary particles. Contrary to our first expectation, the carbon mask was found to have no significant effect on the first layer background rate, while some reduction of hits was seen in the second layer. Figure14.12 shows

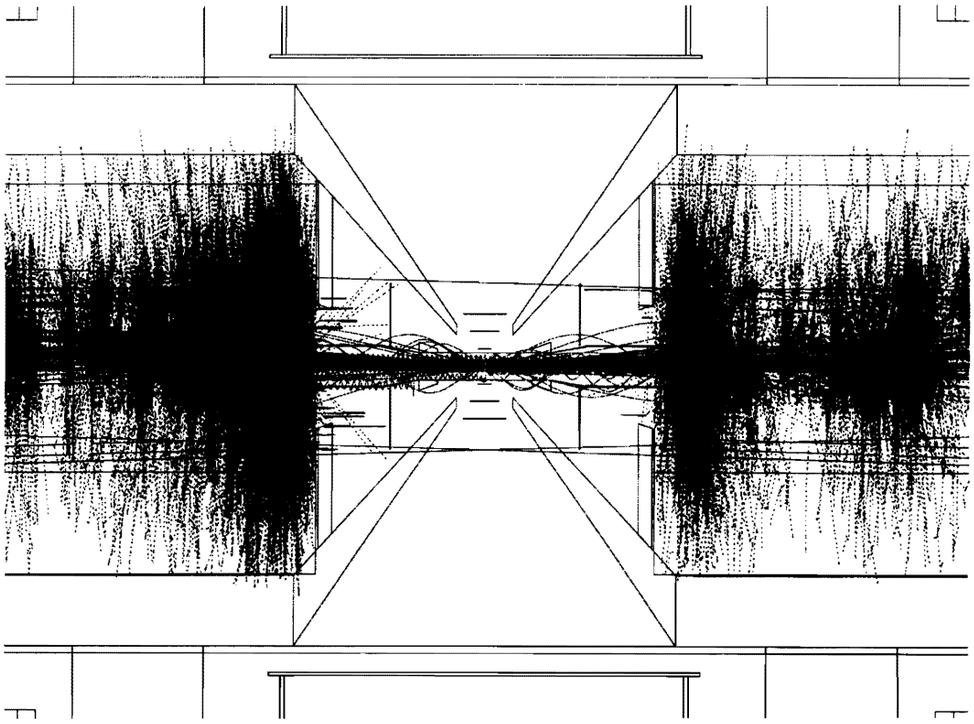

Figure 14.8: *Particles of e^+e^- pairs simulated by the JIM based on GEANT3, where solid and dotted lines are electrons/positrons and photons, respectively. The statistics corresponds to 1/100 of a bunch crossing for a display purpose.*

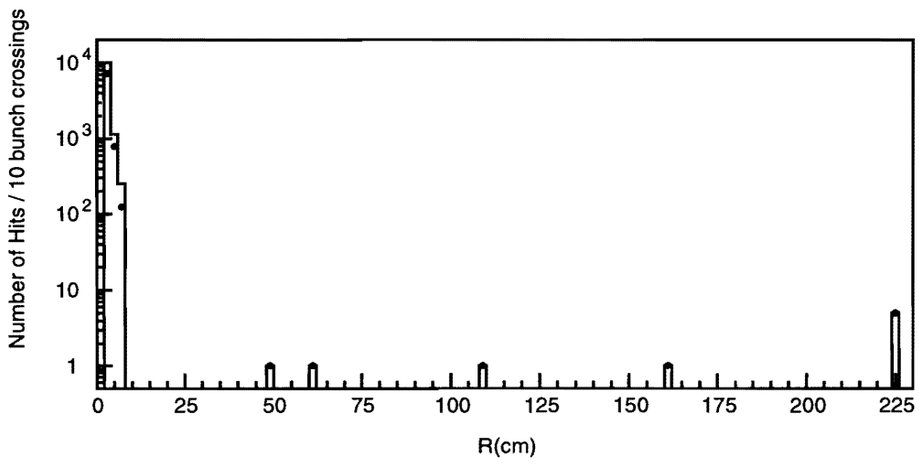

Figure 14.9: *Number of hits detected in the detectors as a function of the radial distance for 10 bunch-crossings, where ones produced by secondary particles are marked by solid circles.*

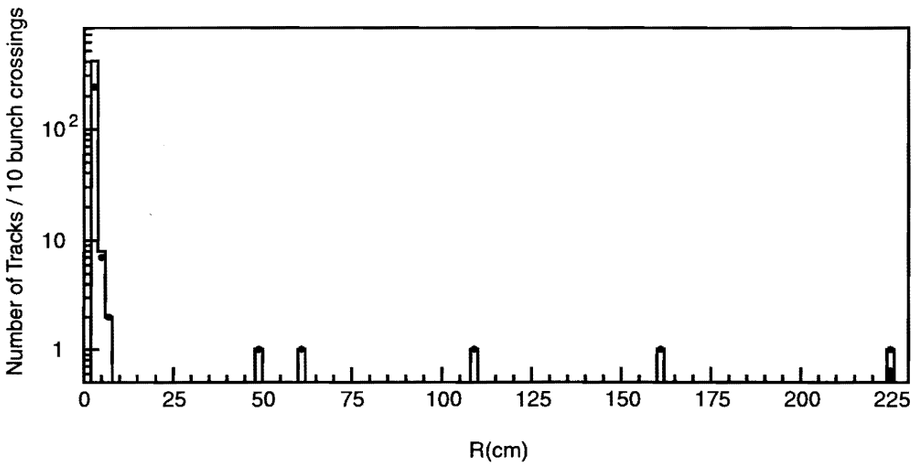

Figure 14.10: *Number of tracks creating the hits in the previous figure as a function of the radial distance for 10 bunch-crossings, where ones produced by secondary particles are marked by solid circles too.*

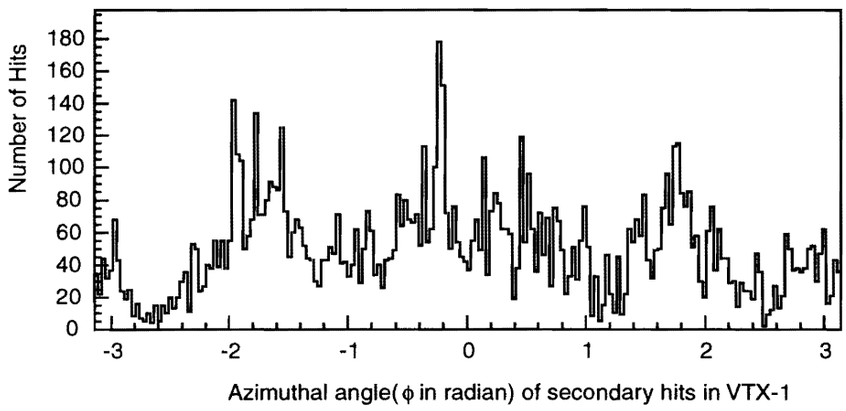

Figure 14.11: *Angular distribution of hits on the first layer of the vertex detector for 10 bunch-crossings.*

transverse vertex positions (x, y for $z > 1.6$ m) of the secondary particles observed in the first layer. It should be recalled that this first layer can clearly see the pole tips of QC1. In fact this may explain why the existence of the carbon mask did not quite help reduce the low-energy pair background on the first layer.

It is considered that more simulation studies and optimization of the relative geometry of carbon masks is necessary. Also, a more detailed calculation of particle tracking with the vertex detector may reveal that for the first layer the background hit rate in excess of 1 hit/mm^2 is actually acceptable. This study should be also pursued.

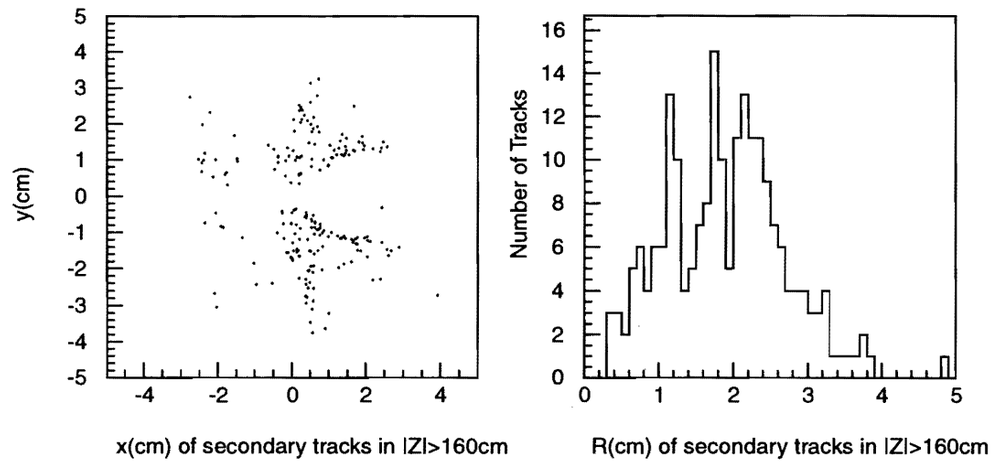

Figure 14.12: *Transverse distribution of the secondary particles at $z > 1.6$m for 10 bunch-crossings.*

In the central tracking region of $r > 45$cm, we expect about one hundred hits machine pulse (85 bunches per pulse at 150 Hz) as shown in Figure 14.9. This hit rate corresponds to ≈ 1 % occupancy in the tracking chamber. Since most of these hits are created by back-scattered photons, they are uniformly distributed in the tracking volume. Also their hit pattern is such that they rarely form contiguous hits that can be misidentified as charged particle tracks that originate from the IP. Therefore, no significant background problems from the pairs are expected in this region.

14.3 Beam Profile Monitor that Takes Advantage of $e^{\pm}$ pairs

As stated earlier, a large number of low-energy electron-positron pairs are produced through beam-beam collisions. Out of these low-energy particles, we hereafter call the ones that have the same charge as the oncoming beam as: "same-charge" particles. Particles with the opposite charge are called "opposite-charge" particles.

Figure 14.6 has shown that "same-charge" particles generally experience large deflections during the collision process because of the strong electromagnetic force due to the oncoming beam. On the other hand, the "opposite-charge" particles tend to oscillate inside the beam size space of the oncoming beam, because of the focusing force that is exerted on them. Consequently, the "opposite-charge" particles are scattered at much smaller angles.

This phenomenon is well described by a scattering process of $e^-(e^+)$ in a two-dimensional Coulomb potential which is Lorentz-boosted to the rest frame of the oncoming beam[10]. Since this potential is produced by the intense electric charge of the oncoming beam, it is a function of the transverse size (σ_x,σ_y) and intensity of that beam. Therefore, the distribution of deflected particles give information on the oncoming beam, in particular its angular distribution. Hence, the measurement of angular distribution of pair particles offers an excellent opportunity for figuring out the beam profile at the IP.

It should be noted that this technique allows to measure the sizes of the two beams independently. This is because the low-energy particles are deflected asymmetrically in the forward and backward angular regions if the two beams have different beam parameters. It should be noted that there are two independent Coulomb potentials due to the two beams that are separated by a large relative Lorentz-boost along the beam axis. With a sufficiently accurate measurement of low-energy particle distributions, we can also measure the relative displacement and transverse rotation of two beams. In addition, this measurement can provide signals that can be used for a real-time, fast feedback to maintain the collision operation of the linear collider without disrupting the data collection by the experimental facility.

The basic characteristics and expected performance of this beam profile measurement technique has been extensively discussed in a published paper[11]. Here, we show some results from the simulation with the JIM code.

We use the monitors that are located at ± 1 m (both sides) from the IP. They are arranged as shown in Figure 14.7. Each monitor consists of two layers of disk-shaped detectors. Each disk constitutes a pixel device which is made of 300μm-thick silicon. The monitor can measure both radial position ($3 < r < 12$ cm) and azimuthal angles ($-\pi < \phi < +\pi$) of traversing particles with pixels of $50 \times 50\mu\text{m}^2$ channel size. In addition, the pixel detectors will be arranged so that they can also measure the energy deposit left by the particles.

Figure 14.13 shows the simulated distributions of hits as measured by the two disks of the monitor at $z = 1$ m. Without taking specific measures to reduce the background, asymmetric angular distributions can be clearly seen over "uniform" backgrounds. The "maximum" radial distance can be found around $r = 5.5$ cm.

Figure 14.14 shows the distribution of energy deposit on the beam profile monitor. The well-separated peak seen in this figure around 90 keV is composed from the primary particles traversing the monitor, while a peak around lower energy deposit of 20 keV is created by the secondary particles which are backscattered from the QC1 and the luminosity monitor. It is seen that the energy deposits are very effective to discriminate the backgrounds. By selecting the hits associated with energy deposits

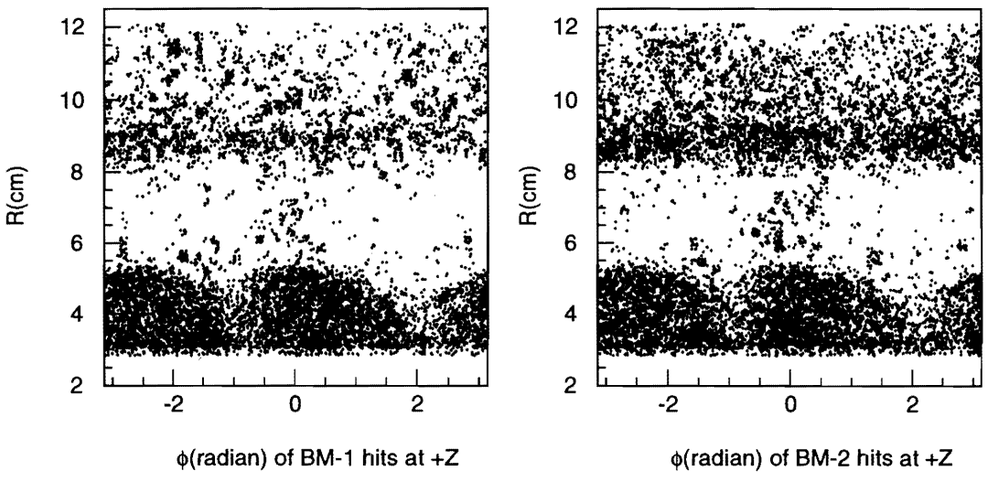

Figure 14.13: *Hits distributions observed at two disks of the beam profile monitor at z=1m for 10 bunch-crossings. BM-2 is behind BM-1 as viewed from the IP.*

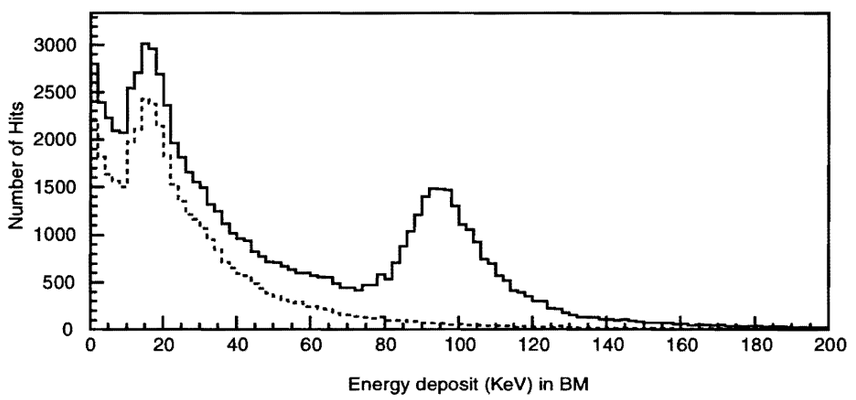

Figure 14.14: *Energy deposits observed at the beam profile monitor for 10 bunch-crossings. The solid and dotted lines are for the total and the secondary particles, respectively.*

> 70 keV, the signals of interest are significantly enhanced as shown in Figure 14.15. Figure 14.16

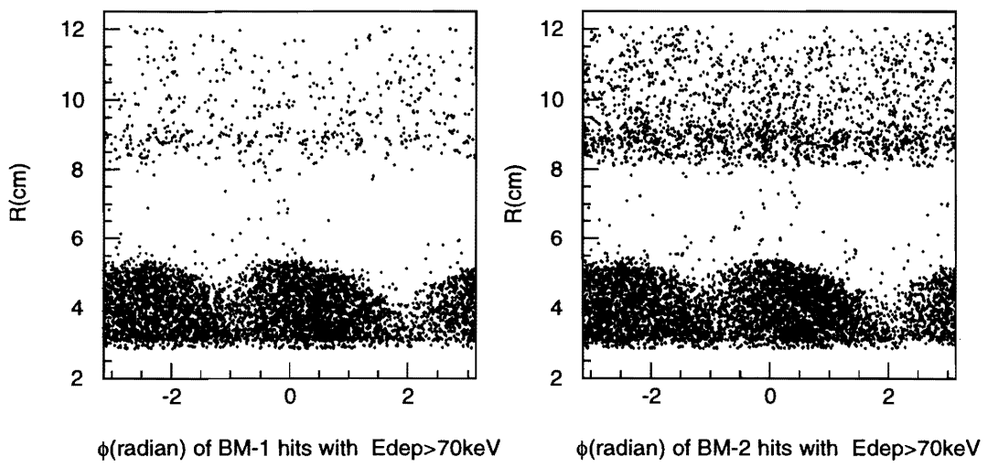

Figure 14.15: *Distribution of hits whose energy deposit exceeds 70keV, as observed at the two disks of the beam profile monitor at $z = 1$ m for 10 bunch-crossings.*

shows the hit angular distributions in the region $4.5 < r < 5.5$ cm. The hit pattern in this region carries an information that is sensitive to the aspect ratio of transverse beam sizes. As clearly seen in these figures, the asymmetric angular distribution can be very well measured with a very small amount of backgrounds.

These results indicate that the beam profile monitor based on measurements of low energy pair particles is a very promising technique.

14.4 Luminosity Spectrum

In typical $e^{\pm}$ colliding experiments, a luminosity is measured by counting the number of small angle Bhabha scattering events. This is a technique under the assumption that the collision energy is reasonably monochromatic, except for the effect of the initial state radiation.

However, this is no longer a valid assumption in high energy linear colliders, including JLC. This is because of the significant energy spread in collisions associated with beamstrahlung energy loss. Rather, the differential luminosity with respect to the effective center of mass energy (hereafter called "luminosity spectrum") needs to be measured. Miller et al. have proposed an idea of measuring the luminosity-spectrum by using acollinearity angle of the large angle Bhabha events[12]. The energy difference between e^+- and e^- beams appears in acollinearity angle of the Bhabha scattering. The potentiality of this idea has been studied by means of a luminosity-spectrum generator and a Bhabha

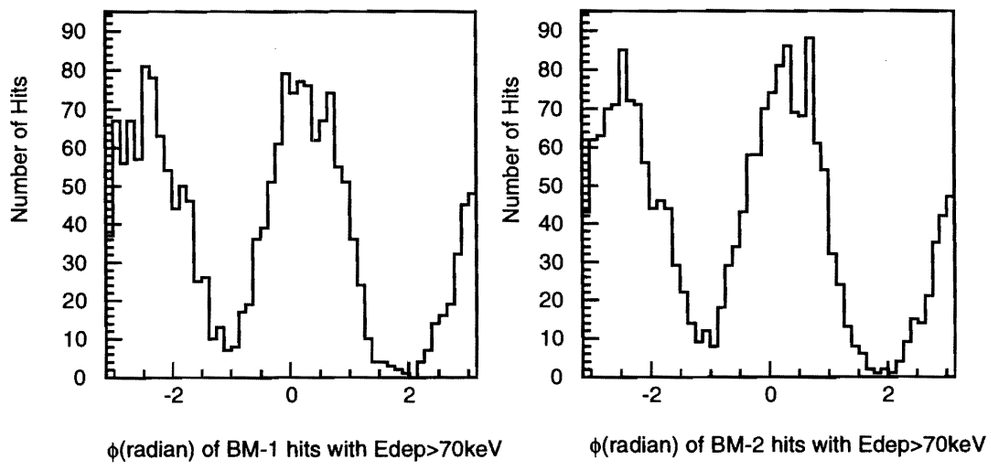

Figure 14.16: *Angular distributions in* $4.5 < r < 5.5cm$ *for the energy deposits of more than 70keV, observed at two disks of the beam profile monitor at z=1m for 10 bunch-crossings.*

event-generator.

14.4.1 Event Generation

In the past an empirical formula to describe the distribution of the collision energy at next-generation linear colliders has been presented by Yokoya and Chen[14]. In addition, a recently developed software CAIN[13] is capable of simulating detailed beam-beam interactions at e^+e^-, $e\gamma$ and $\gamma\gamma$ linear colliders. The function in [14] has been found to give a good approximation to the CAIN calculation as shown in Figure 14.17 at E_{beam}=250GeV. Table 14.1 summarizes the relevant parameters for the calculations.

Figure 14.17 shows that the function reasonably reproduce the CAIN result at $\sqrt{s} > 450$GeV, where a small difference seen in the figure is due to a beam disruption included in the CAIN.

To improve the efficiency of calculations, a luminosity-spectrum generator code has been created[15]. The generator code precisely reproduces the empirical function as shown in Figure 14.18.

It should be noted that besides the beam-beam interactions, the beam-energy spread also affects the luminosity-spectrum. Its effects are simulated and the results are shown in Figure 14.19. In these calculations a uniform energy spread of $\pm 1\%$ is assumed for the original beams. It is seen that the luminosity peaks are smeared around $\sqrt{s}$=500GeV.

Differential cross section of Bhabha scattering process was calculated by GRACE[16]. This is a program package for automatic amplitude calculation. The numerical integration and unweighted event generation were done by two programs, BASES and SPRING[17], respectively. In this study, the lowest order Feynman diagrams of this process have been taken into account, since the effect of the initial state radiation can be precisely estimated[18].

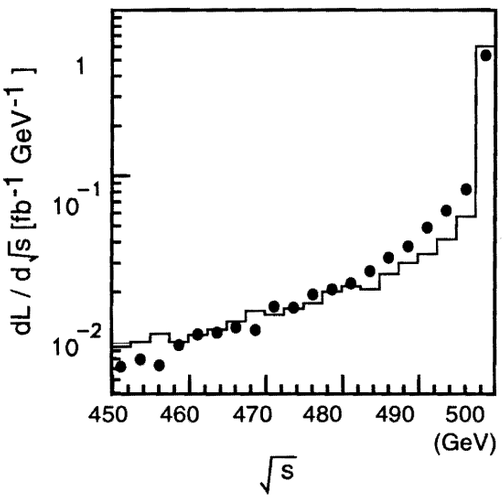

Figure 14.17: Luminosity spectra calculated by the empirical function (histogram) and the CAIN (solid circles).

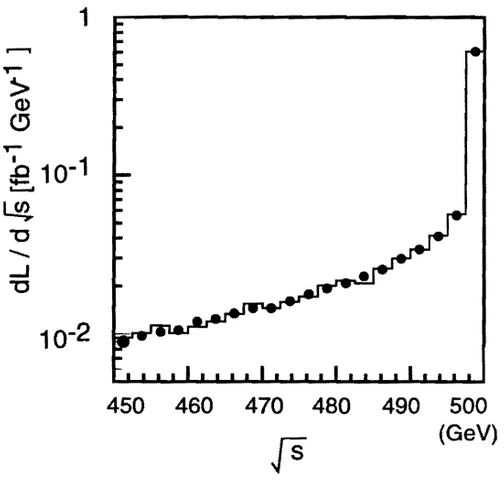

Figure 14.18: Luminosity spectra calculated by the generator (histogram) and the function (solid circles).

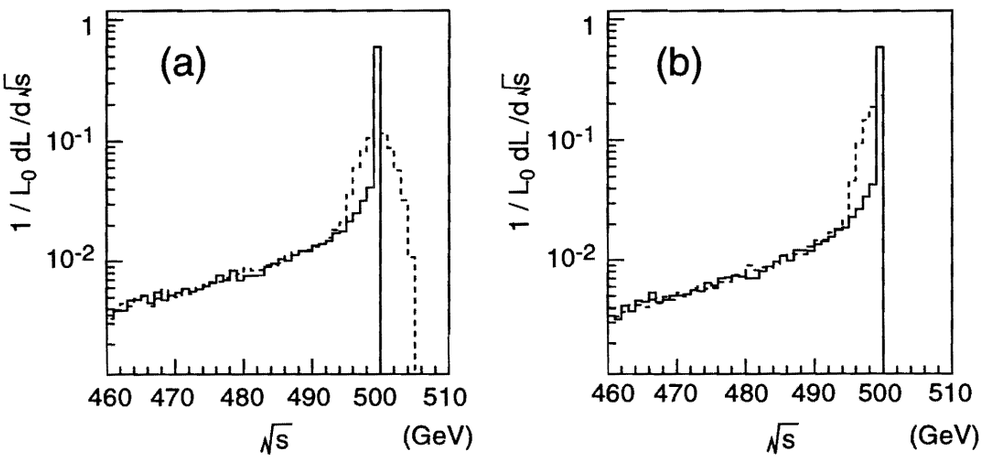

Figure 14.19: (a) The luminosity-spectra weighted by Bhabha cross section, without (with) the ±1% uniform beam-energy spread, which are shown by solid (dashed) histogram. (b) The similar spectra but for calculated ones from acollinearity angles of the Bhabha events. In this case there is no entry above $\sqrt{s}$=500GeV exists by definition.

Item	value	unit
E_{beam}	250	GeV
f_{rep}	150	Hz
n_{bunch}	85	per pulse
$N_{particles}$	0.7×10^{10}	per bunch
ϵ_x	3.3×10^{-6}	m.rad
ϵ_y	0.048×10^{-6}	m.rad
β_x^*	10.0	mm
β_y^*	0.1	mm
σ_x^*	260.0	nm
σ_y^*	3.04	nm
σ_z	90	μm

Table 14.1: *Major parameters of JLC.*

14.4.2 Measurement of Luminosity Spectrum

For Bhabha events, the momentum difference (ΔP) between e^+- and e^--beams can be expressed by;

$$\Delta P = \frac{\theta_A P_b}{\sin\overline{\theta}}, \tag{14.1}$$

where θ_A is acollinearity angle, P_b is nominal beam momentum, and $\overline{\theta}$ is an average of e^+ and e^- polar angles.

Thus, the momentum difference can be calculated from the acollinearity angles of Bhabha events for the known nominal beam energy. The center-of-mass(CM) energy $\sqrt{s_{meas.}}$ can be calculated by;

$$\sqrt{s_{meas.}} = \sqrt{s_{nominal}} - \Delta P, \tag{14.2}$$

where $\sqrt{s_{nominal}}$ is the nominal CM energy, *i.e.* $2 \times E_{beam}$ for head-on collisions. Since θ_A is larger than zero, $\sqrt{s_{meas.}}$ must be less than (or equal to) the $\sqrt{s_{nominal}}$. The beam-energy spread produces events also over the nominal beam-energy as shown in Figure 14.19(a), while the $\sqrt{s_{meas.}}$ distribution is always below the nominal one as shown in Fig14.19(b). This is a limitation of this technique. In order to overcome this limitation for the sizable spread, we will need additional information such as energies of scattered electrons and positrons.

Now, to separately examine the effects of finite angular resolution of the detector, the beam energy spread is turned off. The measured spectrum with a perfect detector, *i.e.* with perfect angular resolution, is compared with those with the angular resolutions(σ_θ) of 3 mrad and 5 mrad in Figure 14.20. In the simulation the polar angles of both tracks are smeared by Gaussian distributions with the assumed angular resolution.

The statistics of the simulation in Figure 14.19 corresponds to an accumulated luminosity of $10fb^{-1}$ (about one year accumulation). The detector is assumed to cover the polar angular region from 45° to

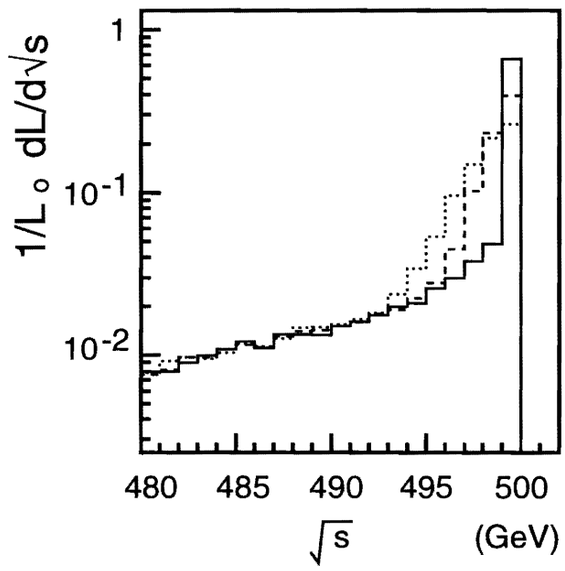

Figure 14.20: *The luminosity-spectra as measured by the acollinearity angles of Bhabha events. Various angular resolutions of measuring the Bhabha scattered particles are considered. Solid, dashed and dotted histograms correspond to angular resolution of σ_θ=0(perfect), 3mrad and 5mrad, respectively.*

135°. The observed spectrum with σ_θ = 1 mrad resolution is hardly distinguishable from the perfect detector case, so it is not independently plotted in Figure 14.20. The spectrum with σ_θ >3 mrad shows a significant smearing effect.

For studies of toponium physics, an accurate knowledge of the luminosity-spectrum within the total decay width of top quark is very important. The top quark decay width is estimated to be 1.55GeV for m_{top} =175 GeV, *i.e.* ±0.5 % of $\sqrt{s_{nominal}}$, according to the standard model. The performance of the accolinearity angle method in this narrow energy region needs to be examined. For this purpose the integral luminosity for 455< $\sqrt{s}$ <450GeV to be actually obtained in collisions and the luminosity values to be "measured" by this method are compared. Figure 14.21 shows the results of this study. The "nominal" (i.e. actual) luminosity are compared with the "measured" luminosity where various detector angular resolution and polar angle coverage are assumed. It is seen that the angular resolution better than 3 mrad is required for $\theta > 45°$ to maintain a satisfactory luminosity measurement performance. We also observe a slightly higher luminosity by 2.5% than the nominal one even with the perfect resolution in Figure 14.21, since the small amount of luminosity must be added in a case that both two beams can loose the same energies with no acollinearity angle, where $\sqrt{s_{meas.}} = \sqrt{s_{nominal}}$ by Equations 14.1 and 14.2.

When Bhabha scattered particles in a smaller polar angle region are included in the analysis the angular resolution of the measurement needs to be substantially improved because of a factor $1/\sin\theta$ in Equation 14.1. On the other hand, the statistics of the Bhabha events increases very rapidly as

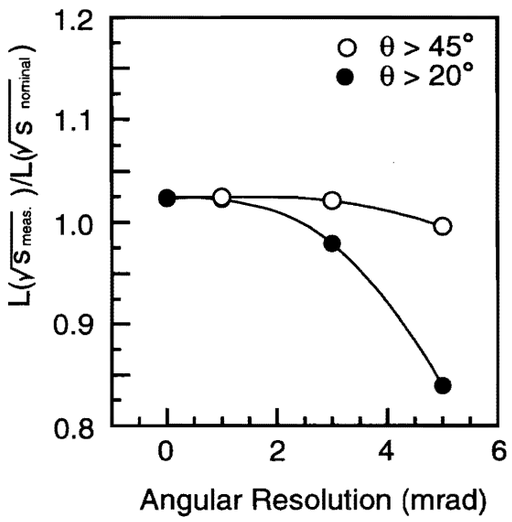

Figure 14.21: The luminosity normalized by the nominal one at $\sqrt{s} > 495GeV$, as a function of σ_θ in two angular regions of $\theta > 45°$ (open circles) and $> 20°$ (solid circles).

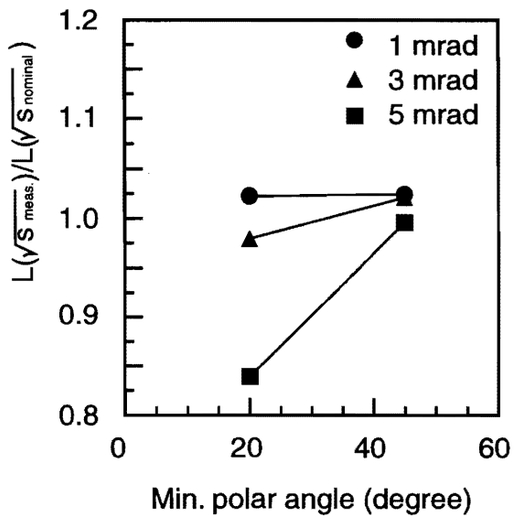

Figure 14.22: The luminosity normalized by the nominal one at $\sqrt{s} > 495GeV$, as a function of minimum polar angle to be measured, for various angular resolutions.

decreasing the minimum polar angle (θ_{min}) to be measured. For example, the statistics for θ_{min}=20° increases about one order of magnitude than that of θ_{min}=45°, therefore the integrated luminosity can be reduced to $1fb^{-1}$ in the requirement. As shown in Figures 14.21 and 14.22, the angular resolution must be 1 mrad at least for θ_{min}=20°. The toponium experiment will involve an energy scan. It will consist of operations at several energy points each for a few fb^{-1}[2]. Therefore, it is essential to have σ_θ <1 mrad for θ >20°. The higher statistics is also favored in the light of reducing possible systematic errors in the measurement of luminosity.

14.4.3 Beam Parameter Fitting

Theoretically the luminosity-spectrum is determined by a set of beam parameters: horizontal, vertical and longitudinal beam sizes ($\sigma_x, \sigma_y, \sigma_z$) and the number of particles in a bunch(N). In the empirical function, two independent-valuables appeared as $B \equiv N/(\sigma_x + \sigma_y)$ and σ_z. They can be calculated from a measured spectrum, since the measured one is the luminosity spectrum convoluted by the cross section of the Bhabha scattering process, which is called the weighted luminosity-spectrum. In this analysis, one of them is obtained by assuming a fixed value of the other and vice versa, *i.e.* one parameter fitting in a likelihood method. The beam energy was set to be 250 GeV and the relevant parameters are listed in Table 14.1, which are called "nominal" beam parameters.

For this study, two kinds of Bhabha events were generated by the method described in the previous

section. They are called 'experimental-data sample' (e-sample) and 'likelihood-function sample' (l-sample). The Monte Carlo statistics of e-samples corresponds to 10fb^{-1} and 1fb^{-1} for the angular regions of $\theta > 45°$ and $\theta > 20°$, respectively. The polar angles of electrons and positrons in the Bhabha events were smeared with a Gaussian distribution of 1mrad resolution, then the weighted luminosity-spectrum was calculated as a function of $\sqrt{s}$ from their acollinearity angles. A number of e-samples were generated with several sets of B and σ_z. To determine a likelihood function, a l-sample was generated with 10 times more statistics than the e-samples with the nominal beam parameters. The weighted luminosity spectrum was obtained in the same way as the e-sample. Dividing the spectrum into 50 bins for 450< $\sqrt{s_{meas.}}$ <500GeV, the normalized likelihood function $\mathcal{L}$ was defined by:

$$\mathcal{L}(I(\sqrt{s}); B, \sigma_z) \equiv N_l(I(\sqrt{s}))/N_{l-sample}, \tag{14.3}$$

where $I(\sqrt{s})$ is a bin-number corresponding to $\sqrt{s}$, $N_l(I(\sqrt{s}))$ is the number of events in $I(\sqrt{s})$'th bin, and $N_{l-sample}$ is the total event number of the l-sample. For the e-sample, the log-likelihood was calculated by;

$$\mathcal{LL} \equiv \sum_{j=1}^{N_{e-sample}} \ln \mathcal{L}_j, \tag{14.4}$$

where $N_{e-sample}$ is the total event number of the e-sample and $\mathcal{L}_j \equiv \mathcal{L}(I_j(\sqrt{s_j}); B, \sigma_z)$ is the likelihood of the j'th event in the e-sample.

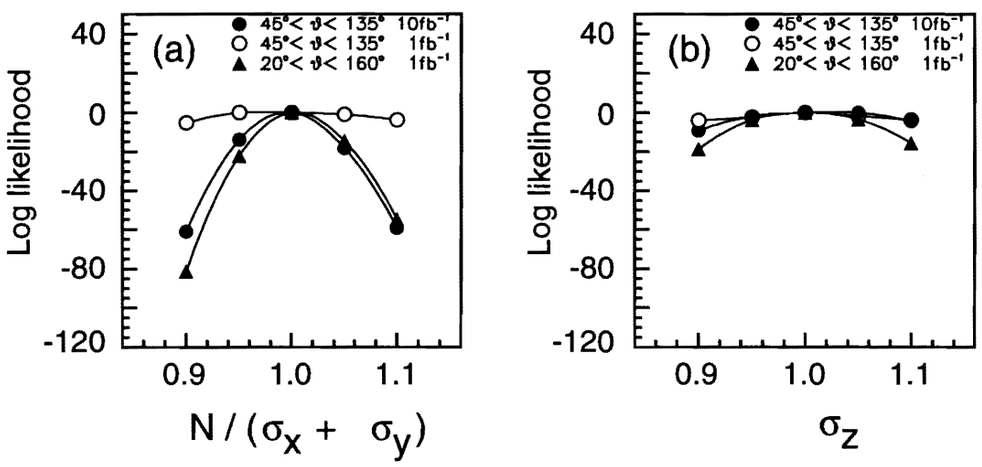

Figure 14.23: *The log-likelihood distributions of the e-samples as a function of (a) $B = N/(\sigma_x + \sigma_y)$ and (b) σ_z, where the parameter was varied for $\pm 10\%$ relative to the nominal value while the other was fixed to the nominal value and vice versa.*

Figure 14.23(a) and (b) shows the log-likelihood distributions as function of B and σ_z, respectively. From these figures it is seen that the beam parameter of B or σ_z can be determined with an accuracy of several % by large ($\theta > 45°$) and small($\theta > 20°$) angle Bhabha events for the integrated luminosity of 10fb^{-1} and 1fb^{-1}, respectively.

As described in the previous section, since the energy scan should be made for the integrated luminosity of a few fb^{-1} each at a number of CM energies around toponium resonance states[2], a 1 mrad angular resolution must be necessary in the small angular region ($\theta > 20°$). In these cases, the integrated luminosity of the peak in the luminosity-spectrum must be precisely determined, although the peak may be smeared by the beam energy spread. It is seen that the present study has demonstrated the feasibility toward this end.

References for Chapter 14

[1] JLC-I, KEK Report 92-16, December, 1992.

[2] K.Fujii, T.Matsui and Y.Sumino,*Phys. Rev.* D **50**, 4341 (1994).

[3] M.M.Nojiri, K.Fujii and T.Tsukamoto, *Phys. Rev.* D **54**, 6756 (1996).

[4] D.Burke, proceedings of Workshop on *Physics and Experiments with Linear* e^+e^- *Colliders*, eds. R.Orava, P.Eerola and M.Nordberg (World Scientific, Singapore, 1992) p51, and references therein.

[5] E.A.Kushnirenko,proceedings of *The International Workshop on Final Focus and Interaction Regions of Next Generation Linear Colliders*, May 2-6,1992, *SLAC report* SLAC-405,p225.

[6] Zeroth-Order Design Report for the Next Linear Collider, LBNL-PUB-5424, also SLAC Report 474 or UCRL-ID-124161, May 1996.

[7] T.Tauchi, K.Yokoya and P.Chen, *Part. Accel.* **41**, 29 (1993).

[8] GEANT3.21-Detector Description and Simulation Tool, Application Software Group, computing and networks division, CERN, CERN Program Library Long Writeup W5013, March 1994.

[9] C.Damerell, private communication.

[10] K. Yokoya and P. Chen, "Beam-beam phenomena in linear colliders", lecture at 1990 US-CERN School on Particle Accelerators, Nov.7-14, 1990, Hilton Head Island, So. Carolina, USA, Lecture Notes in Physics 400. *Frontiers of Particle Beams: Intensity Limitations* , Springer Verlag, pp.415-445.

[11] T.Tauchi and K.Yokoya, *Phys. Rev.* E **51**, 6119 (1995).

[12] M.N. Frary, D.J. Miller, in: e^+e^- collisions at 500 GeV: the physics potential, ed.by P. Zerwas, DESY report 92-123A, 1992,p.379.

[13] P. Chen, G. Horton-Smith, T. Ohgaki, A.W. Weidemenn, K. Yokoya, Nucl. Instr. and Meth. **A355** (1995) 107.

[14] K. Yokoya, P. Chen, 'Electron energy spectrum and maximum disruption angle under multi-photon beamstrahlung', Presented at *the IEEE Particle Accelerator Conference, Chicago, 1989*, SLAC-PUB-4935 (1989).

[15] N. Toomi et al., in preparation.

[16] T. Ishikawa, T. Kaneko, K. Kato, S. Kawabata, Y. Shimizu, H. Tanaka. GRACE manual, KEK report 92-19, 1993

[17] S. Kawabata, Comp.Phys.Comm., **41** (1986) 127; *ibid.*, **88** (1995) 309.

[18] A. Arbuzov et al., Phys. Lett. **B383**(1996) 238.

Authors and Major Contributers of Chapter 14

- Toshiaki Tauchi
- Yoshiaki Fujii
- Yoshihito Namito
- Nobuko Toomi
- Junichi Fujimoto
- Setsuya Kawabata
- Yoshimasa Kurihara
- Takashi Watanabe
- Kaoru Yokoya
- Katsunobu Oide

CHAPTER 15

Gamma-Gamma Collision Option

Contents

15.1 Introduction

A 2nd interaction region is a possible option for a linear collider, and could be used for diagnostic purposes of e^+e^-beams as well as an extension of the physics capabilities of the facility. Besides the beam-diagnostics purpose, possibilities for the 2nd interaction include $\gamma\gamma$ collisions, e-γ collisions, and e^-e^-collisions. e^-e^-collisions can be realized by replacing the positron beam with an electron beam in e^+e^-colliders. For the other two options, $\gamma\gamma$ and e-γ colliders, a photon beam is created by inverse Compton scattering of a laser beam on an electron beam just before the interaction point.

Physics opportunities in $\gamma\gamma$, e-γ and e^-e^-collisions of a few hundreds GeV have been studied by many authors; a summary of their ideas can be found, for example, in [4, 21, 24].

In $\gamma\gamma$ collisions, a Higgs particle is produced via loops of charged particles, light and heavy. In this case, the contribution of any heavy charged particle is not decoupled as long as its mass is generated by the Higgs mechanism. Therefore, a study of the two photon decay width of the Higgs particle in $\gamma\gamma$ collisions provides an important signal beyond the standard model. This kind of information cannot be obtained from e^+e^-collisions [35, 28].

Another feature of $\gamma\gamma$ collisions is that the cross section of the W-pair cross section is large ($\approx$ 90 pb) for $\sqrt{s_{\gamma\gamma}} > 200$ GeV. Since it is $O(10^{1\sim2})$ larger than the second highest process $\gamma\gamma \to f\bar{f}$, a high-energy $\gamma\gamma$ collider is a "W factory" which allows precise measurements of W properties, such as an anomalous coupling constant[5, 31], with high statistics. Since high-energy photons produced by Compton scattering can be polarized circularly as well as linearly, a photon-photon system can form a CP eigen state, which give us other physics opportunities unique to $\gamma\gamma$ collisions[2, 10, 11, 18, 19]. In e-γ collisions, the discovery potential for some new particles is higher than in e^+e^-or $\gamma\gamma$ collisions. Since the initial state of the collision is asymmetric, final state particles do not have to be pair-produced, while it is necessary in most cases in $\gamma\gamma$ /e^+e^-collisions. Using this feature, e-γ collider is a good machine for searching for excited electrons and a supersymmetric partner of electrons[17, 26].

Details concerning physics opportunities have been described in cited references. In this report we describe the status of the R&D for $\gamma\gamma$ colliders. The R&D issues covers a range of engineering and physics fields, such as:

- Optimization of the electron and the laser beam parameters.
- Design of Compton and photon photon interaction region.
- Laser optics.
- Development of high-power, high-repetition-rate laser.

In this report, we do not try to describe a comprehensive design which includes all of the items listed above, but concentrate on making the property of a $\gamma\gamma$ collier clear in the sense of physics experiments, such as the luminosity distribution and beam background. Particularly, to estimate the

realistic luminosity and beam background, an understanding of the laser-electron and electron-electron beam interaction is crucial. For this purpose, a simulation program for laser-electron and electron-electron interactions, CAIN, has been developed by a collaboration of KEK, Hiroshima, SLAC and UCB [8, 7]. We mainly report on results using CAIN in this report.

In the following, an overview of the $\gamma\gamma$ collider is given in the next section, followed by a description of the laser and electron beam parameters. Details concerning the photon-beam generation is described in section 15.2.2. The luminosity distribution calculated by CAIN is described in section 15.2.3, and an estimate of detector background from beam-beam interaction is discussed in section 15.2.4. Finally, a brief comment on the other R&D issues can be found in section 15.2.5.

15.1.1 Gamma-Gamma Collider

The idea of generating high-energy photons by backward-scattered Compton photons has been discussed in [13, 14, 15, 33, 34], and summarized in [4]. In $\gamma\gamma$ colliders, photon beams are generated by inverse Compton scattering of the electron beam and lasers just before the interaction point. By this method, a photon beam of the highest energy close to the original electron beam can be generated. A schematic view of the interaction region is illustrated in Figure 15.1.

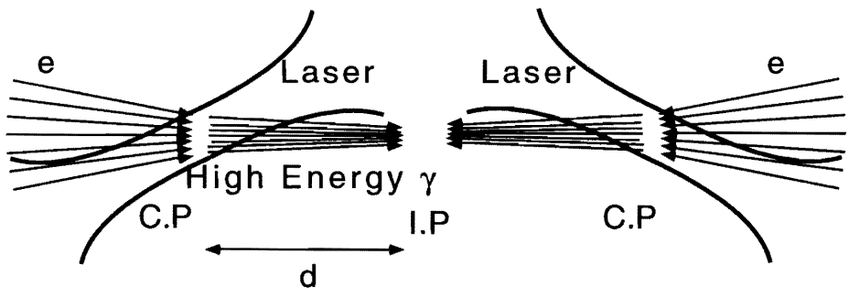

Figure 15.1: *Conceptual view of the interaction region of a $\gamma\gamma$ collider*

Maximum energy of the generated photon is expressed as

$$E_\gamma = \frac{x}{x+1} E_e, \tag{15.1}$$

where x is the kinematics parameter of Compton scattering, defined as

$$x = \frac{4E_e\omega_L}{m_e^2}\cos^2(\theta/2). \tag{15.2}$$

Here, E_e, ω_L and θ are the electron energy, laser photon energy and angle between the electron beam and the laser beam (see Figure 15.2).

A typical photon energy spectra generated by laser Compton scattering are shown in Figure 15.3. As shown in the figure, the energy distribution of the generated photons depends on the polarization

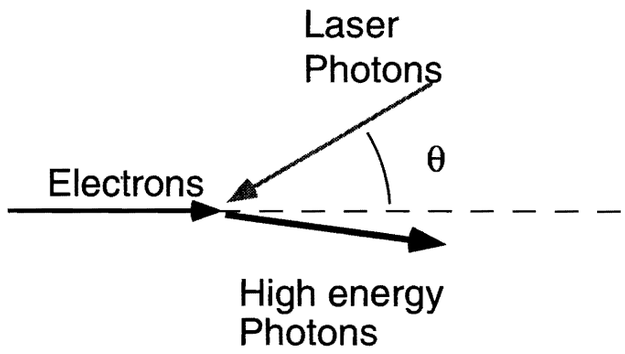

Figure 15.2: *Kinematics of inverse Compton scattering.*

of the electron and laser beams. One can obtain a broad energy distribution or peaked distribution depending on their purpose by controlling the polarization. It should be noted that not only circular polarized, which is the eigenstate of helicity, but also a transverse polarized beam can also be generated that gives another chance of physics to study.

According to Equation 15.2, the maximum photon energy increases as x becomes higher. However, when x exceeds $x = 2(1+\sqrt{2}) \approx 4.83$, the energy of a Compton-scattered photon and a laser photon system becomes greater than the threshold of e^+e^-pair creation. This pair-creation process could waste the generated high-energy photons, and could be an additional source of detector background. On the contrary, the large x value has some advantage in that the photon energy is higher and its spectrum becomes narrower. The possibility of a high-x $\gamma\gamma$ collider is discussed in [25, 34]; however, at least as a first assumption, the x parameter is restricted to be smaller than 4.83 in this report. For the case of an electron beam energy of 250 GeV, the laser energy that makes $x \approx 4.8$ is about 1 μm, which fits the energy of a solid state laser, such as Nd:Glass or YAG type.

Though a precise estimation of the luminosity of $\gamma\gamma$ colliders requires a detailed consideration of the laser-Compton interaction and the geometry of the interaction region, which requires a simulation study of laser-Compton scattering as well as the beam-beam interaction at the interaction point, here we estimate the luminosity of $\gamma\gamma$ colliders by a simple analysis, and describe the details in a later section.

First of all, the Compton conversion probability, i.e., the mean number of Compton interactions of an electron in a laser pulse, is assumed to be 1. Based on this assumption, the ratio k of the number of electrons that interact with a laser photon (that is identical to the number of Compton-scattered photons) and initial number of electrons is, $k = 1 - e^{-1} \approx 0.65$. So the number of scattered photons n_γ is $0.65n_b$, where n_b is number of electrons in a bunch; n_γ includes the whole spectrum of scattered photons, and roughly half of n_γ have an energy greater than 60% of the initial electron energy.

Since the scattered photons from an electron, having a Lorentz factor γ, generally has intrinsic angular spread of $1/\gamma$, the spatial spread of the photons is approximately d/γ at distance d from the Compton

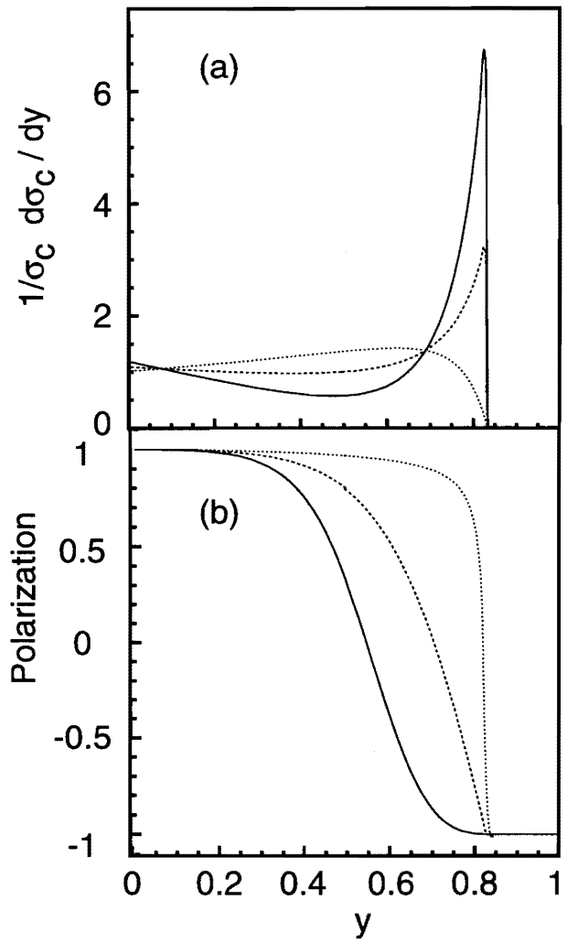

Figure 15.3: *Calculated energy (a) and polarization (b) of high energy photons by laser-electron Compton scattering. Solid, dash and dotted lines correspond to combination of polarization of an electron beam (λ_e) and laser beam (λ_L) as $\lambda_e\lambda_L = -1$, $\lambda_e\lambda_L = 0$ and $\lambda_e\lambda_L = +1$ respectively.*

interaction point. As illustrated in Figure 15.1, scattered photons are boosted in the direction of the parent electron. The spatial size of the high-energy part of the photon beam at d can be estimated as

$$d = \sqrt{(d/\gamma)^2 + \sigma_e^2}, \tag{15.3}$$

where σ_e is the beam size of the electron beam at distance d from the Compton interaction point. In Equation 15.3, d can be interpreted as being the distance between the Compton interaction point (C.P.) and the $\gamma\gamma$ interaction point (I.P.), and σ_e is the electron beam size at the I.P. Equation 15.3 determines the relation between d and σ_e at a fixed electron energy. Usually, d is chosen so that $d/\gamma = \sigma_e$, because the d smaller than $\sigma_e\gamma$ gives no advantage for a luminosity improvement, and just makes the interaction region more complex. For $d = \sigma_e\gamma$, the size of the photon beam is about the same as the electron beam size. Therefore, the higher energy part of the photon i.e., 50% of k, contribute to the luminosity of a $\gamma\gamma$ collier as

$$L_{\gamma\gamma} = (0.5k)^2 L_{ee} \approx 0.1 L_{ee}, \tag{15.4}$$

$$L_{ee} = \frac{f_{rep} n_b^2}{4\pi\sigma_x\sigma_y}. \tag{15.5}$$

The electron beam size is usually smaller for the vertical direction, σ_y, than for the horizontal direction, σ_x. Relation 15.3 is applied to σ_y.

In short, the luminosity of a $\gamma\gamma$ collider is approximately 10% of electron-electron geometric luminosity, and the maximum energy of the $\gamma\gamma$ system is 80% of that of the original electron-electron system.

15.2 Accelerator R&D

15.2.1 Machine Parameters

For studies of $\gamma\gamma$ colliders, we prepared 3 sets of reference parameters: one for a 400 GeV $\gamma\gamma$ collision and 2 sets for a 120 GeV $\gamma\gamma$ collision, as summarized in Table 15.1.

The 400 GeV parameter is designed to obtain the highest-energy $\gamma\gamma$ collision with JLC-I. The 120 GeV parameters are planned mainly for use in a light-Higgs study. For 120 GeV $\gamma\gamma$ collision, 2 sets of parameters have been prepared. The difference in the two comes mainly from the choice of the laser wavelength. Since it is preferable to keep the x parameter close to 4.8 to obtain a narrower luminosity spectrum, parameter (c) is desirable. However, in this case, it is necessary to develop a 4 eV,TW laser to achieve a sufficient Compton interaction efficiency. Though a 4 eV laser may be achievable by the fourth-harmonic generation of Nd:Glass laser, for example, another parameter for 120 GeV was prepared. The laser wavelength of this "backup parameter" is the same as in the 400 GeV case, and is expected to be reliable for laser development. The price to pay for this case is that the x parameter is small, resulting in a broader luminosity spectrum.

Beam energy	E_e	GeV	250(a)	103(b)	80(c)
Particles/bunch	N		0.65×10^{10}		
Repetition rate	f_{rep}	Hz	150	←	←
bunches/pulse	n_b		85	←	←
Bunch length	σ_z	μm	90	←	←
Bunch sizes (C.P.)	σ_x^C/σ_y^C	nm	584/56.1	704/66.4	667/80.5
Bunch sizes (I.P.)	σ_x^*/σ_y^*	nm	58.1/8.86	70.1/10.91	79.5/9.59
Beta functions (I.P.)	β_x^*/β_y^*	mm	0.5/0.8	0.3/0.5	0.3/0.3
Norm. emittance	$\varepsilon_{xn}/\varepsilon_{yn}$	nm·rad	3300/48	←	←
Geom. emittance	$\varepsilon_x/\varepsilon_y$	10^{-12}m·rad	6.75/0.0981	16.4/0.238	21.1/0.307
ρ parameter	$d/(\gamma\sigma_y^*)$		1.15	1.36	1.66
C.P-I.P distance	d	mm	5.0	3.0	2.5
Geom. luminosity	$L_{geom.}^{ee}$	$cm^{-2}s^{-1}$	7.83×10^{33}	5.27×10^{33}	5.28×10^{33}
Laser parameters					
Wave length	λ_L	μm	1.053	←	0.37
Pulse energy	E_L	J	1.0	←	←
Pulse length	σ_z^L	μm	230	←	120
Rayleigh length		μm	120	←	80
r.m.s spot size	σ_r^L	μm	3.17	←	2.17
Peak power density	P_d	W/m^2	8.23×10^{21}	←	6.73×10^{22}
Max. ξ parameter	ξ^2		0.334	←	0.337
x parameter	$4\omega_L E_e/m^2$		4.51	1.86	4.11

Table 15.1: *Reference parameters of the $\gamma\gamma$ collider considered for JLC.*

In all sets of parameters, we assumed that the electron beam parameters are almost identical to those of the e^+e^-collider, and that the differences are the beam size and the β function at the interaction point. Since, as mentioned before, a smaller beam size is better for the $\gamma\gamma$ collider, the beam size and the β function for the horizontal direction is chosen to be smaller than that for the e^+e^-collier. A boundary condition for choosing the parameters is that the hardware of the accelerator is assumed to be the same as e^+e^-collider. Thus, the horizontal beam size of the electron beam is the smallest achievable value without changing the hardware of the accelerator.

For laser beams, the size and power are set to obtain efficient laser-electron scattering at the C.P. The details concerning the choice of the parameters and the obtained photon beams are mentioned in the next section.

15.2.2 Photon Beam Generation

Laser Parameters

At the C.P., low-energy laser photons are converted to high-energy photons by Compton scattering with electrons. To obtain high intensity photon beams, every electron is required to give its energy to a laser photon. Under actual conditions, it is reasonable to assume that an electron is scattered by a laser photon once on the average during one laser pulse. The number of interacted electrons in infinitesimal time and space, dx, dt, can be written as

$$dN_e = -c\sigma_c n_e(\vec{x},t)n_L(\vec{x}+ct,t)dx\,dt, \tag{15.6}$$

where c, σ_c, n_e and n_L are the speed of light, the cross section of Compton scattering, the density function of the electrons and laser photons, respectively. After collisions within a finite time period, the number of scattered electrons is

$$N_e = \int dx n_e(\vec{x},t)\exp[-c\sigma_c \int n_L(\vec{x}+ct,t)dt]. \tag{15.7}$$

Since this integration is complicated, due to double integration, it is convenient to define the luminosity of the collision of an electron bunch and a laser pulse as

$$L_c = \int n_e(\vec{x},z_1)n_L(\vec{x},z_2)d\vec{x}dz_1dz_2. \tag{15.8}$$

Using the Compton luminosity 15.8, the number of scattered electrons, which is identical to the population of generated high-energy photons, can be approximately estimated as

$$N_\gamma \approx n_b(1-e^{-\sigma_c L_c/n_b}). \tag{15.9}$$

The required condition of single electron-laser collision is interpreted as

$$n_b = \sigma_c L_c. \tag{15.10}$$

In order to calculate the requirement for laser power, the density function of the electron bunch and the laser pulse is assumed to be a Gaussian function in all three dimensions; i.e.,
for electron bunches

$$n_e = \frac{n_b}{(2\pi)^{3/2}\sigma_x^e\sigma_y^e\sigma_z^e}\exp[\frac{x^2}{2\sigma_x^{e2}}]\exp[\frac{y^2}{2\sigma_y^{e2}}]\exp[\frac{z^2}{2\sigma_z^{e2}}], \tag{15.11}$$

where the beam-size σ's are calculated from the given beam parameters,
and for a laser pulse;

$$n_L = \frac{J}{(2\pi)^{3/2}\hbar\omega_L\sigma_x^L\sigma_y^L\sigma_z^L}\exp[\frac{x^2}{2\sigma_x^{L2}}]\exp[\frac{y^2}{2\sigma_y^{L2}}]\exp[\frac{z^2}{2\sigma_z^{L2}}]. \tag{15.12}$$

For both expressions z is the distance from focal point of the beam. The transverse spot size of the laser, σ_r^L is expressed while assuming the diffraction-limit wave to be

$$\sigma_r^L(z) = \sigma_0^L\sqrt{1+\left(\frac{z}{Z_R}\right)^2}. \tag{15.13}$$

Here, σ_0^L is the laser beam size at the focal point. Z_R is the Rayleigh length of the laser, which is related to its wavelength, λ_L, and waist size as

$$Z_R = \frac{4\pi\sigma_0^{L2}}{\lambda_L}. \tag{15.14}$$

To calculate the Compton luminosity with the given electron beam parameters, a guideline is necessary to fix the pulse length of the laser. Since a portion of a laser pulse at large z does not contribute to the Compton luminosity, due to the diffraction effect of Equation 15.14, the laser pulse length σ_z^L is set to $2Z_R$ for the calculation. The requirement for the laser to satisfy condition 15.10 was calculated for the case of a 400 GeV $\gamma\gamma$ collider (parameter (a) of Table 15.1). Figure 15.4 shows the relation between the laser power in a pulse and spot size at the focal point. It is found that the laser power

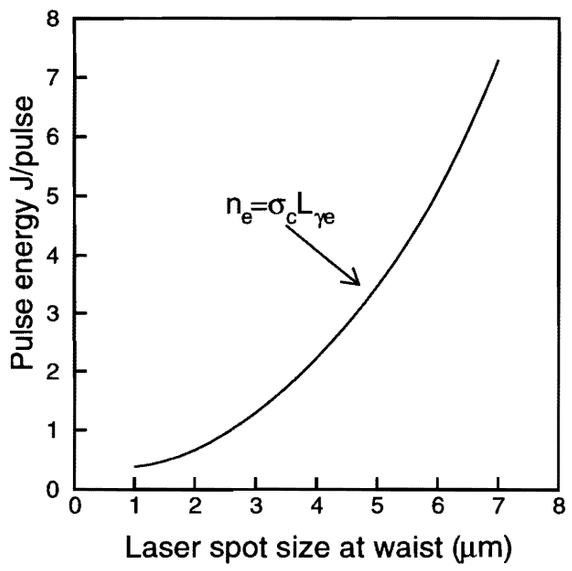

Figure 15.4: *Relation between laser spot size and pulse energy.*

is about 1 J/pulse when it is focused down to $\approx 3\mu m$.

The other factor to be considered is the laser power density. At a focal point of 3 μm, 1 J laser pulse, the power density of the laser approaches 10^{18}W/cm^2. Under this high-power density condition, a nonlinear effect in the Compton scattering, which lowers the peak energy of the generated high-energy photon, while broadening the width of the peak, is not negligible. The nonlinear effect is characterized by the parameter η defined as

$$\eta = \frac{eE}{\omega_L m_e c} \tag{15.15}$$

where e and E are the electron charge and electric field of the laser beam; η can be expressed numerically as

$$\eta^2 = 0.4 \left[\frac{I}{10^{18} W/cm^2}\right] \left[\frac{\lambda_L}{1.054\mu m}\right]^2, \tag{15.16}$$

where I is the power intensity of a laser field. η^2 is about 0.4 for a 1 μm laser of 10^{18} W/cm^2.

The requirement of high Compton conversion efficiency and low non linearity contradict each other. We found $\eta^2 \approx 0.3$, if the laser of 1 J /pulse, $3\mu m$ is chosen. Since the nonlinearity in Compton scattering is about $\eta^2\sigma_c$, $\eta^2 = 0.3$ could be a tolerable value.

The details of the Compton scattering, such as the photon spectrum, including multiple electron scattering in a laser pulse, non-linear Compton scattering, must be studied by simulations, and the results must be fed back to the laser-parameter optimization; however, the above discussion is sufficiently good, and the described laser parameter is close to optimum.

Compton Scattering Simulation

As discussed in the previous section, in order to study the details concerning Compton scattering at C.P., we must count on computer simulations. For this purpose, a computer simulation program called CAIN[8] has been developed by a collaboration of Hiroshima, KEK, UCB and SLAC. CAIN is a comprehensive simulation program for linear colliders, and includes laser-electron Compton scattering at C.P. and the beam-beam interaction at I.P.

For Compton scattering at C.P., CAIN is able to treat nonlinear Compton and Breit-Wheeler interactions. Since the cross section of Compton scattering depends on polarization of the lasers and the electrons, the simulation is designed to treat the spin information of lasers and electrons. In the current version of CAIN, although general polarization information is taken into account for a linear interaction, only the helicity eigenstate is treated in a nonlinear interaction.

The photon spectrum simulated by CAIN after a laser-Compton interaction is shown in Figure 15.5 for 250 GeV electrons and 1.054 μm lasers. The combination of the electron and the laser beam is chosen so that the relation $\lambda_e\lambda_L = -1$ holds. This makes a peak in the highest end of the photon spectrum. The high-energy peak is seen around 190 GeV, which is consistent with expected value from $n = 1$ nonlinear Compton scattering,

$$E_\gamma|_{\max x} = \frac{x}{1+\eta^2+x}E_e. \tag{15.17}$$

Photons having an energy greater than Equation 15.17 can be attributed to the contribution from a multiple photon-absorption ($n \geq 2$) effect, and those in the low-energy part of the spectrum are due to multiple Compton scattering of an electron in a laser pulse.

Figure 15.6 is the electron energy distribution after an interaction with the laser pulse. As expected from the interaction rate $k \approx 0.65$, about one third of original electrons are intact. Multiple Compton scattering produces low-energy photons as well as low-energy electrons which could diffract by a large angle due to the beam-beam interaction at the I.P. Since large-angle electrons are a potential source of detector background, a simulation of these electrons is important for designing a $\gamma\gamma$ collider. Figure 15.7 shows the number of Compton scatterings experienced by a singe electron in a laser pulse.

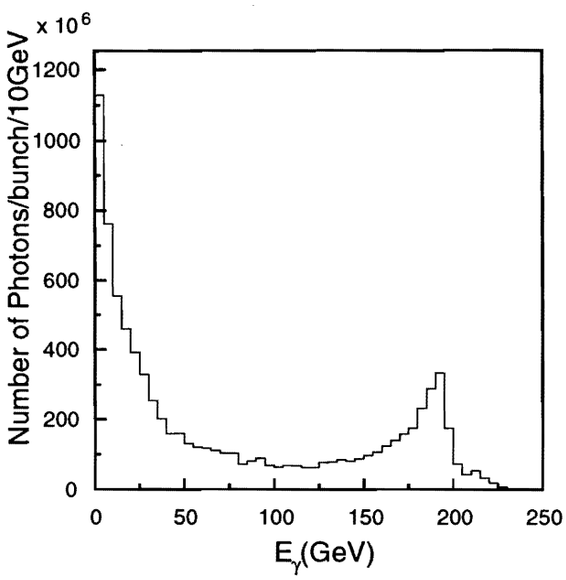

Figure 15.5: *Simulated photon energy distribution by CAIN. The electron energy is 250 GeV and the laser wavelength is 1.054 μm and the polarization of the laser and the electron beam are chosen to make a peak at the energy end of the spectrum.*

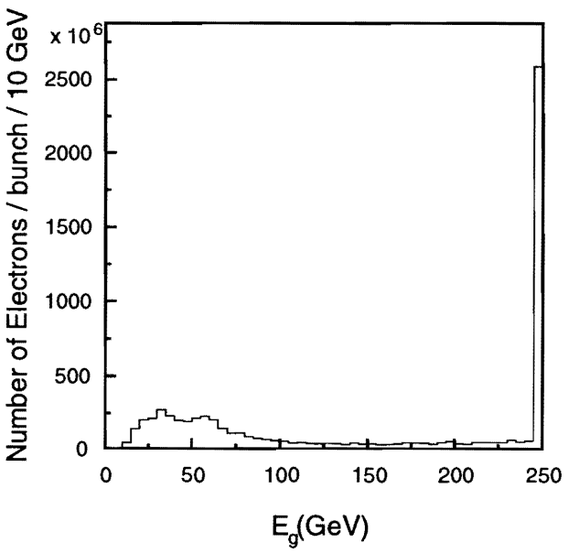

Figure 15.6: *Electron energy spectrum after the Compton interaction point.*

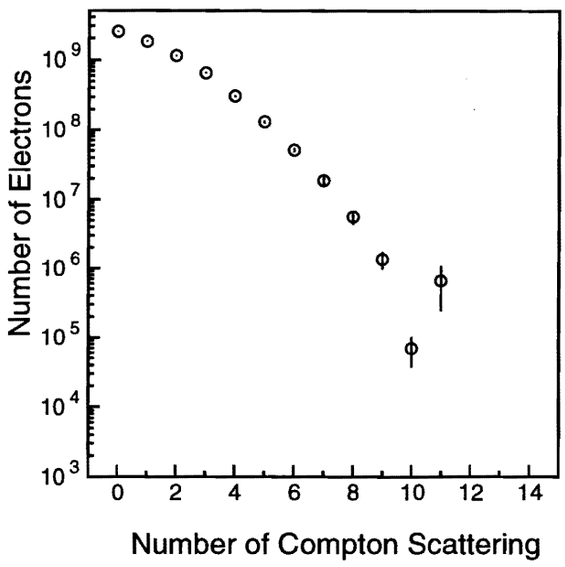

Figure 15.7: *Number of Compton scatterings experienced by an electron in a laser pulse.*

Millions of electrons suffer from more than 10 scatterings in a laser pulse, which may result in an electron energy of a few GeV. In fact, 10 consecutive backward scatterings makes 2 % of the original electron energy[36]. The number of these particles might be on the order of 10^3, which is a very small fraction of number of electrons in a bunch (10^{10}), but is large enough to be a serious background source to detectors. In order to simulate 10^3 out of 10^{10} electrons, CAIN adopts a way to weigh a smaller number of particles [7]. Figure 15.6 was plotted using the weight method, which made it possible to see the contribution of $O(10^2)$ electrons. We found that though the probability of multiple Compton scattering is not small, the probability to produce very low energy electrons of $\leq 2\,\% E_e$ is not a serious cause of additional background to the detectors. The issues concerning the detector background will be discussed in a later section.

15.2.3 Luminosity Calculation

As previously described, the luminosity of $\gamma\gamma$ colliders is approximately 10 % of the e^-e^- geometric luminosity. However, the luminosity value as well as the structure, such as energy dependence, rapidity distribution and angular momentum of the $\gamma\gamma$ system depend on the details of laser-Compton scattering and subsequent beam-beam interactions at the I.P. For a realistic estimation of the luminosity, we used CAIN for calculations.

After a laser-Compton scattering simulation, all particles from C.P. are brought into I.P., and then interact with particles from the opposite beam. During the drift from C.P. to I.P., it may be possible to insert an external magnet to sweep the spent electrons away from the I.P. However, for the case

of small C.P-I.P. distance, it is hard or impossible to insert such an external magnet between C.P. and I.P. In this case, e^-e^- and e-γ as well as $\gamma\gamma$ collisions can occur at the I.P., and the beam-beam interaction at the I.P. changes the luminosity distribution.

In order to simulate these effects, CAIN takes the electron disruption, beamstrahlung, and incoherent and coherent pair production into account as interactions at the I.P. The incoherent and coherent pair productions are sources of low-energy e^+e^- pairs, which will be described in the next section.

The simulated luminosity distributions for 400 GeV $\gamma\gamma$ collider are plotted in Figure 15.8. For this

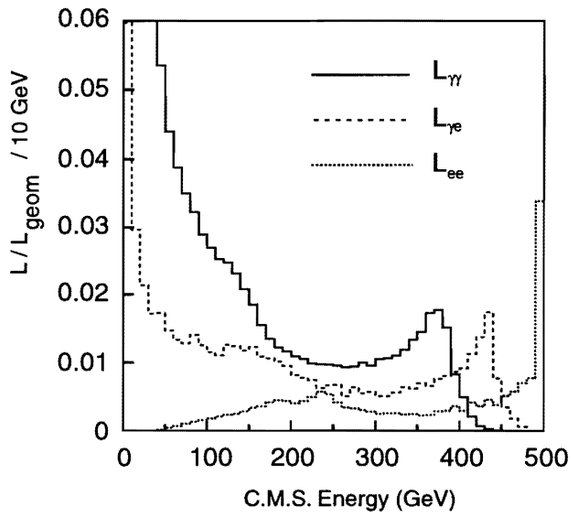

Figure 15.8: *Luminosity distribution simulated by CAIN. The solid, dashed lines are for the $\gamma\gamma$, e-γ and e^-e^- luminosity respectively.*

parameter, we assumed that all particles from C.P. are brought into the I.P. without a sweeper magnet. It is seen that the amounts of e-γ and e^-e^- luminosity are comparable with the $\gamma\gamma$ collisions.

The luminosity for the 120 GeV case is plotted in Figure 15.9 for case (b) and (c) of Table 15.1.

Since the x parameter is smaller (1.86) for case (b) of Table 15.1, luminosity distribution is broader than in case (c). The absolute values of the luminosity are summarized in Table 15.2.

15.2.4 Background

In the reference parameters used for this study, all particles from C.P. are brought to I.P. without using an external sweeping magnet. Under this environment, the interaction region is simpler thanks to non-existence of a magnet in a small area; however, a strong beam-beam interaction at the I.P. could cause a large disruption of spent electrons, the generation of beamstrahlung photons and the pair production of low-energy e^+e^- by incoherent and coherent production.

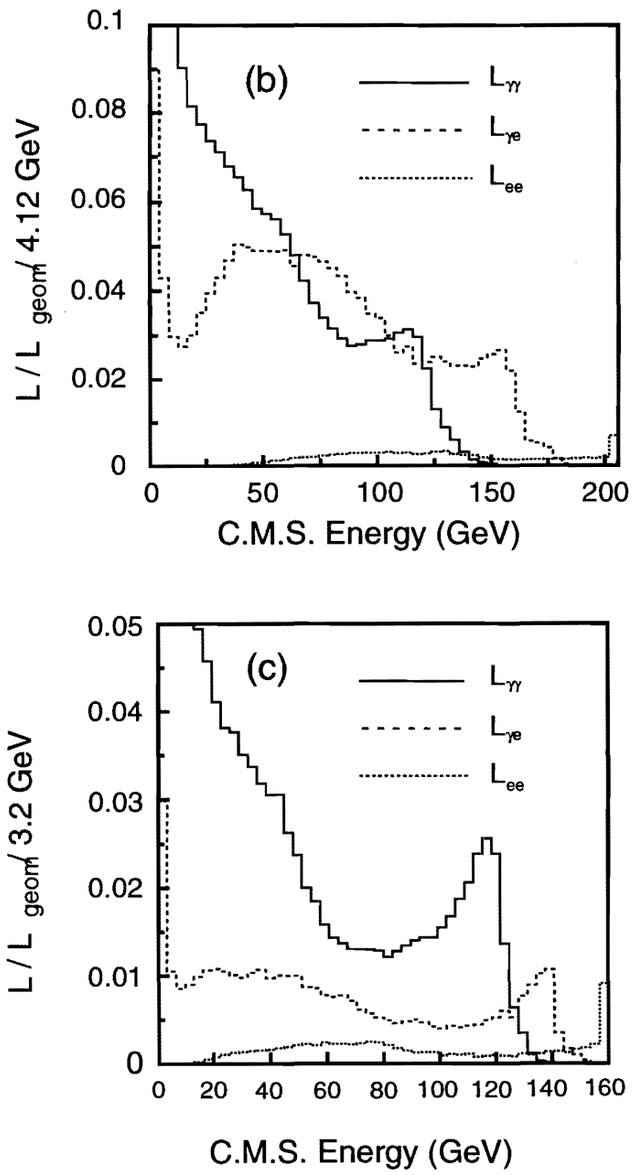

Figure 15.9: *Luminosity distribution simulated by CAIN. The solid, dashed lines are for the $\gamma\gamma$, e-γ and e^-e^- luminosity respectively. The figures with labels b), c) correspond to the parameter sets given in Table 15.1.*

$E_{\rm beam}$ (GeV)	$L_{\gamma\gamma}$ ($z > 0.65$)	$L_{e\gamma}$ ($z > 0.65$)	L_{ee} ($z > 0.65$)
80	1.3 (0.15)	0.36 (0.082)	0.074 (0.029)
103	2.0 (0.12)	0.53 (0.071)	0.088 (0.037)
250	1.3 (0.12)	0.52 (0.12)	0.18 (0.10)

Table 15.2: *Summary of the luminosity of a $\gamma\gamma$ collider*

In order to estimate this beam-beam effect, CAIN was designed to simulate the interaction of electron/positron bunches when they are passing by. The origin of beam-beam interaction part of CAIN is a simulation program developed for e^+e^-colliders, called ABEL[32]. ABEL includes all interactions listed above, except for coherent pair creation, and was incorporated into CAIN.

Figure 15.10 shows the electron disruption angle after, versus the electron energy after the I.P. interactions. The relation between the electron energy and the disruption angles $\langle\theta^d\rangle$ almost agree with

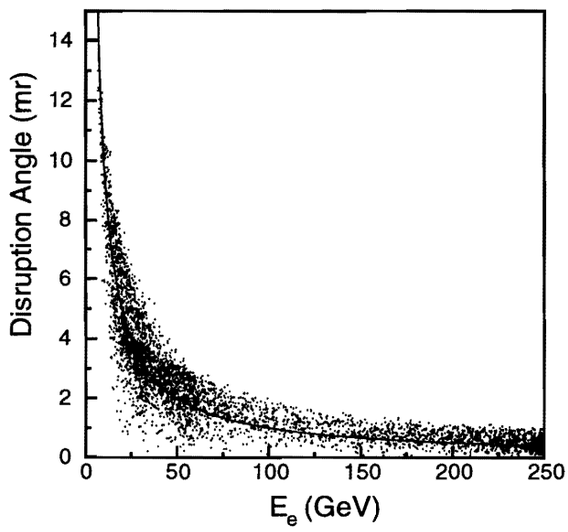

Figure 15.10: *Electron disruption angle after I.P. for the 400 GeV $\gamma\gamma$ parameters. The solid line is an estimation from the disruption parameter (see text).*

the theoretical prediction:

$$\langle\theta^d\rangle \approx \sqrt{\langle\theta_x^d\rangle^2 + \langle\theta_y^d\rangle^2}. \tag{15.18}$$

$$\left\langle\theta_{x/y}^d\right\rangle \approx \frac{0.5 D_{x/y}\sigma_{x/y}}{\sigma_{x/y}} \tag{15.19}$$

where $D_{x/y}$ is the disruption parameter for horizontal (x and vertical (y) direction, defined as

$$D_{x/y} = \frac{2r_e n_b \sigma_z}{\gamma \sigma_{x/y}(\sigma_x + \sigma_x)}. \tag{15.20}$$

Here, r_e is the classical radius of the electron. The largest disruption angle seen in the figure is about 20 mrad, which is small enough not to be a direct background source to the detector. However, the angle is much larger than in the e^+e^-collision case, since the electron energy is almost monochromatic; and to maintain the original energy in e^+e^-colliders, it is necessary to introduce an additional beam crossing angle so as to avoid direct hit of the spent electrons to final quadrupole magnets [36].

Another possible source of background to be considered is low energy e^+e^-pairs produced by incoherent pair production, such as: Breit-Wheeler ($\gamma\gamma \to e^+e^-$), Bethe-Heitler ($\gamma e^\pm \to e^\pm e^+e^-$), and Landau-Lifshitz ($e^+e^- \to e^+e^-e^+e^-$). The contribution of low-energy pairs to the background for vertex detector in an e^+e^-collider was studied in [22]. For the $\gamma\gamma$ collider case, due to a larger e^-e^-geometric luminosity, the effect may be larger than in an e^+e^-collider. The number of hits expected in the vertex detector during each bunch crossing is shown in Figure 15.11 as a function of the distance of the detector from the beam line while keeping the angular coverage of the detector constant.

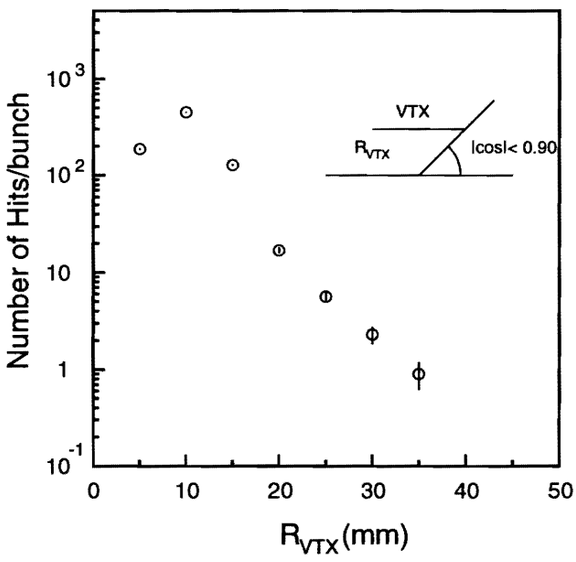

Figure 15.11: *Expected number of background electron hits in the vertex detectors per bunch crossing.*

In the estimation, a magnetic field of 2 T parallel to the beam axis was assumed, and multiple hits by helical tracks were allowed. As can be seen from the figure, the number of hits in each bunch crossing is about 10, corresponding to $O(10^3)$ hits by each pulse train. According to a simulation of Compton and beam-beam interactions, the backgrounds due to direct hits of particles is not serious

to the detectors; however, the effect of secondary interactions must be studied.

15.2.5 Other Issues

In this report we do not intend to cover all of the issues concerning the development of $\gamma\gamma$ colliders, since our activity dose not cover all of them. Among the issues, the development of high-power high-repetition rate laser and related optics is critical for realizing $\gamma\gamma$ colliders. In this section, the status of these issues is briefly summarized. Details concerning the status are described elsewhere [4, 36].

Solid state lasers

As described in the previous section, the laser required for $\gamma\gamma$ colliders has characteristics of: 1 J/pulse, 1 ps width, and 16 kW average power. At the time of this report, no solid state laser could meet this requirement. The status and prospect for the development of solid state lasers for a $\gamma\gamma$ collider can be found in [36]. One of the most promising ways to achieve the performance required for a laser is using Chirped Pulse Amplification (CPA) [30]. By this method, a short-pulse laser is stretched in time by a pair of gratings and amplified to high power; it is then compressed again by another pair of gratings to a short pulse. The concept of CPA is illustrated in Figure 15.12. Since the peak power in lasing material can be reduced by CPA, problems related with high peak powers such as saturation fluence and nonlinear index can be resolved. An example of high peak power laser is ND:Glass laser used in E144 experiment at SLAC[6]. It is $1\mu m$, 1ps 1J , CPA laser and is now operating at 0.5Hz. It should be noted the laser also achieved synchronization with electron bunches within 2ps. The laser meets all requirement except repetition rate which is 4 orders less than for the $\gamma\gamma$ colliders.

For the average power of the laser, the main problem is heating in the laser materials. For example, the Nd:Glass laser adopted in E144 has a low thermal conductivity and thermal shock limit, which prevents us from using it under high-repetition-rate operation. To overcome this problem, a new laser material, such as new glass and Yb:S-FAP, is being developed [12]. In addition, a high-power laser diode for a pumping laser material is required; the current high-power diode laser is 1.45kW[3]. Since the laser wave can be focused down to a μm size, it has to be a diffraction-limited beam. Attention has to be paid to keep the diffraction-limited property during amplification.

As described, the average power for $\gamma\gamma$ colliders is much higher than that of achieved to date. Although it is expected to meet our requirement for the construction of a $\gamma\gamma$ collider, an attempt to reduce the average power is useful. If a laser pulse can be re-used many times, the average power can be drastically reduced. Also, the use of laser pulse stacking mechanism would be useful. This is because the electron beam from the linac, which is operated at a repetition rate of 100 Hz, has up to 85 bunches with a 1.4 ns separation in a single machine pulse.

An idea of multi-pass reflection mirror at the interaction point is discussed in [9, 36]. It comprises a pair of mirrors installed at the Compton interaction point. A laser pulse reflects back and forth between the two mirrors, and meets with electron bunches many times at the Compton interaction

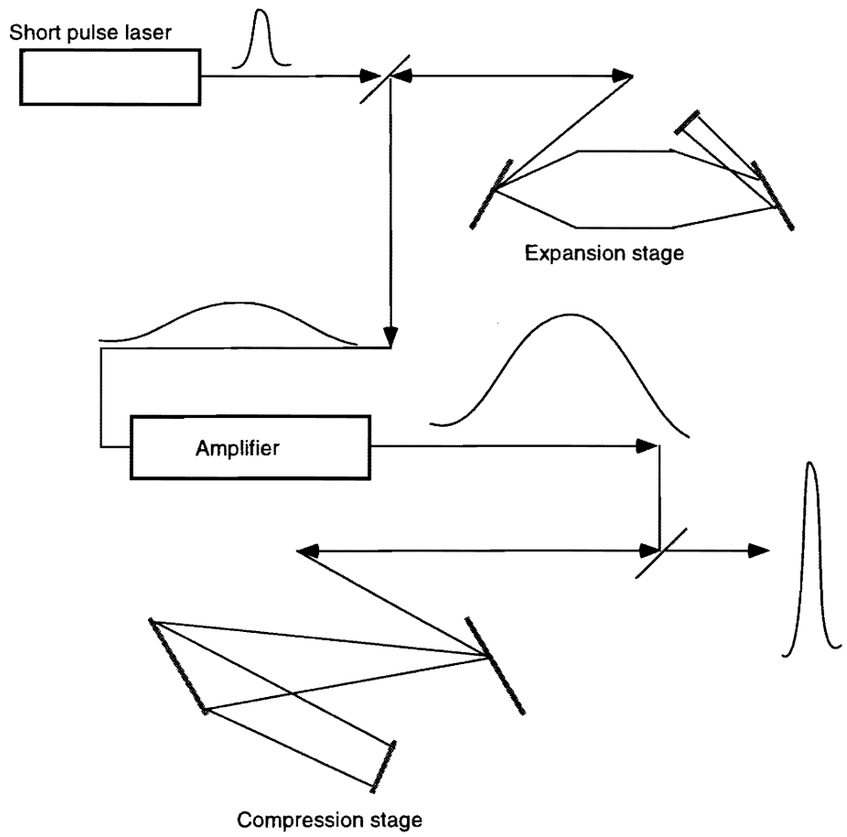

Figure 15.12: *Concept of chirped pulse amplification*

point. In this case, the mirror system can not be large, because it has to be placed into the small area around the interaction pint. Due to the smallness of the system, the damage threshold of the devise is critical. Particularly, the damage on optical devises due to pulse trains (repetition at 100 Hz of 1 J pulse with ns separation) is an open problem. Keeping a small focal point of the laser during reflection is another problem. Due to the build-up of aberration during mirror reflections, the laser spot size is getting larger, which limits the number of reflections in a mirror system.

Another idea concerning a pulse-recycling system is regenerative ring scheme, which was described in [12, 36]. Laser pulses having a relatively low repetition rate are accumulated in the ring cavity, as illustrated in Figure 15.13. In this system, laser pulses of low repetition rate are stacked in to the ring

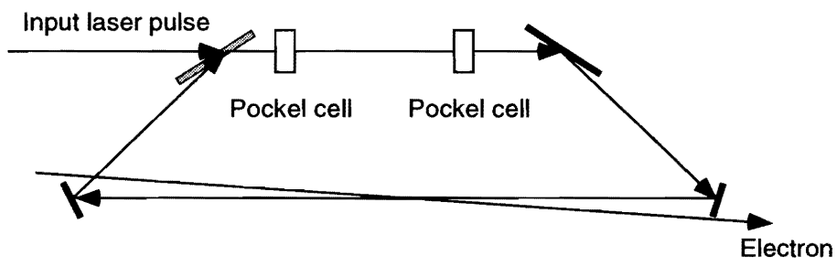

Figure 15.13: *Concept of ring regenerative cavity.*

system, and brought to the Compton interaction point. The quality of the laser can be maintained by utilizing a relay image or internal cavity system.

Free Electron Laser

A Free Electron Laser(FEL) is another candidate for the laser for $\gamma\gamma$ colliders. For higher energy $\gamma\gamma$ colliders, such as 1 TeV center of energy, the laser wave length is about 2 μm for $x \approx 4.8$. Since there are no suitable lasing materials in solid state lasers in this infrared range, it is necessary to apply FELs. The application of FEL for $\gamma\gamma$ colliders is discussed in [4, 36]. Since FEL does not have lasing materials, it does not suffer from any thermal problem, as solid state lasers. However, in order to obtain a high-power laser output, beam current in an electron linac is on the order of kA, and energy is about 100 MeV.

For example, the FEL discussed in [16] has a 150 MeV, 4 kA electron beam which generate 100 GW, 4 μm laser pulse. In [16], the system consist of 10 units of 100 GW FELs, as illustrated in Figure 15.14. Another example is described in [36], which is for 2 J, 1 μm laser pulses. In this example, a CPA is applied to obtain a sufficient gain in the amplification process. The current and energy of the electron linac is assumed to be 1 kA and 100 MeV respectively. For both cases, the energy spread of the electron beam must be of the order of 0.1 % to maintain a sufficient gain in the amplification process.

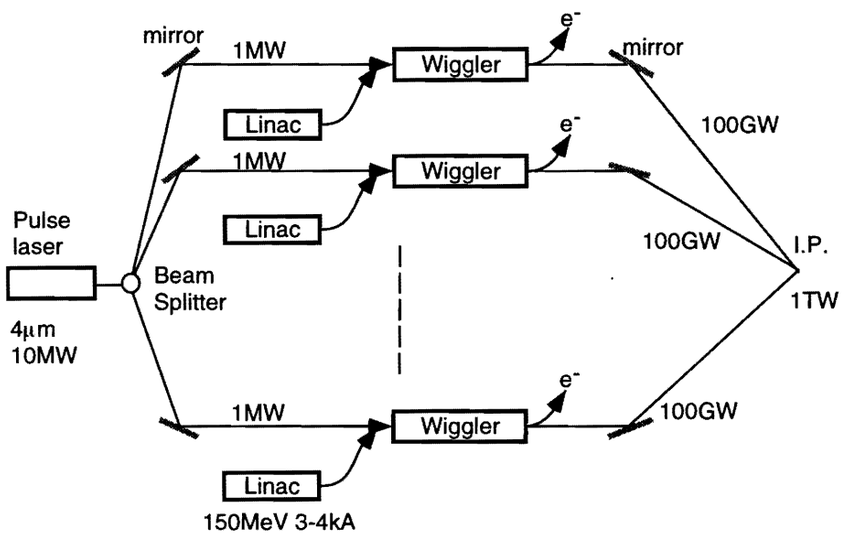

Figure 15.14: *Concept of the FEL system, discussed in [16]*

15.3 Summary and Outlook

In this report, we have described the status of the R&D work for a $\gamma\gamma$ collider. During the past several years, efforts have been made to figure out the overall features and problems of $\gamma\gamma$ colliders. In particular, there has been progress in our understanding of the beam-beam interaction issues, including the laser-electron interaction and such properties as the luminosity distribution and beam background.

On the other hand there are many items to be studied for a realistic design of $\gamma\gamma$ collider, such as:

- Development of high-average power lasers
- Laser Optics for high-power density, including techniques for laser-pulse recycling.
- Development of a magnet system for spent-electron sweep out.
- Design of an interaction region complex which includes all of the items listed above.

Although there are ideas and initial designs for all of the items described in [4, 36], the optimization of the design and the construction of prototypes of subsystems have not yet been performed.

For the further development of R&D studies, it is necessary to make prototype designs of the interaction region while taking into account the beam-beam- and laser-related issues. To carry out the

R&D program, it is necessary to extend the collaboration so as to include laser experts, accelerator physicists and high energy physicists.

References for Chapter 15

[1] K. Abe, et.al., *Phys. Rev. Lett.* A355 (1995)

[2] G. Bélanger and G. Couture, *Phys. Rev.* **D49** (1994) 5720.

[3] R. Beach et. al., *Conf. on Lasers and Electro-optics*, Anaheim,CA (1994)

[4] *Proc. of Workshop on Gamma-Gamma Colliders*, Berkeley, CA, USA, 1994 published in *Nucl. Instr. Meth.* A355 (1995).

[5] M. Baillargeon, G. Belanger, F. Boudjema, ENSLAPP-A-473/94.

[6] C. Bula et.al., it Study of QED at Critical Field Strength at SLAC, E-144 proposal (1992)

[7] P. Chen, T. Ohgaki, A. Spitkovsky, T. Takahashi, K. Yokoya, SLAC-PUB-7426, HUPD-9707, March 1997.

[8] P. Chen, G. Horton-Smith, T. Ohgaki, A.W. Weidemann, K. Yokoya, *Nucl. Instr. Meth.* **A335** (1995) 107.

[9] P. Chen, D. Bullock, D. Yu, *Nucl. Instr. Meth.* **A335** (1995) 130.

[10] S.Y. Choi and K. Hagiwara, *Phys. Lett.* **B359** (1995) 369.

[11] S.Y. Choi, K. Hagiwara and M.S. Baek, *Phys. Rev.* **D54** (1996) 6703.

[12] C. E. Clayton, N. M. Kurnit and D. D. Meyerhofer, *Nucl. Instr. Meth* **355** (1995) 121

[13] I. Ginzburg, G. Kotkin, V. Serbo, V. Telnov, *Pizma ZhETF* 34 (1981) 514; *JETP Lett.* 34 (1982) 491; *Prep. INP* 81-50, Novosibirsk.

[14] I. Ginzburg, G. Kotkin, V. Serbo, V. Telnov, *Nucl. Instr. Meth.* 205 (1983) 47; *Prep. INP* 81-92, Novosibirsk.

[15] I. Ginzburg, G. Kotkin, V. Serbo, V. Telnov, *Nucl. Instr. Meth.* 219 (1984) 5.

[16] S. Hiramatsu, S. Hashimoto and Y. Ishida, *Nucl. Instr. Meth* **355** (1995) 133

[17] A. Goto and T. Kon, *Europhys. Lett.* **19** (1992) 575: T. Kon and A. Goto, *Phys. Lett.* **B295** (1992) 324.

[18] B. Grazadkowski and J.F. Gunion, *Phys. Lett.* **B291** (1992) 361.

[19] J.F. Gunion and J.G. Kelly, *Phys. Lett.* **B333** (1994) 110.

[20] R. Hollebeek, *Nucl. Instr. Meth.* **184** (1981) 333

[21] *Proc. of INS Workshop 'Physics of* e^+e^-, *e-*γ , *and* $\gamma\gamma$ *collisions at Linear Accelerators'* Tokyo, Japan, 1994 published in INS-J-181 (1995).

[22] *JLC-I* KEK-Report 92-16 (1992).

[23] JLC design report in preparation.

[24] *Proc. Physics and Experiment with Linear Colliders* Moriola Appi. World Scientific 1996.

[25] T. Ohgaki and T. Takahashi *Nucl. Instr. Meth.* **A373** (1996) 185

[26] T. Kon, I. Ito and Y. Chikashige, *Phys. Lett.* **B287** (1992) 277.

[27] M. Krämer, J. Kühn, M.L. Stong and P.M. Zerwas, *Z. Phys.* **C64** (1994) 21.

[28] T. Ohgaki, T. Takahashi and I. Watanabe, in preparation.

[29] M. Spira, in Proceedings of AIHENP '96 Workshop, Lausanne, Switzerland, September 1996.

[30] D. Strickland and G. Mourou, *Opt. Comm.* **56** (1985) 219, P. Maine, et.al., *IEEEJ. Quantum Electron.* **QE-24** (1988) 398

[31] T. Takahashi *Proc. of Workshop on Physics and Experiments with Linear colliders* World Scientific (1996) 681

[32] T. Tauchi, K. Yokoya and P. Chen, *Part. Acc.* 41 (1993) 29.

[33] V. Telnov, *Nucl. Instr. Meth* A294 (1990) 72.

[34] V. Telnov, *Proc. of Workshop on Gamma-Gamma Colliders*, Berkeley, CA, USA, 1994 published in *Nucl. Instr. Meth.* A355 (1995) 3.

[35] I. Watanabe, in *Proc. of Workshop on Physics and Experiments with Linear Colliders*, Morioka-Appi, Iwate, Japan, Sep. 8–12, 1995, eds. A. Miyamoto, Y. Fujii, T. Matsui and S. Iwata, World Scientific (1996), pp. 689.

[36] *Zeroth-Order Design Report for the Next Linear Colliders* SLAC-474 (1996).

Authors of Chapter 15

- Tohru Takahashi
- Ichita Endo
- T. Ohgaki
- K. Matsukado
- T. Kon

- I. Watanabe
- T. Takeshita
- N. Matsuda
- Toshiaki Tauchi
- Kaoru Yokoya

CHAPTER 16

Instrumentation

Contents

16.1 Introduction

Depending on the requirements during accelerator operation and beam tuning, a huge number of various beam parameters need to be measured at a linear collider. The fundamental quantities are the beam position (X, Y and Z), its size (σ_x, σ_y, and σ_z) and the intensity (N_e). Most other parameters can be derived from those fundamental quantities by using a variety of techniques. In some cases these quantities must be measured separately for individual bunches in a bunch train. In other cases, this is not required; that is, measuring the parameters that are averaged over a bunch train is sufficient.

In the past several years the development of beam instrumentation for linear colliders has been conducted in close association with the operation of existing accelerators and the construction of new test facilities. The basic direction of development is to obtain high resolution, high precision and resolving power in multi-bunch beam operations. Some new techniques and designs of beam instrumentation have been developed by the research staff from KEK and their collaborators. The details of these developments are summarized in this Chapter.

16.2 Beam Position Monitors (BPM)

16.2.1 Transverse Position

The transverse positions of a beam are most typically measured with strip-line BPMs (Beam Position Monitors), button BPMs and the microwave cavity BPMs. With these monitors the positions of individual bunches in the bunch train can be separately measured by using a window gate in front of the processing circuits. However, in most cases, only the average signal is needed for the beam orbit control. Strip line BPMs are frequently used in beam transport lines and linacs, because a good resolution is available with low-frequency electronics. The button BPMs are typically used in the damping ring because of its low coupling impedance with the beam. The microwave-cavity BPM is a relatively new technology. At linear colliders they are considered to be promising for use in conjunction with the accelerating structure, because they have excellent performance for a precise center definition of the structure.

FFTB Strip Line BPM[1]

The strip-line beam position monitors have been widely used in beam transport-lines and linear accelerators. Examples of development includes that at the FFTB[2] and ATF Linac[3].

In FFTB, a BPM is directly installed inside the quadrupole bore aperture, and is fixed together with the quadrupole magnet, as shown in Figure 16.1. Pickup electrodes were placed between the pole pieces, utilizing the free space within the quadrupole magnet. The length of the strip line was determined by the available space inside the bores of the quadrupole magnets. As a result, 457.2 mm (18") was chosen for its length. One end of each strip is shorted to the chamber wall.

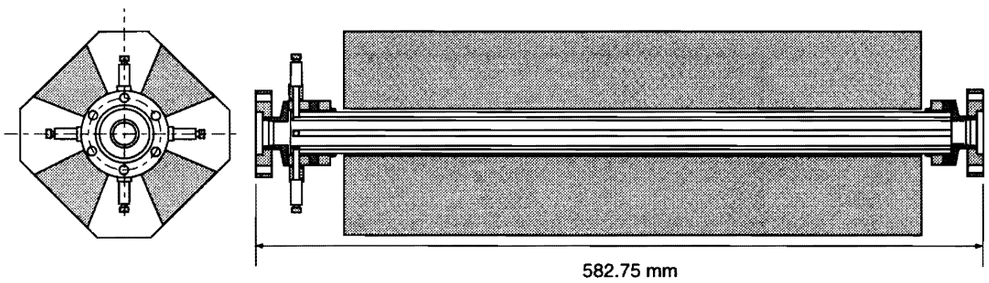

Figure 16.1: *FFTB BPM chamber installation into the quadrupole magnet.*

Figure 16.2 shows a cross section of the monitor. The vacuum chamber is made of extruded aluminum. It has four hyperbolic surfaces to fit inside the quadrupole pole tips and to be attached to them. The extrusion aperture was chosen to accommodate a beam stay clearance of 10σ. The transverse dimensions of the electrode were determined using the code "POISSON" to give a characteristic impedance of $50\,\Omega$.

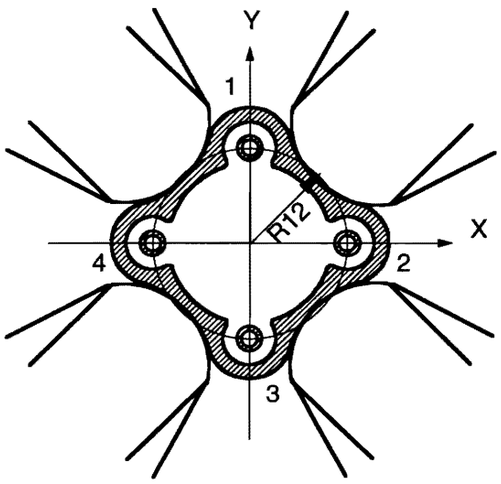

Figure 16.2: *Cross-sectional view of the FFTB BPM.*

The calibration of the electrical center to the magnetic center was performed by using the stretched-wire technique at the calibration stand. A singing-wire method has been developed to determine the

magnetic center. There, pulse signals are applied to the wire, and the wire position is electrically measured by detecting the induced signals on the BPM electrodes. Figure 16.3 shows the distribution of the measured offset of BPM electrical centers according to this calibration. After a calibration measurement, the quadrupole magnets with BPM are brought together into the FFTB tunnel.

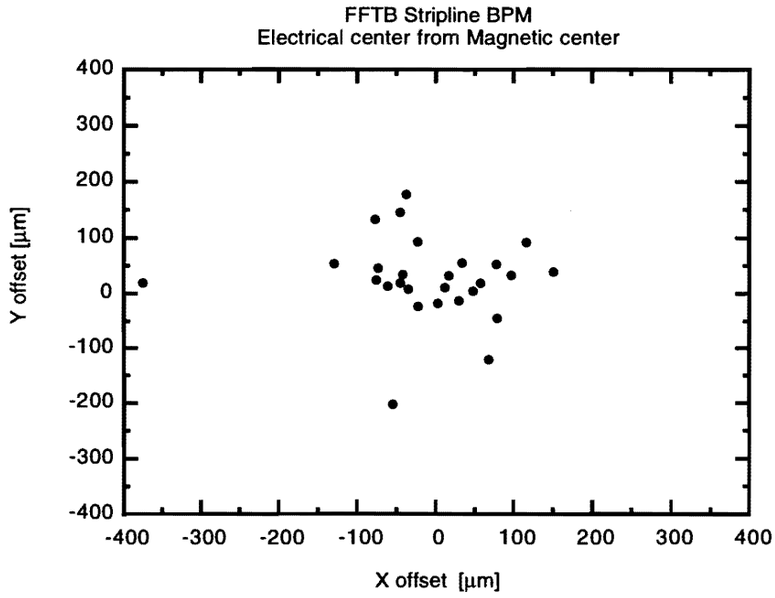

Figure 16.3: *Distribution of the electrical center offset relative to the magnetic center for the FFTB BPM.*

This design and installation method of FFTB BPMs has an advantage that it offers good precision in the relative alignment between the BPM electrical centers and quadrupole magnetic centers. A BPM will measure the beam position at the longitudinal center of each quadrupole magnet. Generally, long strip-line electrodes are preferred in the light of enhancing the low-frequency components of the signals for improving the S/N ratio in the low-frequency regime. However, the installation and support of longer strip-lines can become problematic, because of difficulties with mechanical fittings and sagging of the strip-lines.

A signal-processing electronics unit has two identical channels for two pickup electrodes. One unit of the electronics package measures one coordinate (x or y) of the beam position. It consists of a pulse-stretcher amplifier (called Head Amp), track-and-hold (T&H), digitization (NiTNH) and a pulse generator for electronics calibration (TPG). The signals are fed through long cables into the Head Amp, then amplified and stretched by Gaussian low-pass filters to obtain a good signal-to-noise ratio (S/N). The outputs of the Head Amp are given to the input of the NiTNH through matched RG-223/u cables. The input signals are tracked and held at their first extreme by the self-generated trigger inside NiTNH. After bing held, the signals are digitized by 16-bit ADCs, and are latched until

the read operation is completed.

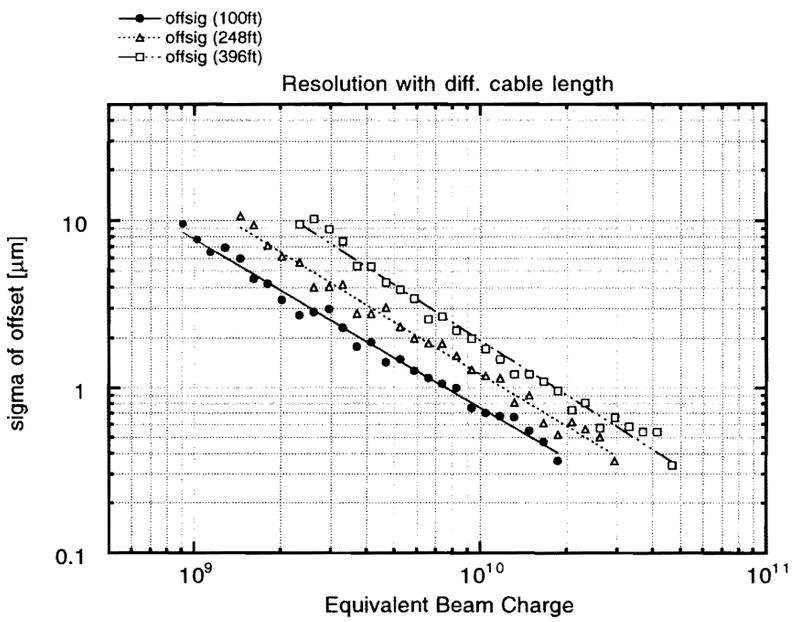

Figure 16.4: *Estimated resolution for the FFTB BPM.*

The estimated resolution is shown in Figure 16.4, which is obtained by running the electronics with a test pulser. Pedestal levels are measured during calibration in advance. Those pedestal values are subtracted from the readings to remove the electrical offset. The beam position will be calculated by

$$X' = k \times \frac{V_2 - G_x V_4}{V_2 + G_x V_4}, \tag{16.1}$$

$$Y' = k \times \frac{V_1 - G_y V_3}{V_1 + G_y V_3}, \tag{16.2}$$

where k is a geometrical coefficient. The G_x and G_y are the gain ratios V_{2c}/V_{4c} and V_{1c}/V_{3c} for the x and y channels, respectively. They are to be obtained by calibration in advance. The deviation in the gain ratio from one would cause a position offset, as shown in Figure 16.5. Since the electronics is adjusted to have a very flat gain ratio with the amplitude, the gain ratios are taken as being either a constant or a linear function of the amplitude summation ($V_2 + V_4$ or $V_1 + V_3$). These calculated positions X' and Y' are only a first-order approximation. To obtain $1\,\mu$ precision, we should go to the next higher order correction. That is, using the other geometrical coefficients k' and k",

$$X = X' + k'X'(X'^2 - Y'^2) - k''(4X'^3 - 3(X'^2 + Y'^2)X'), \tag{16.3}$$

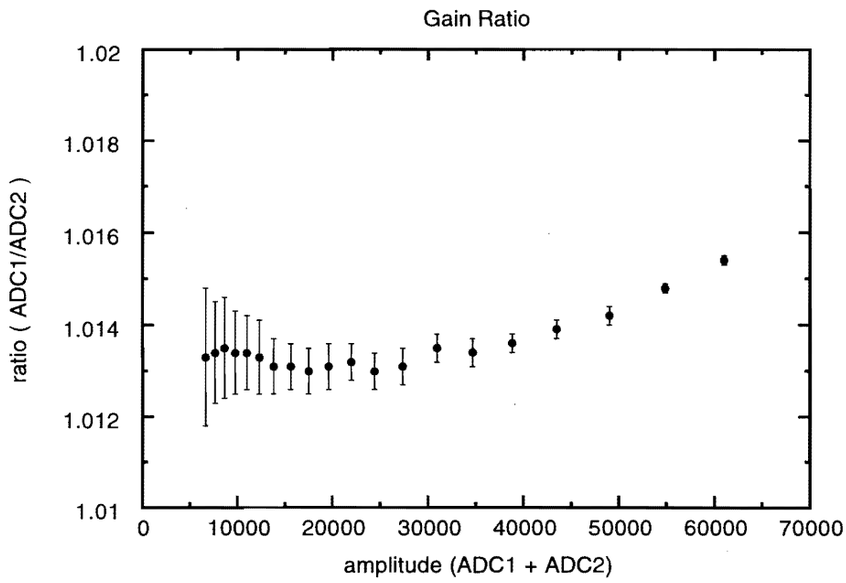

Figure 16.5: *Example of the electronics offset for the FFTB BPM.*

$$Y = Y' + k'Y'(Y'^2 - X'^2) - k''(4Y'^3 - 3(X'^2 + Y'^2)Y'). \tag{16.4}$$

In the case of a simple cylindrical BPM, the geometrical coefficients k, k' and k'' can be written analytically as

$$k = \frac{r/2}{\sin\Delta\varphi/\Delta\varphi}, \tag{16.5}$$

$$k' = \frac{\sin 2\Delta\varphi/\Delta\varphi}{r^2}, \tag{16.6}$$

$$k'' = \frac{\sin 3\Delta\varphi/3\Delta\varphi}{(\sin\Delta\varphi/\Delta\varphi)r^2}, \tag{16.7}$$

where r is the location of the pickup electrode from the center and D_j is the half-opening angle of the pickup electrode from the center. This formula gives a good approximation with less than a 0.01 μm error for a 500 μm off-centered beam, and less than a 3 μm error for a 2 mm off-centered beam.

ATF Strip-Line BPM[4]

The strip-line BPM of ATF Linac has 80 mm-long strips, which are shorted on one end to the chamber wall (Figure 16.6). The mechanical design of the strip line is simple compared with the FFTB BPM. The short strip that extends from the chamber will make the strip support more rigid and fabrication more easy. To achieve a 1 μm resolution, the inner diameter of the strip-line was selected as being

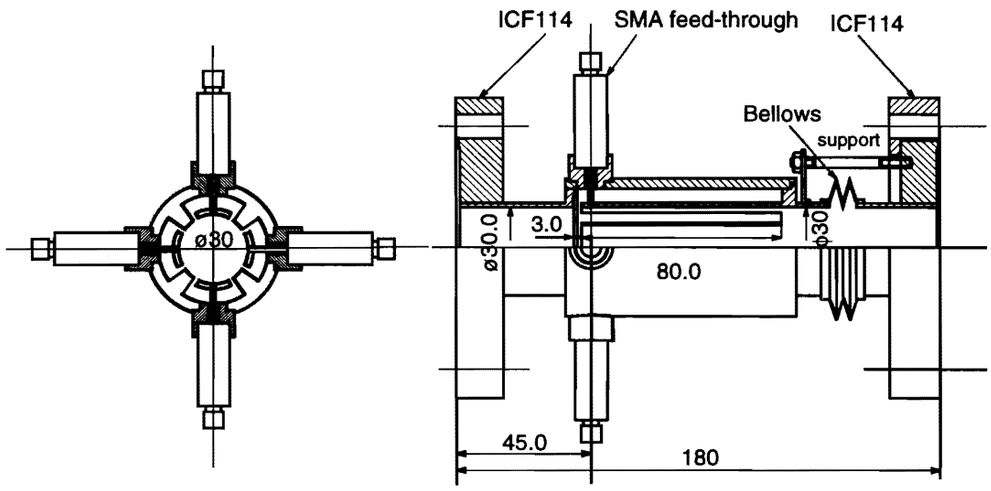

Figure 16.6: *Stripline BPM of the ATF Linac.*

small as possible. In ATF, a 30 mm diameter was selected. The width of the strip was designed to be as wide as possible in order to obtain a larger beam signal. The electrode transverse dimensions were determined using the code "POISSON" to give a 50 Ω characteristic impedance (Figure 16.7).

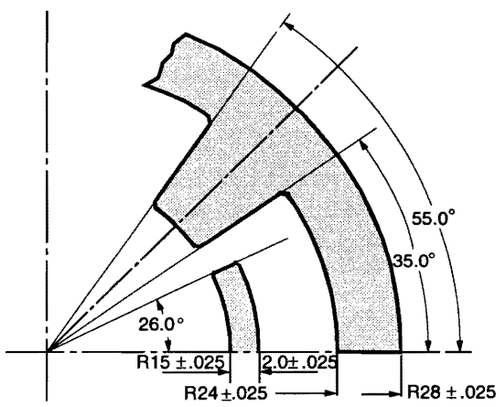

Figure 16.7: *Cross-section of ATF Stripline BPM.*

The strip-line pulses are 0.5 ns apart, which corresponds to twice the length of the strip-line. Since the bunch length is a few millimeters, we can treat the induced signal as impulses. The expected signal wave form is calculated by an approximation formula[5] which estimates the impulse response for long dispersive cables. The impulse areas are estimated using the charge in the bunch and the beam-coupling coefficient to the pickup electrode. A geometrical coupling coefficient of 0.167 is used.

Four RG-223/u coaxial cables are used in one BPM for signal transmission from the strip line pickups to the electronics front end. The four cables have identical lengths matched to within 100 ps. The unit lengths vary from 30 m to 50 m, depending on the distances from the electronics hut. Since the electronics works at about 50 MHz, signal reduction by the coaxial cables is expected to be -3.2 dB to -5.5 dB at that frequency.

The processing electronics system consists of a head amp and a track-hold circuit, which is based on the design that is derived from the FFTB BPM electronics. The block diagram of the electronics is shown in Figure 16.8. Two sets of amplifying gains are provided for processing single-bunch signals as well as multi-bunch signals. Signals under multi-bunch operation have an enhanced low-frequency component than in the case of single-bunch operation. Therefore, a 17 db gain reduction in the head amp is introduced, for processing multi-bunch signals. This gain reduction is achieved by bypassing the front rf amplifier produce a 2-times S/N enhancement.

Figure 16.9 shows an estimated resolution as obtained by using a test pulser in the laboratory. About a 0.7μm resolution for a 2×10^{10} single-bunch beam, and 0.35 μm for a 20 multi-bunch beam are obtained in the case of 50 m RG-223/u cables.

The calibration of the BPM electrical center offset from the mechanical center of the BPM chamber was obtained using stretching wires[6]. The wire was 50 μm gold-plated tungsten, which was stretched and measured regarding its absolute position by a 3-dimensional coordinate machine to an accuracy of 12 μm. After the measurement, a pulse, which simulated a beam, was fed into the wire. The position detected by the electronics represents an offset. Figure 16.10 shows the distribution of the electrical offset of several ATF strip line BPMs. These offsets are subtracted by the position measurement in the beam operation.

In the ATF linac, BPM electronics is installed using a multiplexing method as an inexpensive installation [7]. A head amp is prepared for each BPM chamber. The multiplexer is used for the output signal of the head amp for low-frequency signal processing. One set of the track-and-hold circuit is used for six BPMs, as shown in Figure 16.11. It takes a few 10 seconds to obtain the entire beam orbit in the linac. It is noted, however, that a full set of electronics is quite necessary for a real-life linear collider.

Multibunch Position Detection by the ATF Strip Line BPM[8]

The strip line BPM of ATF Linac has 80 mm length strips which are shorted on one end to the chamber wall. The signal from the strip line consists of two pulses which are of opposite polarity and 0.533 ns separation. This signal is slowed by the slow cable response, and has a long tail after a long dispersive co-axial cable. In order to resolve the position of each bunch out of 20 multi-bunch, of the ATF beam, which has a 2.8 ns bunch separation, the tails of the signal should not overlap each other.

The short co-axial cable for signal transmission is necessary for multi-bunch position detection. Furthermore, the fast sample-hold circuit is also necessary to digitize the signal peak for position detection. In order to realize a multi-bunch BPM, an 80 mm strip-line BPM, 10 m of RG-213/u cable, an 850 MHz

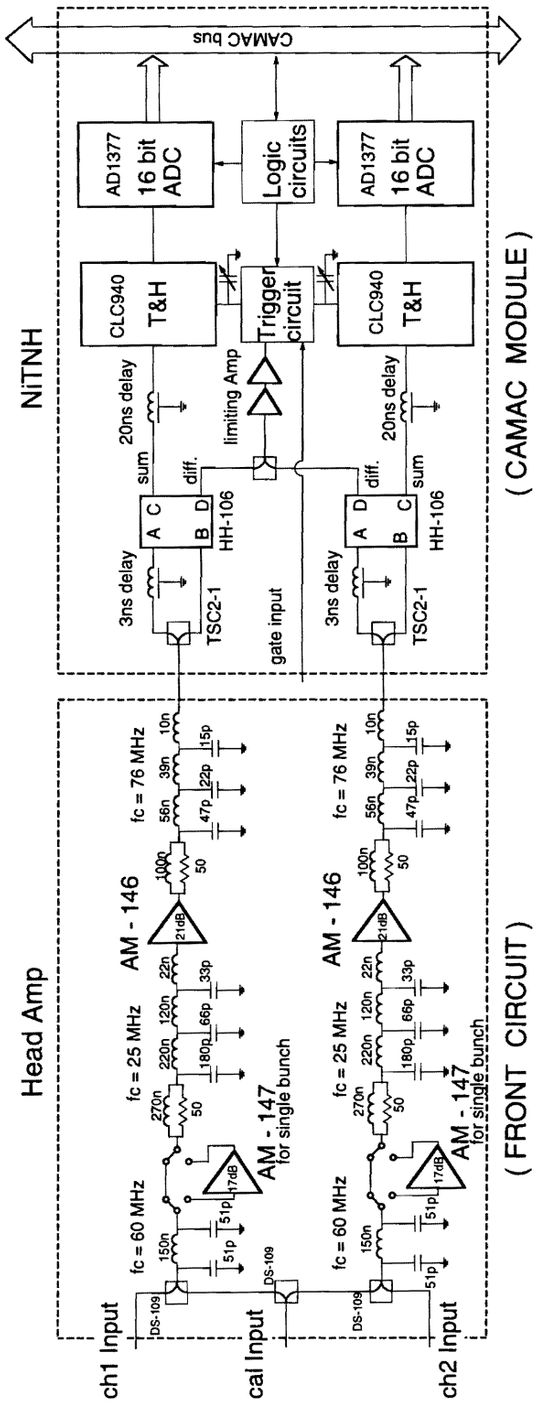

Figure 16.8: *Block Diagram of the processing electronics for the strip-line BPM.*

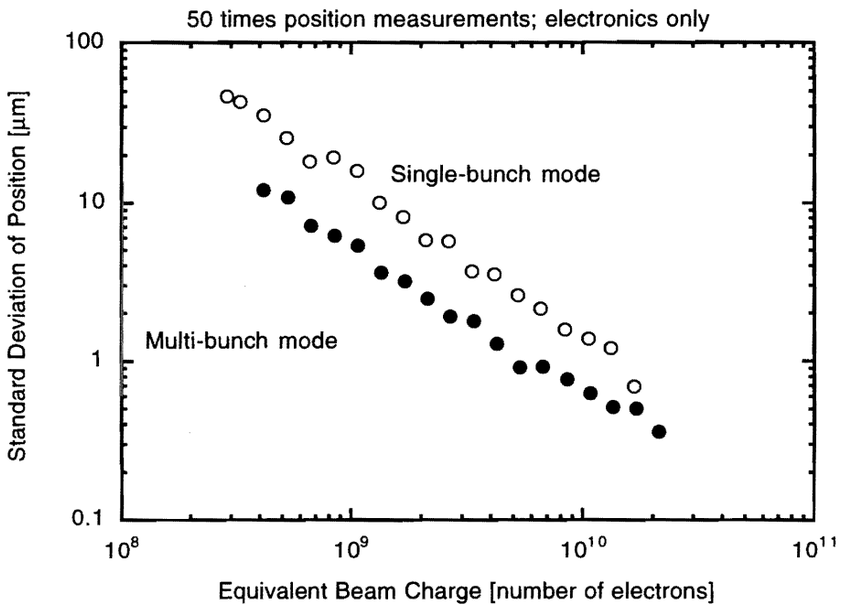

Figure 16.9: *Resolution estimation for ATF strip-line BPM.*

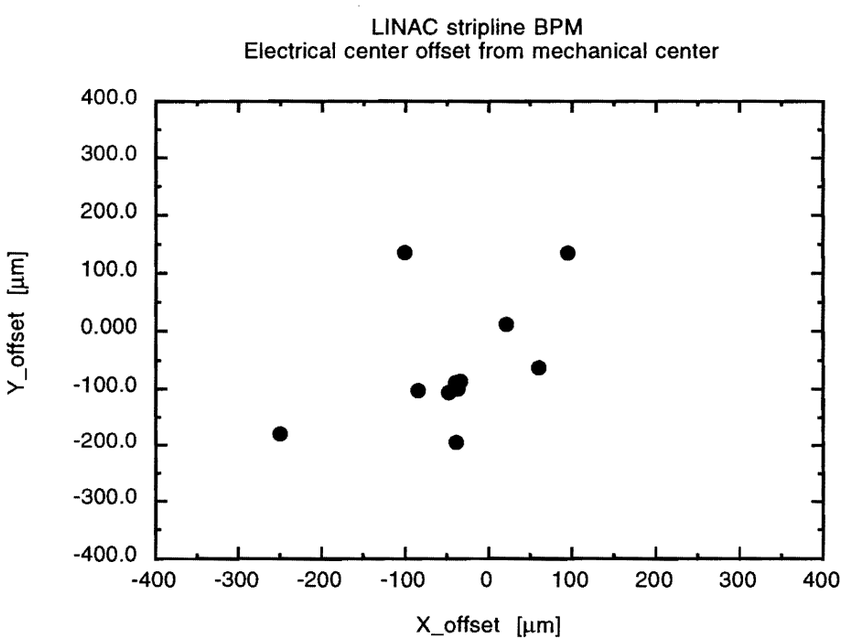

Figure 16.10: *Electrical offset distribution of ATF strip-line BPM chamber*

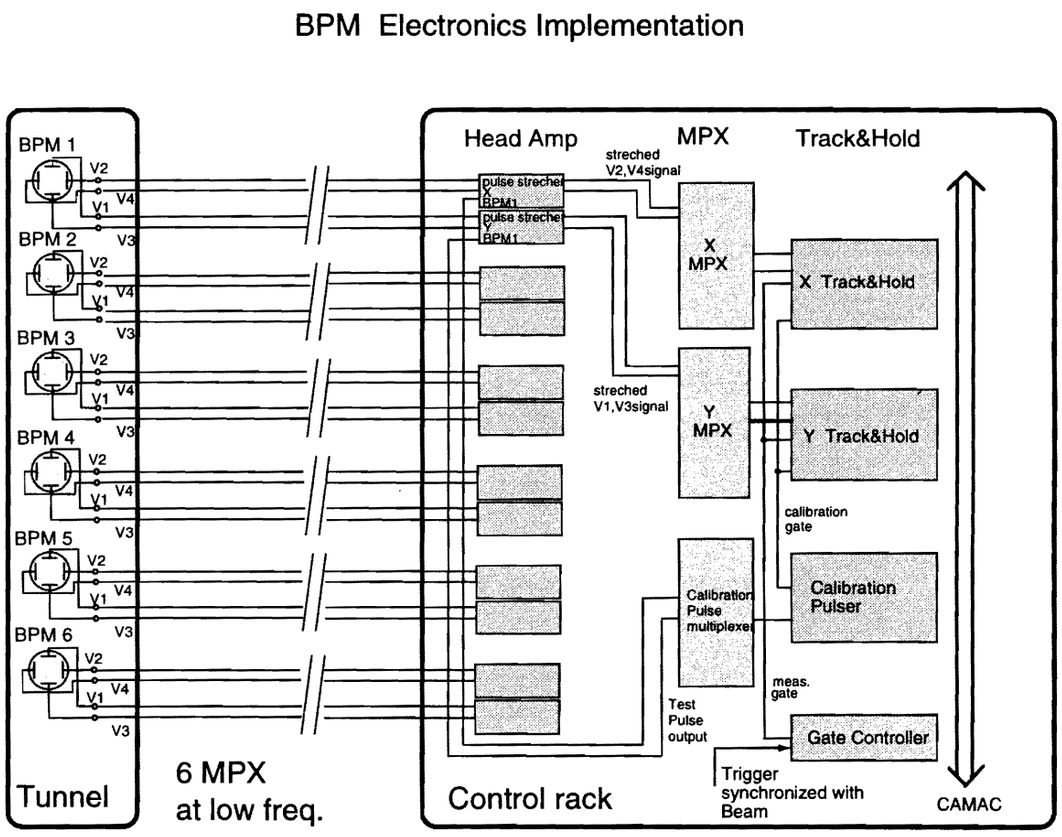

Figure 16.11: *Multiplexing electronics for ATF Linac commissioning.*

low-pass filter for signal stretching and 1 GHz band width of a sample hold circuit were used in the ATF beam experiment, as shown in Figure 16.12.

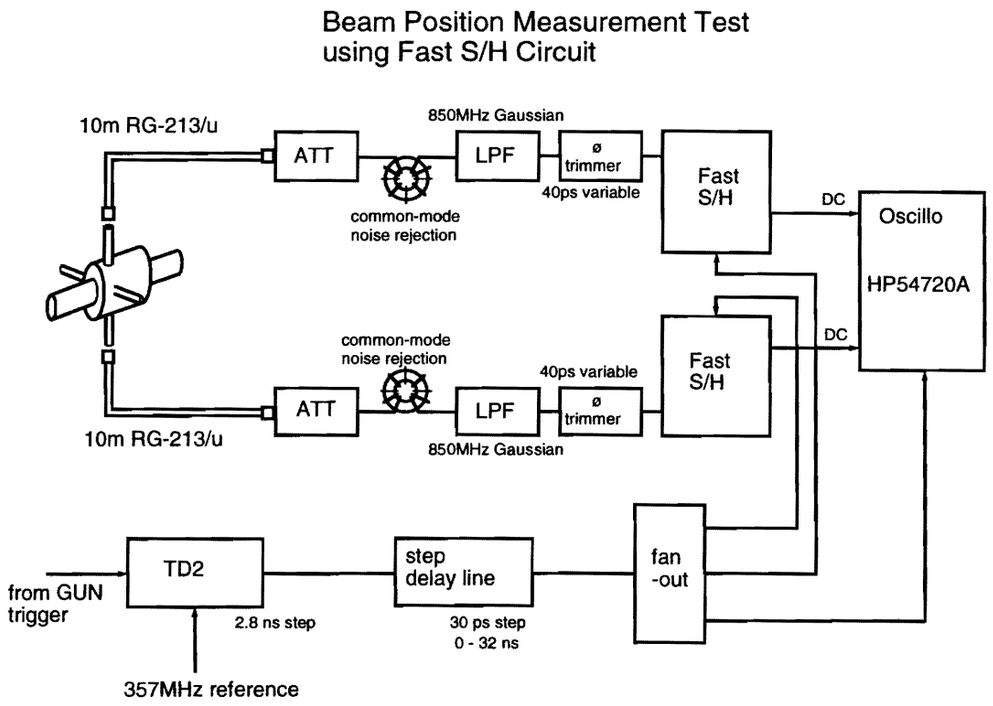

Figure 16.12: *Experimental setup of a multibunch BPM test.*

The sample-hold circuit shown in Figure 16.13 has 400 ps strobe gate for fast sampling which follows a 400 ns slow strobe gate of signal holding. The circuit, therefore, works at a slow sampling rate of about 1 kHz. The position measurement by this circuit is done for one bunch in a train at one time. The resolution was estimated from the signal-to-noise ratio; in the case of the ATF strip line BPM, it would be 0.8 μm without sampling trigger jitters and 6.9 μm with ATF trigger jitters. The signal tail mixture into the next following bunch signal was estimated to be about 2 % in this setup. An example of multi-bunch beam-position measurement is shown in Figure 16.14; it was performed at the ATF linac pre-injector.

ATF Button BPM[9]

The button beam position monitors are used for the ATF Damping Ring, because of the limited space and the relatively low parasitic mode loss. To avoid an instability due to parasitic mode loss, the longitudinal impedance must be less than 0.2 Ω. The impedance of the button BPM was calculated and compared to that of the strip line. The result showed that the impedance, which was 8 mΩ for

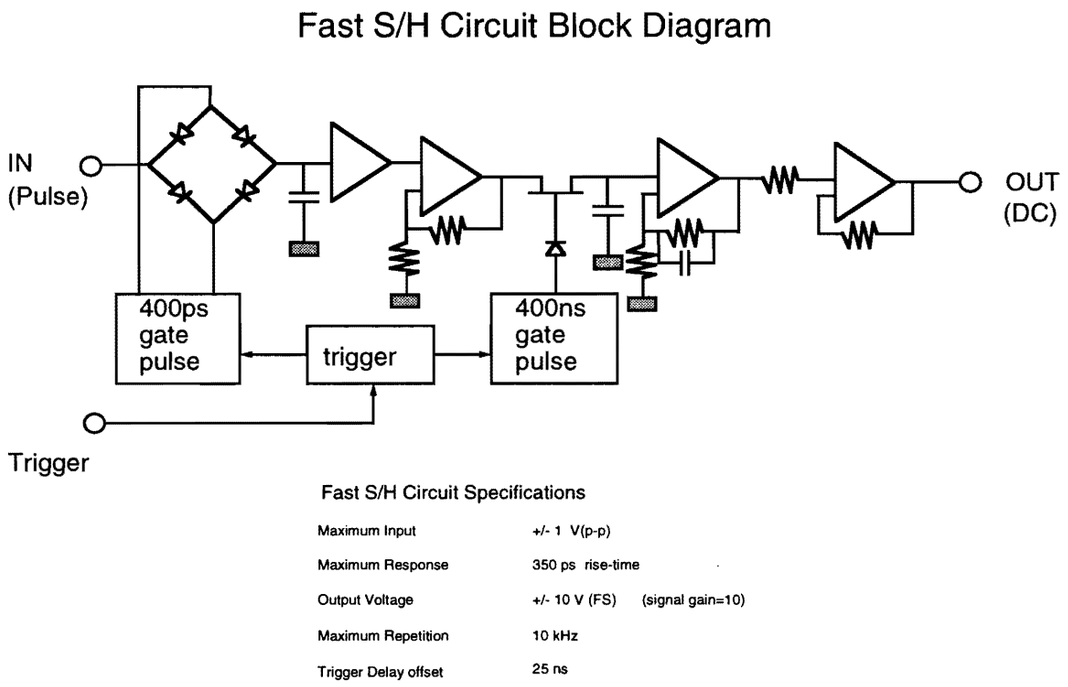

Figure 16.13: *Circuit Diagram of the fast S/H for the multibunch BPM.*

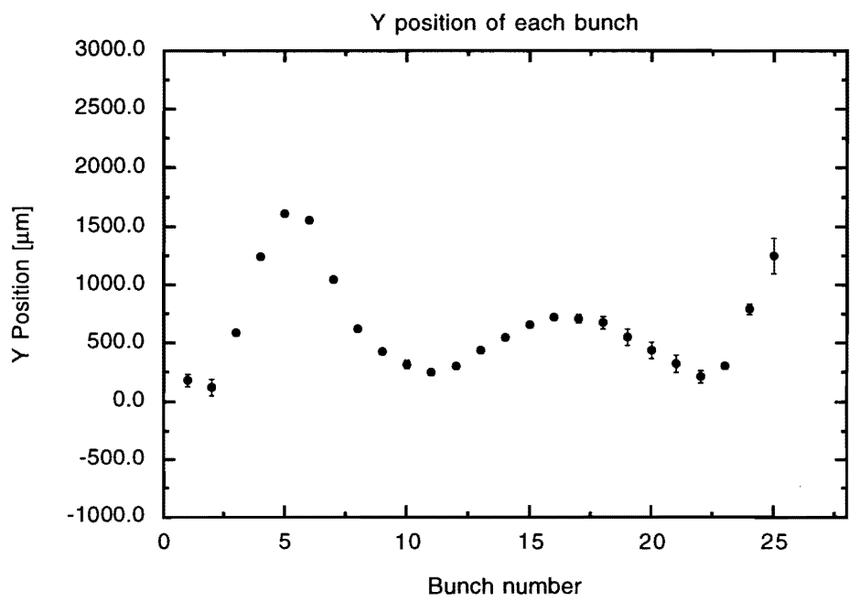

Figure 16.14: *Measurement example of multibunch beam position in ATF.*

100 BPMs, was very small. A consideration of the heating-up by beam interception and synchrotron radiation has been made.

In order to avoid direct irradiation to the electrode, the electrode axis were rotated by 45 degrees. A special feed-through design was made in order to reduce the resonance below 10 GHz by good matching to 50 Ω cables. The resolution requirement is 5 μm in order to measure the small dispersion at the wiggler section in the ATF damping ring. To obtain such a high resolution by a button electrode, a large-diameter electrode was used. The electrode was directly welded to the feed-through with a short center conductor which avoids mechanical vibration (Figure 16.15).

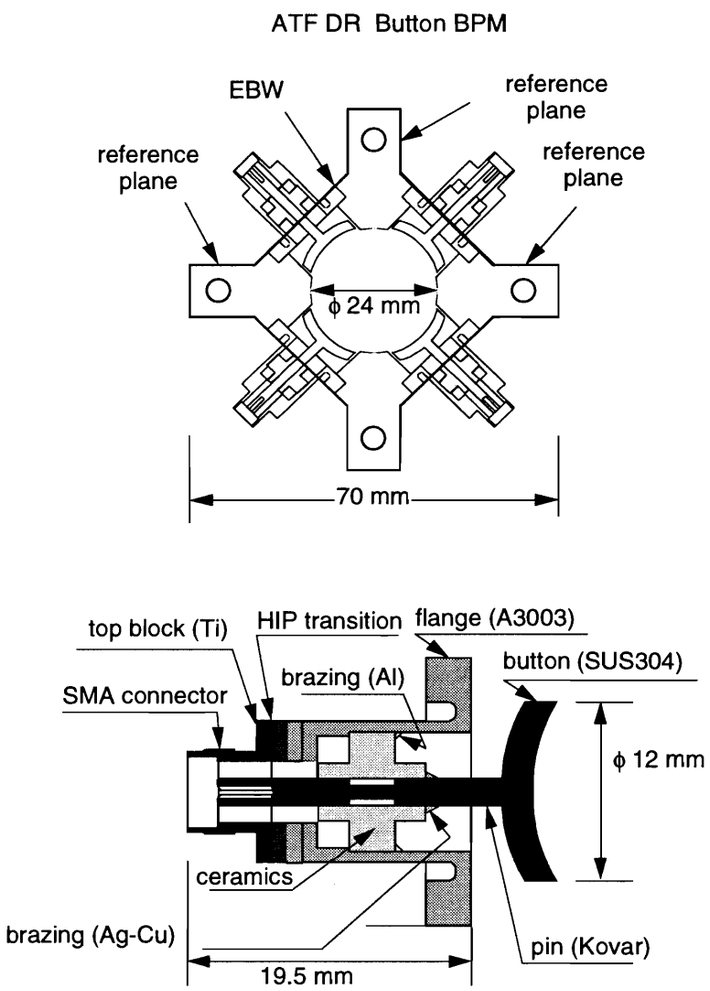

Figure 16.15: *Button BPM block of ATF DR.*

The feed-through consists of a central conductor, an outer conductor and a ceramic insulator forming

an SMA connector. The SMA connector comprises parts made of titanium and an aluminum-alloy which are joined through HIP transition. The mechanical strength of the SMA connector is, thus, increased from that of the aluminum alloy connector. Every feed-through was tested by applying a 60 kg tensile force and a heat cycle from liquid nitrogen temperature to 200 degrees. The four electrodes with feed-throughs were welded into the BPM block, which was machined precisely from a mass of aluminum alloy.

The BPM block has a horizontal reference surface and a vertical reference surface which have a 50 μm accuracy from the BPM block center. The block was welded to an aluminum vacuum chamber, and fixed to a quadrupole magnet using a stainless-steel attachment. After an installation, the mechanical center of the BPM block from a quadrupole mechanical center was measured.

An electrical center relative to the mechanical center of the BPM block was measured before welding the block into the vacuum chamber. An electrical pulse on a stretched wire was used to determine the mechanical center and to simulate a beam signal. The 50 μm tungsten wire was set to the center of the BPM block with an accuracy of better than 40 μm using a gauge and a microscope. In Figure 16.16, the distribution of the electrical center offset for 40 BPM blocks is shown. The mean values of the offset

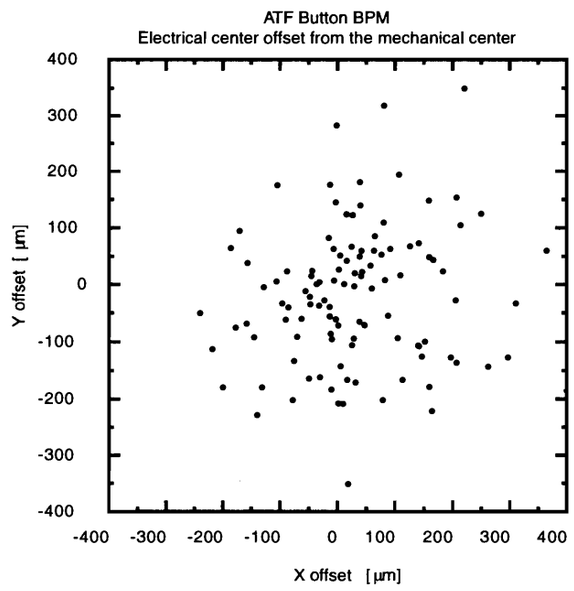

Figure 16.16: *Distribution of the electrical center offset relative to the mechanical center of the ATF-DR button BPM.*

were $-19\,\mu$m in the horizontal direction and $58\,\mu$m in vertical direction, and its standard deviation was around $90\,\mu$m in both directions. In order to confirm the uniformity of position detection, the wire was moved so as to map out the central region of the BPM. The wire was moved using a stepping motor stage with $0.1\,\mu$m accuracy. As shown in Figure 16.17, the distortion was less than $10\,\mu$m in center region and $100\,\mu$m 2 mm away from the center. The position calculation was performed using

a first-order approximation without a higher order correction.

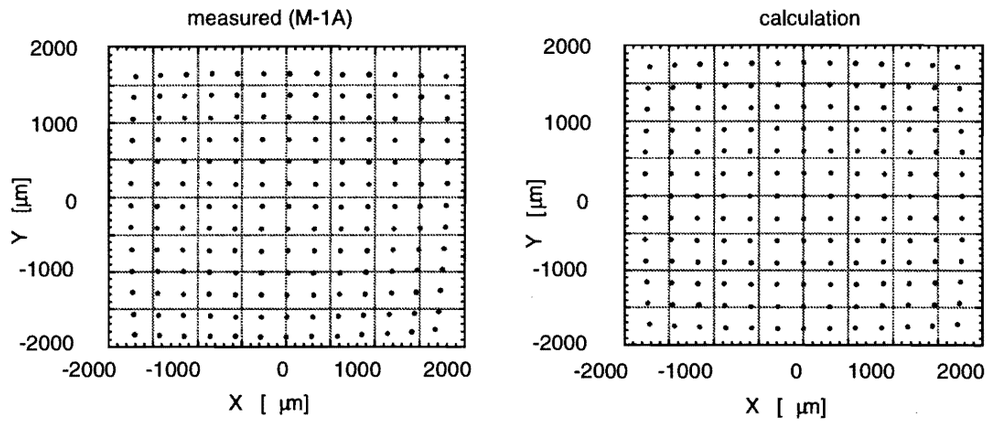

Figure 16.17: *Distortion of the detected position by a linear formula (ATF-DR button mapping).*

The detection electronics for the ATF Damping Ring is base-band detection, which involves the charge integration of the negative swing signal cut out by the clipping module amplifier. The advantage of this method is a simple and inexpensive circuit compared with other single-shot electronics. The performance is shown in Figures 16.18 and 16.19.

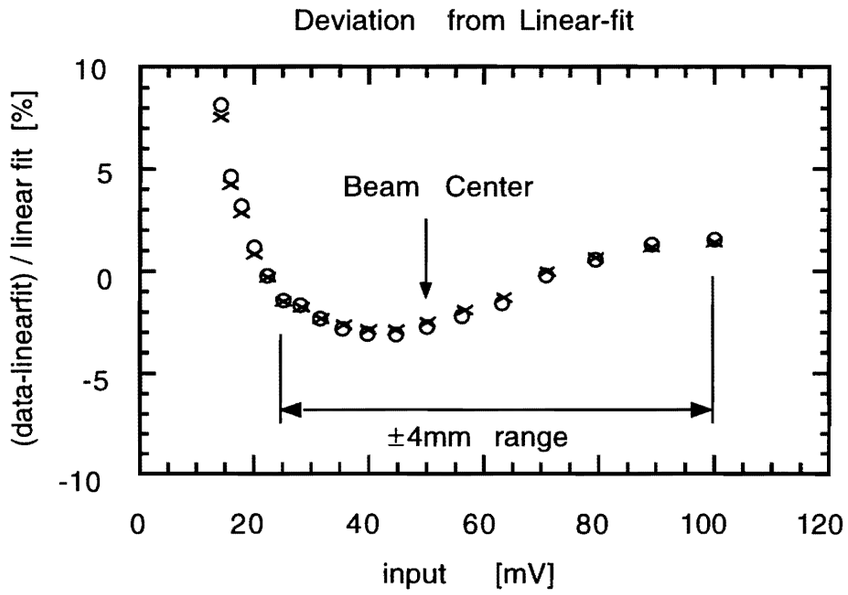

Figure 16.18: *Linearity of the detection circuit for the ATF-DR button BPM.*

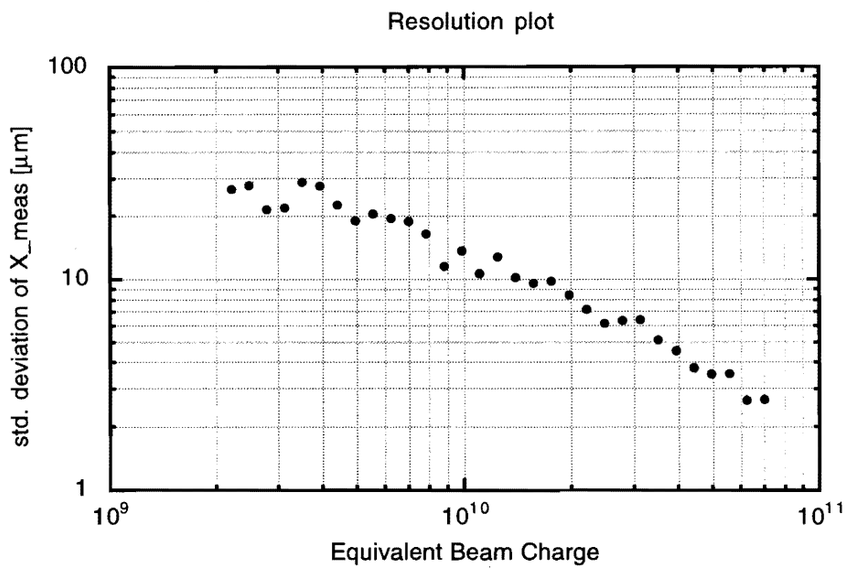

Figure 16.19: *Estimated resolution for the ATF-DR button BPM.*

FFTB Microwave Cavity BPM[10][11]

In order to measure the beam position at the final focus line, a microwave cavity is used as a high-resolution, high-precision beam position monitor for the nano-meter range. The cavity monitor uses the TM110 mode, whose signal intensity is directly coupled to the transverse beam offset. The zero-signal output corresponding to that the beam is in the BPM center within the accuracy of machining. The precision of the beam offset position directly depends on the beam intensity and the accuracy of the cavity symmetric machining. Therefore, the cavity BPM is adequate for detecting the center relative to the outer surface of its body.

The cavity BPM test was performed at the FFTB of SLAC using a sub-micron size beam. The purpose of the test was to verify that the cavity BPM has a nm resolution and is a certain candidate for the final focus BPM. The cavity BPM installed in the FFTB beam line consists of three identical TM110 (f = 5.712 GHz) cavities and a TM010 (f = 5.712 GHz) cavity. These cavities are assembled in one block, as shown in Figure 16.20, with a vertical stepping motor mover housed in a vacuum chamber. The intrinsic resolution of this BPM was obtained by having the beam passing through it and by analyzing the correlation of signals obtained from the three cavities.

In order to obtain high resolution, in addition to high-precision machining in fabrication of the BPM cavities, rejection of common-mode noises (around 90 dB rejection) is essential. The common-mode rejection is achieved by an external circuit which consists of a phase shifter and a variable attenuator. The two symmetric pickup antenna following this rejection circuit are connected to the down-conversion electronics (Figure 16.21). The 5.712 GHz signals are converted to 500 MHz using

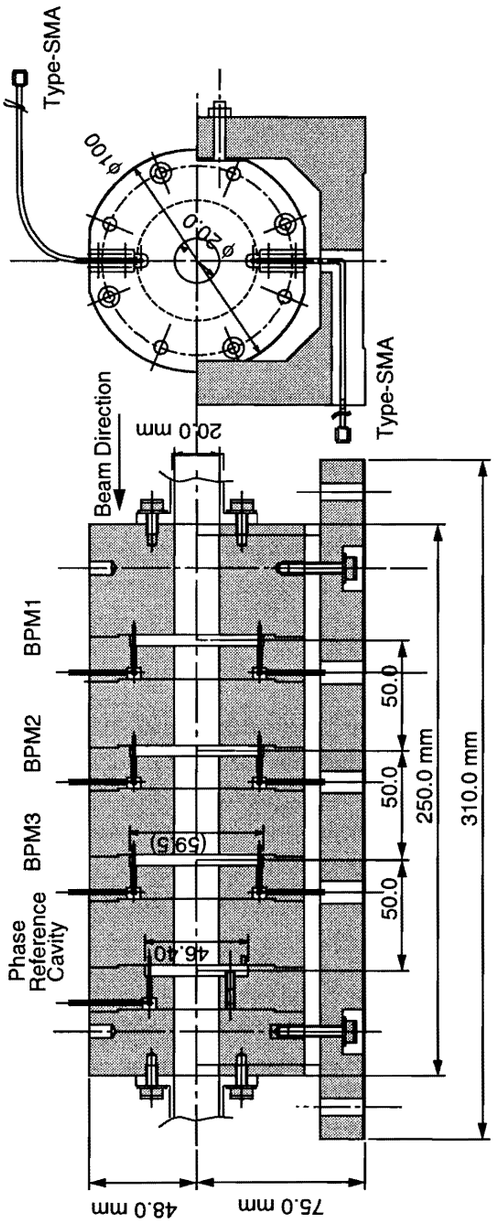

Figure 16.20: *Pickup cavity assembly of FFTB cavity BPM.*

a 5.212 GHz local oscillator. The converted signal from the TM010 cavity is used for the synchronous detection of the TM110 signal. The detected signals are filtered by a 50 MHz low-pass-filter, and are sampled by a S/H circuit.

The characteristics of the FFTB beam used for this test were: 50 GeV, single-bunch, 30 Hz repetition and 1 nC charge intensity. The calibration of the position coefficient was performed using a vertical mover. In order to obtain an intrinsic BPM resolution using three BPM read-outs (y_1, y_2, y_3), correlation plots of y_2 and $(y_1 + y_3)/2$ were made, as shown in Figure 16.22. The estimated intrinsic resolution for this setup and for the beam intensity was 28 nm, calculated from the fitted width along minor axis of the distribution. The beam position jitter was 10 μm in this case.

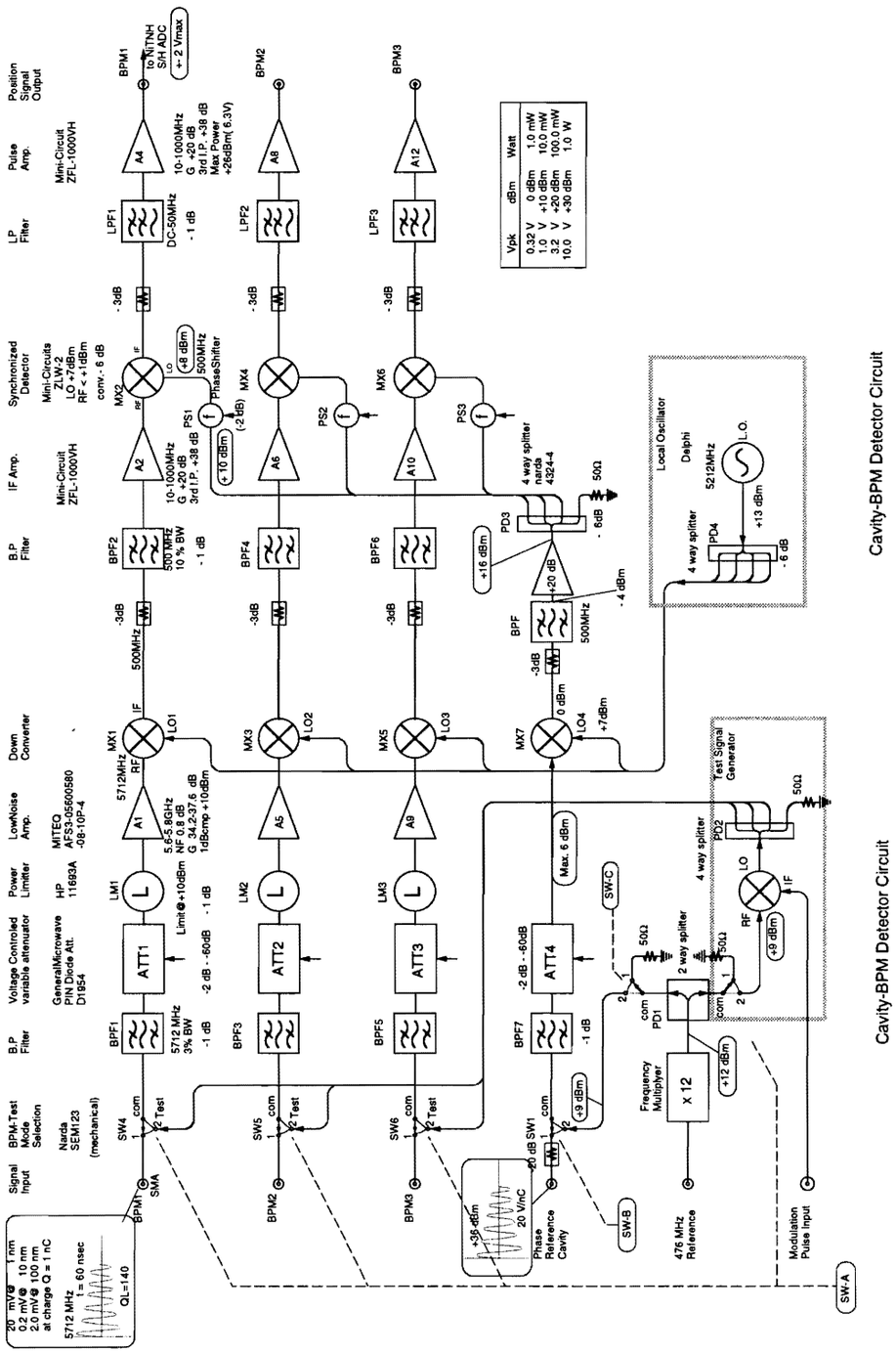

Figure 16.21: *Processing electronics for FFTB cavity BPM.*

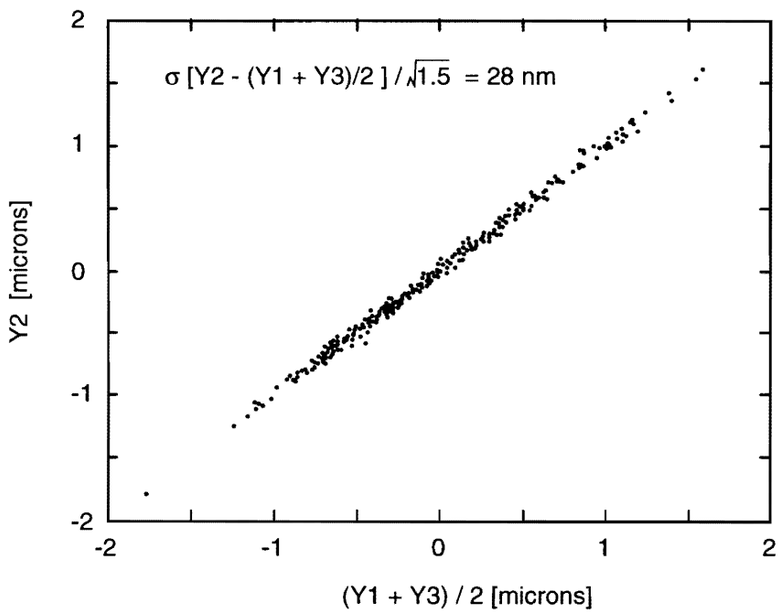

Figure 16.22: *Correlation plot of BPM readings from FFTB cavity BPM.*

16.2.2 Longitudinal Position

The longitudinal position of the beam, which means the relative spacing of individual bunches within a bunch train, will be measured by analyzing the intensity distribution of Cerenkov radiation or synchrotron radiation of the beam. This measurement can be achieved by the auto-correlation method, or by using a streak-camera system which is now available with a resolution of 0.2 ps[12]. These monitors can be achieved by an extension of the ordinary techniques currently available. A detailed discussion will given in the section of the bunch-length monitor. No development or no experiment has yet been performed for this monitor. A measurement test of the bunch spacing will be made at the extraction line of the ATF Damping Ring.

16.3 Beam-Size Monitors (BSM)

16.3.1 Transverse Spread

The transverse spread of a beam which is related to the transverse emittance, will be measured using a phosphor screen, a wire scanner, synchrotron radiation, and laser-Compton scattering. These monitors will be applied at an appropriate position in the accelerator.

A phosphor screen, which is a destructive and relatively low-resolution beam-size monitor, will be fit to the low-energy part and a beam of mm-size.

The wire-scanner beam-size monitor, which is placed anywhere in the accelerator has an advantage in that measurement with this monitor is relatively non-intrusive. However, it has a a disadvantage of being a multi-shot monitor. It requires many beam pulses for a complete size measurement. During wire scanning, the beam should maintain the same parameters.

A synchrotron-radiation monitor uses radiation emitted by a beam in the bending field. It can be applied to any location having a bending magnet or a wiggler magnet in the accelerator. Its resolution is limited by the diffraction of synchrotron light, which greatly depends on the radiation opening angle. The expected resolution will be around 10 to 50 μm, depending on the observation wavelength.

The laser beam size monitor is categorized in two types, depending on the interaction method between the laser and the beam. One is a fringe monitor, which uses the interaction of the beam with the interference fringes of the laser. The other is the laser-wire monitor or the laser beam scanner, which uses the interaction of the beam with the laser beam itself as an scanning probe. Since both are necessary to scan the beam, they are multi-shot monitors.

Phosphor Screen Profile Monitor[13]

Beam-profile measurements at around a few 10 μm accuracy will be carried out by inserting a phosphor-screen in the beamline. It is noted that the screen stops some part of the beam, and because of multiple-scattering it makes the beam diverge after passing. The radiation emission to downstream must be considered for the installation. Since fluorescence light comes from excitation of the phosphor by the beam, the thickness of the screen substrate should be thinner in order to avoid multiple scattering of electrons. In the ATF development as shown in Figure 16.23, the phosphor substrate was polished

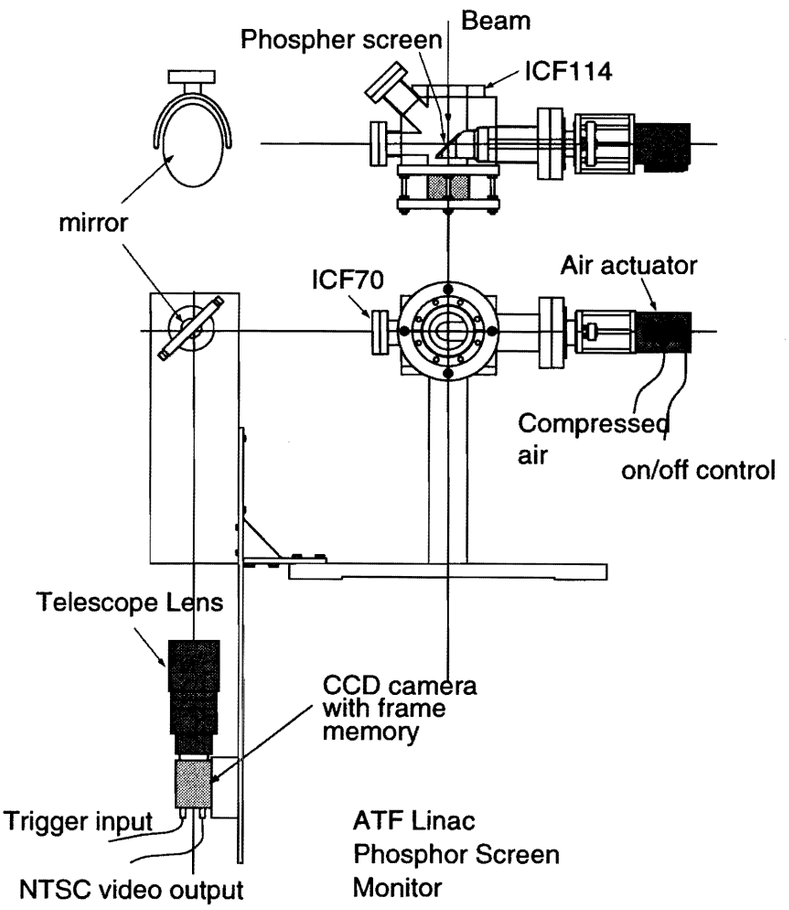

Figure 16.23: *ATF Phosphor screen profile monitor.*

to 130 μm thickness to obtain around 20 μm resolution by electron multiple scattering. Though the light yield from the thin screen decreased, the optical telescope should be set at high magnification for high-resolution imaging. The detected beam image, therefore, tends to be dark compared with an ordinary screen.

The resolution of the optical-telescope system, which was needed to avoid radiation damages, was estimated to be around 20 μm, which was mainly determined by the pixel granularity in a CCD camera. The main radiation damage was caused by direct gamma rays from the phosphor screen. A mirror of 90-degree reflection was used to avoid direct radiation from the screen. An optical telescope and a gated CCD camera were installed downstream of the first mirror. The gate time, synchronized with the beam, was set to be 17 ms long, because of the long decay time of the fluorescence light. The beam image was frozen and converted to an NTSC video signal by the CCD camera driver. An analysis of beam size was performed using off-line analysis software for a beam size of around 300 μm sigma. An example of the beam image is shown in Figure 16.24. The measured emittance was in good agreement with the wire-scanner result.

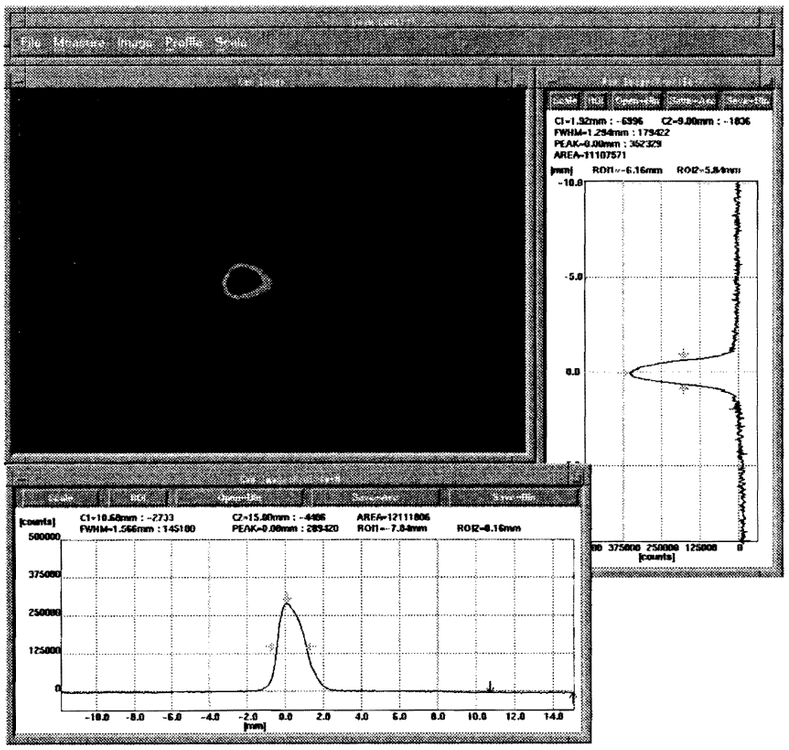

Figure 16.24: *Example of the beam image obtained by the phosphor screen profile monitor.*

Transition-Radiation Profile Monitor[14]

To obtain a bunch-by-bunch beam profile, transition-radiation light was used along with a fast-gate camera. The transition light was created by a polished stainless-steel plate located on the beam line at the ATF linac preinjector. Since the radiation from a point charge spreads like a ring distribution,

the observed image will be a convolution of its distribution and beam-charge distribution. The beam size should, therefore, be greater than the ring distribution. The imaging technique is the same as that of the phosphor screen. However, a 2.5 ns gate could distinguish each bunch within the 2.8 ns spacing of the ATF multi-bunch (Figure 16.25). For applying this monitor in the high-energy part of the accelerator, we should consider the beam loss and radiation emission by a transition light radiator.

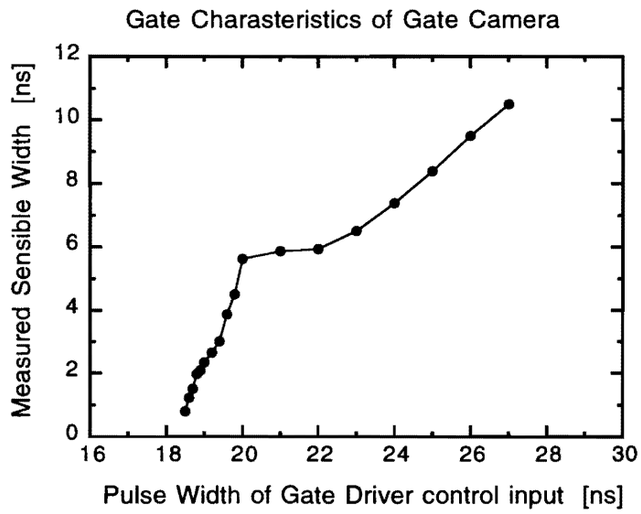

Figure 16.25: *Gate characteristic of the fast gate camera.*

Wire Scanner Profile Monitor[15]

Beam-profile measurements at around 1 μm accuracy is made using the wire scanning method. For fine-resolution measurements, a thin carbon wire of 4 μm diameter was used on the mover, which uses a stepping motor stage of 0.5 μm step resolution with a 0.1 μm repeatability. Detection of the profile is done by measuring the gamma-ray yield synchronized with the wire movement downstream of the wire scanner. This wire scanner will be tested on a 10 μm beam of the ATF extraction line.

The development of the wire scanner monitor was performed using a 50 μm gold plated tungsten wire, instead of carbon wire, at the Tohoku University linac and ATF linac by collaboration with Tohoku University. The wire was stretched in three directions by one wire, as shown in Figure 16.26. By this stretching method, one-way slide of the wire mount could perform a beam-size measurement in three different directions (X, Y, U) at one time. The beam size determined by the U-wire was used for a coupling measurement between the X and Y directions. The wire mount was fixed to both ends with the linear slider in order to avoid mechanical vibration during a scan. The vacuum chamber housed the wire mount, which was held at an angle of 45 degrees. One of the sliders was the stepping-motor stage, which had a 0.5 μm step resolution and a 0.1 μm repeatability. The gamma-ray signal and

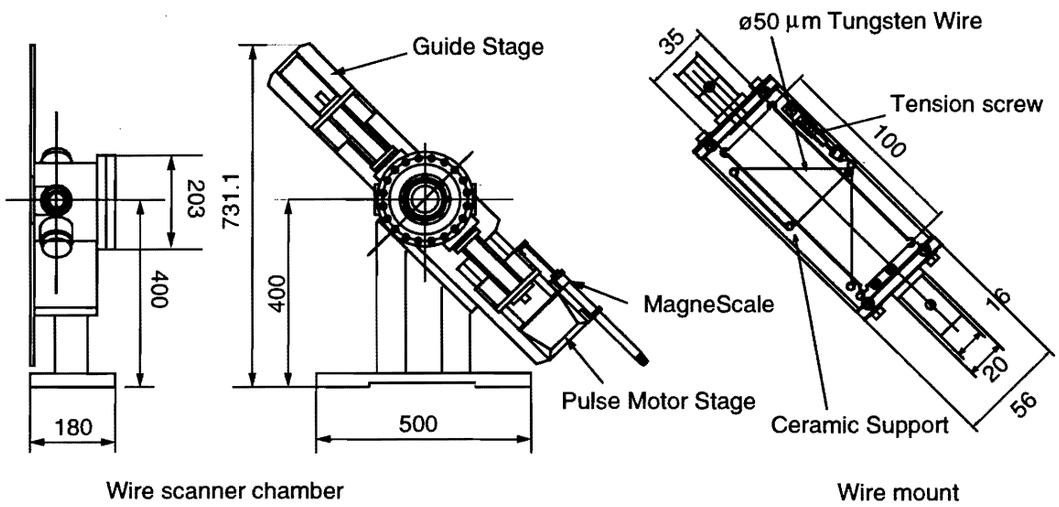

Figure 16.26: *Wire scanner chamber for ATF linac.*

knock-on electron signal were used for detecting the beam-wire interaction. A photo-multiplier with a plastic scintillator was used for the gamma-ray detection, placed at downstream of the wire scanner with around 10-degree scattering angle. This is in order to avoid beam halo gamma-ray background. In the case of knock-on electron detection, a detector that was the same as that mentioned above was placed in a position perpendicular to the beam line with a thin plastic window in order to avoid the absorption of scattered electrons. A beam-size measurement using this wire scanner was performed on a beam having around a 1 mm transverse size. The functioning of the wire-scanning method was confirmed by the results in Figure 16.27, which show a clear measurement of the beam size by a 50 μm probe.

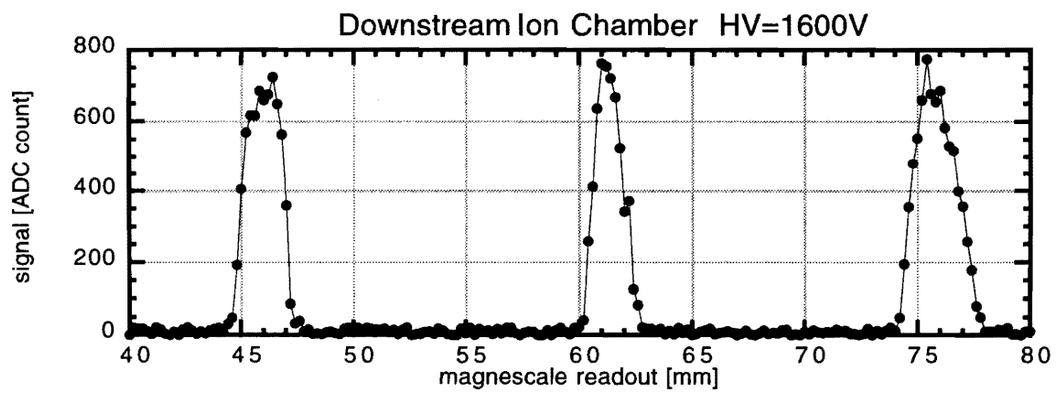

Figure 16.27: *Example of a beam-size measurement using the wire scanner.*

A measurement of the beam size for each bunch in the bunch train was developed by using a photo-multiplier tube (PMT) with a fast gate. The PMT has a photo-cathode with a grid and two stacks of multi-channel plates (MCP) for electron amplification. The grid has a response time of less than 5 ns gate width for an on/off ratio of 4 × 105. The 2.5 ns gate width was applied to the PMT in order to distinguish a gamma-ray from each bunch out of a 2.8 ns interval multi-bunch train. A beam experiment of this multi-bunch beam-size measurement using a wire scanner was conducted at the ATF Linac pre-injector using the same scanner chamber and ATF 2.8 ns spacing multi-bunch beam. The detection of gamma-rays was made using a bare PMT without a scintillator converter. Electron emission from the photo-cathode was expected by the direct excitation of electrons and Cerenkov light in a glass window of a PMT by a converted electron. The PMT was placed downstream of the wire scanner chamber at an angle of 14.2 degrees away from the beam line. Lead blocks shielded the PMT from the halo gamma-rays of the linac. An example of a wire scan focused on the 6'th bunch in a 20 multi-bunch is shown in Figure 16.28. In this way, the beam size in the multi-bunch train can be measured for each bunch, as shown in Figure 16.29.

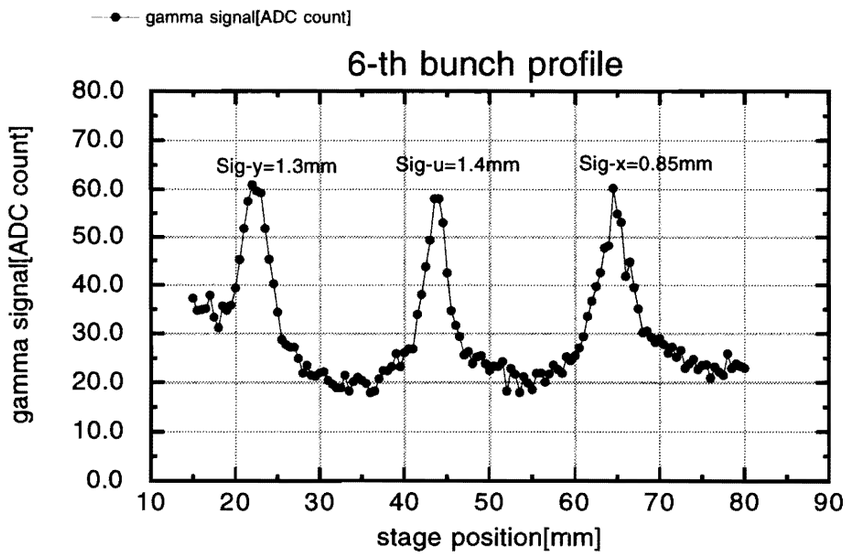

Figure 16.28: *6th beam profile within a 20-bunch train, obtained by the wire scanner and gate PMT.*

Synchrotron-Radiation Profile Monitor[16]

Non-destructive beam profile measurements at around 50 μm resolution will be carried out using synchrotron radiation. To avoid blurring of the image due to diffraction of synchrotron light, a shorter wave length will be used for imaging. This monitor is installed in the Damping Ring to monitor the beam size turn-by-turn along with the beam-size damping.

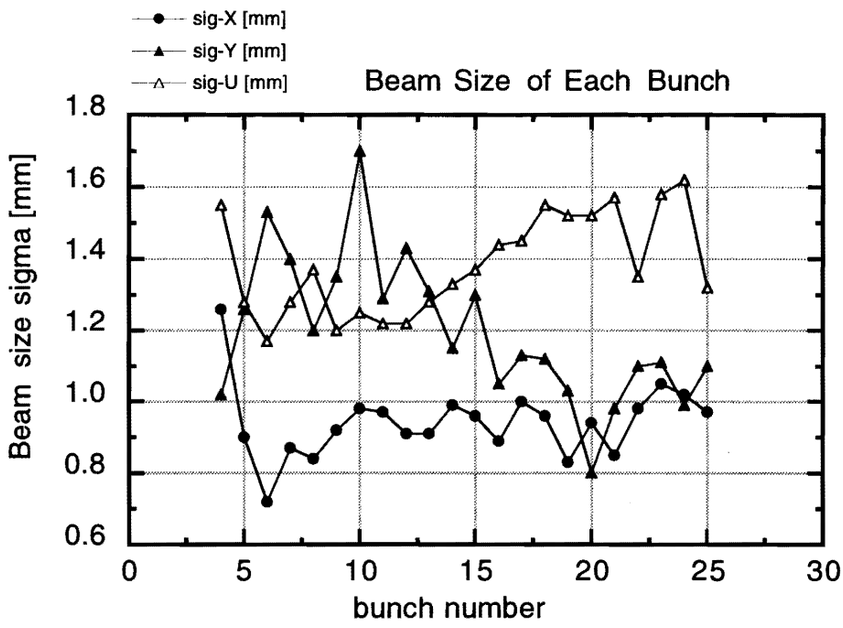

Figure 16.29: *Beam size measurement of multi-bunch beam.*

A synchrotron-radiation (SR) monitor was developed in collaboration with the Institute of Nuclear Science of the University of Tokyo[1] using their Electron-Synchrotron (ES). The ES is a fast-cycle synchrotron accelerator with 20Hz repetition and 1.2 GeV top energy. Since the beam cycle and damping along the acceleration are similar to that of the ATF Damping Ring, SR monitor development was started using the ES beam before commissioning the Damping Ring (Figure 16.30). The vacuum chamber of the bending magnet was modified so as to attach an extraction port for synchrotron radiation. The extraction port, including the first mirror, which reflected visible light and avoided X-rays and other radiation, was pumped out to the 10^{-7} Pa level to avoid dust from being trapped on the mirror surface. The mirror was made of aluminum-coated glass with a very low thermal-expansion coefficient. The distortion of the mirror due to the absorption of synchrotron-radiation energy was kept small. Two sets of appocromatic lenses were used to obtain about a factor 1.0 magnification of the image. A fast-gate camera using a gate photo-cathode, an MCP, a light converter and a CCD was used for single-shot imaging with around 10 μm granularity. The fast-gate camera could be operated with a 2.5 ns gate width, which was confirmed by this beam test. The resolution of this optical system was mainly limited by the diffraction determined by the radiation opening angle. The diffraction determined by the opening angle of the optical system. These contributions were estimated to be about a 50 μm increase in the image width. As a result, point-source imaging with less than 50 μm radius would be difficult by the SR monitor. This situation is the same as in the case of Damping Ring. Since the ES beam size was greater than 500 μm, the measurement was successfully performed,

[1] Starting April of 1997, INS was detached from University of Tokyo, and has become part of High Energy Accelerator Research Organization, KEK, formerly known as National Laboratory for High Energy Physics.

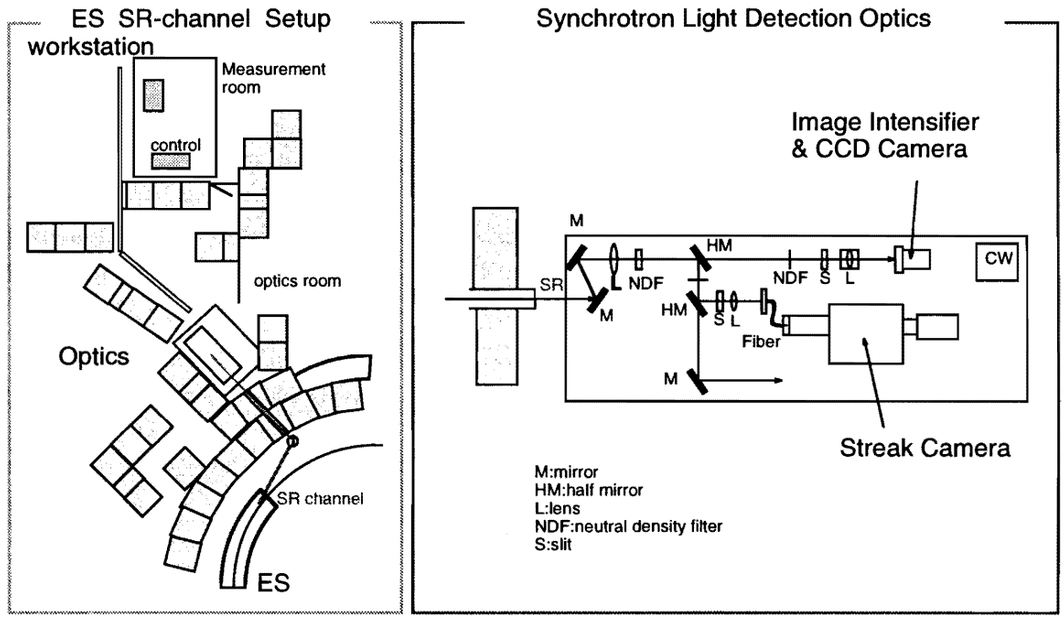

Figure 16.30: *SR extraction and optics of the ES SR monitor.*

as shown in Figure16.31. On the other hand, since a measurement in the Damping Ring is limited by diffraction, the measured beam size reaches equilibrium far away from the true beam size.

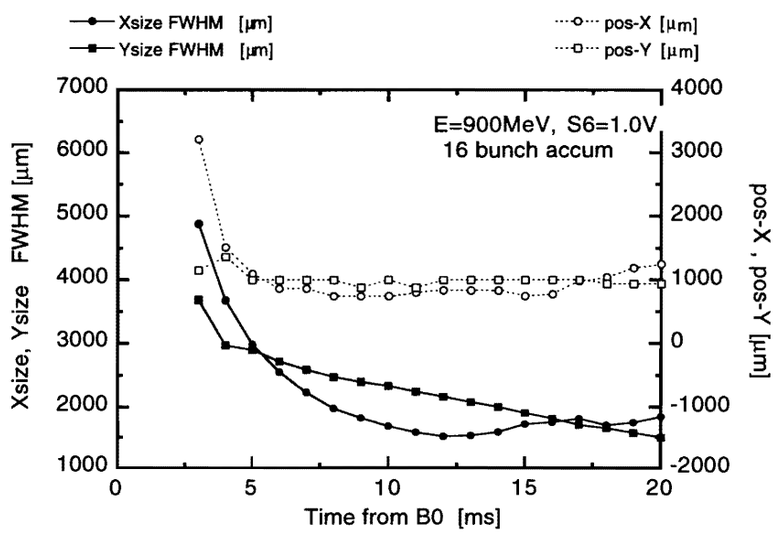

Figure 16.31: *Beam-size measurement along 20ms acceleration in the ES.*

Laser-Profile Monitor (Fringe Monitor)[17]

For the final focus beam line, a very precise profile monitor of nano-meter beam size is required for focus tuning. A novel technique has been developed where the interaction of the beam with a laser interference fringe pattern which has a pitch size of sub-microns is utilized. The beam would interact with the laser fringe pattern and produce a Compton-scattered gamma-rays. The flux of the scattered gamma-rays is measured downstream as a function of the steered beam position. Modulation of the gamma-ray intensity gives information about the beam size. This profile monitor was installed and tested in the FFTB at SLAC.

The monitor consists of a Nd:YAG pulse laser, 20 m of laser transport line into the tunnel, an interferometer stage in the beam line and a gamma-ray detector using Cerenkov light. The laser output is a 200 mJ and 9 ns pulse at 1064 nm wavelength which is stabilized by a seeding laser injection technique for improving the coherency and a spatial distribution. The interferometer stage stands perpendicular to the beam line. It is an optical table that has a size of 1.5 m in the horizontal direction, 1.6 m in the vertical direction and a thickness of 110 mm.

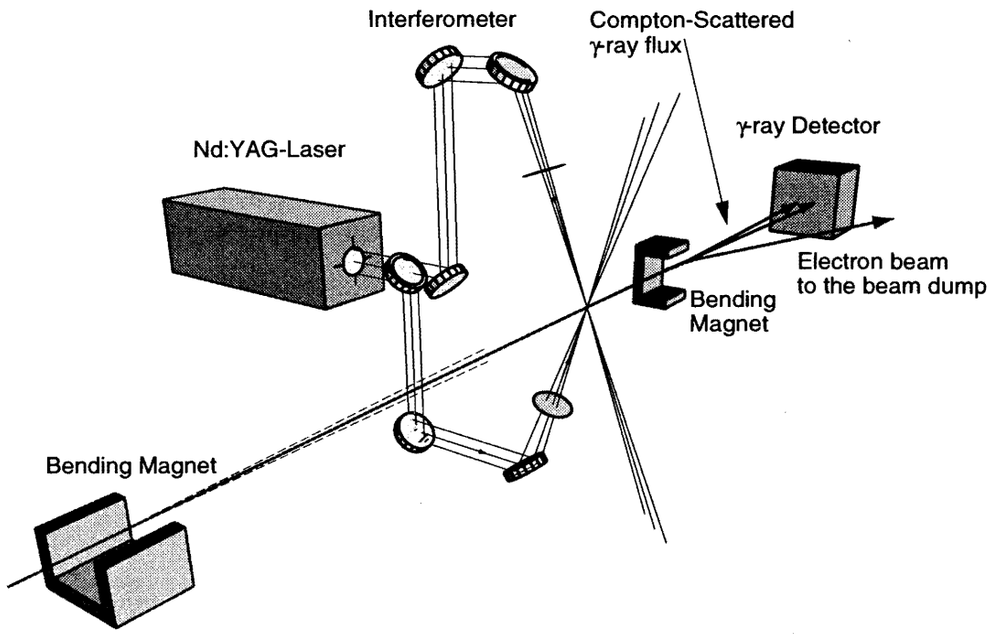

Figure 16.32: *Principle of the laser fringe profile monitor.*

The optical system is arranged in the stage so as to produce interference fringes in the center vacuum chamber, which is connected into the beam line (Figure 16.32). There are three operation modes for three different spacings of the interference fringe, as shown in Figure 16.33. 'Mode 1' generates a 0.53 μm spacing vertical fringe which is used for 40 to 180 nm vertical beam size measurements. 'Mode

2' generates a 2.1 μm fringe for 160 to 720 nm vertical size. 'Mode 3' generates a horizontally spaced fringe of 10.2 μm for 0.76 to 3.4 μmm horizontal beam size measurement.

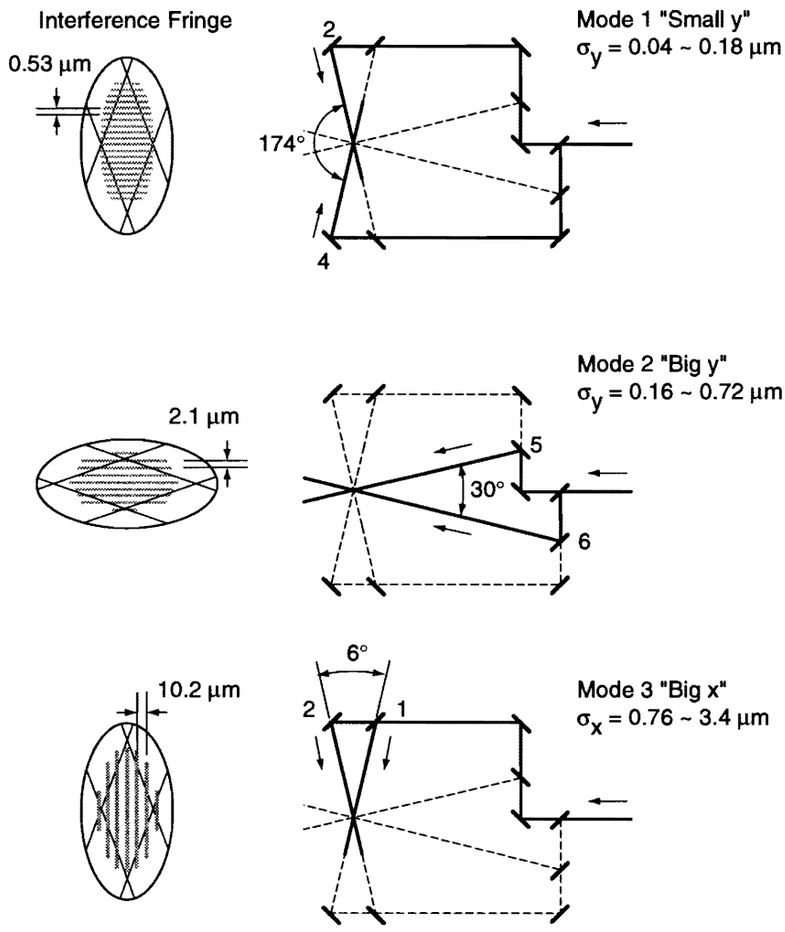

Figure 16.33: *Three operation modes of the laser fringe profile monitor.*

The gamma-ray detector placed downstream of the interferometer stage consists of a lead converter, a gas Cerenkov periscope and a photo-multiplier tube with a lead shield. The laser was operated at 10 Hz and the FFTB beam was operated at 30 Hz. A noise pedestal measurement for pedestal subtraction was made with a near-time position of the signal measurement.

A measurement of the modulation of the gamma-ray intensity from the interaction of the laser fringe was performed by moving the beam vertically with a fine step of around 30 nm. From the observed intensity modulation, the beam size was calculated to be 66 nm in the vertical in the case of Figure 16.34. The measured spot-size distribution for 3 hours (Figure 16.35) indicates a stable beam size and a stable measurement of around 70 nm.

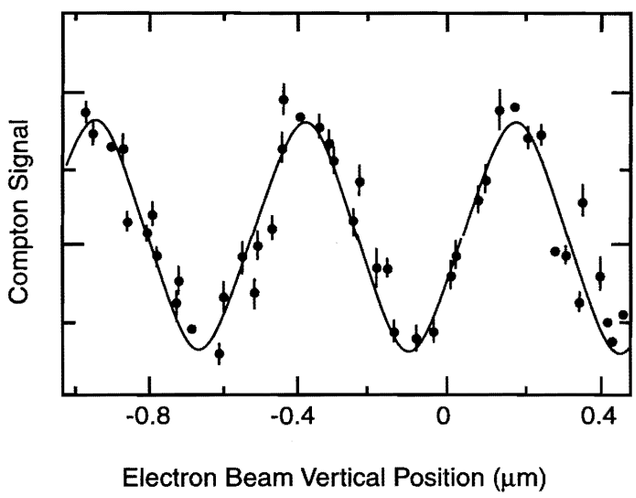

Figure 16.34: *Observed gamma-ray intensity modulation in the case of a 70 nm beam size.*

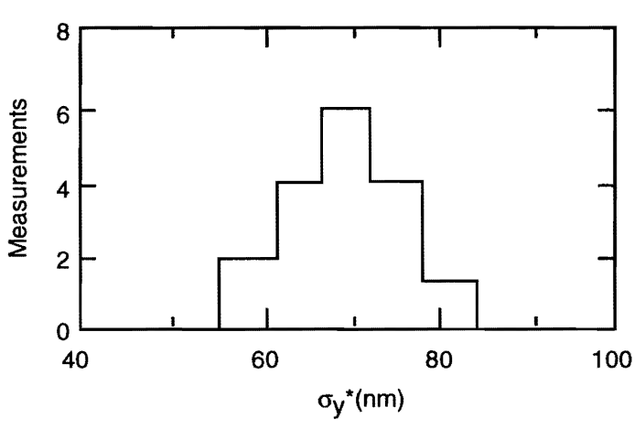

Figure 16.35: *Beam size distribution measured by the laser fringe monitor.*

16.3.2 Bunch Length Monitors

The longitudinal spread of the beam (bunch length) will be measured by the intensity distribution of Cerenkov radiation, synchrotron radiation or transition radiation of the beam. This measurement can be achieved by the spectrum-conversion method or by a streak-camera system which, is the same as that for measuring the longitudinal position.

Streak Camera[18]

A streak-camera (FESCA-500 from Hamamatsu Photonics Co.) is used in the ATF linac preinjector to measure the bunch length using transition light from a stainless-steel plate. The camera consists of an input slit, an input optical lens, a photo-cathode, an MCP, fluorescence light converter, an output lens and a CCD camera. The light which passes through the slit and input lens is focused on the photo-cathode. The emitted electrons are accelerated by a high-voltage field and swept by a fast sweeping field. The swept electrons are amplified by the MCP and hit a fluorescent screen. The image on the screen is captured by the CCD camera. These working principle of the streak camera are illustrated in Figure 16.36. The maximum resolution of the FESCA-500 is 0.6 ps in the case of a 60 ps

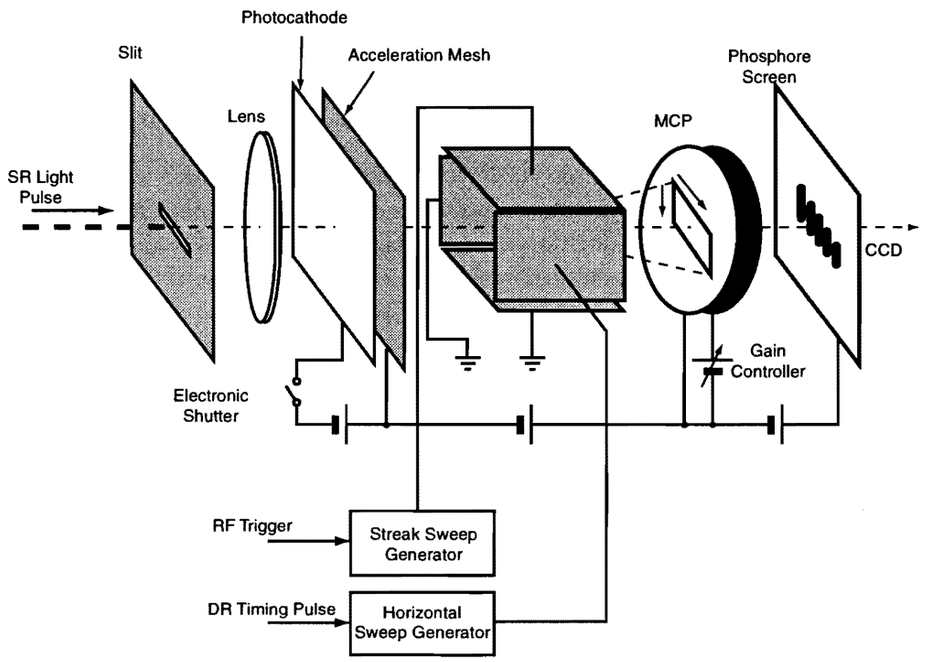

Figure 16.36: *Principle of streak camera.*

full-sweep range. The streak camera is placed outside of the linac tunnel. The transition light from the beam line is transported by an optical system which consists of a $f = 500\,\text{mm}$ object lens, three

mirrors and a $f = 50\,\text{mm}$ focusing lens. The measurement is usually performed without a wavelength filter. The error coming from the time difference due to the different wavelengths is estimated to be 2 ps. The other error coming from the effect of an infinite scanning beam width is estimated to be 4.5 ps in the case of a 500 ps sweep range. The measured bunch length of the multi-bunch shown in Figure 16.37 is around 15 ps with these errors subtracted.

The bunch-length measurement in the ATF Damping Ring is performed by a two-axis sweep streak-camera, which can sweep the SR light several times during the damping process. Two sets of sweep electrodes are installed in the streak tube. One electrode sweeps the beam slowly (such as 20 ms full range), while the other sweeps it very quickly (such as 0.2 ns full range). The image taken by the one-cycle scan gave a set of bunch-length information along the damping process. The bunch-length monitor of the ATF Damping Ring is installed using the same optics line as that of the SR beam size monitor. The development of this monitor was also done at the ES SR monitor line. An example of the result is shown in Figure 16.38, which shows a bunch length shrunk during acceleration.

Spectrum Measurement[19]

For a short bunch length measurement of less than 1 ps, a spectrum measurement of the coherent radiation has been proposed [19]. Since the spectrum of coherent radiation is proportional to the bunch form-factor, an FFT conversion of the spectrum expresses the longitudinal charge distribution. The development of a bunch-length monitor of this method was started at Tohoku University. A beam test using the ATF linac preinjector was done in collaboration with Tohoku University.

Two different detectors were used for spectrum detection of transition radiation from a thin aluminum foil. One was a spectrometer using a diffraction grating and a Si-bolometer. It could measure the spectrum very precisely with a scanning time of several hours. The other was an InSb detector array with a diffraction grating, which could detect each spectrum component at the same time. This type of detector, which is illustrated in Figure 16.39, sample the spectrum shot-by-shot of the linac beam. Since the linac beam was too long to detect the bunch length by these detectors, against our expectation, the measured beam size did not agree with the streak-camera measurement. An additional trial will be held in the near future.

16.4 Bunch Charge Monitors

16.4.1 Charge of Each Bunch

The amount of charges in each bunch and total charge of a whole bunch train is measured by a wall-current monitor (WCM) and a current transformer (CT). In order to measure the response of each

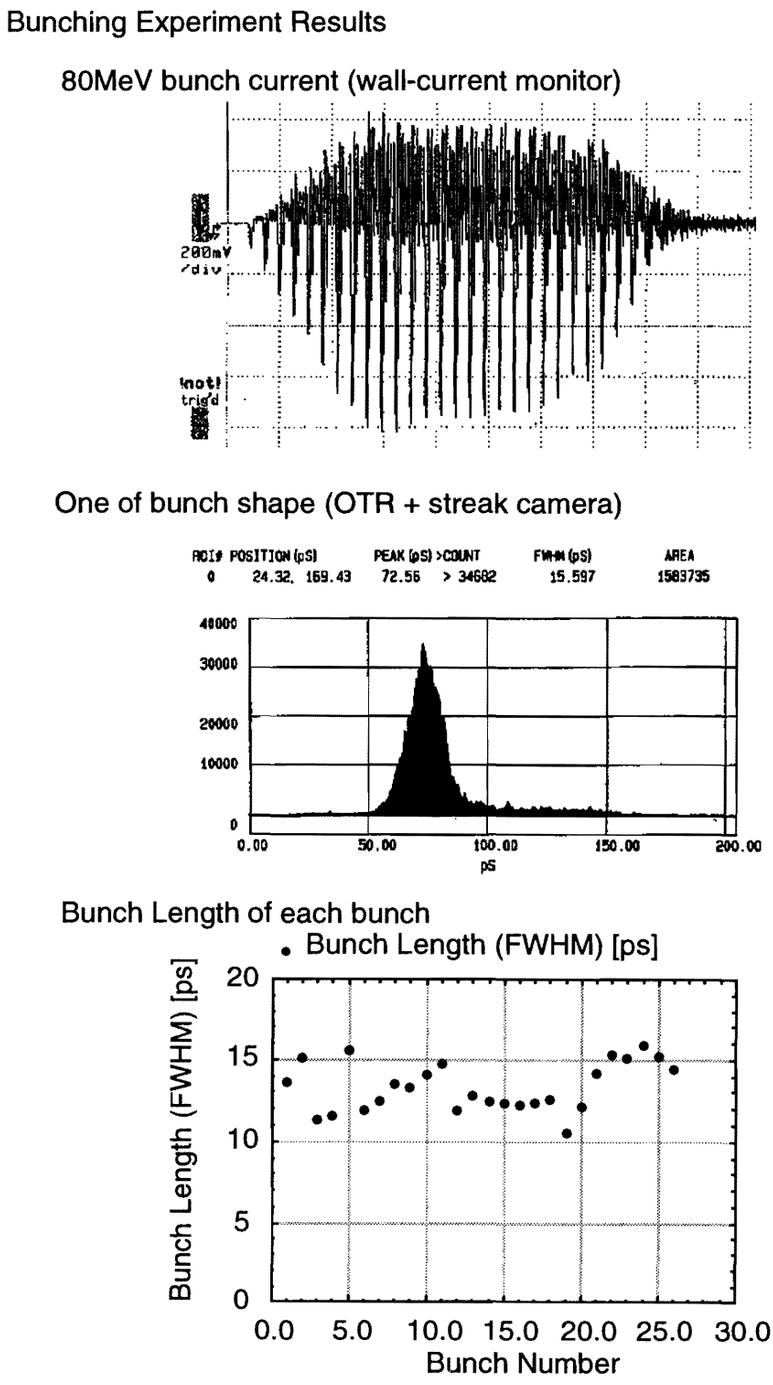

Figure 16.37: *Example of bunch length measurement for the ATF linac multi-bunch.*

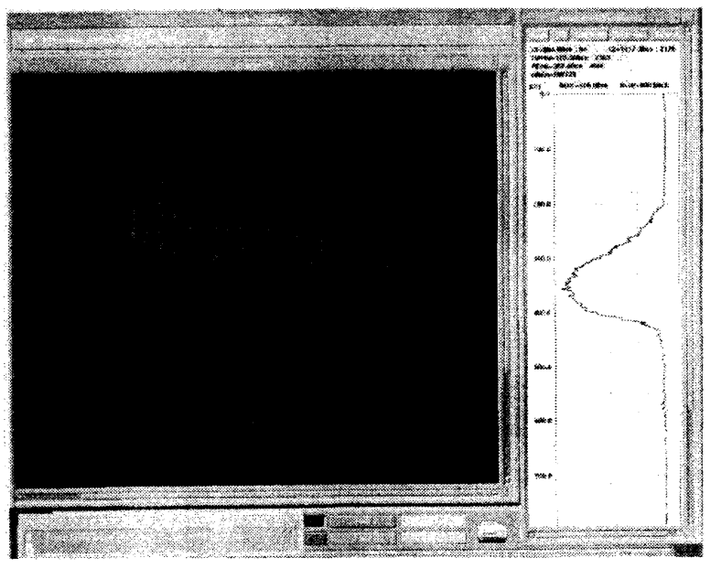

Figure 16.38: *Example of a bunch-length measurement during 20 ms acceleration of the ES beam.*

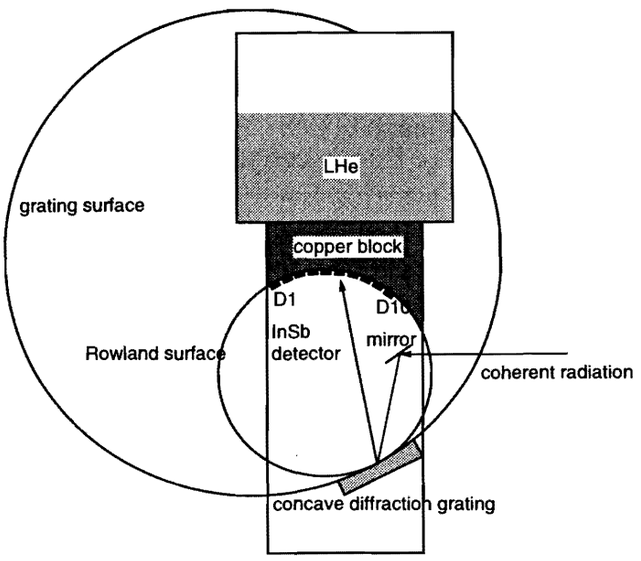

Figure 16.39: *Spectrum detector of coherent transition radiation.*

bunch, which has a 1.4 ns bunch spacing, fast-response pickups, short-length cables and fast response digitizers are required. The WCM with around a several 100 ps response time using a chip resistor can measure each bunch intensity by using a short co-axial cable and a wide-band sampling oscilloscope. On the other hand, a CT having a relatively slow response will be used for total-charge measurements.

Wall Current Monitor

The vacuum chamber of the wall current monitor has a ceramic insulator, shown in Figure 16.40. The chip resistors, which have low inductance at high frequencies, are soldered between the insulator gap. A symmetric connection of four cables can be used for signal extraction. The combined signals of the four extracted cables does not have a beam-position dependence, which is useful for current measurements. The outer sides of the resistors are shielded by a cylindrical aluminum case with a microwave absorber inside. The observed signal by this WCM, as shown in Figure 16.41, has a ringing

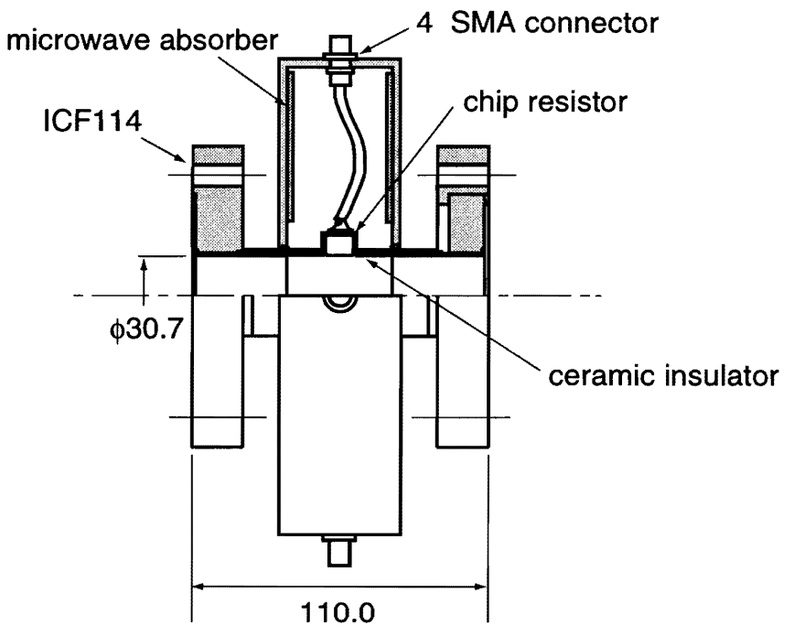

Figure 16.40: *Wall current monitor chamber of ATF linac.*

tail, which results from reflections of the wall current and resonance. Therefore, a further study is necessary for a precise measurement of the bunch current.

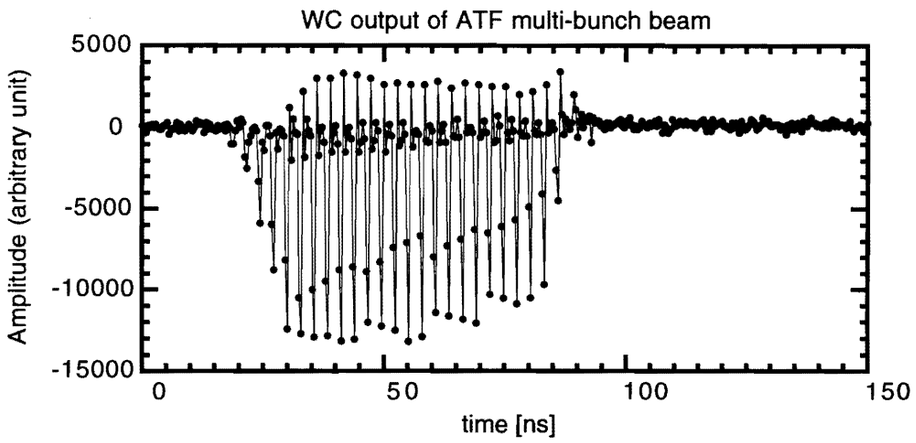

Figure 16.41: *Observed multibunch signal by the wall current monitor in ATF linac.*

Integration Current-transformer Monitor

The integration current-transformers (ICT) from Bergoz Co. are used in several places of the ATF. The ICT integrates a very fast beam pulse on the order of 20 ns. A measurement of the current

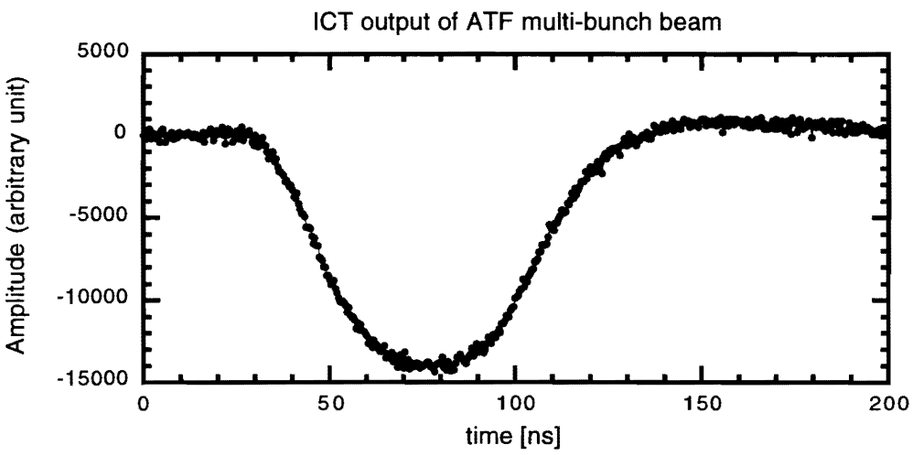

Figure 16.42: *Example of the waveform output from the integration current-transformer monitor.*

of a short pulse is possible with less than 0.1 % error. On the other hand, this is not suitable for a multi-bunch beam of 60 to 130 ns corresponding to the ATF beam and, also, the Linear Collider beam. An example of the response is shown in Figure 16.42. It is necessary to develop a multi-bunch charge measurement.

.6.5 Other Quantities

Other quantities to be measured frequently at JLC include the transverse emittance ϵ_x, ϵ_y, the beam energy E, and the energy spread σ_E. They are derived from the transverse beam profile σ_x, σ_y using the beam-optics parameters, beam position and profile using a bending field. Thus, a measurement of these quantities can be made by combining the above-mentioned monitor outputs and optics parameters.

References for Chapter 16

[1] H. Hayano et al., "High Resolution BPM for FFTB," N.I.M. A320, 47-52(1992)

[2] D. Burke, "FFTB Project," SLAC-PUB-5517, and IEEE PAC San Francisco May(1991) D. Burke, "Results from the FFTB," SLAC-PUB-6609, and EPAC94 London July(1994)

[3] H. Hayano et al., "An 80MeV Injector for ATF Linac," 17th Int. Linac Conf.(Linac94) Tsukuba August(1994) H. Hayano, "The KEK Accelerator Test Facility,"EPAC96 Sitges June(1996) H. Hayano, "ATF Linac Commissioning," 18th Int. Linac Conf.(Linac96) Geneva August(1996)

[4] H. Hayano et al., "Submicron Beam Position Monitors for Japan Linear Collider," 16th Int. Linac Conf.(Linac92) Ottawa August(1992) H. Hayano et al., "Strip-line BPM for ATF,"17th Linear Accelerator Meeting in Japan Sendai September(1992)

[5] R.L. Wiginton et al., Proc. IRE 45, 166(1957)

[6] S. Kashiwagi et al., "Calibration of Stripline BPM for ATF Linac,"20th Linear Accelerator Meeting in Japan Osaka September(1995)

[7] H. Hayano, "BPM System of ATF Linac,"21th Linear Accelerator Meeting in Japan Tokyo September(1996)

[8] H. Hayano, "Development of Multi-bunch Beam Position Monitor,"20th Linear Accelerator Meeting in Japan Osaka September(1995)

[9] M. Tejima et al., "Beam Position Monitor of the ATF-DR," 17th Int. Linac Conf. (Linac94) Tsukuba August(1994) F. Hinode et al., "Beam Test of a Button-type Beam-Position Monitor for the ATF Damping Ring," IEEE PAC Dallas May(1995)

[10] S.C. Hartman et al., "Nanometer Resolution BPM using Damped Slot Resonator," IEEE PAC Dallas May(1995)

[11] T. Shintake, "Experimental Results from FFTB December 1995 Run," report of FFTB run, December(1995) unpublished

[12] A. Takahashi et al., "A New Femtosecond Streak Camera," SPIE Vol.2002, 22(1993)

[13] T. Naito, "Beam size measurement by phosphor screen monitor," report of beam experiment at Tohoku University, March(1993) unpublished

[14] T. Naito et al., "Bunch by Bunch Beam Monitor for ATF Injector Linac," 17th Int. Linac Conf.(Linac94) Tsukuba August(1994)

[15] H. Hayano et al., "Beam Test of Wire Scanner Beam Size Monitor,"18th Linear Accelerator Meeting in Japan, Tsukuba September(1993)

[16] M. Muto, "SR monitor development," LC96, Tsukuba March(1996) Y. Hashimoto et al., "R&D of Electron-Beam Diagnostic System Using Synchrotron Radiation and a Study of the Beam Dynamics in the INS Electron Synchrotron," INS annual report 1994

[17] T. Shintake, "Proposal of a Nanometer Beam Size Monitor for e+e- Linear Colliders," N.I.M. A311, 453-464(1992) T. Shintake et al., "Design of Laser-Compton Spot Size Monitor," 15th Int. Conf. on High Energy Accel.(HEAC92) Hamburg July(1992) T. Shintake, "High Precision Spot Size Monitors for e+e- Linear Colliders," 17th Int. Linac Conf.(Linac94) Tsukuba August(1994) T. Shintake et al., "Experiments of Nanometer Beam Size Monitor at FFTB using Interferometry," IEEE PAC Dallas May(1995) T. Shintake, "Beam-Profile Monitors for Very Small Transverse and Longitudinal Dimensions using Laser Interferometer and Heterodyne Techniques," Beam Inst. Workshop ANL may(1996)

[18] H. Hayano, "Bunch Length Measurement by Streak Camera" report of beam experiment February(1994) unpublished

[19] T. Nakazato et al., "Bunch Length Measurement by using Coherent Radiation," Research Report of Laboratory of Nuclear Science Tohoku University vol.26 December(1993)

Author of Chapter 16

- H. Hayano

Contributers to the work presented in Chapter 16

- S. Kashiwagi
- M. Tejima
- F. Hinode
- J. Urakawa
- N. Terunuma
- T. Shintake
- T. Naito
- M. Muto
- Y. Hashimoto
- M. Oyamada
- T. Nakazato

Acknowledgments

We express our gratitude to the following colleagues from SLAC who have done important R&D work for beam instrumentation of LC, which are presented in this chapter: J.-L. Pellegrin on FFTB BPM electronics, S. Smith on FFTB BPM electronics, S. Williams on FFTB BPM fiducialization, M. Ross on ATF wire scanner, D. McCormick on ATF wire scanner, and S.C. Hartman on FFTB cavity BPM.

CHAPTER 17

Accelerator Tunnel and Facilities

Contents

17.1 Introduction

An appropriate site for JLC should satisfy the following technical criteria:

1. A geologically and geohydrologically stable area for the constructions of a long linac tunnel and a large detector-hall. A low level of seismic and micro seismic activity for the alignment of the final focus system, the main linacs, and the damping rings.
2. Availability of large electric power ($\sim$ 300 MW) and enough water-cooling capacity for linear-collider operation. An area close to an existing AC power line from a power station to industrial cities is favorable in this respect.
3. Easy access to the site from a highway, major railways such as Shinkansen, and an airport.

Keeping these criteria in mind, possible main tunnel designs are being studied. In this chapter, the main tunnel design based on both the blasting method (so-called NATM) and boring method (so-called TBM) is given after a short historical review of the design based on the shield method.

17.1.1 Tunnelling Methods

The construction methods for the main tunnel and detector-hall have been investigated for the following three cases:

- Shield method,
- Blasting method,
- Tunneling boring machine.

In an early stage of the JLC project design, the shield method seemed to be the most appropriate to reduce land cost. At that time the utilization of a deep underground location was attracting people's attention as a solution to obtain land for public use during the inflation period of the land price triggered by rapid economical growth. The Ministries started to prepare a draft of a law for the utilization of deep underground space in the metropolitan area. The objective of the draft was to allow the construction of public facilities at a depth deeper than 50 m underground without distinction of superficies. Assuming that the law would be enacted within a few years, we have elaborated a plan to construct the main tunnels and a detector-hall at a depth of 100 m underground in the Tsukuba area, so that the detector-hall could fit in the present KEK site. This would also allow the construction of the injector complex, including damping rings, injector linacs, and a positron production linac, on the ground of the KEK site. Outside of the present KEK site, several spot sites were required to construct pits dug in the ground for access to the main tunnels, as in the case of LEP and HERA. The accelerator and detector components could then be transported through the pits by lifts.

The Shield Tunnelling Method is applied for tunneling when water-tightness in poor-soil conditions is required. The Shield Tunnelling Methods are typically utilizing for under-sea tunnels, such as the Dover Tunnel and the Trans-Tokyo Bay Tunnel. The Shield Tunnelling Methods are also utilized for subway tunnels in urban areas in order to reduce sound and vibration to the environments. If we use shield machines, the cross section of the main tunnel should be circular, and its diameter should be constant over the full length of the main tunnel. Deep underground, the wall of the tunnel should be strong enough to sustain a high earth pressure, and should also be made water-tight by chemical processing in order to cope with high water pressure. The construction cost depends on the depth of the tunnel. The cost has been estimated to be approximately 20-30 MYen/m, referring to the Trans-Tokyo Bay Tunnel which connects Chiba and Kawasaki by a highway (under construction). A technical difficulty lies in the construction of access pits of 100 m in depth. There remains a subtle problem concerning the interpretation of the word "metropolitan area": whether the law can be applied to the Tsukuba area or not. In the meanwhile a sudden collapse of the so-called bubble economy in 1990 induced a recession and caused a drop in the price of land, which diminished interest in the utilization of deep-underground locations.

Since then, interest in the site was changed to hard-rock mountains, which would provide small vibration and long-range stability for stable beam collisions at the interaction point. In order to excavate the main tunnel inside of a rock mountain, the following two tunneling methods are applicable: a blasting method (so-called NATM) and a boring method (so-called TBM) to excavate the main tunnel inside rock along a ridge of mountains. The design of a facility has been investigated for these two tunneling methods.

17.2 NATM

The concept of NATM (New Austrian Tunnelling Method) was developed as the result of findings by Rabcewicz in 1944 concerning the importance of the time-dependent behavior of a rock mass; a study was made by Fenner in 1938 on the reciprocal relationship between radial deformations and the required support resistance in tunnels. Some basic requirements had already been established at the beginning of the century, such as the rapid installation of a support in full contact with an unexcavated rock surface.

The application of NATM began with the use of shotcrete in small water tunnels with poor rock conditions. The construction of the 6.4 km-long Tauern tunnel in Austria was a milestone application of NATM. The Tauern tunnel was a significant stage, since for the first time extremely difficult rock-pressure phenomena resulted from primary stresses had been observed. In addition, the phyllite in the area had very poor physical characteristics. Deformations of 10 to 20 cm or more on short sections necessitated the use of longitudinal contraction joints in the shotcrete to allow more flexibility of the lining. The stabilizing effect of fully mortar-embedded rock bolts in the very poor ground was obvious.

Subsequently, NATM was used for road and railway tunnels, and large openings for various purposes.

Some promising developments in technology were found from the 1970's in Europe, especially in North Europe. The NATM technology was imported from Europe in the early 1980's to Japan. At present, NATM has been one of the most popular tunneling methods for small water tunnels, railway tunnels, road tunnels, oil-storage tunnels and large amusement halls in rock mountains.

17.2.1 Characteristics of NATM

The principal concept of NATM is that the ground (rock or soil) which surrounds the excavation can be made to acts like a load-bearing ring, thus enabling the ground to become an important support member in itself. In other words, the surrounding area of the excavation acts like an arch-dam for supporting the high pressure of large amount of water mass. For this, the following basic requirements have to be taken into account:

- Consideration of the geomechanical ground behavior;
- The most suitable static shape of the profile;
- Avoidance of any unfavorable stresses and deformations by adopting suitable support works, installed in the correct sequence;.
- Optimization of the support resistance as a function of the allowable deformations; and
- Control by in-situ measurements.

When a tunnel is excavated, the prevailing primary state of equilibrium is transformed in several intermediate steps of stress re-distributions to a new secondary state of stable equilibrium. The aim of NATM is to influence these processes in a way which is both technically safe and economical. During excavation, the soil or rock deformations should therefore be controlled in such a way that they remain small enough to avoid a decrease in the rock strength, but large enough to mobilize the rock to form a load-bearing ring, thus reducing the required support resistance.

Rock bolts are the most important support element for squeezing and swelling ground. In poor geological conditions due to the abnormal rock pressure phenomena, the complex of the rapidly applied a shotcrete and rock bolting can improve the situation considerably.

The procedures of excavation by NATM are schematically shown in Figure 17.1. It goes through the following steps:

1) Excavation and shotcrete

- The blast depth is determined from the condition of the rock determined by in-situ measurement.
- Drilling the rock at the face of the tunnel by a drill jumbo with several booms. The drilling depth is adjusted by the blast depth.
- Insertion of explosives into the drilled holes and connection of a leading wire to the exploder.

- Taking the drill jumbo backward so as to avid any damage from the blasting.
- Blasting by explosion.
- Mucking by a shovel car to muck loaders. See Figure 17.2.
- The drill jumbo approaches the face of the tunnel and the shotcrete is sprayed by two or four spraying machines on the jumbo. The depth of the shotcrete is determined by the condition of the rock.
- Systematic rock bolting is carried out if the rock condition is poor.

The depth of the blasting and shotcrete, and the length and density of the rock bolting are determined by the rock condition. Five patterns have been standardized by both the Ministry of Construction and the Ministry of Transport in this country. An in-situ measurement of the deformation of the rock surroundings after evacuation determined the next step of the excavation and shotcrete. The above basic procedure requires about 6 hours for one cycle. In general, four cycles of blasting and shotcrete are carried out per day.

2) Water-proofing and lining

- Installation of a drain on the side wall of the tunnel.
- Water proofing with a chemical sheet using a traveling form.
- Arch lining by a traveling form.

3) Invert concrete

- Water drain on the floor at both sides of the tunnel.
- Invert concrete for the floor of the tunnel.

In-situ Measurement of Deformation after Excavation

The inner dimensions of the tunnels are measured after blasting during the period of deformation. The deformation in an ordinal rock mountain is damped in two weeks, except in very poor rock conditions. The following data show typical examples of the deformation of rock tunnels in two different rock conditions. The data were obtained at tunnels for an experimental railway of the JR Superconducting Linear Motor Car excavated near Mt.Fuji. From those data, the deformations in the main-tunnels of JLC excavated by NATM can be estimated, since the tunnel size is similar to the size of the main-tunnel of JLC. As shown in Figure 17.3, in Tuff rock, which is of relatively poor condition, the maximum deformation of the width of the tunnel is 22 mm. The deformation in the level of civil engineering is damped in two weeks. In Quartz Prophyry rock, which is relatively hard rock, the maximum deformation is 5.5 mm, and is damped in 10 days. See Figure 17.4. No detailed data

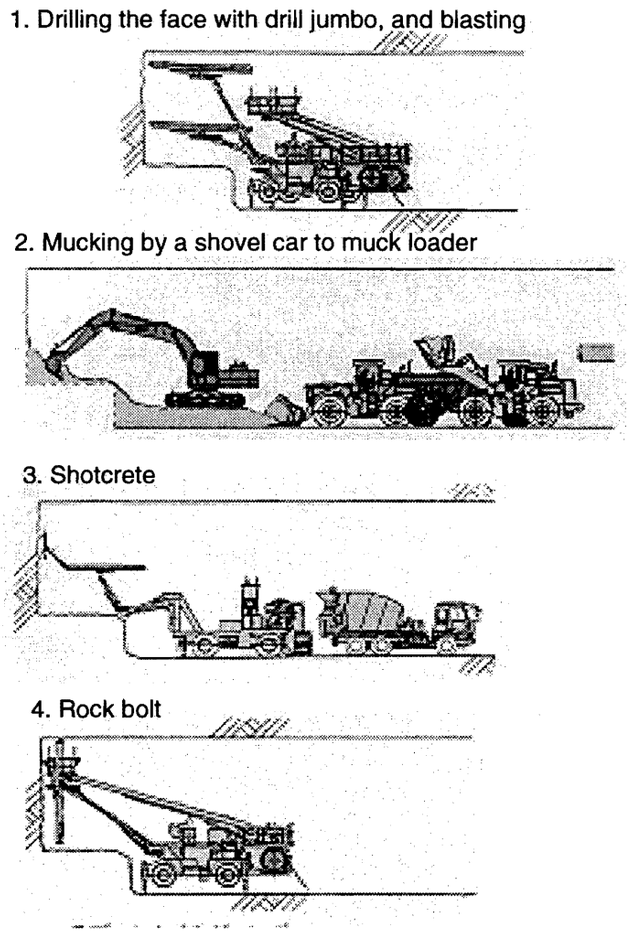

Figure 17.1: *Procedure of NATM.*

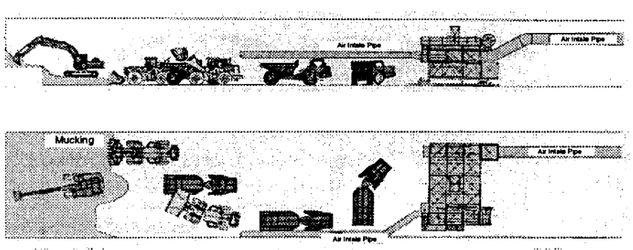

Figure 17.2: *Face of the tunnel at the mucking.*

concerning deformations during many years have been measured; however additional deformations on the level of civil engineering have not been observed. In Granite rock, the deformation would be smaller than in the above two examples, since the rock condition is hard.

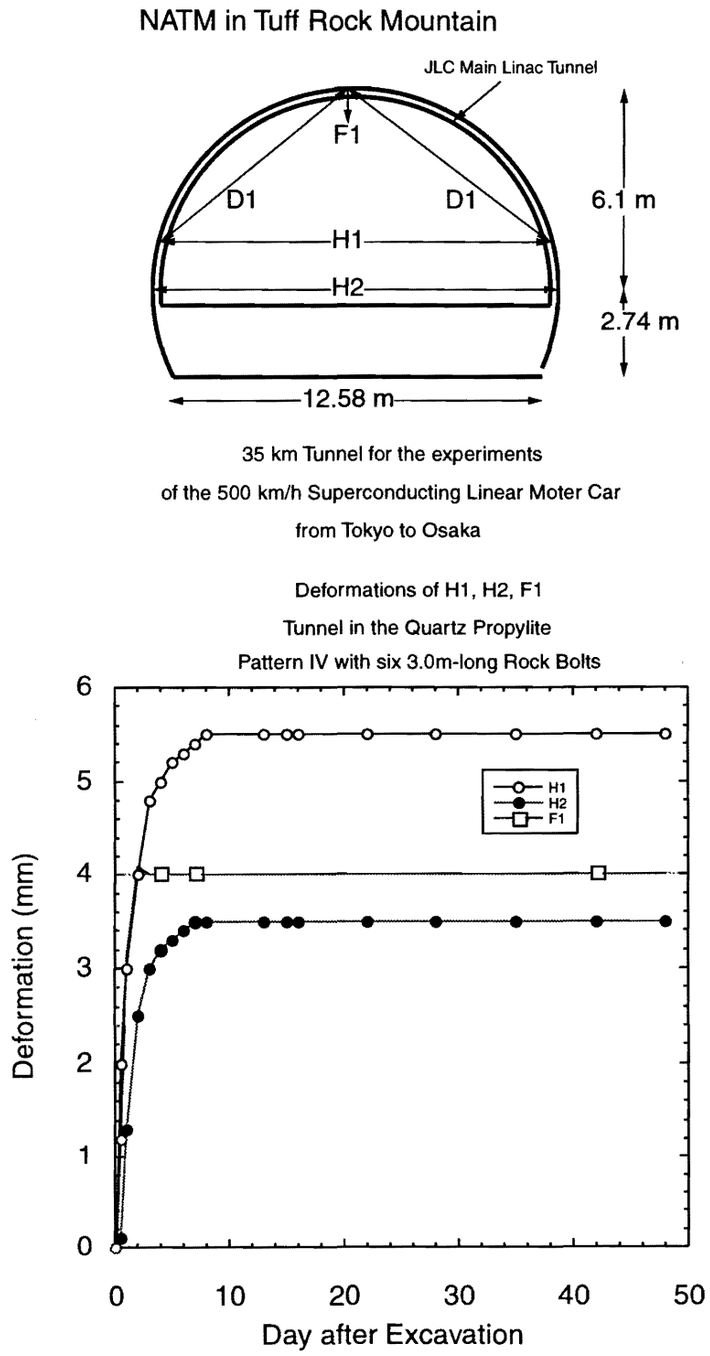

Figure 17.3: *Deformation of a tunnel excavated in the Tuff rock mountain*

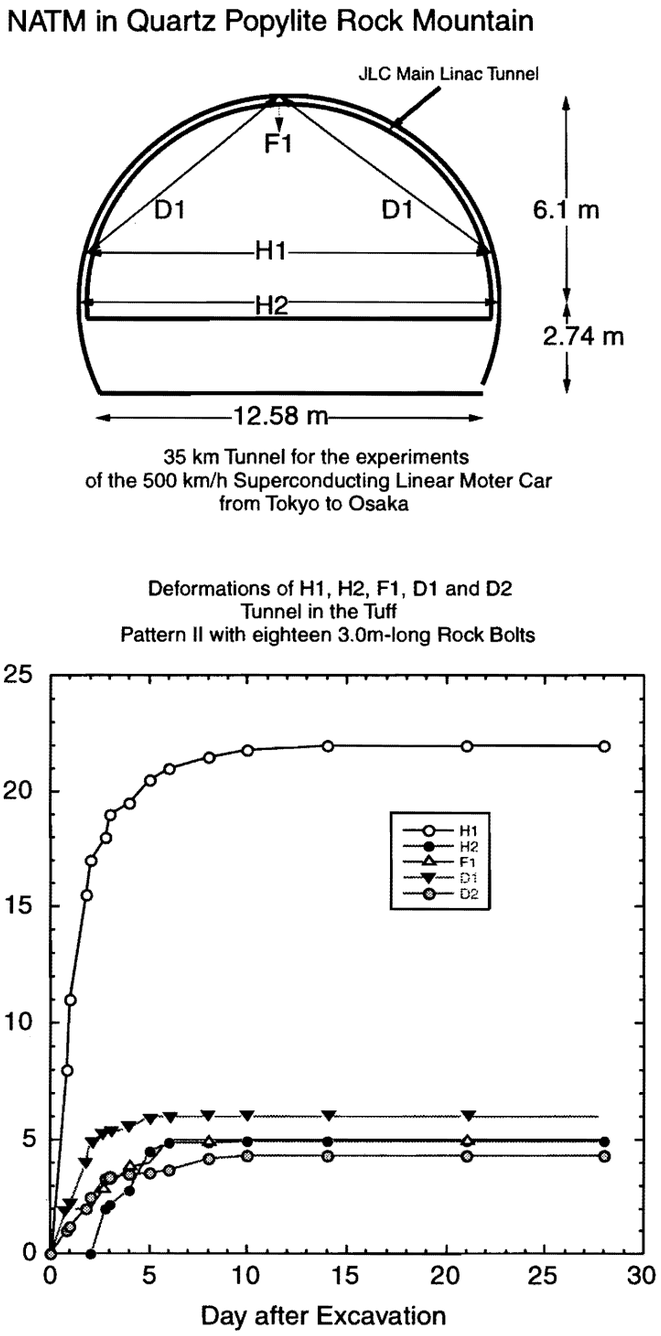

Figure 17.4: *Deformation of a tunnel excavated in a Quartz Popylite rock mountain*

17.2.2 Design of the Tunnels Excavated with the NATM Technique

Access Roads

A total design of the JLC Facility was performed using the NATM technique. At the starting point of the construction, access roads are constructed from the existing roads to the access points where the construction work offices are built. After that, the construction materials are brought into the assembly areas near to the construction work offices.

The total number of access points should be determined by both the construction period and the total cost of construction. Assuming a 5-year construction period, the total number of access points is nine, as shown in Figure 17.5. A large-scaled access point is placed at the interaction region for the detector which requires the transportation of a superconducting solenoid magnet of large diameter into the detector-hall. Another eight access points are utilized for the accelerator. The access points are required for each of the main linac and one access point for each injector complex, including bunch compressor. Assuming that the total length of the JLC is 28 km and the distance between the access points of the main linac is 3.2 km, one access points near to the injector complex should serve as access to the bunch compressor and main linac. These access roads would be utilized for access from the outside to the accelerator for maintenance.

Access Tunnels

In the second stage, the access tunnels would be excavated by NATM to the location of the accelerator tunnels, such as the main-tunnel, the pre-accelerator complex, the injector complex and the detector-hall. The number of access tunnels to the main tunnel would depend on the required construction period of the total facility. The speed of excavation is determined by the blast depth, which depends on the rock condition. Assuming that the rock condition is typical Granite existing in this country, the excavation speed of main tunnel is estimated to be about 150 m/month. Consequently, the access tunnels should be placed every $3 \sim 5$ km of the main tunnel. These access tunnels would be utilized for the mucking, gallery ventilation as well as the transportation of the construction materials. The cross section of the access tunnels should be determined, based on the following conditions:

- Two lanes for 25 t dump trucks.
- Sufficient size for the easy transport of construction materials.
- Space for the duct of gallery ventilation.
- The average slope should be less than 1:10 in order to allow easy mucking by heavy dump trucks.
- Sufficient size for transporting accelerator components and detector components after constructing the facility.
- The average slope should also be less than 1:10 in order to maintain easy transport of the accelerator and detector components

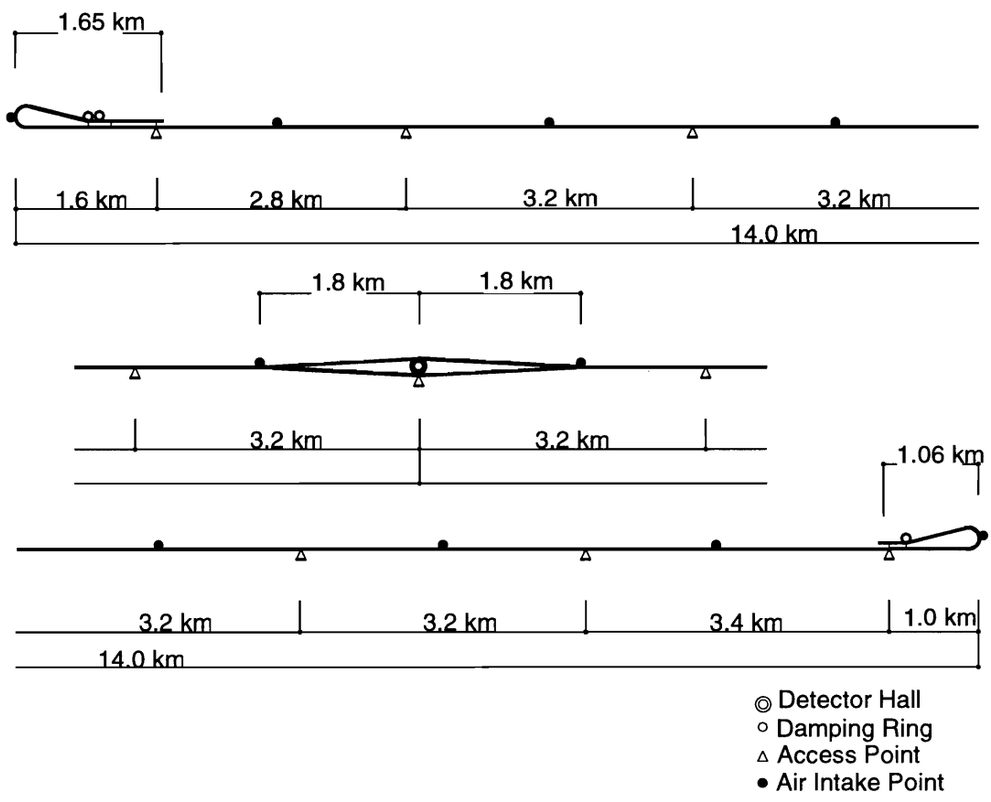

Figure 17.5: *Access points to the detector-hall, main linac, injector complex and bunch compressors.*

- The cross section should satisfy the above conditions and should be minimized for the cost of construction

Figure 17.6 shows the cross section of the access tunnel to that of the main linac. The geometry of this access tunnel is approximately equivalent to the JR Shinkansen two-lane tunnels. Table 17.1 gives the parameters of the access tunnel.

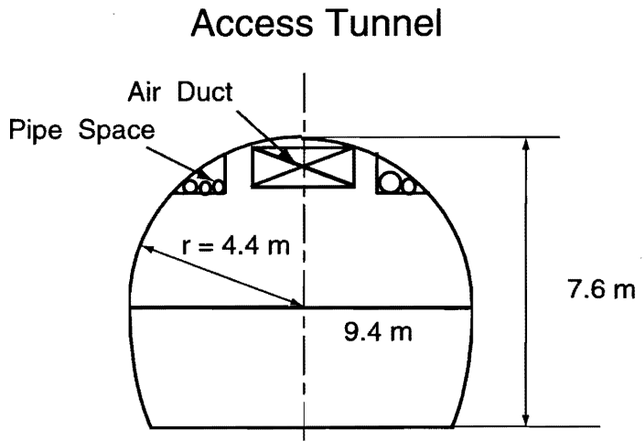

Figure 17.6: *Cross section of the access tunnel to the main linac excavated by NATM.*

Table 17.1: *Parameters of excavation of the access tunnel.*

Shotcrete	
Thickness	$t = 0.1$ m
Rock bolts	
Length	$L = 2.5$ m
Density	5.5 bolts/m
Invert	
Thickness	$t = 0.2$ m

Air-Intake Shafts and Detector-Hall Access Shaft

Shafts with a relatively small diameter are required at the middle points between the access tunnels in order to intake fresh air during the excavation and machine operation. In the present design, ten shafts will be constructed by shaft excavators, as follows: eight shafts for the main tunnels and detector-hall, and two shafts for the bunch compressors and injector complex, as shown in Figure 17.5.

Access to the detector-hall can be provided through a large-scale NATM access tunnel or large-scale

shaft excavated by NATM. In the present design, the above two options have been studied. The access shafts comprise two shafts.

The first one is for transporting tools and excavation components as well as transporting detector components, such as superconducting magnet, cryostat system and electronics. The diameter of the shaft is ϕ =12.0 m of inner diameter, so that a superconducting magnet having a diameter of 10 m can be brought in. The cross section of the access shaft is shown in Figure 17.7.

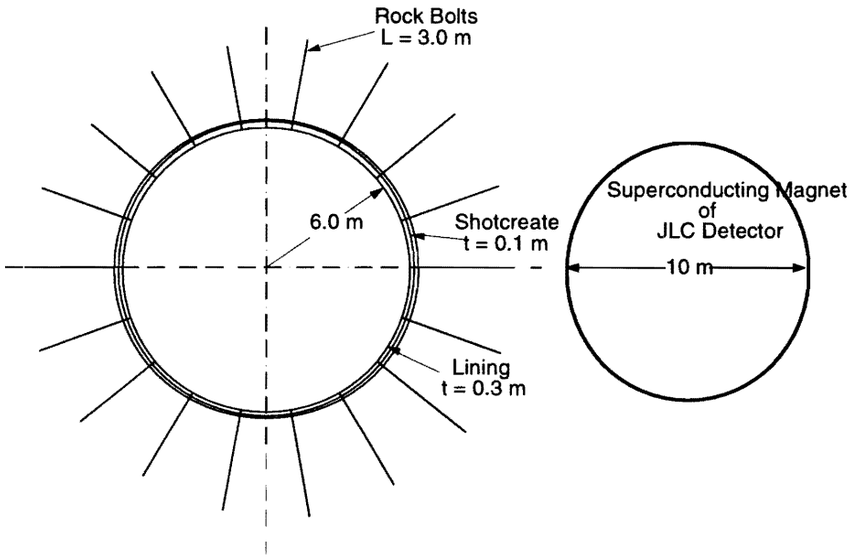

Figure 17.7: *Cross section of the access shaft to the detector-hall for the accelerator components. The shaft is excavated by NATM.*

The second one is for the personnel and workers. The diameter of the shaft is about ϕ =6.0 m and an elevator and emergency staircase are installed inside. The cross section of the access shaft is shown in Figure 17.8.

The procedure for excavating the shaft is similar to that of the main tunnel by NATM, as shown in Figure 17.9.

Main Tunnels excavated by NATM

In the third stage, the construction materials are brought into the face of the access tunnels to start excavating the main tunnels. A drill jumbo, or drill carriage, with multi-booms and shotcrete spray arms, is built from the machine components. In order to shorten the construction period, two drill jumbos can be installed in the face of the access tunnel. In this case, each system excavates in different directions along the main tunnel, respectively. The excavation procedures by NATM are described in the previous section.

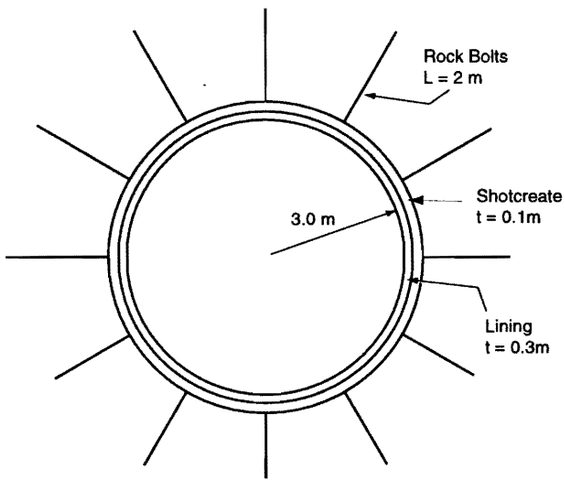

Figure 17.8: *Cross section of the access shaft to the detector-hall for personnel. The shaft is excavated by NATM.*

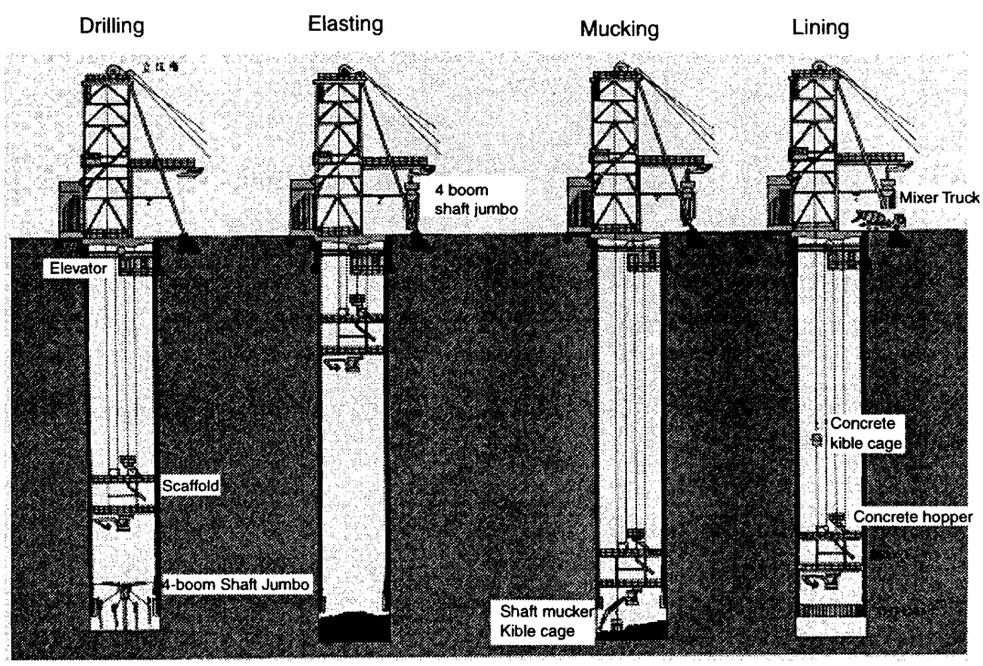

Figure 17.9: *Excavation procedures of large-scaled shaft by NATM*

The cross section of the main tunnel would be 12 m in width and 5.8 $\sim$ 7.6 m in height, as shown in Figure 17.10. This size is relatively wider than highway tunnels with two lanes and railway tunnels with two lanes, and relatively higher ratio of flatness. However, an actual long tunnel with a wider width by NATM has already been achieved. The experimental line of JR, the Superconducting Linear Motor Railway was excavated near Mt.Fuji having a total length of about 35 km. The width and height of this tunnel are 12.58 m and 8.8 m, respectively. Since NATM has flexibility in excavation compared with the TBM construction method, side-rooms can easily be constructed along the main tunnel. These spaces are to be utilized for shield door, electricity, water cooling system and air-conditioning systems as shown in Figure 17.11.

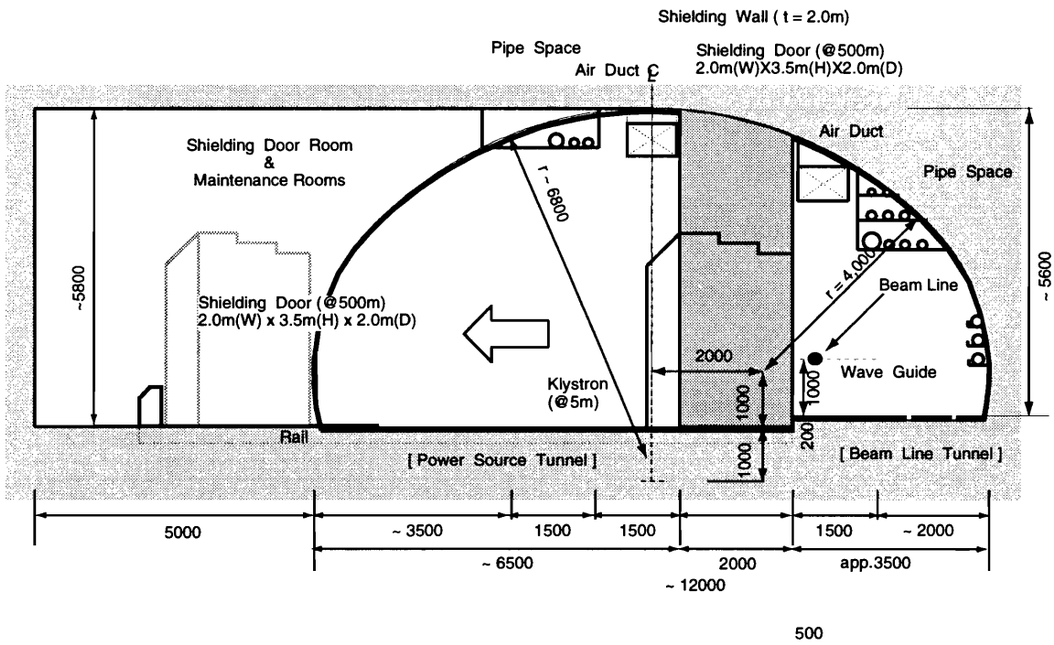

Figure 17.10: *Cross section of the main tunnel excavated by NATM.*

Five patterns of the support system for different rock conditions have been standardized by both the Ministry of Construction and the Ministry of Transportation. The pattern of the main tunnels is shown in Fig 17.12, which is referred to from the pattern of the tunnel of JR Superconducting Linear Motor Railway. The thickness of the shotcrete and the density of the rock bolts provide the optimum support for different rock conditions. Figure 17.2 shows the classification of rock conditions and examples of the rock mass. Assuming that the main tunnels are excavated in granite rock mountain, the patterns required to excavate the main tunnel would be of two types (Pattern V or IV). The technical experiences obtained by NATM during more than 20 years in this country shows that Pattern III is sufficient to support the granite rock mass under poor conditions.

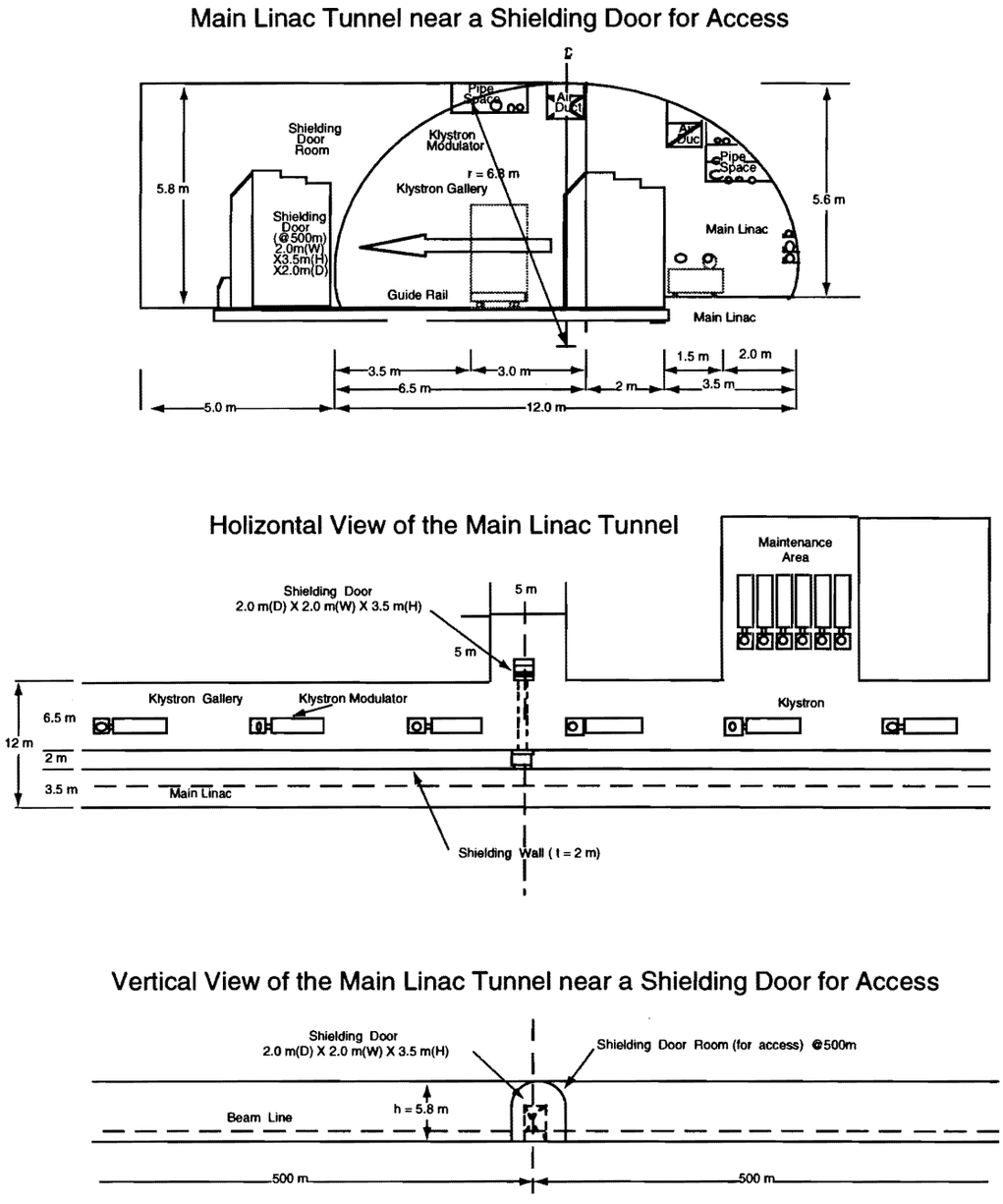

Figure 17.11: *Cross section of the main tunnel excavated by NATM. The area of an access door between the klystron gallery and the accelerator room.*

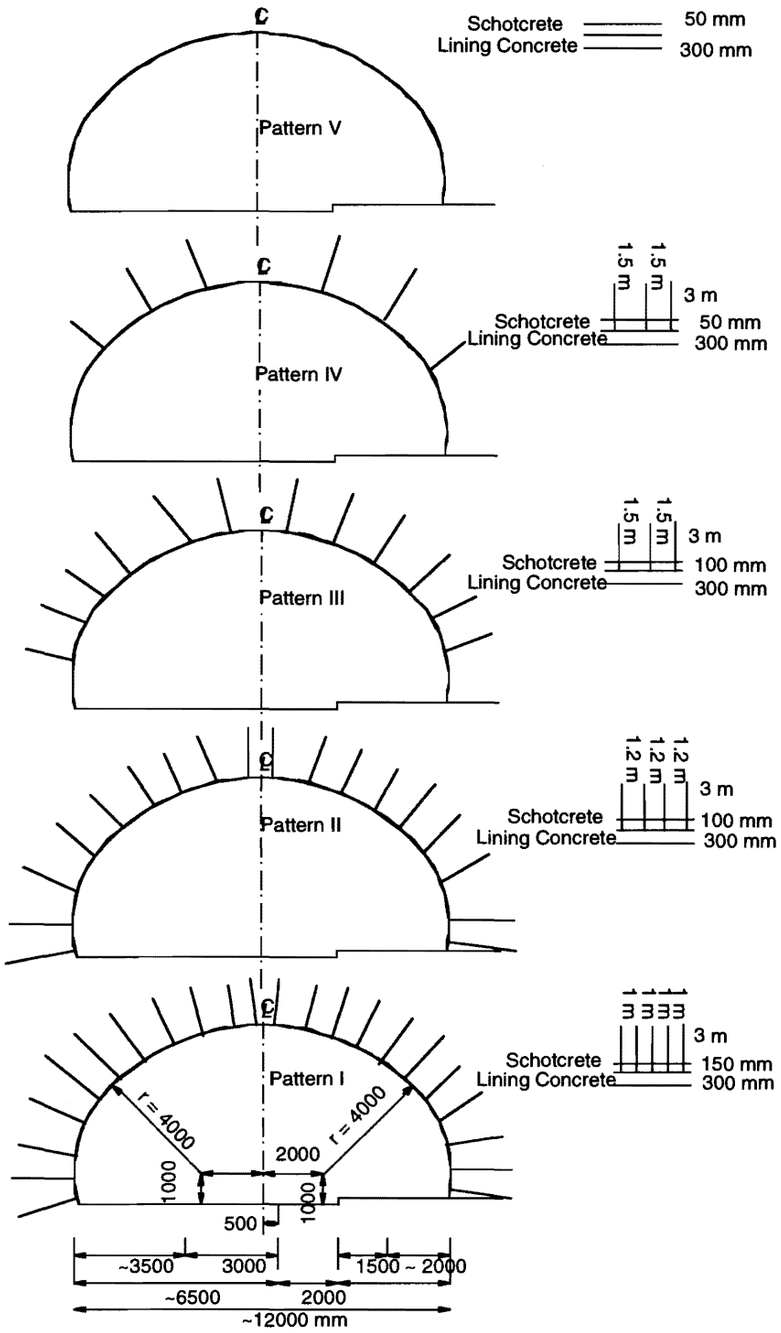

Figure 17.12: *Different patterns of support for different rock conditions.*

Table 17.2: Classifications of the five patterns

	Conditions of Rock Mass	Example
Pattern V	Stable	Plutonic Rock:(Granite, Granoiorite, Diorite, Gabbro) Hypabyssal Rock:(Porphyrite, Quartz Porphyry, Diabase) Volcanic Rock:(Basalt)
Pattern IV	Fragile	Metamorphic Rock, Paleozoic Rock
Pattern III	Crushed	Volcanic Rock:(Rhyolite, Andesite) Old Tertiary System (Tuff, Shale, Sandstone)
Pattern II	Fragment	Old Tertiary System (Mudstone, Sandstone, Tuff, Silt etc.)
Pattern I	Mironite	New Tertiary System (Mudstone, Sandstone, Tuff, Silt etc.)

Tunnels for an Injector Complex and Bunch Compressor

Figures 17.13 and 17.14 show tunnels for the injector complex and bunch compressors. These tunnels will also be excavated by NATM.

As shown in Figure 17.13, the injector complex for positron consists of a 10 GeV S-band positron production linac and a 1.98 GeV S-band damping ring injector linac; the bunch compressor consists of an 8 GeV S-band pre-linac and a 4 GeV S-band linac. The injector complex for electrons is composed of a 1.98 GeV S-band injector linac, and the bunch compressor comprises an 8 GeV S-band pre-linac and a 4 GeV S-band linac. The geometry of the main tunnel is adopted to the S-band linacs in the injector complex and bunch compressor.

The pre-damping ring is installed in a hall excavated by NATM since the size of the ring is relatively small. The facility of the damping ring is similar to that of the ATF damping ring.

The damping ring is installed in a ring tunnel excavated by NATM. A hall excavated near to the center of the ring tunnel provides a space for installing damping-ring components, such as rf sources, power supplies and modules for beam instrumentation. This hall also provides a standard level of alignment for the initial installation of the damping-ring components.

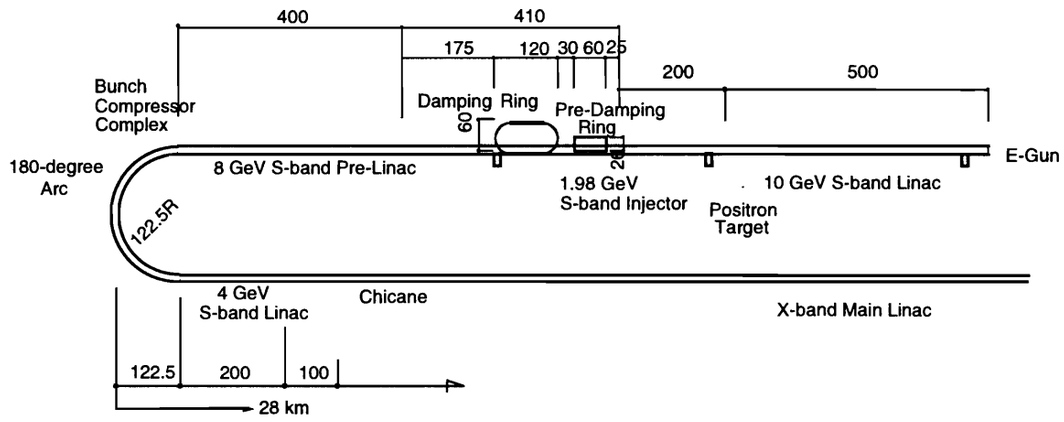

Figure 17.13: *Tunnels of the injector complex and bunch compressor for positrons.*

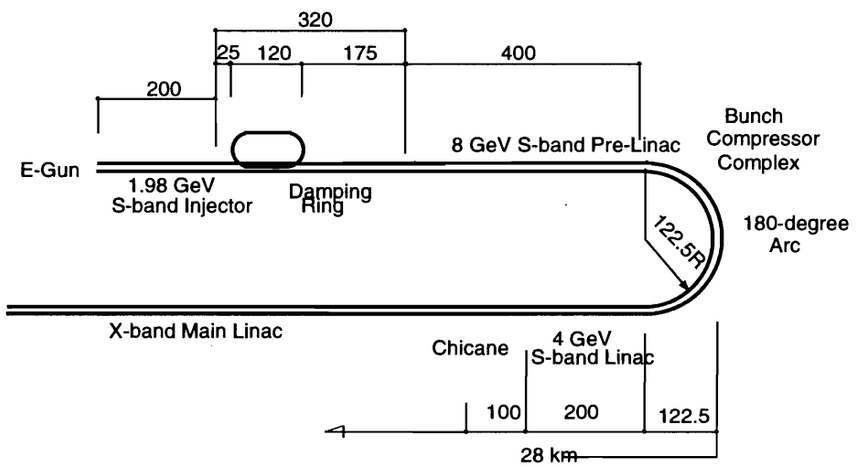

Figure 17.14: *Tunnels of the injector complex and bunch compressor for electrons.*

Tunnels for the Collimator and Final Focus System

Figure 17.15 shows the tunnels for the collimators and final focus system that was originally considered for 0.5 TeV JLC-I. At the end of the main linac, the width of the tunnel is expanded from 12 m to 17 m. The end of the 17 m width tunnel, and the two collimator tunnels are connected. NATM has the flexibility to connect tunnels with different geometries. The technology is similar to the construction of a large-scaled subway station with subway tunnels. The size of the collimator tunnels is 5 m width and 5.8 m height, which is relatively smaller than the access tunnels. The distance between the two final-focus system is 48 m at the end of the collimators.

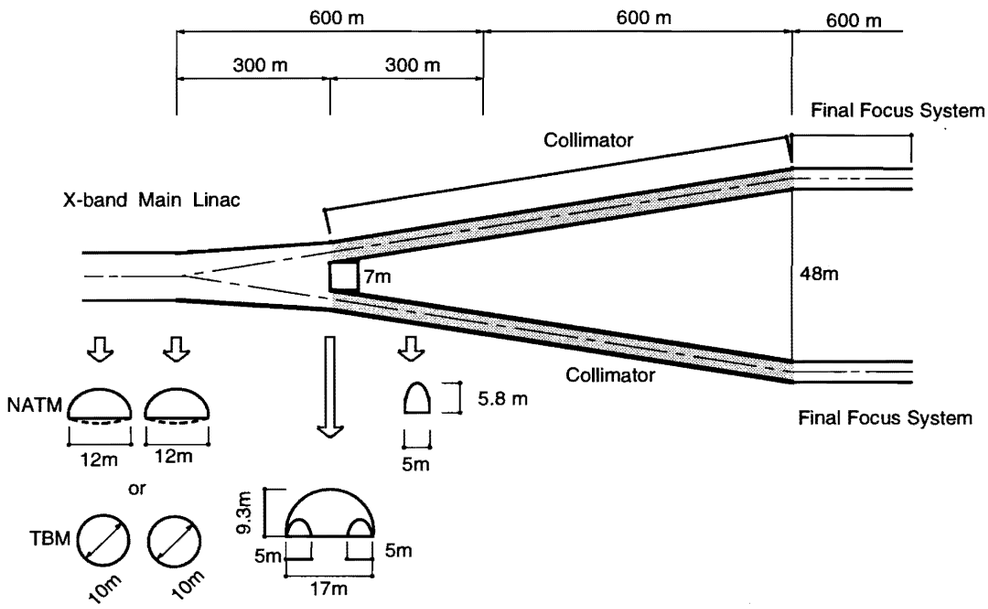

Figure 17.15: *Tunnels from the main linac to the final focus system, originally considered for 500 GeV JLC-I.*

Figure 17.16 shows the tunnels for the final focus system in 0.5-1.5 TeV JLC, which is consistent with the design of the final focus system presented in Chapter 13. At the end of the main linac, the width of the tunnel decreases from 12 m to 5 m in order to connect the collimator tunnel of 1.2 km in total length. The final focus tunnel is followed to the collimator tunnel. The distance between the two final-focus system is 20 m at the end of the collimators.

Tunnels for the Detectors

Figure 17.17 shows the schematic drawing of the facility from the main linac to the interaction points for 0.5 TeV JLC-I (consistent with Figure 17.15). The present design shows that the distance between the two final focus system is about 48 m which is sufficient to install two detectors.

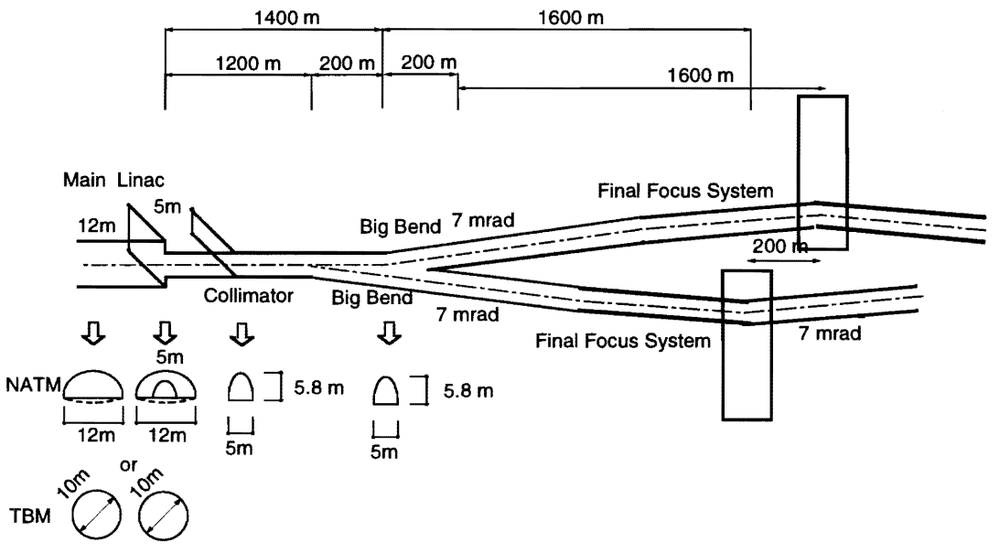

Figure 17.16: *Tunnels from the main linac to the final focus system that is compatible with the new layout presented in Chapter 13.*

Figure 17.18 shows the schematic drawing of the facility from the main linac to the interaction points for 0.5–1.5 TeV JLC (consistent with Figure 17.16). The distance between the two final focus system is about 20 m. The horizontal offset of 200 m between two interaction points provides two detector halls.

We have two options concerning the access tunnels for installing the detector components. One is a large-scaled shaft excavated by boring machines. The construction of a large-scaled shaft requires one of the most difficult tunneling methods. We have another option of a long access tunnel excavated by NATM. The optimum choice should be chosen based on the site conditions and cost estimation.

A cross section view of the tunnel for the detectors is shown in Figure 17.19. The size of the JLC detector design by the JLC physics group is 15 m×15 m×15 m. The width is 40 m and height is 26 m. The length of the detector tunnel is 190 m, which is sufficient to install two detectors, a maintenance area and two access tunnels.

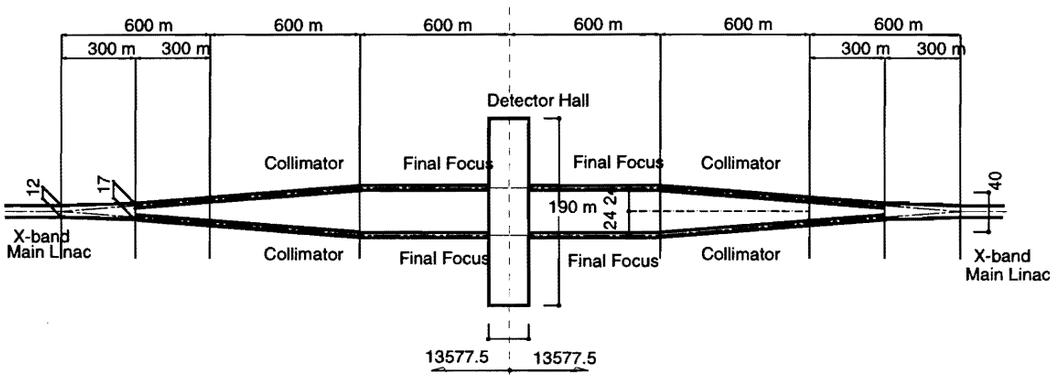

Figure 17.17: *Schematic view of the tunnel arrangement near to the interaction point of 0.5 GeV JLC-I. The initial scheme.*

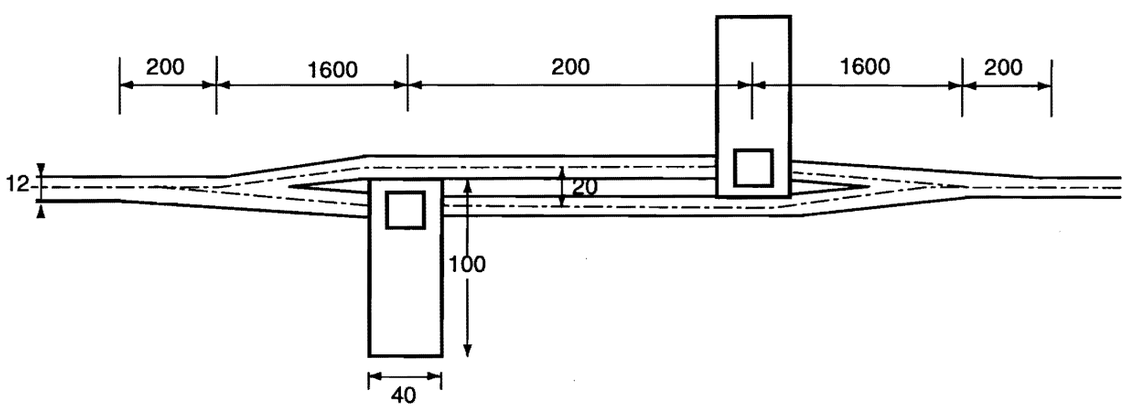

Figure 17.18: *Schematic view of the tunnel arrangement near to the interaction point of 0.5–1.5 GeV JLC. This layout is compatible with the new layout as presented in Chapter 13.*

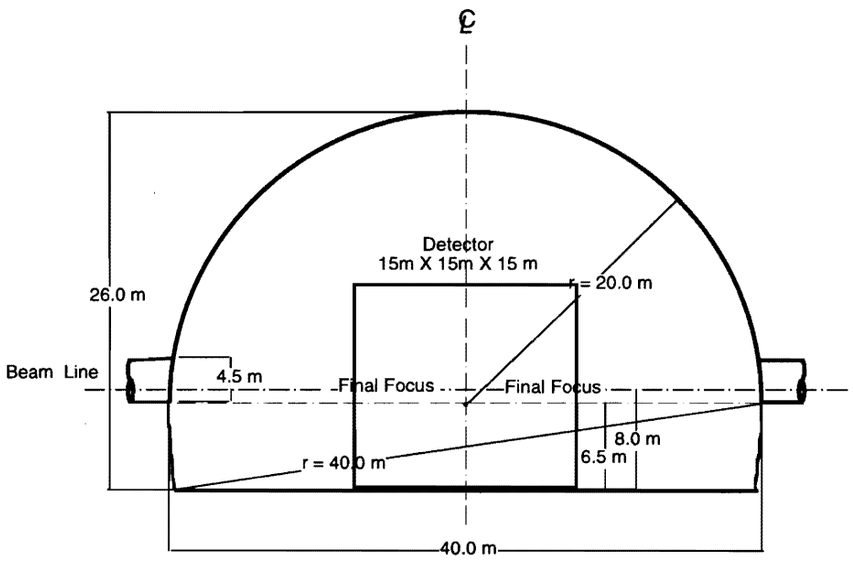

Figure 17.19: *Tunnels for detectors.*

Total Facility of JLC

A bird's-eye view of the total facility of the JLC tunnels is shown in Figures 17.20 and 17.21.

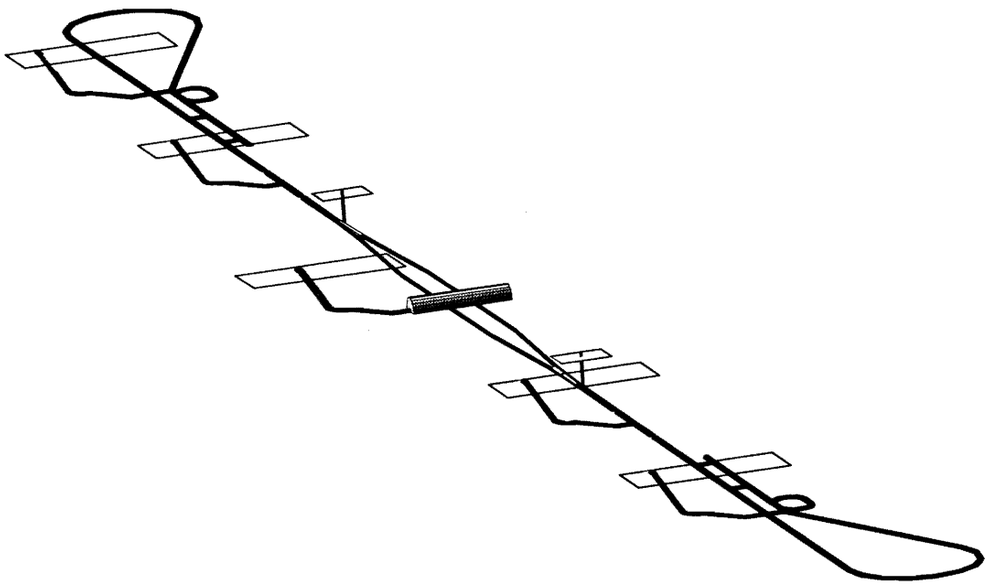

Figure 17.20: *Bird's-eye view of the total facility of the JLC tunnels.*

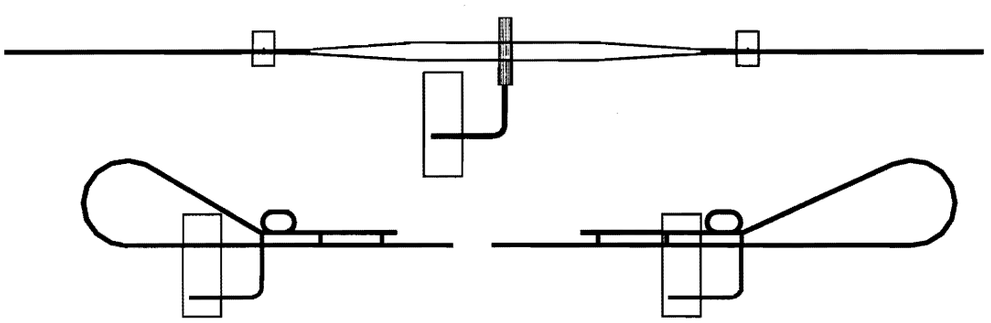

Figure 17.21: *Bird's-eye view of the total facility of the JLC tunnels.*

17.2.3 Support System for the Accelerator Components

The supports of the accelerator components should be directly connected to a large rock mass in order to avoid any misalignment due to external incoherent vibration. However, a fracture zone comprising micro cracks may be produced after excavation by a change in the stress of the rock mass. In addition, a fractual zone comprising cracks can be produced by the shock of blasting. The thickness of a fracture zone is estimated to be $10 \sim 50$ cm in a Granite rock mass according to an ultrasonic velocity test, a boring test and so on.

The rock mass consists of blocks of rock pressurized by intense earth pressure. After the excavation, a decrease in the stress expands the interstitial of the rocks. By measuring the water flow around the tunnels, the coefficient of permeability of the water increases to be ten-times higher than the rock mass without excavation. The thickness of the fracture zone around the tunnel is estimated from the change in the coefficient of permeability. In a Granite rock mass, the thickness of a fracture zone is estimated to be about one radius of the tunnel.

The change in the stress in the rock mass in the floor is smaller than in the rock mass in the tunnel sides. In addition, the rocks in the floor of the tunnels would have a fracture zone caused by the blasting as well as the forces from the excavation machines and mucking machines. The floor, where the accelerator supports will be installed, should be modified by the rock-bolting method. A base plate is directly connected to the undamaged rock mass deep-inside with long rock bolts.

17.3 TBM

The concept of the TBM (Tunnelling Boring Machine) was developed as an open-type boring machine in coal mines. The application of an open-type boring machine, the so-called partial face machine, road header and partial cutting machines, to the excavation of a rock mountain was started many years ago. In this country, its first application was the construction of a railway tunnel in Kyusyu Island in 1969.

The TBM, as a full-face tunneler, was first applied to the construction of a water tunnel of 2.3 m diameter at Niihama, Shikoku Island in 1964. A full-face tunneler consists of a rotating cutter head, a front body, a second body and a belt conveyer for mucking. The main clippers installed in the second body are expanded in the radial direction, and fixed to the inner surface of the tunnel. The total thrust force is made by four thrust jacks while the main clippers support the second body. The direction of the excavation is controlled by adjusting the thrust force of each jack. In a hard rock mass, an intense total thrust force can be generated, and the cycle length becomes shortened. After one cycle length, the front clippers are expanded and support the front body. The main clippers are ducked and the thrust jacks are shortened in order to move the second body to the front. One round of excavation by the full-face tunneler is shown in Figure 17.22.

The cross section of tunnels excavated by TBM is a circle. At present, the main application of the TBM by a full-face tunneler is the excavation of the water tunnels for hydroelectric power stations, sewer tunnels, and water-way tunnels. The diameter of the most popular TBM is 2 $\sim$ 30 m diameter could be constructed in the near future.

The application of the TBM to the accelerator facility is popular in Europe and US. A part of the LEP tunnel was excavated by using full-face tunneler.

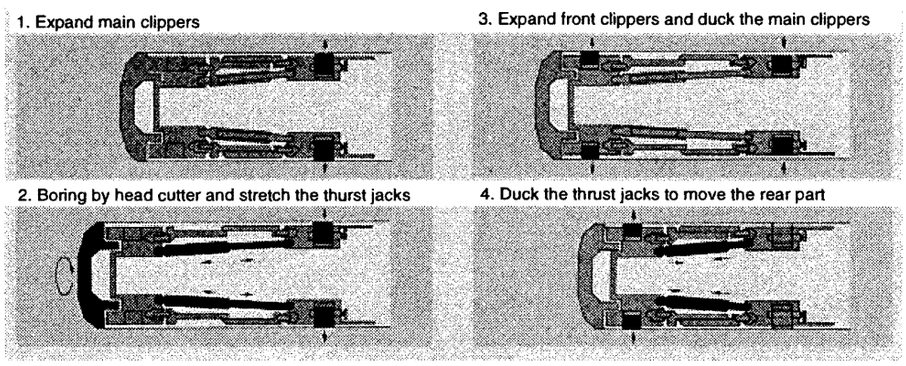

Figure 17.22: *Procedure of boring by TBM.*

17.3.1 Characteristics of the TBM

The principal concept of the full-face tunneler TBM involves a new type of tunneling method using computer-controlled automatic procedures. The environment at the face of a tunnel for workers is better than that for a NATM tunnel. In a NATM tunnel a large amount of fresh air is required to exhaust the micro dust produced by blasting. The noise environment in a NATM tunnel is the continuous sound of air flow and instantaneous shock of explosion. The environment in the TBM tunnel during construction is quite noisy with continuous sound and vibration generated during boring.

The cross section of the TBM tunnel is a complete circle. After excavation, the ground (rock or soil) which surrounds the tunnel is made to act like a load-bearing ring, enabling the ground to become an important support member in itself. In a poor geological section due to abnormal rock pressure phenomena, the NATM procedures should be required. The complex of rapidly applied shotcrete and rock bolting can improve the situation considerably.

The excavation procedures by the TBM method are as follows:

1) Cycle of the boring

- Main clippers installed in a second body are expanded in the radial direction.
- The main clippers are fixed to the rock mass bored in the previous round.
- The pressure of the main clippers to the rock mass should be high so as to obtain the total thrust force for boring.
- The front clippers with a cutter head are ducked, and then the front body is supported by four thrust jacks.
- Start the rotation of the cutter head.
- Total thrust force is made by four thrust jacks.
- The direction of boring is controlled by adjusting the thrust force of each jack.
- Mucking by a conveyer system near to the TBM. A diesel locomotive or battery locomotive is utilized for mucking in a long tunnel.
- When the thrust jacks are completely expanded, the rotation of the cutter head is paused.
- The front clippers are expanded in the radial direction and support the front body to the rock mass.
- The main clippers are ducked so as to be free from the rock mass.
- The thrust jacks are shortened so as to move the second body to the front.

The depth of excavation in one cycle is determined by the length of the thrust jacks. In general, 2 - 3 hours is required for one cycle. Any worn cutters should be replaced with new ones and the boring is interrupted for 4 - 7 days. The life-time of the cutter depends on the rock condition.

Water proofing has not been required for water tunnels bored by TBM. TBM has insufficient experience to be used as a technique for water proofing and lining. For the accelerator tunnel, water proofing and lining is one of the most important issues for maintaining a high reliability of machine operation. The following procedures would be required:

2) Water proofing and lining with concrete segments

- Shotcrete to proof against water leaks.
- Water proofing with a chemical sheet by using a traveling form.
- Water flows outside the segment ring
- Lining with concrete segments

Concrete segments are utilized for lining TBM tunnels. In general, an invert segment for lining is placed on the bottom of the tunnel in order to install the conveyer system at the tunnel's face, and to install the rails of locomotives for mucking in a long tunnel. After boring is completed, the concrete segments are transported by a segment wagon from outside and attached on the tunnel wall by a segment hanger. The standard segment width is about 1 m, and a segment joint is connected by bolts. The clearance between the surface of excavated rock mass and the outer surface of the segment ring is filled with concrete. The key issue is the technique of the invert segment in the TBM tunnel excavated for accelerators.

The supports of the accelerator components should be directly connected to a large rock mass so as to avoid any misalignment due to external incoherent vibration. However a fracture zone comprising micro cracks may be produced after boring. The diameter of the tunnel is slightly shrunk by intense earth pressure. Consequently, the micro cracks may be produced after boring due to a change in the stress of the rock mass. The thickness of a fracture zone is estimated to be $10 \sim 30$ cm in Granite rock. In general, the fracture depth of a NATM tunnel is three-times longer than that of a TBM tunnel.

Even by TBM, the fracture zone under the floor segments would cause loose contact with the accelerator supports. In addition, the segments interrupt any direct connection between the rock mass and the accelerator supports. The role of the segment ring is to support the rock mass and water proofing; also, all of the floor segments can not be removed. However, if floor segments are removed at intervals, the concrete with rock bolts drilled deeply inside the rock mass would be able to connect the accelerator support to the rock mass.

2) Base for the accelerator support

- Remove invert segments at intervals.

- Shotcrete and rock bolting to construct the base for the accelerator support.

17.3.2 Design of the Tunnels by the TBM

A total design of the JLC Facility was carried out by using the TBM. The advantage of the TBM is to excavate straight and long tunnels at a higher excavation speed than when using NATM. In the present design, the TBM is adapted to bore only the main linac tunnels; all other tunnels are excavated by NATM.

Access Roads

An access roads are required for the construction of work offices, and to bring in the construction materials such as the components of the TBM and NATM. The total number of access points should be determined by both the construction period and the total cost of construction. The cost of the TBM machine, itself, represents the main part of the total cost of the tunnel construction. In order to reduce the total cost of construction, the total number of machines should be reduced by reducing the cost of the construction period. The excavation speed of the TBM is higher than that of NATM. Assuming a 5-year construction period and a total length of 28 km, the span between the access points should be about $3.8 \sim 4.4$ km, which is longer than the design case of using NATM, as shown in Figure 17.23.

Access Tunnels

In the second stage the access tunnels are excavated by NATM to the location of the accelerator tunnels, such as the main-tunnel, the pre-accelerator complex, the injector complex and the detector-hall. The requirements of access tunnels are different from those of the NATM case. The tools of NATM include small-size components, and an access tunnel of smaller size is sufficient for bringing them into the main tunnel. However, the TBM includes some large-size components, such as the cutter head, the front body and the second body. The largest diameter of the TBM is equal to the diameter of boring; in addition, a clearance is required during transportation through the access tunnel.

- Sufficient size for easy transport of the TBM. Some clearance is required for transporting the cutter head, front body and second body of the boring machine.
- Sufficient size for transporting accelerator components can be provided after constructing the facility, since the largest size is the boring-machine component.
- The average slope should be less than 1:10 in order to allow easy mucking by a belt conveyer. It is also required for the easy transport of the accelerator components.
- The cross section should satisfy the above conditions, and should be minimized considering the cost of construction.

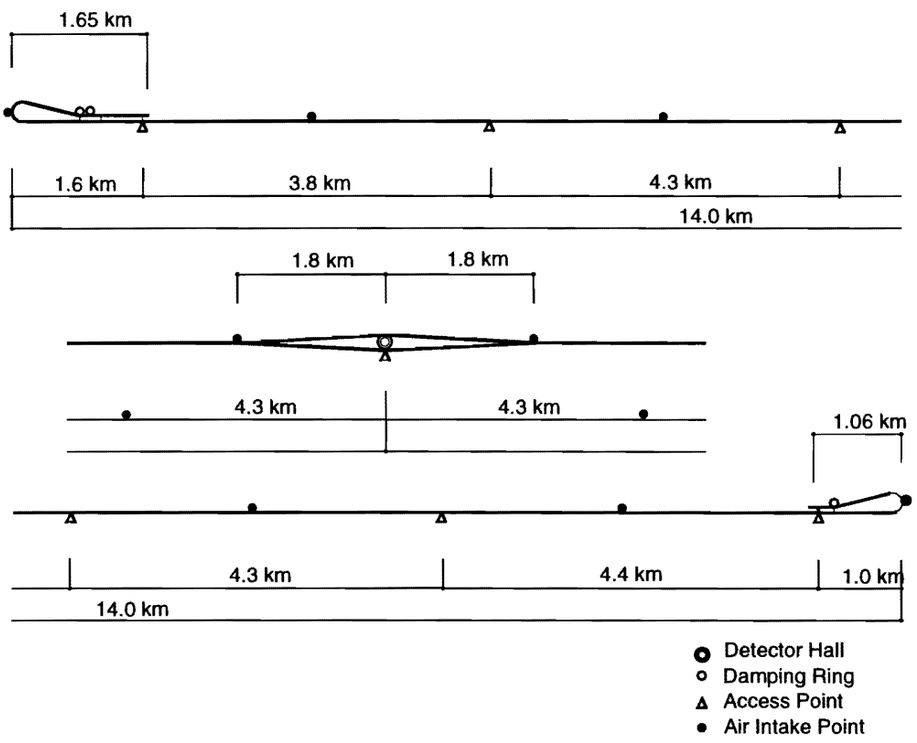

Figure 17.23: *TBM — Access points to the detector-hall, main linac, injector complex and bunch compressors.*

Figure 17.24 shows the cross section of the access tunnel to the main linac. The geometry of this access tunnel is slightly larger than that of the JR Shinkansen two-lanes tunnels. Table 17.3 shows the typical parameters of NATM.

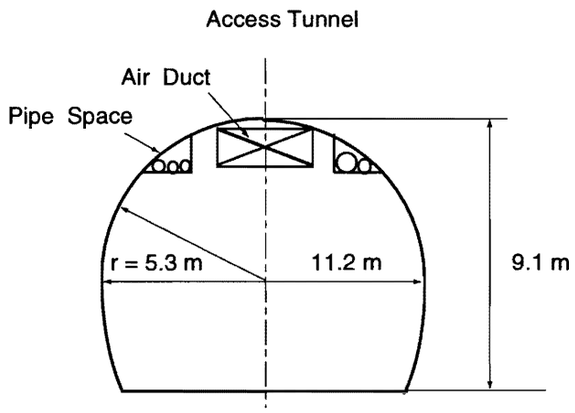

Figure 17.24: *Cross section of the access tunnel (excavated by NATM) to the main linac excavated by TBM.*

Table 17.3: *Excavation parameters of the access tunnel for TBM.*

Shotcrete	
Thickness	$t = 0.1\ m$
Rock bolts	
Length	$L = 2.5\ m$
Density	5.5 bolts/m
Invert concrete	
Thickness	$t = 0.2\ m$

-

Air-Intake Shafts and Detector-Hall Access Shaft

The shafts, such as that for air intake, and access to the detector-hall are common in design in the case of NATM described above.

Main Tunnels excavated by TBM

In the third stage, the construction tools and materials are brought into the face of the access tunnel to start excavation of main tunnel. The largest tool is the head cutter, front body and second body

of the TBM (Tunnelling Boring Machine). Figures 17.25 and 17.26 show drawings of the assembly space of the TBM before boring of the main tunnel is started.

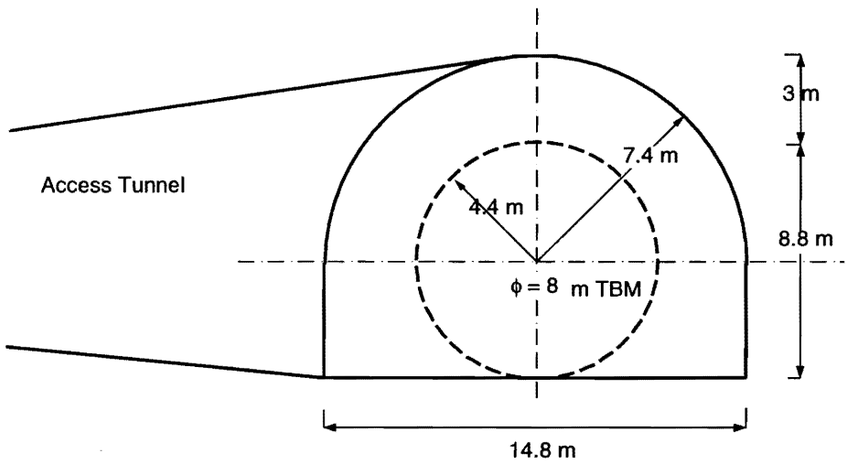

Figure 17.25: *Cross section of the preparation space that is required before starting excavation of the TBM-based main tunnel.*

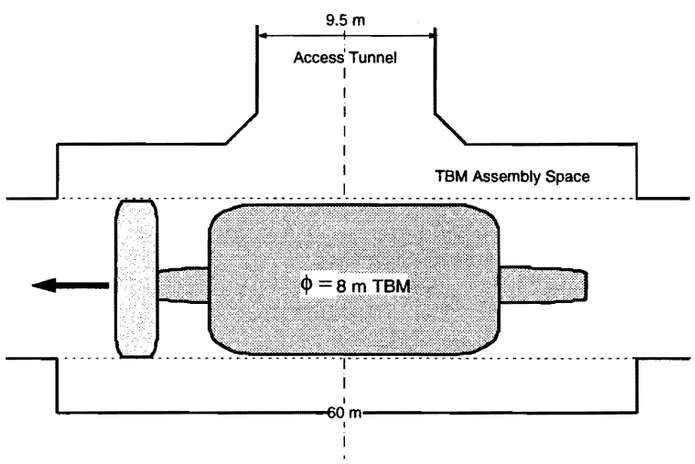

Figure 17.26: *Approach to the main tunnel (to be excavated with TBM) from the access tunnel. It shows the space that is required for assembling the TBM machine.*

After assembling the TBM, a belt conveyer system is installed in the access tunnel and assembly space. The TBM is connected by wiring with a computer-control system in the worker's office in the access point.

Two options of TBM tunnels with different diameter have been studied.

8 m Diameter TBM Option

The cross section of the main tunnel after lining would be smaller than the outer radius of the TBM. Assuming that the thickness of the lining, including shotcrete is 0.4 m, the effective inner diameter is 7.2 m. Shielding concrete is required between the accelerator room and klystron gallery in order to satisfy radiation shield. Since the cross section of TBM tunnel is completely circle, the double-decker style is effective for utilizing the space in a cylindrical tunnel. An access floor should be required for installing the accelerator components, maintenance of the accelerator, and emergency escape. Assuming that the thickness of the shield concrete is 1.0 m, the cross section of an 8 m diameter TBM tunnel becomes as shown in Figure 17.27. The dimensions of the klystron gallery are 7.2 m W × 3.6 m H, and those of the accelerator room are 2.6 m W × 2.6 m H. An access floor should be required for installing the accelerator components, maintenance of the accelerator, and emergency escape. If a larger thickness of the shield concrete is required due to radiation-management considerations, the height of the klystron gallery and the accelerator room should be less. The effective space depends on the thickness of the radiation shielding.

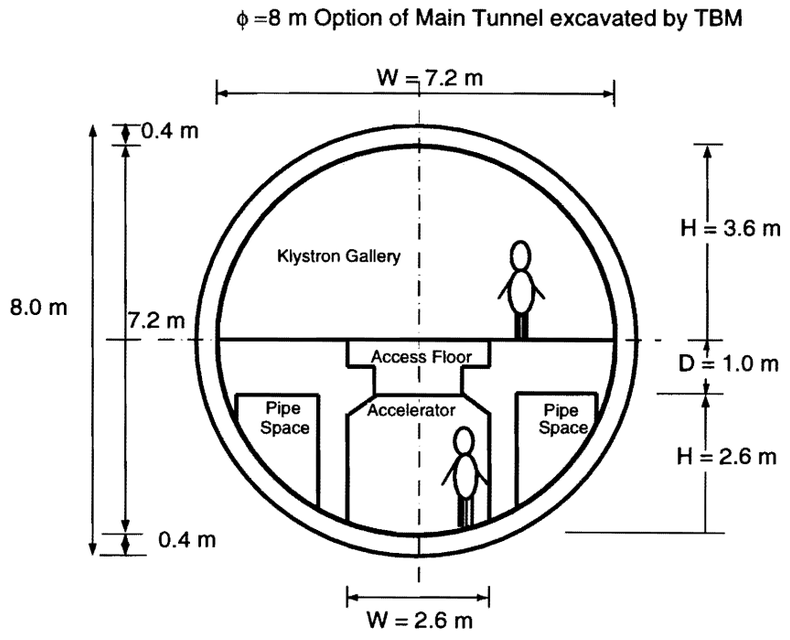

Figure 17.27: *Cross section of the main tunnel excavated by the TBM. The option by using an 8 m diameter TBM and 0.5 m thickness of the floor.*

10.8 m Diameter TBM Option

The cross section of the main tunnel after lining would be smaller than that of the outer radius of the TBM. Assuming that the thickness of the lining including shotcrete is 0.4 m, the effective inner

diameter is 10.0 m. Assuming the thickness of the shield concrete is 1.5 m, the cross section of the 10.8 m diameter TBM tunnel becomes as shown in Figure 17.28. The dimensions of the klystron gallery are 10.0 m W × 5.0 m H, and those of the accelerator room are 5.4 m W× 3.5 m H. An access floor should be required for installing the accelerator components, maintenance of accelerator, and emergency escape.

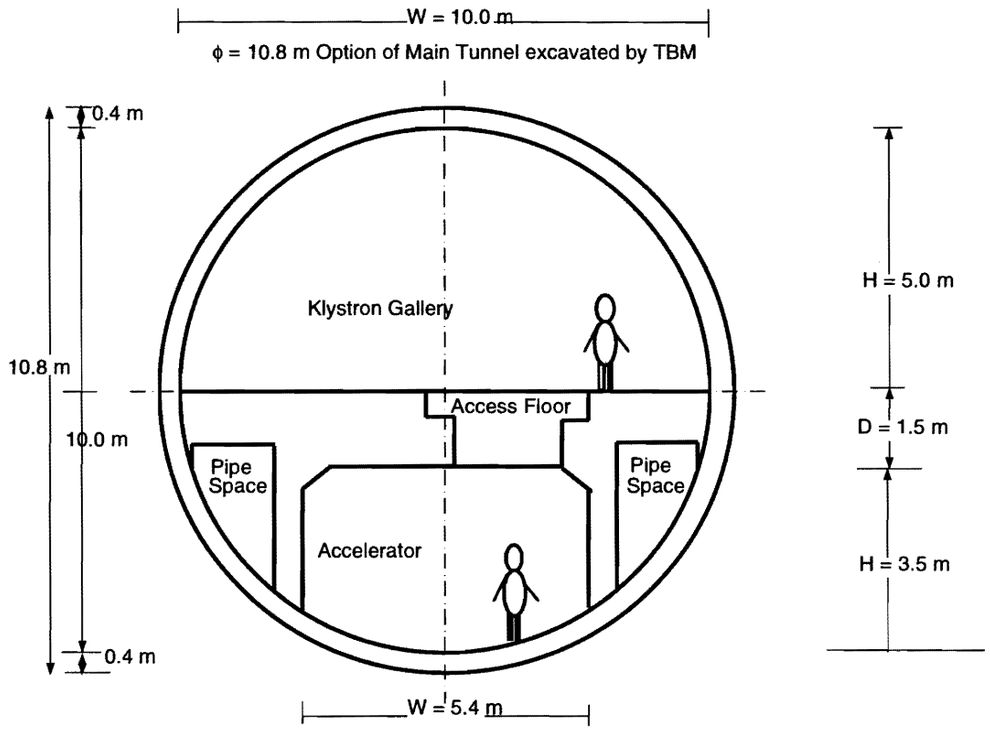

Figure 17.28: *Cross section of the main tunnel excavated by the TBM. The option by using a 10.8 m diameter TBM.*

Comparison of Three Options

The NATM (W=12 m) tunnel and ϕ8.0 m TBM tunnel use the existing technology of civil engineering. The largest size TBM which has ever been constructed is about 8 m. It should be possible to construct a ϕ10.8 m TBM by extending the technology of the ϕ8 m TBM and ϕ12 m shield-type tunneling boring machine now operating.

Three options for tunnels are compared, as shown in Table 17.4. The unit volume of excavation is almost the same between the NATM (W=12 m) tunnel and the ϕ8.0 m TBM tunnel. The shape of the NATM tunnel is a semi-circle while that of the TBM tunnel is a circle. Two rooms for the klystron gallery and the accelerator are required in one tunnel; the rooms should be separated by a

thick concrete shield. The concrete shield in the NATM tunnel is a shield wall, while that in the TBM tunnel is floor. In the TBM tunnel, the main linear accelerator is installed on the lower floor and the klystrons and modulators are installed on the upper floor. The effective floorage where the accelerator can be installed is not wide, since the floor is curved with the radius of excavation. Comparing the unit floorage and unit space between the NATM (W=12 m) tunnel and the ϕ8.0 m TBM tunnel, the TBM tunnel has a disadvantage of a circle shape. If a radiation shield of 2.0 m of thickness is required for radiation protection, a larger diameter of TBM tunnel is required to keep sufficient space and floorage. If the ϕ10.8 m TBM is used for excavating the main tunnel, sufficient space and floorage can be reserved for the klystrons, modulators and accelerator. The total cost of construction has been evaluated by rough estimation. The cost of the TBM tunnel depends on the diameter of the full face tunneling machine, itself. The cost of construction of the ϕ10.8 m TBM is 1.4-times higher than the ϕ8 m TBM and W=12m NATM tunnel.

Table 17.4: *Comparison of three options of tunnels.*

	W=12 m NATM	ϕ8.0 m TBM	ϕ10.8 m TBM
Unit Volume of Excavation (m^3)	55	50.3	91.6
Unit Space (m^3) with t=1.0 m shield			
Klystron Gallery	33.3	20.4	39.2
Accelerator Room	22.2	6.8	21.6
Unit Floorage (m^2) with t=1.0 m shield			
Klystron Gallery	7.0	7.2	10.0
Accelerator Room	4.0	2.6	5.4
Unit Volume (m^3) of t=1.0 m concrete shield	6	10	14
Unit Space (m^3) with t=2.0 m shield			
Klystron Gallery	30.2	16.8	34.2
Accelerator Room	13.5	5.5	18.9
Unit Floorage (m^2) with t=2.0 m shield			
Klystron Gallery	6.5	7.1	10.0
Accelerator Room	3.5	2.6	5.4
Unit Volume (m^3) of t=2.0 m concrete shield	11	16	23
Relative Total Cost	1.0	0.95	1.4

Double Tunnel Option

The concept of double tunnels was studied using the shield tunneling method at an early stage of the R&D, as shown in Fig 17.29. This option can be applied to the TBM double tunnels again, but it has not been studied in detail. This option has an advantage that the rock mass between the two tunnels can be utilized as a radiation shield, while the other options require a concrete shield inside the tunnels. This eliminates the cost of shield construction, and realizes a higher efficiency of utilizing excavated space. At a higher rf frequency, the loss in the rf waveguide is not negligible, and shorter length of the rf waveguide is preferable for reducing the rf loss in the waveguide. Therefore, several

thousands of small tunnels should be required between the two tunnels to transfer rf power from the klystrons to the accelerating structures in shortest distance. It is not difficult to bore between two tunnels separated by the distance of several meters. However, this increases the cost of the total construction. A supplemental radiation shield is required for the waveguide straight tunnels without a maze.

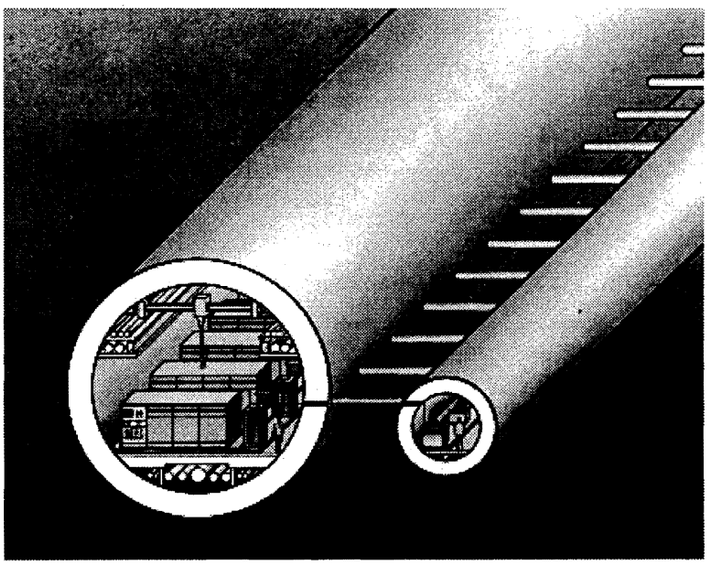

Figure 17.29: *Double tunnel option excavated by two TBM.*

17.4 Environmental Control Inside the Accelerator Tunnels

17.4.1 Air-Conditioning System and Room Temperature

The design of the air-conditioning system in the main tunnel has been carried out. The temperature of the rock mass is relatively lower than the room temperature in the tunnel. If the room temperature is similar to the temperature of the outlet air from the duct, the temperature of the tunnel wall is low enough to make dew on the wall surface.

The relation among the room temperature, wall temperature and temperature in the rock mass is expressed by the following equation;

$$\alpha_i(\theta_{room} - \theta_{wall}) = \frac{(\theta_{room} - \theta_{rock})}{\frac{1}{\alpha_i} + \frac{d}{\lambda}}, \tag{17.1}$$

where θ_{room} is the room temperature, θ_{wall} is that of the tunnel wall surface, and θ_{rock} is that of the rock mass; d is the thickness of wall concrete, λ is 1.4 kcal/$mh°C$, and α_i is the thermal conductivity on the inner wall of the tunnel. The wall temperature can be expressed by

$$\theta_{wall} = \theta_{room} - \frac{1}{\alpha_i} \times \frac{(\theta_{room} - \theta_{rock})}{\frac{1}{\alpha_i} + \frac{d}{\lambda}}. \tag{17.2}$$

The velocity of air motion (v) in the tunnel is evaluated to be 0.4 m/s from the total air ventilation and cross section of the tunnel. In the case that the velocity of air motion is less than 5 m/s, (α_i) on the rough surface can be expressed by

$$\alpha_i = 5.3 + 3.6 \times v. \tag{17.3}$$

Consequently the thermal conductivity on the inner wall of the tunnel, α_i, can be estimated to be 6.74 kcal/m^{2}h°C.

The temperature of the rock mass has been evaluated based on the annual temperature change of the site candidate. The rock mass temperature is 17 °C in the warmest site candidate and 9.8 °C in coldest site candidate. The upper limit of the room temperature without making dew on the wall is estimated to be 20 °C in the warmest district and 22.5 °C in the coldest district. Both temperatures are comfortable for persons working in the klystron gallery and accelerator room during maintenance.

17.4.2 Dewatering and Water Flow in the Rock Mass

Environmental safeguard is the one of most important key issues under all circumstances during the construction of a long tunnel. There are important problems related to water, such as well dry, shortage of water, ground water decline and water pollution. There is much experience involving countermeasures considered from a technological point of view to construct a long tunnel.

The radiation not only from the accelerator, but also from beam dumps, should be taken into account, since high-energy beams are thrown away at the beam dumps after collisions at the interaction point. From the point of a high-energy accelerator, we are interested in the water flow in the rock mass after being excavated from a long tunnel.

During excavation, a large amount of water inflow is sometimes generated at the face in the tunnel. This interrupts the excavation of tunnel until the stored water in the rock mass is exhausted. After that the volume of water inflow decreases to the small amount at the steady state, which is called normal water flow. In a tunnel such as under-see tunnel, and a tunnel in rock mass with a high coefficient of permeability, the normal water flow is higher than that in other general-purpose tunnels.

There is much data concerning normal water flow in various length tunnels constructed in the past. From these data, the normal water flow (Q (m^3/min)) is expressed by

$$Q = 0.14L^{1.8}, \tag{17.4}$$

where L (km) is the total length of the tunnel. The correlation coefficient of this equation is 0.53. From this equation the normal water flow in the JLC tunnel of 28 km can be estimated to be 5.9 m^3/min.

In this data, the 30 examples of tunnels with a relatively high normal water flow, such as the Rokko Tunnel, the New Shimizu Tunnel and the Tanna Tunnel, show the relation of normal water flow as the following equation:

$$Q = 4L^{0.32}. \tag{17.5}$$

By using this equation, the normal water flow in the JLC tunnel of 28 km can be evaluated to be 11.6 m^3/min. From the above two estimations, normal water flow in the JLC tunnel would be in the range of 5.9 to 11.6 m^3/min. After constructing the main tunnel, this amount of water would flow outside of the tunnel along the long tunnel.

17.4.3 Components in Normal Water Flow

The components in normal water flow in granite, basalt and tuff are given in Table 17.5.

Table 17.5: *Comparison of three options of tunnels. ——* indicates that no data is available.*

	Granite	Basalt	Tuff
pH	6.64 ~ 9.6	7.7 ~ 10.0	5.9 ~ 10.5
Eh (mV)	-350 ~ -30	——*	——*
Na (mg/l)	8.3 ~ 4037	30.0 ~ 300	50.0 ~ 56.0
K	1.0 ~ 45	2.51 ~ 9.0	4.2 ~ 6.8
Ca	5 ~ 1900	1.01 ~ 6.5	14.0 ~ 10.0
Mg	0.2 ~ 250	1.0	1.9 ~ 3.0
Fe	0.005 ~ 9.01	0.3	0.001 ~ 0.21
SiO_2	12 ~ 40	25 ~ 100	29.0 ~ 70.0
HCO_3^-	10.3 ~ 286	58 ~ 146.0	98.0 ~ 135
Cl^-	2 ~ 5500	14.4 ~ 152	6.0 ~ 7.5
SO_4^{2-}	8.6 ~ 1560	11.1 ~ 108	16.0 ~ 22.0
F^-	0.2 ~ 3.7	0.7 ~ 52.0	2.0 ~ 2.3
BO_3^-	9.8	——*	——*
HS^-	0.01 ~ 2.7	——*	——*

References for Chapter 17

[1] JLC-I, KEK Report 92-16, December, 1992.

[2] Unpublished papers by the collaboration with Shimizu Corporation.

[3] Unpublished papers by the collaboration with Nikkenn Sekkei Corporation.

[4] Unpublished papers by the collaboration with Kumagai Gumi Co., Ltd.

[5] Unpublished papers by the collaboration with Takenaka Corporation.

Author of Chapter 17

- Seishi Takeda

CHAPTER 18

Outlook

Contents

18.1 General Issues

Figure 18.1 shows a schematic diagram of JLC. There are a number of serious technical challenges that we must face when JLC is actually fully designed and built. At the risk of being too simplistic, we will list here four major issues:

1. **RF Power Sources and Accelerating Structure for the Main Linac**

   To achieve e^+e^- collisions at $E_{\rm CM} = 0.5 \sim 1$ TeV, we have to build a pair of linear accelerators with a high accelerating gradient of ~ 50 MV/m. Even when this high gradient is realized, to reach the designated energy goal, we end up with a facility having a total length of $20 \sim 30$ km. Real estate of this length is considered to be close to the maximum that is realistically available. Then, these linacs need to be driven by several thousand klystron tubes that feed RF power onto some tens of thousands of accelerating structure units. Notice that no large linear accelerators of this scale with such a field have ever been operated in the past.

   Therefore, the first challenge in the development of JLC is how to establish the design of a large number of high-field, high-precision accelerating structure units and actually procure them, and, of course, how to build reliable high-power RF source systems, and operate them at a high energy efficiency with good control.

2. **Realization of an Ultra-Low Emittance Beam and its Focusing**

   JLC at $E_{\rm CM} = 0.5$ TeV operation needs to produce a very high luminosity, higher than that of TRISTAN by factor ~ 100, despite a much lower collision rate of $100 \sim 150$ Hz. One way of increasing the luminosity is to raise the bunch intensity. However, because of the limitation of the RF power that can be stored in the accelerating structure and for other reasons, it is impossible to raise the bunch intensity in the linac much beyond what has been achieved at existing storage ring machines.

   Consequently, a linear collider must look to squeeze the beam size at the interaction point (IP) to an extremely small scale, in order to achieve the required high luminosity. In practice, the IP beam spot size at an LC usually needs to be smaller than that of the typical storage ring IP spot size by $\sim 1/1000$, which means the order of nano-meters.

   Therefore, the second challenge in the JLC design is to find out how to create extremely low-emittance beams, accelerate them without diluting this small emittance, focus the beam to the nano-meter scale, and maintain all of these actions in a well-concerted fashion.

3. **Optimization of Design Parameters**

   Any accelerator design work is an act of parameter optimization, and, in a way, a compromise. The JLC design is no exception. Actually, the LC design optimization has generally been known to be much more complicated than machines in the past.

   For instance, when two nano-meter-sized beams collide, besides the elementary-particle physics processes of interest, beamstrahlung photons are emitted because of the very strong electromagnetic field that these bunch particles exert on each other. Also, a large number of low-energy

e^+e^- pairs are produced. They are all unwelcome background events for experimenters. The number of low-energy e^+e^- pairs to be produced is related to the bunch population and the horizontal bunch size at IP. Therefore, keeping the population of low-energy e^+e^- pairs below a certain limit means that there is a boundary condition between the bunch population and the horizontal beam spot size. These parameters are, in turn, related to the operating condition of the accelerator, beam emittance and many other parameters.

The design of JLC needs to disentangle the myriad of such relations and must come up with a set of conditions that can be achieved by realistic hardware construction.

4. **Reliability / Availability / Maintainability**

In addition to achieving a good instantaneous luminosity, a collider facility must deliver high luminosity with a good up-time. Otherwise, it is rendered useless for experimenters. Therefore, the design of a machine needs to take into account the issues of reliability, availability and maintainability of individual components, and also as the entire system.

This means that the design needs to incorporate certain operational margins. Also, close attentions must be paid to many, many details. It is very important for designers to articulate what the critical points are in the fabrication, assembly and installation processes of accelerator components; and that message has to be clearly communicated to the staff in the field. If the field staff finds something not adequately achievable, they must be heard immediately and seriously by the designers, and improvement measures should be explored. This is really an iterative process that has to continue from an early stage of the design, throughout the entire construction phase, and even during the commissioning period.

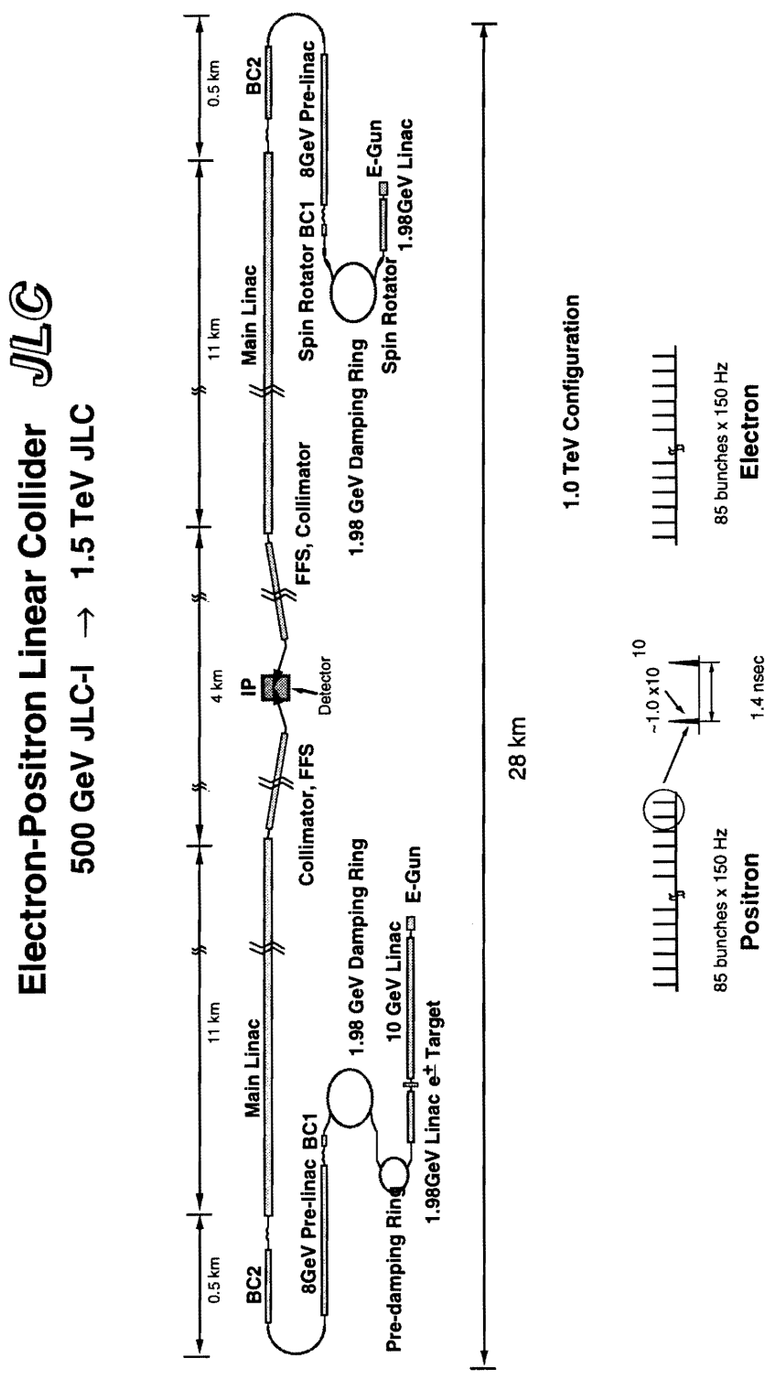

Figure 18.1: *Schematic layout of JLC in its E_{cm} = 1000 GeV configuration.*

18.2 Where We Are

RF Power Sources, Accelerating Structure and Low Emittance

In these two areas we have almost reached the "proof-of-principle" stage, or will be getting there during the next year or two.

One of such items is klystron development. While work at KEK and Japanese industry has not quite reached this stage, efforts at SLAC have produced quite stable 65 MW X-band klystrons that can produce 1μsec pulses at 60 Hz with a respectable efficiency of 47.5 %. This was accomplished by the use of traveling-wave output cavities that allow the extraction of high RF power without causing a HV break-down; and by the use of stainless-steel material in some parts of the tube to reduce excitation of spurious electromagnetic field modes and associated multi-pactoring. Another major progress made at SLAC is development of the use of permanent magnets as the creator of focusing fields for electron beams to pass through the klystron tube. This improvement totally eliminates the need for the DC power that has been previously consumed on the focusing solenoid coils. Also eliminated is the need for cooling-water circuits and interlock complications associated with the solenoid magnets.

Another item that belongs to this area is the development of X-band accelerating structures. The cell fabrication and structure assembly here requires a tolerance of $O(10)$ μm or better. While a number of technical issues remain, the R&D has reached the point where such a tolerance is claimed to be basically achievable. The "Detuned Structure" and "Damped-Detuned Structure" that have been developed at KEK and SLAC have shown reasonably good performance in a beam test at the ASSET (SLAC) facility during the summer of 1996. The test result demonstrates their real potential for use at an LC. It should be noted that all individual cells that are used to assemble those structures have been fabricated at KEK.

Yet, one more item that belongs here is the work at ATF. While ultra-low emittance beams have not yet been created at ATF, the commissioning of the ATF damping ring is among the top priority topics of JLC R&D at KEK in 1997. The plan is to observe good damping in single-bunch operation by the Summer of 1997, and then to proceed with multi-bunch operation.

Optimization of Design Parameters

A theoretical understanding of the inter-relationships among various operating parameters are, by now, relatively well established. Computerized algorithms exist to numerically analyze the design parameters quickly, given an adequately complete set of inputs. Based on such analysis, a list of specifications has been given to accelerator physicists responsible for various areas and components of JLC.

The problem to be recognized is that some of the given specifications may not be always achievable

in real-world hardware systems. To accommodate such cases, some sort of design margins need to be introduced. At present, the feedback process from the hardware staff to the parameter designers in this aspect is not quite complete, because of the long time-period required to go through a hardware R&D cycle. This will take a long iterative process, during which one should not try to take a hasty short-cut.

Reliability / Availability / Maintainability

Without doubt, in the next few years' R&D towards JLC, this will become the biggest issue. There are obviously several ways to attack this area: for instance, one might argue that we should not jump onto too big of a technical challenge in the R&D to begin with; however, another might state that with a proper focus of the resources we may see a break-through in a seemingly difficult technology, that, once successful, will offer a great benefit to everyone. In short, there is no uniquely superior attitude to address this "RAM" issue, and many approaches need to be tried and maintained. An important point is to stay open-minded and to encourage the emergence of creative ideas, while clearly noting that all of these efforts will have to be eventually put together into one working accelerator system.

With the project scale of JLC, it is essential to plan ahead for smooth technology transfer to the industrial sector. This is so as to ensure timely procurement of a large number of accelerator components in cost-effective ways. For this reason it is beneficial to have the industry sector involved from an early stage of the R&D work. However, it should be also noted that a fundamental understanding of "requirements, specifications, their rationale and priorities for the hardware" needs to be established by the research people who will be responsible for operating the facility. An LC is not something for which the scientists simply write a set of specifications and the great industry would do everything for us (In fact this has never been the case with any major accelerators anyway). The R&D capabilities of research facilities, such as those at KEK and collaborating institutes, need to be continuously improved and strengthened. Specifically, it is essential to train a reasonably large number of engineering and support staff, in addition to research scientists at a research laboratory and collaborating institutes, and to maintain a fair influx of such manpower in a continuous and consistent way.

The reliability of the accelerator system depends not only on radically new hardware, but also on "bread-and-butter" components. They are, for instance, the devices that stabilize the AC power amplitude and frequency, standard normal-conducting magnets, magnet power-supplies, all kinds of environmental monitor and control devices, cable routing, reduction of ground loops, cooling-water flow switches, quality hoses, vacuum pumps, flanges, bellows, safety interlock circuits, crate cooling fans, work room in the accelerator housing, availability of cranes and access vehicles in the tunnel, abundant air-conditioning capability or humidity-control in the accelerator complex, LAN bandwidth capacity and so on. Overseeing the reliability of these items requires a great deal of will-power of the accelerator team which maintains the collective memory of lessons learned from past project experience as well as the foresightedness towards challenges to encounter at the LC. One thing that certainly helps is to avoid demanding this staff to cut the price of the accelerator too much and too soon, although the cost-reduction for construction of the real-life LC is certainly a very important,

high-priority issue.

18.3 Remaining R&D and Design Tasks

The global four-area list in previous sections does not quite cover the specific work items that need to be worked on in the next few years. While partially repetitive, and inevitably incomplete, some highlighting items for individual subsystems are listed below:

Parameters

- The energy and luminosity requirements have been already specified. In addition to the target numbers of these goals, it is useful to establish the desired time profile of the energy and luminosity improvement. This is not limited to the timing of transition from the Phase-I (500 GeV) to Phase-II (1 TeV) upgrade and beyond; it includes the desired time profile of performance improvement within the Phase-I operation, also. This is to clarify how this machine should be operated as best competitive and complimentary with respect to other major accelerator facilities for high energy physics research.

- Depending on the outcome of the hardware R&D and also development of new ideas, many parameters may require revisions in the near future. For example, a possibility exists in revisiting the choice of the bunch spacing (currently 1.4 ns), the aperture of the main linac accelerating structure, and some others.

- Discussions on the so-called "emittance budget" have not been quite complete. This is due mainly to many ambiguities, at this moment, in the hardware performance to be obtained in the real-life JLC.

- Simulation studies of the expected luminosity from the entire JLC, including all possible construction and operational errors would be useful. However, obviously this is a major undertaking. It should also be noted that doing this work without careful preparations could be futile, particularly without having a reasonably thorough understanding of how to adequately parameterize and simulate effects of a variety of errors in all JLC subsystems.

- Characterization and interpretation of the term "design luminosity" needs to be clarified in the context above.

Electron Sources

- We need to develop a thermionic gun system that is capable of producing multi-bunch trains whose bunch spacing is 1.4 ns.

- It is considered beneficial to implement beam collimation in the pre-injector area. Its engineering details should be studied.
- Likewise, we need to develop a 200 kV polarized gun system that is capable of producing multi-bunch trains of electrons. A good understanding and techniques need to be learned on suppression of dark-currents, reducing the surface field and extending the cathode lifetime.
- Related to the item above, R&D of a laser system that is compatible with the real-life polarized electron gun for JLC must be done.
- We should re-initiate and accelerate the R&D work of RF guns in the near future; likely first with unpolarized electrons, then ultimately with polarized electrons.

Positron Sources

Positron System Hardware R&D

- Another testing of the positron-production target material would be useful. This is for re-checking the allowed parameter range of incident electron beam size and intensity. Testing should be done with parameters similar to the environment that is planned for JLC. This is so that confirmation is made that the considered parameter range would not cause damages to the target in a long term.
- Simulation of the behaviors of electrons and positrons in the region immediately downstream of the production target area needs to be done in more details. The study should take realistic magnet field errors, and interactions with the RF structure, into account. Reviews must be made from an RF-technological point of view.
- There is a good possibility that use of an L-band accelerator is preferred, instead of S-band, in the positron collection section. This issue needs to be investigated. If it turns out that the L-band frequency is, indeed, preferred, specific hardware R&D for such a system has to be started soon. Incidentally, at this moment, L-band is the preferred technology for the RF system of the first-stage bunch compressor, also.

Positron System Design Work

- Engineering design of the positron production system, including the rotating production target, with long-term stability and reliability in mind, has to be established.
- Detailed design of the high-current 10 GeV electron linac, for producing electrons to impinge on the target, has to be established.
- Design details of the positron pre-damping ring need to be reviewed. It needs to improve the equilibrium emittance, and, if possible, the dynamic aperture. A total system design is required, including the injection / extraction kicker systems. It might be better (or worse) to design the

pre-damping ring to be capable of storing three or more bunch trains simultaneously. This issue needs to be examined.

- The positron pre-damping ring may suffer from photo-electron-induced instabilities. Solutions need to be explored, possibly with a bunch feed-back system and careful shaping of vacuum chambers.

Damping Rings

Figure 18.2 shows a schematic layout of JLC that expands the area of the injector, damping ring, and bunch compressor sections. The broken line indicates the part whose prototype has been built in the ATF project at KEK.

Damping Ring R&D

- We must commission the ATF, and learn and absorb as much as we can from this facility. We must prove that ultra-low emittance multi-bunch beam can be created, controlled, and measured. It is noted that a large amount of operational experience to be gained at ATF would be fed back to all aspects of the final design of the damping rings, including the ring RF system, vacuum system, magnets and others.
- Injection and extraction kicker magnets with a high-quality flat top and fast rise- and fall-times for multi-bunch operation of the damping rings are crucial for stable operation of JLC, even if a double-kicker system would be implemented for extraction. A thorough understanding of this issue will require more hardware R&D and prototype studies.

Damping Ring Design

- For making the final choice of the lattice scheme, obviously some more systematic and comparative studies of several lattice configurations are required, as discussed in section 5.2.
- Use of long sections of wiggler magnets in the real-life damping rings is very likely. Possibilities must be considered for cases where various excitations of those wiggler magnets are used. This leads to a varying ring circumference. Provisions must be made to operationally adjust the ring circumference and/or the ring RF frequency to cope with such possibilities.
- Dynamic aperture and its sensitivity to the construction and operational errors needs much more systematic studies. For the positron system, this issue needs to be considered in conjunction with the design of the pre-damping ring, and the expected positron beam emittance from the production area.
- Potential problems with the Fast Ion Instabilities (FEI) in the electron damping ring, and the Photo-electron-Induced Instabilities (PEI) in the positron damping ring could be quite serious.

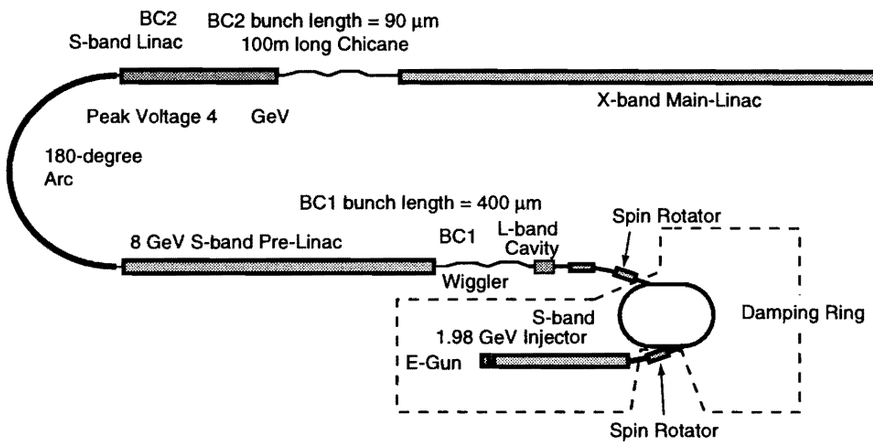

Figure 18.2: *Schematic layout of JLC that expands the area of the injector, damping ring, and bunch compressor sections. The broken line indicates the part whose prototype has been built in the ATF project at KEK.*

Their expected magnitudes and possible cures must be investigated. Experience to be gained from operation of the ATF damping ring, as well as that of KEKB and PEP-II B-factory and other high-current storage rings, would be extremely helpful in understanding these, and to come up with applicable solutions.

Bunch Compressor and Pre-linacs

Bunch Compressor and Pre-linac R&D

- ATF Damping Ring at KEK may allow to test a scheme of the first-stage bunch compressor (BC1), and an upstream portion of the pre-linac. Figure 18.3 shows a schematic diagram of the ATF test site at KEK. The figure includes a possible extension of ATF that accommodates the first-stage bunch compressor, followed by a test section for the pre-linac or the main linac. However, while this testing would be very useful, the time and resources required to conduct such work need to be carefully examined in the context of the schedule of the design and construction of JLC.
- An L-band RF system needs to be developed for use at BC1.

Bunch Compressor and Pre-linac Design

- For the X-band JLC, performing the second-stage bunch compression (BC2) at 10 GeV appears adequate. However, whether the injection to the X-band main linac should take place at the

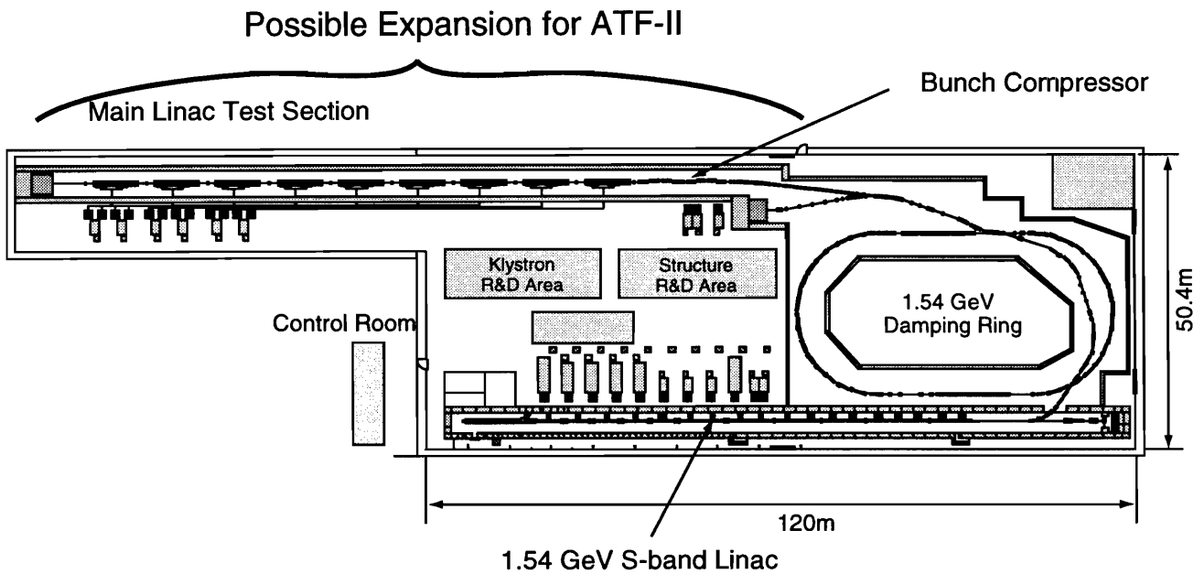

Figure 18.3: *Schematic plan view of ATF at KEK. As of early 1997, the injector linac and the damping ring are completed, and are in operation. This figure includes a possible extension of ATF that accommodates the first-stage bunch compressor, followed by a test section for the pre-linac or the main linac.*

same 10 GeV can still be debatable. A use of S-band or C-band linacs between the BC2 exit and the 20 GeV or so X-band linac injection point may have some advantages. Such a scenario involves a number of possibilities on the accelerating gradient and the focusing strength of the FODO lattice to choose from. This issue has not yet been fully studied.

- The design of the pre-linac requires more work, in particular, concerning the choice of the beam-loading compensation scheme.

- Designs of the bunch compressors and pre-linacs that are compatible with the C-band scheme (i.e. bunch length = 200μm) are still missing.

X-band Main Linac Beam Dynamics

- More work on understanding the behavior of wake-field is required so that we would be able to evaluate effects of all varieties of possible defects that can be introduced during fabrication, assembly and installation processes of accelerating structures, as well as numerous run-time errors during operation of JLC. They are essential for refining the main linac design, for determining the adequate injection energy, and also for making the decision on the type of accelerating structure to adopt.

- At ASSET facility of SLAC, the transverse wake-fields have been experimentally measured with a couple of accelerating structures, including our DS prototype. While the agreement between the measurement and calculations is generally good, there are some inconsistencies that need to be reconciled or be understood.
- While evaluating the effects of linac errors considered in Chapter 8, coupling effects from the horizontal (x) to the vertical (y) plane have been ignored. How this assumption is appropriate needs to be examined.
- Simulation studies of the expected luminosity from the entire JLC, including all possible construction and operational errors, where realistic error correction techniques are applied in a manner similar to a flight-simulator air-pilot training system, would be useful.
- The tunability and operability of the main linacs (and also other subsystems of JLC) need to be examined in conjunction with possible ground-motions and measures to damp them, which are either passive or active. Some pilot studies and measurements have been done in Japan concerning the ground-motion spectra at various sites. However, their results have not been integrated in the design studies presented in this report. This will have to be done soon.

X-band Main Linac Accelerating Structures

Structure R&D

- R&D towards industrial mass-production of accelerating structure is essential. There are major issues to address regarding cell fabrication and structure assembly, in particular, diffusion bonding. We still need to thoroughly refine the techniques currently used within the lab, then, industrialize the procedure for mass production.
- It should be noted that irrespective of the final choice of the accelerating structure to adopt, the techniques to be developed as stated above will be indispensable.

Linac Design

- The final choice of the accelerating structure must be made in the not-so-distant future. Manufacturability of several choices, as well as their required installation tolerances need to be sufficiently evaluated.
- In addition to the type of the structure, the choice of the accelerating field gradient, structure aperture, group velocity, structure length and others may have to be revisited.
- Implementation of some sort of RF-BPMs for precise alignment of the structure with respect to the beam is essential. This has to be done in the sense of engineering design, which also includes the design of a structure support system with, most likely, a mover mechanism.
- Implementation of some sort of beam spoiler to protect the irises need to be included in the structure design.

- Pros and cons of several beam-loading compensation schemes need to be evaluated, and a choice has to be made in the not-so-distant future. This is an important issue common to all linac RF systems (both low-energy and high-energy) within any LC. There, the studies of beam-loading compensation should take the effects of higher modes into account.

X-band Main Linac Power Sources

- We must completely establish the technology related to the X-band RF power source, i.e. power conversion, klystron power-supplies and klystrons. While SLAC in U.S.A. is rapidly establishing the technology of 65 MW-class klystrons, this has not yet been done in Japan.

- Development of highly efficient klystron modulators is still in its infancy world-wide. The work in this area needs to be much accelerated, with special attention to the system efficiency, long-term reliability, maintainability and cost reduction.

- Development of DLDS should be vigorously pursued. Technical details and tuning techniques of this scheme needs to be addressed through a series of low-power and high-power tests.

- While DLDS is very attractive in terms of power efficiency and component count, the nature of the scheme forces us to have three (or four) clusters of accelerating structures, distributed over a length of $\sim$ 80 m or more, to be driven by a common power source unit. This can be problematic in a low-energy part of the main linacs from a viewpoint of fine RF phase control and lattice management when, for instance, a klystron failure takes place. A sophisticated RF control software and associated control hardware need to be developed. It may be that SLED-II, BPC or SLED-III should be introduced in an upstream part of the main linacs. This issue needs to be quantitatively investigated.

- Details of the so-called "low-level" RF system, including master oscillators, delivery of its signals, boosters, monitors, phase controls, local RF feedback systems and others for JLC, have not yet been established. Systematic surveys of these issues need to be initiated soon.

- Practical details of possible energy upgrade scenarios need to be re-examined.

X-band Main Linac Installation Issues

- Systematic studies have been recently started for component installation and alignment in the JLC X-band main linacs. Some hardware development has been already done for the ATF injector linac in this area. However more organized studies and design work have to be made on the accelerator support structure, alignment and measurement schemes.

- The work above needs to take the existence of various additional components into account; examples include quadrupole magnets, waveguides, beam position monitors, tubing for cooling waters, vacuum pumps, and a variety of monitor instrumentation.

- The work above needs to be done with particular attention to how to industrialize the fabrication process of the accelerator support and associated hardware components.
- Issues of ground motions need to be taken into account in the work here.
- All the issues mentioned above should be applicable to other parts of the JLC.

C-band Option

- The topics of R&D tasks in the C-band main linac system are similar to those required for the X-band.
- After conducting the low-power testing of the accelerating structure, SLED-III pulse compression cavities, and initial testing of the klystron, the next step is to perform a high-power "string-test" of a complete RF power source unit which comprises a set of klystrons, waveguide, SLED-III and a choke-mode structure.
- Importance of low-cost, high-efficiency modulators is recognized and some design work has been started. This effort should be encouraged.
- Cross-fertilization between the C-band backup technology and new ideas there, and the efforts for and results from X-band main linac scheme needs to be encouraged.

Beam Delivery and Beam Collimation

A revised final focus optics which can cope with beam energies ranging from 125 GeV up to 750 GeV have been presented. However,

- While the magnet and operational tolerances of this system are expected to be similar to those presented in the JLC-I report for the 250 GeV (beam energy) system, specific calculations have not yet been made. So, they need to be done.
- As stated in Chapter 13, various advanced techniques in improving the performance of the final focus optics design could be incorporated.
- Engineering studies of the collimator designs must be made. Additional beam testing of collimator materials to confirm the currently-conceived beam damage limit would be useful.
- Engineering design of the component support and alignment systems required for this area may be similar to those which would be developed for the main linacs. If special considerations need to be made in some areas in the final focus, they need to be identified time early, and specific hardware design work must be initiated soon.
- Hardware system design of the crab-crossing cavities needs to be developed.
- Design of the beam-line after the collision point towards the beam dump needs to be developed. Special attention should be paid to aspects of radiation safety.

Interaction Region

The basic concept of the design of the beam masking near the collision point has been presented. The scheme appears reasonable. However, a whole set of design reviews from an engineering point of view are missing.

- Specific engineering designs of the final-focus quadrupole magnets together with the shielding solenoid need to be examined and established.
- Design of the hardware support structure in the vicinity of the detector has to be established, with special attentions to isolation of ground motions and environmental noises.

Two-Photon Option

There has been substantial progress in the understanding of the beam-beam interaction issues, including the laser-electron interaction, and such properties as the luminosity distribution and beam background. Remaining major issues are:

- Development of high-average-power lasers for producing a sufficient flux of Compton-scattered photons.
- Laser optics for high-power density, including techniques for laser-pulse recycling.
- Development of an optional magnet system for sweeping out spent-electrons.
- Design of an interaction region complex which includes all of the items listed above.

Beam Instrumentation and Control

- Development of beam instrumentation that is capable of dealing with multi-bunch trains has to be continuously pursued. So far, ATF at KEK has been operating at 2.8 ns bunch-spacing within a bunch train. The beam instrumentation set at ATF is one of the most advanced in the world to use in multi-bunch environments. Nonetheless, more work is needed to handle 1.4 ns bunch separation.
- Fast beam controls and orbit / energy feed-back systems are essential for stable operation of JLC. A number of working ideas in this area have been already invented and implemented for SLC. However, their applications to the JLC environment need to be individually, carefully examined, and, if necessary, substantial improvements and innovations must be added. This is because the required accuracy and the speed of the beam control at JLC would be much more stringent than those at SLC.

- A number of beam dumps and beam repetition rate controls need to be implemented in the JLC beam line as suitable beam disposals. This is so that they serve as radiation safety measures during the beam tuning and commissioning period. They need to be incorporated in the engineering design of JLC from the beginning, not as an after-thought.

- Related to the item above, special beam diagnostic sections should be introduced with an ample amount of beam instrumentation at key junction points within the accelerator complex. Examples include: places near the damping-ring injection / extraction points, BC1 - arc - BC2 junctions, injection point into the main linacs, several points along the main linacs, and the main linac exit.

- General issues of machine protection needs to be systematically and thoroughly reviewed. Its engineering solutions must be devised with sufficient operational margins and reliability.

- The technology of the computers and the network to use at JLC accelerator control system naturally would be of the state-of-the-art models available, when the JLC is to be built. Nonetheless, it would be helpful to evaluate the data transfer rate and network bandwidth required for satisfactorily smooth operation of JLC time early.

- Although the need for development of a solid low-level RF control system has been already mentioned, it is worthwhile repeating it here.

Facilities

- A set of descriptions on the site and infrastructure requirements and models need to be re-evaluated and established.

- Several tunnel excavating techniques have been examined. Their evaluations must be continued so that we maintain more than one technological options at hand. Field-measurement data on the tunnel stability in various site conditions should be collected with maximum efforts.

- Engineering design of the temperature, humidity and vibration controls inside the tunnel needs to be more thoroughly devised.

Overall

- On all subsystems, evaluation of possible construction techniques and schedules need to be developed and established.

- Cost estimates need to be made, with adequate contingency plans.

- Cost reduction must be attempted. However, one should note the discussions in section 18.2. Balancing has to be considered with respect to the system reliability, should there be specific conflicts with cost reduction.

- For remaining major R&D tasks, requirements for possible new test facilities must be identified, and a prioritized list must be produced.
- The list of essential work items above needs to be continually updated, based on new outcomes from the R&D efforts. Consistent yet flexible management of available resources must be executed without hesitation.
- If we are to start construction of JLC (or LC in general) in the early next century, the next few years would offer the last occasion in which the overall technical design strategies and choices can be re-examined. At some point a major review of all technology choices considered for JLC must be made; it has to happen in a not-so-distant future.
- Operational issues, including various safety and environmental concerns, need to be identified and be addressed.

Figure 18.4 shows an example time chart of how the R&D schedule will have to be like if we are to start construction of JLC in the year 2001.

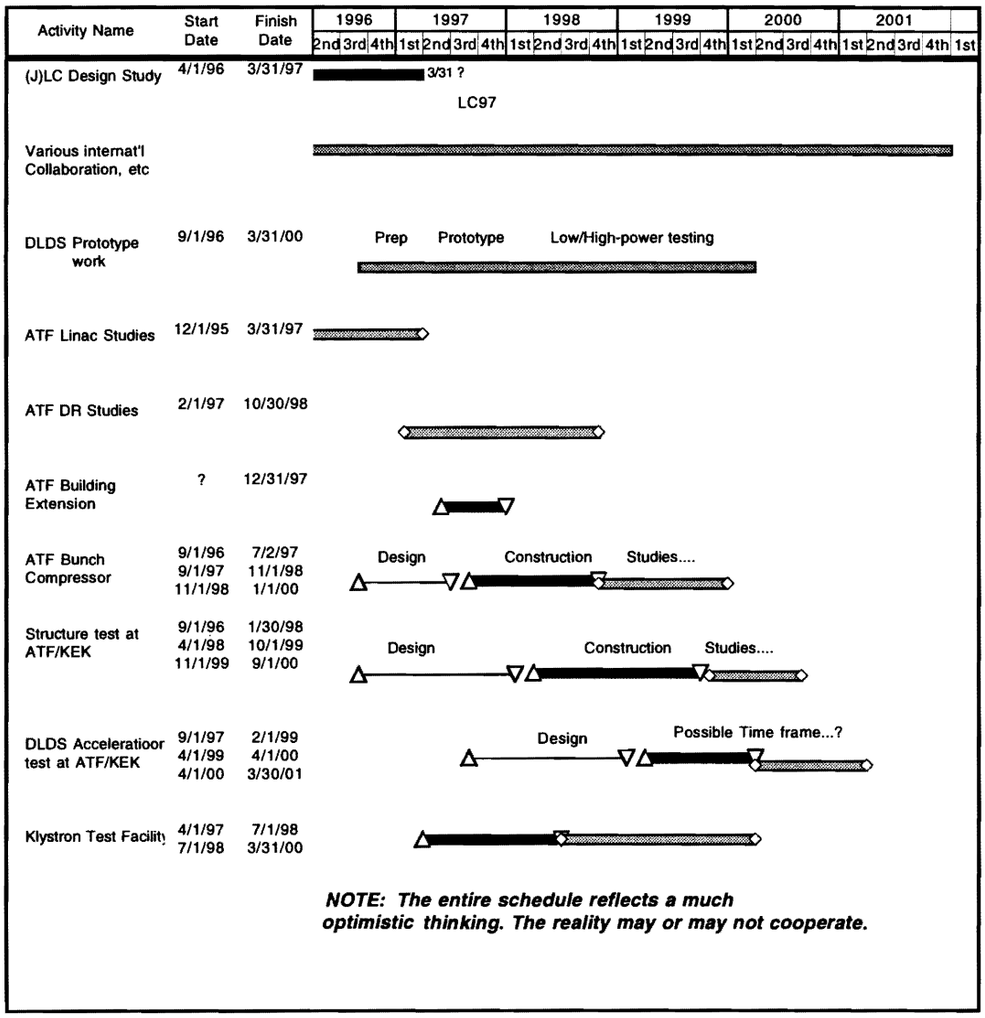

Figure 18.4: *A time chart that shows how the R&D schedule will have to be like if we are to start construction of JLC in the year 2001.*

Author and Major Contributers of Chapter 18

- Nobu Toge
- Hitoshi Hayano
- Yasuo Higashi
- Toshiyasu Higo
- Shigeru Kashiwagi
- Mitsuo Kikuchi
- Kiyoshi Kubo
- Shigeru Kuroda
- Hiroshi Matsumoto
- Hajime Mizuno
- Tsutomu Nakanishi
- Katsunobu Oide
- Toshiyuki Okugi
- Tsumoru Shintake
- Toshikazu Suzuki
- Seishi Takeda
- Toshiaki Tauchi
- Junji Urakawa
- Kaoru Yokoya